

# DIABLO CANYON UPDATED SEISMIC ASSESSMENT

Response to Senate Bill 846



6 March 2024



The following individuals contributed to this Technical Report (alphabetical order):

Linda Al-Atik  
Al Atik Consulting

Nathan Barber  
Pacific Gas and Electric Company

Serkan Bozkurt  
Lettis Consultants International

Jennifer Donahue  
JL Donahue Engineering

Tania Gonzalez  
Earth Consultants International

Nick Gregor  
Nick Gregor Consulting

Albert Kottke  
Pacific Gas and Electric Company

Chris Madugo  
Pacific Gas and Electric Company

Stephen Thompson  
Lettis Consultants International

**Record of Revisions**

<b>Rev. No.</b>	<b>Reason for Revision</b>	<b>Revision Date</b>
0	Initial release.	2/1/2024
1	Inclusion of missing figure, Figure 7-20.	3/6/2024

## Table of Contents

List of Figures .....	viii
List of Tables .....	xx
List of Acronyms and Abbreviations .....	xxiii
EXECUTIVE SUMMARY .....	xxviii
1. INTRODUCTION .....	1
1.1. BACKGROUND AND PREVIOUS STUDIES .....	1
1.2. SCOPE AND OBJECTIVES .....	2
1.3. OVERVIEW OF PROCESS .....	2
1.4. REPORT CONTENTS AND ORGANIZATION .....	2
2. PROJECT PROCESS .....	4
2.1. IMPLEMENTATION OF PROCESS .....	4
2.2. ROLES AND RESPONSIBILITIES .....	5
2.2.1. Technical Integration (TI) Teams .....	5
2.2.2. Hazard Analyst .....	5
2.2.3. Probabilistic Risk Assessment (PRA) Analyst .....	5
2.2.4. Project Technical Integrator .....	5
2.2.5. Project Manager .....	5
2.2.6. Management Support Team .....	6
2.2.7. Project Sponsors .....	6
2.2.8. Participatory Peer Review Panel (PPRP) .....	6
2.2.9. External Reviewers .....	6
2.3. Schedule .....	7
3. KEY TASKS AND ACTIVITIES .....	9
3.1. DEVELOPMENT OF PROJECT PLAN .....	9
3.2. IDENTIFICATION OF ISSUES .....	10
3.3. EVALUATION OF MODELS AND METHODS .....	10
3.4. UPDATED HAZARD AND RISK .....	11
3.5. DOCUMENTATION .....	11
4. GROUND MOTION DATA .....	13
4.1. GROUND MOTION CATALOGS .....	13
4.1.1. Preliminary Turkish Data .....	14



4.1.2.	DCPP Data .....	14
4.1.3.	Preliminary NGA-West3 Data .....	16
4.1.4.	Simulation Data .....	17
5.	EVALUATION OF SEISMIC SOURCE CHARACTERIZATION.....	25
5.1.	OVERVIEW OF THE 2015 SSC MODEL .....	25
5.1.1.	Types of Seismic Sources .....	25
5.1.2.	Primary Contributors to Hazard and Hazard Deaggregation.....	37
5.1.3.	Contributions To Hazard Uncertainty .....	38
5.2.	REVIEW OF NEW INFORMATION .....	39
5.2.1.	Overview.....	40
5.2.2.	New Information on Hosgri Slip Rate .....	54
5.2.3.	New Information on Los Osos Slip Rate.....	56
5.3.	UPDATES TO THE 2015 SSC MODEL.....	57
5.3.1.	Hosgri Fault Source Update.....	57
5.3.2.	Los Osos Fault Update.....	64
5.3.3.	Implementation of the SSC Model Update for the Updated Seismic Hazard Assessment .....	66
6.	EVALUATION OF SSC ISSUES, MODELS AND METHODS RAISED IN PUBLIC TESTIMONY .....	114
6.1.	SUMMARY OF TESTIMONY BY SAN LUIS OBISPO MOTHERS FOR PEACE .....	114
6.2.	GEODETIC MODEL CONSTRAINTS ON DEFORMATION RATES .....	115
6.2.1.	On-Fault Deformation.....	115
6.2.2.	Off-Fault Deformation .....	116
6.2.3.	Alternative Seismicity Model .....	117
6.3.	PROPOSED ALTERNATIVES TO FAULT GEOMETRY, GEOLOGIC SLIP RATES, AND UPLIFT RATES .....	117
6.3.1.	Fault Geometry .....	117
6.3.2.	Geologic Slip Rate .....	118
6.3.3.	Uplift Rate.....	119
6.4.	CONCLUSIONS.....	120
7.	EVALUATION OF GROUND MOTION CHARACTERIZATION .....	124
7.1.	OVERVIEW OF 2015 MODEL .....	124
7.1.1.	Median Model.....	125

7.1.2.	Aleatory Variability Model .....	127
7.2.	EVALUATION OF MEDIAN GROUND MOTION MODEL .....	129
7.2.1.	Review of Potential New Information .....	130
7.2.2.	Sammon’s Mapping Methodology.....	131
7.2.3.	Residual Analyses .....	132
7.2.4.	Hanging Wall Model.....	138
7.2.5.	Directivity .....	138
7.2.6.	Comparison of Non-Ergodic Ground Motion Models.....	143
7.2.7.	Splay and Complex Ruptures.....	148
7.3.	EVALUATION OF ALEATORY VARIABILITY MODEL.....	149
7.3.1.	Evaluation of New Ground Motion Data.....	149
7.3.2.	Between-Event Variability .....	149
7.3.3.	Single-Station Within-Event Variability .....	150
7.3.4.	Single-Station Sigma .....	150
7.4.	CONCLUSIONS.....	151
8.	EVALUATION OF VERTICAL GROUND MOTIONS .....	202
9.	EVALUATION OF SITE CHARACTERIZATION.....	206
9.1.	OVERVIEW OF 2015 MODEL .....	206
9.1.1.	Analytical Approach .....	206
9.1.2.	Empirical Approach .....	208
9.1.3.	Implementation and Results.....	208
9.2.	EVALUATION OF ANALYTICAL SITE FACTORS .....	209
9.2.1.	Approach.....	209
9.2.2.	Characterization of DCPD Target Site Conditions .....	210
9.2.3.	Characterization of Host Site Conditions .....	211
9.3.	EVALUATION OF EMPIRICAL SITE FACTORS .....	213
9.3.1.	New Information Since 2015 .....	213
9.3.2.	Non-ergodic Modeling.....	214
9.4.	CONCLUSIONS.....	219
10.	HAZARD CALCULATIONS AND RESULTS .....	247
10.1.	CALCULATION PROCESS.....	247
10.2.	REFERENCE ROCK HAZARD AND GROUND MOTION COMPARISONS.....	248
10.2.1.	Reference Rock Hazard Curves Comparisons .....	248

10.2.2.	Reference Rock Horizon Uniform-Response Spectra Comparisons.....	257
10.2.3.	Reference Rock Horizon GMRS Comparisons.....	259
10.3.	CONCLUSIONS .....	261
11.	CONTROL-POINT HAZARD FOR RISK ASSESSMENT .....	274
11.1.	DEVELOPMENT OF SITE ADJUSTMENT FACTORS.....	274
11.2.	CONTROL-POINT HAZARD CURVES .....	274
11.3.	CONCLUSIONS .....	275
12.	RISK ASSESSMENT.....	284
12.1.	CALCULATION PROCESS.....	284
12.2.	DISCUSSION AND CONCLUSIONS .....	285
13.	SUMMARY AND CONCLUSIONS.....	286
13.1.	MODEL EVALUATIONS.....	286
13.1.1.	Source Characterization .....	286
13.1.2.	Ground Motion Characterization .....	287
13.1.3.	Site Characterization .....	289
13.2.	HAZARD ANALYSIS .....	290
13.2.1.	Hazard Curve Scaling.....	290
13.2.2.	Summary of Comparisons.....	290
14.	REFERENCES .....	292

Appendix A. Project Plan for 2023 DCPD Updated Seismic Assessment

Appendix B. Minutes from the Working Meeting #1 Held on 21 July 2023

Appendix C. Minutes from the Preliminary Results Meeting #1 Held on 19 September 2023

Appendix D. Minutes from the Workshop #2 Held on 7 November 2023

Appendix E. Minutes from the Final Results Meeting Held on 7 December 2023

Appendix F. Evaluation of Site Terms at DCPD using Updated Methods and Data

Appendix G. Closure Letters

G-1. Closure Letter from the Participatory Peer Review Panel

G-2. Closure Letter from the External Review Panel

## List of Figures

Figure 2-1.	Flowchart for a SSHAC Level 1 PSHA study, indicating the review criteria and potential questions at each point of engagement by the PPRP (from NUREG-2213 [NRC, 2018], Figure 3-2).....	8
Figure 2-2.	Organizational Chart for the Diablo Canyon Updated Seismic Assessment .....	8
Figure 4-1.	Map showing the surface projection of the fault plane (red lines) and ground-motion recording stations (triangles) from the three large earthquakes of the Kahramanmaras event sequence (from GEER Association Report 082, 2023, Figure 3.2).....	19
Figure 4-2.	Earthquake epicenters (blue stars) and ground-motion recording station locations (open red triangles) for the supplemental DCPD California empirical catalog.....	20
Figure 4-3.	Distribution of NGA-West3 data considered in the evaluation plotted as a function of rupture distance and magnitude.....	21
Figure 4-4.	Distribution of NGA-West3 data considered in the evaluation plotted as a function of Ztor (km) and magnitude.....	22
Figure 4-5.	Distribution of SWUS simulation events completed on the SCEC BBP (from GeoPentech, 2015).....	23
Figure 4-6.	CyberShake (2017) study for the Central Coast of California.....	24
Figure 5-1.	Logic Tree Structure for the Primary and Connected Fault Sources (from PG&E, 2015a, Figure 6-1).....	68
Figure 5-2.	Primary and Connected Fault Sources in the Hosgri and Outward-Vergent (OV) Fault Geometry Model (from PG&E, 2015a, Figure 6-2) .....	69
Figure 5-3.	Primary and Connected Fault Sources in the Hosgri and Southwest-Vergent (SW) Fault Geometry Model (from PG&E, 2015a, Figure 6-3) .....	70
Figure 5-4.	Primary and Connected Fault Sources in the Hosgri and Southeast-Vergent (NE) Fault Geometry Model (from PG&E, 2015a, Figure 6-4) .....	71
Figure 5-5.	Primary and Connected Fault Sections in the Fault Geometry Models, Southern Region (from PG&E, 2015a, Figure 6-5) .....	72
Figure 5-6.	Primary and Connected Fault Sections in the Fault Geometry Models, Northern Region (from PG&E, 2015a, Figure 6-6) .....	73
Figure 5-7.	Differences Between Traditional Fault Source and Rupture Source Concepts (from PG&E, 2015a, Figure 6-7).....	74
Figure 5-8.	Example Rupture Sources Associated with the Hosgri Fault Source (from PG&E, 2015a, Plate 9-1). Rupture Sources: a) H85-01; b) H85-04; c) H85-05; d) H85-07 .....	75
Figure 5-9.	Example Rupture Sources Associated with the Outward Vergent (OV) Model (from PG&E, 2015a, Plate 9-2). Rupture Sources: a) OV-02; b) OV-03; c) OV-06; d) OV-08 .....	76

Figure 5-10.	Example Rupture Sources Associated with the Southwest Vergent (SW) Model (from PG&E, 2015a, Plate 9-2). Rupture Sources: a) SW-01; b) SW-05; c) SW-07; d) SW-08 .....	77
Figure 5-11.	Example Rupture Sources Associated with the Northeast Vergent (NE) Model (from PG&E, 2015a, Plate 9-2). Rupture Sources: a) NE-04; b) NE-06; c) NE-08; d) NE-11 .....	78
Figure 5-12.	Magnitude PDFs Used in the 2015 SSC Model (from PG&E, 2015a, Figure 6-8) .....	79
Figure 5-13.	Areal Source Zones Used in the 2015 SSC Model (from PG&E, 2015a, Figure 6-9) .....	80
Figure 5-14.	Reference Rock Hazard (Total and by Source) for 5 Hz Spectral Acceleration ...	81
Figure 5-15.	Reference Rock Hazard (Total and by Source) for 1 Hz Spectral Acceleration ...	82
Figure 5-16.	Reference Rock Hazard (Total and by Source) for 0.5 Hz Spectral Acceleration	83
Figure 5-17.	Deaggregation of the Reference Rock Hazard for 5 Hz Spectral Acceleration for the $10^{-4}$ Annual Hazard Level .....	84
Figure 5-18.	Deaggregation of the Reference Rock Hazard for 1 Hz Spectral Acceleration for the $10^{-4}$ Annual Hazard Level .....	85
Figure 5-19.	Deaggregation of the Reference Rock Hazard for 0.5 Hz Spectral Acceleration for the $10^{-4}$ Annual Hazard Level .....	86
Figure 5-20.	Summary Tornado Plots for the 2015 SSC Model for 5 Hz Spectral Acceleration (from PG&E, 2015a, Figure 14-9) .....	87
Figure 5-21.	Summary Tornado Plots for the 2015 SSC Model for 0.5 Hz Spectral Acceleration (from PG&E, 2015a, Figure 14-10) .....	88
Figure 5-22.	Fault Sources in the DCPV Vicinity Used in the WUS ERF-2023 Study .....	89
Figure 5-23.	Predicted Uplift Rates from Viscoelastic Modeling of the Hosgri Fault Zone (from O'Connell and Turner, 2023, Figure 3) .....	90
Figure 5-24.	Uplift Rates in the DCPV Vicinity as Interpreted by the 2015 SSC SSHAC TI Team (from PG&E, 2015a, Figure 7-4) .....	91
Figure 5-25.	GPS Velocity Field Relative to Fixed Pacific Plate and Coast-Parallel Motion Based on DeMets et al. (2014) (from PG&E, 2015a, Figure 5-13) .....	92
Figure 5-26.	Traces of Virtual Faults Used in the Local Source Zone (from PG&E, 2015a, Figure 13-18) .....	93
Figure 5-27.	Composite Focal Mechanisms and Interpreted Seismicity Lineaments Used to Develop the Geometry and Style of Faulting for Virtual Faults (from PG&E, 2015a, Figure 13-13) .....	94
Figure 5-28.	Hardebeck (2014a) Catalog Seismicity in the DCPV Vicinity (from PG&E, 2015a, Figure 13-2). Local Source Zone Extent Indicated by the Yellow Polygon. ....	95

Figure 5-29.	Catalog Seismicity in the DCPV Vicinity from Hardebeck (2014a) and ANSS ComCat. ....	96
Figure 5-30.	Local Source Zone Seismicity Analysis: a) Magnitude vs. Year; b) Annual Rate vs. Magnitude; c) b-Value vs. Completeness Magnitude.....	97
Figure 5-31.	Map of the Cross-Hosgri Slope, Point Estero Slip Rate Site (from PG&E, 2015a, Figure 8-17) .....	98
Figure 5-32.	New Geophysical (Chirp) Lines and Sediment Cores Collected Near the Cross-Hosgri Slope (from Kluesner et al., 2023, Figure 2) .....	99
Figure 5-33.	Stratigraphic Interpretation of New Chirp and Sediment Core Data Across the Cross-Hosgri Slope (from Kluesner et al., 2023, Figure 6) .....	100
Figure 5-34.	Stratigraphic and Radiometric Age Data from New Sediment Cores Across the Cross-Hosgri Slope (from Medri et al., 2023, Figure 5).....	101
Figure 5-35.	Marine Terrace Uplift Rates on the Irish Hills Coastline from Alternative Models Considered in the 2015 SSC Model (from PG&E, 2015a, Figure 8-4) .....	102
Figure 5-36.	Contours of Paleosea Level Along the California Coast for MIS 5e (from Simms et al., 2016). Central California Coastline (Upper Map) Coincides with the 13 m contour.....	103
Figure 5-37.	Marine Terrace Uplift Rates on the Irish Hills Coastline Comparing Simms et al. (2016) Model to Prior Models. (See Figure 5-35 for Profile Location) .....	104
Figure 5-38.	Hosgri Fault Slip Rate Sites (from PG&E, 2015a, Figure 8-13) .....	105
Figure 5-39.	Hosgri Fault Slip Rate CDF, 2015 SSC Model (from PG&E, 2015a, Figure 8-33) .....	106
Figure 5-40.	Comparison of 2015 SSC Model (Blue), Kluesner et al. (2023) Model (Grey), and SSC Model Update (Red) Input PDFs and Slip Rate CDFs for the Point Estero (Cross-Hosgri Slope) Slip Rate Site on the Hosgri Fault: a) Offset PDFs; b) Age PDFs; c) Slip Rate CDFs .....	107
Figure 5-41.	Hosgri Fault Source Slip Rate CDFs for the SSC Model Update and Comparison with the 2015 SSC Model CDF .....	108
Figure 5-42.	Hosgri Fault Source Slip Rate CDFs for the SSC Model Update and 2015 SSC Model Compared with (a) Plate Boundary Model Constraints by DeMets et al. (2014) and (b) Deformation Model Slip Rates (Means) Used in the WUS 2023-ERF (Field et al., 2023) and UCERF3 (Field et al., 2013) Programs.....	109
Figure 5-43.	Weighted Mean EPHR for the Hosgri Fault Source Based on PG&E (2015a, Chapter 11) and Biasi and Thompson (2018). .....	110
Figure 5-44.	Los Osos Fault Hanging Wall Uplift Rate PDFs Considered in the 2023 SSC Model and Weighted Uplift Rate PDF .....	111
Figure 5-45.	Los Osos Fault Source Slip Rate CDFs for the Alternative Fault Geometry Models, SSC Model Update and Comparison with the 2015 SSC Model CDFs	112

Figure 5-46.	Los Osos Fault Source Slip Rate CDFs for the SSC Model Update Compared with Deformation Model Slip Rates (Means) Used in the WUS 2023-ERF (Field et al., 2023) and UCERF3 (Field et al., 2013) Programs.....	113
Figure 6-1.	Small-Scale Map Showing General Residual Gravity Anomaly Patterns in the United States (from Simpson et al., 1986).....	122
Figure 6-2.	Large-Scale Residual Isostatic Gravity Anomaly Map Showing a Negative Gravity Anomaly Coincident with the Irish Hills (modified from Langenheim et al., 2008 and PG&E, 2011, Figure E-2).....	123
Figure 7-1.	DCPP GMC logic tree for local seismic sources (from GeoPentech, 2015, Figure 1-1).....	152
Figure 7-2.	DCPP GMC logic tree for distant seismic sources (from GeoPentech, 2015, Figure 8.2-3) .....	152
Figure 7-3.	SWUS DCP $\phi_{SS}$ logic tree (from GeoPentech, 2015).....	153
Figure 7-4.	SWUS DCP $\tau$ logic tree (from GeoPentech, 2015).....	153
Figure 7-5.	SWUS DCP single-station sigma logic tree (from GeoPentech, 2015).....	154
Figure 7-6.	Earthquakes (blue stars) and stations (red triangles) in the preliminary NGA-West3 database for recordings with $M \geq 5$ , $R_{RUP} < 120$ km, and $V_{S30} > 250$ m/sec .....	155
Figure 7-7.	Earthquakes (blue stars) and stations (red triangles) in the DCP database for recordings with $M \geq 5$ , $R_{RUP} < 120$ km, and $V_{S30} > 250$ m/sec .....	156
Figure 7-8.	Magnitude-distance (left) and magnitude-Ztor (right) distributions of the Turkish and NGA-West3 data used in the regression analysis. Earthquakes with at least 5 recordings were used.....	157
Figure 7-9.	Magnitude-distance distribution of the DCP data used in the regression analysis. Earthquakes with at least 5 recordings were used. ....	157
Figure 7-10.	Regression constant (top) and between-event and within-event standard deviations (bottom) of the regression analysis of the Turkish and NGA-West3 data .....	158
Figure 7-11.	Between-event residuals of the Turkish and NGA-West3 data versus magnitude for periods of 0.01, 0.1, 0.4, and 1 sec. The robust Lowess fit to the data is shown in red. ....	159
Figure 7-12.	Between-event residuals of the Turkish and NGA-West3 data versus Ztor for periods of 0.01, 0.1, 0.4, and 1 sec. The robust Lowess fit to the data is shown in red. ....	160
Figure 7-13.	Within-event residuals of the Turkish and NGA-West3 data versus distance for period of 0.01 sec. The robust Lowess fit to the data is shown in red. ....	161
Figure 7-14.	Within-event residuals of the Turkish and NGA-West3 data versus distance for period of 0.1 sec. The robust Lowess fit to the data is shown in red. ....	162
Figure 7-15.	Within-event residuals of the Turkish and NGA-West3 data versus distance for period of 0.4 sec. The robust Lowess fit to the data is shown in red. ....	163

Figure 7-16.	Within-event residuals of the Turkish and NGA-West3 data versus distance for period of 1 sec. The robust Lowess fit to the data is shown in red. ....	164
Figure 7-17.	Within-event residuals of the Turkish and NGA-West3 data versus $V_{S30}$ for periods of 0.01, 0.1, 0.4, and 1 sec. The robust Lowess fit to the data is shown in red. ....	165
Figure 7-18.	Regression constant (left) and between-event and within-event standard deviations (right) of the regression analysis of the DCPD database .....	166
Figure 7-19.	Between-event residuals of earthquakes in the DCPD database versus magnitude for periods of 0.01, 0.1, 0.4, and 1 sec. The robust Lowess fit to the data is shown in red. ....	167
Figure 7-20.	Within-event residuals of recordings in the DCPD database versus distance for period of 0.01, 0.1, 0.4, and 1 sec. The robust Lowess fit to the data is shown in red. ....	168
Figure 7-21.	Within-event residuals of recordings in the DCPD database versus $V_{S30}$ for periods of 0.01, 0.1, 0.4, and 1 sec. The robust Lowess fit to the data is shown in red. .	169
Figure 7-22.	Average and plus- and minus-one standard error from the NW of Brea (M 5.09) event for the periods of 0.01, 0.1, 0.4, and 1 sec .....	170
Figure 7-23.	Average and plus- and minus-one standard error from the South Napa (M 6.02) event for the periods of 0.01, 0.1, 0.4, and 1 sec .....	171
Figure 7-24.	Average and plus- and minus-one standard error from the Ridgecrest Sequence (M 7.06) event for the periods of 0.01, 0.1, 0.4, and 1 sec .....	172
Figure 7-25.	Average and plus- and minus-one standard error from the Pazarcik (M 7.8) event for the periods of 0.01, 0.1, 0.4, and 1 sec .....	173
Figure 7-26.	Average and plus- and minus-one standard error from the SE of Ojai (M 5.1) event for the periods of 0.01, 0.1, 0.4, and 1 sec .....	174
Figure 7-27.	Average and plus- and minus-one standard error from the ESE of Alum Rock (M 5.1) event for the periods of 0.01, 0.1, 0.4, and 1 sec .....	175
Figure 7-28.	Average and plus- and minus-one standard error residuals for the six earthquakes evaluated from recordings with distances less than 15 km and spectral period of 0.01 sec. Upper left as a function of magnitude, upper right as a function of $R_{RUP}$ distance, and lower center as a function of $Z_{tor}$ . ....	176
Figure 7-29.	Average and plus- and minus-one standard error residuals for the six earthquakes evaluated from recordings with distances less than 15 km and spectral period of 0.1 sec. Upper left as a function of magnitude, upper right as a function of $R_{RUP}$ distance, and lower center as a function of $Z_{tor}$ . ....	177
Figure 7-30.	Average and plus- and minus-one standard error residuals for the six earthquakes evaluated from recordings with distances less than 15 km and spectral period of 0.4 sec. Upper left as a function of magnitude, upper right as a function of $R_{RUP}$ distance, and lower center as a function of $Z_{tor}$ . ....	178



Figure 7-31.	Average and plus- and minus-one standard error residuals for the six earthquakes evaluated from recordings with distances less than 15 km and spectral period of 1.0 sec. Upper left as a function of magnitude, upper right as a function of $R_{RUP}$ distance, and lower center as a function of $Z_{tor}$ . .....	179
Figure 7-32.	Probabilistic sensitivity analysis of the directivity adjustments to the ground motion at DCPD from the Hosgri fault at period of 3 sec. Directivity implementations of Chiou and Youngs (CY14, 2014) and Watson-Lamprey (WL, 2015) are shown (from GeoPentech, 2015, Figure 6.5.2-3). .....	180
Figure 7-33.	Fault trace (red line), epicentral locations of the hypocenters, and station locations for a simplified strike-slip M 7.0 earthquake rupture. Sites A are located off the end of the fault, Sites B are located at 45° off the end of the fault, Sites C are perpendicular to the end of the fault, Sites D are perpendicular to ¾ of the fault, and Sites E are perpendicular to the middle of the fault (from Al Atik et al., 2023). .....	181
Figure 7-34.	Estimated directivity median adjustment factors for a M 7.0 strike-slip case from the BS13, WL18, BSS20, CS13, and BR20 models for Sites A, B, C, and E at a rupture distance of 5 km (from Al Atik et al., 2023).....	182
Figure 7-35.	Location of the DCPD site (labeled “user site”) and the four neighboring sites used to interpolate the probabilistic directivity adjustment factors at DCPD (from Mazzoni et al., 2023). Fault traces are shown in red. ....	183
Figure 7-36.	Probabilistic ground-motion directivity adjustment factors versus spectral periods at the DCPD site for return period of 2,475 yr (top) and 5,000 yr (bottom) (from Mazzoni et al., 2023) .....	184
Figure 7-37.	Earthquakes and stations in the NGA-West2 database within 50 km of DCPD .	185
Figure 7-38.	DCPD empirical site adjustment factors (from PG&E, 2017b) .....	186
Figure 7-39.	Top: Median predicted response spectra for the Hosgri fault scenario for the reference rock model (Ref. Rock) and site-specific conditions at DCPD (CP). Bottom: Epistemic uncertainty standard deviation of the DCPD median ground-motion model. ....	187
Figure 7-40.	Non-ergodic EAS adjustments at DCPD in LN units for the Hosgri fault scenario based on the LAK21 model. The mean (top) and standard deviation (bottom) of the adjustments over 1000 drawn samples are shown. ....	188
Figure 7-41.	Correlation length of the source term ( $l_{1,e}$ ), anelastic attenuation term ( $l_{ca1,p}$ ), and regional site term ( $l_{1a,s}$ ) in the LAK21 model (from Lavrentiadis et al., 2023) .	189
Figure 7-42.	Comparison of predicted median ground motion at DCPD for the Hosgri fault scenario for ASK14 and LA23 non-ergodic model 1 (top) and CY14 and LA23 non-ergodic model 2 (bottom) .....	190
Figure 7-43.	Comparison of predicted median ground motion at the control point at DCPD for the Hosgri fault scenario for the DCPD model and the LA23 non-ergodic models (top) and of epistemic sigma for the DCPD and the LA23 models (bottom).....	191

Figure 7-44.	Comparison of the range of predicted median ground motion at the control point at DCPD for the Hosgri fault scenario from the DCPD model and LA23 non-ergodic model 1 (top) and the DCPD model and LA23 non-ergodic model 2 (bottom). Dashed lines show median $\pm$ sigma. ....	192
Figure 7-45.	Comparison of predicted median ground motion at DCPD for the Shoreline fault scenario for ASK14 and LA23 non-ergodic model 1 (top) and CY14 and LA23 non-ergodic model 2 (bottom) .....	193
Figure 7-46.	Comparison of predicted median ground motion at the control point at DCPD for the Shoreline fault scenario for the DCPD model and the LA23 non-ergodic models (top) and of epistemic sigma for the DCPD and the LA23 models (bottom) .....	194
Figure 7-47.	Comparison of the range of predicted median ground motion at the control point at DCPD for the Shoreline fault scenario from the DCPD model and LA23 non-ergodic model 1 (top) and the DCPD model and LA23 non-ergodic model 2 (bottom). Dashed lines show median $\pm$ sigma. ....	195
Figure 7-48.	Comparison of predicted median ground motion at DCPD for the Los Osos fault scenario for ASK14 and LA23 non-ergodic model 1 (top) and CY14 and LA23 non-ergodic model 2 (bottom). For the non-ergodic models, the median and median $\pm$ sigma over 1000 drawn samples are shown.....	196
Figure 7-49.	Top: Comparison of predicted median ground motion at the control point at DCPD for the Los Osos fault scenario for the DCPD model and the LA23 non-ergodic models. Bottom: comparison of epistemic sigma for the DCPD and the LA23 models. ....	197
Figure 7-50.	Comparison of the range of predicted median ground motion at the control point at DCPD for the Los Osos fault scenario from the DCPD model and LA23 non-ergodic model 1 (top) and the DCPD model and LA23 non-ergodic model 2 (bottom). Dashed lines show median $\pm$ sigma. ....	198
Figure 7-51.	Example of a complex rupture with the Hosgri and Los Osos faults (blue area is the surface projection of the Los Osos fault plane). DCPD site is indicated with the yellow triangle (from GeoPentech, 2015, Figure 5.2.3-3).....	199
Figure 7-52.	Example splay rupture with the Hosgri and Shoreline faults. DCPD site is indicated by the yellow triangle (from GeoPentech, 2015, Figure 5.2.3-6) .....	199
Figure 7-53.	Comparison of the global $\tau$ model versus magnitude to the SWUS $\tau$ model. Both models are period-independent. Solid lines show the median models and dashed lines show the 5 <sup>th</sup> and 95 <sup>th</sup> percentiles (from INL, 2022) .....	200
Figure 7-54.	Comparison of the global $\phi_{SS}$ model versus magnitude to the SWUS $\phi_{SS}$ models for PGA (top) and period of 1 sec (bottom).....	201
Figure 8-1.	Vertical to Horizontal (V/H) spectral ratio for the controlling scenario event and $V_{S30}$ of 969 m/sec.....	205
Figure 9-1.	Locations of 1-D profiles in the power block and turbine building region used to define the control point (from PG&E, 2015d).....	221

Figure 9-2.	Range of $V_S$ profiles under the power block and the turbine building regions along with the central, upper, and lower $V_S$ profiles (shown in black) for the control point (from PG&E, 2015d) .....	222
Figure 9-3.	Control point $V_S$ profiles compared to the WUS host $V_S$ profile (labeled reference 760) (from PG&E, 2015d) .....	223
Figure 9-4.	Logic tree for the site condition characterization for the DCPD control point used in the PE&A (2015) analytical study (from PG&E, 2015d) .....	224
Figure 9-5.	Modulus reduction and damping curves for the EPRI rock model (from PE&A, 2015) .....	225
Figure 9-6.	Modulus reduction and damping curves for the Peninsular Range model (from PE&A, 2015).....	226
Figure 9-7.	Comparison of modulus reduction (top) and damping (bottom) curves from laboratory testing of DCPD soft rock to the EPRI rock and Peninsular Range models (from PG&E, 2015d).....	227
Figure 9-8.	Analytical site adjustment factors for DCPD for a reference rock PGA of 0.2 g (top left), 1.07 g (top right), and 1.91 g (bottom). The green, red, and blue curves are for the lower, central, and upper $V_S$ profiles. The short-dashed lines are for target kappa of 0.03 sec, the long-dashed lines are for target kappa of 0.05 sec, and the solid lines are for target kappa of 0.04 sec. The black line shows the mean factors. (From PG&E, 2015d).....	228
Figure 9-9.	Top: Components of the epistemic uncertainty of the empirical site term. Bottom: Central, upper, and lower estimates of the empirical site term (from PG&E, 2017b) .....	229
Figure 9-10.	Uniform hazard spectra (UHS) and GMRS for the DCPD control point (from PG&E, 2015d).....	230
Figure 9-11.	Sensitivity of the UHS to the site term approach (from PG&E, 2015d).....	231
Figure 9-12.	Comparison of the GMPE-compatible $V_S$ profiles for ASK14, BSSA14, CB14, and CY14 to the Kamai et al. (2013) reference $V_S$ profile for $V_{S30}$ of 760 m/sec. The control profiles (central, upper, and lower) are shown in cyan. The left panel shows full profile while the right panel shows the profiles in the top 500 m. ....	232
Figure 9-13.	Quarter-wavelength linear site amplifications of the host $V_S$ profiles and the control point target $V_S$ profiles .....	232
Figure 9-14.	$V_S$ -kappa scaling factors for CY14 using the GMPE-compatible host $V_S$ profile and kappa for each of the nine target DCPD $V_S$ and kappa branches .....	233
Figure 9-15.	Comparison of the average $V_S$ -kappa scaling factors for each of the four NGA-West2 GMPEs using the GMPE-compatible host $V_S$ profiles and kappa. The average of the factors over the four NGA-West2 GMPEs is shown with the black curve.....	233

Figure 9-16.	Comparison of the analytical and empirical site factors for DCPD to the analytical factors obtained using the IRVT approach and the GMPE-compatible host $V_s$ profiles and kappa.....	234
Figure 9-17.	Earthquake epicenters (blue stars) and ground-motion recording station locations (open red triangles) for the DCPD expanded dataset used in the non-ergodic analysis.....	235
Figure 9-18.	Magnitude-distance distribution of the expanded dcpp flatfile used in the non-ergodic analysis.....	236
Figure 9-19.	Earthquake epicenters (blue stars) and ground-motion recording station locations (open red triangles) within 50 km of DCPD in the NGA-West2 dataset (top) and the expanded preliminary dcpp dataset (bottom).....	237
Figure 9-20.	Number of FAS data in the usable frequency range versus frequency in the dcpp flatfile. Vertical lines at 0.3 and 11.6 Hz indicate the range beyond which less than 35% of the data remain. ....	238
Figure 9-21.	FAS between-event residuals versus magnitude at frequencies of 0.1, 1, 5, 10, 14.7, and 23.3 Hz. The blue lines show the linear fits to the residuals versus magnitude (from Dr. Sung's report in Appendix F).....	239
Figure 9-22.	FAS site-to-site terms versus $V_{S30}$ at frequencies of 0.1, 1, 5, 10, 14.7, and 23.3 Hz. The blue datapoints show bin averages of the site-to-site residuals. (from Dr. Sung's report in Appendix F).....	240
Figure 9-23.	Top: DCPD site term ( $\delta S2S$ ) and its regional ( $\delta S2S_{reg}$ ) and uncorrelated ( $\delta S2S_{unc}$ ) components in FAS domain. Bottom: Epistemic uncertainty of the regional and uncorrelated components of the site term. ....	241
Figure 9-24.	Comparison of site term and its regional and uncorrelated components in the FAS and PSA domains.....	242
Figure 9-25.	Number of recordings versus frequency for the dataset used in the FAS non-ergodic modeling approach (Data1) and in the PSA sensitivity analysis (Data2) (from Dr. Sung's report in Appendix F).....	243
Figure 9-26.	Comparison of the PSA regional site term (plot c), uncorrelated site term (plot f), and total site term (plot g) obtained from the FAS analysis via RVT for Data1 and Data2 and directly from the PSA analysis for Data2 (from Dr. Sung's report in Appendix F).....	244
Figure 9-27.	Comparison of the 2015 empirical site term (LN units) for DCPD to the site term and its regional and uncorrelated components obtained from the non-ergodic approach (updated study) with the preliminary expanded ground-motion dataset.....	245
Figure 9-28.	Ratio of the empirical site term for DCPD obtained from the non-ergodic modeling approach (updated) to the 2015 site term.....	245
Figure 9-29.	Comparison of the 2015 site term and its epistemic uncertainty (5 <sup>th</sup> and 95 <sup>th</sup> percentile labeled as lower and upper, respectively) and the updated empirical site	

	term obtained from the non-ergodic modeling approach. The average analytical linear site term is shown in black.....	246
Figure 10-1.	Mean hazard curves from the 2015 study (solid lines) and updated scaled results (dashed lines) for the Los Osos fault source (green lines), Hosgri fault source (black lines) and total hazard curves (blue lines) for 100 Hz (PGA).....	263
Figure 10-2.	Mean hazard curves from the 2015 study (solid lines) and updated scaled results (dashed lines) for the Los Osos fault source (green lines), Hosgri fault source (black lines) and total hazard curves (blue lines) for 50 Hz .....	263
Figure 10-3.	Mean hazard curves from the 2015 study (solid lines) and updated scaled results (dashed lines) for the Los Osos fault source (green lines), Hosgri fault source (black lines) and total hazard curves (blue lines) for 33.333 Hz .....	264
Figure 10-4.	Mean hazard curves from the 2015 study (solid lines) and updated scaled results (dashed lines) for the Los Osos fault source (green lines), Hosgri fault source (black lines) and total hazard curves (blue lines) for 20 Hz .....	264
Figure 10-5.	Mean hazard curves from the 2015 study (solid lines) and updated scaled results (dashed lines) for the Los Osos fault source (green lines), Hosgri fault source (black lines) and total hazard curves (blue lines) for 13.333 Hz .....	265
Figure 10-6.	Mean hazard curves from the 2015 study (solid lines) and updated scaled results (dashed lines) for the Los Osos fault source (green lines), Hosgri fault source (black lines) and total hazard curves (blue lines) for 10 Hz .....	265
Figure 10-7.	Mean hazard curves from the 2015 study (solid lines) and updated scaled results (dashed lines) for the Los Osos fault source (green lines), Hosgri fault source (black lines) and total hazard curves (blue lines) for 6.667 Hz .....	266
Figure 10-8.	Mean hazard curves from the 2015 study (solid lines) and updated scaled results (dashed lines) for the Los Osos fault source (green lines), Hosgri fault source (black lines) and total hazard curves (blue lines) for 5 Hz .....	266
Figure 10-9.	Mean hazard curves from the 2015 study (solid lines) and updated scaled results (dashed lines) for the Los Osos fault source (green lines), Hosgri fault source (black lines) and total hazard curves (blue lines) for 4 Hz .....	267
Figure 10-10.	Mean hazard curves from the 2015 study (solid lines) and updated scaled results (dashed lines) for the Los Osos fault source (green lines), Hosgri fault source (black lines) and total hazard curves (blue lines) for 3.333 Hz .....	267
Figure 10-11.	Mean hazard curves from the 2015 study (solid lines) and updated scaled results (dashed lines) for the Los Osos fault source (green lines), Hosgri fault source (black lines) and total hazard curves (blue lines) for 2.5 Hz .....	268
Figure 10-12.	Mean hazard curves from the 2015 study (solid lines) and updated scaled results (dashed lines) for the Los Osos fault source (green lines), Hosgri fault source (black lines) and total hazard curves (blue lines) for 2 Hz .....	268
Figure 10-13.	Mean hazard curves from the 2015 study (solid lines) and updated scaled results (dashed lines) for the Los Osos fault source (green lines), Hosgri fault source (black lines) and total hazard curves (blue lines) for 1.333 Hz .....	269

Figure 10-14. Mean hazard curves from the 2015 study (solid lines) and updated scaled results (dashed lines) for the Los Osos fault source (green lines), Hosgri fault source (black lines) and total hazard curves (blue lines) for 1 Hz .....	269
Figure 10-15. Mean hazard curves from the 2015 study (solid lines) and updated scaled results (dashed lines) for the Los Osos fault source (green lines), Hosgri fault source (black lines) and total hazard curves (blue lines) for 0.667 Hz .....	270
Figure 10-16. Mean hazard curves from the 2015 study (solid lines) and updated scaled results (dashed lines) for the Los Osos fault source (green lines), Hosgri fault source (black lines) and total hazard curves (blue lines) for 0.5 Hz .....	270
Figure 10-17. Mean hazard curves from the 2015 study (solid lines) and updated scaled results (dashed lines) for the Los Osos fault source (green lines), Hosgri fault source (black lines) and total hazard curves (blue lines) for 0.333 Hz .....	271
Figure 10-18. UHS from the 2015 study (solid lines) and the updated results (dashed lines) for hazard levels of $10^{-4}$ (blue lines), $10^{-5}$ (red lines), and $10^{-6}$ (green lines) .....	271
Figure 10-19. Ratio of UHS from the 2015 study and the updated results for hazard levels of $10^{-4}$ (blue line), $10^{-5}$ (red line), and $10^{-6}$ (green line) .....	272
Figure 10-20. GMRS for the reference rock horizon from the 2015 study (solid line) and updated results (dashed line).....	272
Figure 10-21. GMRS spectral ratio (Updated/2015) for the reference rock.....	273
Figure 11-1. Hazard curve ratio (i.e., scaled hazard divided by 2015 hazard) plotted as a function of 2015 total hazard (solid blue line), scaled total hazard (dashed green line), and selected scale factor (dashed red line) for 100 Hz (PGA) .....	276
Figure 11-2. Hazard curve ratio (i.e., scaled hazard divided by 2015 hazard) plotted as a function of 2015 total hazard (solid blue line), scaled total hazard (dashed green line), and selected scale factor (dashed red line) for 20 Hz .....	277
Figure 11-3. Hazard curve ratio (i.e., scaled hazard divided by 2015 hazard) plotted as a function of 2015 total hazard (solid blue line), scaled total hazard (dashed green line), and selected scale factor (dashed red line) for 10 Hz .....	278
Figure 11-4. Hazard curve ratio (i.e., scaled hazard divided by 2015 hazard) plotted as a function of 2015 total hazard (solid blue line), scaled total hazard (dashed green line), and selected scale factor (dashed red line) for 5 Hz .....	279
Figure 11-5. Hazard curve ratio (i.e., scaled hazard divided by 2015 hazard) plotted as a function of 2015 total hazard (solid blue line), scaled total hazard (dashed green line), and selected scale factor (dashed red line) for 2.5 Hz .....	280
Figure 11-6. Hazard curve ratio (i.e., scaled hazard divided by 2015 hazard) plotted as a function of 2015 total hazard (solid blue line), scaled total hazard (dashed green line), and selected scale factor (dashed red line) for 1 Hz .....	281
Figure 11-7. Hazard curve ratio (i.e., scaled hazard divided by 2015 hazard) plotted as a function of 2015 total hazard (solid blue line), scaled total hazard (dashed green line), and selected scale factor (dashed red line) for 0.5 Hz .....	282

Figure 11-8. Selected scale factors (open blue circles) for the seven spectral frequencies and 5 Hz value (dashed black line)..... 283

## List of Tables

Table 2-1	Schedule for the Diablo Canyon Updated Seismic Assessment
Table 4-1	Table of Events in the Türkiye Database Within the Sub-selection Search Parameters
Table 4-2	Table of Events in the DCPD California Database Within the Sub-selection Search Parameters
Table 4-3	Table of New Events Added Since the NGA-West2 Database to the NGA-West3 Database Within the Sub-selection Search Parameters
Table 5-1	Models That Comprise the Primary Fault Source Characterization
Table 5-2	Fault Geometry Models (FGMs) and Logic Tree Combinations
Table 5-3	Rupture Source Types
Table 5-4	Rupture Source Types and Magnitude PDFs
Table 5-5	Grouping of Rupture Sources by Fault Source for Hazard Sensitivity
Table 5-6	Fractional Contribution of the Hosgri Fault Source to the Total Hazard at the $10^{-4}$ Annual Hazard Level
Table 5-7	Deaggregation for Reference Rock Site Hazard at the $10^{-4}$ Annual Hazard Level
Table 5-8	Primary Fault Source Characterization Model Elements and Summary of New Information
Table 5-9	Summary of New Information for the Local Areal Source Zone
Table 5-10	Comparison of Fault Source Geometries, 2015 SSC Model and WUS ERF-2023 Fault Model
Table 5-11	Comparison of Fault Source Slip Rates, 2015 SSC Model and WUS ERF-2023 Deformation Models
Table 5-12	Comparison of Hosgri Fault Slip Rate Sites, 2015 SSC Model
Table 5-13	Changes to the Uncertainty PDF, Offset of Cross-Hosgri Slope
Table 5-14	Changes to the Uncertainty PDF, Age of Cross-Hosgri Slope Offset Feature
Table 5-15	Hosgri Fault Slip Rate CDFs at the Point Estero (Cross-Hosgri Slope) Site, 2015 SSC Model and the SSC Model Update
Table 5-16	Hosgri Fault Slip Rate Study Sites, and Qualitative Ranking of Criteria for Weighting
Table 5-17	Scale Factors for Weighted Mean Slip Rate, Hosgri and Los Osos Fault Sources
Table 5-18	Weighted Mean EPHR Values for the Hosgri Fault Source
Table 7-1	Selected Candidate GMPEs for the Median Ground-Motion Model for DCPD (from GeoPentech, 2015)



Table 7-2	Events with More than Two Recordings Within 15 km for Residual Analyses
Table 7-3	Summary Results from Residuals Analysis for Events with Stations Less than 15 km for Spectral Period of 0.01 sec
Table 7-4	Summary Results from Residuals Analysis for Events with Stations Less than 15 km for Spectral Period of 0.1 sec
Table 7-5	Summary Results from Residuals Analysis for Events with Stations less than 15 km for Spectral Period of 0.4 sec
Table 7-6	Summary Results from Residuals Analysis for Events with Stations less than 15 km for Spectral Period of 1.0 sec
Table 7-7	Stations Within 20 km of DCPD in the NGA-West2 Database
Table 7-8	Deterministic Scenarios Used for Comparisons with Non-ergodic Ground-Motion Models
Table 8-1	Vertical to Horizontal (V/H) Spectral Ratio Results for the Scenario Event from the Gülerce and Abrahamson (2011) and Bozorgnia and Campbell (2016) Models
Table 9-1	Host Kappa for the NGA-West2 GMPEs for $V_{S30}$ of 760 m/sec Based on the GMPE-Compatible Method and the PE&A (2015) Analysis
Table 9-2	Summary of the Lavrentiadis et al. (2023) Model Parameters and Hyperparameters (from Lavrentiadis et al., 2023, Table 2)
Table 10-1	Scaling Factors for the Adjustment to the Mean Slip Rate, EPHR, and Combined Factor for the Hosgri Fault Source
Table 10-2	Scaling Factors for the Adjustment to the Mean Slip Rate for the Los Osos Fault Source
Table 10-3	Mean Total Hazard Curve from the 2015 Study, Updated Mean Total Hazard Curve, and Hazard Curve Ratio for the 100 Hz (PGA) Spectral Frequency
Table 10-4	Mean Total Hazard Curve from the 2015 Study, Updated Mean Total Hazard Curve, and Hazard Curve Ratio for the 50 Hz Spectral Frequency
Table 10-5	Mean Total Hazard Curve from the 2015 Study, Updated Mean Total Hazard Curve, and Hazard Curve Ratio for the 33.333 Hz Spectral Frequency
Table 10-6	Mean Total Hazard Curve from the 2015 Study, Updated Mean Total Hazard Curve, and Hazard Curve Ratio for the 20 Hz Spectral Frequency
Table 10-7	Mean Total Hazard Curve from the 2015 Study, Updated Mean Total Hazard Curve, and Hazard Curve Ratio for the 13.333 Hz Spectral Frequency
Table 10-8	Mean Total Hazard Curve from the 2015 Study, Updated Mean Total Hazard Curve, and Hazard Curve Ratio for the 10 Hz Spectral Frequency
Table 10-9	Mean Total Hazard Curve from the 2015 Study, Updated Mean Total Hazard Curve, and Hazard Curve Ratio for the 6.667 Hz Spectral Frequency
Table 10-10	Mean Total Hazard Curve from the 2015 Study, Updated Mean Total Hazard Curve, and Hazard Curve Ratio for the 5 Hz Spectral Frequency

Table 10-11	Mean Total Hazard Curve from the 2015 Study, Updated Mean Total Hazard Curve, and Hazard Curve Ratio for the 4 Hz Spectral Frequency
Table 10-12	Mean Total Hazard Curve from the 2015 Study, Updated Mean Total Hazard Curve, and Hazard Curve Ratio for the 3.333 Hz Spectral Frequency
Table 10-13	Mean Total Hazard Curve from the 2015 Study, Updated Mean Total Hazard Curve, and Hazard Curve Ratio for the 2.5 Hz Spectral Frequency
Table 10-14	Mean Total Hazard Curve from the 2015 Study, Updated Mean Total Hazard Curve, and Hazard Curve Ratio for the 2 Hz Spectral Frequency
Table 10-15	Mean Total Hazard Curve from the 2015 Study, Updated Mean Total Hazard Curve, and Hazard Curve Ratio for the 1.333 Hz Spectral Frequency
Table 10-16	Mean Total Hazard Curve from the 2015 Study, Updated Mean Total Hazard Curve, and Hazard Curve Ratio for the 1 Hz Spectral Frequency
Table 10-17	Mean Total Hazard Curve from the 2015 Study, Updated Mean Total Hazard Curve, and Hazard Curve Ratio for the 0.667 Hz Spectral Frequency
Table 10-18	Mean Total Hazard Curve from the 2015 Study, Updated Mean Total Hazard Curve, and Hazard Curve Ratio for the 0.5 Hz Spectral Frequency
Table 10-19	Mean Total Hazard Curve from the 2015 Study, Updated Mean Total Hazard Curve, and Hazard Curve Ratio for the 0.333 Hz Spectral Frequency
Table 10-20	Original 2015 UHS and Updated UHS for the Three Hazard Levels of $10^{-4}$ , $10^{-5}$ , and $10^{-6}$
Table 10-21	UHS Ground Motion Ratios (Updated/2015) for the Three Hazard Levels of $10^{-4}$ , $10^{-5}$ , and $10^{-6}$
Table 10-22	Original 2015 GMRS for the Reference Rock Horizon
Table 10-23	Updated GMRS for the Reference Rock Horizon
Table 10-24	GMRS Ratios for the 2015 Study Results and the Updated Results for the Reference Rock Horizon
Table 11-1	Selected Scale Factors for the Control Point Hazard Curves Based on the Scaling Adjustments

## List of Acronyms and Abbreviations

1-D	one-dimensional
2-D	two-dimensional
3-D	three-dimensional
AB	State of California Assembly Bill
ANSS	Advanced National Seismic System
ASK	Abrahamson, Silva, and Kamai
BBP	broadband platform
BC	Bozorgnia and Campbell
BR	Badie Rowshandel
BS	Bayless and Somerville
BSS	Bayless, Spudich, and Somerville
BSSA	Boore, Stewart, Seyhan and Atkinson
CB	Campbell and Bozorgnia
CBR	center, body, and range
CCCSIP	Central Coastal California Seismic Imaging Project
CCSN	Central Coast Seismic Network
CDF	cumulative distribution function
CDF	core damage frequency
CEC	California Energy Commission
CFR	Code of Federal Regulations
CHIRP	compressed high-intensity radar pulse
CHS	cross-Hosgri slope
ComCat	Comprehensive Earthquake Catalog
CP	control point
CPUC	California Public Utilities Commission
CY	Chiou and Youngs
DCISC	Diablo Canyon Independent Safety Committee
DCPP	Diablo Canyon Power Plant
DPP	direct point parameter
DWR	Department of Water Resources

EAS	effective amplitude spectrum
EPHR	equivalent Poisson hazard ratio (referred as equivalent Poisson ratio (EPR) in PG&E (2015a)
EPRI	Electric Power Research Institute
EQID	earthquake ID
EQ or Eqk	earthquake
ERF	earthquake rupture forecast
FAS	Fourier amplitude spectrum
FGM	fault geometry model
FIRS	foundation input response spectra
ft	feet
FW	footwall
$G/G_{\max}$	normalized shear modulus
GEER	Geotechnical Extreme Events Reconnaissance
GIA	glacio-isostatic adjustment
GMC	ground-motion characterization
GMM	ground-motion models
GMPE	ground-motion prediction equation
GMRS	ground-motion response spectrum
GPS	global positioning system
HB	Hanks and Bakun
HID	hazard input document
HW	hanging wall
Hz	Hertz
INL	Idaho National Laboratory
IOF	inferred Offshore fault
IRVT	inverse random vibration theory
ka	thousand years ago
km	kilometer
kyr	thousand years
LA	Lavrentiadis and Abrahamson
LAK	Lavrentiadis, Abrahamson, and Kuehn
LERF	large early release frequency

LN	log-normal
LTFM	long-term fault memory
LTSP	Long-Term Seismic Program
<i>m</i>	magnitude
m	meter
<b>M</b> or <b>M<sub>w</sub></b>	moment magnitude
Ma	million years ago
MBES	multibeam echosounder
<i>m<sub>c</sub></i>	completeness magnitude
<i>M<sub>char</sub></i>	characteristic magnitude
md or <b>M<sub>d</sub></b>	duration magnitude
MDM	magnitude distribution model
MFD	magnitude-frequency distribution
MIS	marine (oxygen) isotope stage
ml or <b>M<sub>L</sub></b>	local magnitude
mm	millimeter
<i>M<sub>max</sub></i>	maximum magnitude
<i>M<sub>min</sub></i>	minimum magnitude
mm/yr	millimeters per year
MRD	modulus reduction and damping curves
NE	northeast-vergent
NGA	Next Generation Attenuation
NRC	U.S. Nuclear Regulatory Commission
NSHM	U.S. National Seismic Hazard Model
NTTF	Near-Term Task Force
NUREG	Reports or brochures, produced by the NRC, on regulatory decisions, results of research, results of incident investigations, and other technical and administrative information
OSL	optically stimulated luminescence
OV	outward-vergent
PDF	probability density function
PE&A	Pacific Engineering and Analysis
PG&E	Pacific Gas & Electric Company

PGA	peak ground acceleration
PNNL	Pacific Northwest National Laboratory
POANHI	Process of Assessment of Natural Hazard Impacts
PPRP	Participatory Peer Review Panel
PRA	probabilistic risk assessment, also see SPRA
PSA	pseudo spectral acceleration
PSHA	probabilistic seismic hazard analysis
PTI	Project Technical Integrator
RAW	risk achievement worth
RESORCE	Reference Database of Seismic Ground Motion in Europe
R <sub>RUP</sub>	closest distance to coseismic rupture (km)
RVT	random vibration theory
R <sub>x</sub>	horizontal distance from top of rupture measured perpendicular to fault strike (km)
SAF	San Andreas fault
SB	State of California Senate Bill
SCEC	Southern California Earthquake Center
sec	second (a unit of time)
SHIFT	Seismic Hazard Inferred From Tectonics
SLOMFP	San Luis Obispo Mothers for Peace
SLPB	San Luis–Pismo structural block
SONGS	San Onofre Nuclear Generating Station
SPRA	seismic probabilistic risk assessment
SRSS	square root of the sum of the squares
SSC	seismic source characterization
SSCs	systems, structures and components
SSHAC	Senior Seismic Hazard Analysis Committee
SSN	station sequence number
SW	southwest-vergent
SWBZ	Southwestern Boundary Zone
SWUS	Southwest United States
TDI	technically defensible interpretations
TI	Technical Integration

UC	University of California
UCERF	Uniform California Earthquake Rupture Forecast
UCERF3	Third Uniform California Earthquake Rupture Forecast
UHS	uniform hazard spectrum
USGS	U.S. Geological Survey
V/H	vertical to horizontal spectral ratio
$V_{S30}$	average shear-wave velocity over the uppermost 30 m of a geologic column
WAACY	Wooddell, Abrahamson, Acevedo-Cabrera, and Youngs
WL	Watson-Lamprey
WUS	Western United States
yr	year
Ztor	depth to the top of rupture (in km)

## EXECUTIVE SUMMARY

This document presents the results of a seismic hazard evaluation and analysis update for the Pacific Gas & Electric Company (PG&E) Diablo Canyon Power Plant (DCPP). The seismic update was performed in response to Senate Bill 846, which was passed in September 2022 to extend operation of the power plant and included a covenant to perform a seismic analysis update.

The starting seismic hazard model for the update was developed in 2015 and was based on new information from two programs. The first program involved extensive new seismological, geophysical, and geological data collection at and near the DCPP site under PG&E's Long Term Seismic Program (LTSP) and California Assembly Bill 1632. This program of extensive new data collection supplemented ongoing seismic data collection and research conducted under the LTSP, including continuous earthquake monitoring by the PG&E Central Coast Seismic Network (CCSN). The second program involved developing new models for probabilistic seismic hazard analysis (PSHA) under the Senior Seismic Hazard Analysis Committee (SSHAC) Level 3 process in response to a request from the U.S. Nuclear Regulatory Commission (NRC) following the Fukushima Dai-Ichi accident in Japan. The SSHAC Level 3 studies examined new information and technically defensible data, models, and methods that could impact seismic hazard or represent a significant change in seismic risk.

Even though the 2015 SSHAC Level 3 PSHA model was used as a starting basis for the seismic update, considerable effort was spent to critically review the existing model and integrate any new significant information or updates to approaches.

The 2023 seismic update was conducted from June 2023 to January 2024. The update was organized following best practices of a SSHAC Level 1 study, which includes defining Technical Integration (TI) teams of subject matter experts to conduct the work and a Participatory Peer Review Panel (PPRP) to review the process of data and model evaluation, development, and documentation by the TI teams. The participants in the update are topical experts in the areas of seismic geology, seismology, earthquake engineering and seismic risk, have considerable experience performing nuclear seismic SSHAC studies, and were involved with the 2015 SSHAC studies for DCPP. In accordance with the SSHAC process, the TI teams were responsible for evaluating the data, models, and methods, integrating the data into updates to the hazard models, and developing documentation. Participatory review occurred at two levels. The first level was the PPRP, a standard element for a SSHAC study. Additionally, a team of external reviewers from the University of California (UC) Los Angeles Garrick Risk Institute and UC Santa Barbara provided a second level of external review that focused on the evaluation process. The project was planned and executed with oversight from the Diablo Canyon Independent Safety Committee (DCISC) and the California Department of Water Resources (DWR), which managed the project for the State of California. The DCISC and DWR participated in technical workshops addressing review of previous studies, new information and models, impact evaluation and analyses results.

In PSHA, the seismic source characterization (SSC) defines the sources of earthquakes that can produce ground motions of engineering significance and the magnitudes and rates of those



earthquakes. In site-specific PSHA, the SSC modelling approach includes a screening process to evaluate the most significant sources and focuses effort on those seismic sources that contribute most to the annual hazard at the site at the hazard levels and spectral frequencies that are the most important to seismic safety. The sources from the 2015 SSC model (that was developed under the 2015 SSC SSHAC study) that contribute most to this hazard are the Hosgri, Los Osos, Shoreline, and San Luis fault sources and the local background seismic source zone.

For the SSC model component of the 2023 seismic update, a review of recently published data, models, and methods found that most new information is consistent with information available to the 2015 SSC SSHAC TI team, and no new information, including proponent models offered through public testimony, warrants changes to the model. The exception to this general finding is new information from several publications concerning the Hosgri and Los Osos fault slip rates. Based on new research on the origin, stratigraphic development, and age of a sea-floor feature that crosses the Hosgri fault north of DCP (offshore Point Estero), the estimated geologic slip rate at this site is interpreted to be more reliable than it was during the 2015 SSC studies. As a consequence of this new information, the geologic slip rate of the Hosgri fault near DCP has been recalculated in this update, and the weighted-mean slip rate of the Hosgri fault source is 26% higher than in the 2015 SSC model (2.14 mm/yr weighted-mean slip rate compared to 1.70 mm/yr in the 2015 SSC model). This increase in mean slip rate has resulted in a change in another SSC model element called the equivalent Poisson hazard ratio (EPHR) that captures uncertainty related to time-dependent earthquake recurrence behavior. The change in mean EPHR for the Hosgri fault source due to the increase in mean slip rate is an increase of approximately 3%, from an EPHR of 1.20 in the 2015 SSC model to 1.24. In addition to the revision to the Hosgri fault source slip rate, the slip rate of the Los Osos fault source has been revised in this seismic update. The change in Los Osos fault slip rate is based on a new model of tectonic uplift rates along the central California coast as recorded by marine terraces. This new model provides more refined estimates of paleosea levels at the time of marine terrace formation based on the incorporation of local glacio-isostatic adjustment effects. Including the new uplift rate model in the Los Osos fault source slip rate calculations results in a decrease in mean slip rate compared to the 2015 SSC model of about 9% to 15%. The magnitudes of the changes in mean slip rate for the Los Osos fault source range between 0.02 and 0.04 mm/yr, which are an order of magnitude less than the 0.44 mm/yr change in mean slip rate for the Hosgri fault source. No changes to the mean EPHR for the Los Osos fault source were warranted.

A review of proponent models, methods and interpretations presented in public testimony for consideration in an update to the SSC model were reviewed as part of this assessment. The review found that while some models or model elements are used in regional seismic hazard assessments, they are not appropriate for direct input into the SSC model for site-specific seismic hazard analysis of a critical facility. Proponent interpretations of tectonic rates, fault geometries, and fault slip rates beneath DCP were found to be either considered in the 2015 SSC model, inconsistent with available information, or technically incorrect.

In PSHA, the ground-motion characterization (GMC) quantifies the ground shaking associated with seismic sources. The GMC model defines the median, aleatory variability, and epistemic uncertainty of ground motion. The ground-motion characterization for the 2015 study for DCP followed a partially non-ergodic approach as part of the 2015 Southwest United States (SWUS) model. In this current project, the median ground-motion model was evaluated in terms of (1) approach, (2) treatment of features such as location relative to the hanging wall, directivity, splay

ruptures, and complex ruptures, and (3) performance compared to recent preliminary empirical ground-motion data. Based on this evaluation, the median ground-motion predictions from the SWUS ground-motion model were found to be generally consistent with new empirical data, and comparisons of the median predictions from the DCP model to available non-ergodic ground-motion models also indicated consistent results. The aleatory variability model developed as part of the SWUS study was also evaluated. It was determined that the newly developed preliminary datasets are not sufficiently complete in terms of the metadata to be used to calculate updated components of aleatory variability for the large-magnitude and short-distance ranges of interest for DCP (e.g.,  $M > 5$  and  $R_{RUP} < 50$  km). Furthermore, components of the DCP aleatory variability model were compared to more recent studies. The model was found to be consistent in the approach, elements of the logic tree, and results in the magnitude and distance ranges of interest. Based on these conclusions, no changes are warranted for the median and aleatory variability models of GMC.

In 2015, site-specific adjustment factors were developed to adjust the SWUS GMC model to site-specific conditions at DCP. These site-specific adjustments were developed using analytical site-response analysis, as well as an empirical approach based on recordings at the plant. No new ground-motion data were recorded at the plant since the conclusion of the 2015 study. The site-adjustment approaches were reviewed, and no changes are warranted. A preliminary non-ergodic ground-motion modeling approach was applied to estimate the empirical site term at DCP and its regional and uncorrelated components. Results from the non-ergodic analysis indicate that the regional site term in the vicinity of DCP shows a below-average trend in ground motion consistent with that observed in the 2015 empirical site term at frequencies greater than 1 Hz. This consistency in the trends between the regional and the site-specific empirical terms supports and explains the 2015 site terms. The site term from the non-ergodic analysis was not adopted due to the preliminary nature of the dataset used and the preliminary nature of the analysis performed.

Probabilistic seismic hazard analysis computes the rate of ground-motion exceedance based on the rate of earthquakes and the probability distribution of ground shaking. It permits consideration of all potential events, event-to-event variability, and uncertainties in the ground-motion modeling calculations. The findings from the evaluation of the 2015 SSC and GMC models guided the approach taken to perform the seismic hazard update. The SSC model evaluation resulted in changes to the slip rates associated with the Hosgri and Los Osos fault sources, and a change to the EPHR for the Hosgri fault source. No changes to the median and the aleatory variability of the SWUS ground-motion model were recommended. Because the recommended changes to the models are limited to SSC parameters that affect the rate of earthquakes from specific seismic sources, the updated hazard can be captured through scaling the 2015 PSHA hazard results. The same scaling approach is justified for the recommended adjustment of the EPHR for the Hosgri fault. This scaling process was performed for 17 spectral frequencies from 100 Hz to 0.333 Hz. Scaled updated mean hazard curves for each spectral frequency for the reference rock horizon were computed, and the resulting uniform hazard spectra and ground-motion response spectrum (GMRS) were estimated. A comparison of these results with the previous 2015 UHS results shows an increase in ground motions of about 5–7% in the lowest frequencies range and about 3–4% in the intermediate to high-frequency ranges.

The probabilistic risk analysis (PRA) is based on the control-point horizon's hazard curves and ground motions. For DCP, the hazard curve for the 5 Hz spectral frequency is used as the input

into the PRA. Hazard curves for the control-point horizon were estimated based on the hazard-curve ratio factors developed from the reference rock horizon scaling results given that the original site adjustment factors were found to be applicable for this evaluation. As a result, hazard-curve ratio factors based on the reference-rock hazard curves were directly applied to the control-point hazard curves from the 2015 study. Scale factors for the hazard values (i.e., hazard value ratio of the scaled results divided by the original 2015 results) were selected based on the evaluation of scale factors at seven select frequencies at the  $10^{-5}$  hazard level.

Impacts of the changes in scaled hazard for plant risk were evaluated utilizing the current Diablo Canyon PRA model of record, a full-scope model including internal events, internal flooding, internal fire, and seismic hazards. This model was recently updated in August of 2023 and includes updates to equipment reliability data and resolutions to industry peer-review comments. The results of this assessment indicate that the total core damage frequency (CDF) and large early release frequency (LERF) for DCPD remain below region II risk criteria from Regulatory Guide 1.174 Revision 3 (total CDF and LERF are less than  $10^{-4}$  yr<sup>-1</sup> and  $10^{-5}$  yr<sup>-1</sup>, respectively) for all the hazard scaling factors used in this assessment.

In summary, the 2023 seismic update found that continued research since 2015 has identified minor changes in the seismic source characterization of hazard-significant seismic sources. Those changes were included in the updated seismic hazard and risk. The risk assessment indicates that total core damage frequency (CDF) and large early release frequency (LERF) for DCPD remain below region II risk criteria from the US Nuclear Regulatory Commission Regulatory Guide 1.174 Revision 3.

# 1. INTRODUCTION

## 1.1. BACKGROUND AND PREVIOUS STUDIES

Since the start of operation of the Pacific Gas & Electric Company's (PG&E) Diablo Canyon Power Plant (DCPP) (1984 and 1985 for Units 1 and 2, respectively), numerous studies and updates of the seismic hazard and seismic risk have been performed. In addition, PG&E has maintained a Geosciences Department and the Long-Term Seismic Program (LTSP) focused on monitoring earthquakes, keeping track of scientific studies and state of knowledge on earthquake sources and hazards applicable to the site, and has directed and funded new research through collaboration with a range of research institutions and agencies, such as the U.S. Geological Survey. To sustain this work, PG&E and the U.S. Nuclear Regulatory Commission (NRC) agreed to an operating license commitment to continue the Geosciences Department and LTSP for the duration of the plant's operating licenses (PG&E Letter No. DCL-91-091).

In addition to the studies performed by PG&E under the LTSP, additional studies related to the seismic hazards applicable to the DCPP were performed by PG&E following the recommendations of the California Energy Commission (CEC) in response to State of California Assembly Bill 1632. These were performed between 2006 and 2014 (PG&E Letter No. DCL-14-081) and included new information characterizing seismic sources, velocity structure, and reliability of the plant. Also, in responding to the NRC's Request for Information related to Recommendation 2.1 (Seismic) of the Near-Term Task Force (NTTF) Review of Insights from the Fukushima Dai-Ichi Accident (NRC, 2012b), PG&E updated seismic hazard and seismic probabilistic risk assessments for DCPP (PG&E Letter No. DCL-18-027, 2018). This work included a probabilistic seismic hazard analysis (PSHA) that was completed in 2015. The PSHA followed the NRC guidelines for a Senior Seismic Hazard Analysis Committee (SSHAC) Level 3 hazard study described in NUREG-2117 (NRC, 2012a) and included a Participatory Peer Review Panel (PPRP) to provide the confident technical basis and mean-centered estimates of the ground motions. This multi-year study addressed all aspects of the seismic hazard at the DCPP and included a comprehensive summary of studies and databases used to support the seismic hazard assessment for the plant (PG&E, 2015a, 2015b). In December 2016, the NRC stated that the reevaluated seismic hazard for DCPP (i.e., the results of the PSHA) is suitable for use in the other seismic assessments associated with the 10 CFR 50.54(f) letter. The seismic hazards developed through the PSHA served as input to the updated DCPP seismic probabilistic risk assessment (SPRA). In January of 2019, the NRC stated that the updated SPRA met the requirements specified in the 10 CFR 50.54(f) letter and that no further response or regulatory actions were required (NRC No. ML18254A040).

Since the completion of the AB 1632 and NTTF Recommendation 2.1 studies, monitoring of earthquakes and targeted research under the ongoing LTSP have continued, with updates provided to the California Public Utilities Commission (CPUC) Independent Peer Review Panel (IPRP) and the Diablo Canyon Independent Safety Committee (DCISC). These continuing studies and reviews have served to keep DCPP current on seismic activity around the plant, including new sources, ground motion and hazard data or methods that could potentially impact hazard or risk at the plant, as well as advance the science and engineering so that the earthquake risk at DCPP can be better quantified.

## **1.2. SCOPE AND OBJECTIVES**

This project provides a seismic hazard assessment update for DCPD to satisfy the covenant for the performance of a seismic update associated with the State of California Senate Bill (SB) 846 plant license extension. SB 846 states that the loan agreement with the California Department of Water Resources (DWR) must include:

*A covenant that the operator shall conduct an updated seismic assessment.*

The objective of this project is to address this covenant with an updated seismic hazard and risk assessment no later than the end of August 2024, which is prior to the expiration of the current operating licenses for DCPD.

## **1.3. OVERVIEW OF PROCESS**

Performance of a seismic assessment for the area in proximity of the DCPD addressed several important considerations: (1) the previously completed PSHA, (2) recent seismic monitoring, and (3) new or improved data, methods, or research relevant to seismic hazard and risk assessment of the DCPD developed by the research community and under the LTSP. Since the completion of the SSHAC Level 3 in 2015, there has been limited time for new methodologies to mature or information to be collected or developed. With these considerations, PG&E followed an incremental hazard assessment process that first evaluated new information and models (i.e., comparison of hazard inputs). The project team then reviewed if any hazard-significant discrepancies are found with the previous 2015 study; if updated inputs are outside of the center, body, and range of the previous study; and if evaluators do not have confidence in their assessment.

During the 19 September 2023 seismic hazard update meeting it was found that new information indicated changes to the estimated slip rates and probability of activity on hazard-significant faults. Given that hazard could potentially increase due to seismic source characterization (SSC) model updates, it was prudent to evaluate the impact of model changes through updated logic trees, hazard calculation, and risk assessment. Since the changes were limited to slip rates, the hazard was modified using scale factors for various combinations of branches of the logic tree. The changes in hazard were input into the probabilistic risk assessment (PRA) model to assess how the changes in hazard impact key risk metrics.

The DCISC and DWR were invited to be observers during the performance of this assessment and are herein referred to as the stakeholders.

## **1.4. REPORT CONTENTS AND ORGANIZATION**

The report contains sections specific to the seismic hazard evaluation, with supplemental information provided in appendices. Chapter 2 provides an overview of the process and the organization of participants involved. Chapter 3 provides key tasks and activities performed in the study. The remaining sections describe the technical aspects of the project, as follows: Chapter 4 presents ground motion data in the form of earthquake catalogs; Chapter 5 provides a review of the 2015 SSC for the DCPD, review of new technical information relevant to the SSC model and updates to the 2015 SSC model; Chapter 6 describes the evaluation of proposed SSC models and the opinions about the 2015 model presented in public testimony; Chapter 7 presents the evaluation of the ground-motion characterization (GMC); Chapter 8 summarizes the

evaluation of vertical ground motion; and Chapter 9 describes the evaluation of the site characterization. Hazard scaling and results are presented in Chapter 10, the control point for risk assessment is discussed in Chapter 11, and the probabilistic risk assessment (PRA) update is presented in Chapter 12. The summary and results are provided in Chapter 13. Finally, Chapter 14 lists the references for the report.

## 2. PROJECT PROCESS

### 2.1. IMPLEMENTATION OF PROCESS

The SB-846 covenant provides no criteria for the technical approach or scope for the updated seismic assessment. Without this guidance, it was decided to follow a process modelled on essential features of the Senior Seismic Hazard Analysis Committee (SSHAC) framework, which is the requirement for hazard assessments performed for the NRC. The NRC SSHAC process is defined in NUREG/CR-6372 (Budnitz et al., 1997) and NUREG-2117 (NRC, 2012a), with the latest guidance provided in NUREG-2213 (NRC, 2018). The SSHAC framework provides for varying levels of effort and permits adjustments based on the specific needs of a particular project.

The essential features of a SSHAC study are provided in Section 2.1 of NUREG-2213 (NRC, 2018) and are summarized as:

- Clearly defined roles for all participants
- Objective evaluation of data, models, and methods proposed by the larger technical community that are relevant to the hazard analysis
- Integration of the data into hazard models that represent the center, body, and range of technically defensible interpretations considering the evaluation process
- Documentation that provides a complete and transparent record of the evaluation and integration
- Independent participatory peer review

These activities were performed as prescribed in the project plan, “Project Plan for 2023 DCPD Updated Seismic Assessment,” which was developed during the process. The project plan identifies the scope, organization, deliverables, schedule, quality requirements and application of the SSHAC process. The project plan is reproduced in Appendix A.

The “Evaluation” portion, as defined on Figure 2-1, compared the 2015 model against potential new information to determine if the “Integration” step was necessary or warranted. Hazard sensitivities that highlight which parameters in the 2015 models are most hazard-significant were used to prioritize which data, models and methods were to be reviewed for this seismic hazard assessment. Based on evidence of potential impacts to the hazard, a limited “Integration” step was performed. Instead of running a full PSHA, given the changes as will be described in later sections, a scaling of the hazard was performed that provides insight into potential results if changes are warranted. The “Documentation” activity follows the previous two activities and culminates with this report.

A unique aspect of this project was that participatory review occurred at two levels. The first level was the Participatory Peer Review Panel (PPRP), which is standard in a SSHAC study. The second level was provided by a team of External Reviewers, which focused on the process. In this study, interaction with stakeholders took place during the development of the study plan, summary of the evaluation, and once the scaling of the hazard calculations was completed. Stakeholders had the opportunity to observe and provide written feedback.

Seismic hazard SSHAC studies typically do not include an evaluation of the seismic performance of the facilities, as this is implemented as a next phase of study using the SSHAC results as hazard input. However, this study is an incremental update to an earlier robust SSHAC study and SPRA evaluation, and as a result, the risk impact on structures, systems, and components important to safety due to changes in hazard could be compared in a screening approach. Therefore, a risk screening evaluation is included in this study that focuses on key seismic risk metrics used for previous evaluations of the plant.

## **2.2. ROLES AND RESPONSIBILITIES**

Participants for the seismic update cover the range of technical specialties required for the full scope of the hazard evaluation and experience implementing the SSHAC process for nuclear power plant assessments. Figure 2-2 provides an overview of the project organization.

### **2.2.1. *Technical Integration (TI) Teams***

The TI Teams were responsible for reviewing and analyzing the SSC and GMC models and logic-trees, which together defined inputs to the 2015 Diablo Canyon SSHAC Level 3. Three participants, Steve Thompson, Linda Al Atik, and Nick Gregor fulfilled the roles and responsibilities for the SSC and GMC TI Teams (Figure 2-2). Each TI Team member objectively examined the available data and various models for the 2015 study, challenged the technical bases and underlying assumptions of the models, reviewed data and models published since the 2015 study and, in some cases, tested models against observations. They compared these models to the full range of data, models, and methods that exist in the technical community.

### **2.2.2. *Hazard Analyst***

The hazard analyst was responsible for executing all PSHA scaling calculations for sensitivity studies according to the Hazard Input Document (HID) developed by the SSC TI Team. Based on the evaluation, there are no recommended adjustments for the GMC model by the GMC TI team. Nick Gregor performed these responsibilities as the hazard analyst for the project (Figure 2-2).

### **2.2.3. *Probabilistic Risk Assessment (PRA) Analyst***

The probabilistic risk analyst was responsible for assessing how changes in the hazard assessment impact key risk metrics. Nathan Barber performed these responsibilities (Figure 2-2).

### **2.2.4. *Project Technical Integrator***

The Project Technical Integrator (PTI) was responsible for ensuring coordination and compatibility between the GMC and SSC studies being conducted. This role required a technical expert with knowledge of the SSHAC process, GMC and SSC studies, and site-specific application for site response effects. Albert Kottke performed these responsibilities (Figure 2-2).

### **2.2.5. *Project Manager***

The Project Manager (PM) was responsible for managing the schedule, budget and coordinating the execution of the project. In addition, the PM interacted with the Project Sponsors and the



Management Support Team to keep them informed on the progress. This role was filled by Jennifer Donahue (Figure 2-2).

### **2.2.6. Management Support Team**

Members of the Management Support Team were responsible for the project logistics and coordination of the execution of the project. Their responsibilities included contract management and maintaining clear lines of communication between the Sponsors, TI Teams, PPRP, External Reviewers and DCCP. The Management Support Team also attended working meetings and reviewed technical documents. These roles were provided by Jeff Bachhuber and Jearl Strickland (Figure 2-2).

### **2.2.7. Project Sponsors**

The Project Sponsors provided financial support and own the results of the study in the sense of property ownership. The Project Sponsors, Albert Kottke and Chris Madugo (Figure 2-2), attended project meetings, reviewed project documents, and facilitated data gathering.

### **2.2.8. Participatory Peer Review Panel (PPRP)**

The PPRP was responsible for *technical* and *procedural* reviews to ensure the approach was implemented per regulatory guidance. For the technical reviews, the PPRP ensured that the full range of data, models, and methods had been duly considered in the assessment, and all technical decisions were adequately justified and documented. For the procedural reviews, they ensured that the process conformed to the requirements of level commensurate with a SSHAC-style approach. They also ensured adequate oversight and assurance that the *Evaluation* aspects of the TI Teams' assessments had been performed appropriately.

For the Diablo Canyon Updated Seismic Assessment project, the PPRP's participation began at the initial kick-off meeting where they provided input to the development of the work plan; they then reviewed the work plan and provided comments. Throughout the process, they participated in the scheduled conference calls and reviewed the preliminary findings. The PPRP addressed concerns of the TI Team, guided selection of scaling analysis, reviewed SSC, GMC, site amplification, and PRA update developments, and reviewed the scaling results. They revised the draft report and concurred with the final report. The PPRP members for this seismic update were Thomas Rockwell and Norman Abrahamson (Figure 2-2).

### **2.2.9. External Reviewers**

The external reviewers were responsible for the *procedural* review of the approach taken. The reviewers, who are experts with SSHAC methodology and PSHA experience, provided external review of the process, methodology and documentation of the project. They ensured that the approach was consistent with the intent of the covenant. This was achieved through review of the workplan, participation in meetings, and review of the draft report. The external reviewers for this seismic update were engaged through the University of California Los Angeles Garrick Risk Institute and included Ali Mosleh, Yousef Bozorgnia, and Ralph Archuleta (Figure 2-2).

### 2.3. Schedule

The Diablo Canyon Updated Seismic Assessment project began in April 2023 and concluded on 1 February 2024. A summary of the schedule is found in Table 2-1.

**Table 2-1. Schedule for the Diablo Canyon Updated Seismic Assessment**

<b>Stage</b>	<b>Date</b>	<b>Action</b>
Planning	April 2023	Gather stakeholder feedback
	May 2023	Initiate data collection and review of background documentation
Evaluation	1 June 2023	Work Commences
	26 June 2023	<b>Kick-off Meeting</b>
	21 July 2023	<b>Working Meeting #1:</b> Present summary of existing models and data and develop project plan
	19 September 2023	<b>Workshop #1:</b> Present comparison of new or improved hazard significant data, methods and models and recommendation for next steps
	7 November 2023	<b>Workshop #2:</b> Present model updates and decide hazard and risk processes next steps
Documentation	7 December 2023	<b>Results Presentation:</b> Present hazard and risk results
	18 December 2023	Draft report to PPRP, External Reviewers and Regulator Observers
	10 January 2024	Review comments due
	22 January 2024	Final report to PPRP
	1 February 2024	PPRP closure letter, Tech Editing Complete, Report to stakeholders

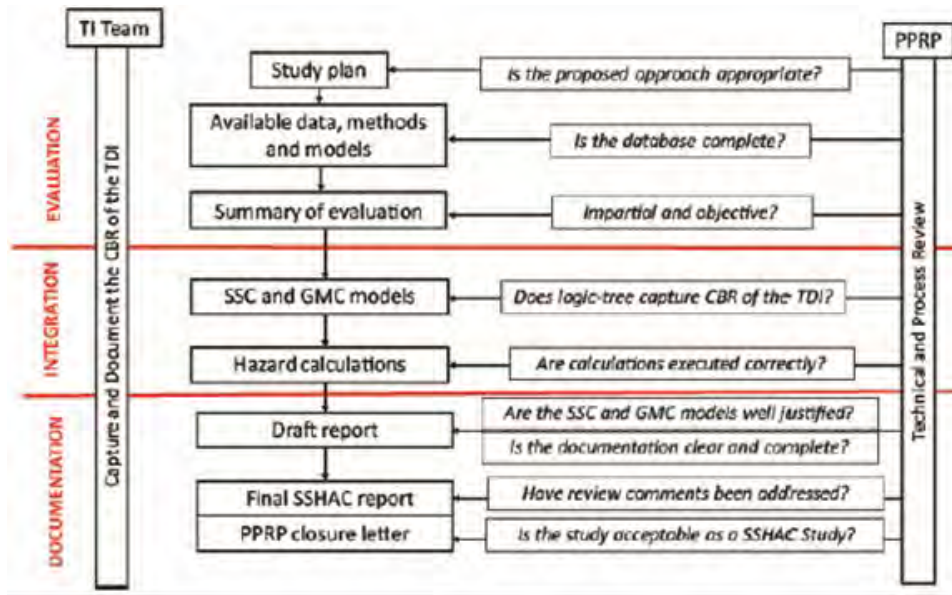
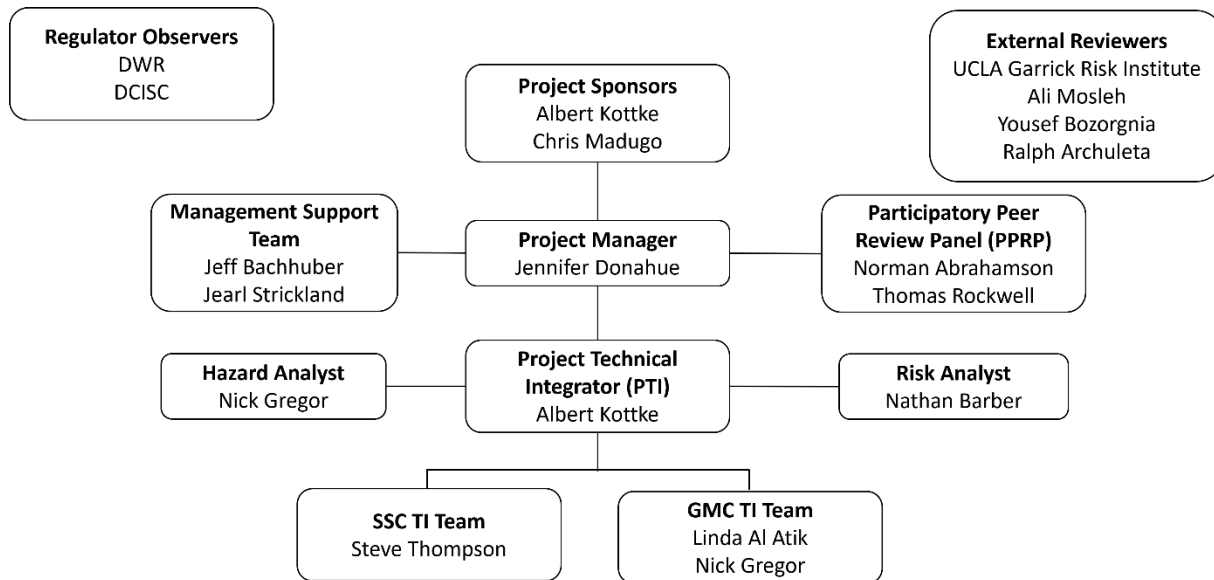


**Figure 2-1. Flowchart for a SSHAC Level 1 PSHA study, indicating the review criteria and potential questions at each point of engagement by the PPRP (from NUREG-2213 [NRC, 2018], Figure 3-2)**



Note: Specialty Contractors, Resource Experts, and Proponent Experts are not included on this project

**Figure 2-2. Organizational Chart for the Diablo Canyon Updated Seismic Assessment**

### 3. KEY TASKS AND ACTIVITIES

This chapter discusses the key tasks that fulfill the main four components associated with the SSHAC study: evaluation, integration, participatory peer review, and documentation as described in Section 2.1.

#### 3.1. DEVELOPMENT OF PROJECT PLAN

An initial project plan was developed by the PG&E Geosciences team that outlined a potential path forward in responding to the SB-846 covenant. Development of the plan was informed by the tornado diagram that was developed as part of the 2015 study, as well as knowledge of advancements in source characterization and ground-motion modeling. A tornado diagram quantifies the impact on the ground motion of alternative branches in the logic tree. Logic tree branches are used to capture epistemic uncertainty, which can be reduced through gaining more information. The plan identified the following potential topics:

- Refinement of Inputs for the Seismic Source Characterization (SSC):
  - New data, models, or methods with the potential to change hazard-significant seismic source parameters, especially for seismic sources closest to the plant, including the Hosgri, Los Osos, San Luis Bay and Shoreline faults, and the Background source. Tornado plots from the 2015 study can be used to identify hazard-significant source parameters and help understand the impact of parameter changes.
  - Updated earthquake catalog—over 6000 earthquake events have been recorded by the PG&E Central Coast Seismic Network (CCSN) since 2015 and may inform fault geometry and rates of areal source zones
  - Background model—accounts for earthquakes that occur off recognized fault sources or secondary low-slip-rate sources
- Refinement of Parameters for the ground-motion characterization (GMC):
  - Review of ground-motion models (GMM) to include: median, variability, and uncertainty
  - Directivity models
  - Updates to the local earthquake catalog, in particular, the four events within 100 km with a magnitude greater than **M** 4
  - Non-ergodic models and their potential application—these models are still being developed, but many advancements have been made and are considered
- Additional Topics:
  - Potential updates to empirical site amplification models—there are two instruments near the project site; one is on the site property and records triggered events, the other is off-site and provides a continuous record
  - Recent modifications to the software HAZ used to compute the PSHA—review modifications made to the code HAZ and impact of those changes. The end goal of this task is to run old hazard inputs on a new Fortran program executable.
  - Consideration of knowledge gained from recent global large earthquakes that have been well instrumented

- Updates to the Probabilistic Risk Assessment (PRA):
  - Assessment of the risk impact—review of the change in seismic hazard and assessment of the change in risk to operation of the plant expressed in terms of core damage frequency and large early-release frequency

After development of an initial project plan, it was presented to both DCISC and DWR for their input.

This SB-846 updated seismic assessment was conducted using working meetings, workshops, and other technical activities as defined below. Working meetings were held in person to facilitate the exchange of information and ideas. Bi-weekly meetings with the TI team were used for tracking ideas and study progress, but also sharing information to improve integration.

### **3.2. IDENTIFICATION OF ISSUES**

A key task of the project was to identify which elements of the SSC, GMC, and PRA models may have changed to enable the TI teams to focus their efforts on the development of those parts of the hazard review. Identifying the greatest contributors to the overall uncertainty allowed data-compilation and data-collection efforts to be as focused as possible. To meet these objectives, the TI teams met during a kick-off meeting on 26 June 2023 to identify and begin to compile pertinent datasets through discussion of past studies and visualization of the current state of knowledge. During a follow-up working meeting on 21 July 2023, the previous hazard study was discussed in detail and potential areas of improvement or reconsideration were identified. The information presented in this meeting was used to update the project plan and focus on topics that were both hazard-significant and have new information available since the 2015 hazard model.

### **3.3. EVALUATION OF MODELS AND METHODS**

In similar fashion to the SSHAC process, for this project it was essential to review the center, body, and range (CBR) of the technically defensible interpretations (TDI) of both new and previously available data, models, and methods. As will be discussed in the following chapters, the first task of the TI Teams was a documentation review of what methods and models were used in 2015 and what new information has become available since that time. Consistent with the SSHAC process, not all new material was incorporated into the models. Each TI Team, with oversight from the PPRP, evaluated new data and applied appropriate criteria for inclusion. This step of determination of inclusion is supported in NUREG 2213 (NRC, 2018).

*“The imperative to capture the full range of the integrated distribution should not lead the experts doing the model-building to include alternatives in their models only as a means to convey the impression of broad capture of epistemic uncertainty. The integration process need not be inclusive of all available interpretations and those interpretations deemed not credible by the TI Team must be culled from analysis.”*

While the TI Team members reviewed a broad range of data, models and methods in their review of published and unpublished literature, including from public testimony, they included only models and parameter values defensible for site-specific hazard and risk analysis in their final analyses. These decisions were reviewed by the PPRP team and documentation of these

decisions is included in this report.

As part of the SB-846 updated seismic assessment of the DCP, the team met on 19 September 2023 to discuss the findings from the “Evaluation” stage of the project. These evaluations considered new information that might influence the seismic source, ground motion, and site effects characterization. The purpose of this meeting was to determine if new information was available that warranted further study and adjustment of the models developed during the 2015 SSHAC study. The following conclusions were reached:

- New information indicated changes to the slip rates and probability of activity on hazard-significant faults:
  - Higher mean Hosgri slip rate than in 2015 model based on new data from one of four slip rate sites used in 2015 model, updated regional geodetic models and testing of uncertainties for 2015 offshore rates
  - Lower mean slip rate for the Los Osos fault based on revision of Irish Hills uplift rates from post-2015 marine terrace study
- No significant change in seismicity rate based on the post-2015 earthquake catalog
- No need to modify the ground-motion characterization, as there is good agreement with the new data and models for the median and epistemic uncertainty
- No need to modify the site effects, as there are no additional data available at the plant location and preliminary assessments indicate agreement with non-ergodic models

Based on the new information presented during the meeting regarding potential changes to the hazard, it was established that a new estimate of the PRA model was appropriate. Furthermore, additional work was conducted to examine the potential of using spatially varying non-ergodic models and weak-motion data to develop new site factors.

### **3.4. UPDATED HAZARD AND RISK**

Scaling of the hazard was performed for this project. The hazard scaling was based on the new HID and was included in the presentation to the project team at a meeting in Oakland, CA on 7 November 2023. Important contributors to the hazard results were assessed and scaling factors were provided from the SSC Team to the GMC Team. These analyses identified the SSC issues of greatest significance to the mean hazard at the annual frequencies of interest.

Review of the site amplification factors was also performed for this project. Upon assessment of several components, including the use of non-ergodic site amplification factors, changes to the DCP site amplification factors were discussed in team meetings on November 7 and December 7, 2023.

The Diablo Canyon PRA model was utilized to assess the impact on operational risk as a result of hazard scaling factors. These scaling factors were used to change the hazard input information used in the seismic PRA model and resulted in new estimates of seismic core damage frequency (CDF) and large early release frequency (LERF).

### **3.5. DOCUMENTATION**

For this project, draft and final reports were prepared. Due to the accelerated schedule for the project, the draft report was completed immediately after presentation of results. The draft report

was provided to the Technical Editor, PPRP, External Reviewers, and the DCISC for review on 18 December 2023. Minor comments were tracked in the electronic documents whereas major comments were provided separately. The TI team addressed the comments from the PPRP and External Reviews through documented responses, and changes were made to the report as necessary. Once all comments were incorporated or resolved, the final draft report was provided to the PPRP and External Reviewers for final review and preparation of the closure letter. The PPRP's review and closure letter fulfilled the review process for the project. The final report was issued on 1 February 2024.

## 4. GROUND MOTION DATA

### 4.1. GROUND MOTION CATALOGS

For the Southwest United States (SWUS) study (GeoPentech, 2015), both empirical datasets and simulation datasets were evaluated. These evaluations were for the development of both the median ground-motion model and the sigma model. Given that the SWUS model was for both DCPD and Palo Verde, with different controlling seismic sources and general tectonic environments (GeoPentech, 2015), a dual focus on empirical datasets was performed. The SWUS study evaluated four primary datasets:

- NGA-West2 (Ancheta et al., 2014)
- Dawood et al. (2015) Japanese database
- Residual database from earthquakes in Taiwan described in Lin et al. (2011)
- Reference Database of Seismic Ground Motion in Europe (RESORCE) as described in Akkar et al. (2014c)
- Arizona earthquake database (Kishida et al., 2014)

For DCPD, only the first three databases were evaluated given that the other two databases were focused on normal faulting events and local Arizona earthquakes that are not relevant for the DCPD site. The NGA-West2 database was used for the development of the median ground-motion model. The Dawood et al. (2015) database was evaluated for potential hanging-wall effects. However, given its sparse data distribution, it was ultimately not used in the development of the hanging-wall model. Finally, the Lin et al. (2011) database was used for the development of the aleatory sigma model.

It should also be noted that the ground-motion recordings from two additional well-recorded normal faulting earthquakes not contained in the NGA-West2 database were also processed and evaluated as part of the SWUS study. However, these events, being normal mechanism events, were focused on the Palo Verde ground motions from the SWUS study and not the DCPD model.

Since the completion of the SWUS study, considerable new empirical data from crustal earthquakes in active tectonic regions have become available. Note, however, that there have not been any moderate- to significant-sized earthquakes along the Central Coast of California near DCPD during the past 8 years. The next version of the NGA project for crustal earthquakes (NGA-West3) was initiated in 2023. Currently, the compilation, processing, and estimation of metadata information is being conducted and is expected to continue through 2024. However, for this current sensitivity evaluation for DCPD, a preliminary version of the working NGA-West3 database was obtained to perform comparisons between the newer empirical data and the SWUS median ground-motion models. It should be noted that, given the preliminary status of the NGA-West3 database and the expectation that a significant amount of additional data will eventually be compiled and included in the final NGA-West3 database when released in the future, these evaluations are preliminary in nature and should be revisited when the final NGA-West3 database is released.

Recently, in February 2023, several large crustal earthquakes occurred in Türkiye. Quality recordings of these events (Kahramanmaraş earthquake sequence) were collected throughout the region, generating a large dataset of strong ground motions. The data from three of these events



are being included as part of the NGA-West3 project and a preliminary database including metadata information was retrieved for this study.

Separate to the efforts being conducted for the NGA-West3 project, ground-motion recordings were obtained and processed for earthquakes located within about 320 km of DCPD since the ending date of the NGA-West2 database (i.e., Bozorgnia et al., 2014). Several of these events will eventually be included in the NGA-West3 database. This preliminary database was also included in the evaluation of the SWUS median ground-motion model.

Additional details and information for these three empirical datasets of events since the SWUS and NGA-West2 projects are presented in the next sections of this report.

#### 4.1.1. Preliminary Turkish Data

In February of 2023, a series of several large and destructive crustal earthquakes struck the region of southeastern Türkiye and northern Syria. The regional tectonics in this area are dominated by the Dead Sea Transform and Eastern Anatolian faults. The **M** 7.8 mainshock event occurred on 6 February 2023 followed shortly on the same day by an **M** 7.6 aftershock. Following these two significant earthquakes, another aftershock (**M** 6.3) occurred on 20 February 2023. Overall, this region of Türkiye is well instrumented, with more than 100 strong ground-motion stations. A map from these three events with the recordings stations in the region is provided as Figure 4-1.

Given the significance of this dataset, the ground-motion data are being processed and included as part of the NGA-West3 project. To assist in this DCPD study, the preliminary data from these three events were also retrieved and evaluated. The event metadata from these three earthquakes are listed in Table 4-1.

**Table 4-1. Table of Events in the Türkiye Database Within the Sub-selection Search Parameters**

EQID	Event Name	Date	Magnitude	Z <sub>tor</sub> (km)	Mechanism	Number of Recordings R <sub>RUP</sub> ≤120km	Number of Recordings R <sub>RUP</sub> ≤15km
7001	Pazarcik	6 Feb. 2023	7.8	0.0	Strike-slip	83	30
7002	Elbistan	6 Feb. 2023	7.7	0.0	Strike-slip	52	0
7003	Yayladağı	20 Feb. 2023	6.3	4.0	Strike-slip	24	2

#### 4.1.2. DCPD Data

To supplement the NGA-West3 preliminary data, a search of ground-motion recordings from earthquakes within 320 km of DCPD that have occurred post NGA-West2 was performed. The earthquake epicenters and station locations based on these search criteria are plotted on Figure 4-2. As noted earlier, there are no new earthquakes in the immediate region around DCPD, nor are there any ground-motion recordings at DCPD based on this data retrieval. The initial database

is sub-selected to be consistent with the NGA-West3 preliminary dataset. Specifically, the events selected have magnitudes equal to or larger than 5.0, distances equal to and less than 250 km, and  $V_{S30}$  values equal to and larger than 250 m/sec. The sub-selection for distances less than 320 km (i.e., 250 km) is based on use of this data for the evaluation of the median GMM, the applicable range of the median GMM, and the range of significant contributing sources to the hazard at DCP. Given these sub-selection criteria, a total of seven events are retained. Note that one event, the 24 June 2020 earthquake SSE of Lone Pine is also contained in the NGA-West3 preliminary dataset and the NGA-West3 data will be adopted for the analysis. The details of these seven events are listed in Table 4-2.

The retrieved ground motions were processed using the automated *GMprocess* (Hearne et al., 2019) script. Although this script, and its implementation, follows a similar standard time history processing methodology as that used for the NGA-West projects, differences may be observed in the processed ground motions based on the specifics of the approaches (e.g., filter corners). However, for the subsequent preliminary residual analyses and observations presented later in this report, these differences are not expected to be significant. Restricting the data to stations within 15 km of the rupture significantly reduces the number of recordings, as indicated in the last column of Table 4-2. Also indicated in Table 4-2 are the event metadata information that are inferred (e.g., mechanism and Ztor depth).

**Table 4-2. Table of Events in the DCP California Database Within the Sub-selection Search Parameters**

EQID	Event Name	Date	M <sup>1</sup>	Mechanism <sup>2</sup>	Ztor (km) <sup>4</sup>	Number of Recordings	
						R <sub>RUP</sub> ≤120km	R <sub>RUP</sub> ≤15km
ci37908735 (8001)	SW of Santa Cruz Isl	5 April 2018	5.3	Strike-slip	5.28	53	--
ci38457687 (8002)	ESE of Little Lake	6 July 2019	5.5	Strike-slip	4.29	41	2
ci38457703 (8003)	E of Little Lake	6 July 2019	5.0	Strike-slip	6.96	15	--
ci38457847 (8004)	E of Little Lake	6 July 2019	5.4	Strike-slip	4.77	30	--
ci39493944 (8005)	SSE of Lone Pine	24 June 2020	5.8	Normal/Oblique	1.59 <sup>5</sup>	46	1
ci39645386 (8006)	SE of Ojai	20 Aug. 2023	5.1	Reverse/Oblique <sup>3</sup>	4.84 <sup>6</sup>	153	6
nc73799091 (8007)	ESE of Alum Rock	25 Oct. 2022	5.1	Strike-slip	6.38	201	9

<sup>1</sup> M = magnitude

<sup>2</sup> Mechanism implied from USGS event page fault plane solution.

<sup>3</sup> Mechanism from Temblor article (<https://temblor.net/temblor/ojai-earthquake-unrelated-to-tropical-storm-hilary-15466/>) and USGS event page (<https://earthquake.usgs.gov/earthquakes/eventpage/ci39645386/executive>).

<sup>4</sup> Inferred from empirical relationship given magnitude and mechanism.

<sup>5</sup> Estimate from NGA-West3 database.

<sup>6</sup> Taken as minimum between default value of 7.31 km and hypocenter depth of 4.84 km.

### 4.1.3. Preliminary NGA-West3 Data

For the evaluation of the NGA-West3 data, the working flatfile dated 28 July 2023 is analyzed ([https://www.uclageo.com/gm\\_database](https://www.uclageo.com/gm_database)). Note that this flatfile contains all of the data from NGA-West2 plus the additional (as of 28 July 2023) new data compiled after NGA-West2. The uniform NGA standard data processing methodology is applied to these new data and estimates of the metadata are also provided. Given the hazard-significant events for DCPD and the applicable range for the SWUS GMM, a sub-selection of this preliminary NGA-West3 data is performed. This sub-selection is focused on events with magnitudes equal to or greater than 5.0 and stations with distances less than 120 km. To be consistent with the approach used in the SWUS study, only stations with  $V_{S30}$  values equal to or greater than 250 m/sec are retained.

Based on the sub-selection of the primarily NGA-West3 data, a total of 14 events are selected. These are listed in Table 4-3 along with the metadata information and number of recordings with distances less than 120 km and 15 km, respectively, and  $V_{S30} > 250$  m/sec. The 14 December 2016 earthquake NW of the Geysers listed in Table 4-3 is identified as an induced earthquake and thus is not included in the analysis. All but two of the remaining events are strike-slip, with one reverse/oblique event NW of Brea and one normal/oblique event SSE of Lone Pine. The distribution of these data is plotted on Figure 4-3 as a function of magnitude and distance between the recording station and the rupture ( $R_{RUP}$ ). The distribution of the same event data as a function of  $Z_{TOR}$  (km) and magnitude is plotted on Figure 4-4. The foreshock  $M$  6.48 event from the Ridgecrest sequence and the mainshock  $M$  7.06 event both had observed surface rupture and thus have  $Z_{TOR}$  values of 0.0 km.

**Table 4-3. Table of New Events Added Since the NGA-West2 Database to the NGA-West3 Database Within the Sub-selection Search Parameters**

EQID	Event Name	Date	M	Ztor (km)	Mechanism	Number of Recordings	
						$R_{RUP} \leq 120\text{km}$	$R_{RUP} \leq 15\text{km}$
2013	NW of Mogul, NV	26 April 2008	5.01	0.85	Strike-slip	2	1
2023	Central California	21 Oct. 2012	5.29	5.86	Strike-slip	25	0
2025	WNW of Greenville, CA	24 May 2013	5.69	4.69	Strike-slip	8	0
1901	NW of Brea, CA	29 March 2014	5.09	2.87	Reverse/Oblique	346	31
1915	South Napa, CA	24 Aug. 2014	6.02	5.75	Strike-slip	336	11
2034	NNE of Upper Lake, CA	10 Aug. 2016	5.09	12.73	Strike-slip	17	0
2035	NW of The Geysers, CA	14 Dec. 2016	5.14	1.5 <sup>1</sup>	Strike-slip (Induced)	42	0
2036	SW of Hawthorne, NV	28 Dec. 2016	5.66	7.59	Strike-slip	21	0
2078	SSW of Petrolia, CA	23 June 2019	5.58	14.27	Strike-slip	30	2
2100	2019 Ridgecrest EQ Sequence	4 July 2019	6.48	0	Strike-slip	69	2

EQID	Event Name	Date	M	Ztor (km)	Mechanism	Number of Recordings	
						R <sub>RUP</sub> ≤120km	R <sub>RUP</sub> ≤15km
2101	2019 Ridgecrest EQ Sequence	5 July 2019	5.47	4.4	Strike-slip	47	2
2102	2019 Ridgecrest EQ Sequence	6 July 2019	7.06	0	Strike-slip	65	7
2072	SE of Bodie, CA	11 April 2020	5.24	8.63	Strike-slip	24	0
2074	Monte Cristo Range, NV Earthquake	15 May 2020	6.49	5.45	Strike-slip	30	0
2075	SSE of Lone Pine, CA	24 June 2020	5.8	1.59	Normal/Oblique	45	1

<sup>1</sup> Hypocenter depth (km)

#### 4.1.4. Simulation Data

As part of the SWUS study, numerous numerical simulations were performed to enhance the empirical dataset, and to develop ground-motion estimates for hanging wall (HW) sites and splay and complex earthquake ruptures. These simulations were performed using the SCEC broadband platform (BBP) (Maechling et al., 2015). To summarize, the focus of those simulations included four main topics:

- Magnitude and scaling of near-fault ground motions
- Rules for estimating ground motions from splay ruptures
- Rules for estimating ground motions from complex ruptures
- Magnitude scaling and HW effects from moderate magnitude events (**M** 5–6)

For the SWUS study, several simulation procedures were used based on version 13.6 of the BBP. Currently the BBP is on version 22.4 (September 2022) with the specific changes related to each release version documented on the SCEC BBP repository website (<https://www.scec.org/software/bbp>). The distribution of simulation events performed as part of the SWUS study is plotted on Figure 4-5.

The open-source framework of the SCEC BBP allows for any user to conduct numerical simulations. These simulations are not required to be collected on a repository and thus, it is plausible that additional simulations applicable and/or of interest for DCPD may have been conducted by others in the past eight years. Nonetheless, to our knowledge no additional simulations have been performed using the SCEC BBP or other simulation procedures for application to DCPD. Future evaluations could make use of the SCEC BBP for additional evaluations.

Following the SWUS study, SCEC has also embarked on a regional (i.e., California-wide) 3D simulation program called CyberShake (<https://www.scec.org/software/cybershake>). CyberShake is a physics-based numerical simulation program developed primarily for the purpose of calculating probabilistic seismic hazard curves for sites in California. For these calculations, which take advantage of superpower computing platforms, the ground motions are numerically simulated given an adopted 3-D velocity structure model, as well as a seismic source

characterization model. For a given site location, the PSHA is computed based on the occurrence of earthquakes, including their rates of occurrence, on specific faults and the resulting numerical simulation of the ground motions given the earthquake and the 3-D velocity structure.

These simulations, given their large regional nature and adopted 3-D velocity structure, are not replacements for a fully site-specific PSHA study such as the one performed for DCPD. These simulations are limited by their 3-D velocity structure and are primarily valid for spectral periods of 1 sec and longer. As an example, in 2017, a CyberShake simulation was performed for the Central Coast region of California, shown by the pink polygon on Figure 4-6. The drop pin markers of various colors shown on Figure 4-6 are the locations for which the hazard curves were computed. The central coast 3-D velocity structure model used for this simulation has a minimum shear wave velocity of 900 m/sec. For the SSC model, the UCERF2 ERF model (Field et al., 2008) was implemented. Both the velocity structure and the SSC used in the CyberShake study are different than the SSHAC Level 3 SSC and the well-studied velocity structure for DCPD. Given these differences, and the lesser importance for DCPD of ground motions with spectral periods greater than 1 sec, the CyberShake hazard curves and ground motions developed for the 2017 Central Coast simulation were not evaluated in this study, but could be evaluated in future work or if longer spectral periods become more important for DCPD.

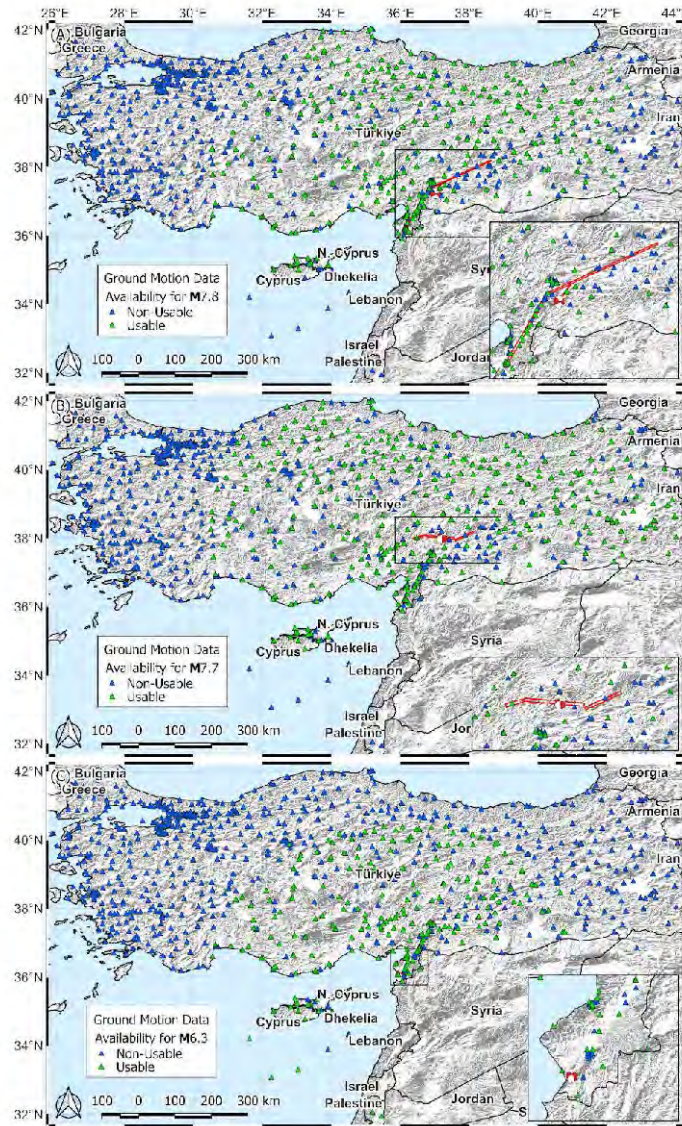


**Figure 4-1. Map showing the surface projection of the fault plane (red lines) and ground-motion recording stations (triangles) from the three large earthquakes of the Kahramanmaras event sequence (from GEER Association Report 082, 2023, Figure 3.2).**



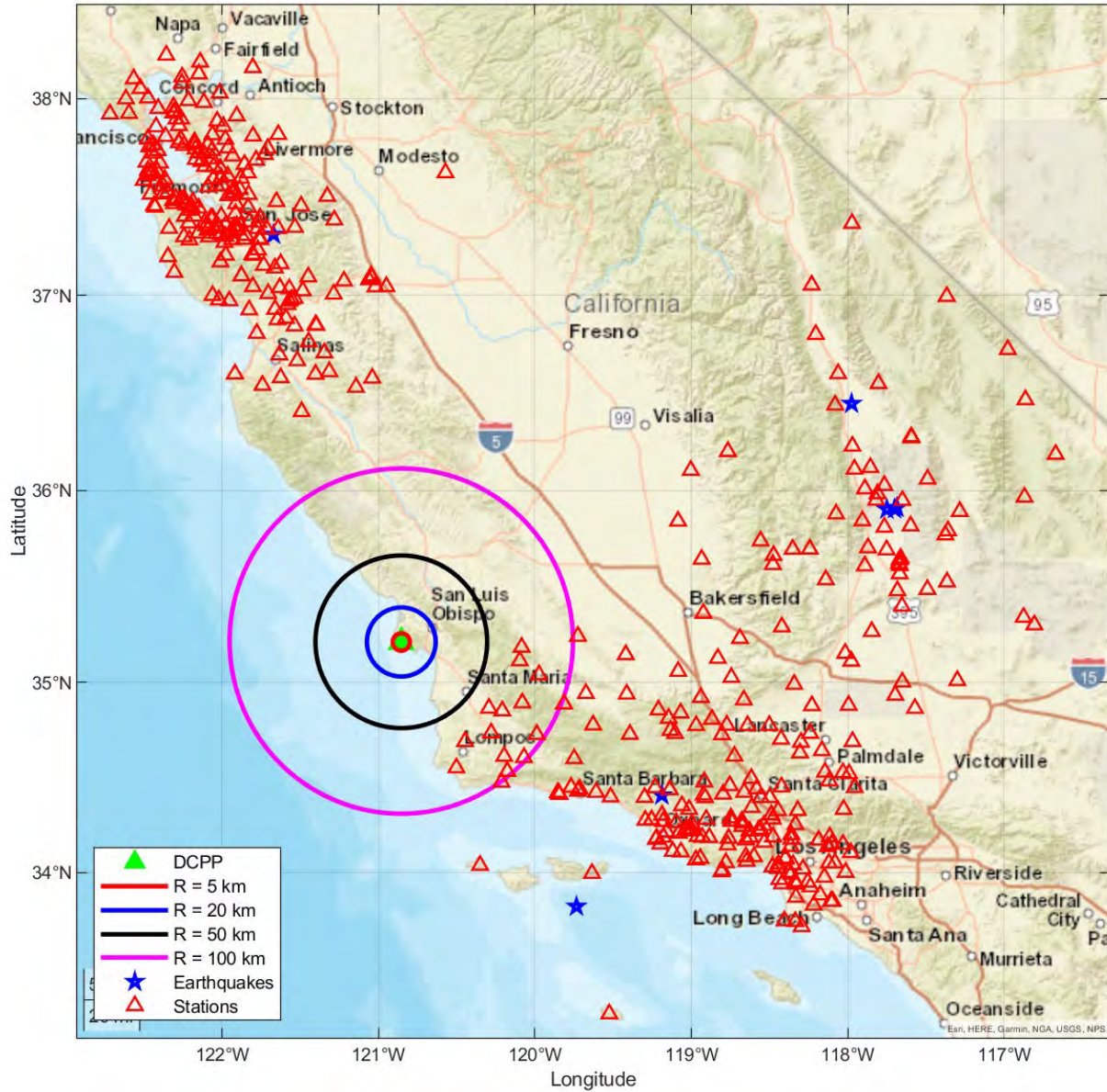


**Figure 4-2. Earthquake epicenters (blue stars) and ground-motion recording station locations (open red triangles) for the supplemental DCPD California empirical catalog**

### NGA-West3 Database: New Events since NGA-West2

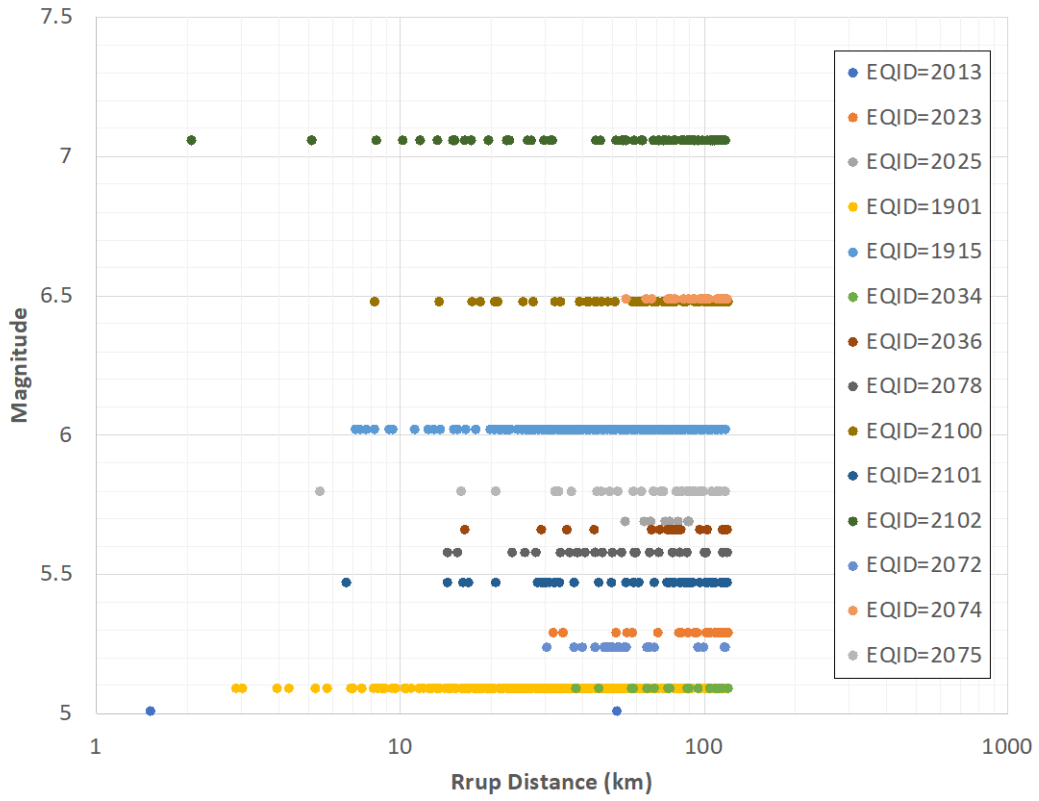


**Figure 4-3. Distribution of NGA-West3 data considered in the evaluation plotted as a function of rupture distance and magnitude**



### NGA-West3 Database: New Events since NGA-West2

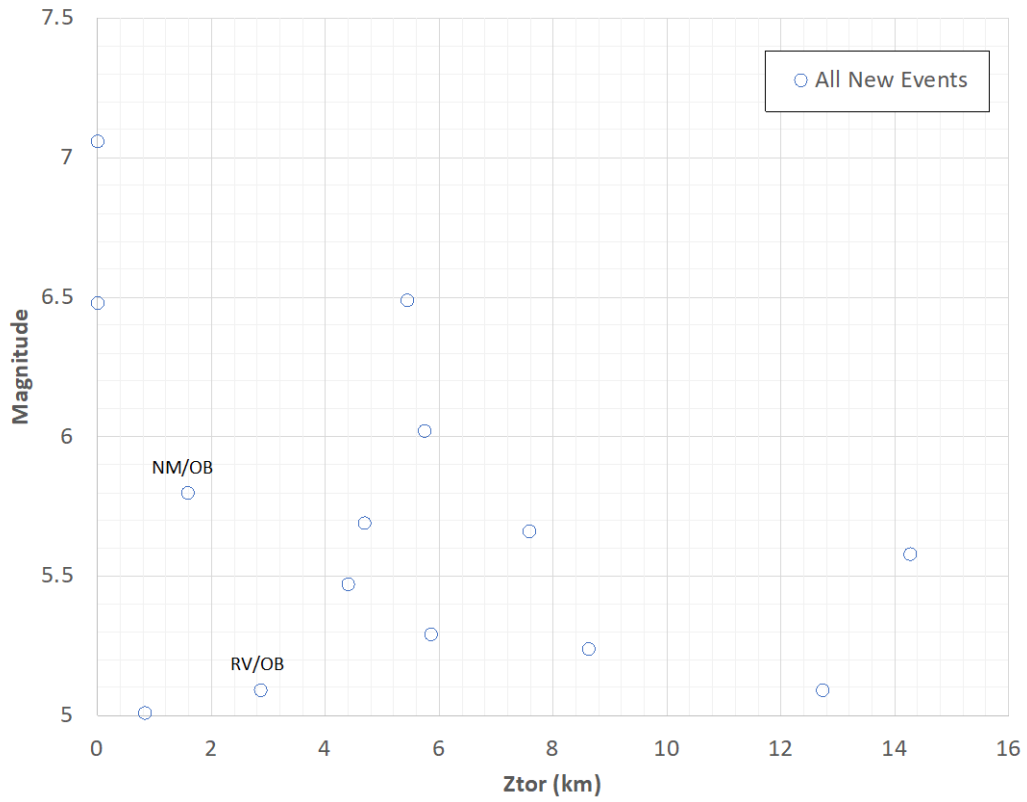


**Figure 4-4. Distribution of NGA-West3 data considered in the evaluation plotted as a function of Ztor (km) and magnitude**

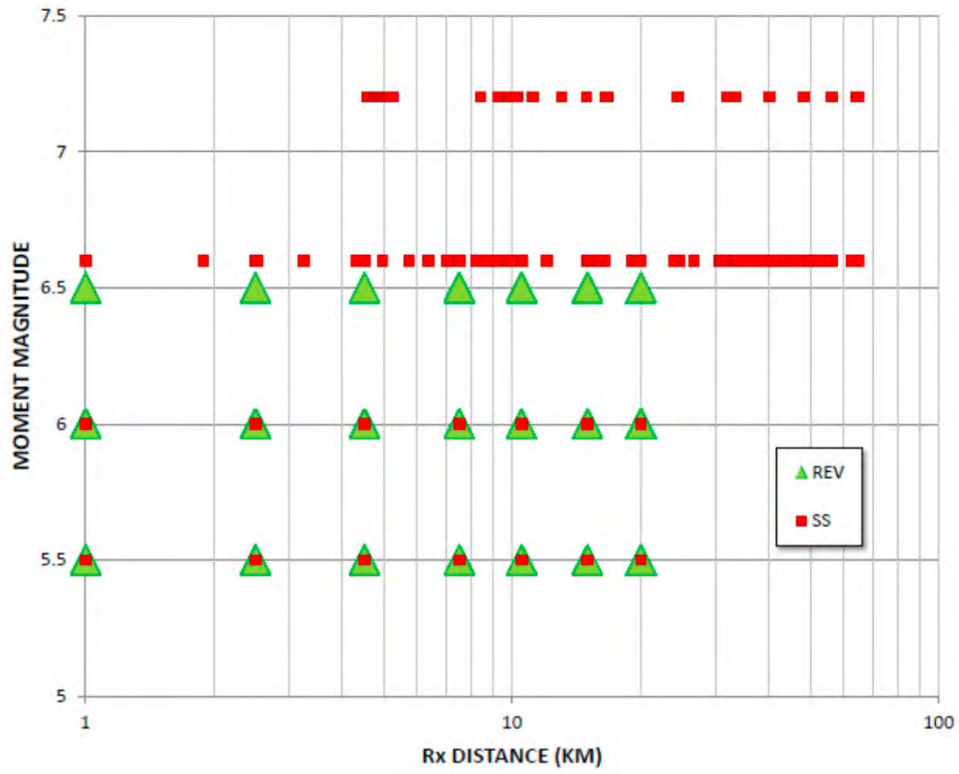
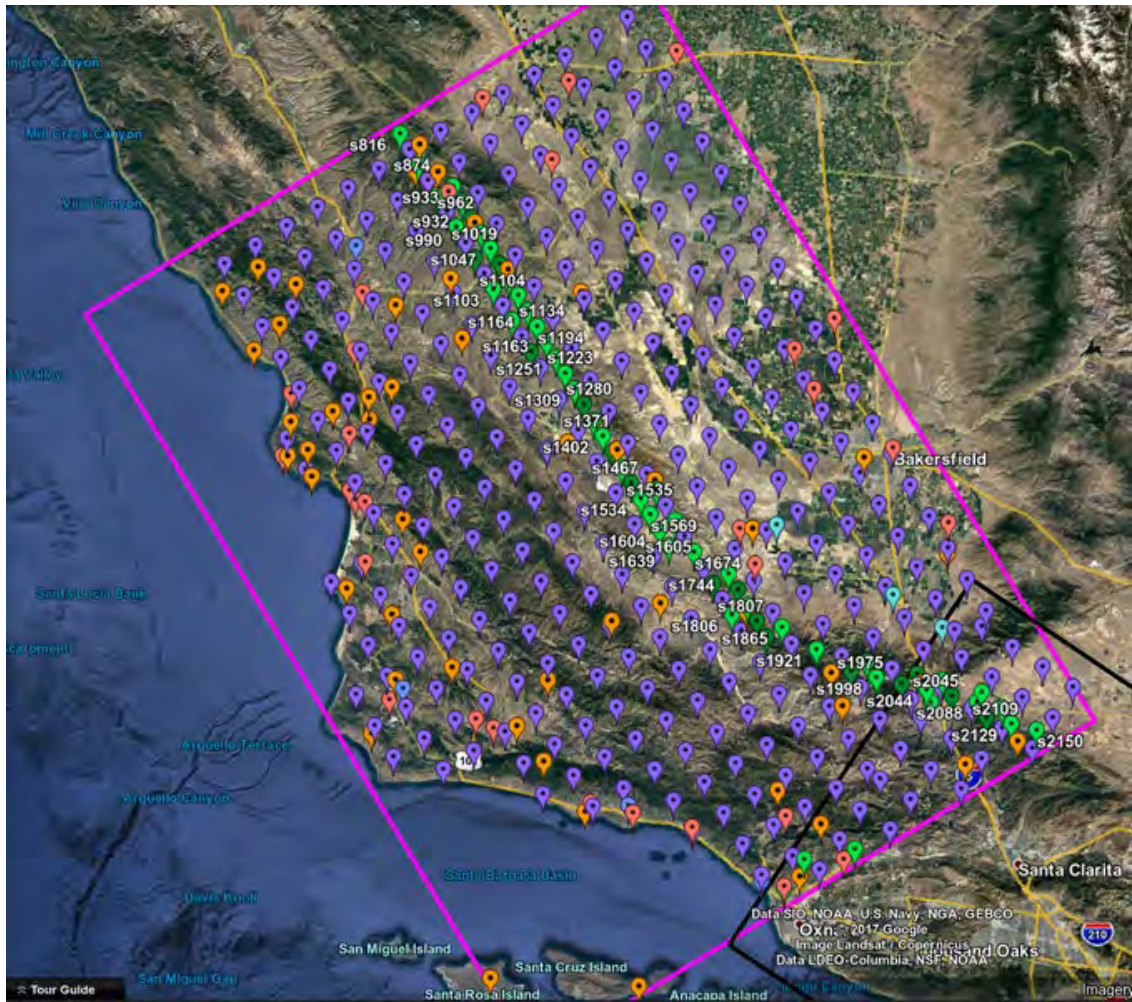


Figure 4-5. Distribution of SWUS simulation events completed on the SCEC BBP (from GeoPentech, 2015)



**Figure 4-6. CyberShake (2017) study for the Central Coast of California**

## 5. EVALUATION OF SEISMIC SOURCE CHARACTERIZATION

In seismic hazard analysis, the SSC defines the sources of earthquakes that can produce ground motions of engineering significance, as well as the magnitudes and rates of those earthquakes. In site-specific seismic hazard analysis, the SSC model includes greater detail for seismic sources that contribute most to the annual hazard at the site at the hazard levels and spectral frequencies that are the most important to seismic safety, and less detail on seismic sources that contribute little or negligible amounts to the total hazard. Accordingly, the SSC for the DCPD focuses on characterizing seismic source parameters and parameter uncertainties for a handful of sources that contribute most to the total hazard at annual hazard levels of  $10^{-4}$  to  $10^{-6}$  yr<sup>-1</sup>. The sources from the 2015 SSC model that contribute most to this hazard are the following:

- Hosgri fault source
- Los Osos fault source
- Shoreline fault source
- San Luis Bay fault source
- Local seismic source zone

This section summarizes the 2015 SSC model, describes a review of new technical information relevant to the SSC model for the DCPD (i.e., focused on the five listed sources), and presents updates to the 2015 SSC model that are consistent with the technical approach of this seismic hazard assessment (Section 1.3).

### 5.1. OVERVIEW OF THE 2015 SSC MODEL

This overview of the 2015 SSC model logic-tree framework is provided so that the evaluation of new information and the updates to the 2015 SSC model have some organizational and technical context. A more expansive overview of the 2015 SSC model is provided in Chapter 6 of the SSC SSHAC report (PG&E, 2015a).

#### 5.1.1. Types of Seismic Sources

The 2015 SSC model has two types of seismic sources: (1) fault sources and (2) seismic source zones. Fault sources are piecewise planar sources of earthquakes that are model representations of well-defined geologic fault zones that are seismogenic. A seismogenic fault is defined as being capable of generating moderate to large earthquakes ( $M \geq 5$ ) in the contemporary tectonic environment. Seismogenic faults that cannot be distinguished and characterized as fault sources are represented in the SSC model by seismic source zones (PG&E, 2015a).

Fault sources are characterized by their location, geometry, depth extent, slip sense, slip rate, magnitude-frequency distribution shape, and probability of occurrence of an earthquake in a given time period. Several terms used to describe fault sources are as follows:

- *Primary Fault Source*—A fault source that has been shown to contribute significantly to the seismic hazard at the DCPD. There are four Primary fault sources (Hosgri, Los Osos, Shoreline, and San Luis Bay fault sources), all within 12 km of the DCPD at their closest source-site distance.
- *Connected Fault Source*—A fault source that connects to a Primary fault source (either directly or via another Connected fault source) in the SSC model.

- *Fault Section*—A portion of a Primary or Connected fault source that is used to define rupture sources.
- *Rupture Source*—A series of adjacent fault sections that are considered capable of hosting a maximum earthquake (i.e., rupture over the entire area of the combined fault sections) and smaller, floating earthquakes (i.e., not confined to a specific section or sections of the rupture source).
- *Regional Fault Sources*—Fault sources within the DCPD site region other than the Primary and Connected fault sources. Types of regional fault sources include the San Andreas fault source, UCERF3 regional fault sources, and non-UCERF3 regional fault sources.

Historical earthquakes have shown that fault ruptures may span multiple connected faults and include various fault branching relationships. Historical earthquake ruptures in transpressional and transtensional tectonic regimes provided analogs that were used to inform possible rupture source geometries in the 2015 SSC model. The Primary and Connected fault sources in the 2015 SSC model include complex ruptures that span multiple named faults and have branching relationships (PG&E, 2015a). In order to capture this complexity, the 2015 SSC model distinguishes fault sources and fault sections (with a geometry and target slip rate) from rupture sources (with a geometry consisting of multiple fault sections and a slip rate that represents a portion of the target fault slip rates that has been allocated to that rupture source).

Seismic source zones, or areal source zones, are sources of earthquakes from volumes of crust occurring on non-specified fault planes. Source zones are characterized with a defined location, crustal thickness, rate of earthquakes, maximum earthquake magnitude ( $M_{max}$ ), and magnitude-frequency distribution shape. There are three areal source zones in the Diablo Canyon SSC model. These are named the Regional, Vicinity, and Local areal source zones, based on their increasing proximity to the DCPD (PG&E, 2015a). For the Local source zone in which the DCPD lies, future earthquakes are modeled as occurring on “virtual faults,” with the assessments provided with future earthquake characteristics, such as location, dip, and slip sense.

#### 5.1.1.1. Primary and Connected Fault Sources

The Primary fault sources are divided into two groups: (1) the Hosgri fault source and (2) other Primary fault sources. The other Primary fault sources are located east of the Hosgri fault zone and are either within or bounding the San Luis–Pismo structural block (SLPB; Lettis et al., 1994). The other Primary fault sources, which include the Los Osos, Shoreline, and San Luis Bay fault sources, when discussed as a group, are referred to as the SLPB fault sources.

The SSC for Primary and Connected fault sources is organized into a series of models for each fault parameter that, in combination, describe the Primary fault source characterizations and their logic tree parameterization for hazard calculation. The models are listed in Table 5-1.

**Table 5-1. Models That Comprise the Primary Fault Source Characterization**

<b>Model Name</b>	<b>Description</b>
Fault Geometry	Location, dip, and width of fault sections
Fault Slip Rate	Slip rate and sense of slip on fault sections. Used as target rates for the slip rate allocation model.
Rupture	Combinations of fault sections that may rupture together
Slip Rate Allocation	Portion of fault slip rate allocated to each rupture source
Magnitude Distribution	Range and relative rate of earthquake sizes occurring on each rupture source
Time Dependency	Equivalent Poisson rate of earthquakes on each rupture source

The SSC logic tree structure for the Primary and Connected fault sources is shown on Figure 5-1. The SSC logic tree is defined as the logic tree that is modeled by the Hazard Analyst for PSHA. In addition to the SSC logic tree, there are supporting logic trees that consist of additional nodes, branches, and weights. These supporting logic trees are used to calculate parameters that are needed to develop branch values and weights in the SSC logic tree. An example of this is the supporting logic trees that are used to calculate fault source slip rates, which are in turn used to develop the slip rate allocation model.

The following subsections describe the roles of the models listed in Table 5-1 that make up the SSC model for Primary and Connected faults.

#### 5.1.1.1.1. Fault Geometry Models

The Fault Geometry Models (FGMs), which are described in detail in PG&E (2015a, Chapter 7), define the location, dip, depth, and width of fault sections that make up the Primary and Connected fault sources. Uncertainty in fault location, geometry, and depth is accounted for in the SSC model through the combination of FGMs. Three alternative FGMs for the Hosgri fault source and three FGMs for the SLPB fault sources allow for the uncertainties in fault location, dip, and connectivity to be correlated among the fault strands within the Hosgri fault zone and among faults within the SLPB. The correlation of fault geometries within each FGM acknowledges that in many cases the uncertainty in dip of one fault source is not independent of the dip uncertainty of a nearby fault source, especially if the fault sources likely intersect at depth.

As shown in the matrix in Table 5-2, nine combinations of Hosgri FGMs and SLPB FGMs are possible for the Primary fault sources in the SSC model. Figure 5-1 shows a portion of the logic tree for the combination of the “Hosgri 85 (H85)” FGM and the “Southwest-Vergent (SW)” FGM.

Each Primary and Connected fault source listed in Table 5-2 is divided into fault sections that are named with unique two-letter codes as shown on Figures 5-2 to 5-6. Descriptions of each fault section are provided in PG&E (2015a, Chapter 7). Each fault section is specified to define a unique set of surface coordinates that constitutes the surface location, or updip projection, of a

particular reach of a fault source. Not all fault sections are included in every FGM; Figures 5-2, 5-3, and 5-4 show differences between the three SLPB FGMs near the DCP. Boundaries between fault sections are specified at locations where fault sources intersect in at least one FGM. Fault sections are allowed to rupture together in various combinations as alternative rupture sources involving sets of fault sections (PG&E, 2015a).

**Table 5-2. Fault Geometry Models (FGMs) and Logic Tree Combinations**

Hosgri (H) FGMs	SLPB FGMs		
	Outward-Vergent (OV)	Southwest-Vergent (SW)	Northeast-Vergent (NE)
Hosgri 90 (H90)	H90/ OV	H90/ SW	H90/ NE
Hosgri 85 (H85)	H85/ OV	H85/ SW	H85/ NE
Hosgri 75 (H75)	H75/ OV	H75/ SW	H75/ NE

The downdip geometries of the fault sections—including bends, changes in dip, and related changes in width and angular relationships between branching fault sources—are different among FGMs. These values and differences are described in PG&E (2015a, Chapter 7).

Sensitivity analyses during the SSC SSHAC study showed that variability in the depth of seismogenic faulting has very little effect on hazard at the DCP. Accordingly, epistemic uncertainty is not characterized for this parameter. The maximum rupture depth is 12 km for all fault sources in the SLPB group, as well as for fault sources in the Hosgri group for events with  $M < 7.4$ . For events with  $M \geq 7.4$ , the maximum rupture depth for Hosgri group fault sources is 15 km. The 12 and 15 km values are further discussed in PG&E (2015a).

#### 5.1.1.1.2. Fault Slip Rate Model

The Fault Slip Rate Model describes the slip rate and its uncertainty for each Primary fault source and certain Connected fault sources. Fault slip rates and their uncertainties are presented as cumulative distribution functions (CDFs) that represent the 2015 SSC model’s effort to capture the center, body, and range (CBR) of technically defensible slip rates. This model is described in greater detail in PG&E (2015a, Chapter 8). The SSC logic tree for Primary and Connected fault sources does not use fault slip rate as direct input to the logic tree (Figure 5-1). Instead, fault slip rate CDFs provide target slip rate budgets that must be accounted for among the various earthquake rupture sources modeled to occur on the network of fault sources described in each FGM. In the 2015 SSC model, this is done by assigning fractions of the fault slip rates to multiple rupture sources that occupy single or multiple fault sections of the FGMs. This process is part of the Rupture Model and is described generally below and in detail in PG&E (2015a, Chapter 9).

#### 5.1.1.1.3. Rupture Models

Each FGM has a corresponding Rupture Model that describes the combinations of fault sections that may rupture together. The Rupture Models consist of sets of rupture sources. A rupture source is a series of adjacent fault sections that are considered capable of hosting a maximum

earthquake and smaller, floating earthquakes. All rupture sources are considered to occur within each Rupture Model. Thus, the rupture sources represent aleatory variability, not epistemic uncertainty, in how earthquake ruptures may span various fault sections. The Rupture Models and rupture sources are defined and described in PG&E (2015a, Chapter 9). This section discusses the general characteristics of the approach and the motivations for implementing it.

## **Approach**

The rupture model approach, which defines combinations of fault sections spanning multiple named faults, is a deviation from standard fault source characterizations, which typically define fault sources as single or multiple fault sections within a single named fault zone or recognized laterally continuous fault system. The differences between the newer rupture model and standard fault source concepts are presented graphically on Figure 5-7.

In the rupture model approach, the FGMs provide alternative sets of fault geometries and senses of slip, but the combinations of adjacent fault sections that are involved in earthquake rupture are considered independently of the named fault zone. The term rupture topology describes the combinations of adjacent fault sections that may rupture in maximum earthquakes (over the entire area of the combined fault sections) and smaller earthquakes (over portions of the fault sections). Each rupture source within a Rupture Model defines a certain rupture topology, and the SSC model describes the slip rate and relative size distribution of earthquakes that may occur on that rupture topology. Examples of rupture sources that include the Hosgri fault sections closest to the DCPD are shown on Figure 5-8. Examples of rupture sources that include the SLPB sources are shown on Figures 5-9 to 5-11 (for the OV, SW, and NE fault geometry models, respectively).

## **Motivation**

The primary motivation for constructing the 2015 SSC model with the rupture model approach is that the SSC SSHAC TI Team recognized that there are several branching relationships between fault sections among the Primary and Connected fault sources and that earthquake ruptures near the DCPD may take various pathways through those branching relationships. For example, the Shoreline and Los Osos faults both have branching relationships with the Hosgri fault zone northwest of the DCPD, and the Los Osos and San Luis Bay fault zones likely have a branching relationship at depth beneath the Irish Hills (PG&E, 2015a, Chapter 5). Recent historical earthquake ruptures that spanned multiple faults and/or crossed various branching relationships include the 1992 Landers, California, and 2002 Denali, Alaska, earthquakes, among others. Because of the lack of information on past earthquake ruptures in the DCPD vicinity, and the current lack of detailed understanding of what controls rupture pathways and rupture terminations (e.g., Wesnousky, 2006, 2008; Biasi and Wesnousky, 2016, 2017), the uncertainty in rupture topology is captured through the consideration of various alternative branching relationships (rupture sources) among fault sections in the 2015 SSC model.

The rupture model approach is a forward-modeling method that relies on judgment, simple rules, and simple bookkeeping in its construction. An alternative approach that includes multi-fault and multi-segment ruptures on an interconnected, branching network of fault sources is the inverse modeling approach used in the UCERF3 model for California (Field et al., 2013). That approach, which also requires expert judgment in parameterizing the logic tree branch values and weights that are used to constrain the inversion, has certain advantages and disadvantages over the



forward-modeling method used for the Diablo Canyon SSC model. An advantage of the inverse approach is that it provides a measure of objectivity to its solutions—the “grand inversion” algorithm used in the UCERF3 model solves for a set of rupture topologies, earthquake magnitudes, and rates that are permitted within the defined rules of rupture connectivity and that minimize misfits with available constraints on fault parameters such as fault slip rate and paleoseismic data (Page et al., 2013). This type of approach has many advantages over a forward-modeling approach for a statewide model in which model boundary conditions (e.g., an overall target rate of  $M \geq 5$  earthquakes) are relatively well constrained.

Some major disadvantages to using an inverse approach apply in cases of a site-specific PSHA where hazard is dominated by low-slip-rate faults, or in the Diablo Canyon situation, where details of the Hosgri fault and lesser faults proximal to the site are important. For UCERF3, the vast majority of ruptures in the overall inverse solution are on the San Andreas fault and branching high-slip-rate faults such as the San Jacinto fault in Southern California and the Calaveras and Hayward faults in Northern California. The UCERF3 rupture solution for faults in the DCPD vicinity—including the Hosgri, Los Osos, Shoreline, and San Luis Bay faults—is within the noise of the overall model, and thus the statewide model solution is not sensitive to variability in ruptures on these fault sources. This fact, along with the consistent findings that some of the highest contributors to hazard uncertainty at the DCPD from the SSC model are uncertainties in slip rate and in the dip of local nearby faults (PG&E, 2015a), led to a clear decision by the SSC SSHAC TI Team not to include the actual UCERF3 model results as a logic tree branch. Because of the dominance of the San Andreas fault solution and other “statewide” parameters used in the inversion, it was further decided not to propose modifications to the UCERF3 model for use at the DCPD (e.g., by proposing several alternative fault geometry models or by proposing a broader range of target fault slip rates).

The construction of smaller inverse models—models that might have their geographic extent limited to the DCPD site vicinity—was considered by the TI Team but rejected in favor of the forward-modeling rupture model approach. A primary reason for rejecting the construction of a smaller inverse model was that it would have the disadvantage of few constraints on the overall inversion solution. For example, the statewide UCERF3 model has a relatively extensive record of  $M \geq 5$  earthquakes that can help determine the overall target earthquake budget. The DCPD site vicinity has extremely few  $M \geq 5$  earthquakes. The statewide model—in which hazard is dominated by high-slip-rate faults—includes opportunities to evaluate results against paleoseismic data. Such evaluations are helpful for gaining confidence in the results of this new approach. The available paleoseismic data on the Hosgri fault (Hall et al., 1994), Los Osos fault (Lettis and Hall, 1994), and San Luis Bay fault (Lettis et al., 1994) are few and insufficient to provide meaningful constraints on an inversion. Lastly, the inverse model approach has the additional disadvantages of being a new model approach with limited time to gain broad acceptance in the hazard community, and being more difficult than a forward model to dissect and explore from a hazard sensitivity standpoint.

In summary, the TI Team opted for the forward-model approach over an inverse approach, believing it to be more practical to implement for a site-specific PSHA, and more tractable to understand and review what contributes most to hazard uncertainty.

## Rupture Source Types

The rupture models describe the number of rupture sources, the fault sections involved in each rupture source, the sense of slip for each fault section in the rupture source, and the type of rupture source. The rupture source type is a classification scheme used in the 2015 SSC model for PSHA in two ways. First, the rupture source type alerts the Hazard Analyst to conditions that require special treatment in the GMC model. Second, the rupture source type is related to the functional form of earthquake sizes (the magnitude probability density function, or magnitude PDF) that occur on a rupture source (this is described further in Section 5.1.1.1.4). The four rupture source types are named and described briefly in Table 5-3. Further description of the four types of rupture sources is provided in PG&E (2015a, Chapter 9).

**Table 5-3. Rupture Source Types**

Type	Explanation
Characteristic	Rupture source is confined to a single named fault of limited length that has a uniform sense of slip.
Linked	Rupture source includes fault sections of multiple named faults of the same sense of slip.
Complex	Rupture source contains multiple named faults and more than one sense of slip on adjacent fault sections.
Splay	Rupture source includes overlapping faults that rupture simultaneously.

The complex and splay rupture sources require special consideration by the ground-motion model regarding how to implement ground-motion contributions from multiple portions of the fault rupture (GeoPentech, 2015). For complex rupture sources, where different portions of the rupture source have different senses of slip, two parts are identified: the larger (“primary”) part, and the smaller (“secondary”) part. For splay rupture sources where there are overlapping portions of the rupture source resulting in two source-to-site distances, the fault sections are identified as part of either the larger (“main”) area, or the smaller (“splay”) area of the rupture source. Examples of complex and splay rupture sources are shown on Figures 5-9 to 5-11.

### 5.1.1.1.4. Slip Rate Allocation Models

A Slip Rate Allocation Model describes the slip rate allocated to individual rupture sources in a single Rupture Model. Accordingly, there is one Slip Rate Allocation Model for the Hosgri Rupture Model (that applies to all three Hosgri FGMs) and three Slip Rate Allocation Models for the SLPB Rupture Models, one each for the OV, SW, and NE Rupture Models. The Slip Rate Allocation Models are presented as part of the Rupture Models in PG&E (2015a, Chapter 9).

The slip rate of each rupture source represents some fraction of the total fault slip rate determined from the Fault Slip Rate Model for each fault source involved in the rupture. Because the Rupture Model contains rupture sources that link across numerous faults with different fault slip rates, the Slip Rate Allocation Model creates a slip rate for each rupture source such that when the contributions from all rupture sources that include a particular fault are summed, the combined slip rate equals the target slip rate budget for that particular fault. The rationale and

criteria used to allocate a fraction of the total fault slip rate to individual rupture sources are discussed in PG&E (2015a, Chapter 9).

For characteristic and linked rupture sources, the slip rate is uniform over the entire rupture source. For complex and splay rupture sources, the slip rates are uniform over each part of the rupture source, but the parts have different slip rates. Slip rates are different for each part (e.g., the *primary* and *secondary* parts) principally because of the method selected for modeling ground motions for these two rupture source types in the ground-motion model (GeoPentech, 2015). The ground-motion model requires that for a given complex or splay rupture source, two magnitudes be defined—one each for the larger and smaller parts of the rupture source. In order to have a constant occurrence rate of the splay and complex earthquake scenarios, the slip rate of the larger fault source (the *main* or *primary* fault for splay and complex cases, respectively) must be greater than the slip rate of the smaller fault source (the *splay* or *secondary* fault for splay and complex cases, respectively) by an amount that is proportional to the estimated seismic moments of each part of the rupture source (PG&E, 2015a, Chapter 9).

Uncertainty in slip rate for each rupture source is handled as epistemic uncertainty in the SSC logic tree with three-point weighted distributions. The three-point weighted distributions are selected from slip rate CDFs that are, in turn, calculated based on the fault slip rate CDFs and the fraction of slip rate allocated to each rupture source.

#### 5.1.1.1.5. Magnitude Distribution Models

A Magnitude Distribution Model (MDM) describes the minimum ( $M_{\min}$ ) and maximum ( $M_{\max}$ ) magnitudes and the relative frequency of earthquake magnitudes from  $M_{\min}$  through  $M_{\max}$  that may occur on a rupture source. Four earthquake magnitude-frequency distribution (MFD) functional forms are used in the 2015 SSC model. These functional forms are called magnitude *probability density functions* (magnitude PDFs); the term *MFD* is reserved for the distribution of annual rate (in  $\text{yr}^{-1}$ ) plotted against magnitude calculated by combining the magnitude PDF with the rupture source area, slip rate, and bounding magnitudes ( $M_{\min}$ ,  $M_{\max}$ , and/or characteristic magnitude,  $M_{\text{char}}$ ).

The paucity of information available on past moderate to large earthquake ruptures on the Primary fault sources was considered in developing an approach to constructing MDMs that accounted for both epistemic and aleatory uncertainty (PG&E, 2015a). No large earthquakes ( $M$  6 or larger) have occurred historically on the Hosgri, Shoreline, Los Osos, or San Luis Bay faults (McLaren and Savage, 2001; PG&E, 2015a). The paleoseismic data collected on these faults are very limited, with a few estimates of the timing and amount of slip on past earthquakes on the Hosgri fault north of San Simeon (Hall et al., 1994), on the Los Osos fault near San Luis Obispo (Lettis and Hall, 1994), and on the San Luis Bay fault near Avila Beach (Lettis et al., 1994). These paleoseismic records, however, do not have well-constrained or well-determined information about earthquake timing, slip per event, or completeness of the stratigraphic record. In all cases, the number of events captured is very few or is difficult to assess.

The construction of MDMs also considers the geometry of the Primary fault sources. As described in PG&E (2015a, Chapters 5, 7, and 10), the best available mapping of the Hosgri–San Gregorio fault zone shows that there is a reasonably well-defined southern end point to the Hosgri fault near Point Arguello. There are no gaps, step-overs, or sharp double bends in the fault zone between Point Arguello and the northern end of the San Gregorio fault zone at Bolinas

Lagoon that are sufficiently large to preclude the possibility of a throughgoing earthquake rupture. The Primary faults of the SLPB group—the Shoreline, Los Osos, and San Luis Bay—all appear to have branching relationships with the Hosgri fault or with one another that also are not sufficiently understood to accurately model, much less preclude, the continuity of earthquake rupture through the intersections. Likewise, fault geometries and senses of slip along and between the Primary and Connected faults east and west of the Hosgri fault contain relatively abrupt changes in strike, geomorphic expression, and rake, but few are sufficiently large to preclude throughgoing fault rupture based on observations from other segmented strike-slip fault systems (Biasi and Wesnousky, 2016, 2017). These physical characteristics suggest that, in the absence of “behavioral” information on the size and timing of past earthquake ruptures, there is little basis to confidently define specific lengths, or segments, of the faults and rupture sources that are meaningful for narrowly constraining the sizes and relative frequencies of earthquake magnitudes.

### **Approach**

Despite the paucity of paleoseismic data, and the lack of historical data and clearly defined fault or rupture segment end points that would limit earthquake rupture, there are alternative models, methods, and empirical observations available to construct models for the earthquake size distribution on the Primary and Connected faults.

The MDMs developed for the Primary and Connected fault sources are derived by assessing possible rupture segmentation of each rupture source, evaluating lengths and areas of possible characteristic and maximum earthquake ruptures, assigning earthquake magnitudes to characteristic and maximum ruptures, and defining magnitude PDFs to characterize the MFDs of earthquakes on the rupture sources. Aspects of the development of the MDMs are described in greater detail in PG&E (2015a, Chapter 10).

Maximum earthquake sizes are subject to epistemic uncertainty but are limited ultimately by the maximum dimensions of the rupture source. Characteristic earthquake rupture dimensions, which are not as clearly constrained, are more challenging to define and defend in the Diablo Canyon SSC model as explained above. The absence of behavioral information or clear segmentation boundaries, however, is not a rationale for precluding characteristic-model behavior as part of the technically defensible range of models. The characteristic earthquake hypothesis—defined herein as the repeated occurrence of earthquakes of similar size over a similar portion of a fault that is more common than would be predicted from an exponential MFD—appears to apply well to certain continental faults where paleoseismic information can be evaluated (Schwartz and Coppersmith, 1984; Stirling et al., 1996; Ishibe and Shimazaki, 2012). Furthermore, empirical data from paleoseismic sites on displacement-at-a-point are consistent with the characteristic earthquake hypothesis and would appear to reject an exponential magnitude size distribution for faults (Hecker et al., 2013). We do not suggest that all portions of all faults rupture in characteristic earthquakes, and we recognize that many faults and portions of fault networks that have been modeled with characteristic earthquakes can also be successfully represented with exponential size distributions (Kagan, 1993; Parsons and Geist, 2009; Page et al., 2011). However, as noted by Field et al. (2014), the results of the grand inversion used in UCERF3 have demonstrated challenges with the Gutenberg-Richter hypothesis for individual faults.

The rupture model concept allows for a broad range of earthquake sizes to be present on the Primary and Connected fault sources. Because alternative rupture topologies coexist on the same

branching fault network with varying lengths, some rupture sources host maximum earthquakes that approach or exceed the size of historical earthquakes that have occurred on similar types of ruptures observed worldwide, whereas other rupture sources repeatedly produce earthquakes of a much more limited size range.

The MDMs are constructed with the site-specific nature of the PSHA in mind. This arises in two ways: (1) in selecting fault lengths for both maximum and characteristic earthquake ruptures, and (2) in modeling the location of earthquake ruptures in the hazard code for PSHA. Just as the rupture topologies defining the rupture sources are created with the DCPD-specific application in mind, the fault sections and lengths considered to define alternative values of  $M_{char}$  on a rupture source are fault sections and lengths nearest to the DCPD. In other words, portions of Connected faults farther from the DCPD that may be considered to define a characteristic rupture are considered less or not at all when compared to portions closer to the DCPD.

Determination of characteristic earthquakes based on fault segmentation has been a durable feature in PSHA (e.g., Schwartz and Coppersmith, 1984), even if it has received much scrutiny (Field et al., 2013). Although the TI Team used concepts of fault segmentation to estimate the size of characteristic earthquakes, they acknowledged that there are many instances of earthquake ruptures that do not behave, even in hindsight, according to commonly applied segmentation rules (PG&E, 2015a). The TI Team accounted for these instances in the SSC model by the following means:

- Having weight on an exponential recurrence distribution for many rupture sources.
- Having a very broad range of characteristic magnitudes on the fault network.
- Allowing the hazard model to “float”—and not fix—earthquake ruptures across the originally postulated fault segment boundaries.

Magnitudes of characteristic and maximum ruptures in the MDMs are calculated from the magnitude-area scaling relation of Hanks and Bakun (2014; HB14). The HB14 relation is a bilinear empirical relation developed from a subset of continental strike-slip earthquakes, mostly from California:

$$\mathbf{M} = \log A + 3.98, \quad A \leq 537 \text{ km}^2 \quad \text{Equation (5.1)}$$

$$\mathbf{M} = 5/4 \log A + 3.30, \quad A > 537 \text{ km}^2 \quad \text{Equation (5.2)}$$

where  $\mathbf{M}$  equals moment magnitude and  $A$  equals rupture area in  $\text{km}^2$ .

The HB14 relation was selected for sole implementation from several alternative candidate empirical magnitude-scaling relations after considering the following:

- The dimensions and style of faulting of the Primary and Connected fault sources yield magnitude estimates that span the magnitude range that appears to be best fit by a bilinear empirical relation.
- The transpressional tectonic setting of the DCPD site is characterized by continental strike-slip faults similar to the type of earthquake ruptures used to develop the empirical relation.
- The hazard results are not sensitive to the choice of empirical relation (PG&E, 2015a), which allows for trimming this branch of the logic tree.

A set of proponent models sampled from the range of available models was selected by the TI Team to assess the magnitude PDFs for different types of rupture sources. The set includes the following distributions:

- The truncated exponential, or Gutenberg-Richter, distribution (Gutenberg and Richter, 1944; Kagan, 1993)
- The simplified maximum magnitude distribution (Wesnousky et al., 1983)
- The characteristic earthquake distribution (Youngs and Coppersmith, 1985)
- The modified characteristic earthquake distribution developed during the SSC SSHAC (Wooddell, Abrahamson, Acevedo-Cabrera, and Youngs [WAACY] magnitude PDF model; PG&E, 2015a, Appendix G)

These proposed magnitude PDFs, shown graphically on Figure 5-12, provide a broad range that captures uncertainty in the relative earthquake sizes that may occur on the fault sources.

Each rupture source type (Table 5-3) is associated with one or two magnitude PDFs to be used in the hazard calculations. Table 5-4 shows the associations between rupture source type, the applied magnitude PDF(s), and the branch weights (shown with square brackets) used in the 2015 SSC logic tree. Discussion of the rationale for the selection and weighting of the various magnitude PDFs for each rupture source type is provided in PG&E (2015a, Chapter 10).

**Table 5-4. Rupture Source Types and Magnitude PDFs**

<b>Rupture Source Type</b>	<b>Branch-Weighted Magnitude PDF Branches and Weights</b>
Characteristic and Linked (shorter rupture sources)	Characteristic Earthquake [1.0]
Linked (longer rupture sources)	WAACY [0.8] Truncated Exponential [0.2]
Complex and Splay	Simplified Maximum Magnitude [1.0]

#### 5.1.1.1.6. Time Dependency Model

The Time Dependency Model in the 2015 SSC applies to the recurrence of moderate to large earthquakes. Near the DCPD it applies to the Primary fault sources and Connected fault sources.

Earthquake recurrence in PSHA is commonly modeled as a time-independent Poisson process. There is evidence, however, that earthquake occurrence is too regular on some faults for the Poisson model to be likely (Biasi et al., 2002; Scharer et al., 2010; Fitzenz et al., 2010). Furthermore, simple elastic rebound theory of elastic strain accumulation and release suggests there is some renewal process involved in earthquake recurrence on individual faults. Thus, we find that a non-Poisson model for earthquake occurrence must be considered technically defensible, and thus included in the 2015 SSC model. To account for the probability that moderate to large earthquakes on faults do not follow a Poisson process, equivalent Poisson hazard ratios (EPhRs) are applied to the Primary and Connected fault source rates. The EPhRs (which were called EPRs in the 2015 SSC SSHAC report) are multipliers of the Poisson rate that capture uncertainty in the recurrence functional form, long-term mean recurrence rate of moderate to large earthquakes, coefficient of variation in the recurrence model, and the time

elapsed since the most recent event. The methodology and results to derive the equivalent Poisson rates are discussed in detail in PG&E (2015a, Chapter 11 and Appendix H) and Biasi and Thompson (2018).

The 2015 SSC model incorporates the Time Dependency Model as a global parameter (i.e., it is applicable to all or a group of sources), with a different tree (different branch values and weights) for the Hosgri and SLPB fault source groups (see Figure 5-1 and Table 5-1).

#### 5.1.1.2. Regional Fault Sources

Active fault sources within 320 km (200 mi.) of the DCPD are considered in the 2015 SSC model. The 2015 SSC model refers to the fault sources within this radial distance other than the Primary and Connected fault sources as *regional* fault sources. Sensitivity analyses (PG&E, 2015a) showed that regional fault sources contribute little to the hazard at the DCPD. The largest regional fault source, the San Andreas fault source (SAF), located approximately 80 km northeast of Diablo Canyon, represents a few percent of the total hazard at long periods at the hazard levels being evaluated for the DCPD (PG&E, 2015a). Aside from the SAF source, the other regional fault sources contribute *in the aggregate* less than 1% to the hazard at hazard levels of importance to the DCPD (PG&E, 2015a, Chapter 6).

The approach for including regional fault sources in the 2015 SSC model was to rely on the UCERF3 characterizations for these sources or to develop simplified fault source characterizations for offshore faults that were not considered in the UCERF3 model (PG&E, 2015a, Chapter 12).

#### 5.1.1.3. Areal Source Zones

Earthquakes occurring off the recognized fault sources within the DCPD site region are modeled to occur in areal source zones (Figure 5-13). The 2015 SSC model has three nested areal source zones: Local, Vicinity, and Regional. The Local source zone, which includes the DCPD, is modeled with virtual faults, and the Vicinity and Regional source zones are modeled as point sources from a grid (PG&E, 2015a).

The Local source zone models earthquakes as occurring on a set of subparallel virtual faults with defined aleatory and epistemic uncertainties in location, rake, dip, and  $M_{max}$ . This *host* areal source zone represents an area where the general characteristics of faults are known (to varying degrees of uncertainty) or may be constrained by available information, but where the fault activity and/or slip rate are unresolved. The rates of earthquakes in this areal source zone are determined based on observed seismicity rates and considerations of geologic rates of deformation. More general information about the motivation for the Local source zone is provided in PG&E (2015a, Chapter 13).

The Vicinity and Regional source zones use an alternative method for modeling earthquakes. These source zones represent earthquakes that may occur from faults that are unknown, or known but not sufficiently active, to be considered as fault sources. The SSC models earthquakes in the Vicinity and Regional source zones from a set of point sources on regularly spaced grids. This approach is used at greater distances from the DCPD site where less precision is warranted. The rates of earthquakes in the gridded source zones are calculated based on observed and

spatially smoothed seismicity rates and model predictions about maximum earthquake size. The gridded areal source zones are described in PG&E (2015a, Chapter 13).

### 5.1.2. Primary Contributors to Hazard and Hazard Deaggregation

The 2015 SSC model captures earthquake ruptures on the Primary and Connected fault sources by using numerous rupture sources, with several rupture sources located on the fault sections closest to the DCPD (examples shown on Figures 5-8 to 5-11). To evaluate fractional contribution to total hazard by fault source (and other hazard sensitivities), the rupture sources were grouped by fault source as shown in Table 5-5. The Hosgri fault source is represented by 21 rupture sources across all three Hosgri FGMs (H85, H75, and H90). The Shoreline, Los Osos, and San Luis Bay faults are represented by 11, 8, and 6 rupture sources, respectively, across all three FGMs developed for the SLPB sources: OV, SW, and NE. Nine other rupture sources tabulated under “Other Connected Faults” involve fault sections that are farther from the DCPD (PG&E, 2015a, Chapter 9).

**Table 5-5. Grouping of Rupture Sources by Fault Source for Hazard Sensitivity**

Fault Source Group (Number of Rupture Sources in Group)				
Hosgri (21)	Shoreline (11)	Los Osos (8)	San Luis Bay (6)	Other Connected Faults (9)
H85-01 through H85-07	OV-01, OV-02, OV-03, OV-04	OV-07, OV-08 SW-08	OV-05, OV-06 SW-04, SW-05, SW-06, SW-07	H75-08, H85-08, H90-08
H75-01 through H75-07	SW-01, SW-02, SW-03	NE-05, NE-06, NE-07, NE-08,		OV-09, OV-10 SW-09, SW-10
H90-01 through H90-07	NE-01, NE-02, NE-03, NE-04	NE-11		NE-09, NE-10

Figures 5-14 to 5-16 show total hazard curves and contributing hazard curves from seismic sources in the 2015 SSC model at three spectral frequencies: 5 Hz, 1 Hz, and 0.5 Hz. These hazard curves are based on a reference rock site condition ( $V_{S30} = 760$  m/sec) and the full ground-motion model from the SWUS study (GeoPentech, 2015). The 2015 SSC SSHAC report (PG&E, 2015a, Chapter 14) includes plots of fractional source contributions at 5 Hz and 0.5 Hz, but these plots are based on a simplified ground-motion model. At the hazard levels of interest ( $10^{-4}$  to  $10^{-6}$  yr<sup>-1</sup>), the Hosgri fault is the largest contributor to total hazard, followed by the San Luis Bay, Los Osos and Shoreline fault sources, and by the Local source zone. At the  $10^{-4}$  annual hazard level, the Hosgri fault contributes approximately 50% to 70% to the total hazard (Table 5-6).



**Table 5-6. Fractional Contribution of the Hosgri Fault Source to the Total Hazard at the 10<sup>-4</sup> Annual Hazard Level**

Frequency (Hz)	Fractional Contribution of Hosgri Fault to Total Hazard
5	0.5
1	0.7
0.5	0.7

Hazard deaggregation plots at the 10<sup>-4</sup> annual hazard level for the three spectral frequencies are shown on Figures 5-17 to 5-19. These plots show the contribution to total hazard by magnitude and distance bins. Table 5-7 lists the fractional contributions of each distance bin. For all three spectral frequencies, the large contribution from the **M** 7.0–7.5 and **M** 7.5–8.0 magnitude bins and the 3–6 km distance bin mostly represents earthquakes on the Hosgri fault source (with a closest source-to-site distance of approximately 5 km). The fractional contribution summed across this distance bin is between 0.5 (at 5 Hz) and 0.61 (at 1 and 0.5 Hz). The next-largest peaks in the hazard deaggregation plots, at the **M** 6.0–6.5 and **M** 6.5–7.0 magnitude bins and the 0–3 km, 3–6 km, and 6–10 km distance bins, reflect the contributions from the San Luis Bay, Los Osos, and Shoreline fault sources and the Local source zone. These peaks are more prevalent at the higher frequency (5 Hz) ground motions. The analysis of hazard curves by contributing source and deaggregation plots highlights the dominant contribution of earthquakes on the Hosgri fault source that rupture the fault sections closest to the DCP.

**Table 5-7. Deaggregation for Reference Rock Site Hazard at the 10<sup>-4</sup> Annual Hazard Level**

Distance Range (km)	Fractional Contribution to Total Hazard at Selected Frequencies		
	5 Hz	1 Hz	0.5 Hz
0 – 3	0.23	0.19	0.17
3 – 6	0.50	0.61	0.61
6 – 10	0.19	0.11	0.10
10 – 20	0.04	0.04	0.04
20 – 30	0.01	0.01	0.01
30 – 50	0.03	0.03	0.03
50 – 75	0.00	0.00	0.00
75 – 100	0.04	0.01	0.00
> 100	0.00	0.00	0.00

### **5.1.3. Contributions To Hazard Uncertainty**

The 2015 SSC SSHAC report includes a hazard sensitivity for 5 and 0.5 Hz spectral frequencies (PG&E, 2015a, Chapter 14). Hazard sensitivities at or near these frequencies were evaluated periodically during the development of the 2015 SSC model (PG&E, 2015a, Appendix D).

Hazard sensitivity of the 2015 SSC model was explored by isolating each node (in some cases, groups of nodes) of the SSC logic trees. For the node(s) of interest, one branch was given full weight and the mean hazard was computed by sampling all branches for the other nodes (using a simplified ground-motion model and reference site condition of 760 m/sec). The results of the hazard sensitivity are presented in the form of tornado plots for a given hazard level. The tornado plots show the relative contribution to hazard uncertainty for each node of the logic tree, with the largest contributor to uncertainty placed at the top of the tornado diagram. The tornado plots show the ratio of the ground motion from the individual sensitivity case divided by the ground motion for the full logic tree (called the “base case”).

Summary tornado plots computed for spectral frequencies of 5 and 0.5 Hz, and for the annual hazard of  $10^{-4}$  and  $10^{-6}$  yr<sup>-1</sup>, are presented on Figures 5-20 and 5-21. More detailed sensitivity plots are in the SSC SSHAC report (PG&E, 2015a, Chapter 14). The order of the hazard sensitivities approximately follows the largest to smallest difference from unity in the ground-motion ratios, but the order of the hazard sensitivities is consistent from plot to plot.

The tornado plots indicate that the largest contribution from the 2015 SSC model to ground-motion uncertainty at the DCPD is uncertainty in the slip rate of the Hosgri fault source, followed by the EPHR uncertainty for the Hosgri fault (Figures 5-20 and 5-21). These observations are not unexpected because both slip rate and EPHR contribute directly to earthquake recurrence rate, and the Hosgri fault source is the largest contributor to total hazard at the DCPD site (Figures 5-14 to 5-16). The next largest contributors to hazard uncertainty are the FGMs for the SLPB sources (i.e., the choice of the OV, SW, or NE models) and for the Hosgri fault (which is labeled in the figures as “Hosgri dip”). Other source slip rates, such as the slip rates of the San Luis Bay, Shoreline, and Los Osos faults (as well as the slip rate calculated for the virtual faults in the Local source zone) have a lesser impact on hazard uncertainty. The selection of  $M_{\max}$  and  $M_{\text{char}}$  have a relatively moderate to low impact on hazard uncertainty depending on spectral frequency and hazard level. Note that the rupture model element of the fault source characterization is not represented in the tornado plots. This is because the rupture sources contribute to aleatory variability in the location and complexity of the ruptures. One proxy for the impact of the rupture sources introduced to the 2015 SSC model is the sensitivity showing the impact on hazard if only the primary or main part of the rupture is considered for complex or splay ruptures, respectively. This sensitivity is at the bottom of the plot, and it indicates a decrease in hazard of approximately 5% to 10% if the secondary or splay parts of ruptures are not included.

## 5.2. REVIEW OF NEW INFORMATION

We reviewed new data, models, and methods available through published literature, technical reports, or publicly released datasets. The review focused on those seismic sources and source parameters that contribute most to hazard (Figures 5-14 to 5-19) and hazard uncertainty (Figures 5-20 and 5-21) based on the 2015 SSC model results.

This review of new information is organized as follows. First is an overview of new information by model element for the fault sources (Table 5-1) and areal source zones. Second is a review of new information on specific sources and source model parameters (e.g., Hosgri fault slip rate). The findings of the review form the basis for the development of updates to the 2015 SSC model that follow the approach of the 2023 SB-846 seismic hazard assessment (Section 1.3).

### **5.2.1. Overview**

Tables 5-8 and 5-9 summarize the findings from our review for the fault sources and areal source zones, respectively. For fault sources, the review focused on publications specific to the Primary faults such as fault location, down-dip geometry, geologic slip rate, kinematics, and paleoseismic history. In addition to fault-specific publications, the review examined papers that have a direct bearing on the slip rate of local fault sources such as: (1) Quaternary history and vertical tectonic motion recorded by coastal marine terraces, (2) Quaternary sequence stratigraphy of the Central California continental shelf, (3) tectonic plate-motion studies examining relative motion between the Pacific plate and the western portion of the Sierra Nevada–Great Valley microplate (i.e., motion west of the San Andreas fault), and (4) numerical models of deformation rates and fault slip rates that incorporate global positioning system (GPS) geodetic and other geological or geophysical data.

**Table 5-8. Primary Fault Source Characterization Model Elements and Summary of New Information**

Model Name	New Information Summary
Fault Geometry	No new published information on the location and geometry of the Primary faults near the DCPD other than the updated set of fault sources and geometries for the WUS ERF-2023 project. Published papers on Primary faults present information on fault location and geometry that were known during the 2015 SSC SSHAC study.
Fault Slip Rate	<p>New published information on:</p> <ul style="list-style-type: none"> <li>• The geologic slip rate of the Hosgri fault</li> <li>• The geologic slip rate of the Shoreline fault</li> <li>• Quaternary sequence stratigraphy on continental shelf and slope environments, which has a bearing on the Hosgri and Shoreline fault slip rates</li> <li>• Marine terrace paleosea levels, which have a bearing on the Los Osos fault slip rate</li> <li>• Geodetic- and geologic-based numerical models of slip rate for all Primary faults and off-fault deformation in the DCPD vicinity (prepared in part for the WUS ERF-2023)</li> <li>• A numerical modeling study that examines coastal uplift near the DCPD caused by displacement on the Hosgri fault zone</li> </ul>
Rupture and Slip Rate Allocation	<p>New published information on:</p> <ul style="list-style-type: none"> <li>• Empirical patterns of fault rupture propagation and rupture terminations coinciding with steps and bends in fault traces</li> <li>• Physics-based dynamic rupture models examining steps, bends, and dips for strike-slip and reverse faulting</li> <li>• Insights on rupture connectivity based on evaluating inversion-based earthquake rupture forecast models of California</li> </ul> <p>Publications broadly support the 2015 SSC SSHAC approach to include alternative rupture pathways as well as complex and splay rupture sources. Information is broadly consistent with what was known during the 2015 SSC SSHAC study.</p>
Magnitude Distribution	<p>New published information on:</p> <ul style="list-style-type: none"> <li>• Evidence for and against exponential magnitude-frequency relationships for fault traces</li> <li>• Scaling relations between rupture dimensions and moment magnitude</li> </ul> <p>New publications are broadly consistent with information that was available during the SSC SSHAC study, and this information broadly supports the approach of the 2015 SSC model.</p>
Time Dependency	Very limited new published information on models that could be implemented to capture uncertainty in time-dependent behavior for the Primary faults. New approaches require additional information on paleoseismic rupture history and other data that are not available for the local fault sources.

For areal source zones, the review examined recent earthquake catalog data from the DCPD vicinity as well as papers on statistical seismology methods and models such as declustering and spatial smoothing of seismicity (Table 5-9). We also searched for papers that evaluated the patterns and kinematics of seismicity in the Local source zone that may impact the location, geometry, and kinematics of the virtual faults.

**Table 5-9. Summary of New Information for the Local Areal Source Zone**

Model Component	New Information Summary
Virtual Fault Location and Geometry	No new published information was found on the location and geometry of potentially seismogenic faults (i.e., other than the Primary and Connected fault sources) within the Local source zone.
Earthquake Rate	Catalog seismicity from the Advanced National Seismic System (ANSS) Comprehensive Earthquake Catalog (ComCat) for the DCPD vicinity was downloaded and reviewed for the period June 2013 through August 2023. No significant changes to the rate or pattern of seismicity in the DCPD vicinity were observed compared to the period examined for the 2015 SSC SSHAC study.
Earthquake Magnitude Distribution	<p>New published information on:</p> <ul style="list-style-type: none"> <li>• Methods for measuring off-fault deformation using geodetic data</li> <li>• Models for estimating the magnitude-recurrence relationship (including <i>b</i>-value and rate)</li> </ul> <p>Our evaluation of the newly published information concludes that the approach taken in the 2015 SSC model is appropriate. Some of the new methods and models are determined to not be appropriate and/or sufficiently reliable for inclusion in this SSC model update.</p>

One source of recently published information is a series of datasets and models developed for the conterminous US National Seismic Hazard Model (2023 NSHM; Petersen et al., 2023) and reports that provide technical peer review of these datasets and models. This information includes published papers and datasets for the Western United States (WUS) used in the 2023 earthquake rupture forecast (WUS ERF-2023; Field et al., 2023). Key publications and data releases include the set of fault sources and fault geometries, a series of geodetic- and geologic-based deformation models that include modeled slip rates of the faults, and manuscripts on earthquake catalog processing and spatial smoothing for gridded seismic sources. We also reviewed two manuscripts (Jordan et al., 2023; Johnson et al., 2024) that document peer review of these data and models for their suitability in the WUS ERF-2023 and the 2023 NSHM.

This review focuses on peer-reviewed, published (or soon-to-be published) information. It does not address proponent models offered through testimony, such as the recent testimony statements by Dr. Peter Bird. Such proponent models are discussed in Chapter 6 of this report.

#### 5.2.1.1. Fault Geometry Models for Primary Fault Sources

As noted in Table 5-8, we found no new published information on the location or down-dip geometry of the local fault sources. Published papers that discuss the location of the Hosgri fault near and north of the DCPD (Kluesner et al., 2023; Medri et al., 2023; O’Connell and Turner, 2023) rely on information that was available to the 2015 SSC SSHAC study, or if new, the information is consistent with prior interpretations. Similarly, the Nishenko et al. (2018) paper on

the Shoreline fault slip rate used information that was evaluated as part of the 2015 SSC SSHAC study and was documented in the Central Coastal California Seismic Imaging Project (CCCSIP) report (PG&E, 2014a).

As part of the WUS ERF-2023, the USGS developed a set of fault sources (Hatem, Collett, et al., 2022). The fault sources in the DCPD vicinity were merged from two alternative fault models developed as part of the Third Uniform California Earthquake Rupture Forecast (UCERF3; Field et al., 2013), which was the predecessor earthquake rupture forecast that was reviewed as part of the 2015 SSC SSHAC study. The WUS ERF-2023 fault sources include representations of all Primary and Connected fault sources to a reasonable degree (Figure 5-22), although the WUS ERF-2023 fault sources do not include aleatory or epistemic alternatives in fault location or dip (Table 5-10). Given this simplified representation of the local faults around DCPD contained in the WUS ERF-2023 model, this new information does not represent a complete fault source model and thus was not incorporated in this study.

**Table 5-10. Comparison of Fault Source Geometries, 2015 SSC Model and WUS ERF-2023 Fault Model**

<b>Fault Source and Parameter</b>	<b>2015 SSC Fault Model (PG&amp;E, 2015a)</b>	<b>WUS ERF-2023 Fault Model (Hatem, Collett, et al., 2022)</b>
<b>Hosgri</b>		
Location	Three traces (aleatory variability) closest to DCPD based on seismic-reflection data interpretation (Johnson and Watt, 2012; PG&E, 2014a)	One trace that approximates the central strand offshore DCPD
Dip	Three fault models with dips of 90°, 85° east, 75° east (epistemic alternatives)	80° east
Lower Seismogenic Depth	12 to 15 km (magnitude dependent)	12.2 km
<b>Shoreline</b>		
Location	Follows mapped trace from geophysical data (PG&E, 2011; PG&E, 2014a)	Simplified but similar location near the DCPD
Dip	90° in all fault models	90°
Lower Seismogenic Depth	12 km	12 km
<b>Los Osos</b>		
Location	Follows mapped trace from geological and geophysical data closest to the DCPD (Lettis and Hall, 1994; PG&E, 2014a; PG&E, 2015a)	Simplified but similar location near the DCPD
Dip	Three fault models with dips of 60°, 80°, and 50° southwest (epistemic alternatives)	45° southwest
Lower Seismogenic Depth	12 km	12 km
<b>San Luis Bay</b>		
Location	Follows uplift rate boundary and varies by fault model (PG&E, 2015a)	(San Luis Bay and San Luis Range extended) Follows trace in SW model west of Shoreline fault; to east follows traces of Connected faults
Dip	Three fault models with dips of 75°, 45°, and 70° northeast (epistemic alternatives)	90° (San Luis Bay) 45° northeast (San Luis Range extended)
Lower Seismogenic Depth	12 km	10 km (San Luis Bay) 12 km (San Luis Range extended)

### 5.2.1.2. Fault Slip Rate Models for Primary Fault Sources

There are several new publications that have a bearing on the slip rates of the Primary fault sources (Table 5-8). These new publications are grouped into fault-specific studies, sequence stratigraphic studies, and coastal uplift rate studies.

#### **Fault-Specific Studies**

New studies that specifically address the slip rates of the Primary fault sources include geologic slip rates calculated for the Hosgri (Kluesner et al., 2023) and Shoreline (Nishenko et al., 2018) faults. The new geologic slip rate calculated for the Hosgri fault is an update of an initial study of the cross-Hosgri slope (CHS) feature documented by Johnson et al. (2014) offshore Point Estero that was considered in the 2015 SSC model (PG&E, 2015a, Chapter 8). The updated information includes much greater detail about the origin, stratigraphy, and age of the CHS feature (Kluesner et al., 2023; Medri et al., 2023). Because of the importance of the Hosgri fault slip rate to the seismic hazard and hazard uncertainty, this new information is used to update the SSC model and is discussed specifically in Sections 5.2.2 and 5.3.1 below.

The new publication of the geologic slip rate of the Shoreline fault by Nishenko et al. (2018) is based on information that was evaluated as part of the 2015 SSC SSHAC study and was documented in the CCCSIP report (PG&E, 2014a). As the published slip rate in Nishenko et al. (2018) is nearly identical to the slip rate presented in the CCCSIP report, the new publication does not require any changes to the 2015 SSC model.

#### **Sequence Stratigraphic Models**

The slip rates of the Hosgri and Shoreline faults in the 2015 SSC model relied to some degree on a sequence stratigraphic model of the continental shelf developed based on analysis of seismic-reflection data (PG&E, 2014a, 2015a). Unconformity-bound sequences mapped in the shallow subsurface of the shelf were interpreted to be associated with major sea-level fluctuations associated with Quaternary glacial and interglacial periods. The marine stratigraphy mapped on the continental shelf offshore the DCPD and overlying the Hosgri and Shoreline faults was used to constrain the ages of offset features interpreted from seismic-reflection data at the Estero Bay and Point Sal slip rate sites along the Hosgri fault, and at the offset terrace sequence site along the southern Shoreline fault (described as the paleoshoreline complex by Nishenko et al., 2018). Our review found several new published studies of continental shelf stratigraphy that are consistent with the sequence stratigraphic model approach used in the CCCSIP studies (PG&E, 2014a) and in the 2015 SSC SSHAC study (PG&E, 2015a).

Numerous recent investigations of continental shelves at several locations throughout the world have identified discrete, unconformity-bound sedimentary sequences correlated to 100-thousand-year (kyr) cycles of sea level rise and fall through interpretation of seismic reflection data, piston cores, borings, and age dating (e.g., Mestdagh et al., 2019; Villasenor et al., 2015; Liu et al., 2022; Gauchery et al., 2021). Combined with the studies cited in the previous reports (PG&E, 2014a, 2015a), these studies illustrate that applying sequence stratigraphic concepts to the interpretation of Quaternary shelf stratigraphy is a common and well-accepted approach (e.g., Ridente, 2016). Many of these investigations also recognized distinct changes in sedimentary architecture across the Mid-Pleistocene Transition from smaller-scale 41-kyr sea-level cycles to large-scale 100-kyr sea-level cycles (Liu et al., 2022; Zhuo et al., 2023; Gauchery et al., 2021). These studies document a period of substantial shelf widening during and following the Mid



Pleistocene Transition, which is a key feature of the age model for the Estero Bay and Point Sal slip-rate sites developed for the CCCSIP project (PG&E, 2014a) and by the 2015 SSC SSHAC TI Team (PG&E, 2015a).

### **Coastal Uplift Rate Models**

Other recent publications contain new models about the vertical tectonics of the coastal areas near the DCPD that are relevant to calculated geologic slip rates for the Los Osos and San Luis Bay faults. Simms et al. (2016) present a new model for paleosea levels along the Pacific coast of North America during the marine isotope stage (MIS) 5e, 5c, and 5a highstands that are approximately 120 thousand years old (ka), 105 ka, and 85 ka, respectively. The new modeling evaluated elevations of flights of marine terraces of these ages (including the marine terraces near the DCPD at Point Buchon) and compared regional variations in their elevations with glacio-isostatic adjustment (GIA) predictions. Their model represents an improvement over prior estimates of highstand paleosea levels that represented global average conditions (e.g., Hanson et al., 1994). The impact of this new model is an improved estimate of the vertical rates of tectonic motion near the DCPD.

As the Los Osos fault slip rate calculations in the 2015 SSC model use a hanging wall uplift rate based on the Q<sub>2</sub> terrace that has a preferred correlation with MIS 5e (PG&E, 2015a, Chapter 8), the new paleosea-level model and uplift rates of Simms et al. (2016) have a bearing on the net slip rate calculated for the Los Osos fault source. This model is discussed in greater detail in Section 5.2.3 and is used to update the 2015 SSC model slip rates (Section 5.3.2). The Simms et al. (2016) study does not impact the geologic slip rates calculated for the San Luis Bay fault, however, as that fault slip rate is calculated based on differential elevations of the Q<sub>2</sub> terrace (PG&E, 2015a, Chapter 8). Only the stratigraphic and age interpretation of the Q<sub>2</sub> terrace, therefore, would impact the San Luis Bay fault slip rate calculation. As the Simms et al. (2016) study adopts the same, preferred terrace correlation model (by Hanson et al., 1994) in the 2015 SSC SSHAC study, there is no change in the calculated slip rate.

O’Connell and Turner (2023) present a numerical model that predicts the pattern and rates of vertical motion along the western margin of the Irish Hills and adjacent shelf based on the geometry, slip rate, and kinematics of the Hosgri fault zone. Hosgri fault zone parameters are based on information in the 2015 SSC model (Hanson et al., 2004; Johnson and Watt, 2012; PG&E, 2015a). The viscoelastic deformation modeling result matches the pattern of uplift rate along the shelf east of the Hosgri fault (PG&E, 2011) and matches the coastal marine terrace uplift rates of Hanson et al. (1994) that are based on the elevation of the MIS 5e terrace (and a global-average paleosea level for the initial terrace elevation) (Figure 5-23). O’Connell and Turner (2023) note that this model accounts for the observed pattern of uplift rates without the need for the San Luis Bay or Los Osos faults.

Although the O’Connell and Turner (2023) model presents an interesting alternative framework for interpreting coastal uplift rates near the DCPD and questions the need for a Los Osos or San Luis Bay fault source to accommodate uplift of the Irish Hills, we have decided not to update the 2015 SSC model based on this model result. The first reason is that, while the model accounts for uplift of the outer coast of the Irish Hills near the DCPD, it does not account for interpreted differential uplift between the Irish Hills and Los Osos Valley along the northern (inland) border of the Irish Hills as interpreted on Figure 5-24 (Lettis and Hall, 1994; PG&E, 2015a), and it does not account for block uplift interpreted along the southeastward continuation of the San Luis

Range (along the Edna sub-block of Lettis et al., 1994; see PG&E, 2015a, Chapters 5 and 7). Without further study of the model relationship between the Hosgri fault (with its slip rate, slip direction, and geometry), coastal uplift east of the Hosgri, and mapped late Pleistocene faults that readily explain shortening across and uplift of the San Luis Range, we do not have confidence in an adjustment to the SSC model that would involve either reducing the slip rate of the Los Osos and/or San Luis Bay faults, or reinterpreting the San Luis Bay fault source with a lower probability of activity.

### **Geodetic Data and Model Constraints**

In addition to publications that address geologic slip rates of fault sources, our literature review included publications that examined plate tectonic constraints on coast-parallel deformation and publications of fault slip rates based, in part, on GPS geodetic data. In the 2015 SSC model, an important constraint on the modeled slip rate of the Hosgri fault source was the interpreted deformation along the eastern margin of the Pacific plate from the plate interior to the San Andreas fault (PG&E, 2015a, Chapter 8). DeMets et al. (2014), with funding from PG&E to support the 2015 SSC SSHAC study, concluded that the total coast-parallel velocity budget available for faults west of the Oceanic–West Huasna fault zone (which includes the Primary and Connected fault sources at the latitude of the DCP) is  $3.4 \pm 0.4$  mm/yr if one assumes a rigid Pacific plate with no internal deformation offshore, or  $1.8 \pm 0.6$  mm/yr if the Pacific plate deforms internally as indicated by GPS stations on Clarion, Socorro and Guadalupe Islands (Figure 5-25). This constraint is important because fault slip rate studies using mostly onshore GPS station velocities may not have good resolution on the rates of coastal and offshore faults due to the absence of velocity data on the western (seaward) sides of the faults. We did not find any publications since DeMets et al. (2014) that revised or presented alternatives to this analysis, so these estimates of coast-parallel, strike-slip motion continue to be the best available constraints for an independent measure of maximum slip rate for the Hosgri fault source.

As part of the WUS ERF-2023, five deformation models were published that include calculated slip rates and slip directions (rakes) for the WUS fault sources (Pollitz et al., 2022). The deformation models include a geology-based model (Hatem, Reitman, et al., 2022a, 2022b) and four numerical models that use a set of horizontal velocity vectors from the WUS (Zeng, 2022a) plus additional geological and/or geophysical data. The four numerical models, listed alphabetically, are the following:

- Evans (2022)
- Pollitz (2022)
- Shen and Bird (2022)
- Zeng (2022b)

Summary explanations of the different approaches taken by the models are provided in Pollitz et al. (2022). Of the candidate models, the Evans (2022) model was determined to be much less reliable than the others by a review team (Johnson et al., 2024), and this model was weighted significantly lower than the other models in the WUS ERF-2023 (Jordan et al., 2023; Field et al., 2023). For this reason, we do not include the results of the Evans (2022) model in further comparisons with the 2015 SSC model or updated results.

Table 5-11 lists the 2015 SSC model Primary fault slip rates along with the equivalent fault slip rates from the four main deformation models (geologic model plus three numerical models)

being considered for the WUS ERF-2023. Mean slip rates and standard deviations are listed for the WUS ERF-2023 models; the 2015 SSC model slip rates listed are the mean rates and the 5–95 percentile ranges from the slip rate CDFs (PG&E, 2015a, Chapter 8). The large standard deviations reported for the Pollitz (2022), Shen and Bird (2022), and Zeng (2022b) models are not explained in sufficient detail to understand what contributes most to the model slip rate uncertainty, and therefore comparable 5–95 percentile ranges are not tabulated. For the San Luis Bay fault source, we report deformation model slip rates from the WUS ERF-2023 for the longer San Luis Range (extended) source, which has a 45° dip in the USGS geometry model, instead of the slip rates for the vertical San Luis Bay source. We do this substitution because it is unclear how the deformation models would resolve reverse, dip-slip displacement on a vertical fault based on a horizontal GPS velocity field. The San Luis Range (extended) model slip rates are greater than the model slip rates for the San Luis Bay source by up to a factor of 2.

The comparison suggests generally consistent results in fault slip rates, with all but two deformation model slip rates falling within the 90% confidence range of the 2015 SSC model slip rates (Table 5-11). The Pollitz (2022) model mean slip rate for the Hosgri fault (3.8 mm/yr) exceeds the 95% probability level (3.0 mm/yr), and the Pollitz (2022) model mean slip rate for the Shoreline fault (0.01 mm/yr) is lower than the 5<sup>th</sup> probability level for the Shoreline fault (0.03 mm/yr). The large reported standard deviations in the Pollitz (2022) model indicate that the 2015 SSC model slip rates are not outside the deformation model uncertainty range.

**Table 5-11. Comparison of Fault Source Slip Rates, 2015 SSC Model and WUS ERF-2023 Deformation Models**

Fault Source	2015 SSC Model Rates (mm/yr)	WUS 2023-ERF Deformation Model Slip Rates (mm/yr)			
		Geologic	Pollitz	Shen-Bird	Zeng
Hosgri (all FGMs)	1.7 (0.6-3.0)	2.5 ± 1.0	3.8 ± 1.3	1.0 ± 0.5	2.8 ± 0.7
Shoreline (all FGMs)	0.07 (0.03-0.16)	0.1* ± 0.125	0.01 ± 0.08	0.05 ± 0.10	0.11 ± 0.90
Los Osos OV	0.26 (0.17-0.39)	0.39* ± 0.2	0.25 ± 0.07	0.24 ± 0.08	0.21 ± 0.91
Los Osos SW	0.19 (0.13-0.27)				
Los Osos NE	0.42 (0.31-0.55)				
San Luis Bay OV	0.16 (0.10-0.24)	0.2*† ± 0.125	0.20† ± 0.10	0.12† ± 0.09	0.13† ± 0.7
San Luis Bay SW	0.22 (0.13-0.32)				
San Luis Bay NE	0.16 (0.10-0.24)				

\* A category slip rate; not based on site-specific data

† Slip rate listed for the 45° San Luis Range (extended) source, which has a higher slip rate than the vertical San Luis Bay source in the ERF-2023 model.

In the 2015 SSC SSHAC report, a prior generation of deformation models developed for the UCERF3 project, including three geodesy-based models, were considered, and documented for comparison (PG&E, 2015a, Chapter 13). In addition, Dr. Peter Bird provided a proponent model that examined strain rates from GPS data resolved as on-fault horizontal slip rates for faults in south-central coastal California using the NeoKinema model (PG&E, 2015a, Chapter 5; Bird,

2012). The slip rates calculated from these studies were not used directly in the development of the fault slip rate CDFs for the following reasons:

- The calculated slip rates do not explicitly account for site-specific geologic information
- The slip rates use as input a fixed set of fault locations and geometries that do not reflect the best-available data near the DCP
- Given the density of fault sources near the DCP, there is low confidence that geodetic data could resolve the rates and kinematics of individual faults
- The coastal location of the Primary fault sources presents a challenge given the absence of offshore GPS velocities
- The uncertainties within each model are poorly understood, which reduces confidence in the robustness of the mean model result

The same findings regarding the confidence in the GPS-based deformation models apply to this SSC model update. We consider the WUS ERF-2023 deformation models to be insufficiently documented and tested for their reliability and suitability to be included directly in the calculation of fault slip rate CDFs. The fixed fault geometries, the density of fault sources relative to onshore distribution of GPS stations, the challenges of calculating slip rates for coastal and offshore faults with the absence of velocity information on the seaward side of the faults, and the lack of understanding of what factors contribute to the uncertainties within the models together form a basis for not including these model slip rate results in the fault slip rate model for this site-specific seismic hazard assessment. A peer review of these deformation models for general use in the WUS ERF-2023 project raised similar concerns about a lack of understanding of what contributes to the model uncertainties (Johnson et al., 2024), and these concerns were echoed in summary reports for the WUS ERF-2023 (Field et al., 2023) and the 2023 NSHM update (Petersen et al., 2023). A comparison of the WUS ERF-2023 deformation models provides sufficient documentation to demonstrate the general consistency between the Primary fault source slip rate CDFs and available geological and geodetic data, models, and methods.

#### 5.2.1.3. Rupture and Slip Rate Allocation Models for Primary Fault Sources

Recently published papers on rupture complexity and factors that promote or control dynamic rupture propagation include empirical studies and numerical studies. Empirical studies on rupture propagation published since the 2015 SSC SSHAC study include Biasi and Wesnousky (2016), which studied the sizes and patterns of fault stepovers that were ruptured through or that coincided with rupture terminations, and Biasi and Wesnousky (2017), which studied bends in faults that were ruptured through or that coincided with rupture terminations. In both studies, the authors developed data and empirical models on passing probabilities. The general finding of these studies—that there are examples of ruptures that are both arrested by and rupture through geometric complexities in faults that represent challenges to dynamic rupture propagation—was understood by the 2015 SSC SSHAC TI Team through earlier publications (e.g., Wesnousky, 2008; Biasi et al., 2013) and incorporated in the Rupture Models and Slip Rate Allocation Models (PG&E, 2015a, Chapter 9). The new passing probability information does not warrant a revision to the 2015 SSC model.

New publications on dynamic rupture modeling continue to explore geometrical and physical factors that promote or inhibit rupture propagation. Examples of papers published since the 2015 SSC SSHAC include Lozos et al. (2015), Oglesby (2020), and Lozos (2021). The additional

insights from these models are generally consistent with the understanding of geometric challenges to rupture propagation (e.g., Harris and Day, 1999; Lozos et al., 2011) when developing the rupture sources in the 2015 SSC model.

#### 5.2.1.4. Earthquake Magnitude Distribution Models for Primary Fault Sources

The shape of the earthquake magnitude-frequency distribution for fault sources is a topic of appreciable discussion (Hecker et al., 2013; Field et al., 2017; Kagan et al., 2012; Parsons et al., 2018). The 2015 SSC model (PG&E, 2015a, Chapter 10) used a variety of functional forms of the distribution depending on the nature of the rupture source, including the maximum magnitude distribution of Wesnousky et al. (1983), the characteristic magnitude distribution of Youngs and Coppersmith (1985), and a modification of the characteristic magnitude distribution that allows for earthquake magnitudes greater than those estimated to be “characteristic” but with empirical data constraints (the WAACY model documented in the 2015 SSC SSHAC report; PG&E, 2015a, Chapter 10). For longer rupture sources, a weight of [0.2] was also given to the doubly truncated exponential magnitude-recurrence model (Cornell and Vanmarcke, 1969).

Our review did not encounter any publications that suggest the magnitude distributions considered in the 2015 SSC model should be revised or re-weighted. We recognize that some SSC model approaches, such as the Seismic Hazard Inferred From Tectonics (SHIFT) model of Bird and Liu (2007), implement an exponential magnitude-recurrence relationship with parameters (effective elastic thickness, beta value, and corner magnitude) based on aggregated information from global seismicity data. As discussed in Chapter 6, we do not consider this method to be a valid alternative for a site-specific seismic hazard study of the DCPD because it relies on global-average information rather than site-specific information.

Additionally, sensitivity analyses documented in the 2015 SSC SSHAC report (PG&E, 2015a, Chapter 14) and summarized here (Figures 5-20 and 5-21) show that the choice of WAACY versus doubly truncated exponential models for the longer rupture sources has a minimal impact on hazard.

#### 5.2.1.5. Time Dependency Models for Primary Fault Sources

New publications of models that explore how to incorporate time-dependent behavior of fault sources for PSHA include Biasi and Thompson (2018) and Neely et al. (2022). The Biasi and Thompson (2018) contribution is the EPHR methodology that was developed specifically for and used in the 2015 SSC model (PG&E, 2015a, Chapter 11 and Appendix H). Neely et al. (2022) present a new methodology for calculating earthquake probabilities for fault sources based on the long-term fault memory (LTFM) model introduced in Salditch et al. (2020). The LTFM earthquake probability model has advantages over the use of single earthquake recurrence models (such as the exponential, lognormal, Brownian passage time, and Weibull models, e.g., Matthews et al., 2002) in that it can model the temporal patterns of earthquake strain accumulation and release, including earthquake clustering. To account for partial strain release on faults and therefore model where the fault may be in its earthquake cycle, the LTFM model incorporates data on past earthquake timing (Neely et al., 2022).

Although very relevant to well-studied, high-slip-rate faults such as the San Andreas and San Jacinto faults, the LTFM model of Neely et al. (2022) is not well suited for the Primary and

Connected fault sources near the DCPD because there are no reliable paleoseismic records of past earthquake timing. The EPHR methodology was specifically developed to explore uncertainty in the time dependency of fault sources that lack paleoseismic data on the timing or size of the most recent event (Biasi and Thompson, 2018). The SSC model update, therefore, cannot take advantage of the additional insight about partial strain release provided by the LTFM model.

#### 5.2.1.6. Virtual Fault Geometry Model for Local Areal Source Zone

As discussed in Section 5.1.2, the Local source zone in the 2015 SSC model is one of the main contributors to hazard at the DCPD (Figure 5-14). The earthquakes in the Local source zone are modeled as occurring on a set of subparallel virtual faults (Figure 5-26), with defined aleatory and epistemic uncertainties in location, rake, dip, and  $M_{\max}$  (PG&E, 2015a, Chapter 13). The 2015 SSC model logic tree developed the geometric and kinematic parameters for the virtual faults based on an evaluation of local earthquake focal mechanisms, microseismicity trends, and site-specific geological and geophysical data (e.g., Hardebeck, 2010, 2013, 2014b) (Figure 5-27). The virtual faults capture the observed patterns of local seismicity that do not coincide with geomorphically recognized uplift rate boundaries or with active faults recognized in high-resolution seismic data. In this sense, they represent plausible orientations of faults that may rupture in “background” earthquakes.

There are no new published interpretations of the available data that warrant updating of the geometry model for the Local source zone (Table 5-9). The proponent fault geometries proposed by Dr. Bird in written testimony are discussed in Chapter 6 of this report.

#### 5.2.1.7. Earthquake Magnitude-Rate Calculation for the Local Source Zone

The earthquake magnitude-rate relationship for the Local source zone in the 2015 SSC model adopted the doubly truncated exponential magnitude PDF with Gutenberg-Richter  $a$ - and  $b$ -values based on an analysis of catalog seismicity (PG&E, 2015a, Chapter 13). The alternative  $a$ - and  $b$ -value pairs used in the model are based on examination of several earthquake catalogs, including a catalog developed by PG&E, the UCERF3 earthquake catalog (Felzer, 2013), and a catalog developed by Dr. Hardebeck of the USGS (Hardebeck, 2010, 2014a) (PG&E, 2015a, Chapter 13 and Appendix F). No reductions were made to the rate of earthquakes in the Local source zone to account for the rate of  $M \geq 5$  earthquakes modeled to occur on the Shoreline, San Luis Bay, and Los Osos faults. This conservative approach was adopted mostly out of simplicity and, based on the approach taken in this current study, we do not propose any revisions to the 2015 SSC model that would explicitly remove the “double counting” of earthquakes.

The catalog of Dr. Hardebeck (Figure 5-28) was extended from 2013 to the end of August 2023 in the DCPD vicinity to evaluate whether patterns and rates of seismicity in the past approximately 10 years have changed and therefore may indicate a need to revise the  $a$ - and  $b$ -value estimates for the Local source zone (Table 5-9). An update of the Hardebeck (2014a) catalog was the most straightforward way to evaluate changes to the Local seismicity as this catalog is compiled down to a lower cutoff magnitude of 0 and does not include declustering.

Earthquakes of magnitude ( $m$ )  $\geq 0$  from the ANSS Comprehensive Earthquake Catalog (ComCat; USGS, 2017) were downloaded and merged with the Hardebeck (2014a) catalog. A six-month overlap period (between June and November 2013) was used to verify that changes in location and magnitude were minimal. The extended ComCat earthquakes are symbolized with green

squares on Figure 5-29, with bright (neon) green squares for events within the Local source zone and light green squares for events in the surrounding areas. Earthquakes from the earlier Hardebeck (2014a) catalog are displayed in orange circles (magnitudes and depths of these events are shown on Figure 5-28).

The extended ComCat events show a similar spatial distribution as the Hardebeck (2014a) catalog, with a concentration of events northeast of the Oceanic-West Huasna fault zone in the aftershock area of the 2003 San Simeon earthquake (McLaren et al., 2008), and lesser concentrations along the Hosgri fault, near Point Sal, and within the Local source zone that covers the Irish Hills and adjacent Estero Bay (Figure 5-29). The extended catalog included 143 events within the Local source zone in the range  $0.3 \leq m \leq 3.1$ , with all reported magnitudes in the duration magnitude (md) scale except for the largest event, which was measured in the local magnitude (ml) scale. This compares to 627 earthquakes from late 1987 through late 2013 in the range  $0 \leq m \leq 3.5$  within the Local source zone in the Hardebeck (2014a) catalog.

Figure 5-30 summarizes some earthquake catalog statistics comparing information available to the 2015 SSC SSHAC study to information available now. Figure 5-30a shows the distribution of earthquakes by magnitude with time from late 1987 through August 2023. Events in the extended catalog (open squares) show a similar size and frequency pattern as the events in the Hardebeck (2014a) catalog (filled circles), with no change in the maximum magnitude over the extended period. Figure 5-30b shows the log of the cumulative annual rate of earthquakes ( $m \geq m_0$ ) versus magnitude using information from the Hardebeck (2014a) catalog only (filled circles; 25.91-year duration), and from the Hardebeck (2014a) catalog and extended catalog combined (open circles; 35.86-year duration). As documented in PG&E (2015a, Chapter 13), the increase in slope between  $m_0 = 0$  and approximately  $m_0 = 1.1$  clearly shows that the catalogs are incomplete, missing events with magnitudes in this range. Above  $m_0 = 1.1$ , casual inspection suggests the catalog may be complete. The earthquake rate including the extended catalog is comparable to, though slightly less, than the rate calculated for the 2015 study, but the shapes are very similar.

An updated comparison of calculated  $b$ -values from the Local source zone seismicity versus different estimates of the completeness magnitude ( $m_c$ ) is shown on Figure 5-30c. The  $b$ -values are calculated using the maximum likelihood method of Aki (1965) (Equation 13-3 in PG&E, 2015a). The results show a steady rise in  $b$ -value between magnitude 1.0 and approximately 1.5, a consistent  $b$ -value of approximately 1.0 between magnitude 1.5 and 1.9, then a larger  $b$ -value greater than 1.1 for  $m_c = 2.0$ . The  $b$ -values calculated from the Hardebeck (2014a) catalog (filled circles) are very similar to the  $b$ -values calculated with the inclusion of the extended catalog (open circles). As discussed in PG&E (2015a), estimates of  $b$ -value for magnitudes 2 and greater are considered less reliable due to low  $N$  values. The steady rise in  $b$ -value from magnitude 1 to 1.5 before stabilizing suggests that the magnitude of completeness is equal to or greater than approximately 1.5. Importantly, the plots document no significant changes in the rates or distributions of earthquakes in the Local source zone since the 2015 SSC Model, and therefore updates to the  $a$ - and  $b$ -values considered in the 2015 SSC model are not warranted based on a re-evaluation of the local seismicity.

Other sources of new information for the rates of background seismicity in the Local source zone come from the deformation models being considered for the WUS ERF-2023 (Pollitz et al., 2022) (Table 5-9). Three of the numerical models, the Pollitz (2022), Shen and Bird (2022), and Zeng (2022b) models, include calculated off-fault deformation rates that complement their

modeled fault slip rates. The off-fault deformation rates have been proposed as an alternative to catalog seismicity to calculate background earthquake rates in regional studies (Bird and Liu, 2007; Kreemer and Young, 2022; Pollitz et al., 2022). In the numerical deformation models for the WUS ERF-2023, the off-fault deformation is presented as gridded moment rates with a  $0.1^\circ$  spacing. These values may then be converted to background earthquake rates by moment balancing and adopting a shape of the magnitude PDF. Using the commonly applied doubly truncated exponential model, this would require defining a  $b$ -value and  $M_{\max}$ .

We do not consider the off-fault deformation rates estimated by the WUS ERF-2023 numerical deformation models to be technically defensible alternatives to the use of earthquake catalog seismicity for estimating future earthquake rates for the background source zones for the DCP. The concerns we have are similar to those listed in Section 5.2.1.2 for the fault slip rates. Of greatest concern is the lack of understanding of the contributions to model uncertainty and the lack of consideration of site-specific information and alternative fault geometries that may be important for calculating on- and off-fault deformation. Our concerns about a lack of understanding about the components of the off-fault deformation signal and what contributes to model uncertainties are expanded on in the technical peer review reports for the WUS ERF-2023 deformation models (Johnson et al., 2024). Based on these concerns, the off-fault deformation models will not be used to determine the rates of background seismicity for the WUS ERF-2023 (Field et al., 2023; Petersen et al., 2023).

Finally, our review documented new methods for the calculation of earthquake catalog  $b$ -values (e.g., van der Elst, 2021) for earthquake catalog declustering (e.g., Zaliapin and Ben-Zion, 2020; Llenos and Michael, 2020), including discussion of whether declustering should be performed for calculating earthquake rates (Marzocchi and Taroni, 2014), and for spatial smoothing of seismicity (Field et al., 2023). Some of these methods are being implemented for the first time for the 2023 NSHM (Field et al., 2023; Petersen et al., 2023), and investigating their performance and implications for a site-specific study at the DCP would take an extensive effort. Based on the hazard sensitivities performed for the 2015 SSC model (PG&E, 2015a, Chapter 14), it is unlikely that these new models and methods will have a significant impact on the hazard contribution of the Local background model. Therefore, we do not propose any changes to the Local background model for this project based on this new information.

#### 5.2.1.8. Summary of Findings on New Information that Warrant Additional Analysis

The review of new information relevant to hazard-significant faults and parameters in the 2015 SSC model suggests that two items need to be re-evaluated in greater detail. These items are the Hosgri fault slip rate, for which new information is available at the offshore cross-Hosgri slope feature (Kluesner et al., 2023; Medri et al., 2023), and the Los Osos fault slip rate, for which a new model of coastal uplift rates and paleosea levels by Simms et al. (2016) impacts the vertical uplift rate component of the net slip rate. This additional information is presented in greater detail in the subsections below. Updates to the slip rate calculations for the Hosgri and Los Osos fault sources are presented in Section 5.3.



### **5.2.2. New Information on Hosgri Slip Rate**

In the Point Estero study area, Johnson et al. (2014) documented a submerged slope in water depths between about 66 and 73 m that they named the cross-Hosgri slope (CHS) and interpreted as a shoreface that formed seaward of a latest Pleistocene sand spit. They interpreted the feature to have formed slightly below sea level during the Younger Dryas stadial (~12.8–11.5 ka). Johnson et al. (2014) interpreted that the CHS was abandoned during meltwater pulse 1B, directly after the Younger Dryas stadial, when sea level rose rapidly and the shoreface was drowned. Using slope maps derived from a high-resolution multibeam echosounder (MBES) survey collected specifically for the study and slope-normal profiles spaced 12.5 m apart, Johnson et al. (2014) interpreted a lateral offset of  $30.3 \pm 9.4$  m of the lower slope break (Figure 5-31). Assuming an age of the submersion and preservation of the lower slope break estimated from global sea-level curves, they interpreted a lateral slip rate of  $2.6 \pm 0.9$  mm/yr for the primary strand of the Hosgri fault.

For the 2015 SSC model, the TI Team developed a slip rate CDF of the Hosgri fault at this site using offset measurements of the lower slope break and age estimates reported by Johnson et al., (2014). However, the Point Estero slip rate CDF was assigned a weight of [0.2] from a collection of four alternative Hosgri slip rate sites for calculating the Hosgri fault source slip rate CDF to be used in hazard calculations (PG&E, 2015a, Chapter 8). Although the CHS provides a shorter-term (Holocene) slip rate that may better represent the current rate of slip for the Hosgri fault relative to some of the alternative slip rate sites, the relatively lower weight assigned to this site reflected the 2015 SSC SSHAC TI Team's judgment regarding the quality of this feature as a well-constrained piercing point and potential underestimation of the uncertainty in the offset amounts used for slip rate calculations. To be a valid piercing point, a feature must be isolated in space and time, so that the original geometry of the feature at a known time can be reconstructed, and fault deformation of the feature can be distinguished from other processes. For the CHS, the 2015 SSC SSHAC TI Team noted that significant uncertainties existed in the original geometry of the feature and the time that the feature stabilized (or was abandoned), and that these uncertainties were not incorporated into the offset measurements (PG&E, 2015a, Chapter 8). The slope itself includes erosional hollows near the top and depositional lobes near the bottom, suggesting that the CHS has been modified by slumping and, perhaps, incision by submarine currents (Figure 5-31). Slope break measurements from the top and the bottom of the CHS include steps and bulges that appear to be associated with these slumps, suggesting that the top and bottom of the slope have been modified since it was formed. Given the likelihood that the feature is composed of saturated sand and has undergone multiple earthquake ruptures and associated strong ground motion, some slope failures or lateral spreading can be expected.

As shown on Figure 5-31, only a subset of slope break measurements was used by Johnson et al. (2014) to characterize offset of the CHS feature. It is not clear that the subset used to measure offset best represents the original geometry of the feature. The part of the slope directly east of the fault appears to have degraded, and the slope may have widened, moving the lower slope break farther south than its original position. The slope break points that are east of the fault and are used to measure offset, shown as blue circles on Figure 5-31, are significantly farther from the top of the slope than the slope break points from the steeper, and possibly more intact, part of the slope farther to the east. Regressing different subsets or the entire collection of measurements yields markedly different estimates of offset.

Since completion of the 2015 SSC SSHAC study, a substantial volume of new data has been collected that greatly improves our understanding of the genesis and evolution of the CHS. This includes over 450 km of high-resolution seismic reflection data (including both sparker and chirp data), seven vibracores, 30 radiocarbon analyses, and 10 optically stimulated luminescence (OSL) analyses of sediments collected from the vibracores (Figure 5-32). Interpretations of these data, together with the data themselves, are presented in recent publications by Kleusner et al. (2023) and Medri et al. (2023).

The new data demonstrate that the CHS has a complex depositional history and consists of two primary stratigraphic units (Figure 5-33). The lower unit (unit 1) overlies the post-last glacial maximum transgressive surface of erosion and is interpreted as a shoreface deposit based on seismic facies (offshore-dipping reflections), sediment texture (clean fine sand), sediment infauna, and a significant component (~8.4%) of heavy minerals (Kleusner et al., 2023). Radiocarbon and OSL dates from this unit are consistent with deposition during the Younger Dryas stadial (Figure 5-34). This shoreface was likely partially eroded and abandoned during the subsequent pulse of rapid sea-level rise and transgression that ended approximately 7 ka (Kleusner et al., 2023). Unit 2 buries the lower unit 1 and is described by Medri et al. (2023) as a subaqueous clinof orm based on its seismic character. Vibracores reveal that it is composed of beds with an erosive base, overlain by shelly fine sands, and a fining-upward sequence marked by alternating parallel and ripple cross-laminated very fine sands. It is often capped by fine silts interbedded with thin, very fine sand beds. Radiocarbon dating of shells collected just above the erosive base indicate the subaqueous clinof orm initiated progradation approximately 7 ka, nucleating on the seafloor irregularity created by the underlying relict shoreface (Medri et al., 2023). Radiocarbon and OSL dates from samples collected higher in unit 2 show that it has continued to build since then (Figure 5-34). Medri et al. (2023) suggest that unit 2 was created by winter-storm waves mobilizing sands from the inner shelf in water depths up to about 70 m, which transitioned into wave-supported gravity flows. The wave-supported gravity flows may have traveled downslope to water depths of up to about 80 m, corresponding to the foot of the subaqueous clinof orm, a depth at which wave influence is negligible and the shelf gradient is insufficient to maintain movement of the load alone.

This improved understanding of the complexity of the CHS demonstrates that the offset measurements used by Johnson et al. (2014) to calculate slip rate were from a different surface than the shoreface that was abandoned at the end of the Younger Dryas stadial. Kleusner et al. (2023) conclude that the chirp and core data combined indicate that the lower slope break represents the base of the unit 1 shoreface. They note that unit 2 thins downslope, becoming only about 50-60 cm thick at the lower slope break near the Hosgri fault trace, and suggest that the presence of unit 2 does not compromise this distinct geomorphic feature as a piercing point. They also note that even if they ignore or remove the thin unit 2 cover, it would not change the locations of the lower slope break relative to one another on bathymetric slope profiles. As a result, Kleusner et al. (2023) use the same offset amounts and uncertainties characterized by Johnson et al. (2014) to recalculate the Hosgri fault slip rate. They note, however, that “it seems possible that undetected variations in unit 2 thickness could lead to greater uncertainty in locating the minimally buried base of the latest Pleistocene shoreface, but that increase cannot be quantified with current data.”

We agree with Kleusner et al. (2023) that the presence of unit 2 burying the relict shoreface, and the potential variability in the thickness of unit 2, leads to greater uncertainty in locating the base

of the shoreface, and consequently, greater uncertainty in estimates of the amount this feature is offset by the fault. As noted above, fault offset of the shoreface was interpreted from measurements of the break-in-slope between the face of the CHS and the gently sloping seafloor below. The position of the slope break was selected from each profile as the intersection of straight lines fitted to both slopes (Johnson et al., 2014). This method of selecting slope break locations is highly sensitive to the slope of the feature itself, which is defined by the deposition of unit 2 sediments, and not by the top of the shoreface deposits (top of unit 1). Despite this uncertainty, we recognize that the CHS is systematically offset by the Hosgri fault, and that the slope break at the base of the CHS approximately coincides with the top of the unit 1 shoreface deposits.

Based on the improved understanding of the feature, we revise the 2015 SSC model characterization of uncertainty in both offset amount and age of the CHS and calculate a revised slip rate CDF for the Point Estero slip rate site (Section 5.3.1). In addition, the logic-tree weight assigned to the Point Estero slip rate site is revised higher compared to the 2015 SSC model to reflect the greater confidence in understanding the origin and age of the feature.

### **5.2.3. New Information on Los Osos Slip Rate**

The coastal uplift rate model of Simms et al. (2016) refines the paleosea levels (commonly called relative sea levels) along the central California coast near the DCPD during the MIS 5e (~129–119 ka), 5c (~106 ka), and 5a (~86 ka) sea level highstands. This model adopts the same interpretation of the marine terrace stratigraphy in the DCPD vicinity as Hanson et al. (1994), but utilizes an estimate of local paleosea levels based on the incorporation of glacio-isostatic adjustment (GIA) effects. This is an improvement over the Hanson et al. (1994) model, which used paleosea levels that represented global average estimates (i.e., eustatic sea levels).

The Simms et al. (2016) model impacts the calculated slip rate of the Los Osos fault source in the 2015 SSC model because the vertical uplift rate of the Los Osos fault is calculated based on different stratigraphic and geomorphic features for rates of the hanging wall (HW) and footwall (FW) (PG&E, 2015a). The HW uplift rate is based on the well-preserved Q<sub>2</sub> marine terrace along the outer coast of the Irish Hills, between approximately the DCPD and Islay Creek (Figure 5-35). The vertical rate of the Los Osos fault FW is based on older strain markers (PG&E, 2015a, Chapter 8). In the 2015 SSC model, two alternative interpretations of the Q<sub>2</sub> marine terrace are considered: the correlation of the Q<sub>2</sub> terrace with MIS 5e and a paleosea level of +6 m (the Hanson et al., 1994 model shown in blue on Figure 5-35), and the correlation of the Q<sub>2</sub> terrace with MIS 5c, and a paleosea level of +4 m (the Muhs et al., 2012 model shown in red). Because there are local radiometric age and paleoenvironmental data from the Point Buchon area that strongly favor the terrace correlation model of Hanson et al. (1994), that interpretation received a weight of [0.8] in the Los Osos uplift rate calculation (PG&E, 2015a, Chapter 8). The alternative terrace correlation model of Muhs et al. (2012) received a weight of [0.2] because the SSC TI Team judged that it could not be rejected from available data.

The new Simms et al. (2016) model adopts the marine terrace stratigraphic interpretation of Hanson et al. (1994) as a model constraint. Therefore, this new model does not provide new information to affect the weighting allocated by the 2015 SSC TI Team to the alternative stratigraphic interpretation of the Muhs et al. (2012) model. Because of this, the Simms et al. (2016) model does not impact the calculated slip rate of the San Luis Bay fault. The San Luis

Bay fault vertical slip rate is calculated based on the uplift rate change of the Q<sub>2</sub> terrace from Point San Luis to approximately the DCP (i.e., between approximately 0 and 10,000 m distance on Figure 5-35). Because the vertical slip rate is based on the change in uplift rate, only the relative elevations and ages of the Q<sub>2</sub> terrace are used (i.e., no assumption about paleosea level is required).

The Simms et al. (2016) model evaluated the elevations and altitudinal spacing of flights of marine terraces correlated with the MIS 5a, 5c, and 5e sea-level highstands and compared regional variations with GIA models (using the CALSEA program) that account for the variability in ice sheet volume and extent (Nakada and Lambeck, 1987; Lambeck et al., 2012). The MIS 5e has the least amount of elevation variability due to GIA and was used as the main datum for tectonic corrections (Simms et al., 2016). For most of the California coast, the predicted paleosea level for MIS 5e is approximately +13 m (Figure 5-36), which is 7 meters greater than the +6 m paleosea level assumed in the Hanson et al. (1994) model. The higher MIS 5e paleosea level in the Simms et al. (2016) model suggests lower coastal uplift rates than calculated previously because the amount of uplift is less. The revised lower rates of coastal uplift along the California coastline are consistent with uplift rates calculated by Simms et al. (2020) using independent methods at a site in San Diego in a study aimed specifically to test the Simms et al. (2016) model.

The impact of the Simms et al. (2016) model on the uplift rates along the Irish Hills coastline is shown on Figure 5-37. The uplift rate profile for the Simms et al. (2016) model is shown in green alongside the Hanson et al. (1994) model (blue) and the Muhs et al. (2012) model (red). The profile extent is identical to that shown on Figure 5-35, and for simplicity the profiles reflect only the preferred survey elevation data (uncertainties are shown on Figure 5-35). The dashed green lines indicate the values for the uplift rate based on the MIS 5e model with GIA adjustment at Point Buchon calculated by Simms et al. (2016), with the long-dash line representing the preferred uplift rate of 0.14 mm/yr and the short-dash lines showing the  $\pm 0.04$  mm/yr uncertainty. Section 5.3.2 presents a reassessment of the uplift rate PDF for the Los Osos fault HW based on this new information as well as an updated calculation of the Los Osos fault slip rate CDFs.

### **5.3. UPDATES TO THE 2015 SSC MODEL**

Based on the review of new information, the 2015 SSC model is updated to account for the new information supporting the calculated geologic slip rate of the Hosgri fault and for the new information that bears on the geologic slip rate of the Los Osos fault. And because the weighted mean EPR is correlated with weighted mean fault slip rate, the weighted mean EPR for the Hosgri fault is also updated.

No change to the EPR is needed for the Los Osos fault source, as the change in weighted mean slip rate for that fault source is relatively small, and the absolute value of the weighted mean slip rate is also relatively small. These small changes would result in an insignificant change in the EPR estimates for the Los Osos fault source.

#### **5.3.1. Hosgri Fault Source Update**

The 2015 SSC model slip rate CDF for the Hosgri fault was based on developing slip rate CDFs at four sites along the fault within the general vicinity of the DCP (PG&E, 2015a, Chapter 8)

(Figure 5-38). At each slip rate site, the preferred values and uncertainty ranges of both the offset amount and the age of the offset feature were captured using one or more trapezoidal PDFs. As these uncertainties are not correlated, the slip rate CDFs were developed based on Monte Carlo sampling of the offset and age PDFs. The four slip rate sites, their distances from the DCP, and the type and age of the offset feature used to calculate a geologic slip rate are summarized in Table 5-12. Plots of the four slip rate site CDFs and the weighted Hosgri fault CDF are shown on Figure 5-39. This slip rate CDF has a weighted mean slip rate of 1.7 mm/yr with a range of 0.6 to 3.0 mm/yr (approximate 5<sup>th</sup>–95<sup>th</sup> percentile range). As discussed in PG&E (2015a, Chapter 8), the slip rate CDF represents the target slip rate (mean and uncertainty distribution) for the sections of the Hosgri fault source closest to the DCP, which are the sections that contribute most to hazard at the return periods of interest (Section 5.1.2). The rupture sources and slip rate allocation models add additional slip rate to sections of the Hosgri fault source north of the DCP due to the addition of rupture sources involved with the intersections of the Hosgri fault with the Shoreline and Los Osos faults (PGE, 2015a, Chapter 8). This additional slip rate is consistent with the interpretation that the Hosgri-San Gregorio fault system slip rate increases from south to north as fault-parallel motion is transferred to the fault system from intersecting faults to the east.

**Table 5-12. Comparison of Hosgri Fault Slip Rate Sites, 2015 SSC Model**

<b>Study Site</b>	<b>Distance from DCP</b>	<b>Offset Feature</b>	<b>Age of Feature (approx.)</b>	<b>2015 Model Slip Rate (mean)</b>	<b>2015 Logic-Tree Weight</b>
San Simeon	60 km (north)	Marine Terrace	200 ka	1.8 mm/yr	0.3
Point Estero (CHS)	40 km (north)	Relict Shoreface	12 ka	2.5 mm/yr	0.2
Southern Estero Bay	15 km (north)	Buried Channel	700 ka	1.7 mm/yr	0.3
Point Sal	40 km (south)	Buried Channel	700 ka	0.8 mm/yr	0.2

Based on the new information on the CHS published in Kluesner et al. (2023) and Medri et al. (2023) (Section 5.2.2), two changes to the Hosgri fault source slip rate CDF are required. The first is a re-evaluation of the slip rate CDF for the Point Estero (CHS) site. The second is a re-evaluation of the weighting scheme for the four Hosgri slip rate sites. The result of these two re-evaluations is an update of the calculation of the Hosgri fault source slip rate CDF and, based on the approach taken in this seismic hazard update, an update of the weighted mean slip rate.

#### 5.3.1.1. Point Estero (Cross-Hosgri Slope) Slip Rate CDF

The new information on the stratigraphy and age dating of the CHS resulted in changes to the uncertainty PDFs representing the lateral offset amount of the CHS and age of the offset feature. For the lateral offset amount, the update adopts the same preferred range of offset, 26–35 m, as was used in the 2015 model, as we concur with Kluesner et al. (2023) that the approach adopted

by Johnson et al. (2014) remains the best available means to measure the lateral offset of the feature. This range of lateral offset, which is used to define the top of the trapezoidal uncertainty distribution, represents the  $\pm 1$  standard deviation values estimated by Johnson et al. (2014) using the lower slope break of the CHS and the USGS MBES dataset (Table 5-13). As in the 2015 SSC study, we believe that there is no good basis for a preferred offset amount within this range, as there are several remaining uncertainties related to the approach used to define the lower slope break, the number of profiles used to define an original shape of the lower slope break away from the fault, and the multibeam data and data processing itself.

The minimum and maximum offset values in the trapezoidal PDF are expanded in the updated assessment (Table 5-13) to account for additional sources of uncertainty in the offset of the relict shoreface feature. These additional sources of uncertainty are discussed in Section 5.2.2. The updated limits are set to 10 m beyond the  $\pm 2$  standard deviation values from the Johnson et al. (2014) analysis, which we judge to be appropriate based on the new information about the erosional history and stratigraphic complexity of the CHS feature (Kluesner et al., 2023) and the unknown variability or systematic differences in the modification of the feature due to erosion and deposition since its formation during the Younger Dryas stadial and subsequent abandonment. The new full uncertainty range (10 to 50 m) also captures the interpreted offsets of the upper slope break and slope face by Johnson et al. (2014). The offset uncertainty PDF adopted in this update is broader than the  $30.3 \pm 9.4$  m (95% confidence limit) used by Kluesner et al. (2023) in their slip-rate calculation (Table 5-13).

**Table 5-13. Changes to the Uncertainty PDF, Offset of Cross-Hosgri Slope**

Trapezoid	2015 SSHAC	2023 Update	Notes
Min limit	15 m	10 m	Limit extended to 10 m beyond the -2 sigma value of Johnson et al. (2014) to account for unknown variability in the difference between the modern slope surface and the intended strain marker (the shoreface).
Preferred min	26 m	26 m	No change. Represents the -1 sigma value of the estimated offset of the base of the slope using the USGS dataset (Johnson et al., 2014).
Preferred max	35 m	35 m	No change. Represents the +1 sigma value of the estimated offset of the base of slope using the USGS dataset (Johnson et al., 2014).
Max limit	43 m	50 m	Limit extended to 10 m beyond the +2 sigma value of Johnson et al. (2014) to account for unknown variability in the difference between the modern slope surface and the intended strain marker (the shoreface).

For the age of the offset feature, the uncertainty PDF in the 2015 model used a triangular distribution with a preferred value of 12 ka and a minimum and maximum ages of 11.5 and 12.5 ka, respectively, after Johnson et al. (2014). For the 2023 update, we interpret an age uncertainty distribution that has a similar maximum age limit, but has a preferred age range and a minimum limiting age that are younger than the values considered in 2015 (Table 5-14). This adjustment to the age uncertainty PDF is based on radiocarbon ages of reworked shell hash dated by Kluesner

et al. (2023) and the additional age dating and stratigraphic information that suggests the slope was likely active at the end of the Younger Dryas. This age uncertainty PDF encompasses but is broader than the  $11.7 \pm 0.1$  ka age of the CHS lower slope break adopted by Kluesner et al. (2023) in their slip-rate calculations. This narrower age range is based on a preferred age model from Bayesian modeling. The main basis for expanding the age uncertainty range for the SSC model update is because the age of interest for the slip rate calculation is when the offset feature started recording measurable lateral offsets, rather than the interpreted age of the shoreface itself.

**Table 5-14. Changes to the Uncertainty PDF, Age of Cross-Hosgri Slope Offset Feature**

Trapezoid	2015 SSHAC	2023 Update	Notes
Min limit	11.5 ka	10.5 ka	Limit decreased to 10.5 ka to reflect radiocarbon ages of interpreted reworked shell hash over the revetment surface (Kluesner et al., 2023). Reflects possible smoothing/renewing of slope break after shoreface was formed and while offset feature was still subject to strong wave energy.
Preferred min	12 ka	11.2 ka	Represents an age after the end of the Younger Dryas stadial, after shoreface presumably was no longer being formed and as it became more submerged. See Johnson et al. (2014).
Preferred max	12 ka	11.7 ka	Represents a preferred age for the end of the Younger Dryas, and a start of the likely time interval when offset events of the shoreface could be preserved.
Max limit	12.5 ka	12.5 ka	Represents the early part of the Younger Dryas stadial, and represents the possibility that the recently formed shoreface starts to record offset events. Implies that shoreface modification during and since the Younger Dryas occurs mainly in the across-slope direction instead of along-slope, so the shoreface is continuously recording lateral offset.

The updated slip rate CDF for the Point Estero (CHS) site is calculated using Monte Carlo sampling of the offset and age PDFs (Tables 5-13 and 5-14). The results and comparisons with the 2015 SSC model CDF (and the CDF representing the Kluesner et al. (2023) interpretation) are plotted on Figure 5-40 and presented in Table 5-15. The plot and table show the broadening of slip rate uncertainty (1.4 to 3.9 mm/yr range at the 5<sup>th</sup> to 95<sup>th</sup> percentiles, respectively) as well as the slight increase in the mean slip rate (increase from 2.5 to 2.6 mm/yr).

**Table 5-15. Hosgri Fault Slip Rate CDFs at the Point Estero (Cross-Hosgri Slope) Site, 2015 SSC Model and the SSC Model Update**

Percentile	Slip Rate (mm/yr)	
	2015 SSHAC	2023 Update
0.05	1.6	1.4
0.10	1.8	1.7
0.20	2.0	2.0
0.50	2.5	2.6
0.80	2.9	3.3
0.90	3.1	3.6
0.95	3.3	3.9
<b>Mean</b>	<b>2.5</b>	<b>2.6</b>

### 5.3.1.2. Weighting of the Four Slip Rate Sites

Due to the more thorough documentation of the CHS age and stratigraphy (Kluesner et al., 2023; Medri et al., 2023), there is greater confidence now than in 2015 that the geological interpretation of the site is correct and that the slip rate estimated from the site is a reliable estimate of the slip rate for the Hosgri fault source near the DCP. The weighting of the four Hosgri fault slip rate sites in the 2015 SSC model (Table 5-12), therefore, needs to be revisited.

Our basis for reweighting the four slip rates sites is qualitative and considers three main criteria, as follows:

- The age of the offset feature
- The location of the slip rate site along the Hosgri fault and its proximity to the DCP
- The confidence that the interpretation of the site provides a reliable result

These three criteria cover different aspects of the applicability of a calculated slip rate to the goal of defining the center, body, and range of technically defensible interpretations for the Hosgri fault slip rate for the reach closest to the DCP. The first criterion—the age of the offset feature—is related to the confidence that a slip rate averaged over a given time interval can be used reliably to calculate the moment accumulation rate on the fault source for hazard assessment. The second criterion—the location of the slip rate site along the fault and its proximity to the DCP—is related to the kinematic model for a northward increase in slip rate along the fault. The third criterion for assigning relative weights to the four slip rate sites—the confidence that the interpretation of the slip rate site provides a reliable result—recognizes the possibility that a model assumption upon which the geologic slip rate is based may be incorrect, either in part or in its entirety. Thus, the model assumptions behind the calculation of each site



slip rate CDF are subject to epistemic uncertainty. Table 5-16 summarizes the ranking of the four sites relative to the above criteria and shows the revised weights that are used for the SSC model update.

**Table 5-16. Hosgri Fault Slip Rate Study Sites, and Qualitative Ranking of Criteria for Weighting**

Study Site	Applicability of Offset Feature Age	Applicability of Slip Rate Site Location	Confidence in Site Interpretation	2023 Update Logic-Tree Weight
San Simeon	High	Moderate	Moderate	0.25
Point Estero (CHS)	High	Moderate	High	0.50
Southern Estero Bay	Low	High	Low	0.20
Point Sal	Low	Low	Moderate	0.05

The Point Estero (CHS) slip rate site has the highest weight [0.5] of the four sites in the updated weighting scheme (Table 5-16). This weight reflects *moderate* and *high* rankings of all three criteria. The ~12 ka age of the CHS and the general slip rate range of the Hosgri fault suggest that the geomorphic feature has recorded multiple earthquakes over the last several earthquake cycles, and uncertainties related to the timing of earthquakes relative to the formation of the strain marker and time since the most recent event are likely small relative to the geologic slip rate calculation (Styron, 2019). The *high* confidence in the site interpretation is related to the clarity and continuity of the geomorphic feature across the Hosgri fault from the MBES bathymetry and chirp data combined with the recently published information about the age and stratigraphy of the feature. Despite this relatively high confidence, we note that concerns remain related to modification of the CHS since the Younger Dryas raised in PG&E (2015a, Chapter 8) and uncertainty in the initial shape of the feature (Section 5.2.2). The applicability of the slip rate site location is *moderate* to reflect the distance of the site from the DCP (Table 5-12) and the differences in the Hosgri slip rate at the site compared to the slip rate for the sections closest to the DCP. The location of the Point Estero site north of the intersections with the Shoreline and Los Osos faults suggests the slip rate at this location is somewhat greater than directly offshore the DCP (Figure 5-38).

The Point Sal slip rate site has the lowest weight [0.05] of the four sites in the updated weighting scheme (Table 5-16). This weight reflects *low* to *moderate* rankings of all three criteria. The estimated mid-Pleistocene (~700 ka) age of the offset buried channels imaged in 3-D seismic reflection data (PG&E, 2014a) is within the timeframe of the current tectonic regime (PG&E, 2015a, Chapter 5). However, it is plausible that the geologic slip rate on the Hosgri fault has changed over the past 0.5 to 1 Ma with the ongoing tectonic development of the Los Osos domain (Lettis et al., 1994) such that the slip rate averaged over ~700 ka may not reflect the current slip rate and rate of moment accumulation on the fault. This same *low* ranking for the age of the offset feature is assigned to the Estero Bay slip rate site where buried offset channels imaged in seismic-reflection data were interpreted to be of a similar mid-Pleistocene age (PG&E,

2014a; 2015a, Chapter 8). The main reason for the low weight of [0.05] for the Point Sal slip rate site, however, is based on its location approximately 40 km south of the DCP. The concern here is that the slip rate of the Hosgri fault may be significantly lower than the fault slip rate directly opposite the DCP. The preferred interpretation of the Hosgri-San Gregorio fault system is that its slip rate is relatively low at its southern end (offshore Point Pedernales) and increases to the north as intersecting faults add to the overall strike-slip motion (Hanson et al., 2004; Johnson et al., 2014, 2018). A lower slip rate at the Point Sal site may result from strike-slip motion accommodated by branching faults between the DCP and the site (Figure 5-38), or there may be other mechanisms for a decrease in slip rate as a fault approaches its southern end. As an analog, we refer to the reported decrease in the San Jacinto fault slip rate (Clark segment) along strike towards the south, where there are no clear intersecting active faults (Salisbury et al., 2012; Rockwell et al., 2015). We note that the confidence in the interpretation of the Point Sal site (*moderate*) is ranked higher than the confidence in the Estero Bay site (*low*). This is due to the better resolution and mapping of the buried channels in the 3-D seismic-reflection data at the Point Sal site compared to the more limited 3-D data and reliance on 2-D data to map and correlate channels at the Estero Bay site. The confidence in the site interpretation at Point Sal is shown as *moderate* because the channel ages—like at the Estero Bay site—rely on a Quaternary sequence stratigraphic model and interpretations of the development of the continental shelf related to global sea-level changes, and are not constrained by absolute age dating (PG&E, 2014a; PG&E, 2015a, Chapter 8).

The San Simeon and Estero Bay slip rate sites (weights of [0.25] and [0.20], respectively) have weights that are between the Point Estero and Point Sal sites (Table 5-16). The slightly higher weight for the San Simeon site reflects the *high* ranking for the age of the offset feature. The age of the offset Oso terrace (correlated with MIS 7, or ~210 ka) is highly appropriate for capturing the average slip rate of the fault in the current tectonic regime (PG&E, 2015a, Chapter 8). The San Simeon site also has a higher relative confidence (*moderate* versus *low*) that the site has been interpreted correctly. The *moderate* confidence in the slip rate site is based on the lack of continuous preservation of remnant terrace surfaces across the fault zone and the need to implement a log-spiral model to reconstruct the configuration of the headland and initial conditions for the geometry of the marine terrace back edge (Hanson and Lettis, 1994; PG&E, 2015a, Chapter 8).

### 5.3.1.3. Update to the Hosgri Fault Source Slip Rate CDF

The Hosgri fault source slip rate CDF was recalculated based on the updated weights for the four slip-rate sites (Table 5-16) and using the individual slip rate site CDFs (from the 2015 SSC model for the San Simeon, Estero Bay, and Point Sal sites and from the 2023 update for the Point Estero (CHS) site). The slip rate CDFs of individual sites, and the weighted Hosgri fault source CDFs from the 2015 SSC model and the SSC model update are plotted on Figure 5-41. The plot and accompanying table show the higher slip rate in the SSC model update, with a revised weighted mean of 2.14 mm/yr. Sensitivities of the Hosgri fault slip rate CDF show that the updated weighted mean rate is relatively insensitive to small (~5–10%) changes in the relative weighting of the four sites.

Comparisons of the SSC update and 2015 SSC model slip rate CDFs with other slip rate information are shown on Figure 5-42. The upper part of the figure (panel a) shows a plot comparing the slip rate CDFs to the plate motion constraints of DeMets et al. (2014), including

both the preferred slip rate constraint ( $1.8 \pm 0.6$  mm/yr) and maximum slip rate constraint ( $3.4 \pm 0.4$  mm/yr) (Figure 5-25). The lower part of the figure (panel b) shows a comparison of the slip rate CDFs to the mean slip rates from the various deformation models in the USGS NSHM, including the new WUS ERF-2023 (Field et al., 2023) and the older UCERF3 (Field et al., 2013) programs (Table 5-11). In both cases, the slip rate CDFs capture the other available information and demonstrate that the 2023 SSC model CDF appropriately represents the Hosgri fault slip rate near the DCP.

#### 5.3.1.4. Update to the Hosgri Fault Source Mean EPHR

Because the EPHR is a function of fault slip rate, the increase in the weighted mean slip rate of the Hosgri fault source should result in a change of the weighted mean EPHR. As discussed in Section 5.1, the EPHR accounts for uncertainty in the time-dependent behavior of large earthquake ruptures on fault sources.

PG&E (2015a, Chapter 11 and Appendix H) and Biasi and Thompson (2018) explored EPHR for the Hosgri fault for slip rates of 0.7, 1.7, and 2.7 mm/yr (Figure 5-43). The central value reflects the 2015 SSC model weighted mean slip rate of the Hosgri fault, and the lower and higher slip rate values were investigated to demonstrate the impact of slip rate on the EPHR calculations.

The weighted mean EPHR for the Hosgri fault source in the 2015 SSC model is 1.20 (PG&E, 2015a). This value is consistent with results listed in Table 11-1 of PG&E (2015a) for a slip rate of 1.7 mm/yr, a limit on the time since the most recent event ( $T_{\min}$ ) of 242 years (based on the founding of the San Luis Obispo mission), and a weighted average of three recurrence models: the lognormal (weight of [0.25]), Brownian-passage time (weight of [0.25]), and Weibull (weight of [0.5]). We note that the  $T_{\min}$  constraint applies to the section of the Hosgri fault directly opposite the DCP and Irish Hills, and not to the entire Hosgri fault zone, the southernmost portion of which may have been associated with the 1927 Lompoc earthquake (NRC, 1991; see also Hanks, 1979; Helmberger et al., 1992; Satake and Somerville, 1992). Weighted mean EPHR values for slip rates of 0.7 and 2.7 mm/yr using the same  $T_{\min}$  and weighting scheme for alternative recurrence models are 1.07 and 1.29, respectively (Figure 5-43). Interpolating for the 2023 SSC model Hosgri mean slip rate of 2.14 mm/yr (orange square symbol on Figure 5-43) yields an updated mean EPHR of 1.24.

#### 5.3.2. Los Osos Fault Update

The 2015 SSC model developed separate slip rate CDFs for the Los Osos fault based on the different FGMs (OV, SW, and NE). All three slip rate calculations utilized the same uplift rate model for the HW of the Los Osos fault, which was based on the calculated uplift rate of the well-preserved  $Q_2$  marine terrace along the outer coast of the Irish Hills (Figure 5-35) (PG&E, 2015a, Chapter 8). The net slip rates for each FGM differed based on the marker used to estimate the uplift or subsidence rate of the FW, the estimated fault dip, and the style of faulting (rake). Similar to the approach used to calculate the Hosgri fault source slip rate CDF, each parameter used to calculate net slip rate was characterized by an uncertainty distribution captured using one or more trapezoidal PDFs. Final slip rate CDFs were developed based on Monte Carlo sampling of the parameter PDFs.

Based on the new model by Simms et al. (2016) (Section 5.2.3), changes are needed in the calculated HW uplift rate of the Los Osos fault and the calculated net slip rates for the Los Osos

fault source slip rate CDFs. These changes will result in an update to the weighted mean slip rate of the Los Osos fault source that can be used for the 2023 SB-846 seismic hazard assessment.

Two HW uplift rate models were considered in the 2015 SSC model: the Hanson et al. (1994) model and an alternative model based on Muhs et al. (2012) (PG&E, 2015a, Chapter 8). The difference between the models is related to correlations of the Q<sub>2</sub> terrace with MIS 5e (Hanson model) or MIS 5c (Muhs model). Because the two models presumed a similar paleosea level (+6 m and +4 m above modern sea level for the Hanson and Muhs models, respectively), the main difference in calculated uplift rate is related to the differences in terrace age, with a 120–125 ka age used for the MIS 5e terrace and 100–105 ka for the MIS 5c terrace. The uplift rate PDFs for the Hanson and Muhs models are shown on Figure 5-44 as the blue (Hanson) and red (Muhs) lines, and are based on incorporating uncertainties in the elevation of the terrace back edges, uncertainties in the age of the sea-level highstands, and uncertainties in the model paleosea levels. The 2015 SSC model assigned weights of [0.8] and [0.2] to the Hanson and Muhs models, respectively, based on a strong preference for the MIS 5e interpretation of the Q<sub>2</sub> terrace based on age dating and altitudinal spacing arguments. The 2015 SSC SSHAC TI Team argued that the Muhs interpretation was unlikely to be correct, but it could not be precluded (PG&E, 2015a, Chapter 8).

An additional uplift rate PDF is developed to represent the Simms et al. (2016) model (Figure 5-44). The preferred uplift rate range of 0.10 to 0.18 mm/yr represents their preferred uplift rate of  $0.14 \pm 0.04$  mm/yr estimated for the Q<sub>2</sub> terrace at Point Buchon. This preferred uplift rate range is equivalent to a  $13 \pm 3$  m paleosea level for the MIS 5e terrace plus uncertainty in the elevation of the Q<sub>2</sub> terrace used in the 2015 SSC model (Figures 5-35 and 5-36). The minimum (0.06 mm/yr) and maximum (0.22 mm/yr) uplift rates used in the trapezoidal PDF represent a doubling of the error (i.e., preferred rate of  $0.14 \pm 0.08$  mm/yr), which incorporates additional uncertainty comparable to the ranges considered in the Hanson et al. (1994) and Muhs et al. (2012) models (Figure 5-44).

The change in weighting of the alternative uplift rate PDFs followed a simple procedure as the impact of the change in weights and change in Los Osos slip rate has a small impact on the hazard compared to the change in the Hosgri fault slip rate. The [0.8] weight that was assigned to the Hanson et al. (1994) uplift rate model was divided equally between the Simms et al. (2016) and Hanson et al. (1994) models (i.e., [0.4] weight to each), and the Muhs et al. (2012) model retained a smaller weight of [0.2]. Arguably, additional weight could be assigned to the Simms et al. (2016) model at the expense of the Hanson model, but including non-trivial weights to the three alternative models provides additional epistemic uncertainty to the net slip rate calculation that is considered to be appropriate given the scope and approach of this seismic hazard assessment. The weighted uplift rate PDF is shown on Figure 5-44 by a gray line. The impact of the updated weighted uplift rate PDF is a shift in the probability mass to lower uplift rates.

The Los Osos fault source slip rate CDFs were recalculated based on the updated uplift rate PDF for the OV, SW, and NE models. No changes were made to the FW rate, dip, or rake uncertainty PDFs. The slip rate CDFs of each FGM are plotted on Figure 5-45. The plot and accompanying table show the lower slip rates in the SSC model update compared to the 2015 SSC model with changes most apparent at the median and lower percentile slip rates. Revised weighted mean slip rates are 0.22, 0.17, and 0.39 mm/yr for the OV, SW, and NE models, respectively, which represent a decrease in mean slip rate compared to the 2015 SSC model on the order of 9% to

15%. The magnitude of the changes in mean slip rate is approximately 0.02 to 0.04 mm/yr, which is an order of magnitude less than the 0.44 mm/yr change in mean slip rate for the Hosgri fault source (Figure 5-41).

Comparisons of the 2023 SSC update model slip rate CDFs with the mean slip rates from the various deformation models in the USGS NSHM, including the new WUS ERF-2023 (Field et al., 2023) and the older UCERF3 (Field et al., 2013) programs are shown on Figure 5-46. The slip rate CDFs across the three models capture the mean slip rates estimated from the regional deformation models.

### **5.3.3. Implementation of the SSC Model Update for the Updated Seismic Hazard Assessment**

This section represents a hazard input document (HID) that lists changes to the 2015 SSC model to create the SSC model update. The purpose of this HID is to provide clear instructions to the hazard analyst on how to modify the 2015 SSC model for input to the updated seismic hazard assessment.

#### **5.3.3.1. Changes to the Hosgri and Los Osos Fault Slip Rates**

The Hosgri fault source and Los Osos fault source weighted mean slip rates are updated. The changes to the weighted mean slip rate of the Hosgri and Los Osos fault sources are provided as scale factors, which are the ratios of the 2023 SSC updated weighted mean fault slip rates to the 2015 SSC model weighted mean slip rates. Table 5-17 shows the scale factors. These slip rate scale factors are to be applied to the rupture sources listed in Table 5-5. The scale factors for the three Hosgri FGMs are identical. The scale factors for the three Los Osos FGMs are different.

**Table 5-17. Scale Factors for Weighted Mean Slip Rate, Hosgri and Los Osos Fault Sources**

<b>Hosgri Fault Weighted Mean Slip Rate Scale Factors</b>			<b>Los Osos Fault Weighted Mean Slip Rate Scale Factors</b>		
<b>H75-</b>	<b>H85-</b>	<b>H90-</b>	<b>OV-</b>	<b>SW-</b>	<b>NE-</b>
1.259	1.259	1.259	0.846	0.895	0.929

#### **5.3.3.2. Changes to the Time Dependency Model**

The equivalent Poisson hazard ratio (EPHR), which is called the equivalent Poisson ratio (EPR) in PG&E (2015a), is a scale factor to be applied to the activity rate of events on fault sources. Due to the change in weighted mean slip rate of the Hosgri fault source, the weighted mean EPHR for the Hosgri fault source needs to be updated as well. No change to the EPHR is needed for the Los Osos fault source, as the change in weighted mean slip rate for that fault source is relatively small, and the absolute value of the weighted mean slip rate is also relatively small.

Table 5-18 lists the weighted mean EPHR for the Hosgri fault source in the 2015 SSC model, the SSC model updated weighted mean EPHR for the Hosgri fault source, and the change in EPHR expressed as a scale factor.

**Table 5-18. Weighted Mean EPHR Values for the Hosgri Fault Source**

<b>Hosgri Fault Source Weighted Mean EPHR</b>		
<b>2015 SSC Model</b>	<b>SSC Model Update</b>	<b>Scale Factor</b>
1.20	1.24	1.033

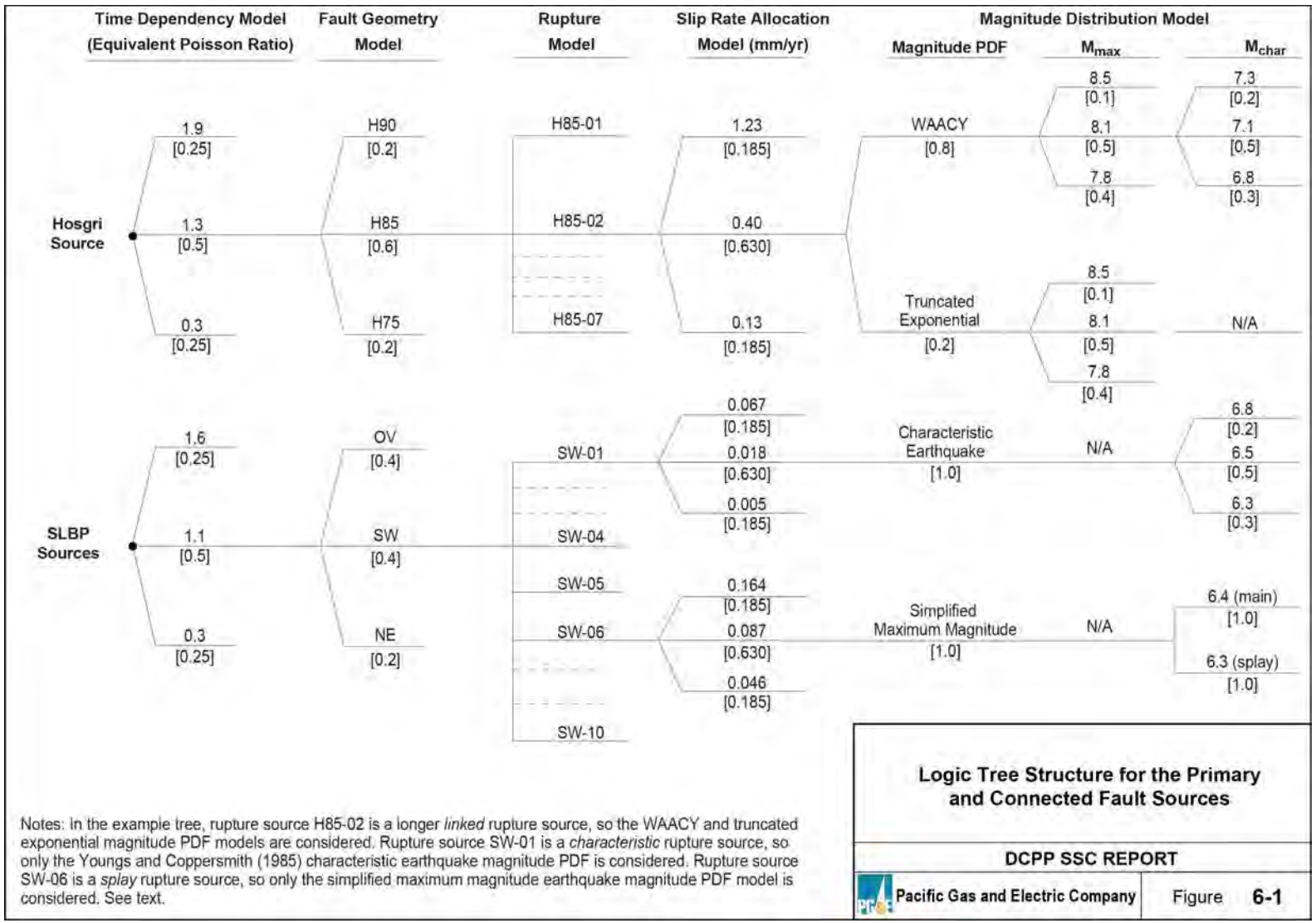


**Figure 5-1. Logic Tree Structure for the Primary and Connected Fault Sources  
(from PG&E, 2015a, Figure 6-1)**



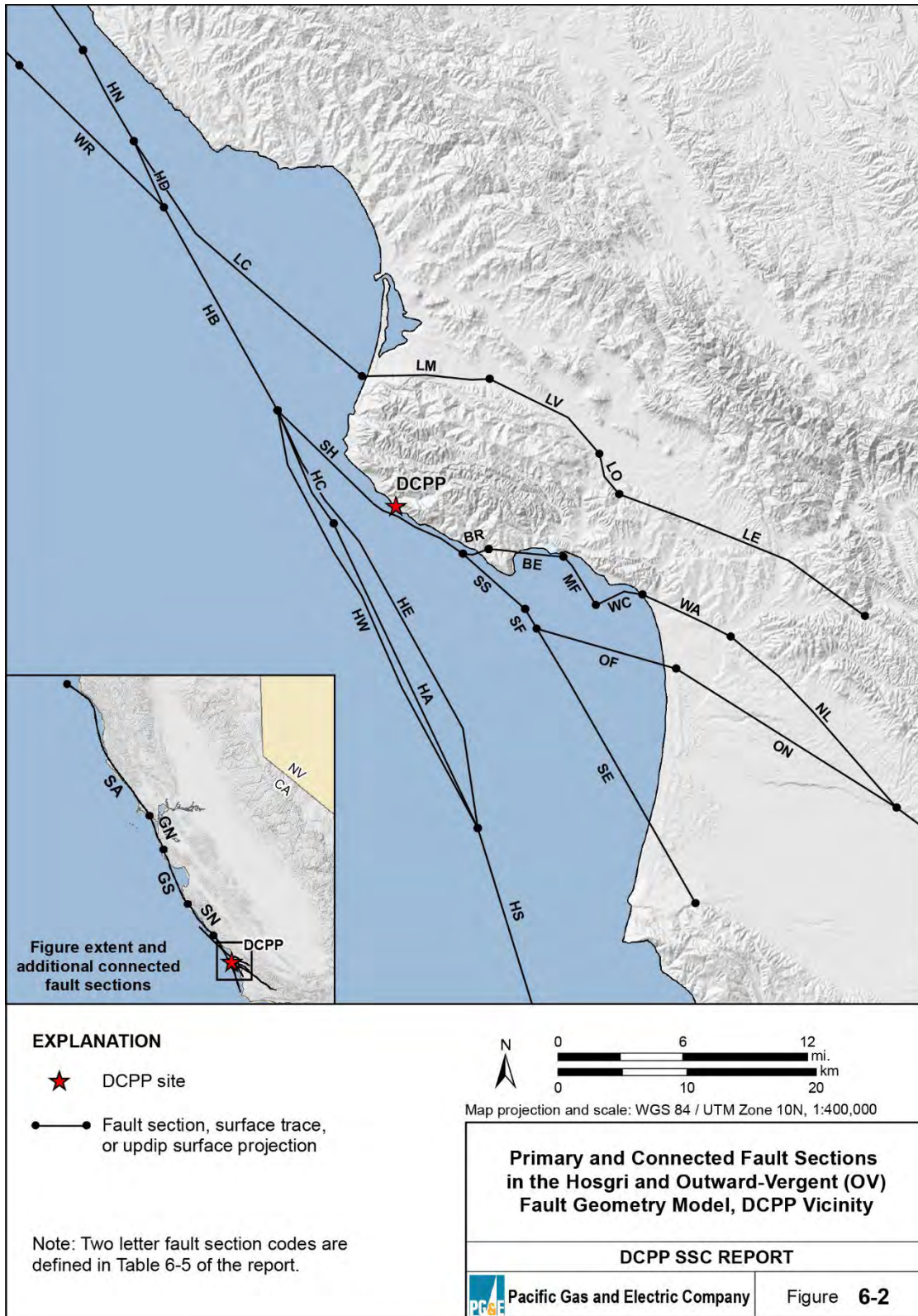


**Figure 5-2. Primary and Connected Fault Sources in the Hosgri and Outward-Vergent (OV) Fault Geometry Model (from PG&E, 2015a, Figure 6-2)**



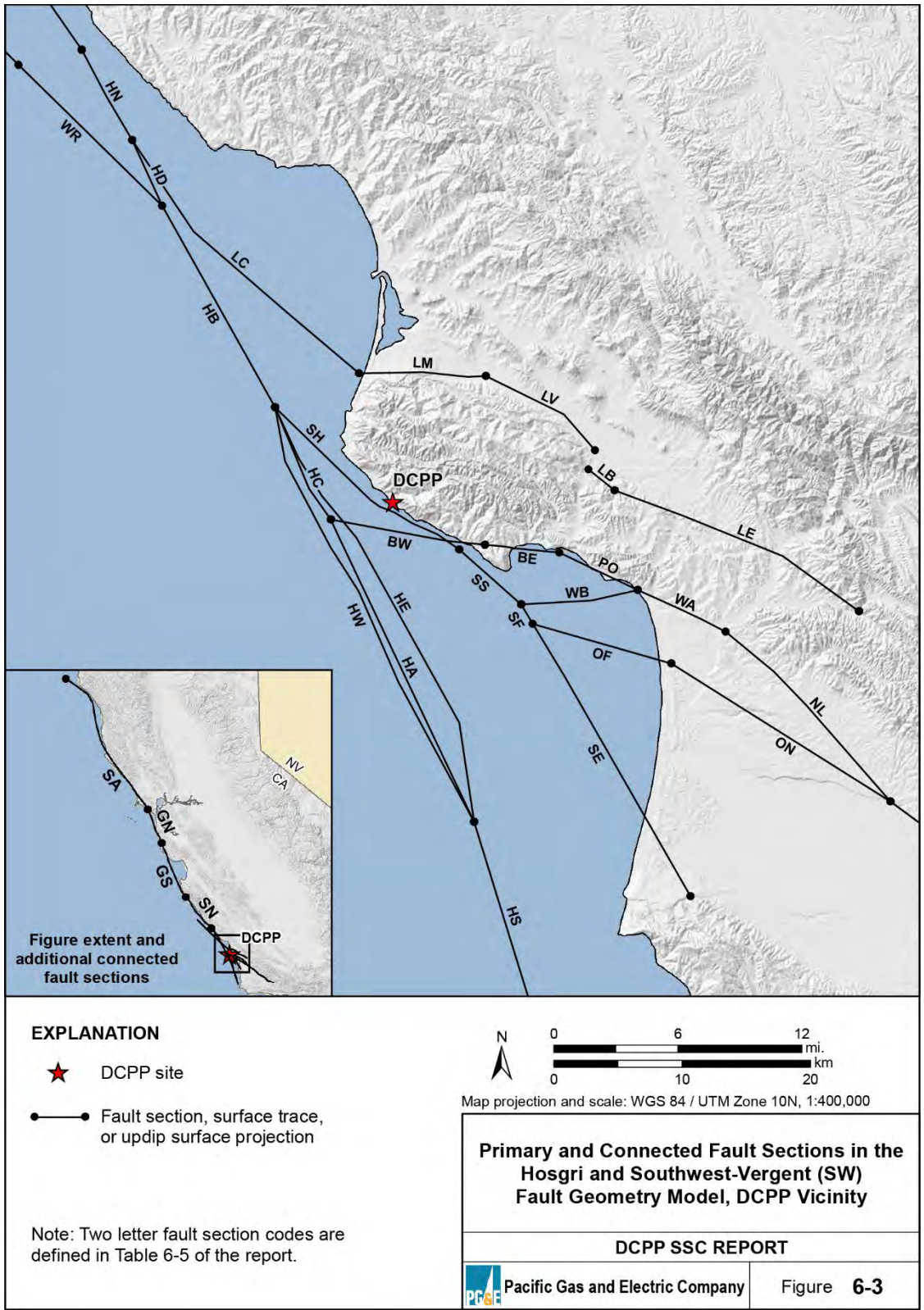
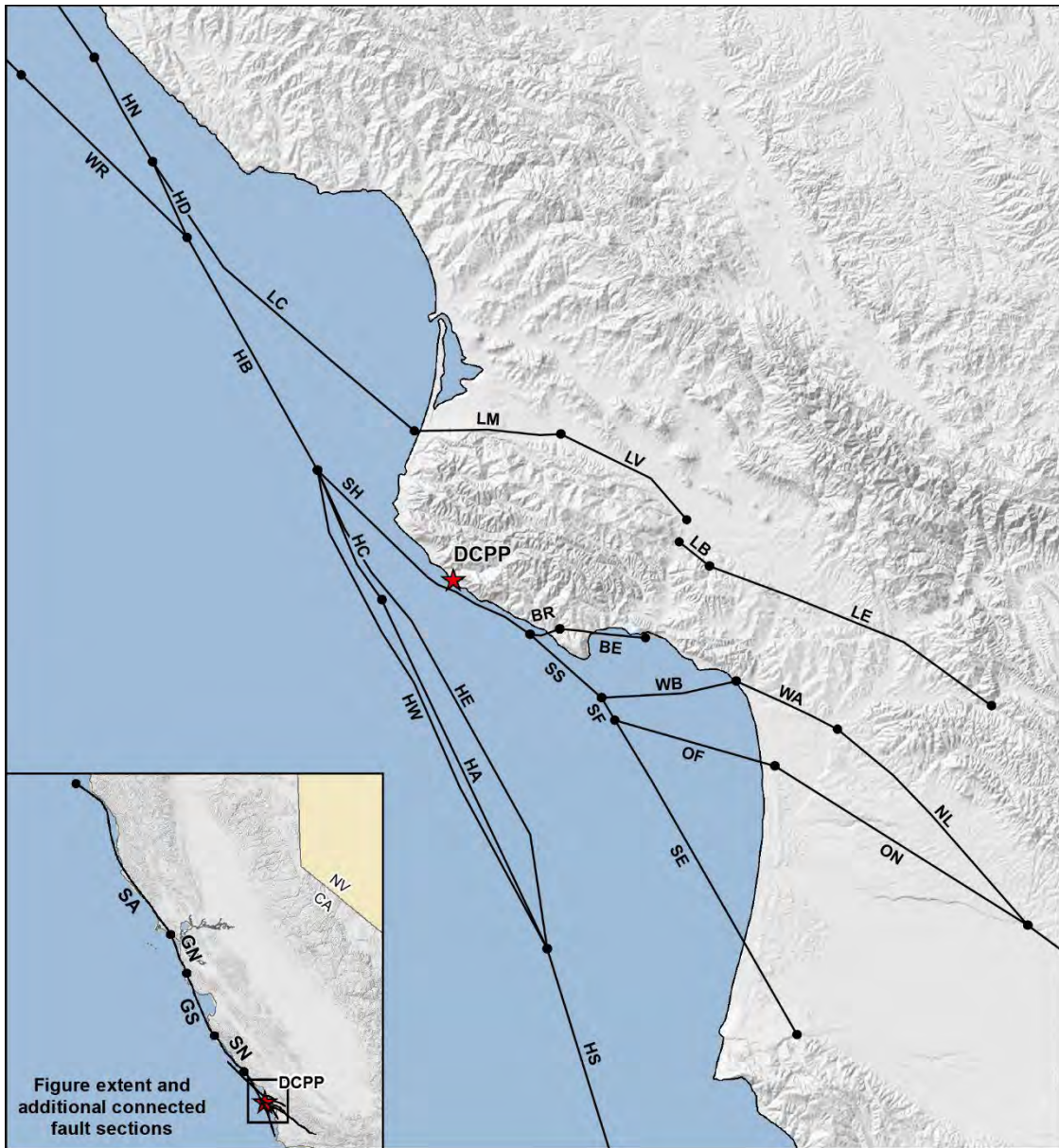


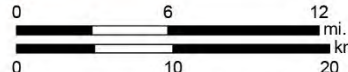
**Figure 5-3. Primary and Connected Fault Sources in the Hosgri and Southwest-Vergent (SW) Fault Geometry Model (from PG&E, 2015a, Figure 6-3)**



**EXPLANATION**

- ★ DCPD site
- Fault section, surface trace, or updip surface projection

Note: Two letter fault section codes are defined in Table 6-5 of the report.



Map projection and scale: WGS 84 / UTM Zone 10N, 1:400,000

**Primary and Connected Fault Sections in the Hosgri and Northeast-Vergent (NE) Fault Geometry Model, DCPD Vicinity**

**DCPD SSC REPORT**

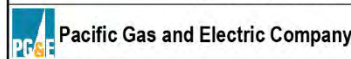
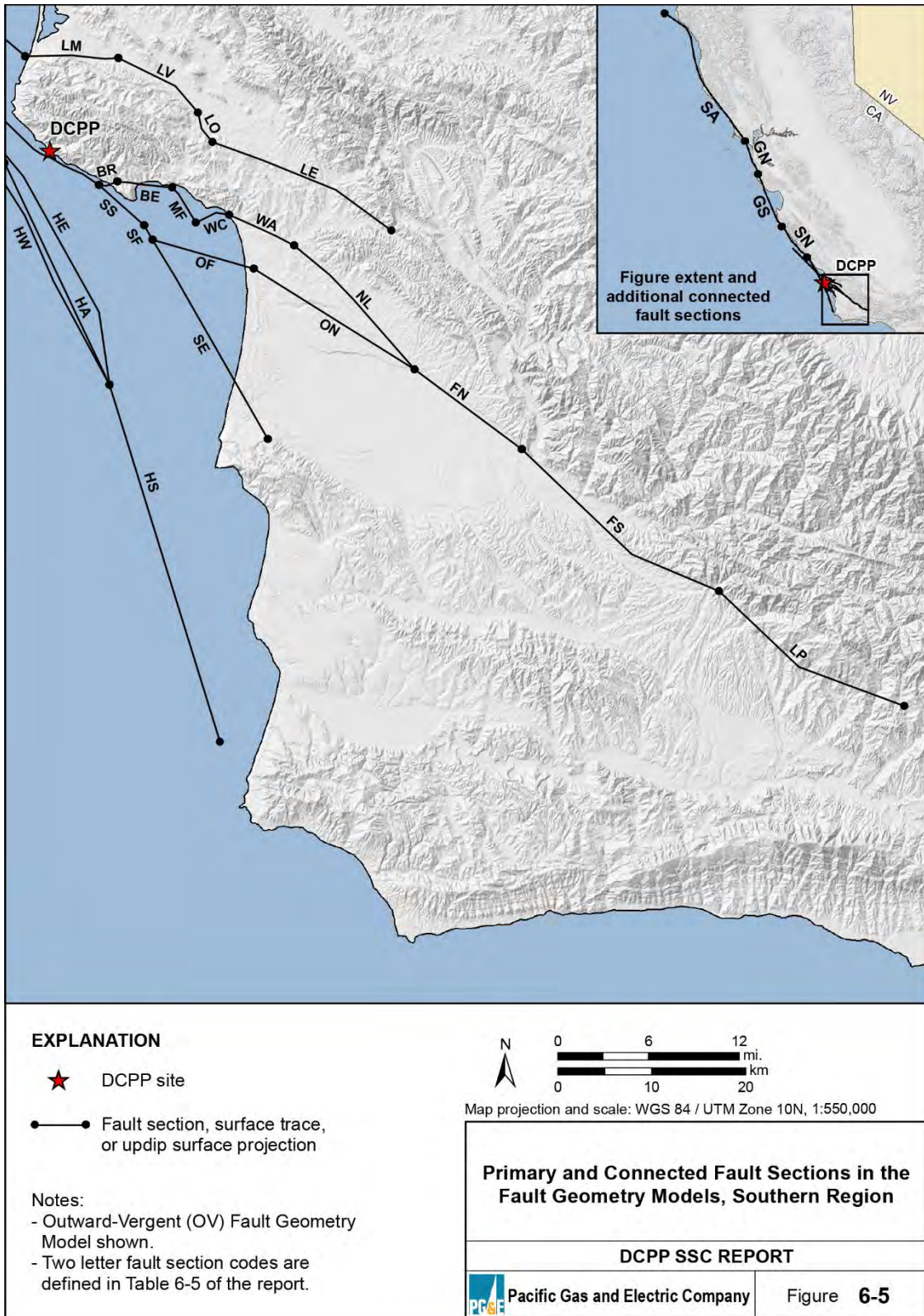


Figure **6-4**

**Figure 5-4. Primary and Connected Fault Sources in the Hosgri and Southeast-Vergent (NE) Fault Geometry Model (from PG&E, 2015a, Figure 6-4)**





**Figure 5-5. Primary and Connected Fault Sections in the Fault Geometry Models, Southern Region (from PG&E, 2015a, Figure 6-5)**

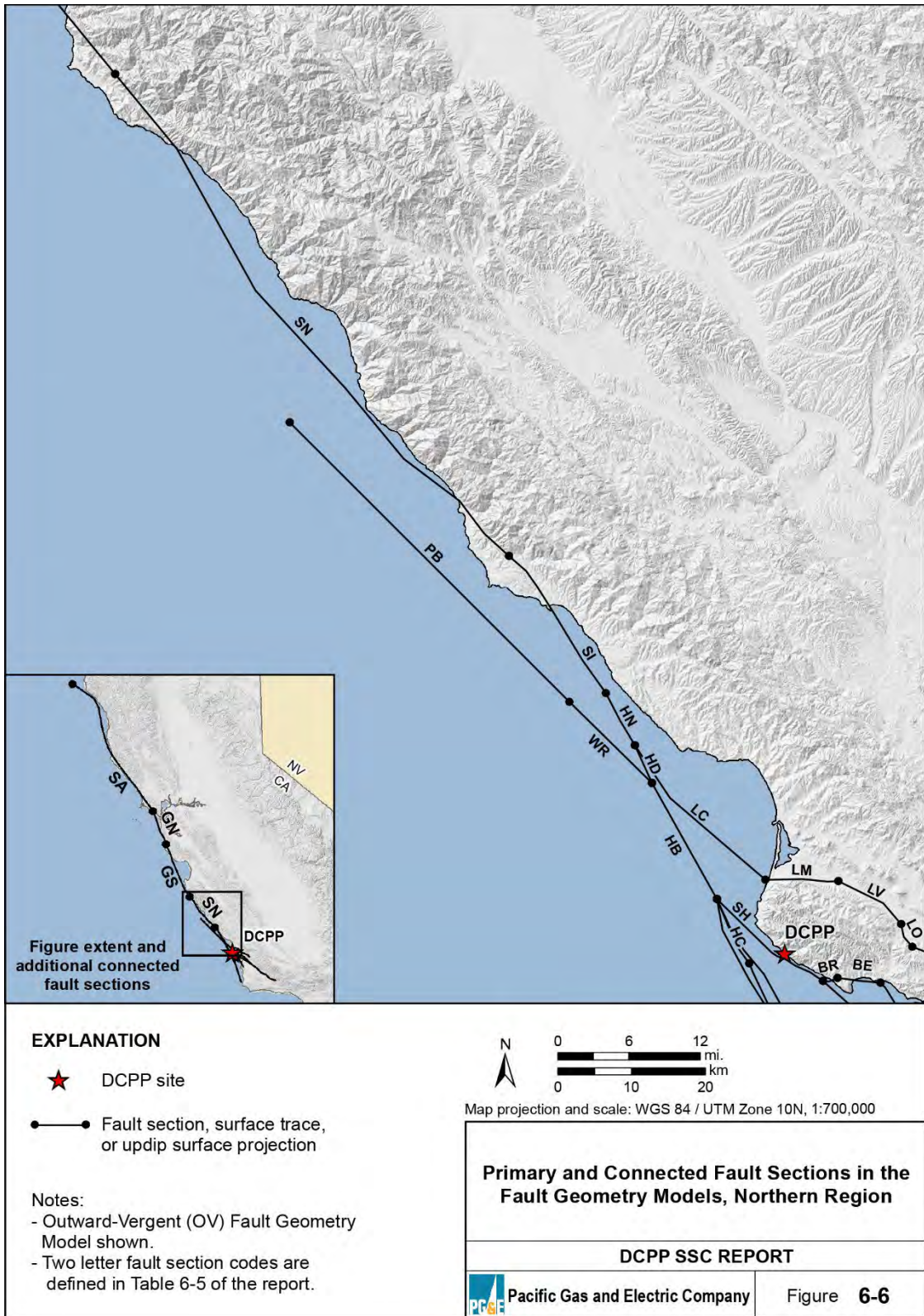


**Figure 5-6. Primary and Connected Fault Sections in the Fault Geometry Models, Northern Region (from PG&E, 2015a, Figure 6-6)**



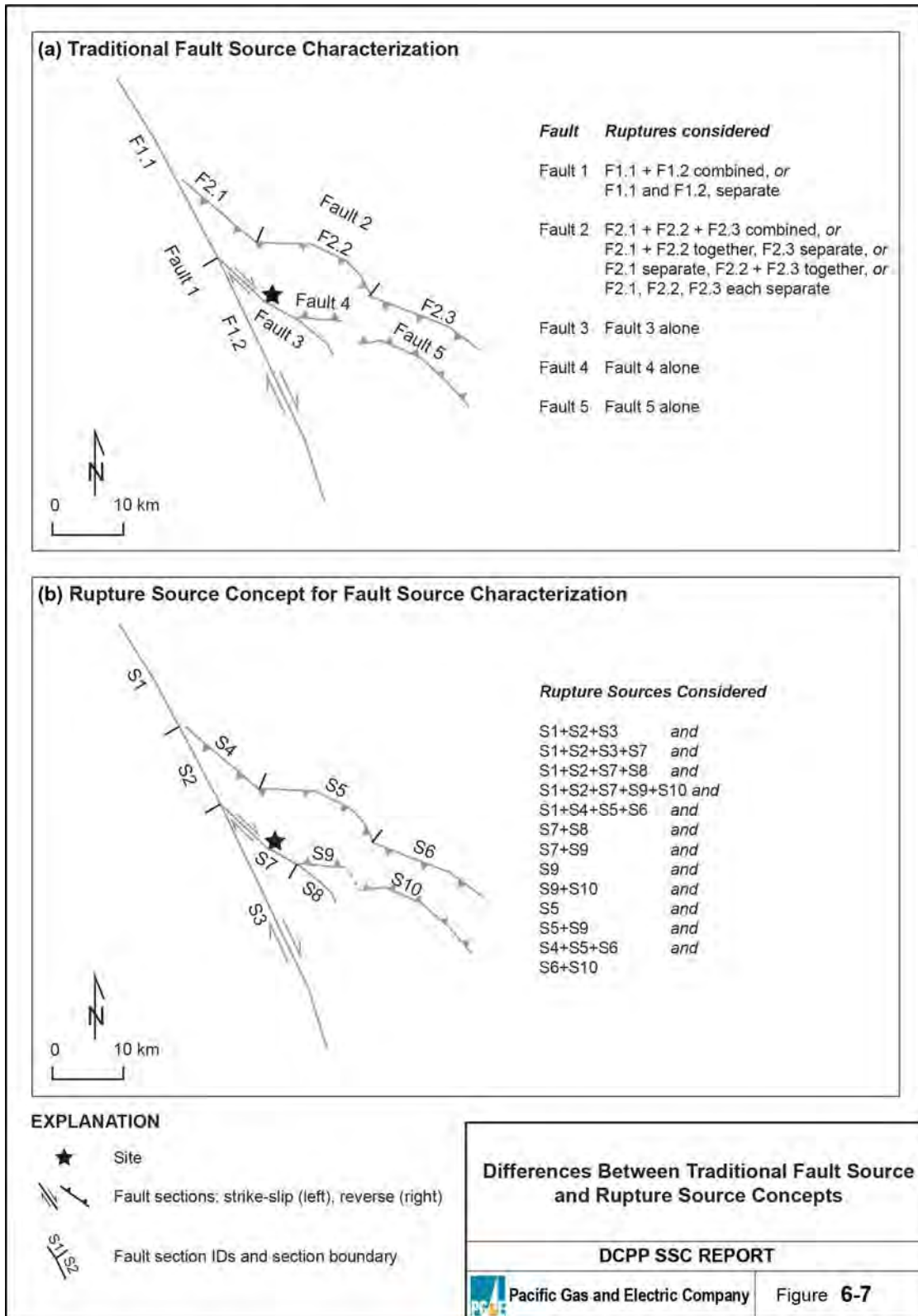


**Figure 5-7. Differences Between Traditional Fault Source and Rupture Source Concepts (from PG&E, 2015a, Figure 6-7)**

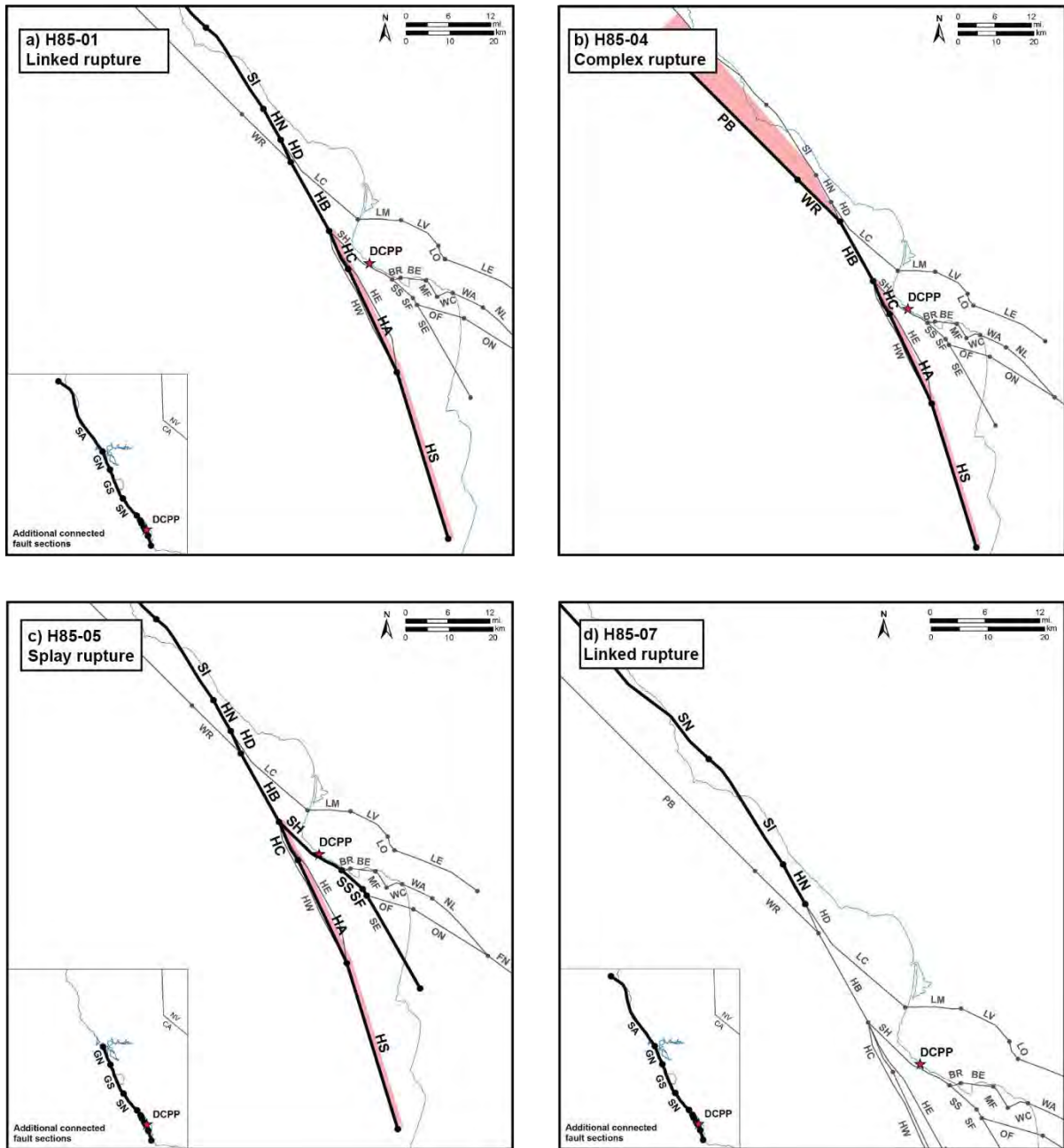
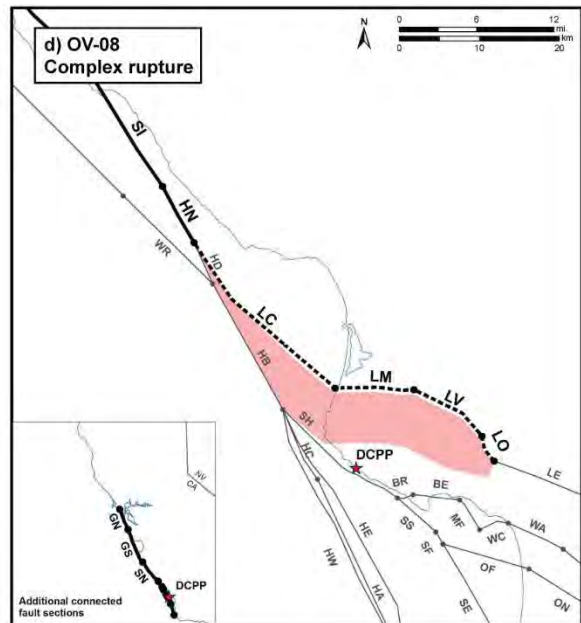
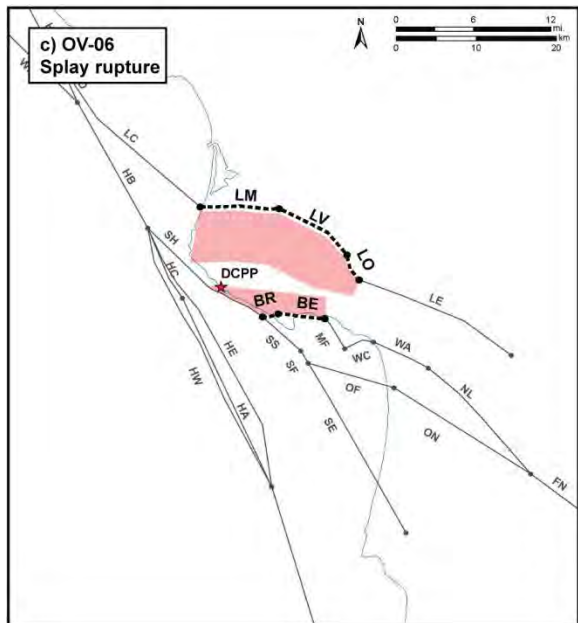
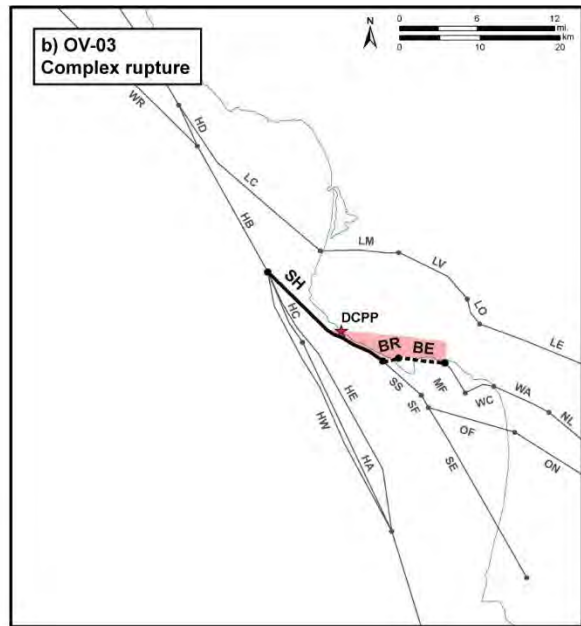
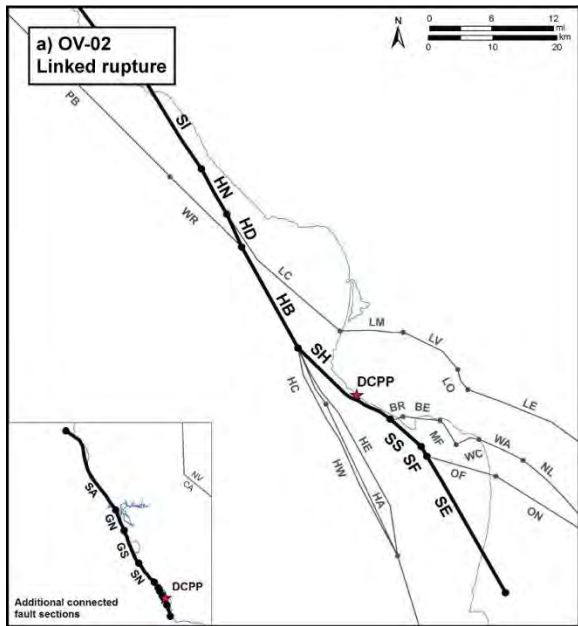
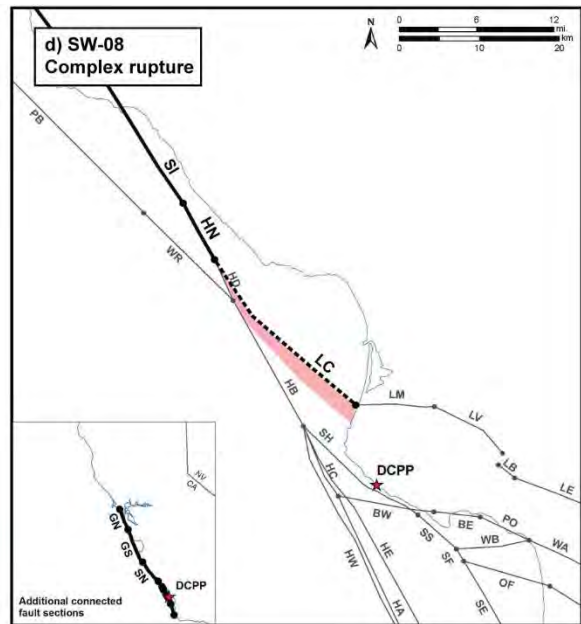
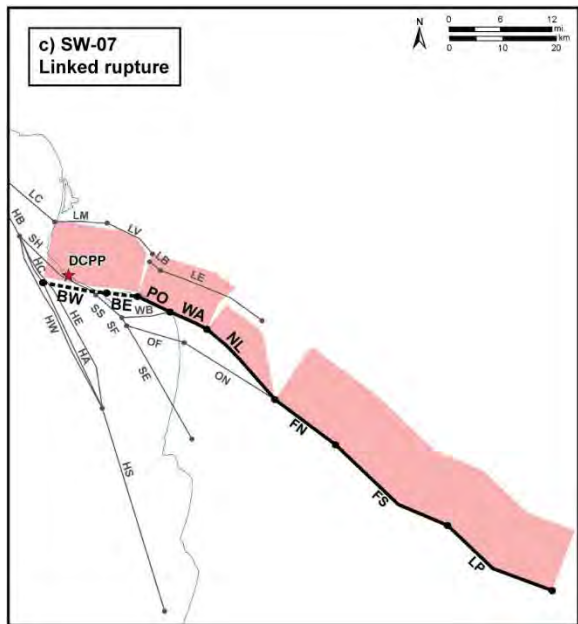
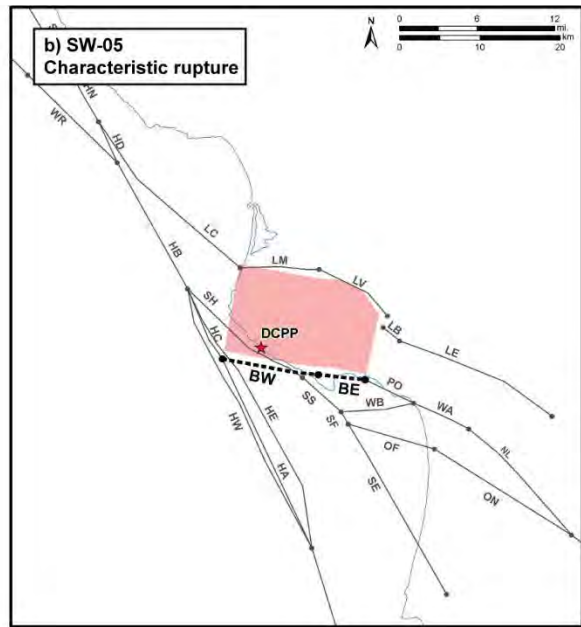
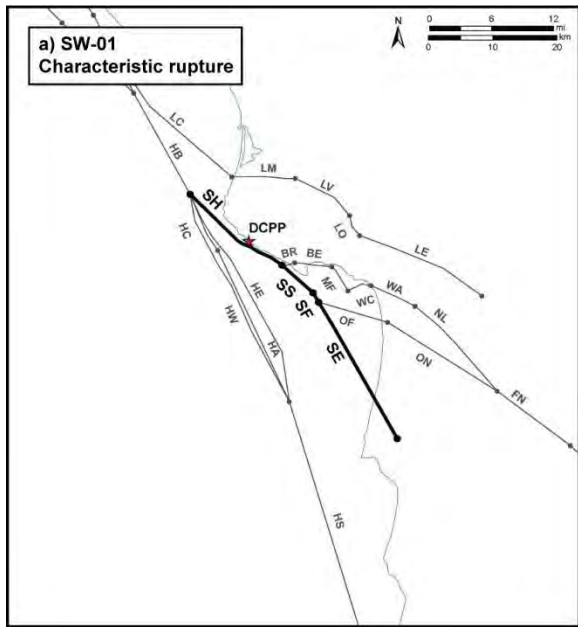


Figure 5-8. Example Rupture Sources Associated with the Hosgri Fault Source (from PG&E, 2015a, Plate 9-1). Rupture Sources: a) H85-01; b) H85-04; c) H85-05; d) H85-07



**Figure 5-9. Example Rupture Sources Associated with the Outward Vergent (OV) Model (from PG&E, 2015a, Plate 9-2). Rupture Sources: a) OV-02; b) OV-03; c) OV-06; d) OV-08**



**Figure 5-10. Example Rupture Sources Associated with the Southwest Vergent (SW) Model (from PG&E, 2015a, Plate 9-2). Rupture Sources: a) SW-01; b) SW-05; c) SW-07; d) SW-08**



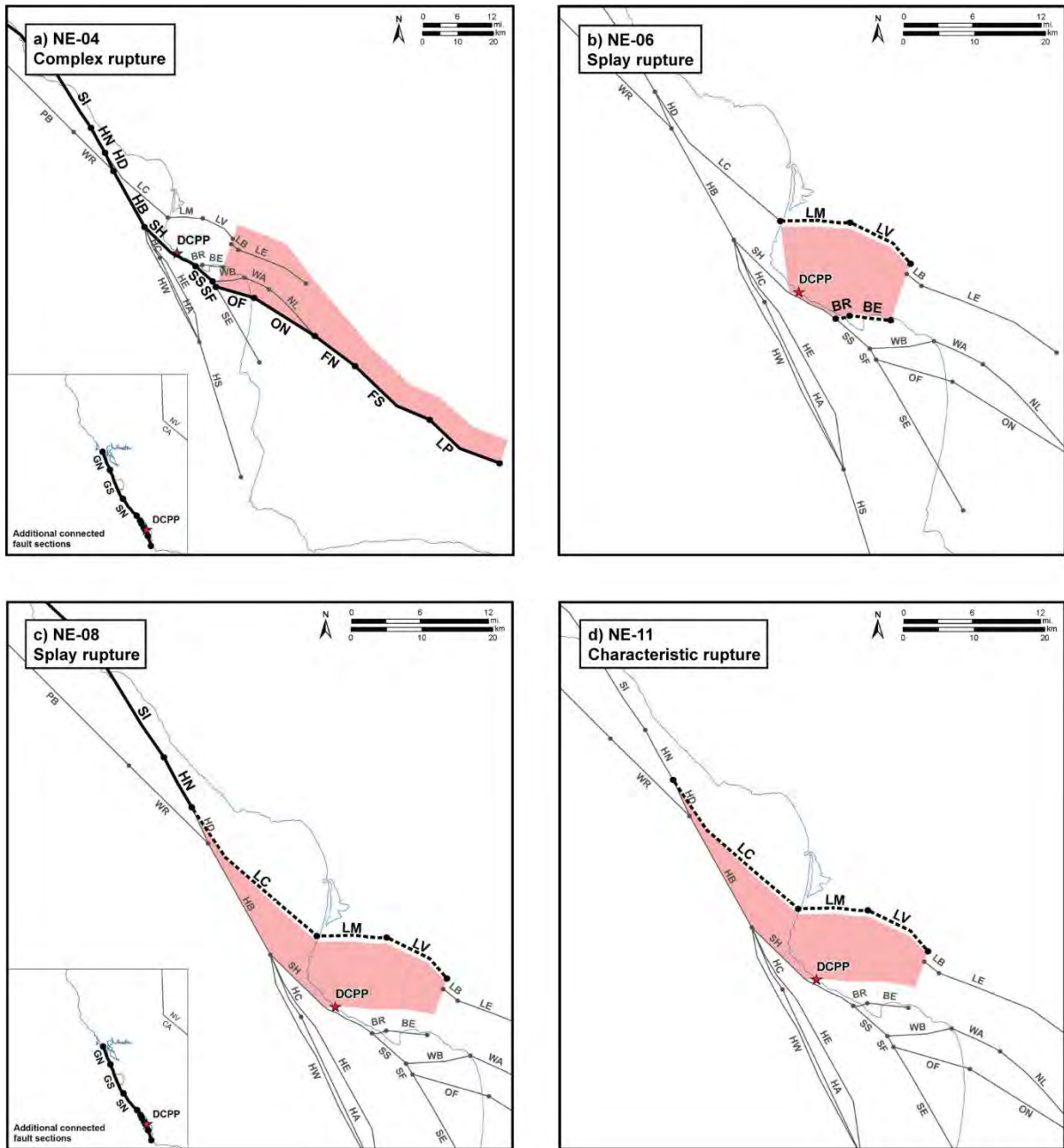


**Figure 5-11. Example Rupture Sources Associated with the Northeast Vergent (NE) Model (from PG&E, 2015a, Plate 9-2). Rupture Sources: a) NE-04; b) NE-06; c) NE-08; d) NE-11**

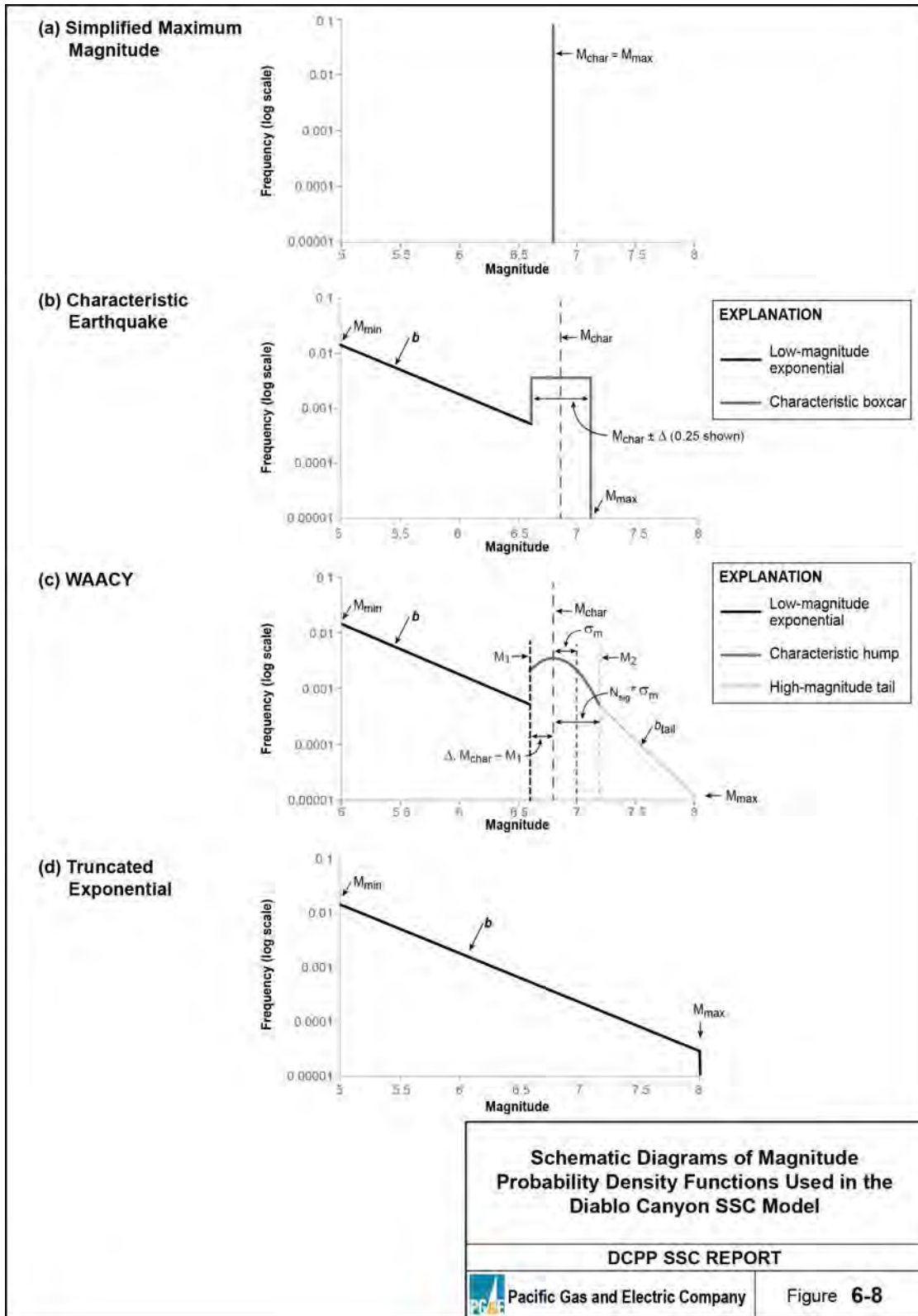


Figure 5-12. Magnitude PDFs Used in the 2015 SSC Model (from PG&E, 2015a, Figure 6-8)

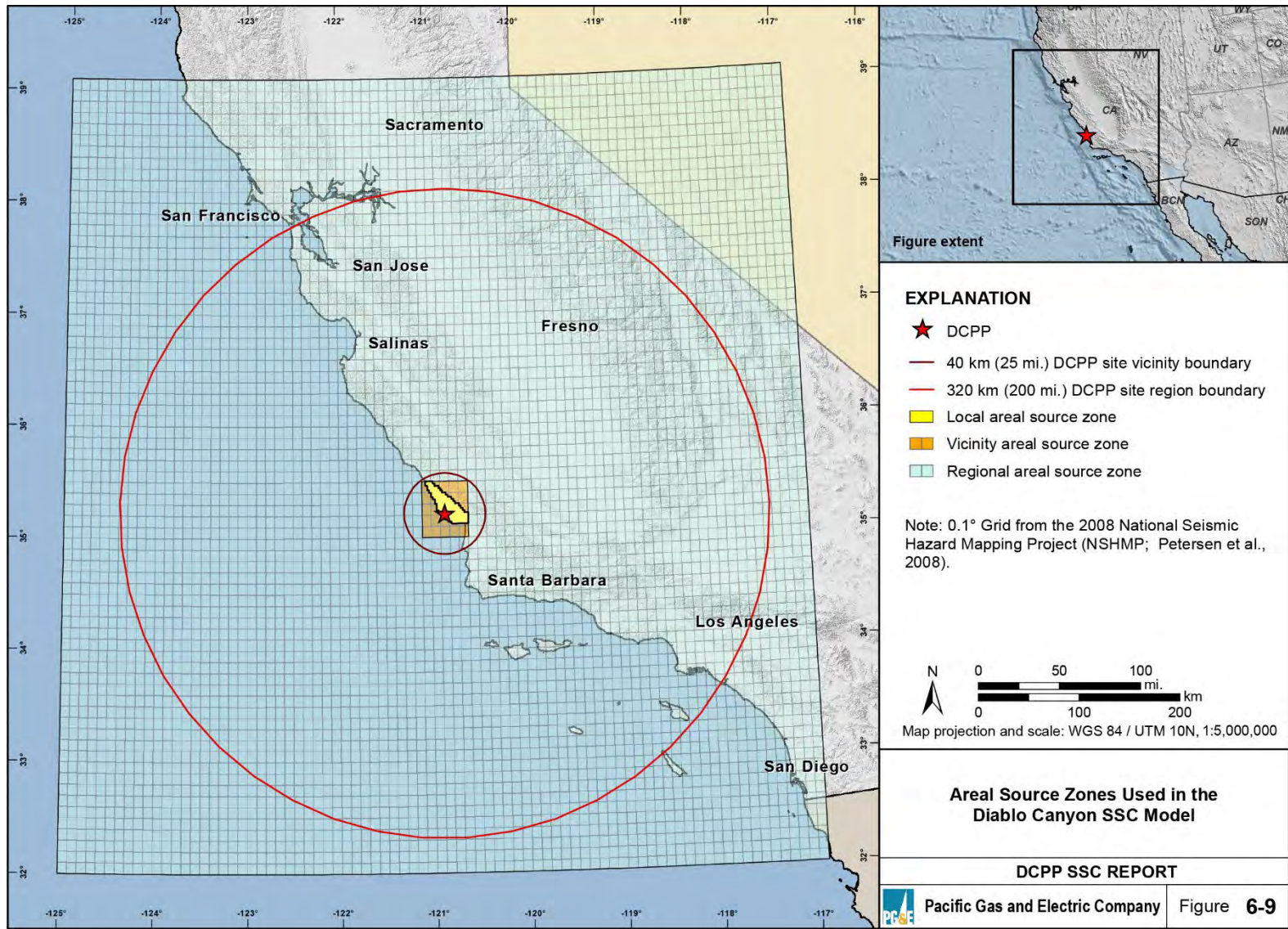


Figure 5-13. Areal Source Zones Used in the 2015 SSC Model  
(from PG&E, 2015a, Figure 6-9)



DCPP: 5 Hz

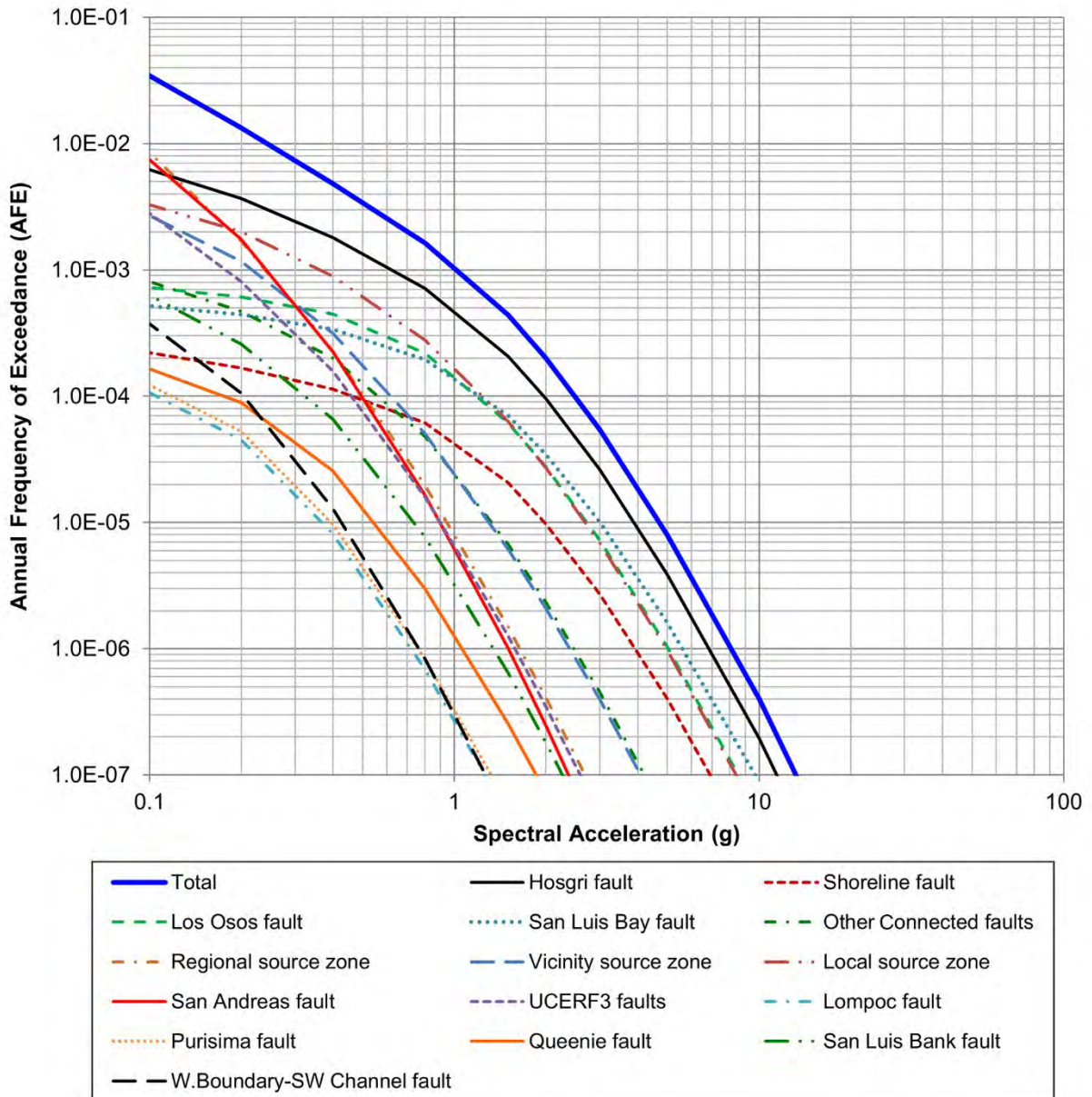


Figure 5-14. Reference Rock Hazard (Total and by Source) for 5 Hz Spectral Acceleration

DCPP: 1 Hz

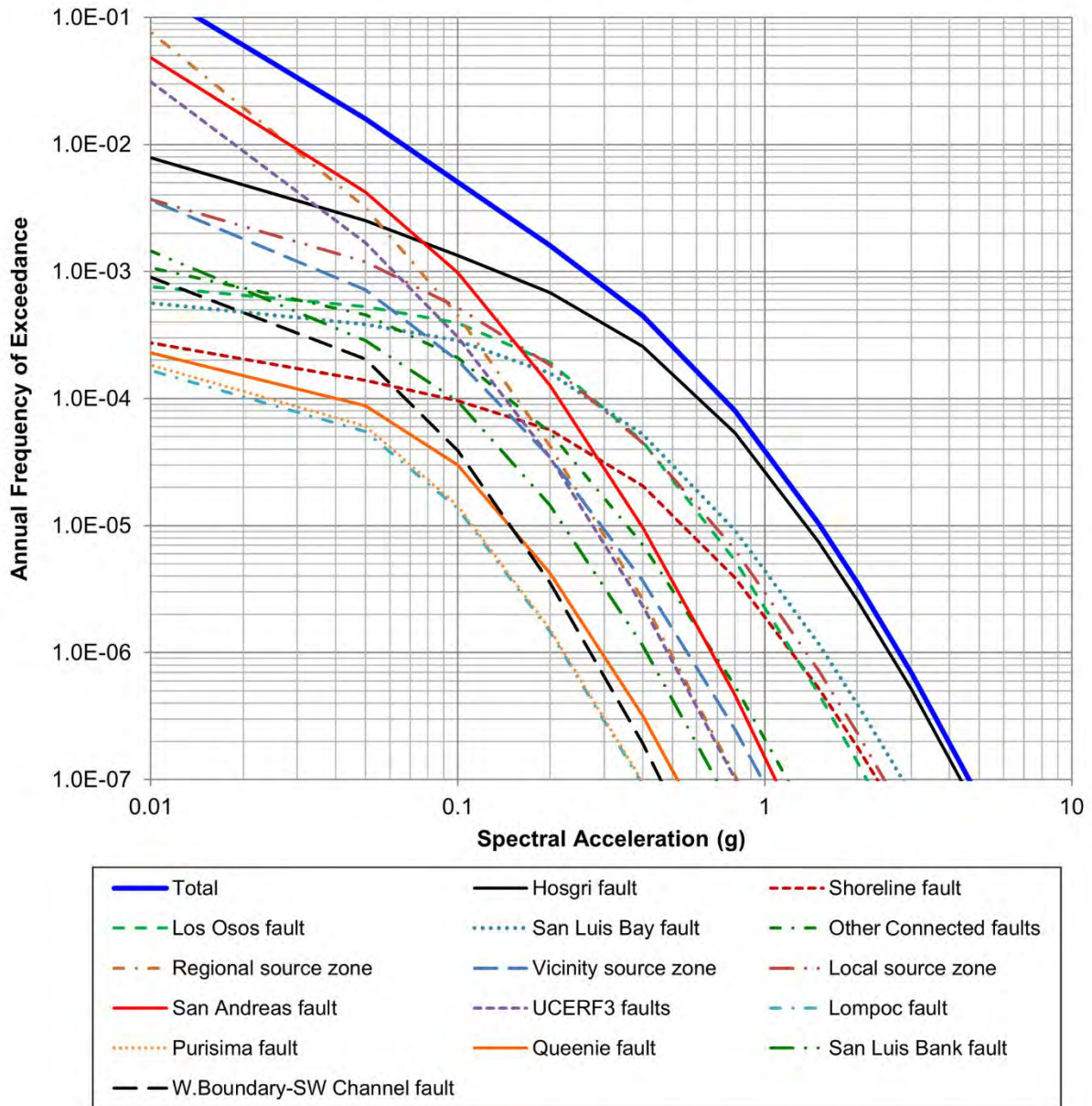


Figure 5-15. Reference Rock Hazard (Total and by Source) for 1 Hz Spectral Acceleration

DCPP: 0.5 Hz

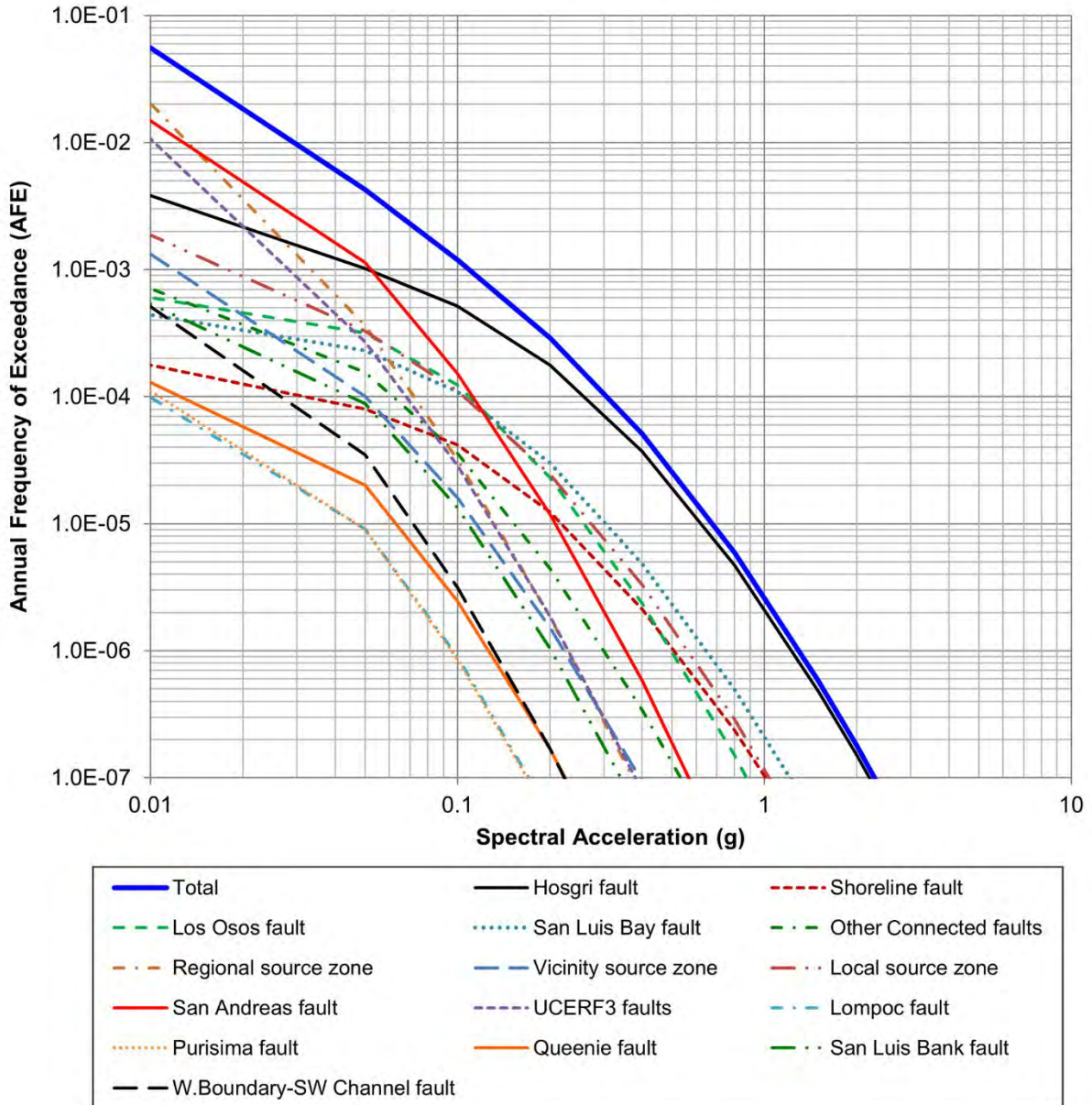
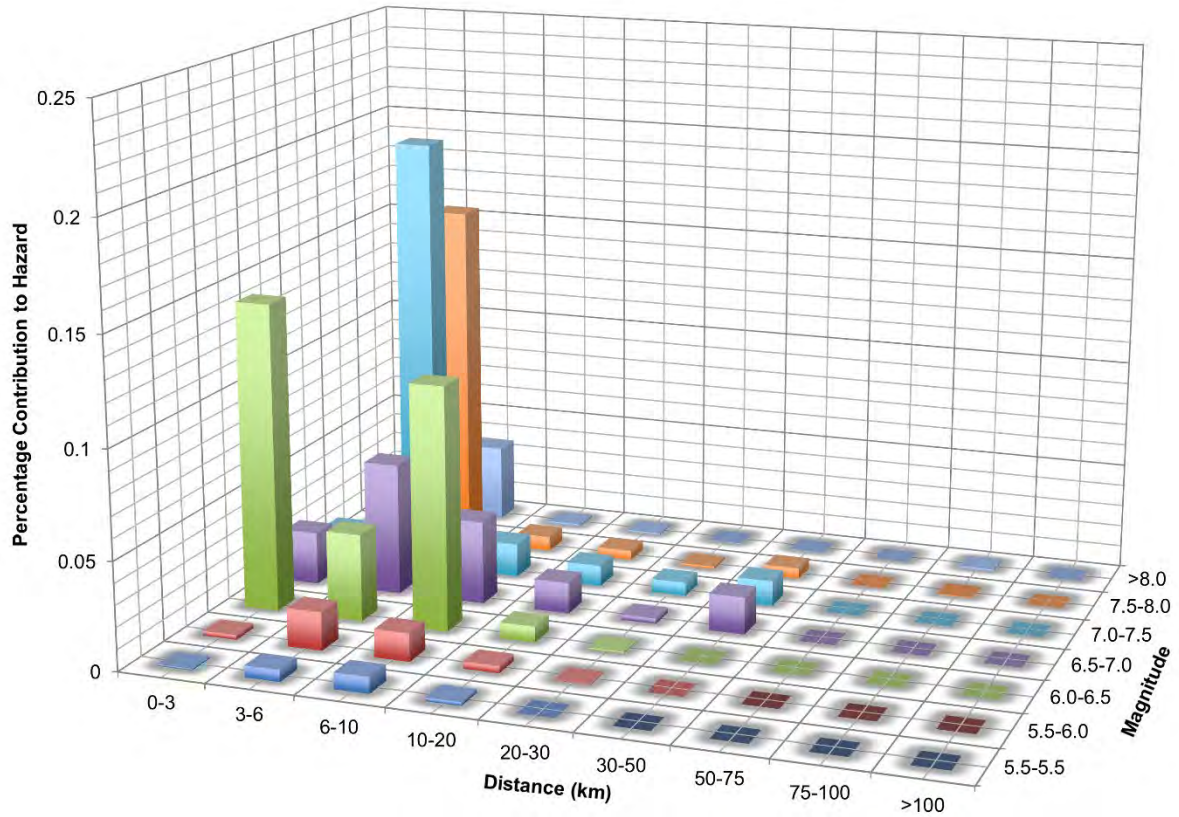


Figure 5-16. Reference Rock Hazard (Total and by Source) for 0.5 Hz Spectral Acceleration



**DCPP: 5 Hz, AFE=1.0E-04**



**Figure 5-17. Deaggregation of the Reference Rock Hazard for 5 Hz Spectral Acceleration for the 10<sup>-4</sup> Annual Hazard Level**

**DCPP: 1 Hz, AFE=1.0E-04**

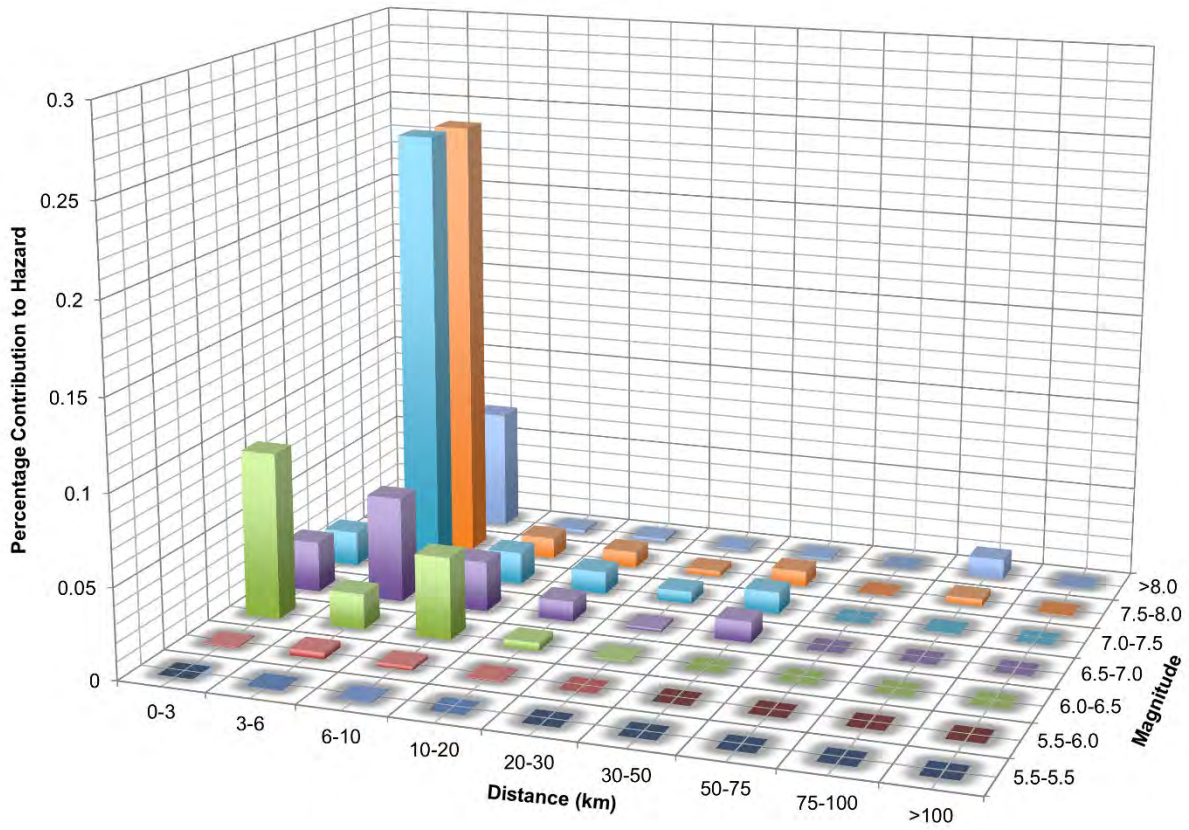


**Figure 5-18. Deaggregation of the Reference Rock Hazard for 1 Hz Spectral Acceleration for the  $10^{-4}$  Annual Hazard Level**



**DCPP: 0.5 Hz, AFE=1.0E-04**

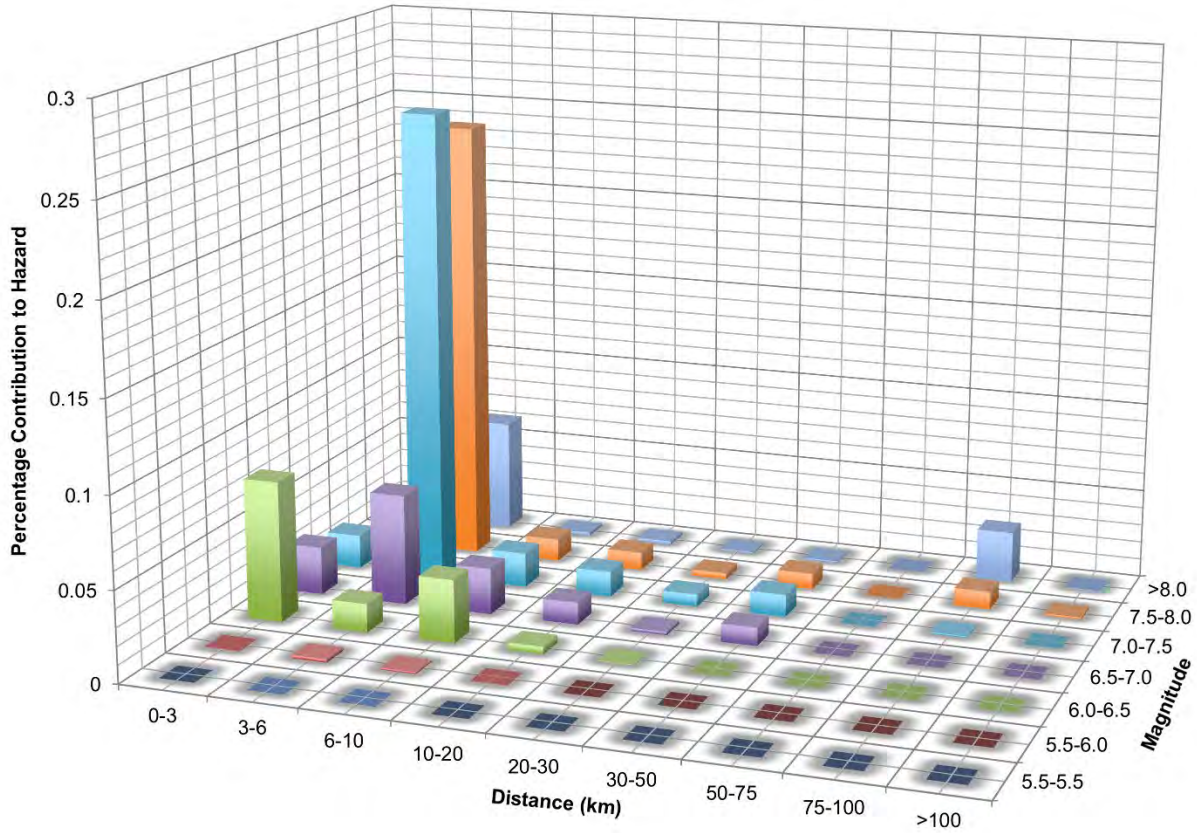
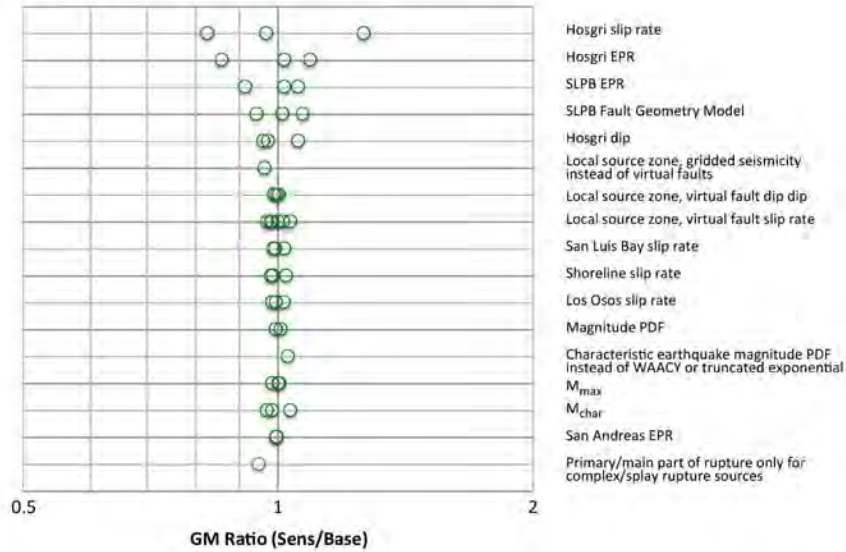
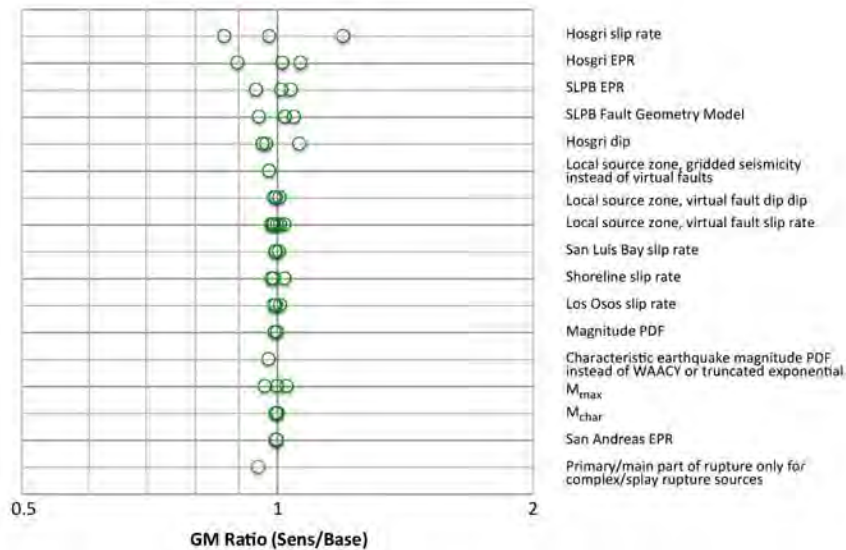


**Figure 5-19. Deaggregation of the Reference Rock Hazard for 0.5 Hz Spectral Acceleration for the  $10^{-4}$  Annual Hazard Level**

(a) DCP: AEP=10<sup>-4</sup>, 5 Hz



(b) DCP: AEP=10<sup>-6</sup>, 5 Hz



Note: Summary tornado plots showing the relative contribution to hazard uncertainty for each sensitivity case tested. The largest contributors to uncertainty are placed at the top of the tornado diagram.

**Summary Tornado Plots for the SSC Model Sensitivity Analyses for 5 Hz Spectral Frequency**

DCPP SSC REPORT

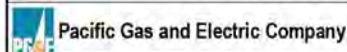
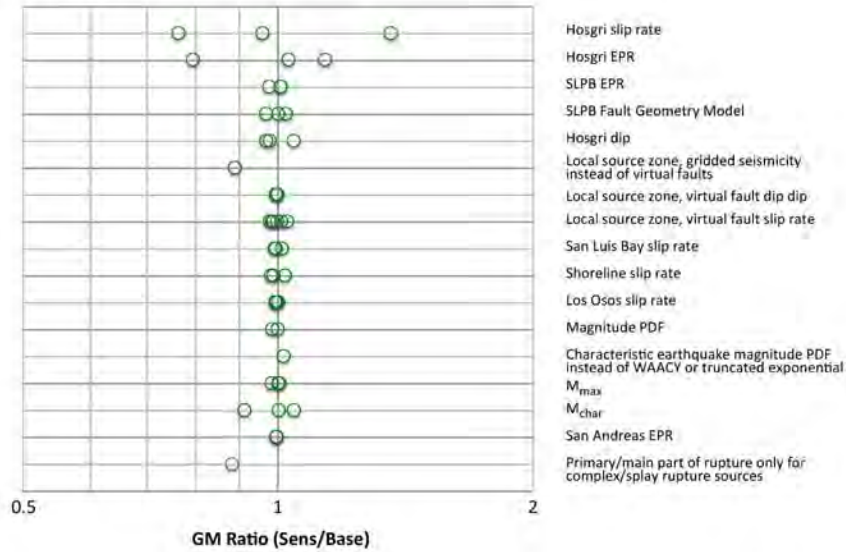


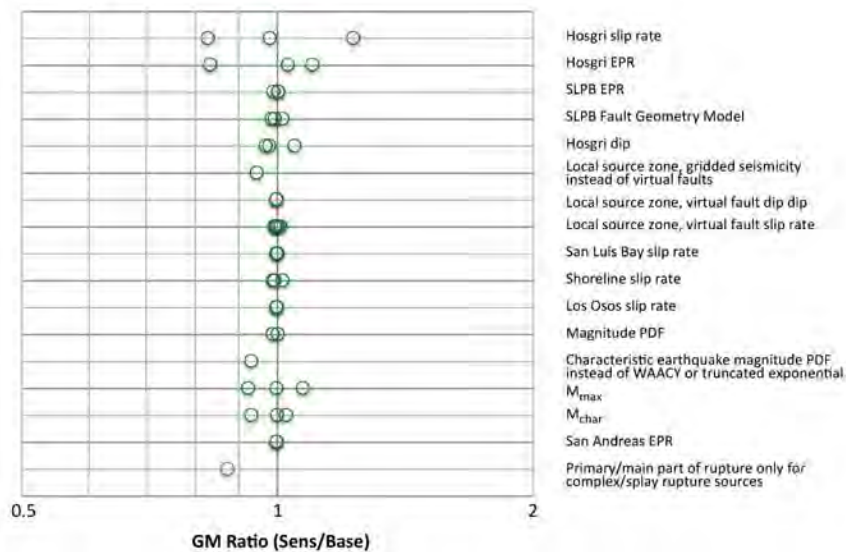
Figure 14-9

**Figure 5-20. Summary Tornado Plots for the 2015 SSC Model for 5 Hz Spectral Acceleration (from PG&E, 2015a, Figure 14-9)**

(a) DCP: AEP=10<sup>-4</sup>, 0.5 Hz



(b) DCP: AEP=10<sup>-6</sup>, 0.5 Hz



Note: Summary tornado plots showing the relative contribution to hazard uncertainty for each sensitivity case tested. The largest contributors to uncertainty are placed at the top of the tornado diagram.

**Summary Tornado Plot for the SSC Model Sensitivity Analyses for 0.5 Hz Spectral Frequency**

DCPP SSC REPORT

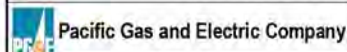


Figure 14-10

**Figure 5-21. Summary Tornado Plots for the 2015 SSC Model for 0.5 Hz Spectral Acceleration (from PG&E, 2015a, Figure 14-10)**



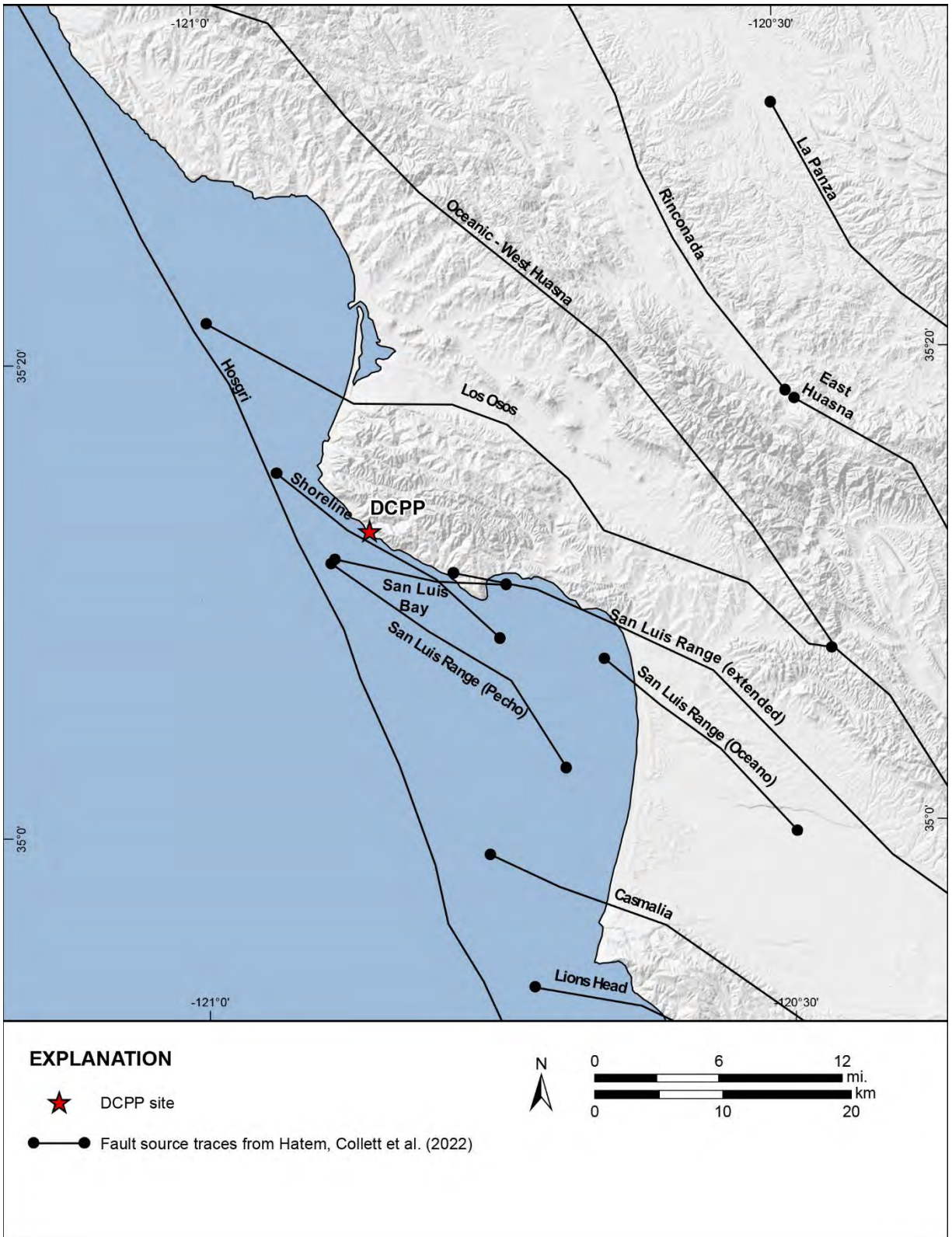
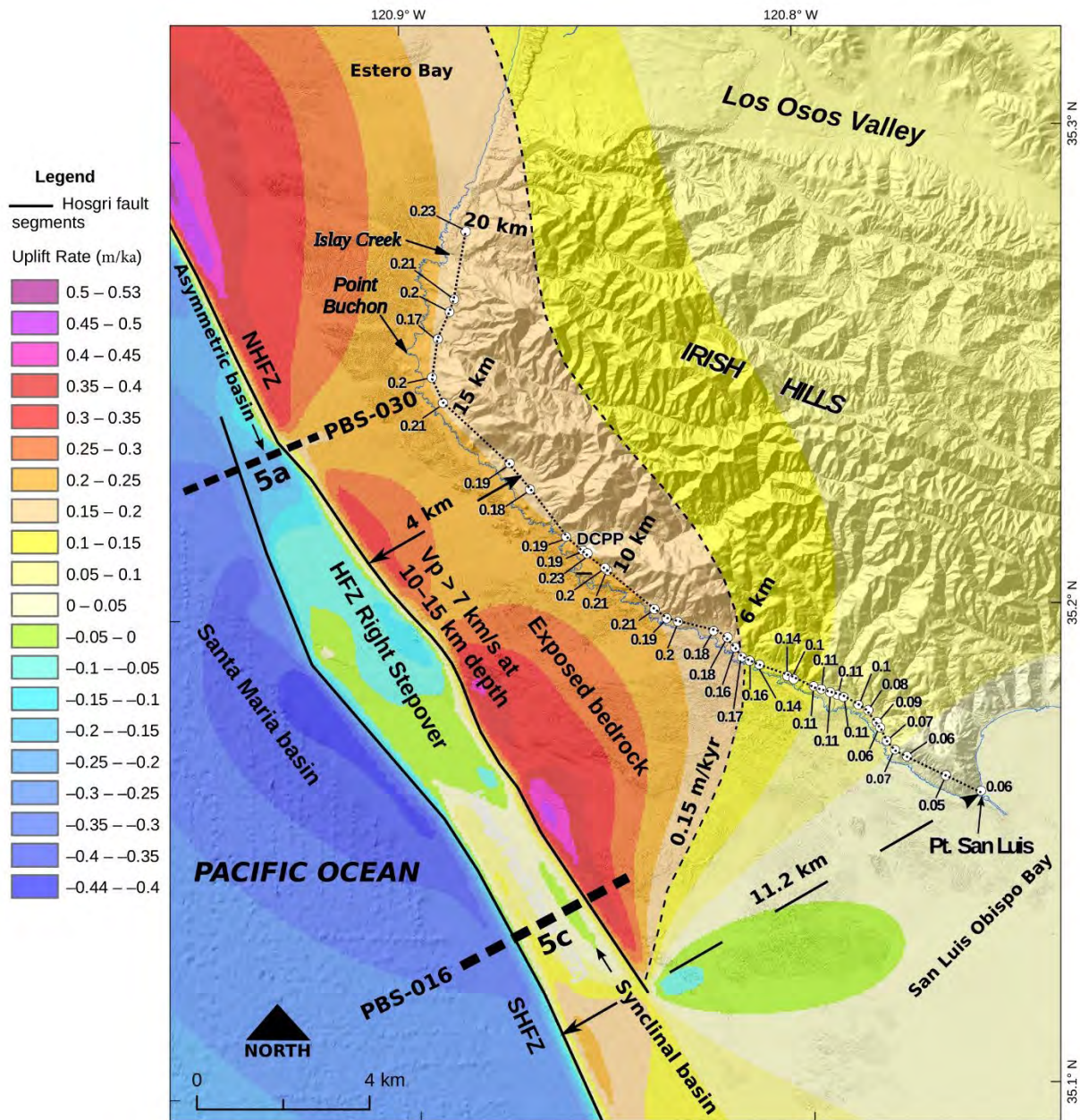


Figure 5-22. Fault Sources in the DCPD Vicinity Used in the WUS ERF-2023 Study





**Figure 3.** Map showing post-125 ka observed uplift rates (white circles labeled with uplift rate values in m/ka) are plotted over color contours of calculated uplift rates produced by the HFZ model in Figure 2b. Dotted black curve traces the uplift rate profile in Figure 2a from zero distance at Pt. San Luis northwestward with Figure 2a distances along the profile of 6, 10, 15, and 20 km labeled. Two seismic reflection profiles (thick black dashed lines) that cross the HFZ stepover between the two HFZ segments that are shown in Figure 5a,c are labeled by figure number and line name

(PBS-030 and 5a for Fig. 5a and PBS-016 and 5c for Fig. 5c). Dashed black arrows show distances from the northern Hosgri fault segment (NHZF) to the closest uplift rate observations (4 km) and the distance of Pt. San Luis from the southern Hosgri fault segment (SHFZ; 11.2 km). Exposed bedrock occurs in the hanging wall of the NHFZ in areas with high uplift rates. The calculated 0.15 m/ka contour in the hanging wall of the NHFZ is the black dashed line.

**Figure 5-23. Predicted Uplift Rates from Viscoelastic Modeling of the Hosgri Fault Zone (from O’Connell and Turner, 2023, Figure 3)**



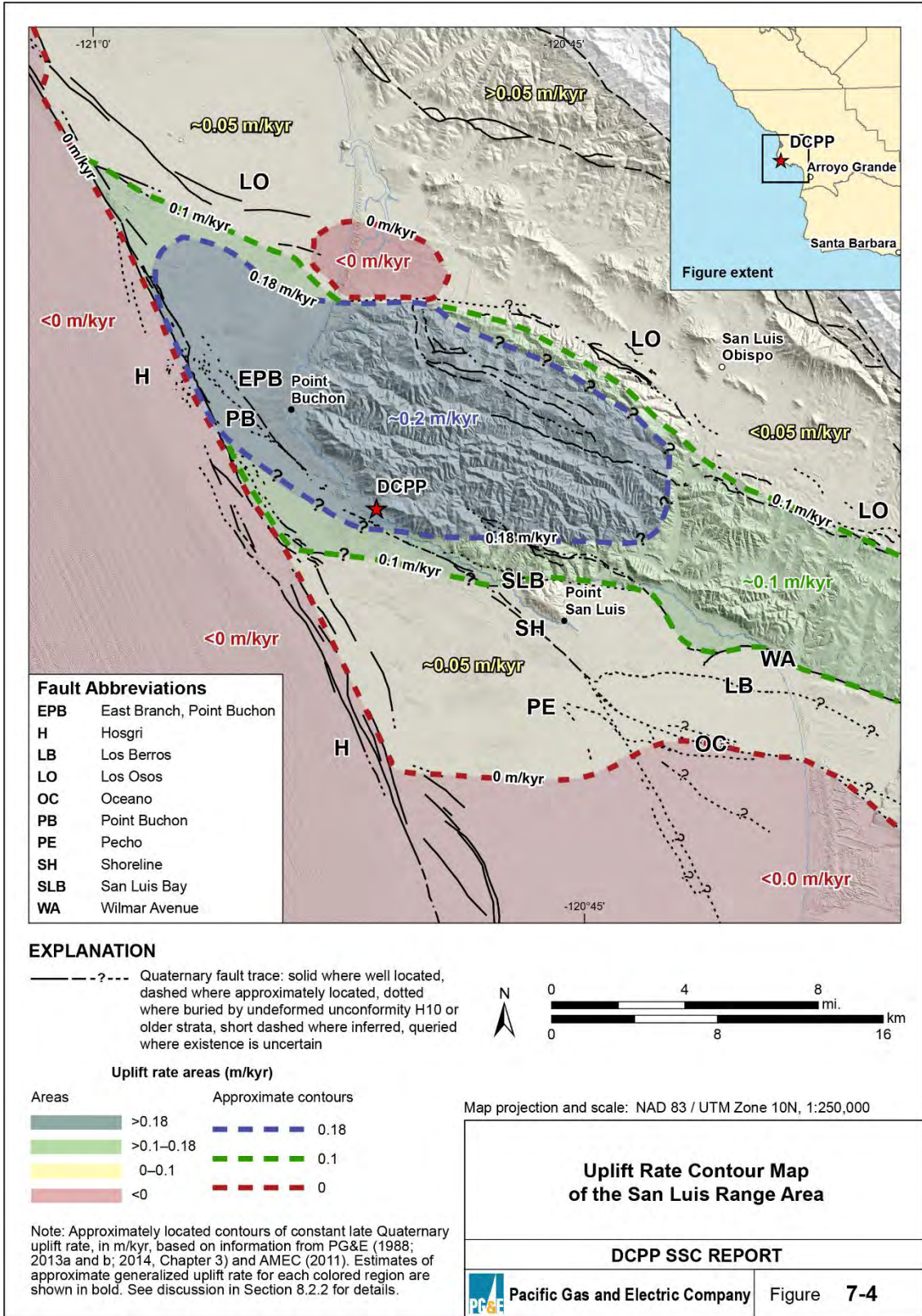


**Figure 5-24. Uplift Rates in the DCPP Vicinity as Interpreted by the 2015 SSC SSHAC TI Team (from PG&E, 2015a, Figure 7-4)**

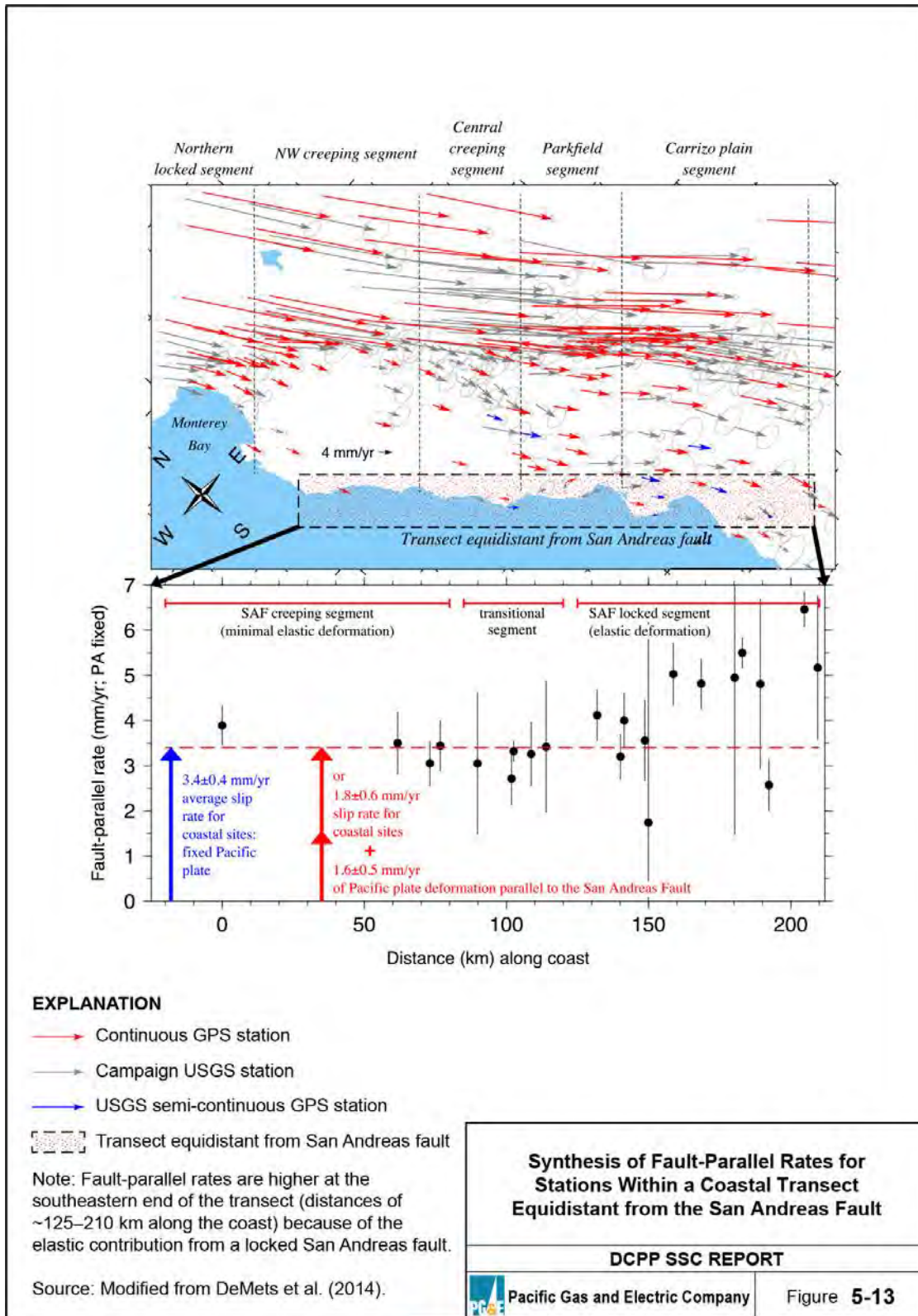


Figure 5-25. GPS Velocity Field Relative to Fixed Pacific Plate and Coast-Parallel Motion Based on DeMets et al. (2014) (from PG&E, 2015a, Figure 5-13)



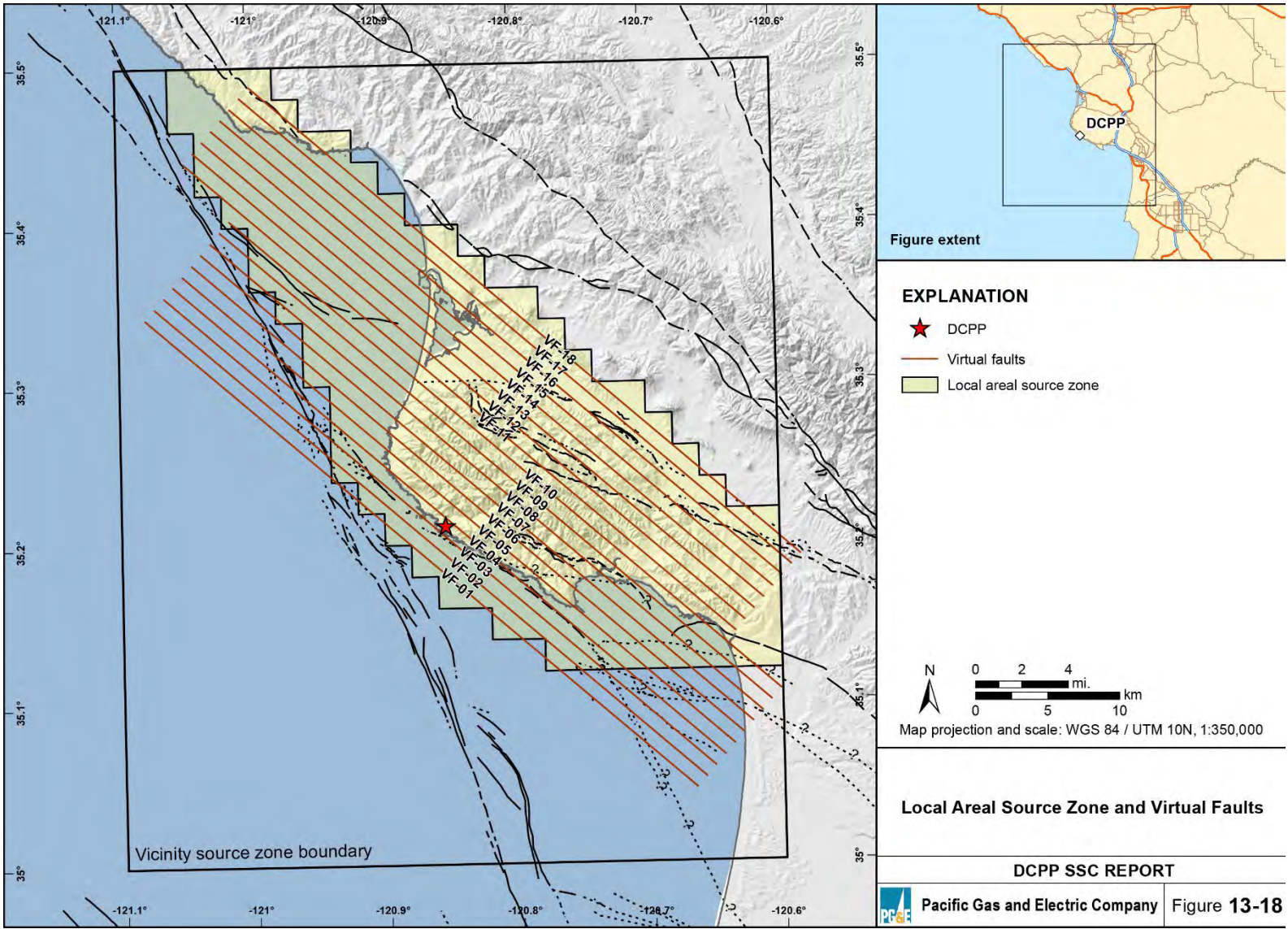
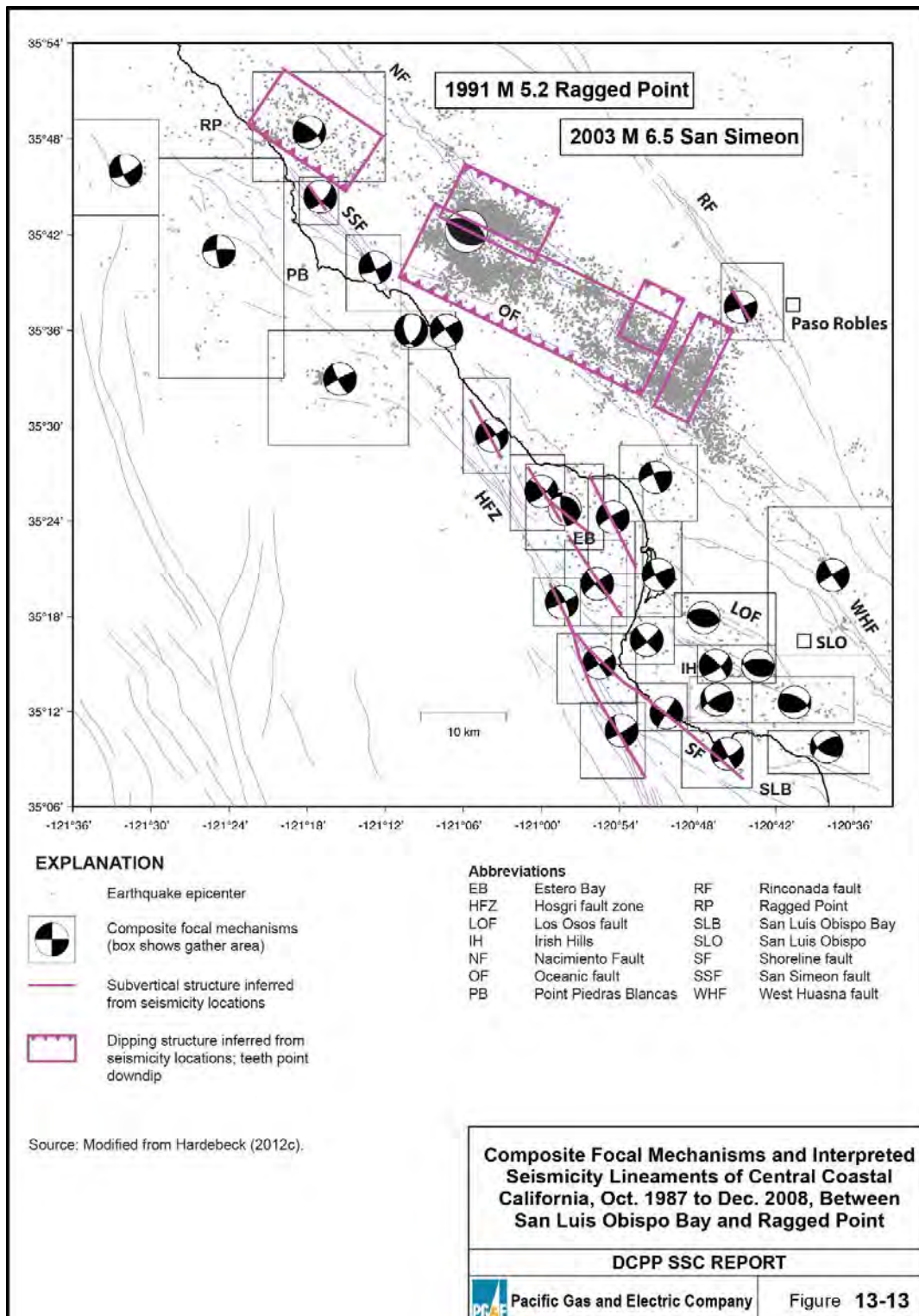


Figure 5-26. Traces of Virtual Faults Used in the Local Source Zone (from PG&E, 2015a, Figure 13-18)





**Figure 5-27. Composite Focal Mechanisms and Interpreted Seismicity Lineaments Used to Develop the Geometry and Style of Faulting for Virtual Faults (from PG&E, 2015a, Figure 13-13)**

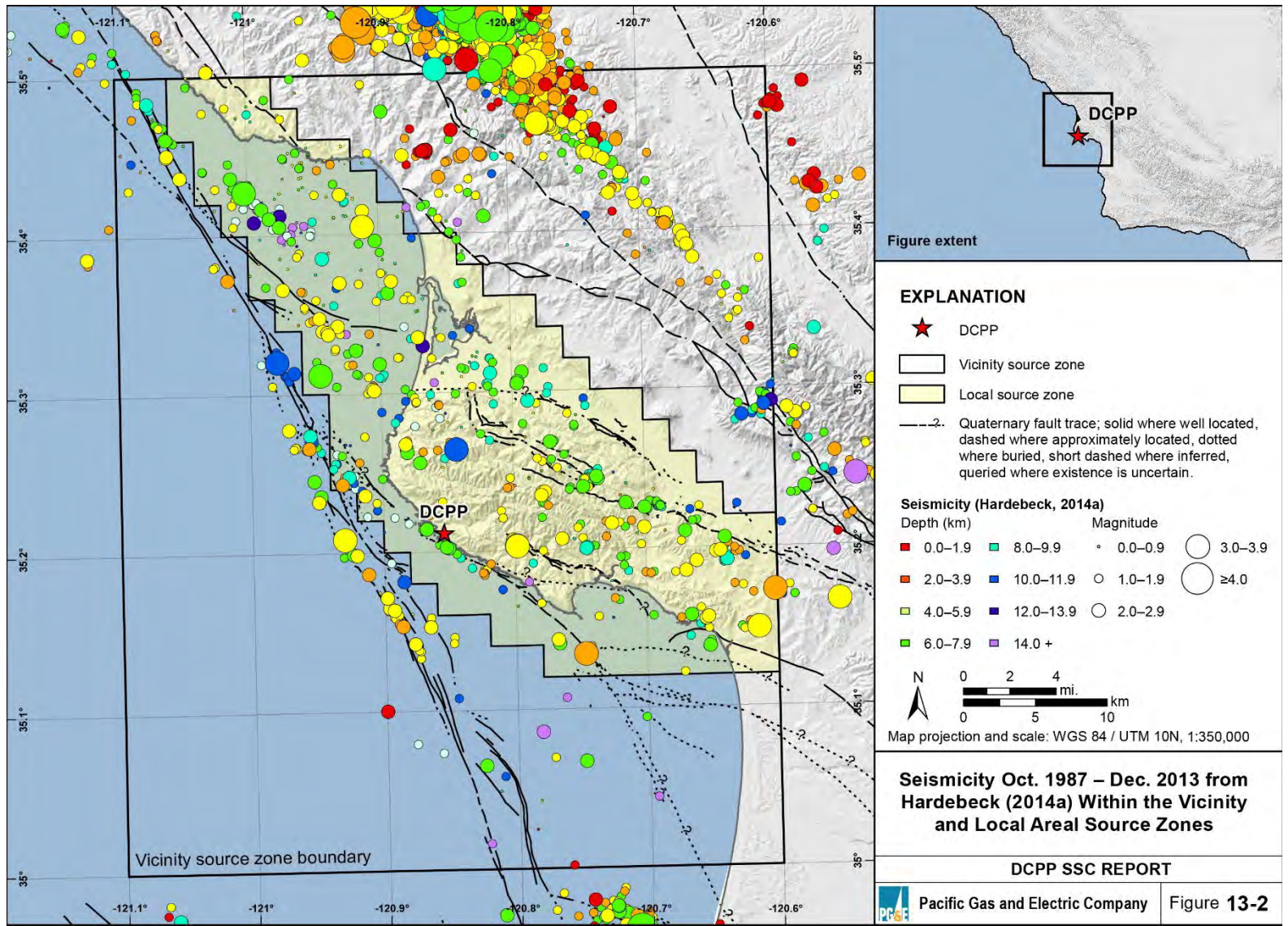
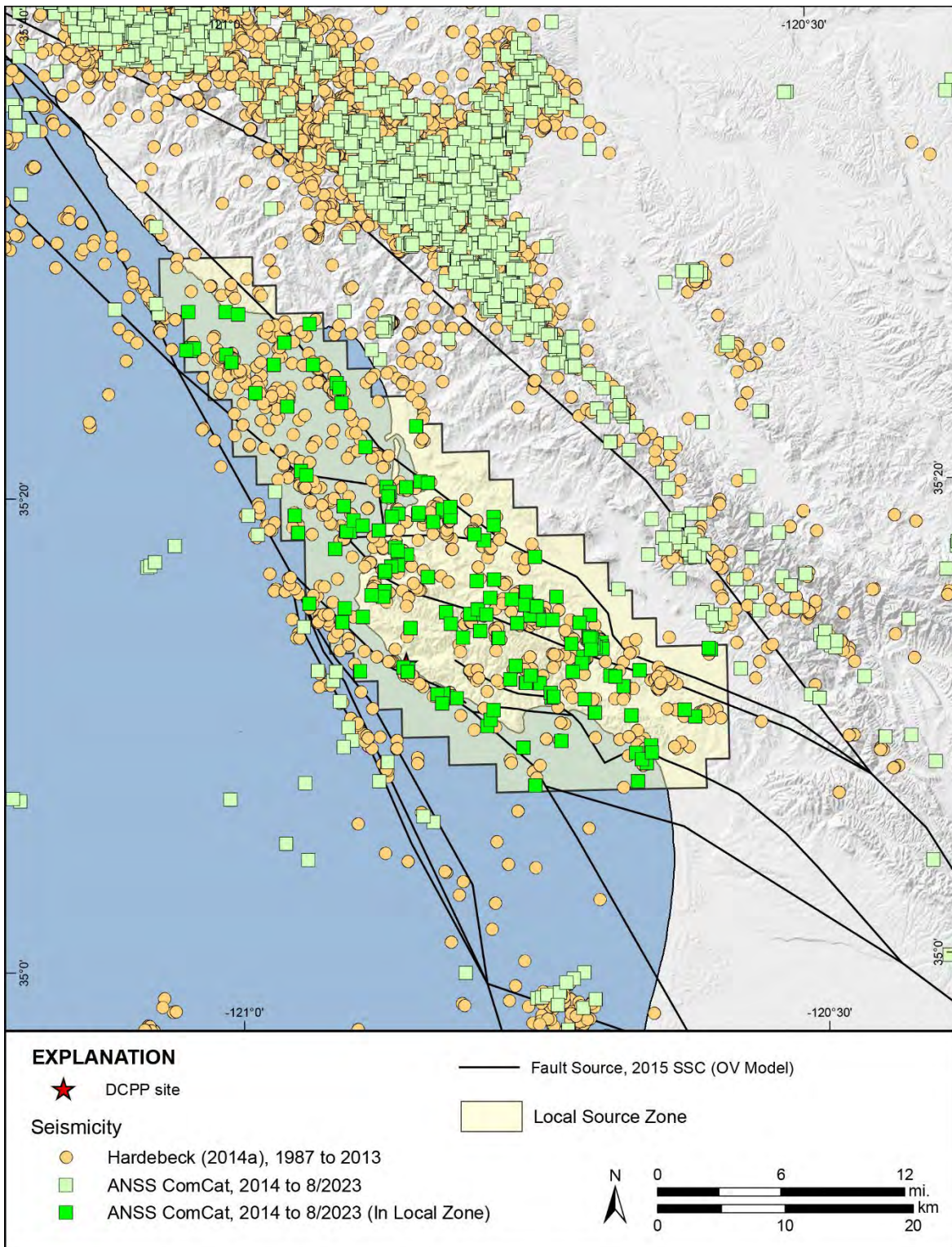


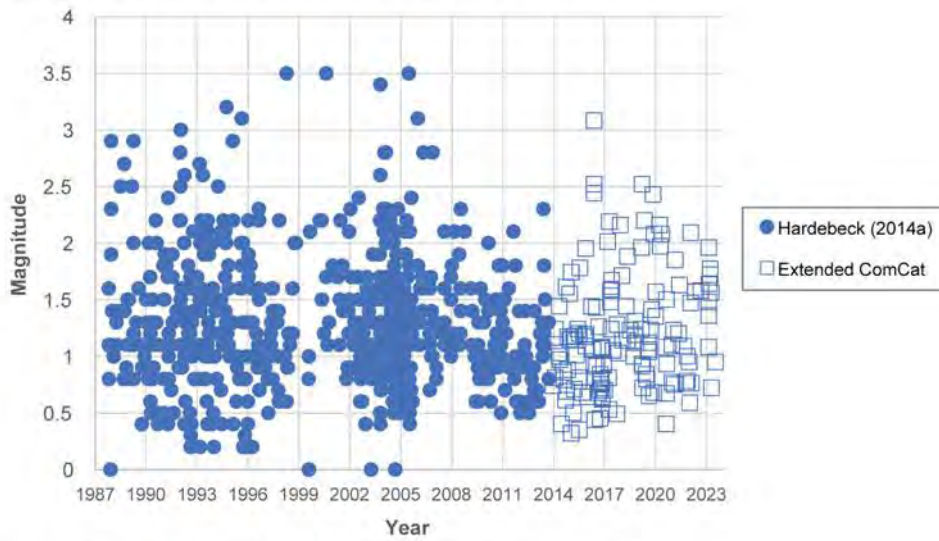
Figure 5-28. Hardebeck (2014a) Catalog Seismicity in the DCPD Vicinity (from PG&E, 2015a, Figure 13-2). Local Source Zone Extent Indicated by the Yellow Polygon.



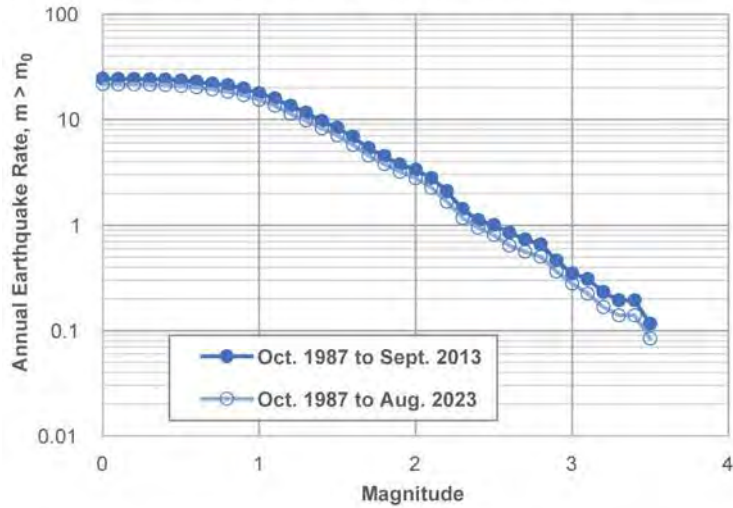


**Figure 5-29. Catalog Seismicity in the DCP Vicinity from Hardebeck (2014a) and ANSS ComCat.**

a) Local source zone seismicity, Oct. 1987 through Aug. 2023



b) Cumulative number of earthquakes versus magnitude



c) *b*-value vs completeness magnitude

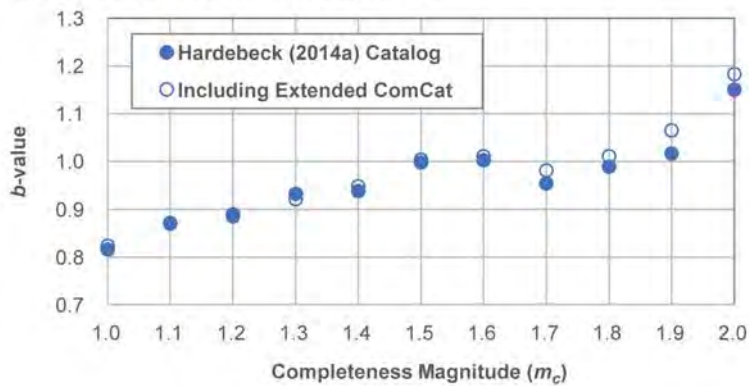


**Figure 5-30. Local Source Zone Seismicity Analysis: a) Magnitude vs. Year; b) Annual Rate vs. Magnitude; c) *b*-Value vs. Completeness Magnitude**



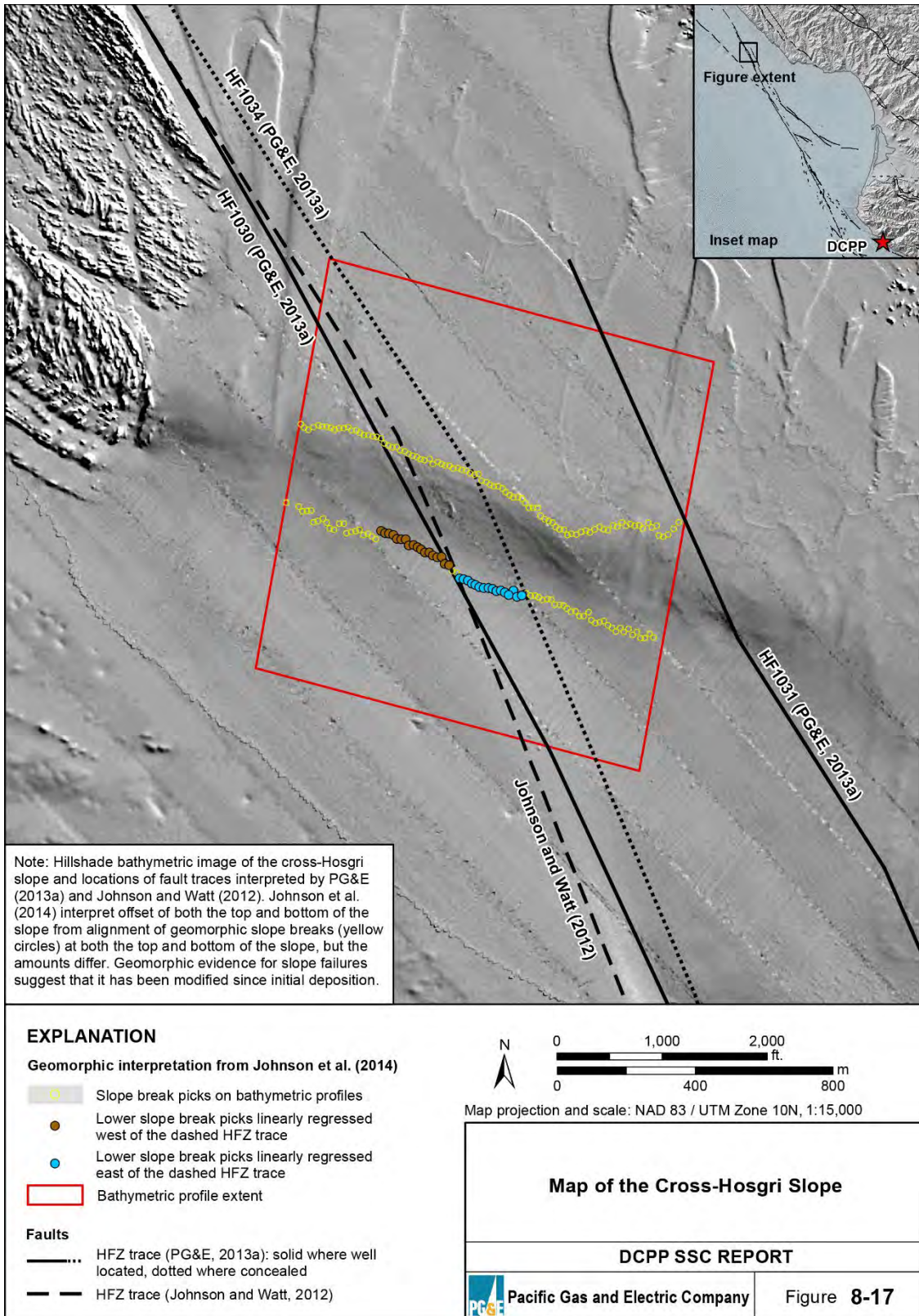


**Figure 5-31. Map of the Cross-Hosgri Slope, Point Estero Slip Rate Site (from PG&E, 2015a, Figure 8-17)**



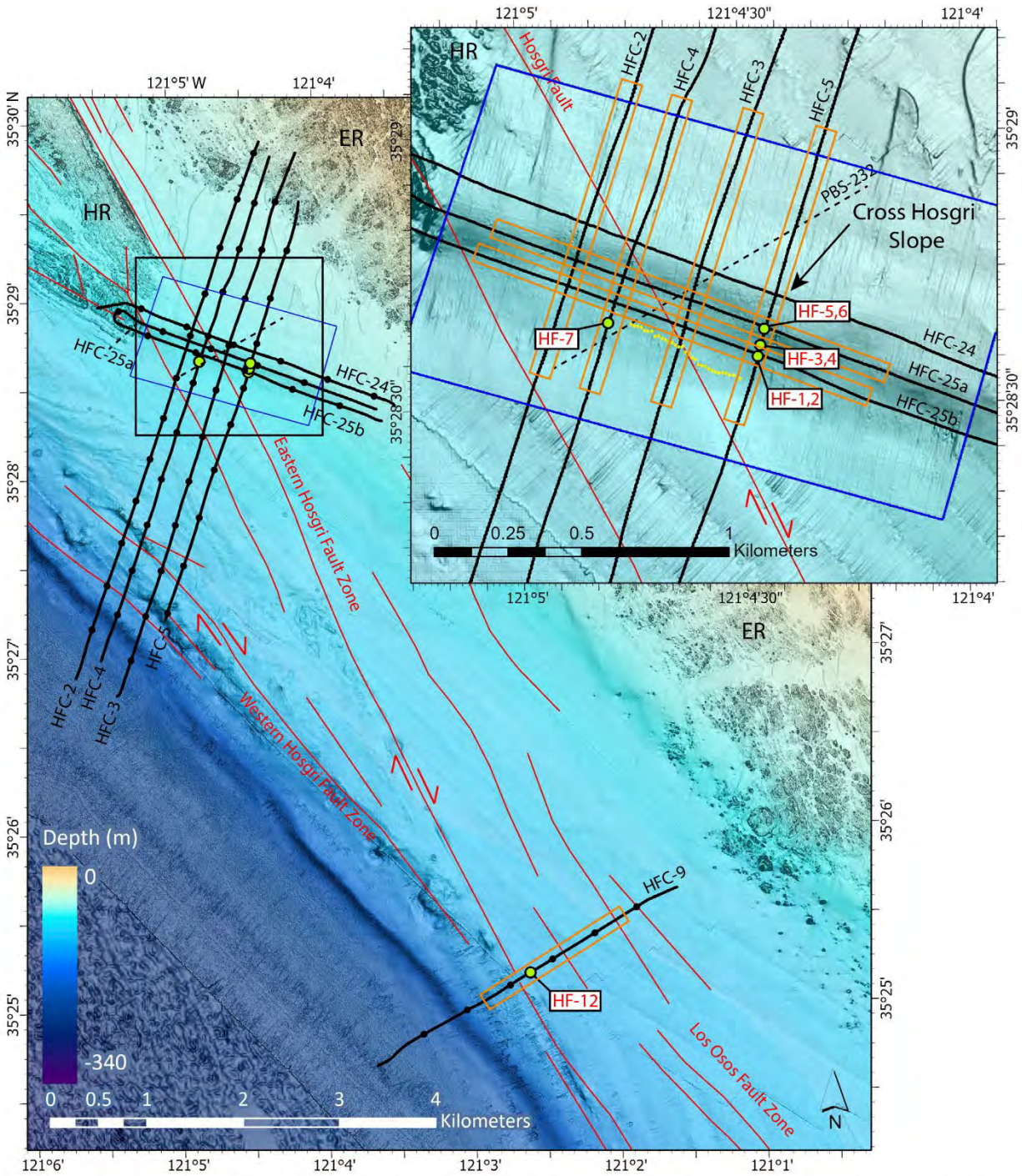


Figure 2. Map showing high-resolution bathymetry and locations of chirp track lines (black lines) and sediment cores (green circles) in the study region. Inset shows details of chirp track lines and core locations along the Cross-Hosgri slope. Inset location is outlined with black rectangle in main map. Orange rectangles show portions of chirp profiles shown in Figures 5 through 8. Red lines denote fault locations from the U.S. Geological Survey (USGS) Quaternary Fault and Fold database (Walton et al., 2020). Black circles along the chirp track lines denote position every 500 shots. Blue polygon outlines USGS-collected Reson 7111 multibeam bathymetry (Hartwell et al., 2013), and yellow points denote lower slope break points used for slip rate analysis in Johnson et al. (2014). Additional bathymetry source includes data from the California Seafloor Mapping Program (Johnson et al., 2017). Dashed black line shows location of sparker profile used in Johnson et al. (2014) and shown in Figure 11. ER—Estero Rocks; HR—Hosgri Ridge.

**Figure 5-32. New Geophysical (Chirp) Lines and Sediment Cores Collected Near the Cross-Hosgri Slope (from Kluesner et al., 2023, Figure 2)**



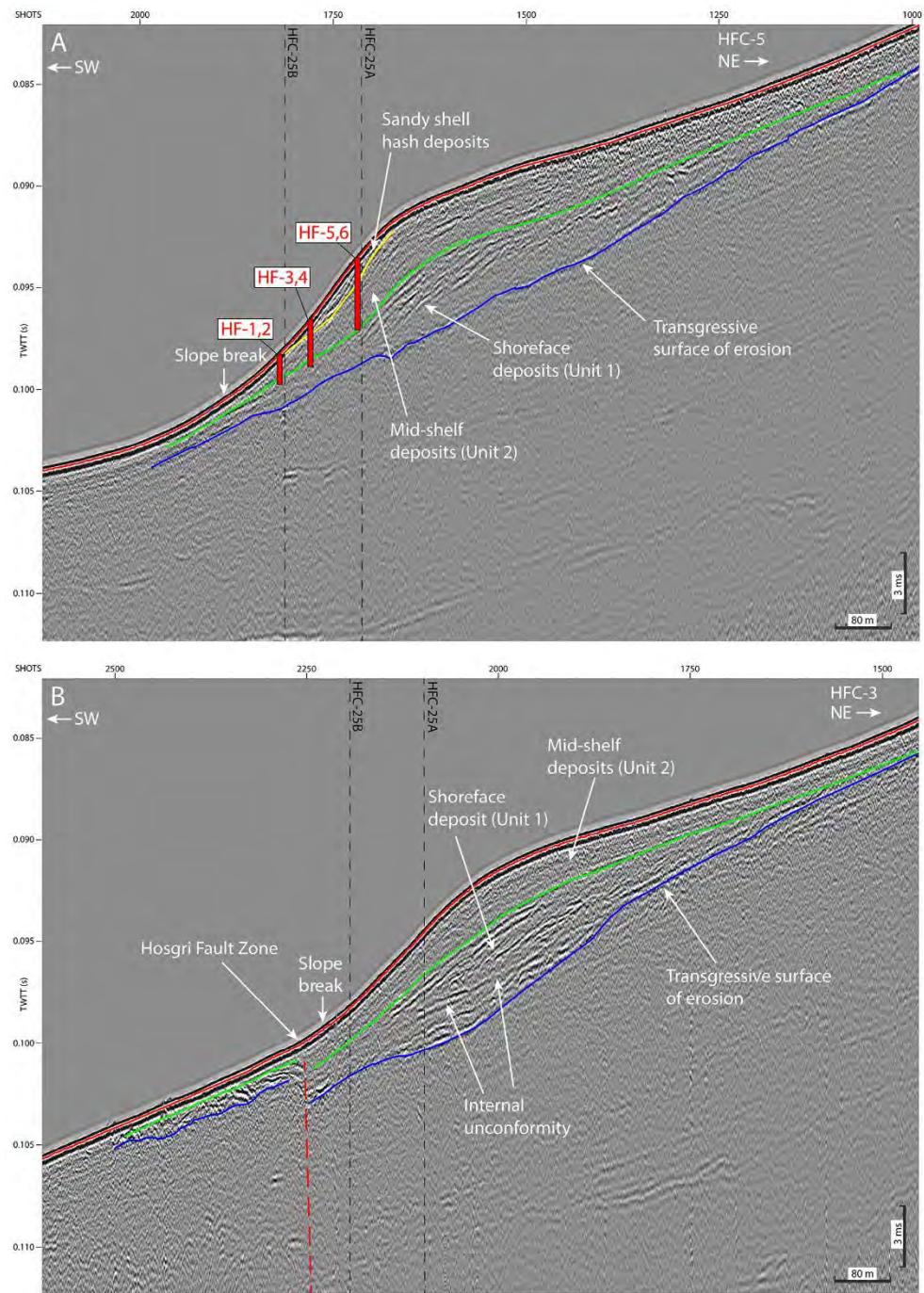


Figure 6. Compressed high-intensity radar pulse (chirp) profiles across the Cross-Hosgri slope (CHS). (A) Chirp profile HFC-5 that crosses core sites HF-1 through HF-6. (B) Chirp profile HFC-3, where offset of the transgressive surface of erosion on unit 1 is imaged near the toe of the CHS. Blue horizon denotes the transgressive surface of erosion, green horizon traces the top of paleoshoreface deposits (unit 1), yellow horizon traces the bottom of the sandy shell hash deposits, and seafloor is delineated in red. Core locations are shown as red rectangles, and the Hosgri fault zone is marked with a dashed red line on panel B. Vertical dashed black lines show locations of crossing chirp profiles HFC-25a and HFC-25b shown in Figure 8. TWTT—two-way traveltime.

**Figure 5-33. Stratigraphic Interpretation of New Chirp and Sediment Core Data Across the Cross-Hosgri Slope (from Kluesner et al., 2023, Figure 6)**

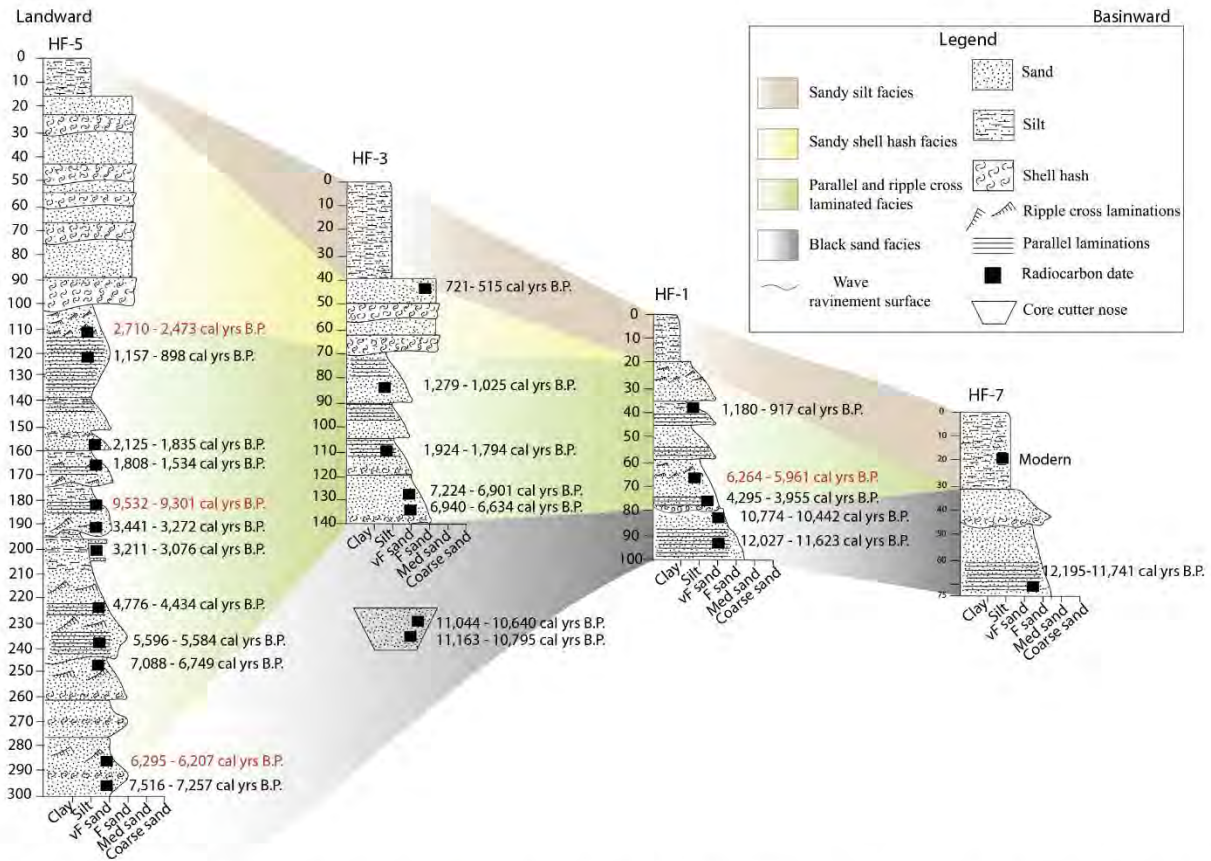
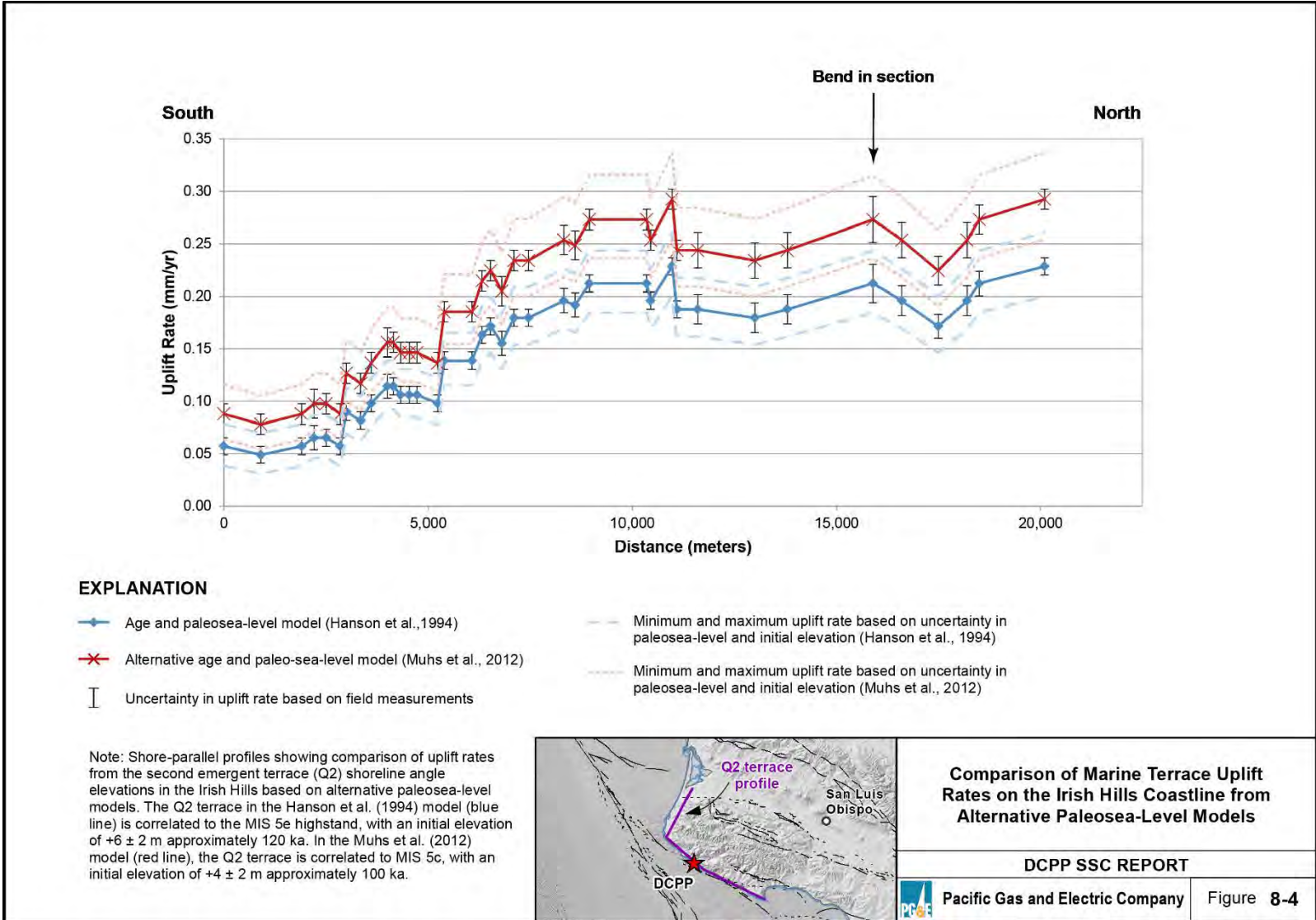


Fig. 5. Stratigraphic logs and correlations from four cores collected on the Cross Hosgri Slope (CHS), along with radiocarbon ages. Dates marked in red are interpreted as out of sequence ages and highlighted by \* in Table 2. (For interpretation of the references to colour in this figure legend, the reader is referred to the web version of this article.)

**Figure 5-34. Stratigraphic and Radiometric Age Data from New Sediment Cores Across the Cross-Hosgri Slope (from Medri et al., 2023, Figure 5)**





**Figure 5-35. Marine Terrace Uplift Rates on the Irish Hills Coastline from Alternative Models Considered in the 2015 SSC Model (from PG&E, 2015a, Figure 8-4)**

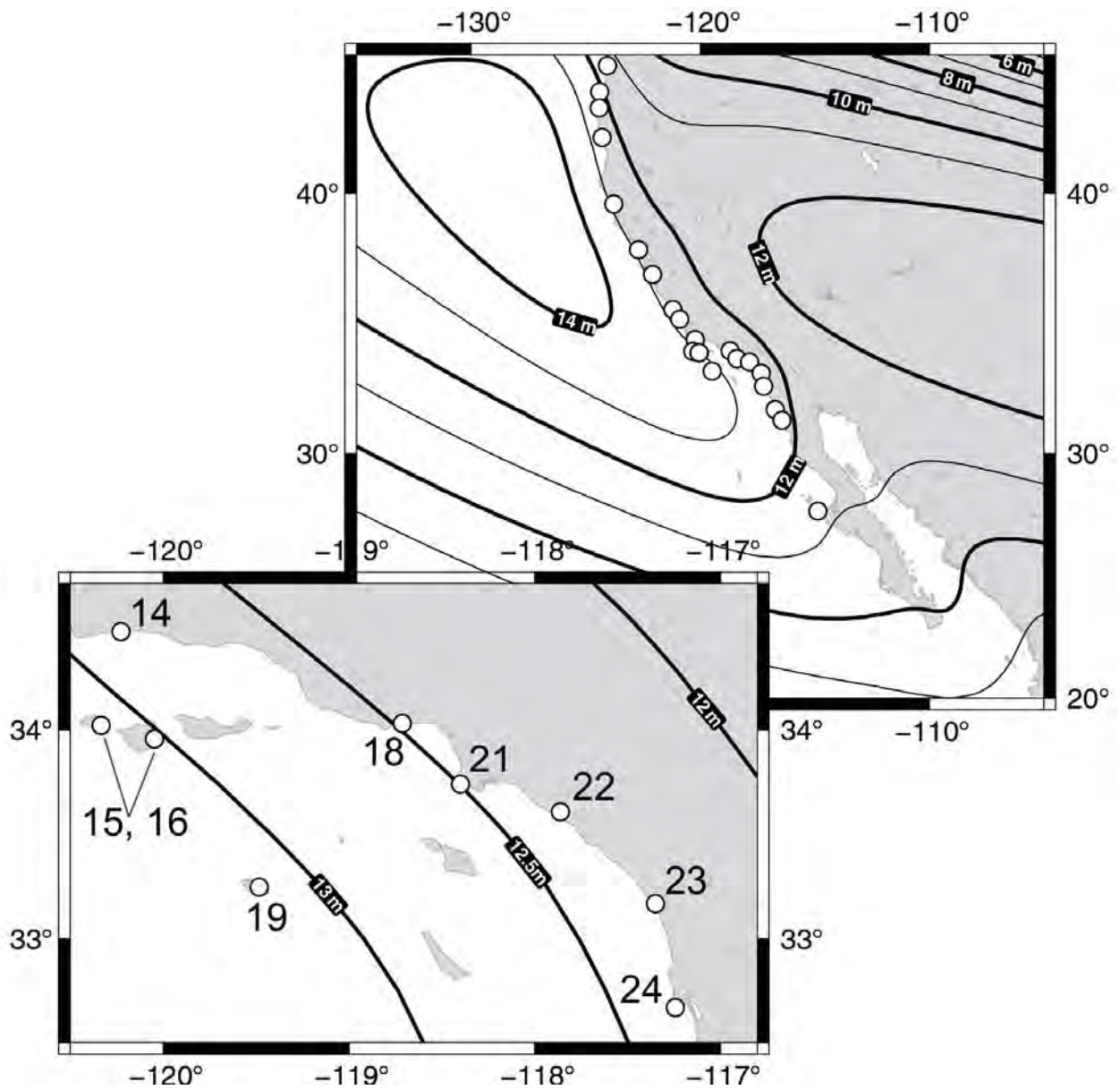


**Figure 5-36. Contours of Paleosea Level Along the California Coast for MIS 5e (from Simms et al., 2016). Central California Coastline (Upper Map) Coincides with the 13 m contour.**

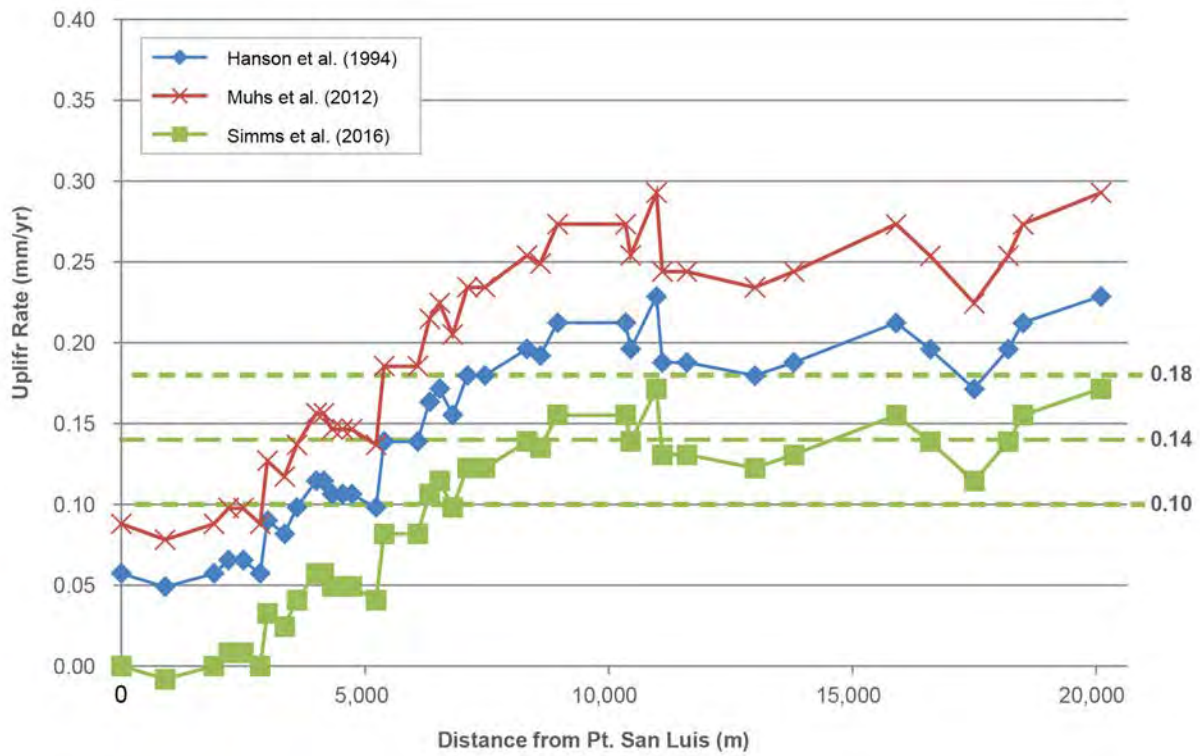


**Figure 5-37. Marine Terrace Uplift Rates on the Irish Hills Coastline Comparing Simms et al. (2016) Model to Prior Models. (See Figure 5-35 for Profile Location)**



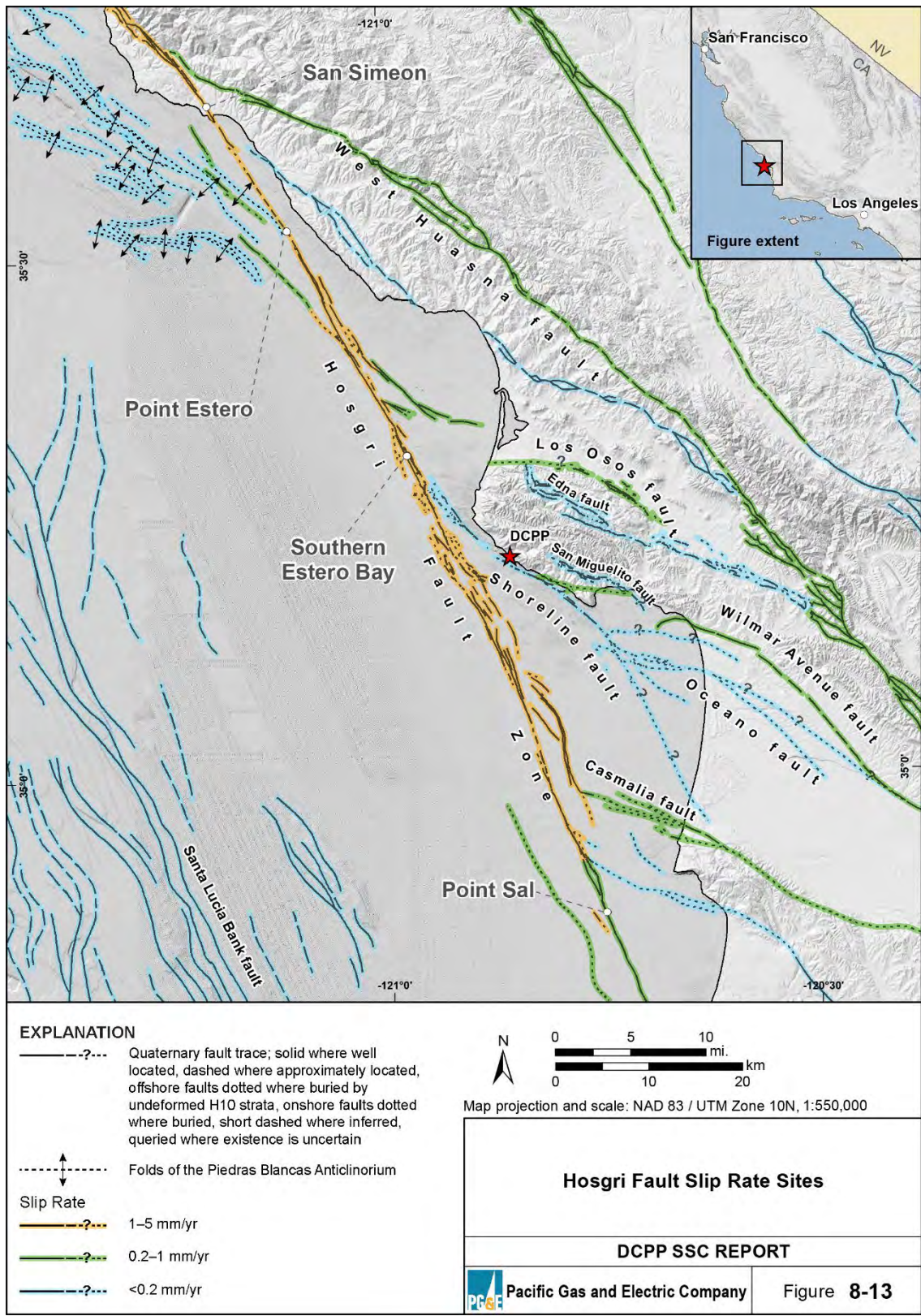


**Figure 5-38. Hosgri Fault Slip Rate Sites (from PG&E, 2015a, Figure 8-13)**

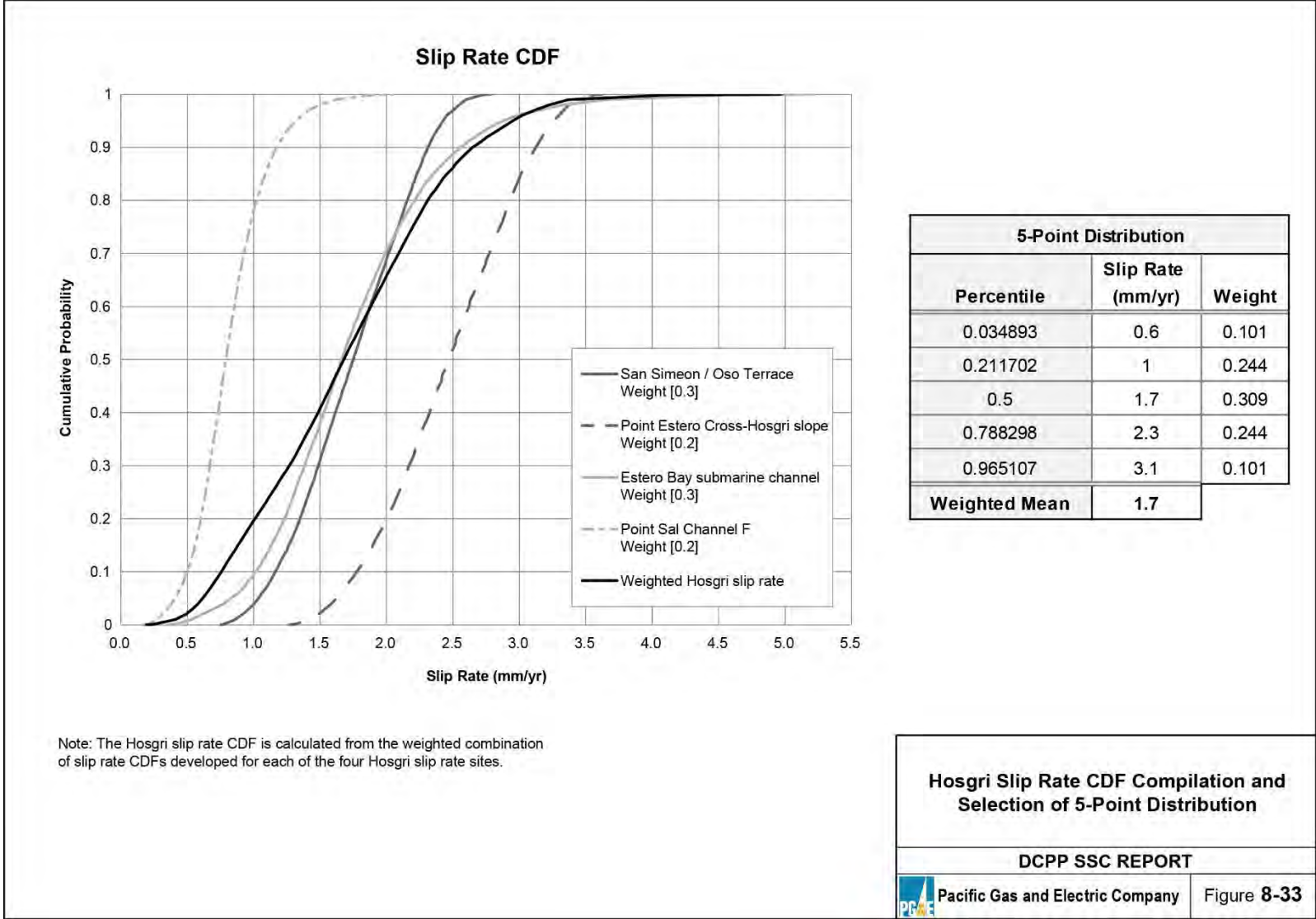
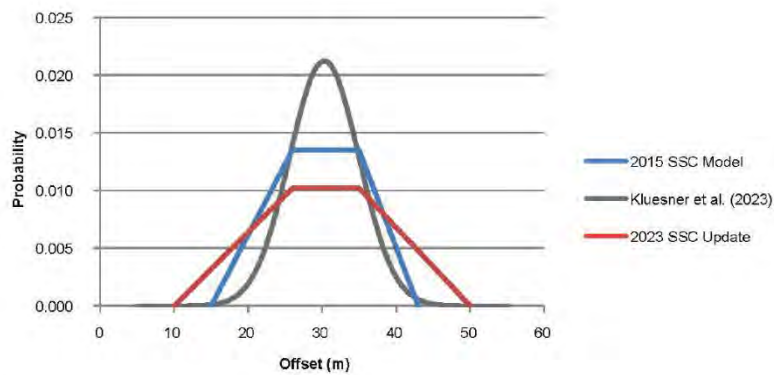
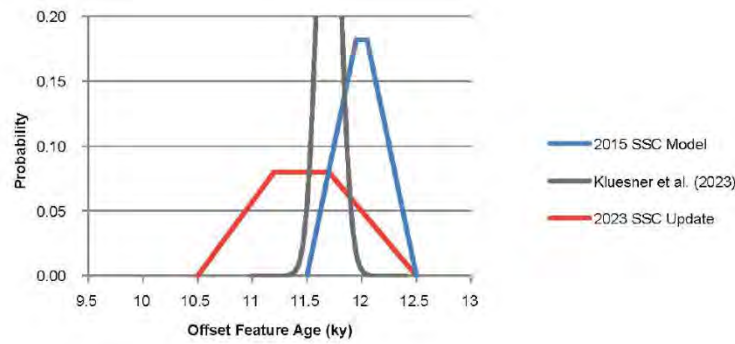


**Figure 5-39. Hosgri Fault Slip Rate CDF, 2015 SSC Model (from PG&E, 2015a, Figure 8-33)**

a) Offset PDF



b) Age PDF



c) Slip Rate CDF

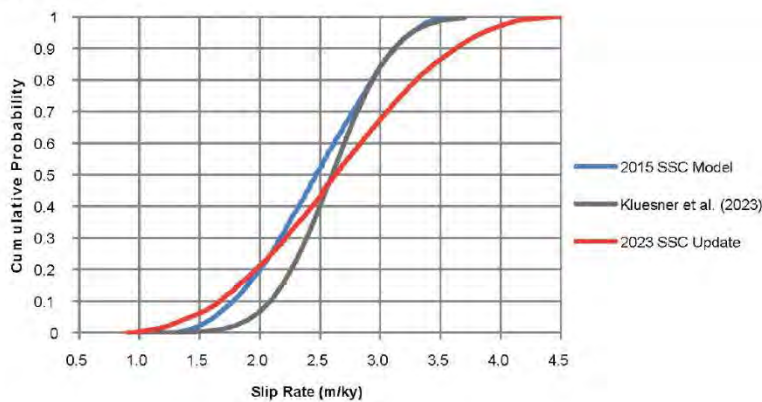
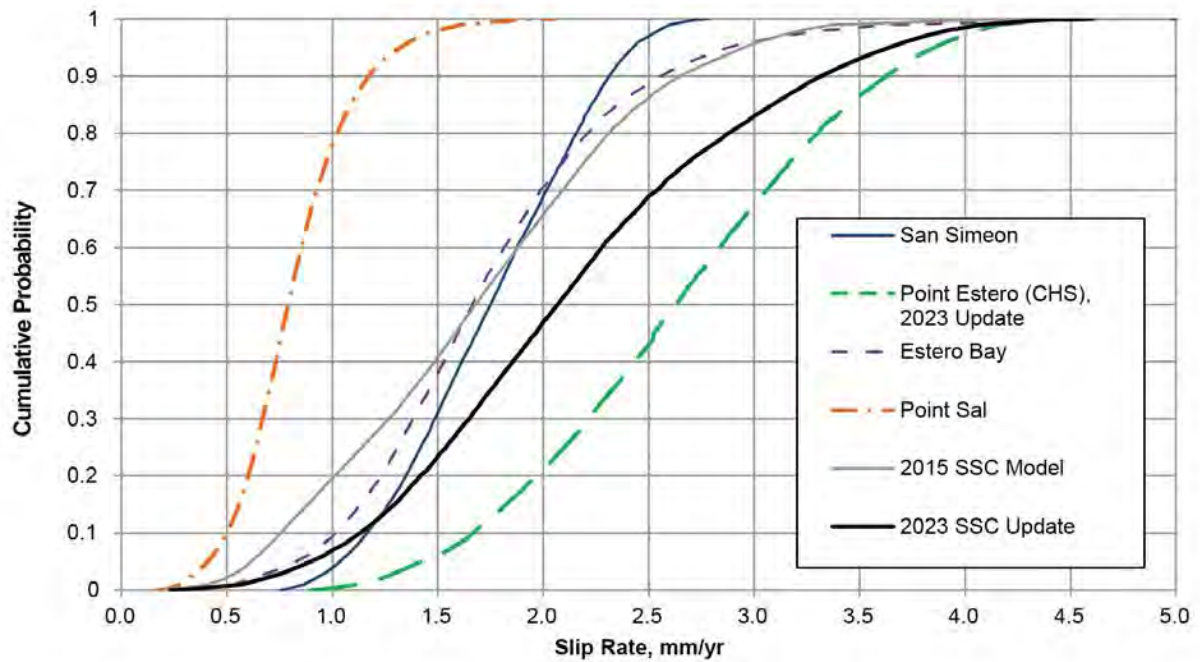


Figure 5-40. Comparison of 2015 SSC Model (Blue), Kluesner et al. (2023) Model (Grey), and SSC Model Update (Red) Input PDFs and Slip Rate CDFs for the Point Estero (Cross-Hosgri Slope) Slip Rate Site on the Hosgri Fault: a) Offset PDFs; b) Age PDFs; c) Slip Rate CDFs





Cumulative Probability	Slip Rate (mm/yr)	
	2015 SSC Model	2023 SSC Update
0.05	0.62	0.90
0.1	0.76	1.13
0.2	1.01	1.42
0.5	1.68	2.07
0.8	2.31	2.88
0.9	2.65	3.32
0.95	2.95	3.64
<b>Mean</b>	<b>1.70</b>	<b>2.14</b>

**Figure 5-41. Hosgri Fault Source Slip Rate CDFs for the SSC Model Update and Comparison with the 2015 SSC Model CDF**

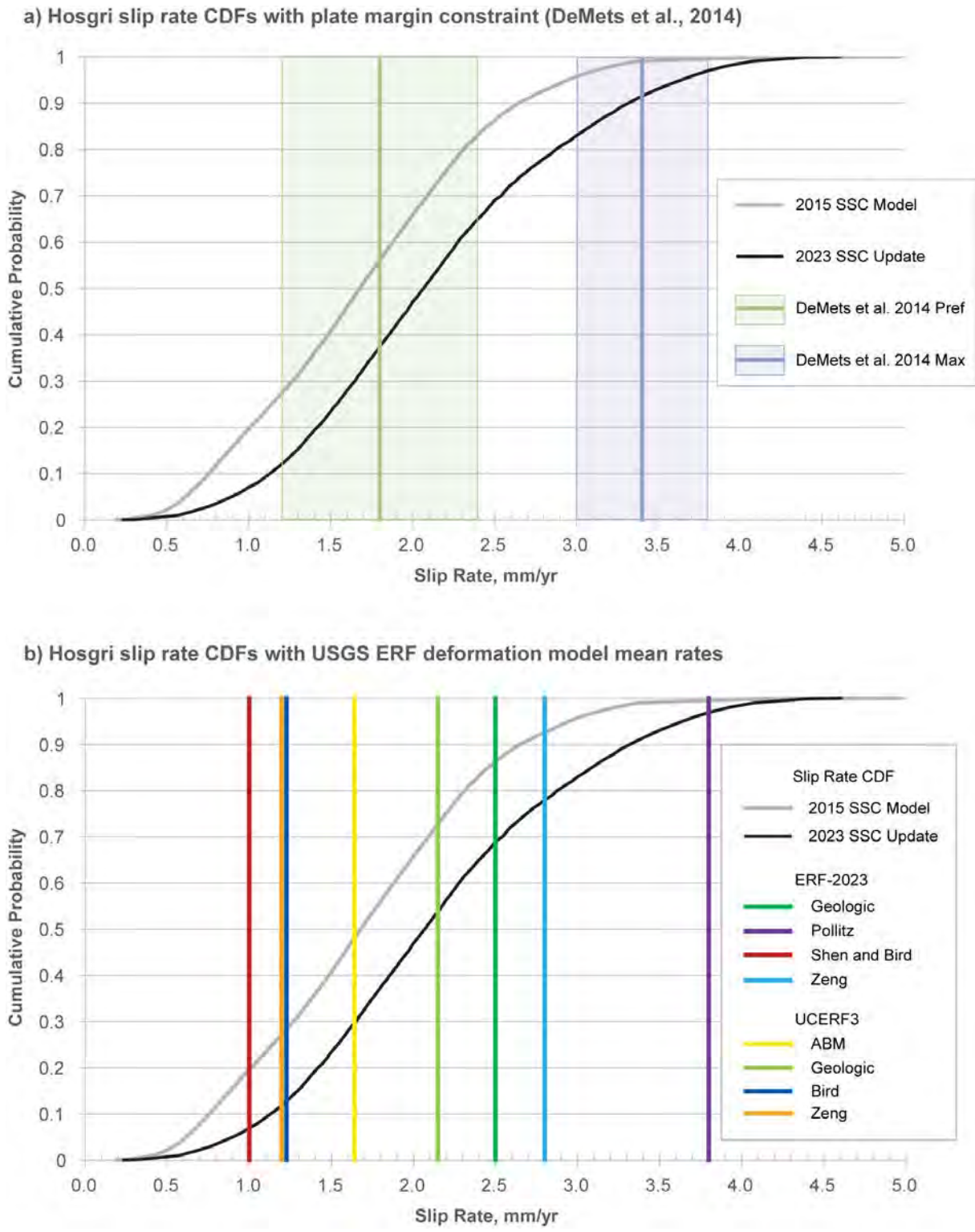
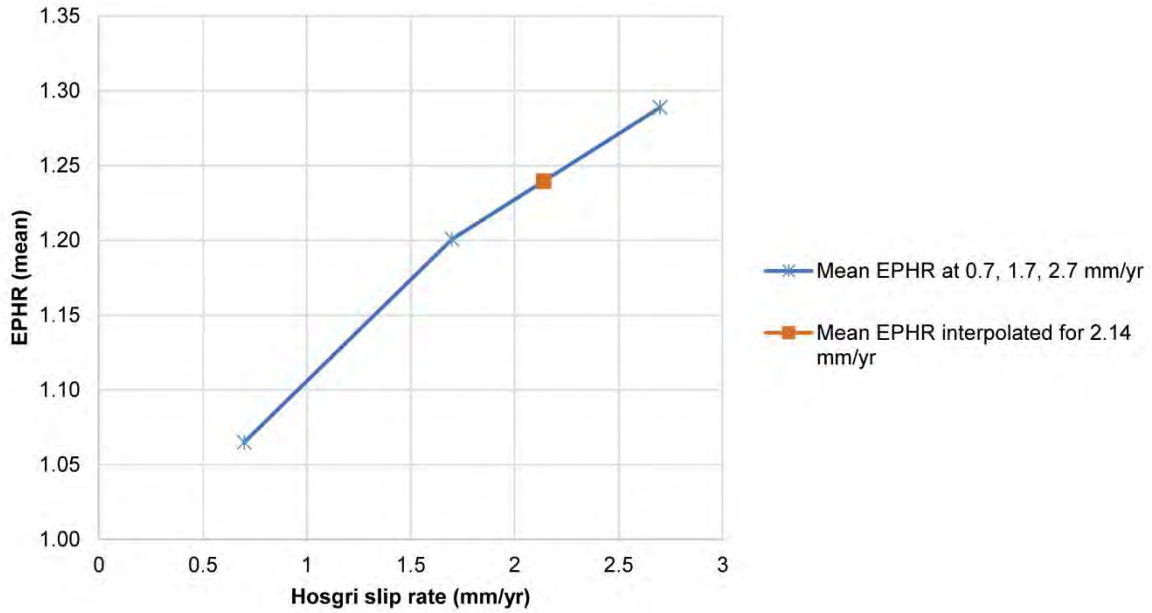


**Figure 5-42. Hosgri Fault Source Slip Rate CDFs for the SSC Model Update and 2015 SSC Model Compared with (a) Plate Boundary Model Constraints by DeMets et al. (2014) and (b) Deformation Model Slip Rates (Means) Used in the WUS 2023-ERF (Field et al., 2023) and UCERF3 (Field et al., 2013) Programs**





Note: Mean EPHR value for the updated mean Hosgri fault source slip rate (2.14 mm/yr) is estimated to be 1.24 based on interpolation of calculated values at 1.7 and 2.7 mm/yr.

**Figure 5-43. Weighted Mean EPHR for the Hosgri Fault Source Based on PG&E (2015a, Chapter 11) and Biasi and Thompson (2018).**

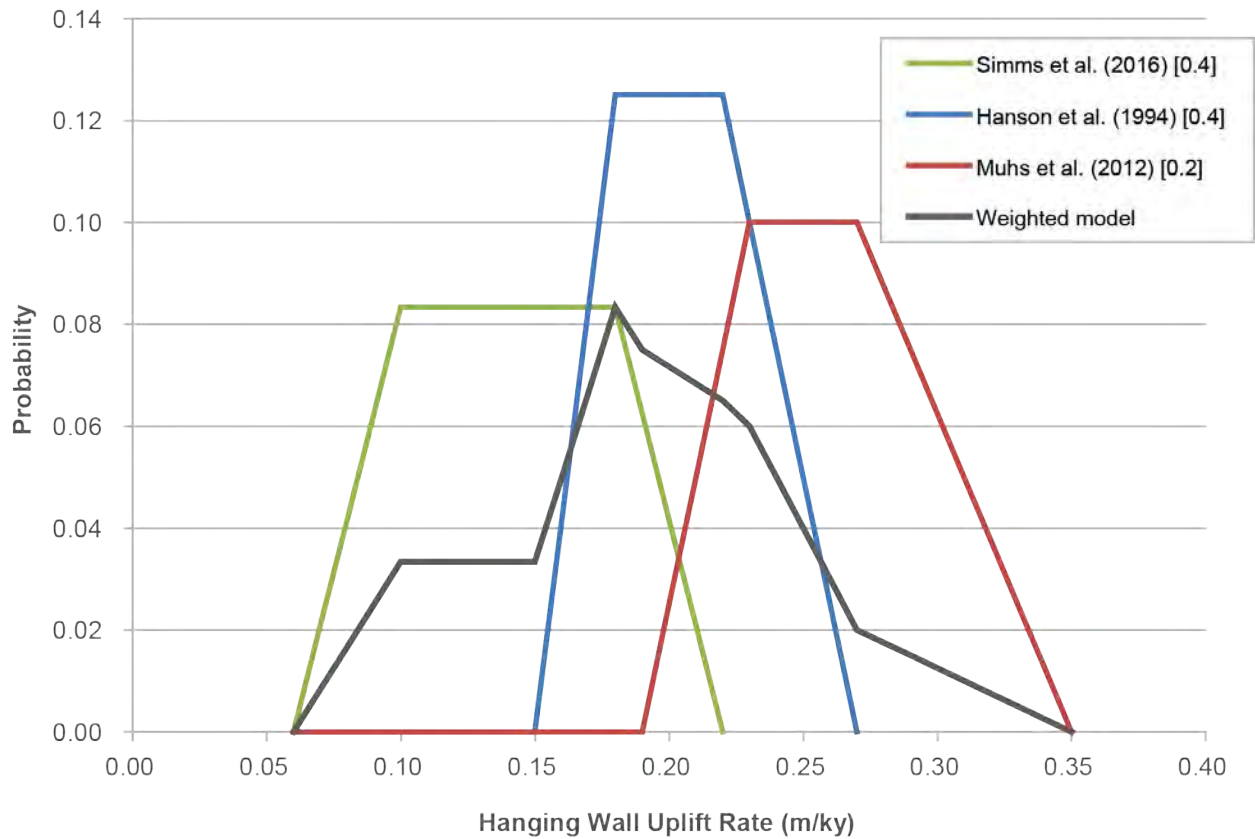
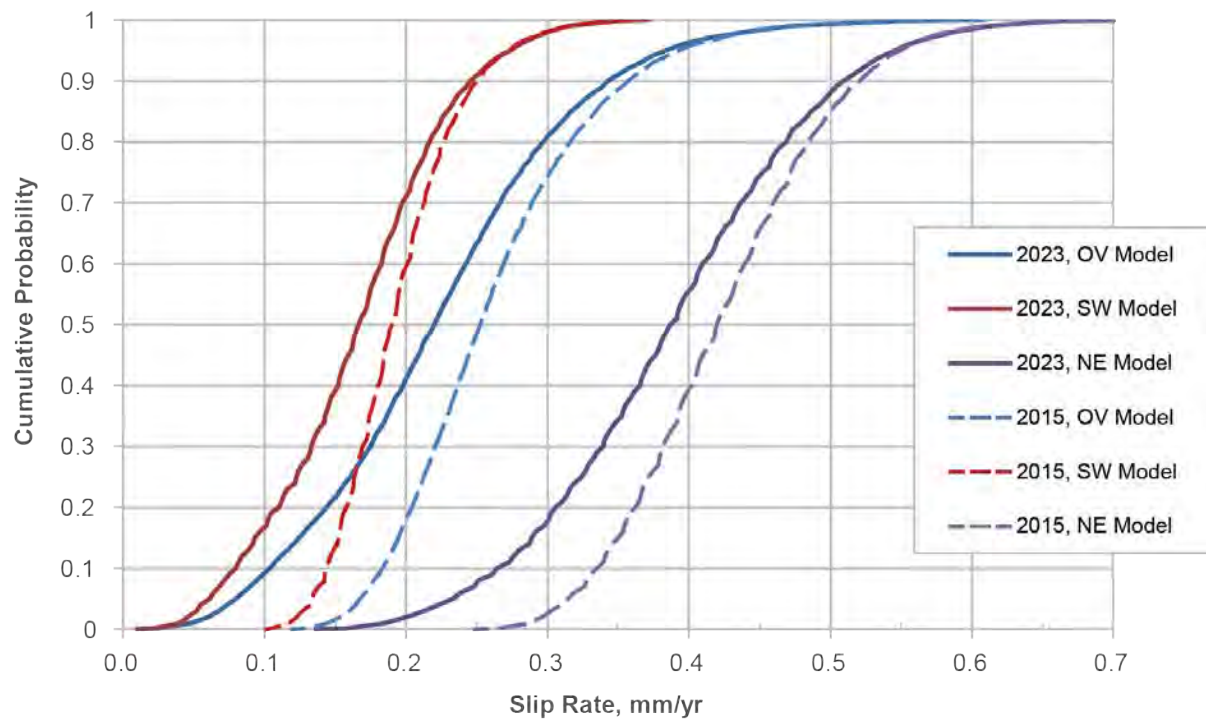
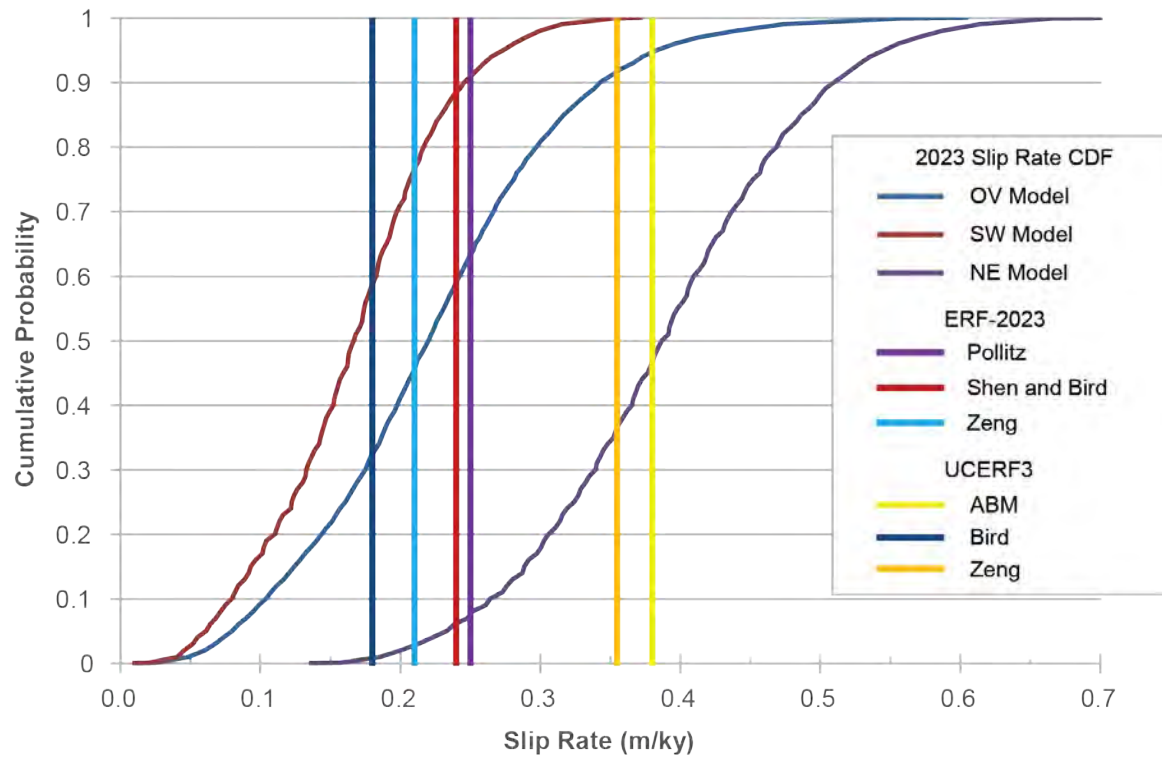


**Figure 5-44. Los Osos Fault Hanging Wall Uplift Rate PDFs Considered in the 2023 SSC Model and Weighted Uplift Rate PDF**



OV Model	Slip Rate (mm/yr)		Change
	2015 SSC	2023 SSC	
95 <sup>th</sup>	0.39	0.38	-2%
50 <sup>th</sup>	0.25	0.22	-13%
5 <sup>th</sup>	0.17	0.08	-52%
<b>Mean</b>	<b>0.26</b>	<b>0.22</b>	<b>-15%</b>
SW Model	Slip Rate (mm/yr)		Change
	2015 SSC	2023 SSC	
95 <sup>th</sup>	0.27	0.27	0%
50 <sup>th</sup>	0.19	0.17	-12%
5 <sup>th</sup>	0.13	0.06	-54%
<b>Mean</b>	<b>0.19</b>	<b>0.17</b>	<b>-15%</b>
NE Model	Slip Rate (mm/yr)		Change
	2015 SSC	2023 SSC	
95 <sup>th</sup>	0.55	0.55	-1%
50 <sup>th</sup>	0.42	0.39	-8%
5 <sup>th</sup>	0.31	0.23	-26%
<b>Mean</b>	<b>0.42</b>	<b>0.39</b>	<b>-9%</b>

**Figure 5-45. Los Osos Fault Source Slip Rate CDFs for the Alternative Fault Geometry Models, SSC Model Update and Comparison with the 2015 SSC Model CDFs**



Note: The Geologic deformation model slip rate (0.39 mm/yr) used in the WUS-ERF-2023 and UCERF3 studies is not plotted because it is a category slip rate that is not based on site-specific information.

**Figure 5-46. Los Osos Fault Source Slip Rate CDFs for the SSC Model Update Compared with Deformation Model Slip Rates (Means) Used in the WUS 2023-ERF (Field et al., 2023) and UCERF3 (Field et al., 2013) Programs**

## **6. EVALUATION OF SSC ISSUES, MODELS AND METHODS RAISED IN PUBLIC TESTIMONY**

The focus of this chapter is a response to testimony submitted on behalf of the San Luis Obispo Mothers for Peace (SLOMFP) that raises concerns about the 2015 SSC model. This response is provided here because the concerns raised in the testimony potentially impact the SSC model update for this SB-846 seismic hazard assessment.

### **6.1. SUMMARY OF TESTIMONY BY SAN LUIS OBISPO MOTHERS FOR PEACE**

SLOMFP submitted comments on the draft environmental impact statement supporting the proposed License Renewal Generic Environmental Impact Statement rulemaking. SLOMFP asserted that certain PG&E models of seismic sources are outdated and inadequate for considering seismic risks at DCP. SLOMFP's comments are discussed in a declaration by Dr. Peter Bird (Bird, 2023a), who formulated his opinions based on a review of a subset of the seismic studies and data developed for the LTSP, AB-1632 studies, and for seismic hazard evaluations of DCP. The declaration did not appear to consider information contained in the comprehensive report on the 2015 SSC SSHAC Level 3 study (PG&E, 2015a).

Dr. Bird also submitted testimony on behalf of SLOMFP on 20 June 2023 to the California Public Utilities Commission that included a review of the 2015 SSC SSHAC report and asserted that the 2015 SSC model for DCP was flawed because: (1) fault slip rates were selected without direct input from geodetic data and models, (2) seismicity rates from unknown faults were not adequately captured, and (3) thrust faults at shallow depth beneath the plant were excluded from the model (Bird, 2023b).

As part of the seismic hazard assessment to fulfill the covenant in SB-846, the project SSC TI Team, PPRP members, and project sponsors reviewed Dr. Bird's declaration (Bird, 2023a) and testimony (Bird, 2023b) to determine whether they contain technically defensible data, models or methods that were not considered during the 2015 SSC SSHAC process and should be included in the SSC model update for the SB-846 seismic hazard assessment. As discussed below, our finding is that many technical points raised by Dr. Bird are points of disagreement regarding the appropriate use of models and methods developed for regional earthquake rupture forecasts or for academic research versus models and methods that should be used for a site-specific seismic hazard analysis of a critical facility. This includes the use of regional deformation models to calculate the slip rates of Primary fault sources and/or the seismicity rates of background earthquakes, and the use of Dr. Bird's "SHIFT" method for developing earthquake magnitude-recurrence distributions. Other points raised by Dr. Bird are interpreted to be technically incorrect or inconsistent with available information. These include assertions about (1) crustal rigidity in the direct vicinity of the DCP and the appropriate use of Airy isostasy principles in the interpretation of vertical tectonic rates, and (2) the geometry and rates of faulting directly beneath the DCP.

## 6.2. GEODETIC MODEL CONSTRAINTS ON DEFORMATION RATES

### 6.2.1. *On-Fault Deformation*

The testimony by Dr. Bird (Bird, 2023b) states that the 2015 SSC model did not make quantitative use of measurements of crustal motion by GPS receivers and long-term crustal strain rates from computer models that consider GPS, geologic and stress data in developing slip rate cumulative distribution functions for fault sources. Dr. Bird is correct in that the slip rates calculated from geodesy-based deformation models were not included as branches in the 2015 SSC model logic tree. However, the deformation models were evaluated as part of the SSHAC process. The results were compared to the slip rates calculated in the 2015 SSC model. As detailed in Section 5.2.1.2 of this report (Geodetic Data and Model Constraints subheading), the 2015 SSC SSHAC report compared the 2015 SSC model fault source slip rates with slip rates from the three geodesy-based deformation models developed for the UCERF3 model (PG&E, 2015a, Chapter 13). In addition, the 2015 SSC SSHAC study considered proponent models using GPS data that examined constraints on fault slip rates using a variety of methods. One of the proponent models was provided by Dr. Bird; this model examined strain rates from GPS data resolved as on-fault horizontal slip rates for faults in south-central coastal California using the NeoKinema model (PG&E, 2015a, Chapter 5). This information was used to develop and support the alternative geometric and kinematic models and to provide general constraints on slip rates, but it was not used to develop epistemic alternative slip-rate models for the Primary faults.

Section 5.2.1.2 outlines the rationale for not including the geodesy-based deformation model slip rates in the calculations of the Primary fault source CDFs. The list of reasons is repeated here:

- The calculated slip rates do not explicitly account for best-available site-specific geologic information
- The slip rates use as input a fixed set of fault locations and geometries that do not reflect the best-available data near the DCP
- Given the density of fault sources near the DCP, there is low confidence that geodetic data could resolve the rates and kinematics of individual faults
- The coastal location of the Primary fault sources presents a challenge given the absence of offshore GPS velocities
- The uncertainties within each model are poorly understood, which reduces confidence in the robustness of the mean model result

The same findings regarding the confidence in the GPS-based deformation models apply to this SSC model update. We consider the WUS ERF-2023 deformation models to be insufficiently documented and tested for their reliability and suitability to be included directly in the calculation of fault slip rate CDFs. The fixed fault geometries that do not reflect the best available information, the density of fault sources relative to the onshore distribution of GPS stations, the challenges of calculating slip rates for coastal and offshore faults with the absence of velocity information on the seaward side of the faults, and the lack of understanding of what factors contribute to the uncertainties within the models together form a basis for not including these model slip rate results in the fault slip rate model for this site-specific seismic hazard assessment. A peer review of these deformation models for general use in the WUS ERF-2023 project raised similar concerns about a lack of understanding for what contributes to the model



uncertainties (Johnson et al., 2024). These concerns were echoed in summary reports for the WUS ERF-2023 (Field et al., 2023) and the 2023 NSHM update (Petersen et al., 2023).

Whereas geodesy-based model slip rates are interpreted to be unreliable for use as direct inputs in the SSC model for DCP, they are useful for comparison and to document whether there are large differences between results. For the SB-846 hazard assessment, we compare Primary fault slip rates from the 2015 and updated SSC model with the equivalent fault slip rates from four deformation models (geologic model plus three numerical models) used in the WUS ERF-2023. (Table 5-11; Figures 5-42 and 5-46). We find generally consistent results, with all but two of the 16 deformation model slip rates (slip rates for the four Primary faults based on the four deformation models) falling within the 90% confidence range of the DCP SSC model slip rates.

### **6.2.2. Off-Fault Deformation**

Dr. Bird argues that the 2015 SSC model does not adequately capture the potential for seismicity that occurs between mapped faults, or on unknown faults beneath the Irish Hills. He advocates for the use of geodesy-based deformation models, such as NeoKinema, to provide quantitative estimates for the rates of this “off-fault” deformation.

We do not consider the off-fault deformation component of these geodesy-based deformation models to be sufficiently reliable for inclusion in the SSC model for DCP. In addition to the concerns stated above regarding the ability of these models to reliably capture on-fault deformation rates, it is unclear whether the calculated off-fault deformation can be entirely attributed to elastic strain accumulation on unknown faults (which is the desired result), or if a significant portion of the calculated off-fault deformation is related to other processes such as rigid-body rotations, anelastic deformation, or local complexities along simplified fault zones. It is also unclear whether the calculated off-fault deformation in these models is consistent with the local tectonic environment. Given these uncertainties, the USGS did not include the geodesy-based off-fault component of deformation models in either UCERF3 (Field et al., 2014), or in the more recent WUS ERF-2023 (Field et al., 2023). A subject matter expert review of the deformation models being considered for the WUS ERF-2023 and 2023 update to the NSHM recommended against the use of the off-fault component of the deformation models because the methodology was considered not yet mature (Johnson et al., 2024). Understanding and validating off-fault deformation from geodetic models is a long-term research goal for the seismic hazard community but is not a reliable source of data for use in a site-specific seismic hazard analysis.

The 2015 DCP SSC model accounted for off-fault seismicity using industry standard-of-practice methods that calculate seismicity rate for unknown faults, or for faults that are not sufficiently active to be fault sources, from the statistical evaluation of earthquake catalogs (Section 5.1.1.3). Seismicity is characterized using areal source zones representing volumes of crust that contain faults where the general parameters (geometry, sense of slip) are known but the rate of activity, and exact extent are unknown. This approach is standard practice to capture off-fault deformation in seismic hazard assessments (e.g., EPRI/DOE/NRC, 2012), including in assessments for SSHAC projects (e.g., Lawrence et al., 2014; PG&E, 2015a) and inversions used in UCERF3 and the WUS ERF-2023 (Field et al., 2014; Field et al., 2023).

### **6.2.3. Alternative Seismicity Model**

Dr. Bird advocates for use of a model called “Seismic Hazard Inferred from Tectonics” (SHIFT) for hazard assessment of DCP. First, we note that this is not a *seismic hazard* methodology for the calculation of ground motions, but rather an alternative methodology for calculating seismicity rates in an area or region. The model calculates the rate of long-term seismicity across a map area using rates of permanent strain from geodesy and fault slip rates (if and where available) and a calibration of global shallow seismicity categorized by plate-tectonic setting to develop a regional magnitude-frequency distribution (Bird and Kagan, 2004; Bird and Liu, 2007; Bird et al., 2010; Bird et al., 2015). The method was not included in the 2015 SSC model and is not incorporated in the SSC model update for the following reasons:

- The SHIFT model relies on the ergodic assumption to a very high degree, and assigns global-average values for maximum magnitude and Gutenberg-Richter *b*-value based on plate-tectonic setting. This approach may be valuable for areas or regions where there is limited information on the local faulting and seismicity. This is not the case for the DCP vicinity, where the *b*-value may be measured based on nearby catalog data and where fault sources that may host the largest earthquakes are relatively well-resolved and can be modeled directly. For modeling the rates and magnitudes of the largest earthquakes in the DCP vicinity, forward modeling of earthquakes on fault sources of the Hosgri-San Gregorio fault system is a much more reliable approach compared to the SHIFT approach, where the maximum magnitude is set based on plate-tectonic setting and modeled to occur anywhere within the study area.
- The SHIFT model has not been implemented in recent updates to regional seismic hazard models that use the latest accepted techniques to characterize seismicity rates, such as the WUS ERF-2023 (Field et al., 2023) and the seismicity rate model for the 2022 New Zealand National Seismic Hazard Model (Gerstenberger et al., 2024).
- To our knowledge, the SHIFT model has not been considered applicable for use in recent SSHAC studies, nor has it been used in site-specific seismic hazard assessments for critical facilities since it was developed in 2004 (PNNL, 2014; INL, 2022). As such, we consider the method to be of academic interest, but not sufficiently evaluated or tested to be reliable for use for site-specific seismic hazard assessments, such as for DCP.

## **6.3. PROPOSED ALTERNATIVES TO FAULT GEOMETRY, GEOLOGIC SLIP RATES, AND UPLIFT RATES**

The June 2023 testimony by Dr. Bird speculates about alternative fault geometries, very-long-term geologic slip rates, and uplift rates. These ideas appear to be based on inferences about the geometry of faulting beneath the Irish Hills, a review of a regional geologic map, and assumptions about the flexural rigidity of the crust beneath the Irish Hills.

### **6.3.1. Fault Geometry**

Dr. Bird (2023b) argues that dips of active faults beneath the Irish Hills, including the Los Osos and San Luis Bay faults, should be less than 30 degrees based on geologic structure and the orientation of the regional stress field. The proposed model is similar to the Inferred Offshore Fault (IOF) model proposed by Nitchman (1988) and the IOF/San Luis Range Thrust model proposed by Hamilton (2012a, 2012b) for uplift of the Irish Hills. Both of these models were

evaluated in detail in PG&E (2014a, Chapter 12), and this evaluation was considered in the 2015 SSC SSHAC process. The evaluation concluded that the IOF/San Luis Range Fault model did not provide a unique solution to the pattern of coastal uplift or seismicity and was inconsistent with onshore and offshore seismic reflection data and bathymetric data (PG&E, 2014a, Chapter 12).

While the 2015 SSC model does not consider the exact parameters of the IOF/San Luis Range Fault model, the Southwest- and Northeast-Vergent fault geometry models and the Local source zone (background) model allow for the general style of deformation proposed in the model. The Southwest-Vergent model includes pure dip-slip reverse motion on the San Luis Bay fault beneath the DCPD with a dip as low as 45 degrees, and the virtual faults used in the Local source zone have dips as low as 35 degrees with pure reverse motion. The 2015 SSC model does not consider a lower fault dip on range-bounding faults, as proposed by Dr. Bird, to be technically defensible because it is inconsistent with the following:

- Seismic reflection data indicate a dip range of 55-80 degrees for the Los Osos fault and 65-85 degrees for the San Luis Bay fault (PG&E, 2014a, Chapters 7 and 9).
- Interpretations of bedrock structure beneath the Irish Hills that consider stratigraphic and structural relations from geologic mapping, well data, aeromagnetic data and gravity data, support moderate to high angle faulting (Graymer, 2012).
- Relocated seismicity beneath the Irish Hills is generally consistent with moderate to high fault dips (Hardebeck, 2014b).
- The width of the Irish Hills uplift relative to the depth of the base of the seismogenic zone requires fault dips >45 degrees on seismogenic faults to be consistent with patterns of rock uplift.

Although we consider the Southwest- and Northeast-Vergent fault geometry models to have similar kinematic interpretations of deformation across the Irish Hills to those advocated by Dr. Bird, the 2015 SSC SSHAC recognized that other fault geometry and kinematic interpretations are consistent with constraints on the deformation pattern of the Irish Hills. To capture the range of technically defensible uplift rate models for the Irish Hills, the 2015 SSC model also includes the Outward-Vergent fault geometry model, which is consistent with:

- Analyses of stress and strain in the Irish Hills based on inversions of seismicity and analysis of moment tensor (Lewandowski, 2014).
- Sand box models of inverted basins that show reactivation of basin-bounding normal faults as reverse faults and breakout reverse faults.
- Tectonic analogues, such as the Gurvan Bogd Range in Mongolia, which has been uplifted by reverse faults along a strike-slip fault system.

Given that no new data were provided by Dr. Bird to support the existence of significant seismogenic faults with dips of less than 30 degrees beneath the Irish Hills, we consider the 2015 SSC model to have adequately captured the uncertainties in fault geometry and kinematics beneath the Irish Hills.

### **6.3.2. Geologic Slip Rate**

Dr. Bird (2023b) estimates vertical throw of the Pliocene Obispo Formation (referred to as unit Tmo) across the Shoreline fault over the last ~5 Ma to calculate a long-term slip rate for the

Shoreline fault or a low-angle equivalent adjacent to the Shoreline fault. We do not consider this rate to be technically defensible for seismic hazard assessment for the following reasons:

- The Pismo Basin, Santa Maria Basin and smaller subbasins formed over a long period of Miocene-Pliocene transtension. It is unclear whether onshore and offshore stratigraphic sections assigned to unit Tmo are correlative, as they may have formed in adjacent basins.
- Given the complicated, multi-stage structural evolution of the central coast of California over the last 5 Ma, a slip rate over this time frame may not be applicable to the current tectonic framework. The relevant time frame of interest for site-specific seismic studies is the Late Quaternary. Slip rates over this time frame have been developed for the Primary hazard-significant faults around DCP, including the strike-slip Shoreline fault.
- The western uplift rate boundary in the area around DCP is the Hosgri fault (Figures 5-23 and 5-24). There is no evidence for significant Late Quaternary uplift across the Shoreline fault, which exhibits only Quaternary strike-slip displacement. A detailed discussion of studies to evaluate the potential for vertical deformation across the Shoreline fault is provided in the Shoreline fault report (PG&E, 2011).

### **6.3.3. Uplift Rate**

To model deformation and develop slip rate estimates for hypothetical thrust faults beneath the Irish Hills, Dr. Bird explicitly assumes an Airy isostatic compensation mechanism for the topography of the hills. In this model, the observed Quaternary surface uplift of the Irish Hills primarily reflects vertical crustal thickening rather than horizontal crustal shortening, and it is accommodated by downward growth of a relatively low-density crustal root beneath the hills. This is analogous to assuming that the Irish Hills is like an iceberg, and that for every one meter of observed uplift of the surface of the hills (the top of the iceberg above the waterline), an assumed low-density crustal root beneath the hills (the part of the iceberg below the waterline) incrementally grows downward by approximately 5 meters.

This model is assessed to be not technically viable because it is inconsistent with the most current gravity data and geophysical modeling in this region, and because it predicts neotectonic effects in and around the Irish Hills that are not observed, as discussed further below:

1. The key data cited by Dr. Bird in support of an Airy model is an isostatic residual gravity anomaly map of the conterminous United States published by Simpson et al. (1986). Dr. Bird states that the absence of a “large” isostatic gravity anomaly over the Irish Hills on this map indicates complete Airy compensation of the topography (i.e., that all observed tectonic surface uplift reflects vertical crustal thickening and progressive growth of a relatively low-density crustal root). The Simpson et al. (1986) map was published as a page-sized document at a scale of approximately 1:23,000,000. At this very small scale, it is not possible to confidently determine the presence or absence of an isostatic residual gravity anomaly over an area the size of the Irish Hills (Figure 6-1).

The Simpson et al. (1986) isostatic residual gravity map for the U.S. was updated by the USGS in 1999 (Kucks, 1999). Although the resolution of the newer map is coarse, it depicts a negative isostatic residual gravity anomaly over the Irish Hills. More recently, the USGS compiled, edited, and reprocessed approximately 30,000 gravity measurements to develop a high-resolution gravity map of the Irish Hills and surrounding regions as part

of the PG&E Shoreline fault investigations (Langenheim et al., 2008). For this study, the USGS calculated an isostatic residual gravity anomaly map by subtracting a theoretical gravity field generated by an idealized Airy root (i.e., the compensation mechanism assumed by Dr. Bird for his model) from the observed Bouguer anomaly. The Langenheim et al. (2008) map shows a well-defined negative residual isostatic anomaly of about 15 to 20 mgal over the Irish Hills, and specifically over the Neogene Pismo basin in the core of the hills, indicating that Dr. Bird's assumption of full Airy compensation for the topography is not consistent with the currently available gravity data and modeling (Figure 6-2).

2. Simpson et al. (1986) acknowledge that the physical assumptions they made to develop the small-scale isostatic residual gravity map cited by Dr. Bird may not be satisfied everywhere. Specifically, they state the following: "One weakness to our approach in this report is that we have ignored crustal and lithospheric strength: the possibility of distributing compensation and of supporting loads regionally by elastic flexure of the lithosphere." In other words, the crust and lithosphere beneath and surrounding the Irish Hills could have elastic strength to bend up or down and mediate the tectonically elevated topography, violating Dr. Bird's assumption that all support is provided by a continuously downward-growing, low-density crustal root.

Recent geophysical studies of crustal strength and rheology in the western United States by Dr. Anthony Lowry and colleagues at Utah State University document that the crust and lithosphere along the central California coast have non-zero elastic strength, which is consistent with the observation (and consensus opinion of the technical community) that elastic strain is broadly stored in the crust and released in moderate to large earthquakes in this region. Specifically, Lowry and Pérez-Gussinyé (2011) find that the effective elastic thickness of the lithosphere along the central California coast, including the Irish Hills and environs, is about 10-15 km, which is comparable to the thickness of the seismogenic crust in this region. The work of Lowry and Pérez-Gussinyé (2011), as well as the occurrence of earthquakes like the 2003 San Simeon earthquake and the presence of a negative isostatic residual gravity anomaly as determined by Langenheim et al. (2008), all indicate that elastic strength and flexural support of topography cannot be assumed to be zero in the Irish Hills, as required for the Airy isostatic compensation model invoked by Dr. Bird.

## **6.4. CONCLUSIONS**

A review of information in the declaration and testimony by Dr. Peter Bird on behalf of SLOMFP for the SB-846 seismic hazard assessment reached the following conclusions:

- On-fault deformation rates from geodesy- and kinematic-based numerical models are useful for comparison to the geologic slip rates calculated for the Primary fault sources near the DCP, but are not appropriate for direct input into the site-specific seismic hazard assessment for DCP due to model uncertainties related to closely spaced faults in the vicinity of the Irish Hills, a lack of offshore geodetic data, and poor characterization of model uncertainties.

- Off-fault deformation rates from geodetic and kinematic deformation models are poorly understood and not yet mature enough for use in regional and site-specific or regional seismic hazard models.
- Seismicity rates developed using the Seismic Hazard Inferred from Tectonics (SHIFT) model are not yet accepted or used broadly by the seismic hazard community and are currently not considered appropriate substitutes for site-specific seismic hazard assessments where fault slip rates and seismicity are well characterized.
- Alternative models for fault geometries were reviewed through the SSHAC process for the 2015 SSC model and were incorporated into six internally consistent fault geometry models (three for the Hosgri fault source and three for the Primary fault sources within the San Luis–Pismo structural block) that are consistent with available data. No new information has been presented to warrant an update to the fault geometry models.
- The proposed estimate of long-term geologic rate of throw for the Shoreline fault exceeds the time frame relevant to seismic hazard assessment and is inconsistent with the Late Quaternary style of deformation on the Shoreline fault.
- Proposed uplift mechanisms for the Irish Hills that invoke Airy isostasy are not consistent with site-specific gravity data.



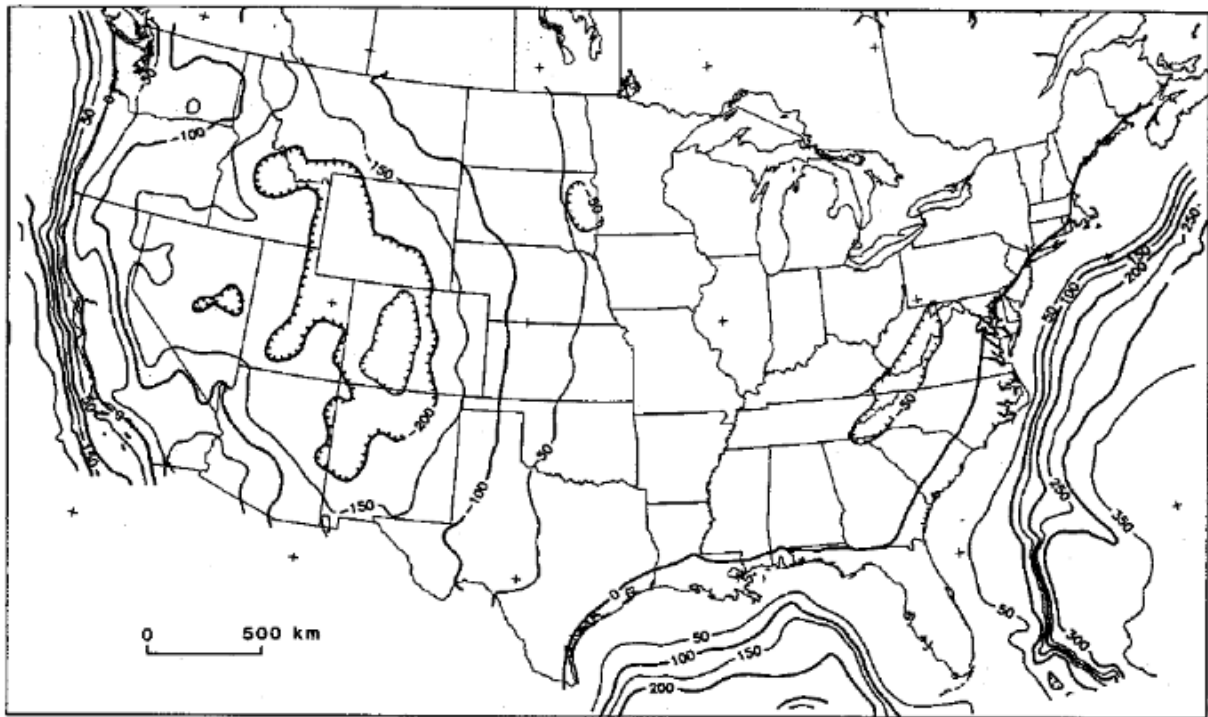


**Figure 6-1. Small-Scale Map Showing General Residual Gravity Anomaly Patterns in the United States (from Simpson et al., 1986)**

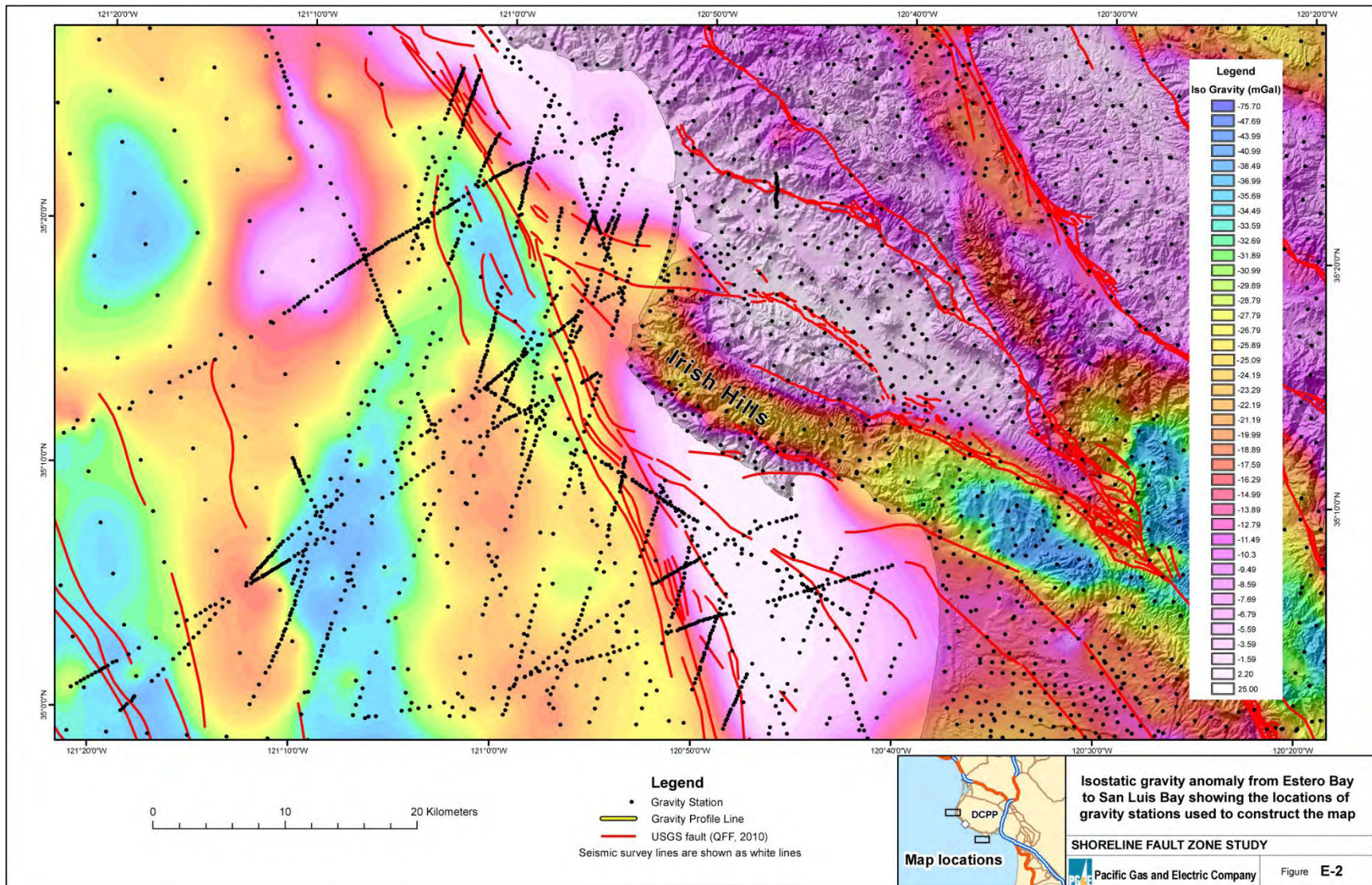


**Figure 6-2. Large-Scale Residual Isostatic Gravity Anomaly Map Showing a Negative Gravity Anomaly Coincident with the Irish Hills (modified from Langenheim et al., 2008 and PG&E, 2011, Figure E-2)**

## 7. EVALUATION OF GROUND MOTION CHARACTERIZATION

The ground-motion characterization for the 2015 SSHAC Level 3 study for DCPD followed a partially non-ergodic approach (Al Atik et al., 2010) in which the site-to-site variability is removed from the within-event standard deviation. The hazard analysis was conducted for a reference rock site condition with  $V_{S30}$  of 760 m/sec. Site-specific adjustments were developed to capture the site response and its uncertainty at DCPD. These site adjustments were convolved with the reference rock hazard to develop a site-specific hazard for DCPD.

The reference rock ground-motion model (GMM) developed as part of the 2015 SSHAC Level 3 study (GeoPentech, 2015) is discussed in this chapter and evaluated relative to new ground-motion data and models that became available since the conclusion of the 2015 study. An overview of the reference rock GMM developed for a reference  $V_{S30}$  of 760 m/sec is first provided describing the median and the aleatory variability components of the model. Next, the evaluation of different components of the median GMM is presented, followed by the evaluation of the components of the aleatory variability model. The development and evaluation of site-specific adjustments are presented in Chapter 9.

### 7.1. OVERVIEW OF 2015 MODEL

As part of the 2015 SSHAC Level 3 seismic hazard study (Budnitz et al., 1997) conducted for DCPD, a collaborative ground-motion study was performed for three nuclear power plant locations in the western United States. These three plants were: (1) DCPD along the central coast of California, (2) San Onofre (SONGS) along the southern coast of California, and (3) Palo Verde in Arizona, west of Phoenix. Although these three site locations would be expected to have different controlling seismic events associated with their individual PSHA results, ground-motion studies indicated that several features of ground-motion models may be common across all three sites. In addition, the general methodology followed by the SSHAC Level 3 study to assess the center, body, and range (CBR) of the technically defensible interpretations (TDI) would be consistent across these three sites. For these reasons, a common SSHAC Level 3 study was conducted for all three sites in developing the necessary ground-motion characterization (GMC) model for each individual PSHA study. That study (GeoPentech, 2015), which developed ground motions for the Southwestern United States (SWUS), formed the basis for the GMC used in the previous (2015) DCPD PSHA study. Note that during the SWUS study, the San Onofre project was dropped, and as a result, GMC models were only developed for the DCPD and Palo Verde site locations.

The DCPD site is located along the central coast of California, a transpressional zone bounded by the San Andreas fault to the east and the Hosgri fault system to the west. Earthquakes in this region are typically defined as either strike-slip or reverse in mechanism. Based on previous PSHA studies (PG&E, 2011), the controlling seismic sources for the hazard levels of interest at DCPD are the Hosgri, Shoreline, Los Osos, and San Luis Bay faults, all of which are located in the immediate vicinity of the site (i.e., distance less than 10 km). Regarding the reverse faults in the area, the DCPD is located on the hanging wall (HW) side of these faults. For completeness, the SWUS GMC study also contained applicable ground-motion models for other more distant seismic sources that contribute less to the total hazard at DCPD.

The GMC model developed as part of the SWUS study characterized both a median ground-motion model and an aleatory variability model. These two models together were adopted and used in the GMC for the DCPD PSHA study (PG&E, 2015a). Given that the DCPD is the focus of both the 2015 and this current study, the aspects of the SWUS model developed for the Palo Verde site are not discussed here.

### 7.1.1. Median Model

The median ground-motion model developed for DCPD as part of the SWUS study (GeoPentech, 2015) was defined for a reference horizon with a  $V_{S30}$  value (travel-time-average shear velocity in the top 30 m) of 760 m/sec and a kappa value of 0.041 sec. Additional adjustments to account for site-specific conditions were based on modifications to the PSHA results from this reference horizon site condition to the site-specific conditions at DCPD. The selection of this reference horizon condition was based on the upper range in site conditions, which were well constrained by the available empirical ground-motion data.

During the evaluation and development of the DCPD GMC, both empirical- and simulation-based ground-motion databases were compiled and examined. For the empirical data, the primary database reviewed was the NGA-West2 database for active tectonic regions (Ancheta et al., 2014). This database was used in the evaluation of the median and aleatory sigma models. For the median model development, the NGA-West2 database was restricted to strike-slip and reverse earthquakes at short distances, which are the events that control the hazard at DCPD. A simulation database was also developed and used in the evaluation of splay and complex ruptures and HW effects; this effort supplemented the empirical database which was limited and/or missing for these types of ground motions. Finally, an additional empirical database (Lin et al. 2011) was retrieved and used in the development of the aleatory model.

The first step in the SWUS model development was to select candidate ground-motion prediction equations (GMPEs) based on their applicability to the seismic hazard sources at DCPD. A set of eight GMPEs were selected; these are listed in Table 7-1. These models, which were the current state-of-practice GMPEs at the time, were classified based on their applicability to either the local, controlling seismic sources, or the less-significant and more-distant seismic sources.

**Table 7-1. Selected Candidate GMPEs for the Median Ground-Motion Model for DCPD (from GeoPentech, 2015)**

GMPE	DCPD	DCPD Distance Sources
Abrahamson et al. (2014), ASK14	X	X
Boore et al. (2014), BSSA14	X	X
Campbell and Bozorgnia (2014), CB14	X	X
Chiou and Youngs (2014), CY14	X	X
Idriss (2014)	X	X
Zhao et al. (2006)	X	
Zhao and Lu (2011) adjustment to magnitude scaling	X	
Akkar et al. (2014a, 2014b)	X	

Given the selected candidate GMPEs, the development of the median ground-motion model was based on the Sammon's (1969) mapping approach. Accordingly, the selected GMPEs were expanded to provide a continuous distribution in model space. To assist in the facilitation of this approach, visualization techniques (Scherbaum et al., 2010) were utilized. Based on this 2-D mapping, a suite of sampled and weighted ground-motion models that represent the center, body, and range (CBR) of the median ground-motion predictions was developed. This new methodology, which was first implemented for SSHAC Level 3 for DCP, provided a more systematic approach for capturing the CBR of the median ground motions by discretizing the space covered by the Sammon's map. Additional checks were performed in hazard space to confirm that this new approach captured the range in hazard expected following the previous standard approach of using the original candidate GMPEs with their epistemic uncertainty. These checks confirmed that the hazard results were consistent between the two approaches.

Following the Sammon's mapping approach, a common functional form based on the  $R_{RUP}$  distance metric was selected for the DCP local sources. This model was defined for the noted reference horizon conditions and for a footwall (FW) site location. It was considered applicable for magnitudes in the range of 5 – 8 and FW  $R_x$  distances of –2 to –200 km. Coefficients were developed for a total of 21 spectral periods spanning the range of  $T=0.01$  sec (PGA) to  $T=10.0$  sec. For each spectral period, a suite of models was sampled to capture the CBR of the median ground motions. This process, and the associated weights, led to approximately 30 ground-motion models for each spectral period. The central model, which has the highest weight, represents the central estimate of the median ground motions for each spectral period. The common form median model was applied to the following seismic sources: Hosgri, Shoreline, San Luis Bay, Oceano, Wilmar, Los Osos, and SWBZ faults, and the Irish Hills background zone.

For the numerous more-distant seismic sources, the use of the common form model was not recommended, as it was not constrained for the more-distant ground motions. For these seismic sources, which contribute significantly less to the total seismic hazard at DCP, the five NGA-West2 GMPEs were applied with equal weights. In addition, the recommended epistemic model of Al Atik and Youngs (2014) was applied to these more-distant seismic sources in modeling the median ground motions.

Given the importance of HW effects in ground-motion estimation, five separate HW models were developed; these were based on limited empirical and simulation data (e.g., Donahue and Abrahamson, 2014). Three of the NGA-West2 GMMs contain a HW model, and these were evaluated along with the ground-motion results from the simulations. The final HW model was based on a functional fit, consistent with the limited empirical and simulation data. This model is a function of magnitude, dip, width, depth to top of rupture, and the distance metrics  $R_x$ ,  $R_{JB}$  and  $R_{RUP}$ . For each common form model, one of these five equally weighted HW models were randomly selected and applied for the PSHA calculations. For the more-distant seismic sources, adjustments for HW sites were deemed not necessary, and as a result, the NGA-West2 models were applied without the application of any HW model.

For longer spectral periods (e.g., greater than 1.0 sec), ground-motion adjustments for near-field rupture directivity effects are typically evaluated in hazard studies. For the DCP site, the long-period hazard is controlled by the Hosgri fault generating strike-slip earthquakes at distances of less than 10 km from the DCP. Given this close proximity to the Hosgri fault, an evaluation of



directivity models was performed as part of the SWUS study. Similar to the HW data, available near-fault rupture directivity data were also limited. The implementation of directivity models in hazard studies requires the randomization of the hypocenter location, a process that adds significant run time. Watson-Lamprey (2015, 2018) developed a simplified implementation of the directivity scaling in CY14 that is based on the Chiou and Spudich (2013) direct point parameter (DPP) model. An evaluation of this simplified model was performed and compared to other existing directivity models for specific scenarios, as well as for the probabilistic hazard at DCPD from the Hosgri fault source.

The SWUS TI team concluded that the effects of rupture directivity would not be included in the GMC model. The justification for this decision was four-fold: (1) directivity has a small impact (i.e., less than 5%) on the long-period hazard at DCPD, (2) there are questions regarding the applicability of the CY14 directivity implementation to other GMPEs, (3) the PPRP expressed concerns about the Watson-Lamprey (2015) model that was unpublished at the time of the study, and (4) the large increase in computation time associated with the use of other directivity models that require hypocenter randomization. The small effect from directivity was thus assumed to be captured by the aleatory variability of the ground-motion models.

The last aspect of the GMC model for DCPD was the estimation of ground motions from splay and complex ruptures defined in the seismic source characterization (SSC) model. These earthquakes as defined in the SSC model have relatively low rates of occurrence, and thus are not significant contributors to the total hazard at DCPD despite their close distances to the site. As part of the evaluation performed during the SWUS study, simulated ground motions based on splay and complex ruptures were analyzed. This led to the recommendation that ground motions from the two separate seismic sources that make up the splay and complex ruptures were to be estimated separately, and the final ground motions would be a combination of the ground motions from each source using the square-root-of-the-sum-of-the-squares (SRSS) approach.

The final DCPD GMC logic tree for the local seismic sources is shown on Figure 7-1. The first level is for all local seismic sources. The second level is for the distance metric, which for DCPD is  $R_{RUP}$ . The third level is for the suite of sampled common-form models, along with the randomly assigned HW model. The final level is for directivity adjustments; as discussed above, these were not applied in the final GMC model.

The DCPD GMC logic tree for the distant seismic sources is shown on Figure 7-2. The first level indicates the five equally weighted NGA-West2 GMPEs. The second level is for the additional epistemic uncertainty model from Al Atik and Youngs (2014). Both the HW and directivity branches shown for the local seismic sources (Figure 7-1) do not apply for the more distant seismic sources.

### **7.1.2. Aleatory Variability Model**

The development of the SWUS aleatory variability model for application at DCPD follows the partially non-ergodic sigma approach (Anderson and Brune, 1999). Specifically, single-station sigma models, which quantify and remove the site-to-site variability from the ergodic ground-motion variability, were developed. The use of single-station sigma requires: (1) adjustment of the median ground motion to site-specific conditions, (2) quantification of the epistemic uncertainty in the site adjustment, and (3) quantification of the epistemic uncertainty in single-



station sigma. These requirements for single-station sigma were satisfied as part of the SWUS study and the subsequent site response analysis that was conducted for the DCPD site.

The SWUS DCPD single-station sigma model was built from individual models for the between-event variability and the single-station within-event variability components that were then combined into single-station sigma. An overview of the different elements of the SWUS DCPD single-station sigma model is provided in this section. We use the notation of Al Atik et al. (2010) to describe the components of ground-motion residuals and variability.

#### 7.1.2.1. SWUS Single-Station Within-Event Standard Deviation

The logic tree for the SWUS DCPD single-station within-event standard deviation ( $\phi_{SS}$ ) is shown on Figure 7-3. The levels in this logic tree represent elements of the model where epistemic uncertainty is characterized. Two datasets of single-station within-event residuals with  $M \geq 5.0$  and distance  $< 50$  km were used to develop the  $\phi_{SS}$  models. The global dataset consists of residuals from the four NGA West2 GMPEs (ASK14, BSS14, CB14, and CY14) supplemented with Taiwanese data from Lin et al. (2011), whereas the California dataset consists of the California subset of the global dataset. Given that the California dataset is more applicable to DCPD (same region), the California dataset was given a higher weight of [0.67].

Data trends derived from the global dataset do not support a magnitude dependence for  $\phi_{SS}$ . Therefore, a homoscedastic  $\phi_{SS}$  model was used with the global dataset. For the California dataset, two magnitude-dependent  $\phi_{SS}$  models were fit to the data. These models differ in their magnitude breakpoint ( $M$  5.5 versus 7.0), and were given equal weights. The epistemic uncertainty in  $\phi_{SS}$  was evaluated based on the station-to-station variability in  $\phi_{SS,S}$ , which represents the differences in  $\phi_{SS}$  at the different stations in the database. A bias-corrected coefficient of variation of  $\phi_{SS,S}$  of 0.12 was used to compute the low (5<sup>th</sup> percentile) and high (95<sup>th</sup> percentile) branches of  $\phi_{SS}$ .

The next level of the  $\phi_{SS}$  logic tree shown on Figure 7-3 involves the directivity adjustment. Based on the directivity discussion presented in Section 7.1, no directivity adjustment was applied to the ground-motion aleatory variability. Finally, the distribution of the ground-motion residuals was evaluated as part of the SWUS study. This evaluation indicated that the traditional lognormal distribution does not capture well the tails of the residuals. A mixture model of two equally weighted lognormal distributions with standard deviations of 0.8 and 1.2  $\phi_{SS}$  were used to adequately fit the heavy tailed distribution of the single-station within-event residuals. The SWUS study assigned weights of [0.8] and [0.2] to the mixture and the lognormal distributions, respectively. These weights reflect favoring of the mixture model because it is supported by statistical evidence. The lognormal distribution was retained with a lower weight of [0.2] because it was still the most widely used model in practice.

#### 7.1.2.2. SWUS Between-Event Standard Deviation

The logic tree for the SWUS DCPD between-event standard deviation ( $\tau$ ) is shown on Figure 7-4. The SWUS  $\tau$  model is based on the published NGA-West2 GMPEs  $\tau$  models (ASK14, BSSA14, CB14, and CY14) and the Zhao et al. (2006)  $\tau$  model. While the four NGA-West2  $\tau$  models are magnitude-dependent, the Zhao et al. (2006)  $\tau$  model is magnitude-independent. The magnitude-dependence of  $\tau$  is a well-established feature based on the analysis of ground-motion datasets

that cover a wide range of magnitudes. The magnitude-independent Zhao et al. (2006)  $\tau$  model was included in the SWUS  $\tau$  model because it is largely based on recordings with  $M > 5$  and therefore considered applicable to the magnitude range of interest at DCP.

The DCP  $\tau$  model was constructed based on the average of the five  $\tau$  models considered. The resulting model is both magnitude-dependent, with a breakpoint at  $M 7.0$ , and period-independent. The observed peak in  $\tau$  around the frequency of 10 Hz was not included in the SWUS  $\tau$  model since this peak was attributed to differences in average site effects (i.e.,  $\kappa$ ) that do not belong in  $\tau$  and are addressed as part of the site response analysis.

The uncertainty in  $\tau^2$  consisted of between-model and within-model components. The within-model component is based on the CY14 regression analysis and represents the statistical uncertainty in  $\tau^2$  given the data. The between-model component is based on the standard deviation of  $\tau^2$  from the five considered models. The total standard deviation of  $\tau^2$  was used to construct the lower (5<sup>th</sup> percentile) and upper (95<sup>th</sup> percentile) branches in the  $\tau$  logic tree.

### 7.1.2.3. SWUS Single-Station Sigma Model

The logic tree for the SWUS DCP single-station standard deviation ( $\sigma_{SS}$ ) is shown on Figure 7-5. The  $\phi_{SS}$  and  $\tau$  models discussed in the subsections above were combined into  $\sigma_{SS}$  models that were then simplified into a single magnitude-dependent model with three branches to capture the uncertainty in  $\sigma_{SS}$ . The SWUS study evaluated the effects of the spatial correlation of the ground-motion residuals on the resulting components of the aleatory variability. This evaluation indicated an overall increase in  $\sigma_{SS}$  of about 4% when accounting for the spatial correlation of ground-motion residuals. This small increase in  $\sigma_{SS}$  was accommodated by modifying the weights of the epistemic uncertainty branches from [0.6], [0.2], and [0.2] on the central, low, and high branches, respectively, to [0.55], [0.15], and [0.3]. These modified weights result in an increase of 3-4% in the mean  $\sigma_{SS}$ , with a minor impact on the epistemic uncertainty in  $\sigma_{SS}$ .

## 7.2. EVALUATION OF MEDIAN GROUND MOTION MODEL

To evaluate the SWUS median GMM, we first compiled and reviewed available applicable data and published studies with an emphasis on the aspects of the SWUS GMM that are important for the seismic hazard at DCP (i.e., crustal faults with distances less than about 10 km). The secondary and less-significant contribution from the splay and complex ruptures, as well as from more distant seismic sources, reduced the need for the evaluation of those aspects of the SWUS GMC model, especially the acquisition of new empirical data. It is expected, however, that more empirical data will be compiled in the future (e.g., NGA-West3 study), which can be used to supplement the evaluation of the SWUS median model presented in this study.

Key aspects and evaluation of the median model are presented in this section and separate subsections, along with recent developments currently used in the practice of ground-motion modeling.

### **7.2.1. Review of Potential New Information**

The SWUS median GMM was developed using the empirical datasets available at the time of the study (e.g., NGA-West2 database), and ground-motion recordings from two post-NGA-West2-database events that were compiled and evaluated as part of the study (GeoPentech, 2015). Given the increase in seismic instrumentation during the past approximately 11 years, since the NGA-West2 database was compiled, numerous strong-motion empirical recordings are now available for several recent earthquakes. These events are being processed and compiled as part of the NGA-West3 database development. A preliminary version of this database for events that would be applicable to the evaluation of the median ground-motion model was accessed and used for this study. In addition, the recent sequence of three large crustal earthquakes in Türkiye has produced a large database of near-fault recordings and these preliminary processed empirical recordings are included in the evaluation of the median ground-motion model. Finally, a local ground-motion database of events within approximately 300 km of the DCPD site location was also compiled, processed and evaluated with the median ground-motion model. A more detailed discussion of the available data used in the evaluation of the median GMM is provided in Chapter 4.

Since the completion of the SWUS study, ground-motion simulations have improved and increased in number. Specifically, the SCEC broadband platform (Maechling et al., 2015) that was used in the original SWUS study for project-specific simulations has continually been updated over the years. As was the case when the SWUS study was conducted, the SCEC broadband platform and associated simulation algorithms are available for the greater community of modelers to perform specific ground-motion simulations. However, since the SWUS project, there have been no additional applicable simulations performed on the SCEC broadband platform that can be used in the evaluation of the median ground-motion model.

A similar simulation platform, CyberShake, also maintained at SCEC, has been developed since the completion of the SWUS study. For these simulations, regional 3-D velocity structures are included, along with the activity rates for the known seismic sources in the region. The goal of the CyberShake platform is to generate simulation-based hazard curves for regions of California based on the frequency of events on the seismic sources and the 3-D modeling of simulation ground motions. Given the number of necessary calculations, these simulations are performed on large mainframe supercomputers. SCEC performed a CyberShake analysis in 2017, after the SWUS study had been completed, for the Central Coast region of California, including the area around DCPD. The seismic source model was based on the UCERF2 (Field et al., 2008) SSC, and the simulation 3-D ground motions were based on a Central California 3-D velocity model with a minimum  $V_{S30}$  value of 900 m/sec. Note that the 3-D velocity structure that has been developed for the region immediately around DCPD has a finer resolution than the regional 3-D velocity structure used in the CyberShake study. Moreover, the results from the CyberShake calculations are for longer spectral periods (i.e., greater than 1 sec) given the limitations of numerical computing. Given the differences in the SSC model used, the lower-resolution 3-D velocity structure, and the spectral period range covered by the CyberShake results, we find that an evaluation of the Central California CyberShake simulations need not be performed. Even with these noted limitations, the ground motions computed from the CyberShake platform could be used to evaluate and inform the potential path effects due to 3-D velocity structure for non-ergodic ground-motion models. Sung et al. (2023) has performed this analysis for Los Angeles

basin in evaluating 3.0 sec ground motions from the CyberShake platform and this same methodology could be applied to the region around DCPD in the future.

### **7.2.2. Sammon's Mapping Methodology**

During the development of the SWUS median ground-motion model, the Sammon's mapping methodology was applied to develop approximately 30 sampled GMMs that provide a continuous distribution of ground motion in terms of the magnitude and distance scaling. Previously, candidate GMMs would have been selected and weighted within a logic tree framework; however, this does not necessarily provide a continuous distribution and would potentially underestimate the CBR of the TDIs. The key input for the Sammon's mapping methodology is the selection of applicable candidate GMMs. A total of eight GMMs were selected for the SWUS study, as follows:

- Abrahamson et al. (2014)
- Akkar, Sandikkaya and Bommer (2014a, 2014b)
- Boore et al. (2014)
- Campbell and Bozorgnia (2014)
- Chiou and Youngs (2014)
- Idriss (2014)
- Zhao et al. (2006)
- Zhao and Lu (2011) as implemented by the TI Team.

These models were considered to be applicable for the controlling seismic sources (i.e., magnitude between 5–8, distances between 0–30 km, periods less than 3.0 sec, strike-slip and reverse faults with sites on the FW location). Limitations for distance less than 3 km and magnitudes greater than 7.5 for both the Idriss (2014) and Akkar, Sandikkaya and Bommer (2014a, 2014b) models were applied based on the behavior of these models. Given these candidate models, a sample space of GMMs was created, and this space was discretized into 30 regions. A representative GMM was selected for each discrete region in the Sammon's map space (Scherbaum et al. 2010).

As part of the evaluation of the Sammon's mapping methodology, a key criterion would be the potential inclusion of more current GMMs. However, since the SWUS model was completed, there have been no new applicable GMMs for active crustal regions that should be considered for this update analysis. Note that a newer crustal model, Zhao et al. (2016) has been developed, but this is primarily based on empirical data from Japan and issues have been reported related to the extrapolation of the magnitude scaling contained in the model. For these reasons, this newer model would not be considered as a selected GMM within the framework of the Sammon's mapping methodology for the SWUS median model for DCPD. Given the above, we conclude that the candidate models used in the 2015 SWUS study represent the range of models that are still currently applicable.

Another technical evaluation question is whether use of the Sammon's mapping methodology is applicable to this study update. The SWUS study was the first SSHAC Level 3 study that implemented the Sammon's mapping methodology. Since its completion, however, several SSHAC Level 3 studies have also used the methodology in various forms. The NGA-East (Goulet et al., 2018) followed the same approach in selecting candidate GMMs and sampling the

magnitude-distance space through the use of a common form model. In a variation of the approach, other SSHAC Level 3 studies (e.g., PNNL, 2014; INL, 2022; Bommer et al., 2015) have used a scaled-backbone approach in place of the common-form model using the Sammon's mapping methodology to confirm that the CBR of the TDI is adequately sampled.

Both applications of the Sammon's mapping methodology assist in the goal of developing a median GMC model that samples the necessary body and range. Following the first use of this approach for the SWUS study, the Sammon's methodology is now standard of practice for high-level (e.g., SSHAC Level 3) studies. As a result, we conclude that the approach used in the development of the median model for the SWUS study is assessed to be current and acceptable.

### **7.2.3. Residual Analyses**

Given the compilation of the new empirical databases, multiple residual analyses are performed to evaluate the median SWUS ground-motion model. Residuals are computed using the central SWUS model, which is the highest weighted model from the suite of approximately 30 weighted models for each given spectral period. This central model is defined for a  $V_{S30}$  value of 760 m/sec for a FW site location. Results are presented for spectral periods of 0.01, 0.1, 0.4, and 1.0 sec.

Two separate mixed-effects residual analyses were performed to evaluate the SWUS DCPD median ground-motion model relative to new empirical ground-motion data. For the first analysis, the combined ground-motion spectral accelerations from the preliminary NGA-West3 and Turkish databases are compiled for magnitudes greater than 5 and distances less than 120 km. Events with less than five recordings are compiled but are not used in the residual calculations given the limited number of recordings for constraining the event term. In addition, station recordings with  $V_{S30}$  greater than 250 m/sec are selected to be consistent with the approach used in the SWUS model development. For empirical recordings with  $V_{S30}$  not equal to 760 m/sec, the  $V_{S30}$  site adjustment based on the Abrahamson et al. (2014) model is applied to the recorded ground motions, again consistent with the approach implemented in the SWUS model development.

The second residual analysis was performed using the DCPD flatfile. This flatfile is not combined with the preliminary NGA-West3 and the Turkish data given the likely overlap of many recordings in the DCPD and the NGA-West3 databases. Given the preliminary nature of the NGA-West3 data used in this analysis, the DCPD flatfile includes recordings not analyzed and included in this early version of the NGA-West3 flatfile. Similar magnitude, distance, and  $V_{S30}$  ranges, minimum number of recordings per earthquake, and  $V_{S30}$  adjustments are used for the DCPD data. The distribution of earthquake epicenters (blue stars) and recording stations (red triangles) for the NGA-West3 data and the DCPD data are plotted on Figure 7-6 and Figure 7-7, respectively. The distribution of recording stations for the Turkish data was presented in Chapter 4, on Figure 4-1.

The magnitude and distance distribution of the empirical data from the Turkish and the NGA-West3 databases used in the regression analysis are plotted in the left side of Figure 7-8. On the right-side plot of Figure 7-8, the magnitude versus depth to top of rupture ( $Z_{tor}$ ) for the earthquakes is presented. The preliminary NGA-West3 and Turkish data in this analysis consist of a total of 1,205 recordings from 16 earthquakes. Figure 7-9 shows the magnitude-distance distribution of the DCPD data used in the mixed-effects regression analysis consisting of a total

of 539 recordings from 7 earthquakes. Note that Ztor values were not available for the DCP flatfile and default values with respect to magnitude were used to estimate the median ground motion for these earthquakes.

For the analysis, residuals are computed based on the following equation:

$$\delta_{es} = \text{Ln}(SA_{obs}) - \text{Ln}(SA_{SWUS}) \quad \text{Equation (7.1)}$$

where  $\delta_{es}$  is the total residual for a given earthquake  $e$  and recording  $s$  in natural log units. The  $SA_{obs}$  is the observed ground-motion value and the  $SA_{SWUS}$  is the median ground motion estimated from the central SWUS model. These residuals are computed for each recording at the four spectral periods that are evaluated. Given the total residuals, a mixed-effect regression is performed to separate the residuals into an average bias (i.e., regression) term  $c$ , event term  $\delta B_e$  with standard deviation  $\tau$ , and within-event residual  $\delta W_{es}$  with standard deviation  $\phi$ .

$$\delta_{es} = c + \delta B_e + \delta W_{es} \quad \text{Equation (7.2)}$$

### 7.2.3.1. Preliminary NGA-West3 and Turkish Dataset

The regression results of the combined NGA-West3 and Turkish data are presented in this section. The average bias for the regression is shown on Figure 7-10 (top panel) for the four spectral periods. Overall, there is a negative average residual between  $-0.2$  to  $-0.6$  indicating an overprediction from the SWUS median ground-motion model relative to the empirical NGA-West3 and Turkish data. Plots of the resulting between-event and within-event standard deviations for the four spectral periods are shown on the bottom panel of Figure 7-10.

The between-event residuals of earthquakes in the Turkish and NGA-West3 datasets are presented on Figure 7-11 as a function of magnitude for the four spectral periods considered. The Turkish data are shown with solid blue symbols. The robust Lowess fit to the residuals is also included in these plots. In general, there is a good distribution of between-event values about the zero line with no strong trends as a function of magnitude. The between-event residuals as a function of Ztor are plotted on Figure 7-12. At the two higher frequency cases (i.e.,  $T=0.01$  and  $0.1$  sec), there is an observed trend with larger Ztor values leading to more negative event terms. This trend is not observed at the two other spectral periods of  $0.4$  and  $1.0$  sec. For those events with Ztor less than  $10$  km, this trend for the two shorter spectral period cases is not observed, with the between-event terms being approximately equally distributed about the zero line.

The within-event residuals as a function of  $R_{RUP}$  distance from the NGA-West3 and Turkish datasets are presented on Figure 7-13 through Figure 7-16 for the four spectral periods considered. Overall, the trends for the combined NGA-West3 and Turkish residuals show a constant positive bias for the sparse data at distances less than about  $10$  km and a positive trend for distances larger than  $40$  km up to the cutoff distance of  $120$  km. The within-event residual plots on Figure 7-13 through Figure 7-16 show a positive average within-event residual at short distances ranging from  $0.25$  to  $0.5$ . Combining the negative constant shown in Figure 7-10 (top panel) with the within-event residuals, the average of these residuals at distances less than  $10$  km ranges between  $-0.1$  and  $0.1$  at periods of  $0.01$  to  $0.4$  sec, and  $0.2$  at a period of  $1$  sec. Given the application of the SWUS median model for the controlling seismic sources with distances less than about  $20$  km, the combined constant and within-event residuals at short distances indicate



no significant underprediction of the new data by the SWUS model. The longer-distance trend is not a significant observation in terms of the evaluation of the SWUS model for DCPD.

The within-event results as a function of  $V_{S30}$  are plotted on Figure 7-17 for the four spectral periods. These results do not show any trends in the residual results between the empirical ground motions adjusted for the reference  $V_{S30}$  value of 760 m/sec and the SWUS median ground-motion model.

In summary, the results of the residual analysis of the preliminary NGA-West3 and Turkish data relative to the SWUS median model presented in this section show an average overprediction of the model compared to the data (negative constant term shown in the top panel of Figure 7-10). The trends in the event-terms versus magnitude and  $Z_{tor}$ , and within-event-residuals versus distance, are generally consistent between the NGA-West3 and the Turkish data. No significant trends are observed in the SWUS model given these new data.

### 7.2.3.2. DCPD Dataset

The regression results of the DCPD database are presented in this section. The average bias for the regression is shown on

Figure 7-18 for the four spectral periods. Overall, there is a negative average residual between  $-0.1$  to  $-0.4$  indicating an overprediction from the SWUS median ground-motion model relative to the empirical data. A plot of the resulting between-event and within-event standard deviations for the four spectral periods is shown in the right-side panel on Figure 7-18.

The between-event residuals of earthquakes in the DCPD dataset are presented on Figure 7-19 as a function of magnitude for the four spectral periods. The robust Lowess fit to the residuals is also included in these plots. In general, there is a good distribution of between-event values about the zero line with no strong trends observed as a function of magnitude.

The within-event results as a function of  $R_{RUP}$  distance for the DCPD dataset are presented on Figure 7-20 for the four spectral periods. Similar to observations for the NGA-West3 database, the results generally show a constant level for distances less than about 20–30 km and a positive trend for larger distances up to the cutoff distance of 120 km. Given the application of the SWUS median model for the controlling seismic sources with distances less than about 20 km, this longer distance trend is not a significant observation in terms of the evaluation of the SWUS model for DCPD. The within-event results as a function of  $V_{S30}$  are plotted on Figure 7-21 for the four spectral periods. These results do not show any trends in the residual results between the empirical ground motions adjusted for the reference  $V_{S30}$  value of 760 m/sec and the SWUS median ground-motion model.

### 7.2.3.3. Total Residuals with $R_{RUP} \leq 15$ km

Next, the total residuals from the NGA-West3, Turkish, and DCPD databases were examined in the distance range  $\leq 15$  km of importance to the hazard at DCPD. This distance restriction reduces the number of available events and recordings. A total of six events have more than two recordings within the 15-km-distance restriction. These events, along with their metadata information, are listed in Table 7-2. For each event, the average residual is computed along with the standard error for the four selected spectral periods. Similar to the previous residual analysis,

the empirical ground motions are corrected for the consistent reference  $V_{S30}$  value of 760 m/sec based on the  $V_{S30}$  site-correction factors from Abrahamson et al. (2014).

**Table 7-2. Events with More than Two Recordings Within 15 km for Residual Analyses**

Event Name	Date	Magnitude	Z <sub>tor</sub> (km)	Mechanism	Number of Recordings $R_{RUP \leq 15km}$
NW of Brea, CA	29 March 2014	5.09	2.87	Reverse/Oblique	31
South Napa, CA	24 Aug. 2014	6.02	5.75	Strike-slip	11
Ridgecrest Sequence	6 July 2019	7.06	0.0	Strike-slip	7
Pazarcik	6 Feb. 2023	7.8	0.0	Strike-slip	30
SE of Ojai	20 Aug. 2023	5.1	4.84	Reverse/Oblique	6
ESE of Alum Rock	25 Oct. 2022	5.1	6.38	Strike-slip	9

The mean residual, and the plus- and minus-one standard error of the results, are plotted on Figure 7-22 for the 31 stations that recorded the (**M** 5.09) earthquake NW of Brea in southern California. The average residuals for this event fall between values of about 0.2–0.5 natural log units indicating a slight underprediction of the observed ground motions by the SWUS model.

The next event is the South Napa earthquake (**M** 6.02) that occurred in northern California. A total of 11 stations are located within 15 km from the fault rupture, and the average residuals are plotted on Figure 7-23 for the four selected spectral periods. On average, these results are approximately distributed about the zero residual line showing a similar or slightly larger range in values as the previous event with about one-third less recordings.

The Ridgecrest sequence in southern California consisted of three crustal earthquakes with magnitudes greater than 5.5 occurring in a span of two days. The largest event (**M** 7.06) occurred on 6 July 2019 and was recorded at seven stations located less than 15 km from the rupture. The average and standard error results from this earthquake are plotted on Figure 7-24. In general, the results show a good consistency between the empirical data and the estimated SWUS median ground-motion values (i.e., residuals distributed about the zero residual line). Even with the relatively small number of recordings, these results do not indicate a trend with rupture distance or an overall average bias for this large-magnitude event.

The largest of the three Türkiye events occurred on 6 February 2023 and had a magnitude 7.8. This event is the largest in the database compiled for the evaluation of the SWUS model, and there are a total of 30 stations within 15 km of the fault rupture. Three stations are assigned distances less than 1 km. Overall, the distribution of the residuals is similar across the four spectral periods, with an average value of approximately zero, as shown on Figure 7-25. This indicates that for this large-magnitude crustal strike-slip event, the SWUS model is consistently estimating ground motions that agree well with the empirical recordings.

The most recent event in the database is the **M** 5.1 earthquake that occurred on 20 August 2023 located SE of Ojai in southern California. Unlike the majority of the events evaluated in this residual database, this event has a reverse/oblique faulting mechanism. The average residual results for this event are plotted on Figure 7-26, which show consistency with the other events, with average values centered about the zero residual line.

The final event evaluated in the residual database is the event ESE of Alum Rock (**M** 5.1) that occurred on 25 October 2022. This strike-slip event has an assigned  $Z_{tor}$  value of 6.38 km based on the empirical relationships from Chiou and Youngs (2014) given the magnitude and mechanism for the event. This estimated  $Z_{tor}$  value is consistent with the depth distribution of seismicity and aftershocks along this section of the Calaveras fault (Hirakawa et al., 2023). No finite fault model is available for this smaller-magnitude event. This central section of the Calaveras fault has historically exhibited widespread aseismic creep and microseismicity (Oppenheimer et al., 1990).

The average and standard error results from this earthquake are plotted on Figure 7-27 indicating large negative residuals for recordings from this event relative to the SWUS model. A recent ground-motion study for this event (Hirakawa et al., 2023) has also computed negative residuals relative to the Boore et al. (2014) ground-motion model based on a larger database of empirical recordings. The authors propose at least two factors from this event that can be the cause of these lower-than-expected (i.e., negative residuals) observations. Firstly, the computed stress drop for the event is about a factor of two lower than for similar-sized events in California (Hirakawa et al., 2023). This reduced stress drop would be expected to result in smaller high-frequency ground motions. Secondly, for the longer period range, Hirakawa et al. (2023) suggest that the effect of rupture directivity, with a southeasterly propagating rupture away from the majority of the recording stations, leads to a lower suite of empirical ground motions. This suggestion regarding rupture directivity and resulting ground motions is supported by the numerical simulations performed by Hirakawa et al. (2023).

Based on the detailed Hirakawa et al. (2023) ground-motion study for the event ESE of Alum Rock, the observed residuals from the SWUS median ground-motion model are consistent in showing larger ground-motion predictions than observed (i.e., negative residuals). Although the residual results show a large overprediction (e.g., negative residuals on the order of  $-1$  to  $-1.5$ ), the observations from this one earthquake would not invalidate the SWUS model and its application to the seismic hazard at DCP.

The summary of the residual analysis from these six events is listed in Table 7-3 for the spectral period of 0.01 sec. The results for the other three spectral periods are provided in Table 7-4 (0.1 sec), Table 7-5 (0.4 sec), and Table 7-6 (1.0 sec). These results are also presented graphically on Figure 7-28 ( $T=0.01$  sec), Figure 7-29 ( $T=0.1$  sec), Figure 7-30 ( $T=0.4$  sec), and Figure 7-31 ( $T=1.0$  sec). In each of these figures, the mean residual and standard errors are shown as a function of magnitude (upper-left plot), rupture distance (upper-right plot), and  $Z_{tor}$  depth (lower-center plot). For the rupture distance plots, the results from each earthquake are graphed at the median distance from the dataset used in the residual analysis.

These plots are consistent with the plots presented for each individual earthquake with the general observation that the residuals are similar for five of the six earthquakes, the outlier being the **M** 5.1 event ESE of Alum Rock. Not including this event, and focusing on the remaining five earthquakes, the results are basically equally distributed about the zero residual line, falling

within values of -0.5 to 0.5. Based on this limited residual analysis of empirical data collected at stations less than 15 km from the rupture, the evaluation of the SWUS median model shows that it is acceptable and consistent with the new empirical data.

**Table 7-3. Summary Results from Residuals Analysis for Events with Stations Less than 15 km for Spectral Period of 0.01 sec**

Event Name	Magnitude	Ztor (km)	Number of Recordings $R_{RUP} \leq 15\text{km}$	Mean Residual	Standard Error
NW of Brea, CA	5.09	2.87	31	0.256	0.090
South Napa, CA	6.02	5.75	11	-0.128	0.155
Ridgecrest Sequence	7.06	0.0	7	-0.047	0.092
Pazarcik	7.8	0.0	30	0.106	0.092
SE of Ojai	5.1	4.84	6	-0.242	0.150
ESE of Alum Rock	5.1	6.38	9	-1.405	0.118

**Table 7-4. Summary Results from Residuals Analysis for Events with Stations Less than 15 km for Spectral Period of 0.1 sec**

Event Name	Magnitude	Ztor (km)	Number of Recordings $R_{RUP} \leq 15\text{km}$	Mean Residual	Standard Error
NW of Brea, CA	5.09	2.87	31	0.350	0.097
South Napa, CA	6.02	5.75	11	-0.272	0.211
Ridgecrest Sequence	7.06	0.0	7	-0.035	0.128
Pazarcik	7.8	0.0	30	-0.009	0.103
SE of Ojai	5.1	4.84	6	0.116	0.173
ESE of Alum Rock	5.1	6.38	9	-1.085	0.167

**Table 7-5. Summary Results from Residuals Analysis for Events with Stations less than 15 km for Spectral Period of 0.4 sec**

Event Name	Magnitude	Ztor (km)	Number of Recordings $R_{RUP} < 15\text{km}$	Mean Residual	Standard Error
NW of Brea, CA	5.09	2.87	31	0.334	0.098
South Napa, CA	6.02	5.75	11	-0.113	0.335
Ridgecrest Sequence	7.06	0.0	7	0.002	0.103
Pazarcik	7.8	0.0	30	-0.096	0.085
SE of Ojai	5.1	4.84	6	-0.158	0.223
ESE of Alum Rock	5.1	6.38	9	-1.363	0.155

**Table 7-6. Summary Results from Residuals Analysis for Events with Stations less than 15 km for Spectral Period of 1.0 sec**

Event Name	Magnitude	Ztor (km)	Number of Recordings $R_{RUP \leq 15km}$	Mean Residual	Standard Error
NW of Brea, CA	5.09	2.87	31	0.496	0.089
South Napa, CA	6.02	5.75	11	-0.162	0.384
Ridgecrest Sequence	7.06	0.0	7	-0.089	0.160
Pazarcik	7.8	0.0	30	-0.046	0.081
SE of Ojai	5.1	4.84	6	0.190	0.265
ESE of Alum Rock	5.1	6.38	9	-0.905	0.115

#### **7.2.4. Hanging Wall Model**

For the SWUS model, the effects from hanging wall locations were modeled using five equally weighted HW models. These models were developed using both simulation data and the empirical HW model contained in the NGA-West2 GMMs. As part of the empirical data evaluation performed for the 2015 SWUS model, the Dawood et al. (2015) dataset was examined for the potential for HW sites and data not contained in the NGA-West2 GMMs. It was concluded, however, that no additional empirical data were available to assist in the development of the HW model from the Dawood et al. (2015) dataset.

Since the completion of the SWUS study (GeoPentech, 2015), no additional recorded empirical data have been observed. Ideally, a well-recorded dipping reverse fault event in the moderate magnitude range (e.g., **M** 6–7) would be beneficial for the evaluation and potential modification or development of a HW model. The occurrence of such an earthquake with well-distributed stations about both the HW and FW sites may happen in the future, which would allow for an evaluation of the current HW models in the SWUS model.

Similarly, additional numerical simulation scenario events could be performed to both evaluate and potentially refine the current HW models. As noted earlier in this report, no additional HW-specific simulations that would assist in this task have been performed since the completion of the SWUS study.

#### **7.2.5. Directivity**

As discussed in Section 7.1.1, the SWUS study evaluated directivity effects at DCPD through the development of a simplified directivity adjustment to the median and the aleatory variability models that removes the need to randomize the hypocenter location in hazard analysis. The SWUS study used what at the time was a draft of the simplified model of Watson-Lamprey (2018 [WL18]), which in turn was based on the Chiou and Spudich (2013 [CS13]) DPP model as implemented in the NGA-West2 GMM of Chiou and Youngs (2014 [CY14]). Figure 7-32 shows the results of a hazard sensitivity analysis of ground motion from the Hosgri fault at DCPD. Specifically, the analysis evaluates the sensitivity of implementing a directivity adjustment to the 3-sec ground motion versus annual hazard using both the CY14 directivity implementation and the simplified WL18 model. This sensitivity analysis conducted as part of the SWUS study

showed that the impact of incorporating directivity effects from these two models on the 3-sec probabilistic ground motion generally results in an increase of 5% or less.

The TI team that conducted the SWUS study decided to not incorporate directivity effects in the hazard analysis at DCPD given the following reasons: (1) directivity effects were shown to have a small impact on the ground motions, as described above and shown on Figure 7-32; (2) the WL18 model was unpublished at the time; (3) the traditional implementation of directivity models was associated with an increase in run times; and (4) there were unresolved questions related to the centering and aleatory variability adjustment of existing directivity models. Excluding the directivity adjustment was also justified with the assumption that the variability of the ground motion due to directivity is captured by the standard deviation model.

In their final letter, the PPRP noted limitations of the directivity evaluation and integration in the SWUS study. These limitations were related to the simplified directivity model being unpublished at the time of the study and the differences observed on Figure 7-32 between this simplified model and the CY14 implementation of directivity at hazard levels below  $10^{-4}$ . As a result, the PPRP found that the zero weighting of the directivity branch of the logic tree to be lacking in sufficient technical justification, given that the key rationale for this weighting is the sensitivity of the hazard to the directivity effect calculated using the Watson-Lamprey (2015) simplified model (GeoPentech, 2015, Appendix B).

As part of this evaluation of directivity effects for DCPD, we review and compare directivity models published since the conclusion of the SWUS study. Issues related to centering of directivity models and treatment of aleatory variability are discussed for these models. Deterministic and probabilistic comparisons from these models are presented for cases relevant to the important hazard sources at DCPD. In terms of new empirical ground-motion data, we note that preliminary analyses of recordings from the **M** 7.8 and **M** 7.5 earthquakes that occurred in Türkiye on 6 February 2023 indicated velocity pulses in recordings at near-field stations that are indicative of directivity effects. These empirical data will be used in future efforts to examine and constrain directivity models.

#### 7.2.5.1. New Directivity Models and Studies

Donahue et al. (2019) evaluated the five directivity models published as part of the NGA-West2 study (Spudich et al., 2013) and found broad consistency in the directivity adjustments to the median ground-motion prediction among the five directivity models for strike-slip scenarios. Directivity models published since the conclusion of the SWUS study include those by Watson-Lamprey (2018), Rowshandel (2018), and Bayless et al. (2020).

The Watson-Lamprey (2018 [WL18]) model is the published version of the simplified model developed and used in the SWUS study. It is based on five simple strike-slip ruptures with **M** 6 to 8 and four simple reverse ruptures with **M** 6 to 7.5. The model captures the average change in the median ground motion over all randomized hypocenter locations, and the change in the aleatory variability that accounts for a reduction in the sigma due to directivity effects in the median and an increase due to hypocenter randomization.

Bayless et al. (2020 [BSS20]) updated the Bayless and Somerville (2013 [BS13]) directivity model to include narrowband characteristics and better accommodate complex and multi-segment ruptures. The BSS20 model generally retains some of the computational simplicity of



the BS13 model and uses both empirical ground-motion data and finite-fault simulations in the model development. Rowshandel (2018) also updated the Rowshandel (2013) directivity model. These updates involve improvements on the narrowband characterization and centering, as well as capturing rupture and slip heterogeneity effects. Finally, Brian Chiou (2020, personal communication) extended the implementation of the Chiou and Spudich (2013 [CS13]) directivity model to ASK14, BSSA14, and CB14. This update, documented in Al Atik et al. (2023), makes the DPP-based directivity implementation GMPE-specific for four NGA-West2 GMPEs (ASK14, BSSA14, CB14, and CY14).

Recently, Al Atik et al. (2023) presented the first comprehensive implementation of near-field rupture directivity effects in a state-wide probabilistic hazard study for California using the UCERF3 seismic source characterization model (Field et al., 2014). Al Atik et al. (2023) evaluated existing directivity models in terms of centering, treatment of aleatory variability, comparisons of median adjustments, and application to complex UCERF3 fault ruptures. The BS13, CS13 with GMPE-specific implementation, and the BSS20 models were selected and weighted for use in the statewide probabilistic study. Probabilistic hazard was performed for 19,316 sites in California based on a grid spacing of 0.05 by 0.05 degrees longitude and latitude. Hypocenter locations were randomized in the hazard analysis, leading to a large computational effort and requiring the analyses to be parallelized and performed on the Amazon Web Services. Hazard results and directivity adjustment factors as a function of return period and spectral period are presented in a companion webtool (Mazzoni et al., 2023), allowing the user to retrieve hazard results for any location in California based on the interpolation of the gridded hazard results.

#### 7.2.5.2. Centering

Centering a directivity model involves predicting an average null change in ground motion over all azimuths at a particular distance from a rupture scenario and for a particular hypocenter location. A directivity model that is not centered could lead to changes in the magnitude-distance scaling of GMPEs. Donahue et al. (2019) discussed directivity model centering in relation to the NGA-West2 directivity models and noted that there are two approaches for centering. Explicit centering involves calculating the average directivity parameter for a “racetrack” of locations around the rupture with the same rupture distance, and removing this average from the value of the directivity parameter at the location of interest. Implicit or empirical centering assumes that a model is centered with respect to the directivity effects implied by that data.

The CS13 and the Rowshandel (2013, 2018) models use explicit centering. While this approach ensures a centered directivity model, it does lead to complexities in the model implementation in hazard analysis due to the need to calculate the average directivity parameter over a racetrack of sites for each rupture and each hypocenter location. WL18 also centered the directivity predictions as part of her model development. In their implementation of the CS13 model, Al Atik et al. (2023) used functional forms to predict the average DPP as a function of distance, hypocenter location, rupture length, and style-of-faulting to simplify the implementation of explicit centering.

Donahue et al. (2019) examined the implicit centering of the NGA-West2 directivity models and concluded that “non-directivity” NGA-West2 GMPEs can be considered to reflect directivity-

neutral conditions by virtue of using, on average, directivity-neutral datasets. Based on this evaluation, the BS13 and BSS20 models can be considered implicitly centered.

Despite these recent studies, debates continue in the scientific community on the issue of centering of directivity models. This is related to the limited empirical dataset of large-magnitude earthquakes at short distances with good azimuthal station coverage for directivity evaluation. Also, models that are implicitly centered by using directivity neutral datasets may not be centered for particular magnitude-distance scenarios. Therefore, further long-term evaluation is needed in relation to implicit centering. For explicit centering, simplifications may be needed to allow for an efficient implementation in hazard analyses without the need to build racetracks around each rupture and hypocenter location, which will significantly increase complexities and affect run time.

#### 7.2.5.3. Treatment of Aleatory Variability

The aleatory variability of ground-motion models is related to simplifications in the modeling of source, path, and site effects. As such, it is generally expected that the adjustment of directivity effects in the median ground-motion prediction be accompanied by a reduction in the aleatory variability of the model. This reduction is expected due to the inclusion of the additional explanatory term modeling directivity effects in the median model. The randomization of the hypocenter location on the rupture surface would lead to an increase in the variability of the ground motion.

While existing directivity models provide an adjustment to the median ground motion, reduction of the aleatory variability of the GMPEs have remained modest to non-existent. This has been generally attributed to the scarcity of data exhibiting directivity effects in the ground-motion datasets as well as the lack of azimuthal variations in the data. The BS13 model noted a minor reduction in the aleatory variability of the residuals as a result of incorporating directivity effects. The aleatory variability of CY14 incorporates a small reduction in sigma as a result of including the CS13 directivity term in their median model. The updated model of BSS20 includes an adjustment to the aleatory variability. Similarly, the Rowshandel (2020, personal communication) model includes a reduction in the aleatory variability. The WL18 model, which does not require an explicit randomization of the hypocenter location over the rupture surface, incorporates the decrease in the aleatory variability of CY14, as well as an increase to account for hypocenter randomization.

Similar to centering, the impact of directivity adjustments on the aleatory variability remains a topic of debate in the scientific community. Resolving this issue requires further long-term studies.

#### 7.2.5.4. Comparisons

Al Atik et al. (2023) performed deterministic and probabilistic comparisons of directivity models that are relevant for this study. Figure 7-33 shows an example of a simple deterministic rupture for a vertical-dip, strike-slip earthquake with magnitude 7.0. Stations are shown at distances of 1, 5, 10, 20 and 50 km from the fault plane and at five specific azimuths: off the end of the fault (Site A), 45 degrees off the end of the fault (Site B), perpendicular to the end of the fault (Site C), perpendicular to  $\frac{3}{4}$  of the fault (Site D), and perpendicular to the middle of the fault (Site E). Figure 7-34 shows the predicted median directivity adjustments as scaling factors to the ground

motion at four locations at a distance of 5 km for the BS13, WL18, BSS20, CS13, and Rowshandel (2018, 2020[BR20]) models. The minimum (dashed lines), maximum (dotted lines) and average directivity adjustment factors (solid lines) are shown on the plots.

The comparisons on Figure 7-34 show a wide variability in the median adjustment from the different models. In general, the average directivity adjustment factors from the CS13, WL18 and BR20 models are the most similar, with the estimated values from the updated BSS20 model typically being higher. The broadband characteristic of the BS13 model is apparent on Figure 7-34, whereas the other models are characterized by narrow bands with the peaks being magnitude-dependent. The BS13 model, in contrast, peaks around 1 sec and then remains approximately constant for the longer spectral periods.

Results from the California statewide directivity-based hazard study of Al Atik et al. (2023) are used to estimate the expected directivity adjustment to the probabilistic ground motion at DCPD due to the incorporation of directivity effects for  $V_{S30}$  of 760 m/sec. In Al Atik et al. (2013), the UCERF3 source model is used, which is not necessarily consistent with the source modeling of the Hosgri fault in the SWUS study. Three directivity models are implemented in Al Atik et al. (2023): BS13, BSS20, and CS13, with preferred weights of [0.25], [0.25], and [0.5], respectively. Adjustments to the median and aleatory variability are implemented for each directivity model as indicated by the different modeling groups.

Using the interactive hazard tool documented in Mazzoni et al. (2023) (<https://www.risksciences.ucla.edu/nhr3/california-directivity>), the probabilistic directivity adjustments at DCPD are interpolated based on the factors at the four neighboring grid sites weighted by inverse the distance of each neighboring site to DCPD. Directivity adjustment factors are defined as the ratio of uniform hazard spectra (UHS) with directivity to the UHS without directivity for a certain return period. Figure 7-35 shows the location of DCPD relative to the four neighboring sites used to estimate the directivity adjustment factors. Figure 7-36 shows the estimated directivity adjustments at DCPD for the 2,475-yr and the 5,000-yr return periods. For each return period, directivity adjustment factors are plotted versus spectral period for each of the individual directivity models, as well as the weighted average of the models. Figure 7-36 illustrates the epistemic uncertainty in the directivity adjustments, with the BSS20 model predicting the largest ground-motion adjustment, and the BS13 and the CS13 models being more comparable. For the return period of 5,000 years, the directivity adjustment of the hazard results at DCPD is on the order of 1.08 and 1.09 at spectral periods of 3 and 5 sec, respectively.

#### 7.2.5.5. Summary

An evaluation of the directivity models published since the conclusion of the SWUS study and their attributes for application to the hazard at DCPD was performed. New models have been published since 2015, but the general state of directivity modeling remains approximately similar to that evaluated in the SWUS study. In particular, issues related to centering of directivity predictions and treatment of aleatory variability remain subjects of debate. Computational demands of implementing directivity models along with randomizing hypocenters still exist, though are now largely alleviated with advances in parallel computing. Deterministic and probabilistic comparisons of directivity adjustments at DCPD, or for cases relevant to DCPD, were presented. A significant epistemic uncertainty can be observed in the directivity adjustments from the available models indicating a lack of consensus in terms of directivity

modeling and predictions. Estimates of the impact of incorporating directivity adjustments in the hazard analysis at DCPD were presented based on the Al Atik et al. (2023) study, which uses the UCERF3 source model. Adjustments were estimated to be on the order of 1.08 at 3 sec for a 5,000-yr return period.

Based on the issues related to directivity modeling and implementation discussed in this section, the relatively small impact expected on the hazard results at DCPD, and the impact being limited to long spectral periods, we conclude that the decision adopted during the SWUS study of not incorporating directivity effects in the hazard analysis remains valid. The evaluation of directivity effects can be revisited in the future, following the publication and evaluation of new models.

### **7.2.6. Comparison of Non-Ergodic Ground Motion Models**

Traditionally, due to the scarcity of available empirical ground-motion data in a small region, ergodic models have been used in probabilistic seismic hazard analysis for the characterization of the median and aleatory variability of ground motion. The ergodic approach assumes that the statistical properties of ground motion do not vary in space (Anderson and Brune, 1999) and allows for the use of global ground-motion data to build ground-motion models. The resulting ergodic ground-motion models tend to have relatively large aleatory variability because they treat systematic source, path, and site effects as part of the random variability of the model.

In recent years, the availability of the NGA-West2 dataset and the increased number of repeated ground-motion recordings at individual stations allowed for the estimation of systematic site effects and their removal from the ground-motion variability. This resulted in partially non-ergodic ground-motion models where the median ground motion is adjusted for site-specific effects and a reduced single-station aleatory variability is used. The use of partially non-ergodic single-station sigma models leads to a reduction in the aleatory variance of about 30% compared to the ergodic models (Lavrentiadis et al., 2023). The site-specific adjustment of the median ground motion accounts for the epistemic uncertainty in the characterization of site-specific effects.

The SWUS DCPD ground-motion model described in Section 7.1 is a partially non-ergodic ground-motion model that captures the systematic site effects at DCPD. The development of partially non-ergodic single-station sigma models for the SWUS study was discussed in Section 7.1.2. Site-specific adjustment factors were developed for DCPD using empirical and analytical approaches as described in Chapter 9. The availability of three ground-motion recordings at stations ESTA27 and ESTA28 at DCPD allowed for the estimation of empirical site factors along with their epistemic uncertainty; these were used to adjust the reference rock hazard results to become site-specific for the DCPD. The scarcity of empirical ground-motion data in the vicinity of DCPD in the magnitude and distance range of importance to the hazard analysis ( $M > 5$  and distance  $< 20$  km) did not allow for the estimation of source and path adjustments for the ground-motion model.

Since the completion of the SWUS study, major progress has been made in ground-motion modeling involving the development of non-ergodic ground-motion models. The increase in the size of recorded ground-motion databases for locations such as California has allowed for the estimation of the repeatable systemic source, path, and site effects, and the adjustment of median ground-motion models to be site-, source-, and region-specific. This has also led to a further

reduction in the aleatory variability, as some of the apparent randomness in the ergodic ground-motion variability has become epistemic uncertainty. Thus, Lavrentiadis et al. (2023 [LAK21]) developed a non-ergodic effective amplitude ground-motion model for California making use of the abundant ground-motion recordings of NGA-West2 from small-magnitude earthquakes to develop non-ergodic adjustments across the state.

Lavrentiadis and Abrahamson (2023[LA23]) then developed a non-ergodic spectral acceleration ground-motion model for California using the LAK21 non-ergodic effective amplitude spectrum (EAS) effects and converting them to response spectra domain through the use of Random Vibration Theory (RVT). More specifically, LA23 developed two non-ergodic ground-motion models, referred to as GMM1 and GMM2, using the ASK14 and the CY14 GMPEs as backbone models, respectively. Figure 7-37 shows the earthquakes and recording stations in the vicinity of DCPD in the NGA-West2 dataset that drive the non-ergodic adjustments at DCPD using the LA23 models. As shown on Figure 7-37, the recordings from ESTA27 and EST28 at DCPD are included in the NGA-West2 dataset where they are grouped as one station. In addition to the DCPD station, there are four other stations within 20 km of DCPD; their properties are listed in Table 7-7. The database includes a total of eight earthquakes with a maximum magnitude of 4.4 within 50 km of DCPD.

In this section, we present deterministic comparisons of the median ground motion at DCPD from the 2015 study to non-ergodic median predictions from the LA23 model. For these comparisons, we select hazard-significant seismic sources at DCPD. These sources are scenarios on the Hosgri, Shoreline, and Los Osos faults, as listed in Table 7-8, including their assumed epicenter locations. For these scenarios, we compare median ground-motion predictions on the FW. For the non-ergodic model, we assume that the hypocenter location and the location of the closest point on the rupture to the site are at the same point. A zero depth to the top of rupture is used for all scenarios. The  $V_{S30}$  value at the control point ( $V_{S30} = 968$  m/sec) is used for the non-ergodic median ground-motion predictions and we specify that the DCPD site is at the location of station SSN 100606 listed in Table 7-7.

For each scenario, median ground-motion predictions are obtained from the 31 reference-rock SWUS ground-motion models for DCPD assuming the site is located on the FW. The empirical site adjustment factors computed for DCPD and discussed in Section 9.1 are applied to the reference rock median ground motion to adjust it to the site-specific conditions at DCPD. The total epistemic uncertainty of the median ground-motion predictions from the DCPD model combines the epistemic uncertainty in the reference rock model and the uncertainty in the empirical site adjustment factors. Figure 7-38 shows the median (central), upper (95<sup>th</sup> percentile), and lower (5<sup>th</sup> percentile) of the DCPD empirical site adjustment factors.

**Table 7-7. Stations Within 20 km of DCPD in the NGA-West2 Database**

Station Name	SSN	Station ID No.	V <sub>S30</sub> (m/sec)	Distance to DCPD (km)	Number of Recordings
DCPD (ESTA28)	100606	DCPD	1100	-	3
DCPD (ESTA27)	100606	DCPD	570	-	1
Diablo Creek Digital	100436	DCD	517	1.3	2
Davis Peak Digital	100437	DPD	382	7.0	6
Point Buchon – Los Osos	1786	36427	486	7.4	2
San Luis Hill Digital	100219	SHD	818	9.8	4

**Table 7-8. Deterministic Scenarios Used for Comparisons with Non-ergodic Ground-Motion Models**

Scenario	Eqk Longitude	Eqk Latitude	Dip	Dip Direction	Mechanism	Magnitude	Width (km)	R <sub>RUP</sub> (km)
Hosgri Fault	-120.9023°	35.1935°	80°	East	SS	7.5	15	4.79
Shoreline Fault	-120.874°	35.213°	90°	---	SS	6.4	12.94	1.76
Los Osos Fault	-120.85°	35.206°	60°	South	RV	6.6	15	0.77

### 7.2.6.1. Hosgri Fault Scenario

The Hosgri fault scenario has a magnitude of 7.5 and is at a distance of 4.79 km from DCPD. Figure 7-39 (top) shows the geometric mean of the median ground motion predicted from the 31 reference rock model branches, and the 16<sup>th</sup> and 84<sup>th</sup> percentiles of the reference rock spectra (blue solid and dashed lines). Figure 7-39 (bottom) shows a comparison of the epistemic uncertainty in the reference rock median ground motion with the empirical adjustment factors and the total epistemic uncertainty in the control point median ground motion. The empirical site factors applied to the median reference rock ground motion result in the control point median spectrum shown on Figure 7-39 (solid pink line in the plot on the top panel). Using the total epistemic standard deviation, the 16<sup>th</sup> and 84<sup>th</sup> percentile spectra are also shown in the figure (dashed pink lines).

For the implementation of the non-ergodic model for ground-motion prediction at DCPD, 1000 EAS samples were drawn using the LAK21 model to capture the range of epistemic uncertainty in the non-ergodic median ground motion. Figure 7-40 shows the constant term, as well as the spatially varying, non-ergodic source, path, and site terms of the LAK21 EAS model at the DCPD site. The mean and standard deviation of these terms in natural log units over the 1000 samples are shown on this figure. The non-ergodic EAS site term consists of regional and site-specific adjustments as shown on Figure 7-40. The regional site term, which has a finite



correlation length, describes the broader adjustments to the backbone model based on regional site effects, while the site-specific term has zero correlation length and describes site-specific adjustments based on the ground motion recorded at DCPD (SSN 100606). The source term captures systematic source effects and is a function of the coordinates of the earthquake scenario, and the path term captures systematic attenuation effects from the source to the DCPD site. The constant term represents the small shift in the non-ergodic model due to the difference in the weighting of residuals between the ergodic and non-ergodic models.

The relative amplitude of the different non-ergodic adjustments shown on Figure 7-40 is a function of ground-motion data availability in the vicinity of DCPD. Figure 7-41 shows the correlation length of the source, path, and regional site terms in the LAK21 model. These correlation lengths indicate the extent of the smooth variation of a parameter spatially, and are on the order of 30, 50, and 18 km for the source, path, and regional site terms, respectively. Given the limited data in the vicinity of DCPD (Figure 7-37) and the correlation lengths shown on Figure 7-41, the source and path adjustment terms at DCPD shown on Figure 7-40 are small, while the regional and site-specific site terms make up most of the non-ergodic adjustment at DCPD.

Given the 1000 samples of non-ergodic ground motion, the median, 16<sup>th</sup>, and 84<sup>th</sup> percentile response spectra for the Hosgri fault scenario at DCPD are plotted on Figure 7-42 for non-ergodic models 1 and 2 compared to the ergodic median predictions from their corresponding backbone models of ASK14 and CY14, respectively. Figure 7-42 indicates a decrease in the short-period non-ergodic ground motion, and an increase at long periods relative to the ergodic backbone models. This is consistent with the observed non-ergodic EAS adjustments shown on Figure 7-40.

The non-ergodic ground-motion predictions at DCPD for the Hosgri fault scenario are compared with the partially non-ergodic predictions from the SWUS DCPD model. Figure 7-43 shows the comparison of the median ground motion along with the epistemic standard deviation for this scenario. This figure indicates a good agreement between the SWUS DCPD model and the LA23 non-ergodic models at short periods both in terms of the median ground motion and its epistemic uncertainty. At long periods, the median ground motion and epistemic uncertainty predicted by the SWUS DCPD model exceed those of the non-ergodic models. Given that the adjustments in the non-ergodic model at DCPD are primarily related to site effects, a good agreement is observed between the non-ergodic models and the site-specific partially non-ergodic SWUS DCPD model. At long periods, the uncertainty in the DCPD site adjustment is relatively large due to the large scatter in the estimated site terms from the three available recordings at these periods. Figure 7-44 shows the median, 16<sup>th</sup>, and 84<sup>th</sup> percentile response spectra for the Hosgri fault scenario at DCPD for non-ergodic models 1 and 2 compared to the predictions from the SWUS DCPD model.

#### 7.2.6.2. Shoreline Fault Scenario

The Shoreline fault scenario has a magnitude of 6.4 and is at a distance of 1.8 km from DCPD. Given the 1000 samples of non-ergodic ground motion, the median, 16<sup>th</sup>, and 84<sup>th</sup> percentile response spectra for this scenario at DCPD are plotted on Figure 7-45 for non-ergodic models 1 and 2 compared to the ergodic median predictions from their corresponding backbone models of ASK14 and CY14, respectively. Similar to the observations made for the previous deterministic

scenarios, Figure 7-45 indicates a decrease in the short-period non-ergodic ground motion and an increase at long periods relative to the ergodic backbone models.

The non-ergodic ground-motion predictions at DCPD for the Shoreline fault scenario are compared with the partially non-ergodic predictions from the SWUS DCPD model. Figure 7-46 shows the comparison of the median ground motion (top) and the epistemic standard deviation (bottom) for this scenario. The plots on this figure show good agreement between the SWUS DCPD model and the LA23 non-ergodic models at short periods both in terms of the median ground motion and its epistemic uncertainty. At long periods, the median ground motion and epistemic uncertainty predicted by the SWUS DCPD model exceed those of the non-ergodic models. Figure 7-47 shows the median, 16<sup>th</sup>, and 84<sup>th</sup> percentile response spectra for the Shoreline fault scenario at DCPD for non-ergodic models 1 and 2 compared to the predictions from the SWUS DCPD model. Given that the adjustments in the non-ergodic model at DCPD are primarily related to site effects, a good agreement is generally observed between the non-ergodic models and the site-specific partially non-ergodic SWUS DCPD model.

#### 7.2.6.3. Los Osos Fault Scenario

The Los Osos fault scenario has a magnitude of 6.6 and is at a distance of 0.77 km from DCPD. Given the 1000 samples of non-ergodic ground motion, the median, 16<sup>th</sup>, and 84<sup>th</sup> percentile response spectra for this scenario at DCPD are plotted on Figure 7-48 for non-ergodic models 1 and 2 compared to the ergodic median predictions from their corresponding backbone models of ASK14 and CY14, respectively. Similar to the observations made for the previous deterministic scenarios, Figure 7-48 indicates a decrease in the short period non-ergodic ground motion and an increase at long periods relative to the ergodic backbone models.

The non-ergodic ground-motion predictions at DCPD for the Los Osos fault scenario are compared with the partially non-ergodic predictions from the SWUS DCPD model. Figure 7-49 shows the comparison of the median ground motion along with the epistemic standard deviation for this scenario. This figure indicates a good agreement between the SWUS DCPD model and the LA23 non-ergodic models at short periods both in terms of the median ground motion and its epistemic uncertainty. At long periods, the median ground motion and epistemic uncertainty predicted by the SWUS DCPD model exceed those of the non-ergodic model. Figure 7-50 shows the median, 16<sup>th</sup>, and 84<sup>th</sup> percentile response spectra for the Los Osos fault scenario at DCPD for non-ergodic models 1 and 2 compared to the predictions from the SWUS DCPD model. Given that the adjustments in the non-ergodic model at DCPD are primarily related to site effects, a good agreement is generally observed between the non-ergodic models and the site-specific partially non-ergodic SWUS DCPD model.

#### 7.2.6.4. Summary of Comparisons

The median ground motions predicted at DCPD by the SWUS DCPD partially non-ergodic model were compared to the LA23 non-ergodic models for a suite of hazard-significant deterministic scenarios. Given the limited empirical ground-motion data in the vicinity of DCPD, the non-ergodic ground-motion adjustment is dominated by site adjustments. Since site-specific adjustments were incorporated in the partially non-ergodic SWUS model, the deterministic comparisons presented in this section indicated a good agreement between the SWUS model predictions and the non-ergodic model at DCPD. Therefore, we conclude that adopting a fully

non-ergodic ground-motion model for the hazard at DCPD is not needed since the non-ergodic adjustments are largely captured with the site factors in the SWUS DCPD model. This can be revisited in the future with increased ground-motion recordings in the vicinity of DCPD that may allow for an update of the non-ergodic models to capture source and path effects.

### **7.2.7. Splay and Complex Ruptures**

Another focus topic for the simulation ground motions performed as part of the SWUS study was the evaluation of ground motions from splay and complex ruptures. As part of the SSC model, splay and complex ruptures from connected fault systems were included in the model. The large crustal 2016 Kaikoura event (M 7.8) in New Zealand has shown the potential for such large and complex ruptures (Xu et al., 2018). Bradley et al. (2017) performed a study on the empirical ground motions from this event, which includes data from four recording stations within approximately 10 km of the closest fault plane. As part of their study, Bradley et al. (2017) performed simulations similar to those performed for the SWUS study based on complex source ruptures consisting of multiple fault planes (i.e., sources) timed in rupture initiation. Their analysis yielded favorable comparisons between the observed ground motions and the simulations. The Bradley et al. (2017) study, however, did not analyze any potential differences in ground motions between the observed ground motions and predicted results using GMMs with a method for combining the ground motions from these multiple seismic sources.

As part of the SWUS evaluation, the question of how to estimate ground motions from these splay and complex ruptures was investigated through the use of simulations. Four potential choices were proposed:

- Square root of the sum of the squares of the ground motions from the individual seismic sources (SRSS)
- Approximate a single fault with an area weighted approach
- Approximate a single fault with a 1/R<sup>2</sup> weighted approach
- Approximate a single fault with the closest segment parameters

As an example, a complex rupture consisting of the Hosgri fault connected to the Los Osos fault is shown on Figure 7-51. The Hosgri fault trace is the red line drawn in the NW direction and the blue area represents the surface projection of the Los Osos fault. The DCPD site is indicated by the yellow triangle. An example of a splay event is plotted on Figure 7-52 with the main trace being the Hosgri fault and the splay fault being the Shoreline fault. As before, the DCPD site is shown by the yellow triangle. Based on the evaluation conducted as part of the SWUS model, combined with the key finding that these splay and complex ruptures do not significantly contribute to the total hazard at the DCPD site, the SRSS method was adopted. This was deemed to be a conservative approach in terms of the ground motions (GeoPentech, 2015).

Although the Kaikoura event is a recent example of a complex rupture, the limited amount of near-fault data obtained from that earthquake does not allow for the robust evaluation of the different methods of estimating ground motions from these types of complex ruptures. Also, as discussed by Bradley et al. (2017), the lack of empirical data from complex or splay ruptures in the near-field requires the calculation of simulation ground motions to assist in the evaluation. Given that several suites of simulation events based on the DCPD SSC model were conducted for the 2015 study, it is expected that additional simulations would not lead to a different conclusion regarding the approach adopted for the SWUS study. Thus, the estimation of ground motions

from these splay and complex ruptures using the SRSS methodology as was conducted for the 2015 study is acceptable based on more recent data and information.

### **7.3. EVALUATION OF ALEATORY VARIABILITY MODEL**

This section evaluates the SWUS aleatory variability model developed for DCP. An overview of the SWUS was presented in Section 7.1.2. A discussion of recent updates to the various components of the model is presented in this section.

#### **7.3.1. Evaluation of New Ground Motion Data**

The SWUS between-event and single-station within-event standard deviation models are largely based on the NGA-West2 empirical ground-motion data and models. Updating these aleatory variability models requires the availability of large empirical ground-motion datasets that cover the magnitude and distance ranges of interest for DCP (e.g.,  $M > 5$  and  $R_{RUP} < 50$  km). Empirical ground-motion data that have become available since completion of the SWUS study in 2015 consist of the NGA-West3 data, the DCP California data, and the Turkish data discussed in Chapter 4.

The current versions of the NGA-West3 and the DCP datasets are preliminary and only include limited data with  $M > 5$  (e.g., 15 and 7 added earthquakes in the current NGA-West3 and the DCP flatfiles, respectively, have  $M \geq 5$ ). While it is expected that new between-event and single-station within-event standard deviation models will be available as part of the NGA-West3 project, these models will not be available until the end of 2024. The current preliminary versions of the empirical datasets of ground motion since the completion of the SWUS study do not currently allow for a revision or an update of the aleatory variability models for DCP.

#### **7.3.2. Between-Event Variability**

Published between-event standard deviation ( $\tau$ ) models since the completion of the SWUS study are evaluated in terms of their applicability to DCP and their differences compared to the SWUS  $\tau$  model. The global  $\tau$  model of Al Atik (2015), developed as part of the NGA-East study, is based on the four NGA-West2  $\tau$  models. The global  $\tau$  model is magnitude-dependent and is applicable to  $M \geq 3.0$ . Similar to the SWUS  $\tau$  model, the global  $\tau$  model is period-independent, smoothing through the peak in  $\tau$  observed at frequencies around 10 Hz. The epistemic uncertainty in the global  $\tau$  model consists of the between-model and within-model uncertainty in  $\tau$ . The global  $\tau$  model was adopted in the SSHAC Level 3 studies for the Idaho National Laboratory (INL, 2022) and in the Sodium Demonstration Project in Wyoming (Sodium, 2024).

Figure 7-53 shows a comparison of the global and the SWUS  $\tau$  models as a function of magnitude. The two models are similar in terms of their central branch and their epistemic uncertainty for  $M \geq 5.5$ . Differences can be observed for  $M < 5.5$  as a result of the different smoothing with magnitude approaches for the two models, and the focus of the SWUS study on  $M > 5$  as opposed to the wider magnitude range ( $M \geq 3.0$ ) for the global  $\tau$  model. Based on the comparison presented on Figure 7-53 and other similarities between the global and SWUS  $\tau$  models (i.e., both models are based on the NGA-West2  $\tau$ , and are magnitude-dependent, period-independent, and similar in their characterization of epistemic uncertainty), we conclude that the

SWUS  $\tau$  model is consistent with later  $\tau$  models that were adopted in other large SSHAC Level 3 studies.

### **7.3.3. Single-Station Within-Event Variability**

Since the completion of the SWUS study, other large SSHAC Level 3 studies (e.g., INL, 2022; Natrium, 2024) adopted the partially non-ergodic approach and characterized the single-station within-event variability. The INL (2022) and the Natrium (2024) studies both adopted the global  $\phi_{SS}$  model of Al Atik (2015). This model was developed based on the analysis of within-event residuals from the four NGA-West2 GMPEs (ASK14, BSSA14, CB14, and CY14) with  $M \geq 3.0$  and  $R_{RUP} \leq 400$  km, and is magnitude- and period-dependent. The epistemic uncertainty in the global  $\phi_{SS}$  model was estimated using the station-to-station variability of  $\phi_{SS}$  (coefficient of variation of  $\phi_{SS,S}$  of 0.12) including the standard error of the model coefficients estimated from the weighted linear fit to the  $\phi_{SS}$  values versus magnitude (Al Atik, 2015). The total uncertainty in  $\phi_{SS}$  was found to be largely due to the station-to-station variability of  $\phi_{SS}$ .

Figure 7-54 presents a comparison of the global  $\phi_{SS}$  model to the three SWUS DCP  $\phi_{SS}$  models for PGA and spectral period of 1 sec. As discussed in Section 7.1.2.1 and shown on Figure 7-54, two of the SWUS models are magnitude-dependent, whereas the third model is magnitude-independent. Figure 7-54 illustrates that the SWUS magnitude-dependent  $\phi_{SS}$  models and the global  $\phi_{SS}$  model are generally comparable for  $M \geq 6.0$ . For smaller magnitudes at PGA, the SWUS models have smaller  $\phi_{SS}$  than the global model as a result of the SWUS study using residuals with  $M \geq 5.0$  to develop the  $\phi_{SS}$  models. The global  $\phi_{SS}$  model uses residuals with  $M \geq 3.0$  to define  $\phi_{SS}$  for  $M \leq 5.0$ . The inclusion of the smaller magnitudes leads to larger average  $\phi_{SS}$  values in the global model at  $M \leq 5.0$ . At the period of 1 sec, the SWUS and the global  $\phi_{SS}$  are comparable.

Based on the comparison presented on Figure 7-54 and other similarities between the SWUS and the global  $\phi_{SS}$  models (e.g., magnitude-dependence, period-dependence, models based on NGA-West2 residuals, characterization of epistemic uncertainty), we conclude that the SWUS  $\phi_{SS}$  model is consistent with later models and does not need to be updated given the currently available empirical datasets. Observed differences between the SWUS and the global  $\phi_{SS}$  models can be attributed to differences in the magnitude and distance ranges used in the development of the SWUS and the global models.

### **7.3.4. Single-Station Sigma**

The SWUS single-station sigma logic tree, first discussed in Section 7.1.2.3, combined the between-event and within-event standard deviation models accounting for the uncertainty in the components of the ground-motion variability. It also accounted for the distribution of the ground-motion residuals and the impact of the spatial correlation of the residuals on the components of the aleatory variability. Later studies (INL, 2022; Natrium, 2024) adopted the SWUS approach of modifying the weights on the sigma branches to account for the spatial correlation of the ground-motion residuals. Therefore, the incorporation of the impact of spatial correlation on the sigma model in the SWUS study is still considered up-to-date and consistent with the approach used in later studies. The impact of the spatial correlation of ground-motion residuals can be evaluated and updated following the NGA-West3 study.

Given the statistical evidence supporting the use of the mixture model to adequately capture the fat tails of the distribution of the within-event residuals, the INL (2022) and the Natrium (2024) studies adopted the mixture model and abandoned the lognormal distribution. The impact of abandoning the lognormal distribution is expected to be small given the assigned weight of [0.2] to this branch in the SWUS logic tree. Moreover, the sensitivity of the hazard results to the aleatory distribution form was evaluated as part of the SWUS study (GeoPentech, 2015). This sensitivity analysis indicated that the difference between the two types of distributions is small and only observed at hazard levels of  $10^{-6}$  and smaller.

#### **7.4. CONCLUSIONS**

The evaluation of the SWUS 2015 GMC model for DCPD was presented in this section. The median ground-motion model was evaluated in terms of: (1) approach; (2) treatment of features such as location relative to the hanging wall, directivity, and splay and complex ruptures; and (3) performance compared to recent empirical ground-motion data. Based on this evaluation, we conclude that the median ground-motion predictions from the SWUS ground-motion model are generally consistent with new empirical data in the preliminary NGA-West3, DCPD, and Turkish databases. In some instances, residual analyses showed some overprediction by the DCPD model compared to the data. The evaluation of directivity, HW effects, as well as the treatment of splay and complex ruptures, did not indicate significant differences between the DCPD ground-motion model and more recent data and models. Comparisons of the median predictions from the DCPD model to available non-ergodic ground-motion models also indicated consistent results. Therefore, we conclude that no changes are warranted for the median model at this time.

The aleatory variability model developed as part of the SWUS study was also evaluated. We conclude that the available preliminary datasets do not currently allow for an update to the calculation of components of aleatory variability for the large-magnitude and short-distance ranges of interest for DCPD (e.g.,  $M > 5$  and  $R_{RUP} < 50$  km). Components of the DCPD aleatory variability model were also compared to models used in more recent studies. These comparisons indicated consistency in the approach, elements of the logic tree, and results in the magnitude and distance ranges of interest. Therefore, the SWUS aleatory variability model developed for DCPD is considered valid and no updates are recommended at the time of this evaluation.

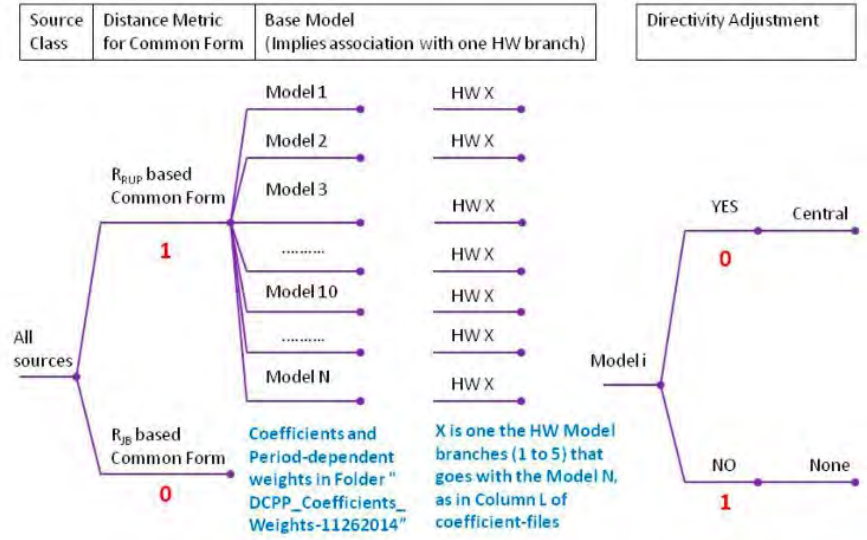


**Figure 7-1. DCPG GMC logic tree for local seismic sources (from GeoPentech, 2015, Figure 1-1)**

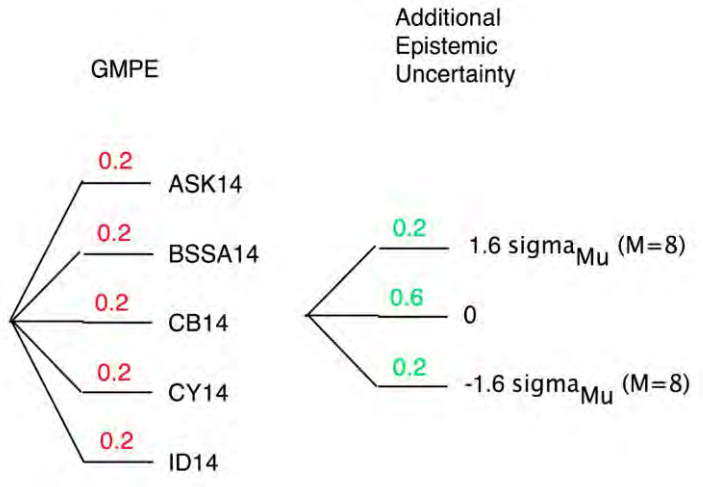


**Figure 7-2. DCPG GMC logic tree for distant seismic sources (from GeoPentech, 2015, Figure 8.2-3)**



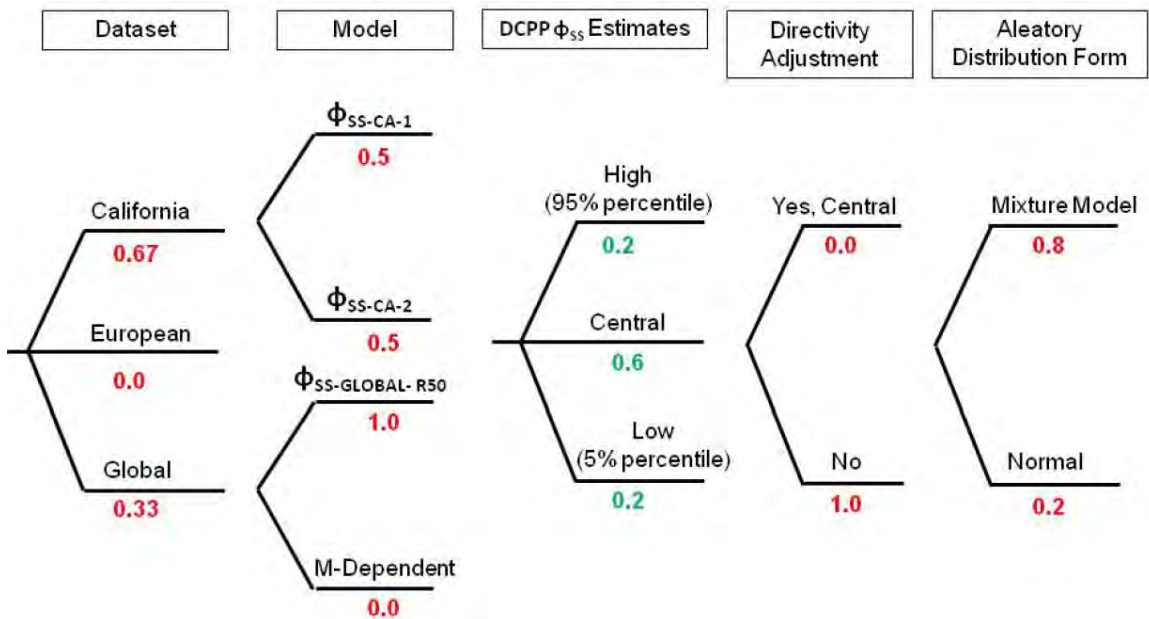


Figure 7-3. SWUS DCPP  $\phi_{ss}$  logic tree (from GeoPentech, 2015)

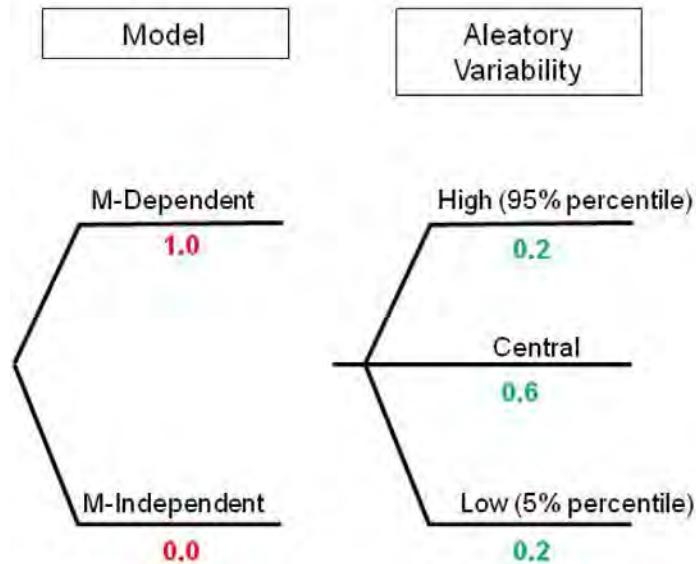


Figure 7-4. SWUS DCPP  $\tau$  logic tree (from GeoPentech, 2015)

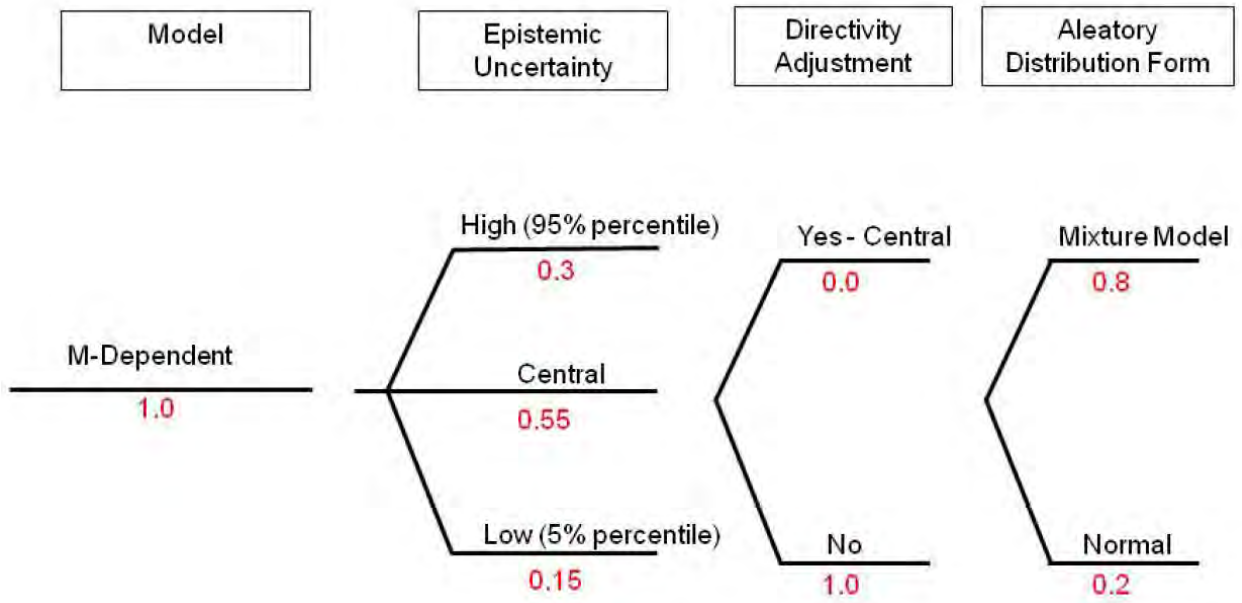
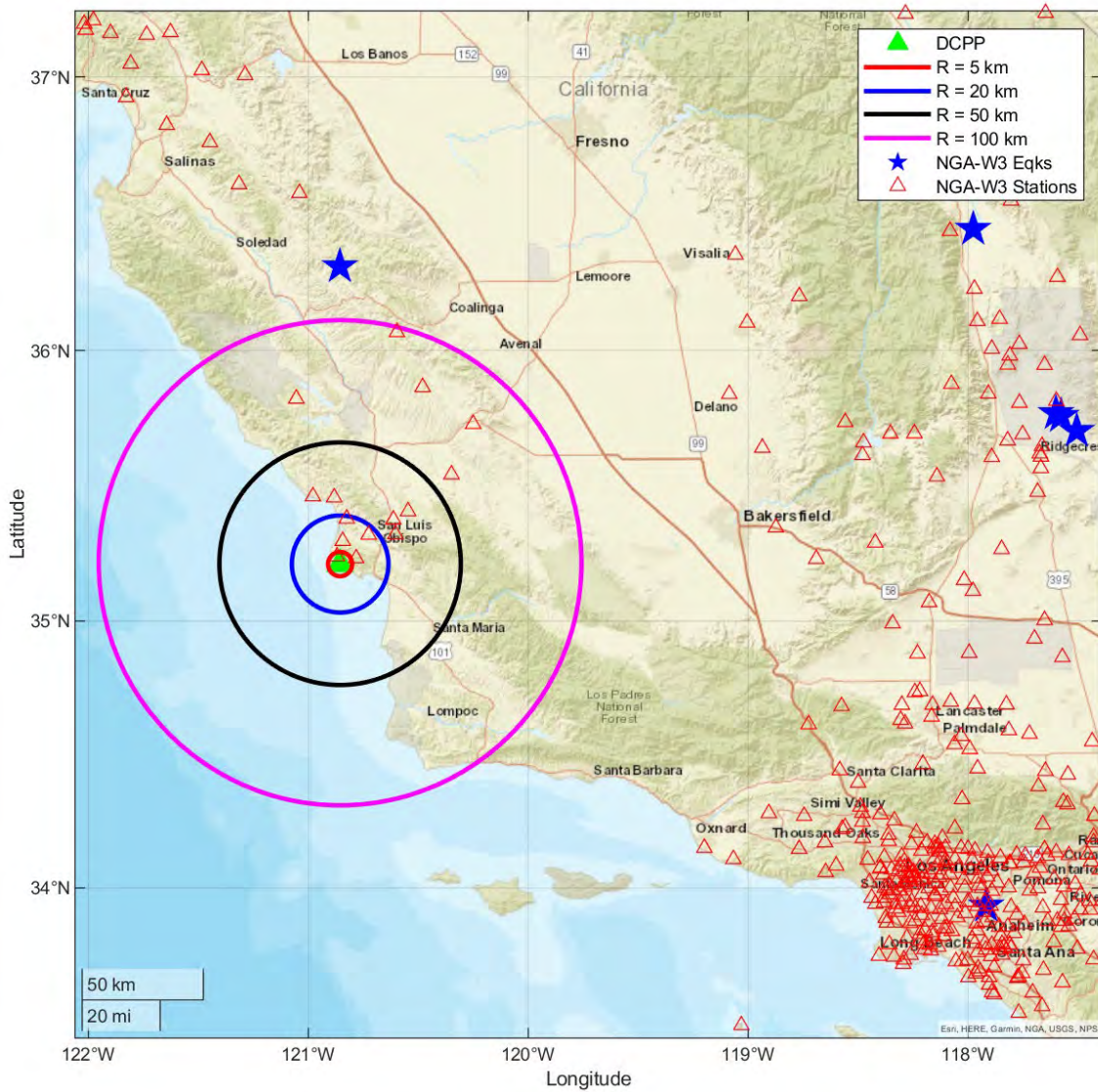
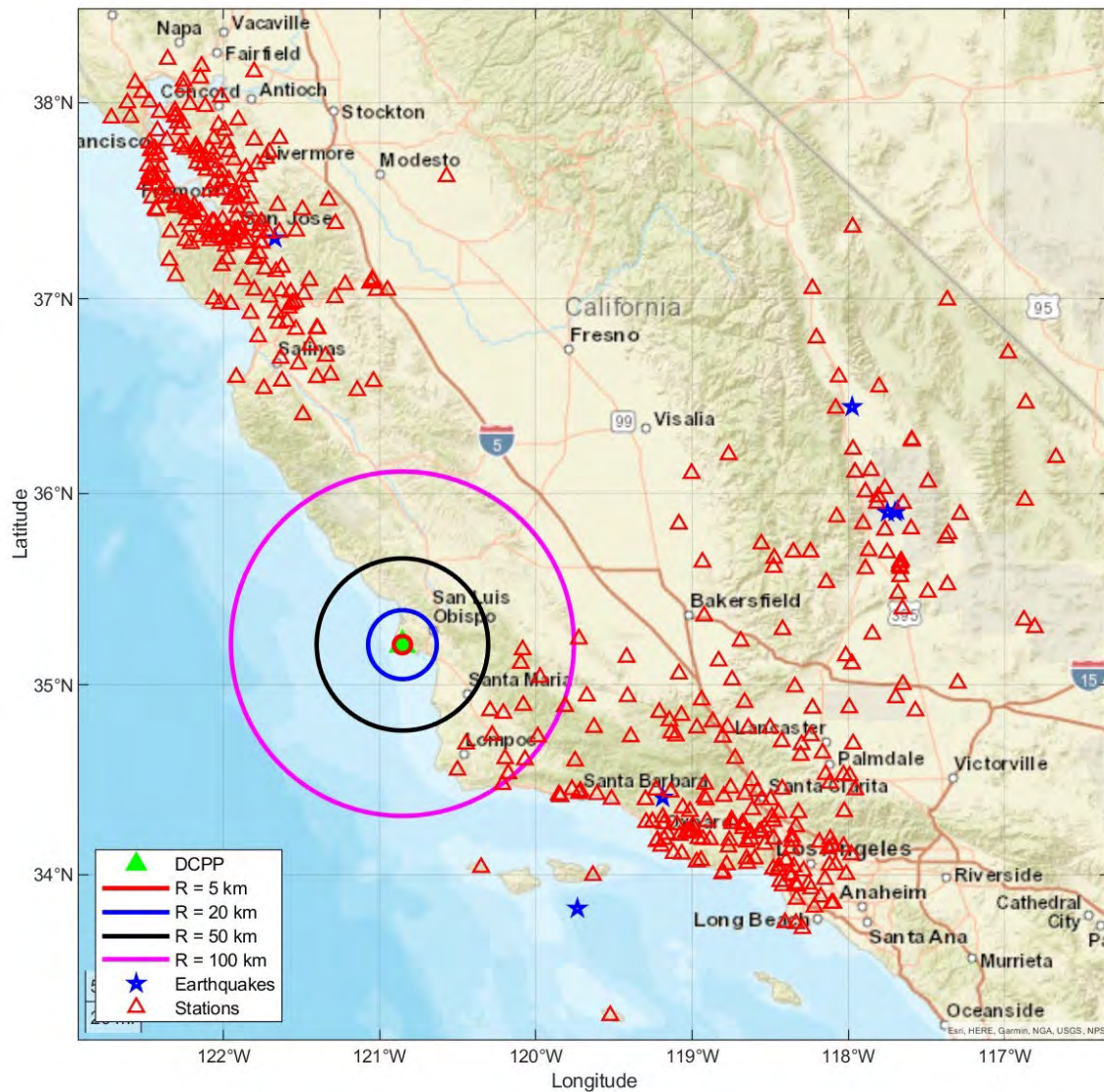


Figure 7-5. SWUS DCP single-station sigma logic tree (from GeoPentech, 2015)



**Figure 7-6. Earthquakes (blue stars) and stations (red triangles) in the preliminary NGA-West3 database for recordings with  $M \geq 5$ ,  $R_{RUP} < 120$  km, and  $V_{S30} > 250$  m/sec**



**Figure 7-7. Earthquakes (blue stars) and stations (red triangles) in the DCPP database for recordings with  $M \geq 5$ ,  $R_{RUP} < 120$  km, and  $V_{S30} > 250$  m/sec**



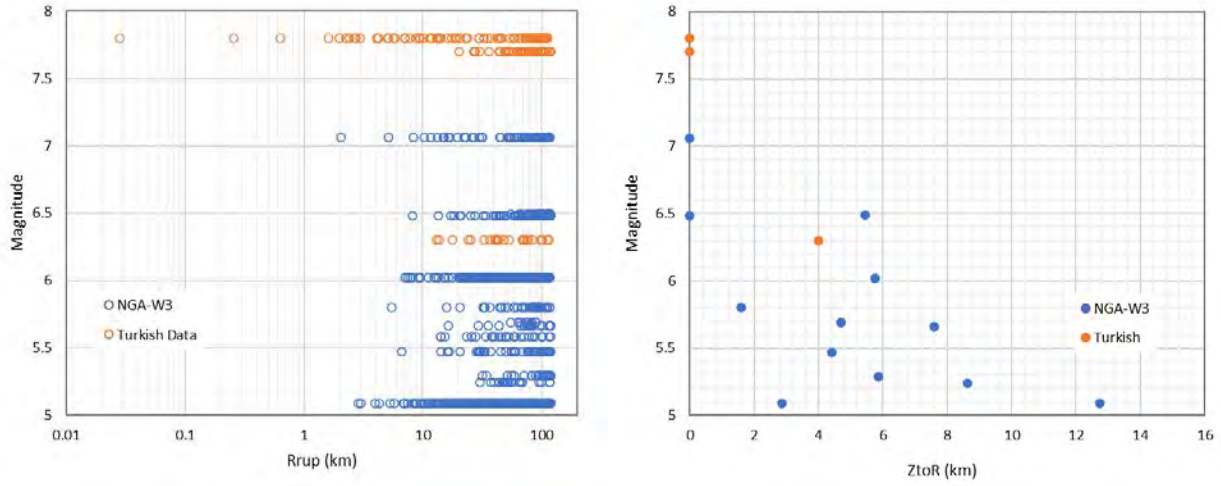


**Figure 7-8. Magnitude-distance (left) and magnitude-Ztor (right) distributions of the Turkish and NGA-West3 data used in the regression analysis. Earthquakes with at least 5 recordings were used.**

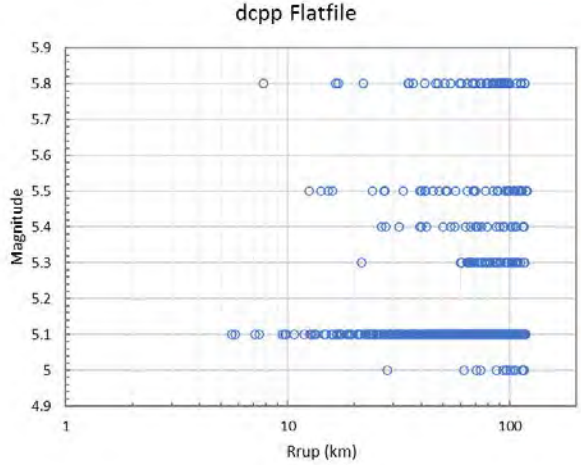


**Figure 7-9. Magnitude-distance distribution of the DCP data used in the regression analysis. Earthquakes with at least 5 recordings were used.**

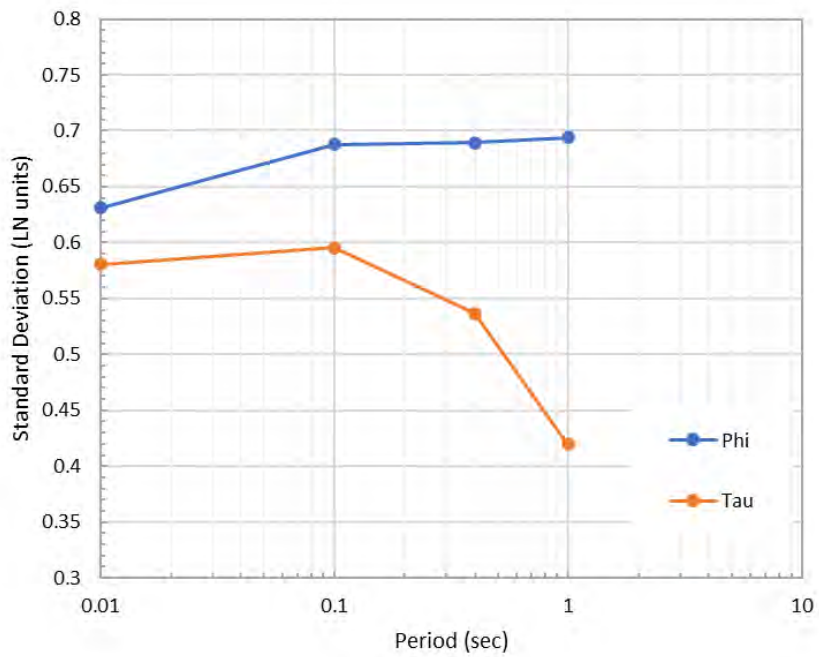
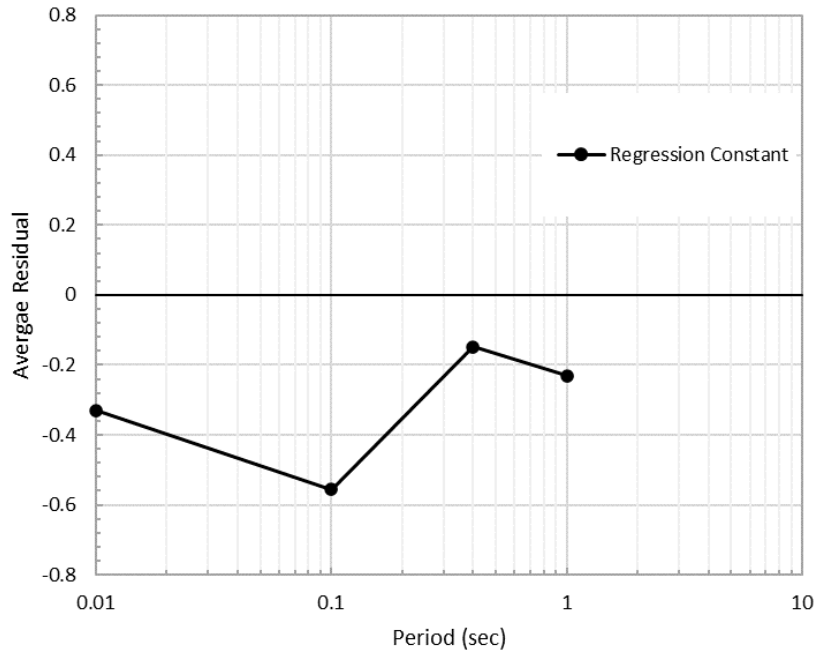


**Figure 7-10. Regression constant (top) and between-event and within-event standard deviations (bottom) of the regression analysis of the Turkish and NGA-West3 data**

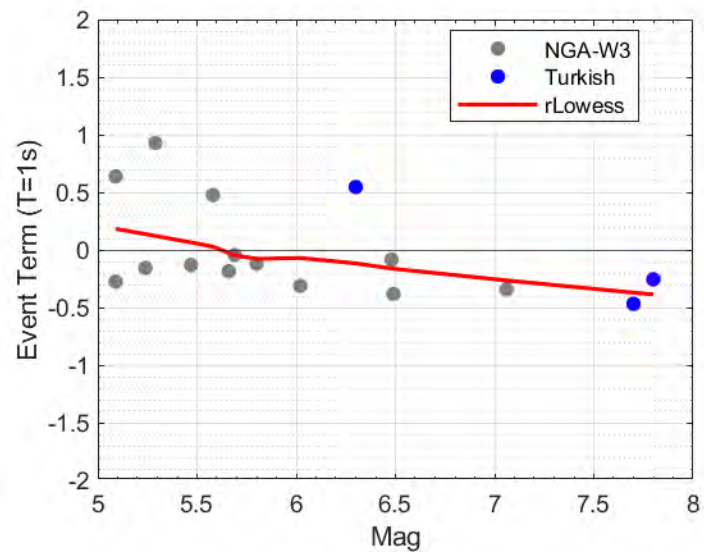
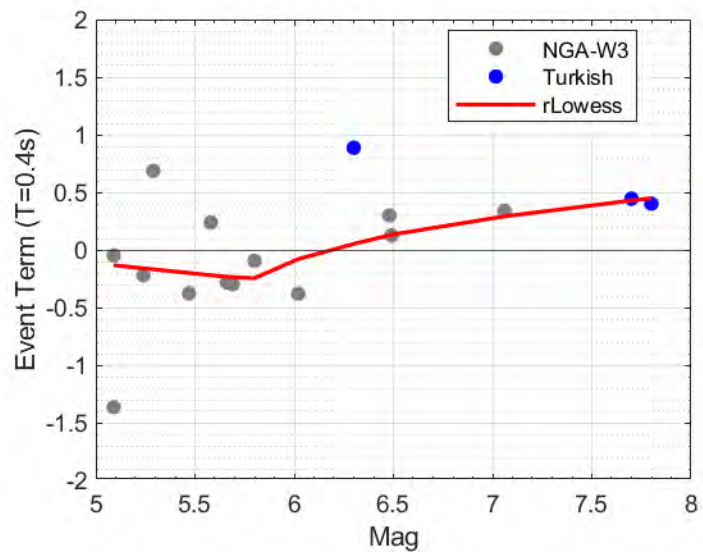
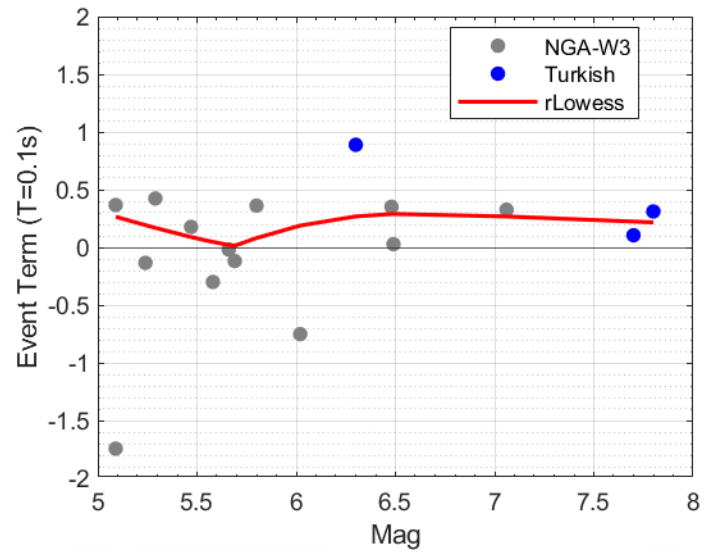
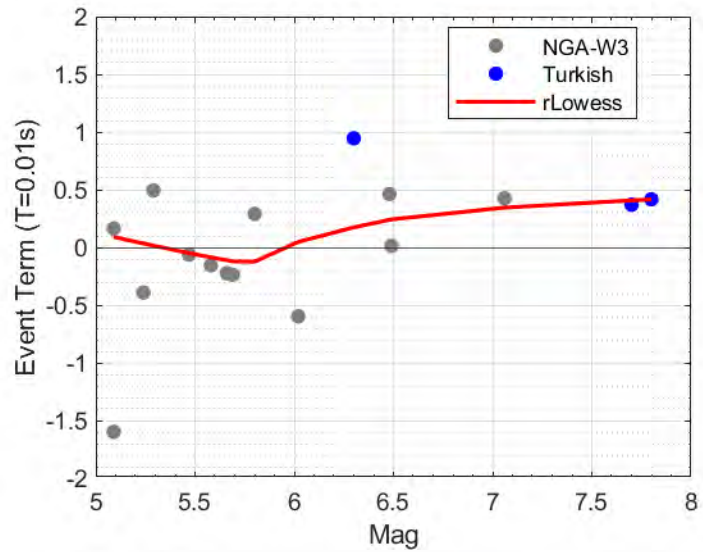
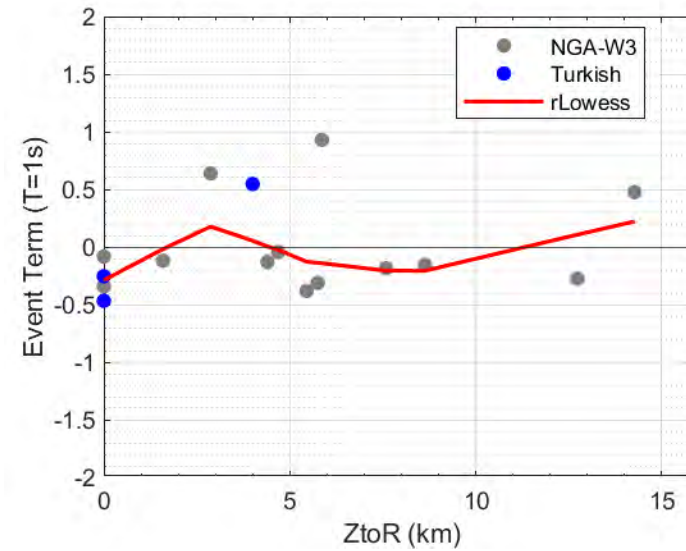
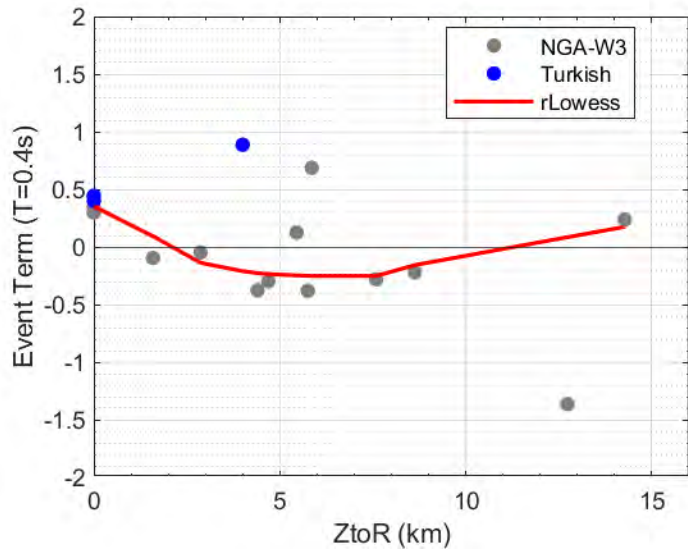
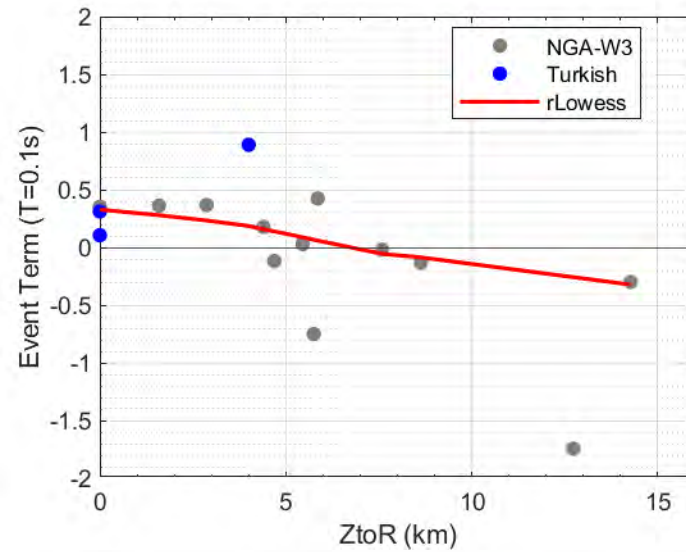
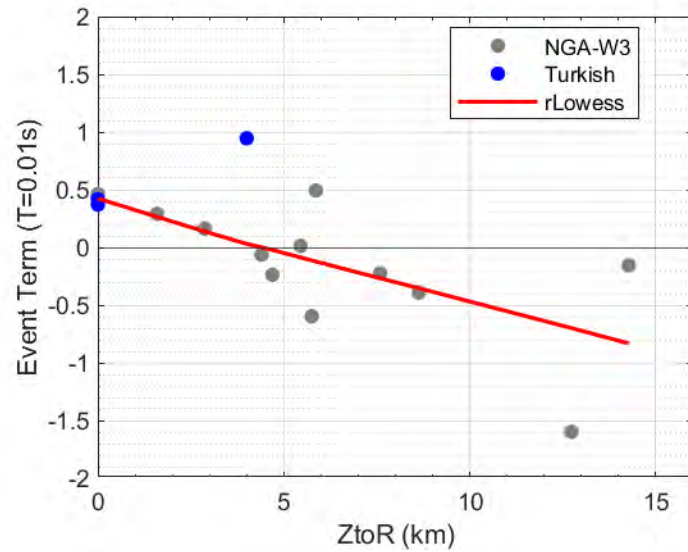
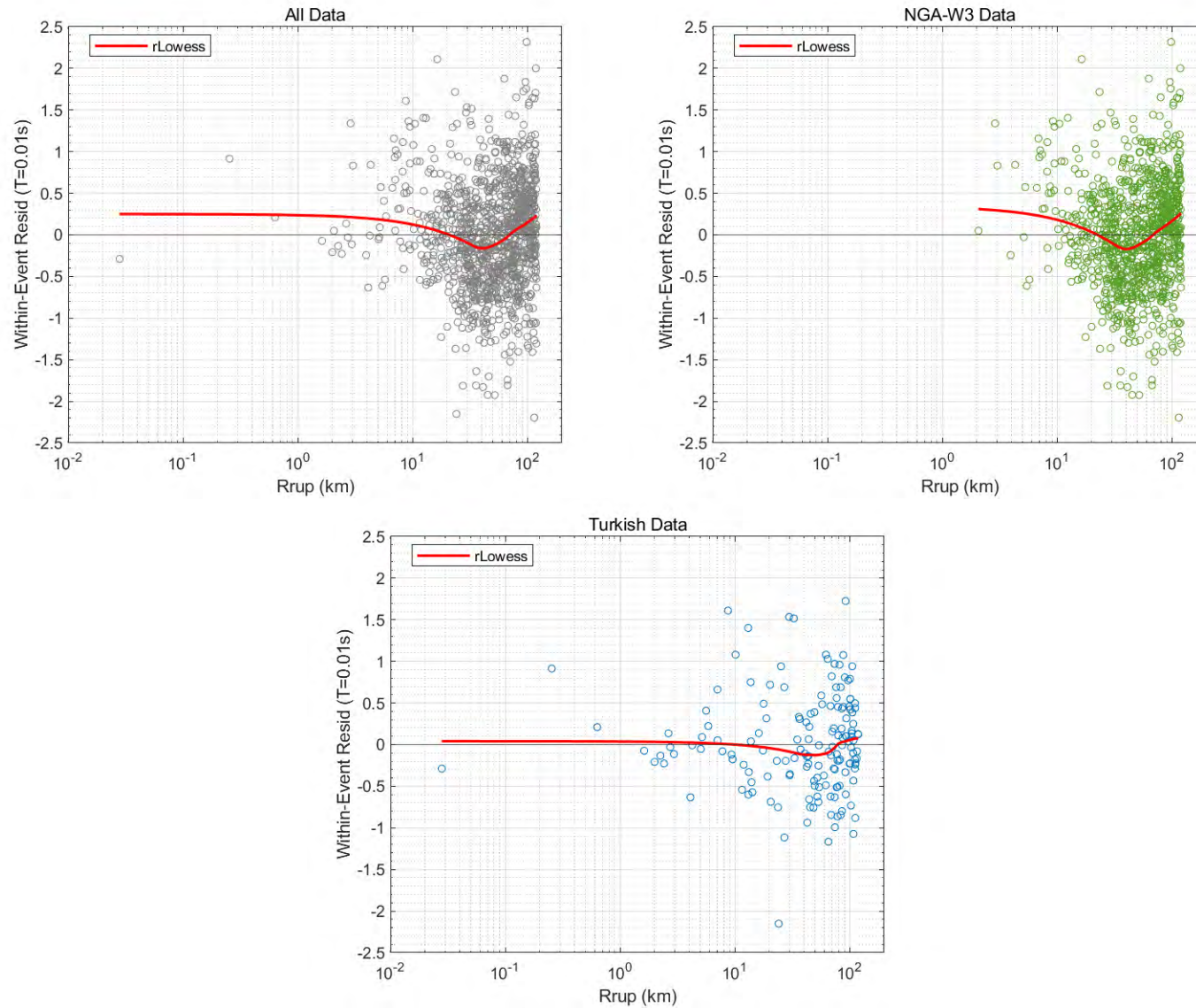


Figure 7-11. Between-event residuals of the Turkish and NGA-West3 data versus magnitude for periods of 0.01, 0.1, 0.4, and 1 sec. The robust Lowess fit to the data is shown in red.





**Figure 7-12. Between-event residuals of the Turkish and NGA-West3 data versus Ztor for periods of 0.01, 0.1, 0.4, and 1 sec. The robust Lowess fit to the data is shown in red.**



**Figure 7-13. Within-event residuals of the Turkish and NGA-West3 data versus distance for period of 0.01 sec. The robust Lowess fit to the data is shown in red.**

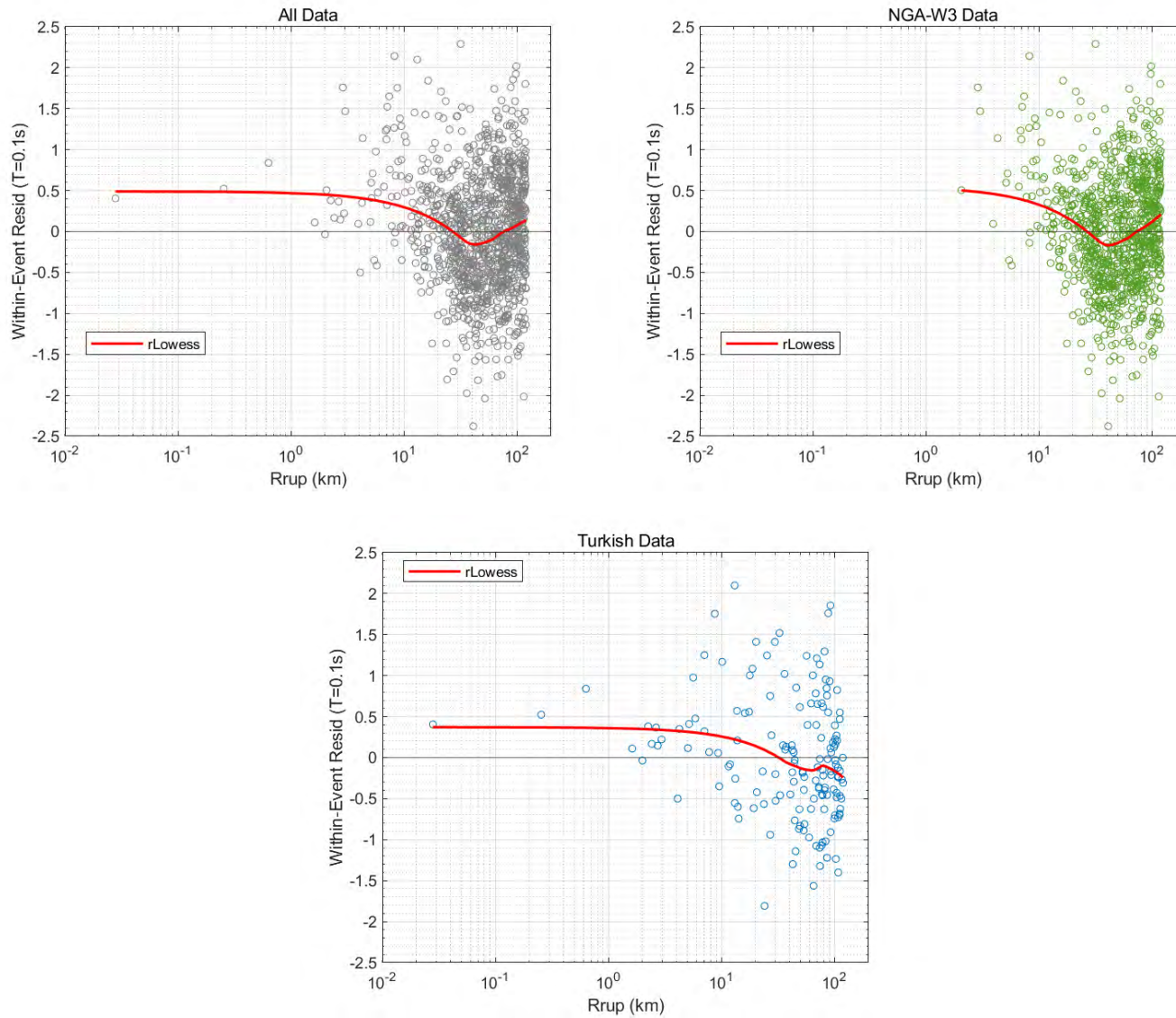


**Figure 7-14. Within-event residuals of the Turkish and NGA-West3 data versus distance for period of 0.1 sec. The robust Lowess fit to the data is shown in red.**



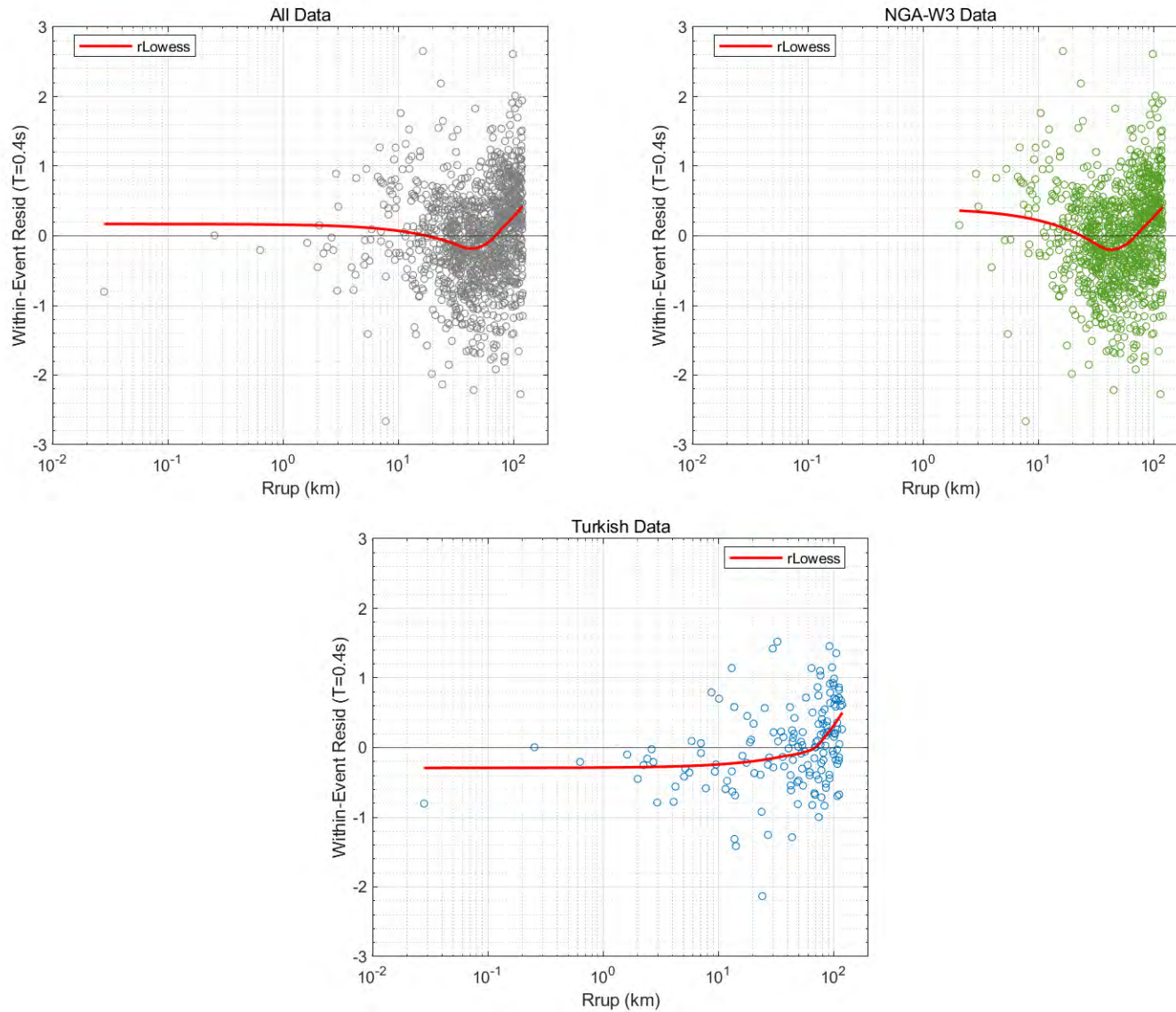


**Figure 7-15. Within-event residuals of the Turkish and NGA-West3 data versus distance for period of 0.4 sec. The robust Lowess fit to the data is shown in red.**

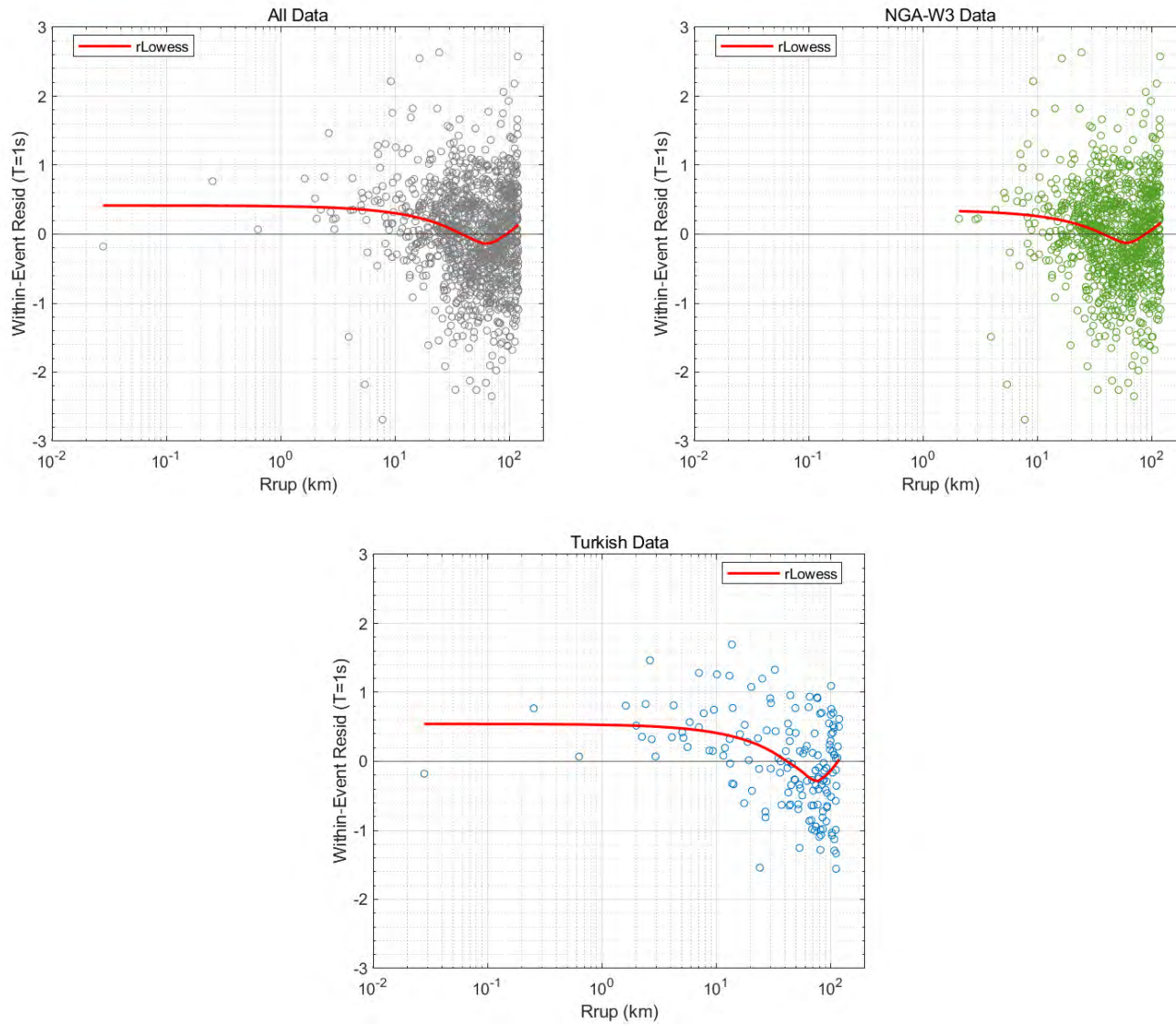


**Figure 7-16. Within-event residuals of the Turkish and NGA-West3 data versus distance for period of 1 sec. The robust Lowess fit to the data is shown in red.**

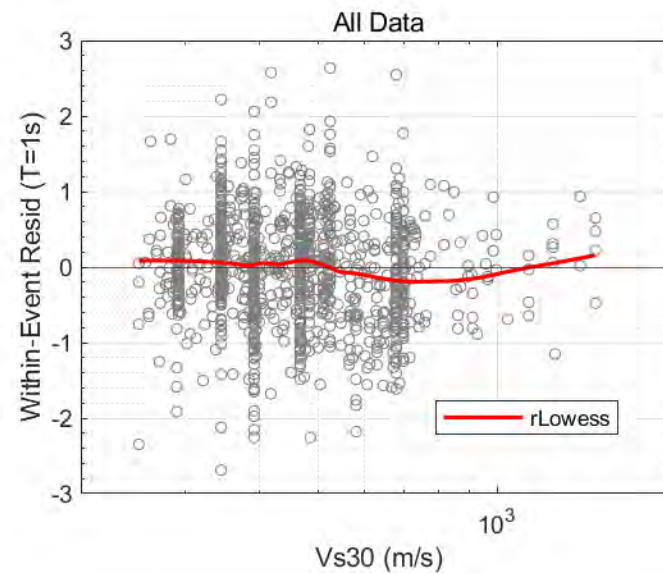
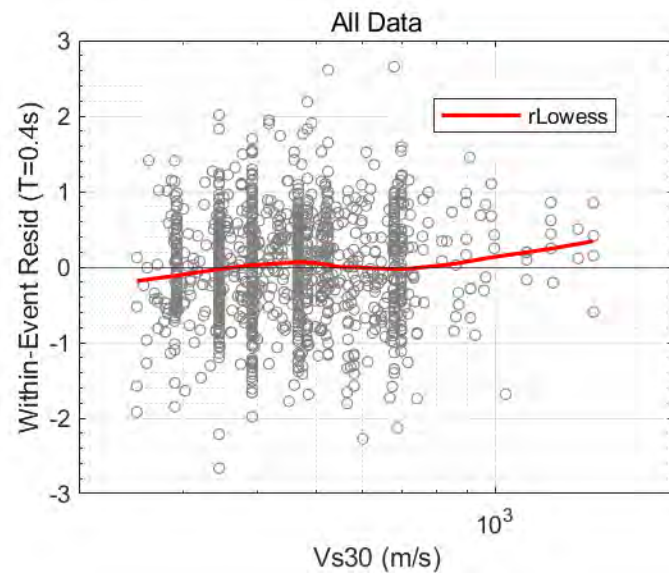
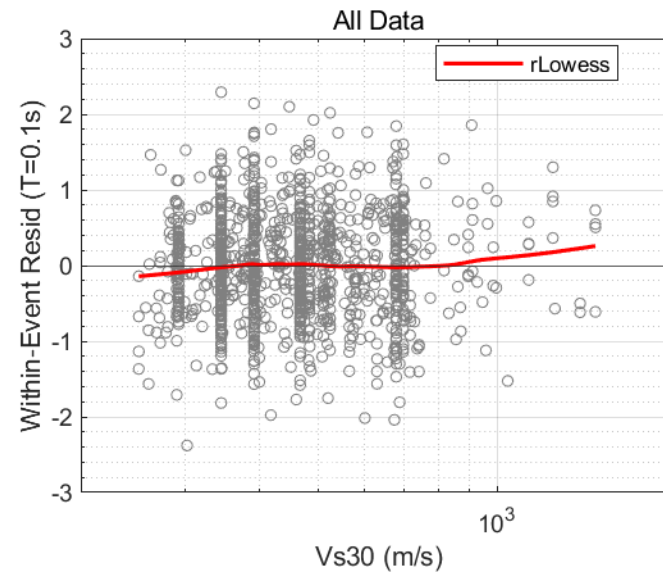
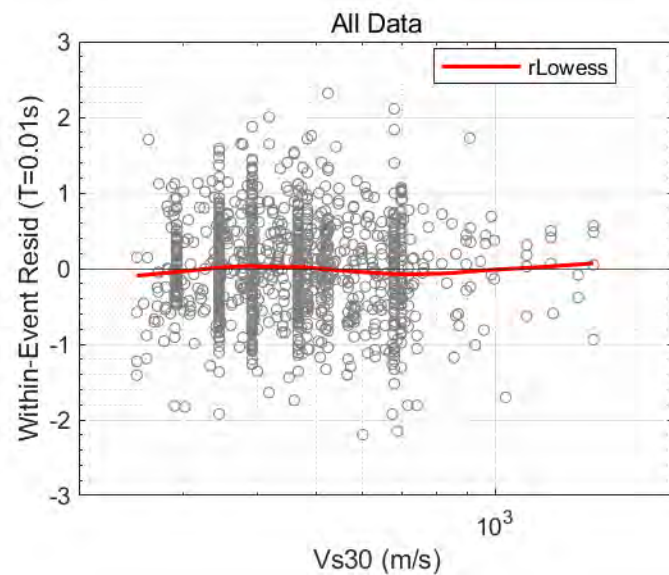
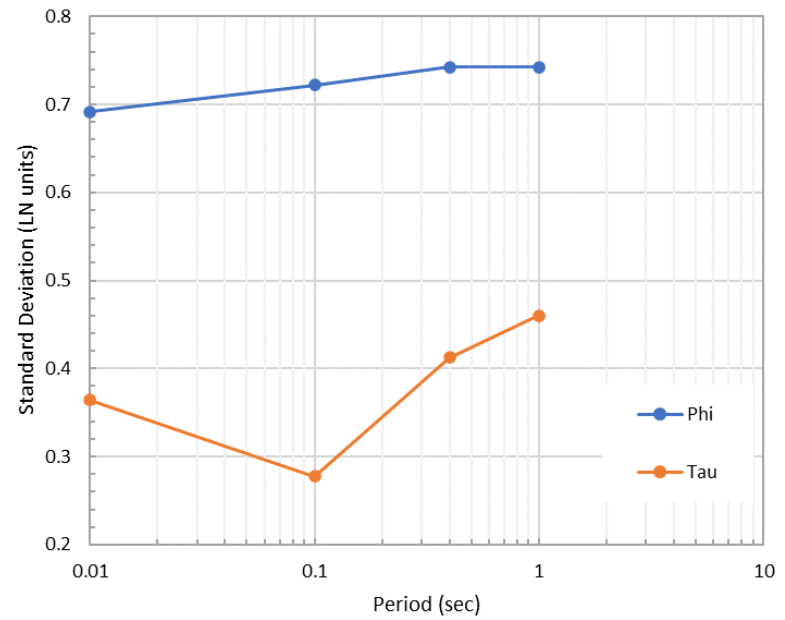
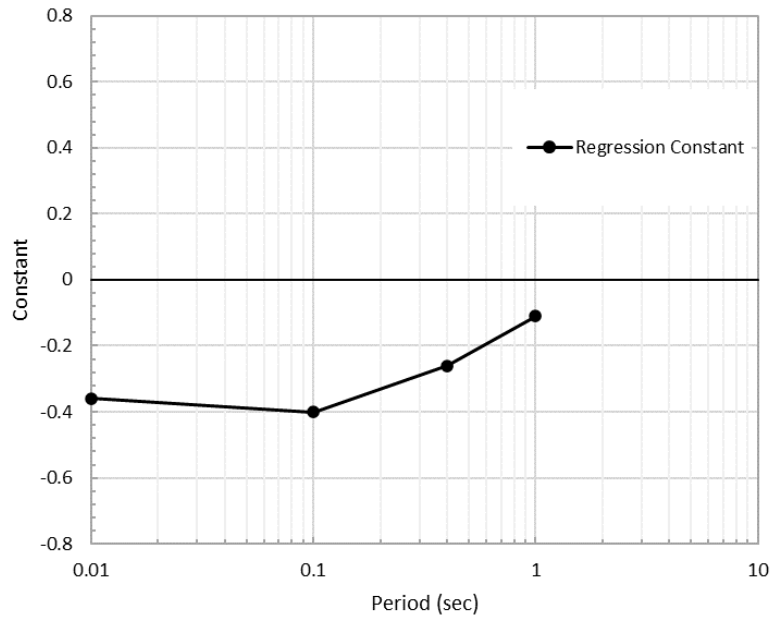
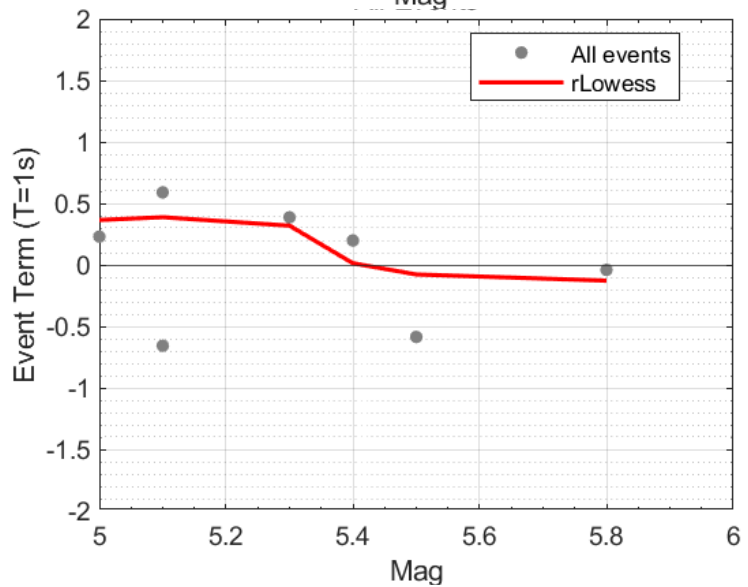
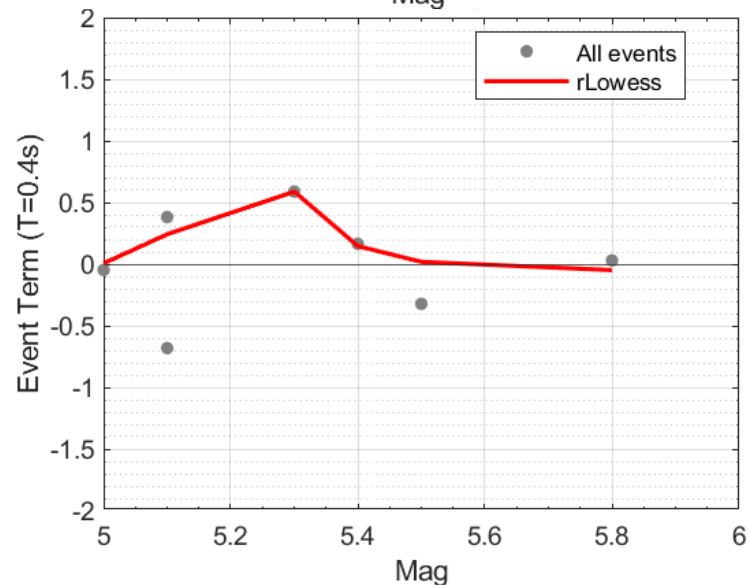
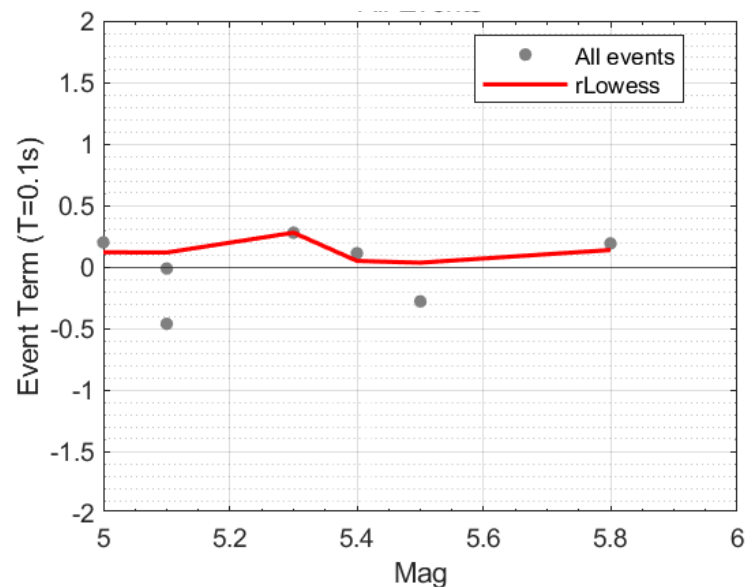
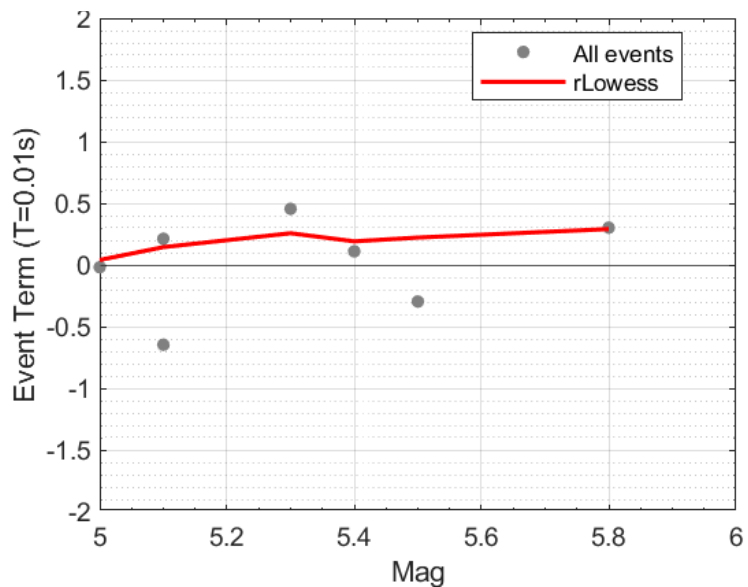


Figure 7-17. Within-event residuals of the Turkish and NGA-West3 data versus  $V_{S30}$  for periods of 0.01, 0.1, 0.4, and 1 sec. The robust Lowess fit to the data is shown in red.



**Figure 7-18. Regression constant (left) and between-event and within-event standard deviations (right) of the regression analysis of the DCPD database**





**Figure 7-19. Between-event residuals of earthquakes in the DCPD database versus magnitude for periods of 0.01, 0.1, 0.4, and 1 sec. The robust Lowess fit to the data is shown in red.**

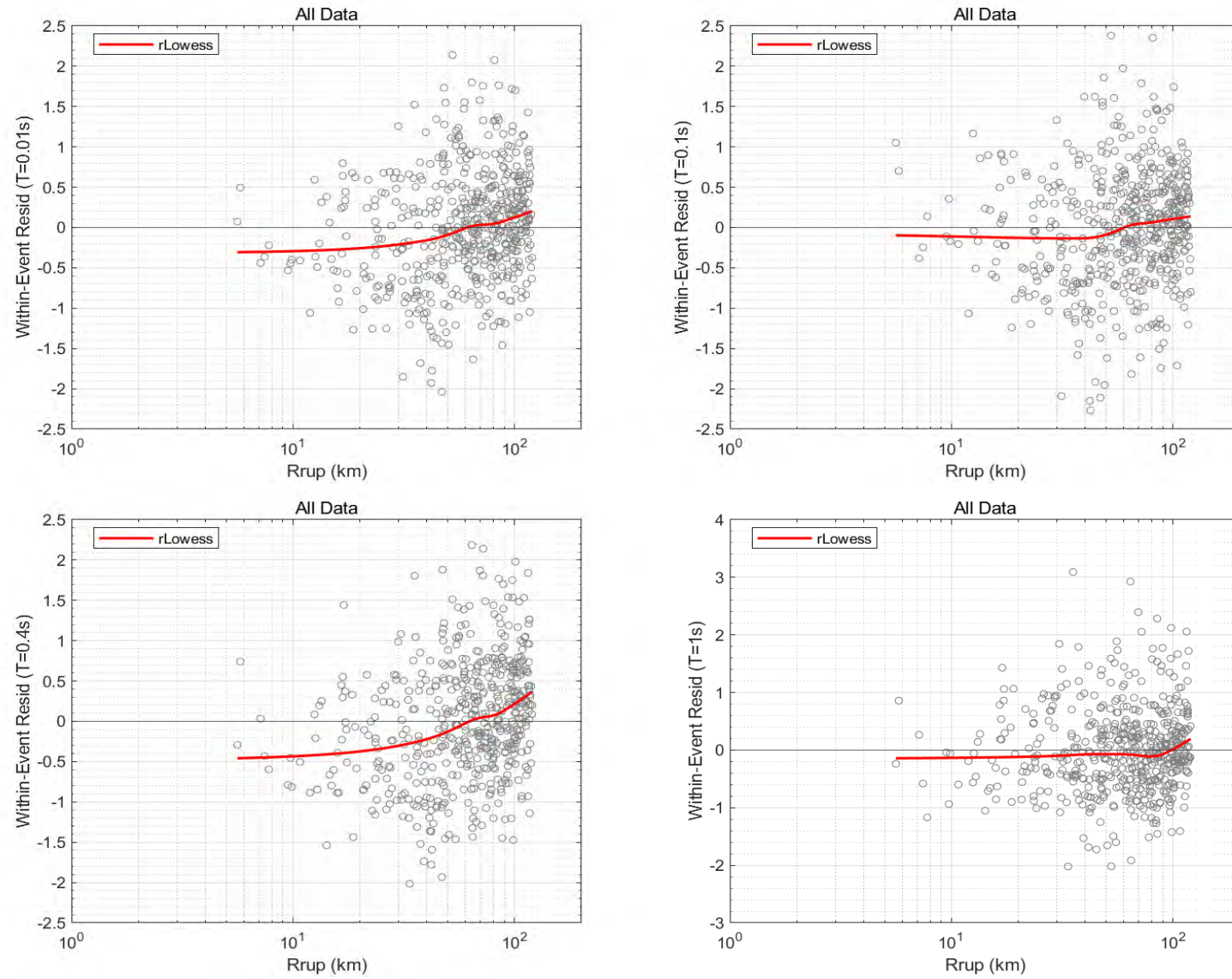


**Figure 7-20. Within-event residuals of recordings in the DCPP database versus distance for period of 0.01, 0.1, 0.4, and 1 sec. The robust Lowess fit to the data is shown in red.**

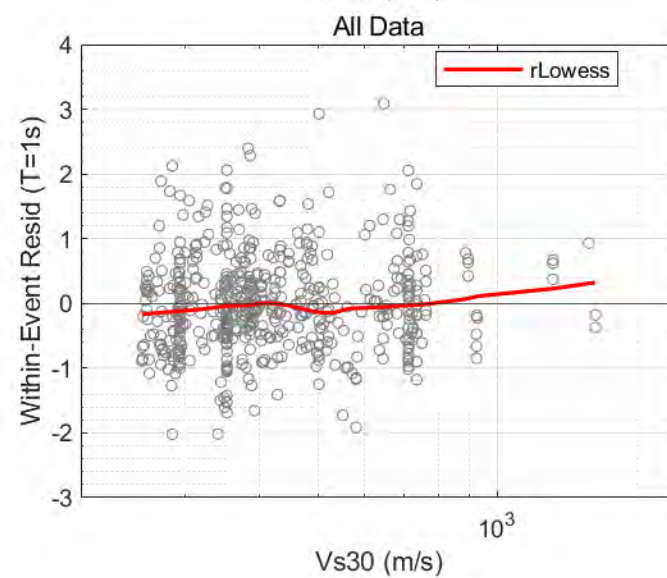
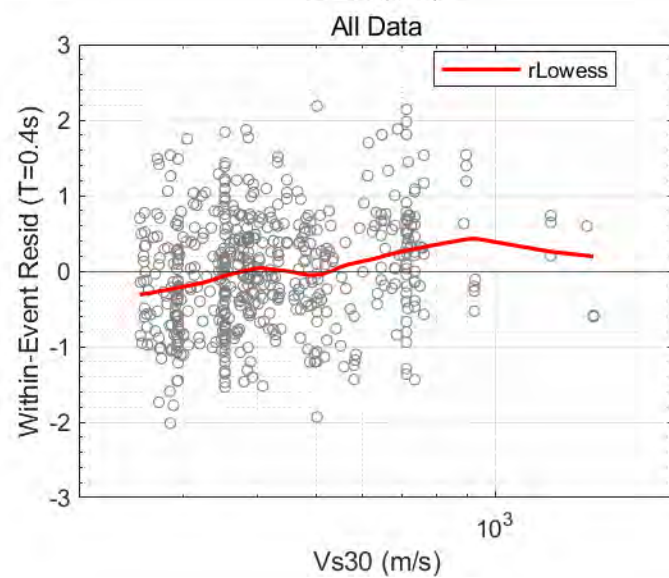
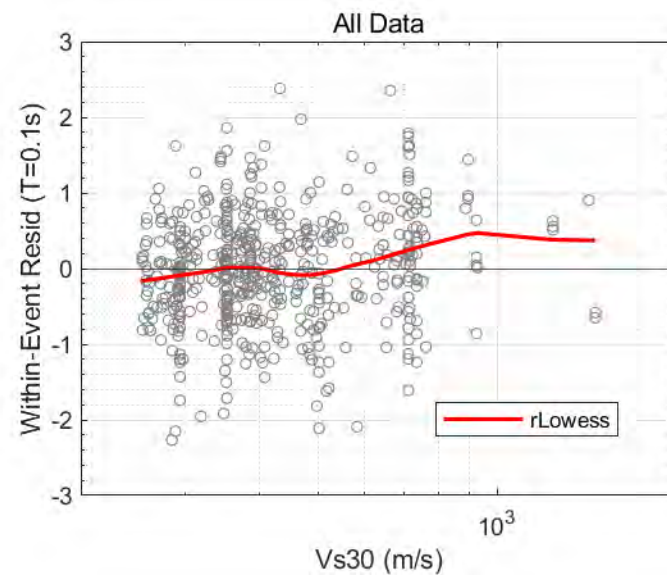
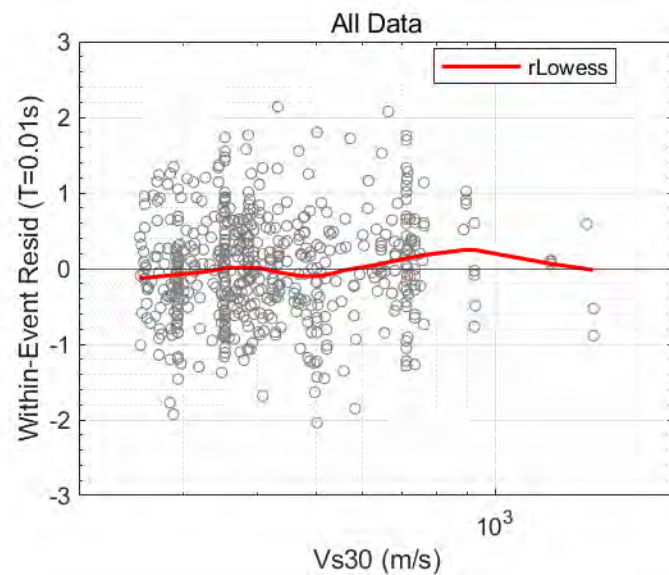


Figure 7-21. Within-event residuals of recordings in the DCPD database versus  $V_{S30}$  for periods of 0.01, 0.1, 0.4, and 1 sec. The robust Lowess fit to the data is shown in red.

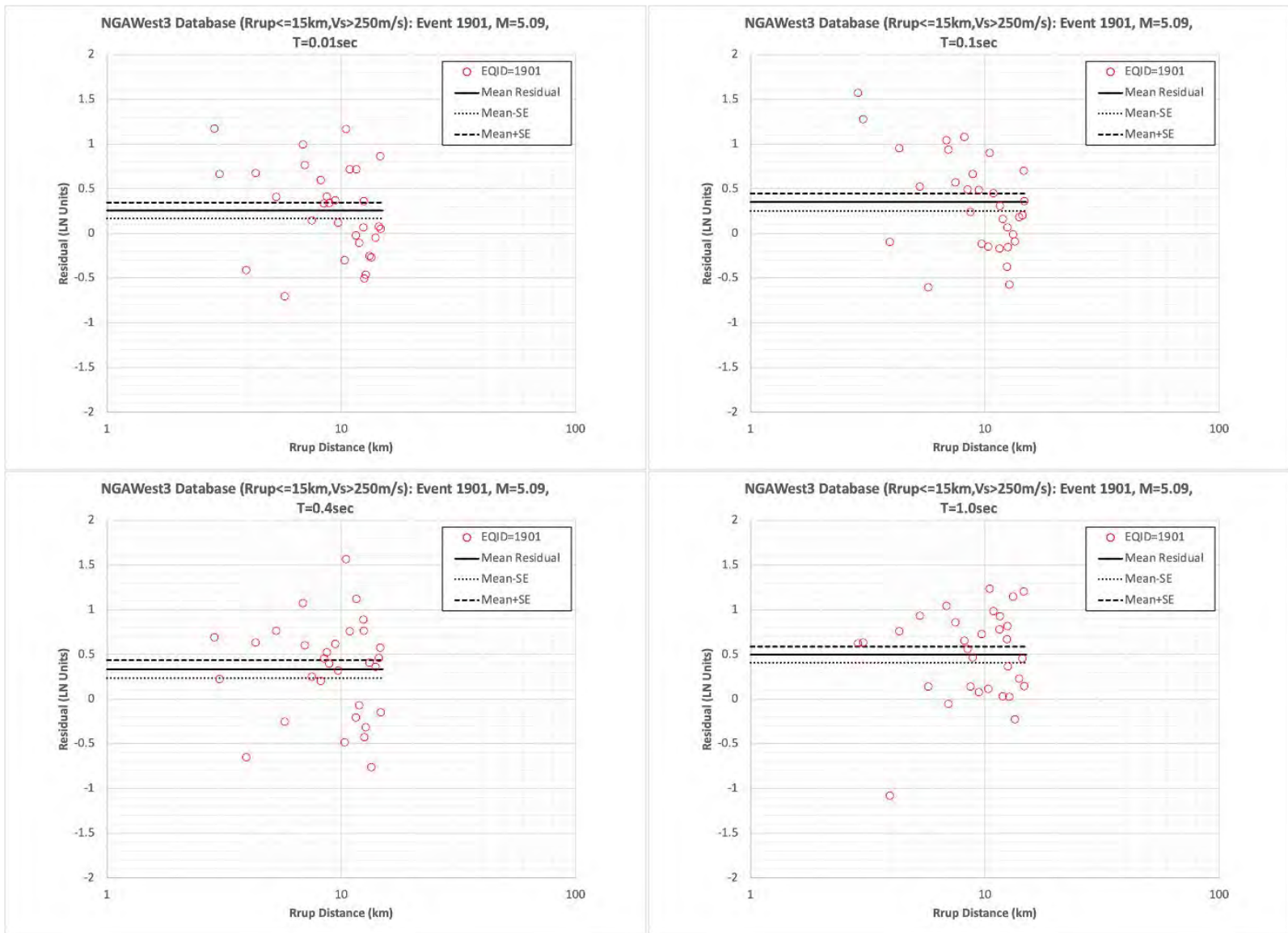


Figure 7-22. Average and plus- and minus-one standard error from the NW of Brea (M 5.09) event for the periods of 0.01, 0.1, 0.4, and 1 sec



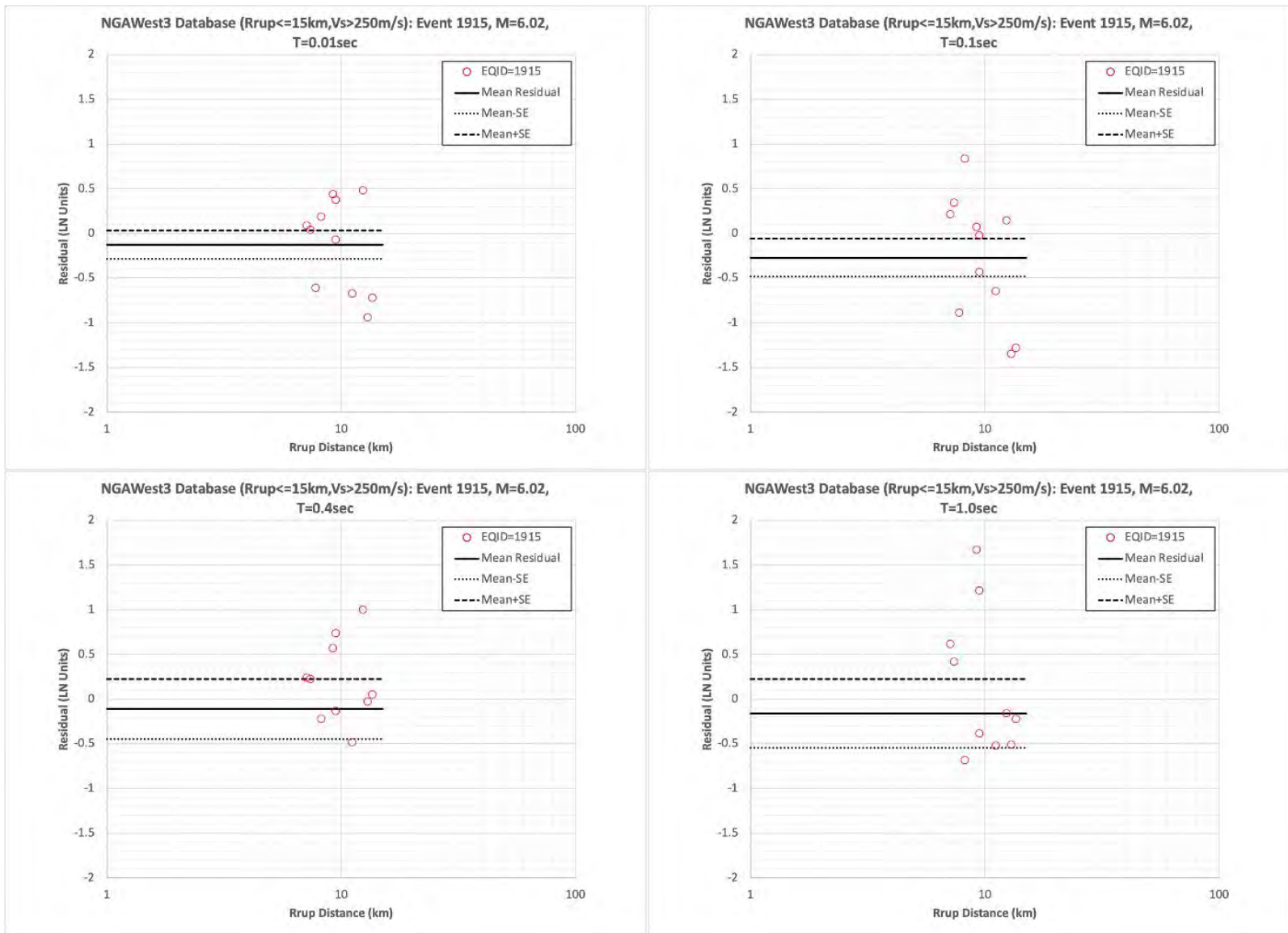


Figure 7-23. Average and plus- and minus-one standard error from the South Napa (M 6.02) event for the periods of 0.01, 0.1, 0.4, and 1 sec

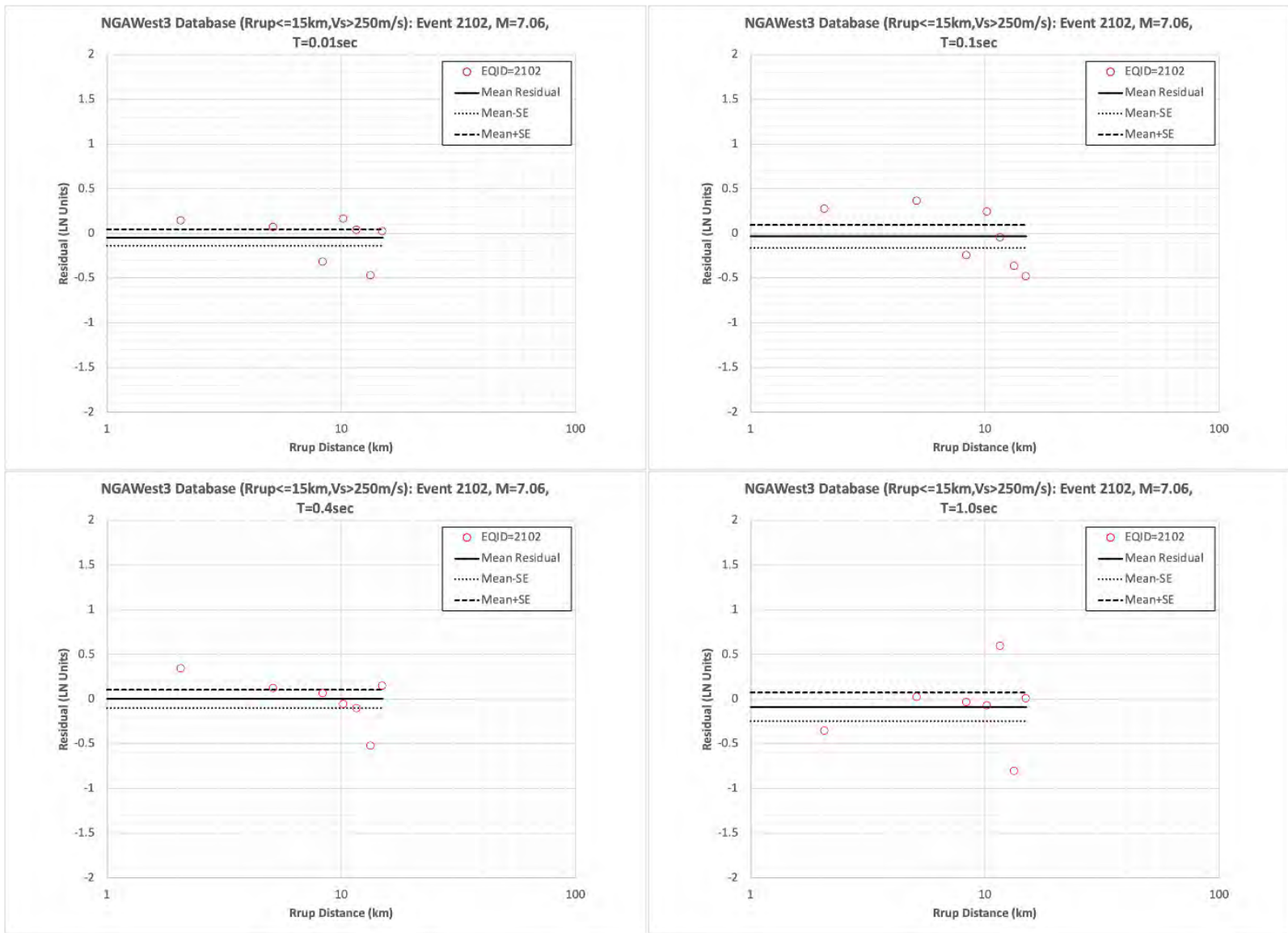
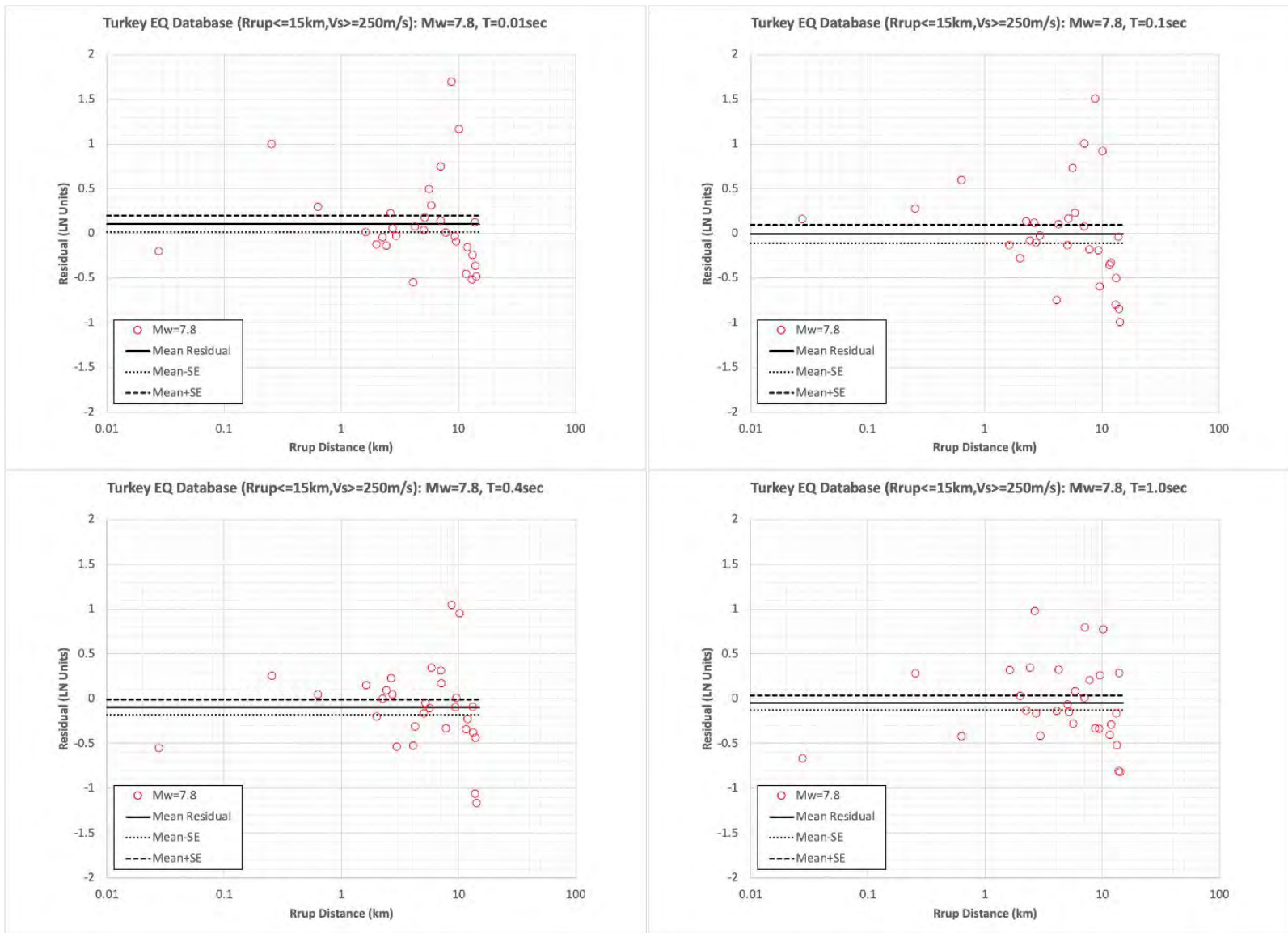
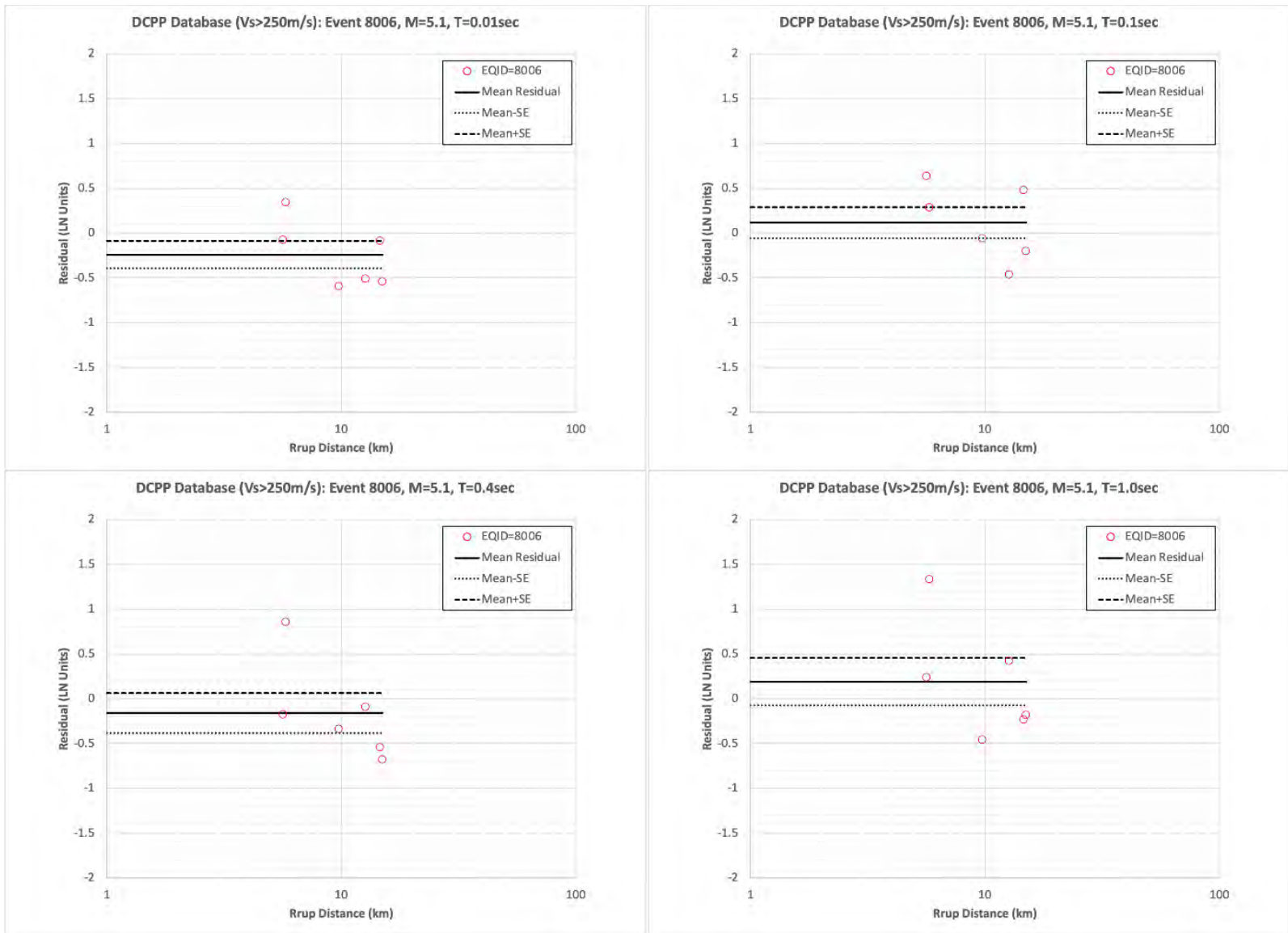


Figure 7-24. Average and plus- and minus-one standard error from the Ridgecrest Sequence (M 7.06) event for the periods of 0.01, 0.1, 0.4, and 1 sec





**Figure 7-25. Average and plus- and minus-one standard error from the Pazarcik (M 7.8) event for the periods of 0.01, 0.1, 0.4, and 1 sec**



**Figure 7-26. Average and plus- and minus-one standard error from the SE of Ojai (M 5.1) event for the periods of 0.01, 0.1, 0.4, and 1 sec**

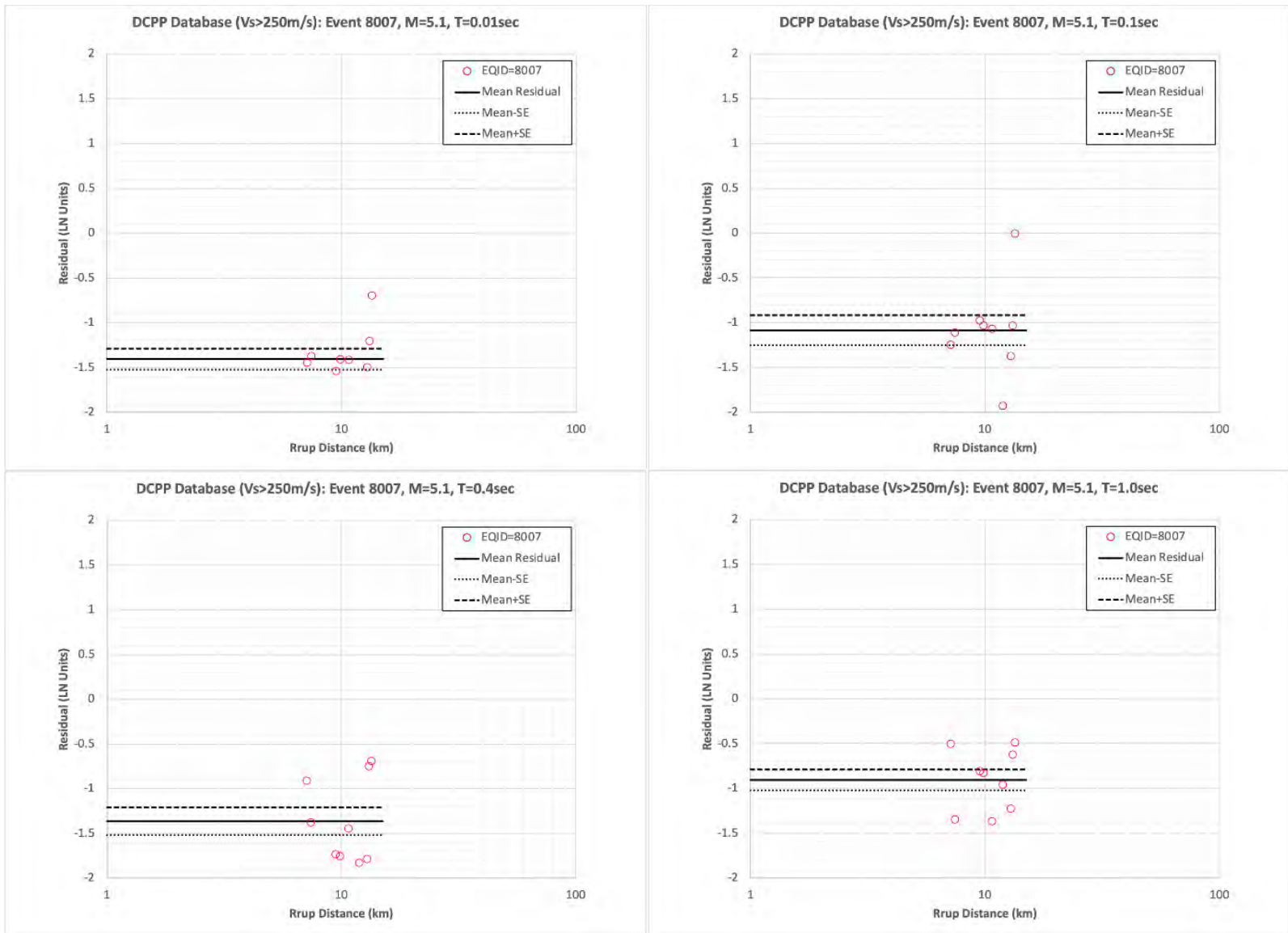
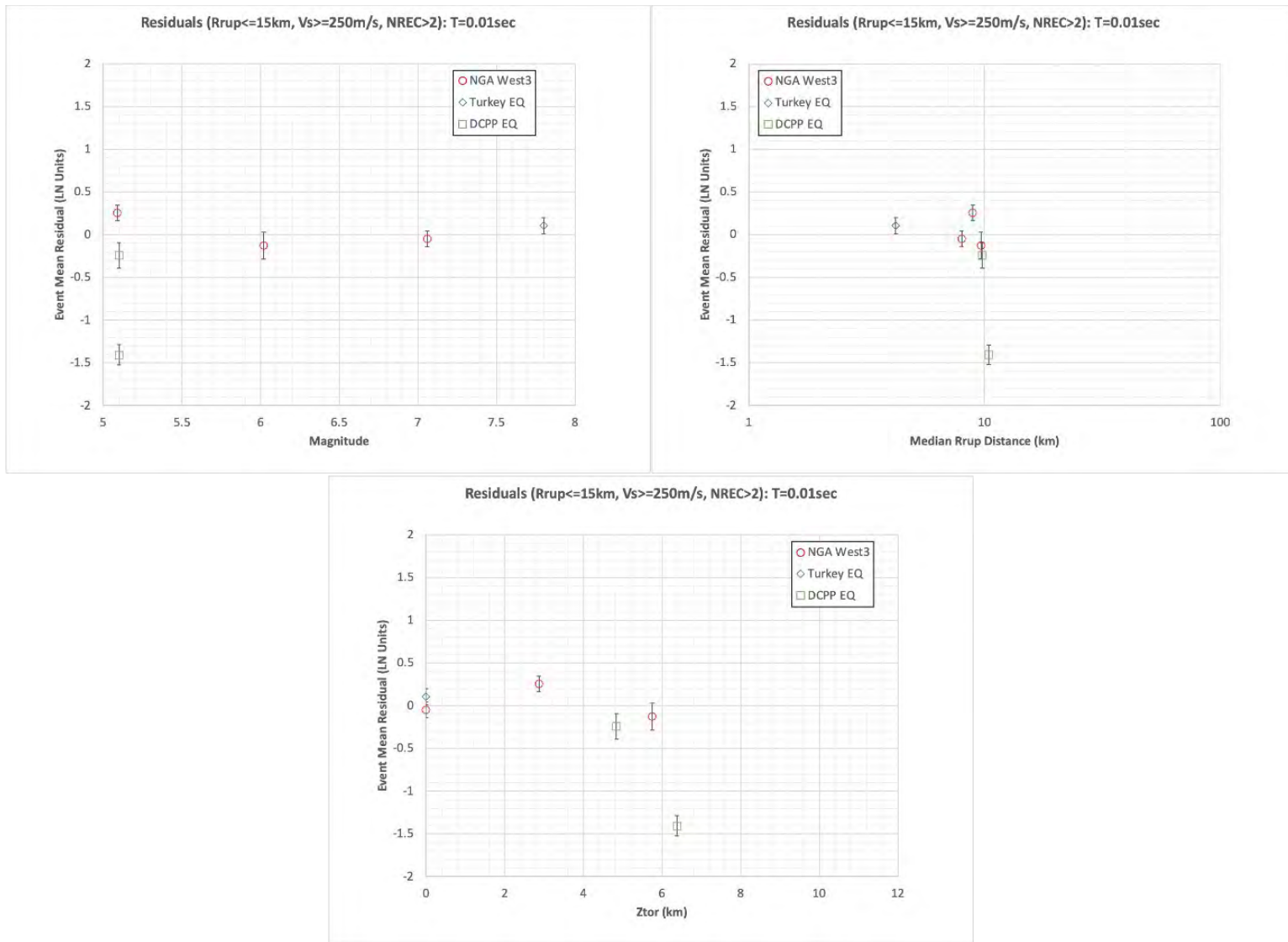
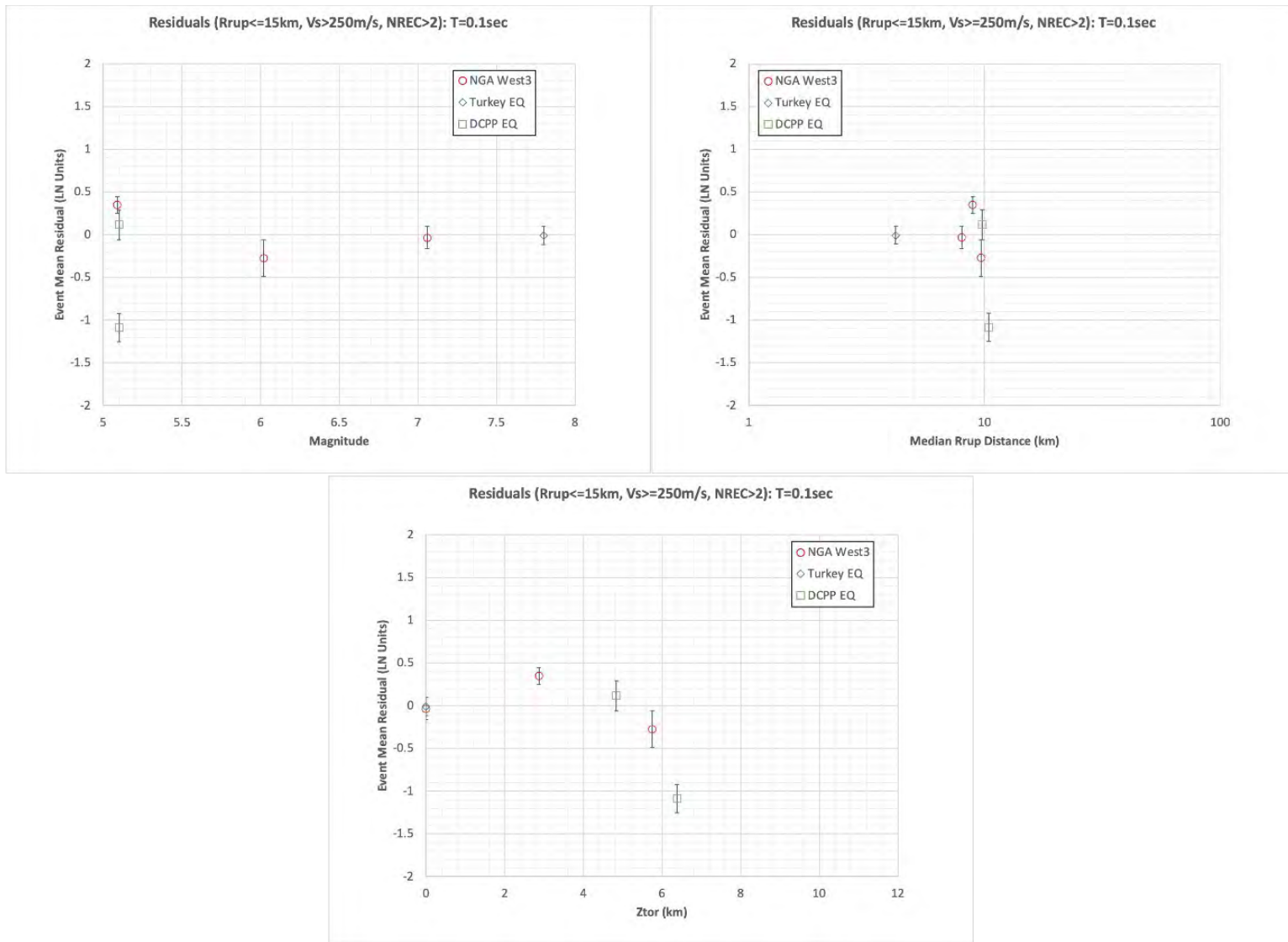


Figure 7-27. Average and plus- and minus-one standard error from the ESE of Alum Rock (M 5.1) event for the periods of 0.01, 0.1, 0.4, and 1 sec



**Figure 7-28. Average and plus- and minus-one standard error residuals for the six earthquakes evaluated from recordings with distances less than 15 km and spectral period of 0.01 sec. Upper left as a function of magnitude, upper right as a function of  $R_{RUP}$  distance, and lower center as a function of  $Z_{TOR}$ .**



**Figure 7-29. Average and plus- and minus-one standard error residuals for the six earthquakes evaluated from recordings with distances less than 15 km and spectral period of 0.1 sec. Upper left as a function of magnitude, upper right as a function of  $R_{RUP}$  distance, and lower center as a function of  $Z_{TOR}$ .**

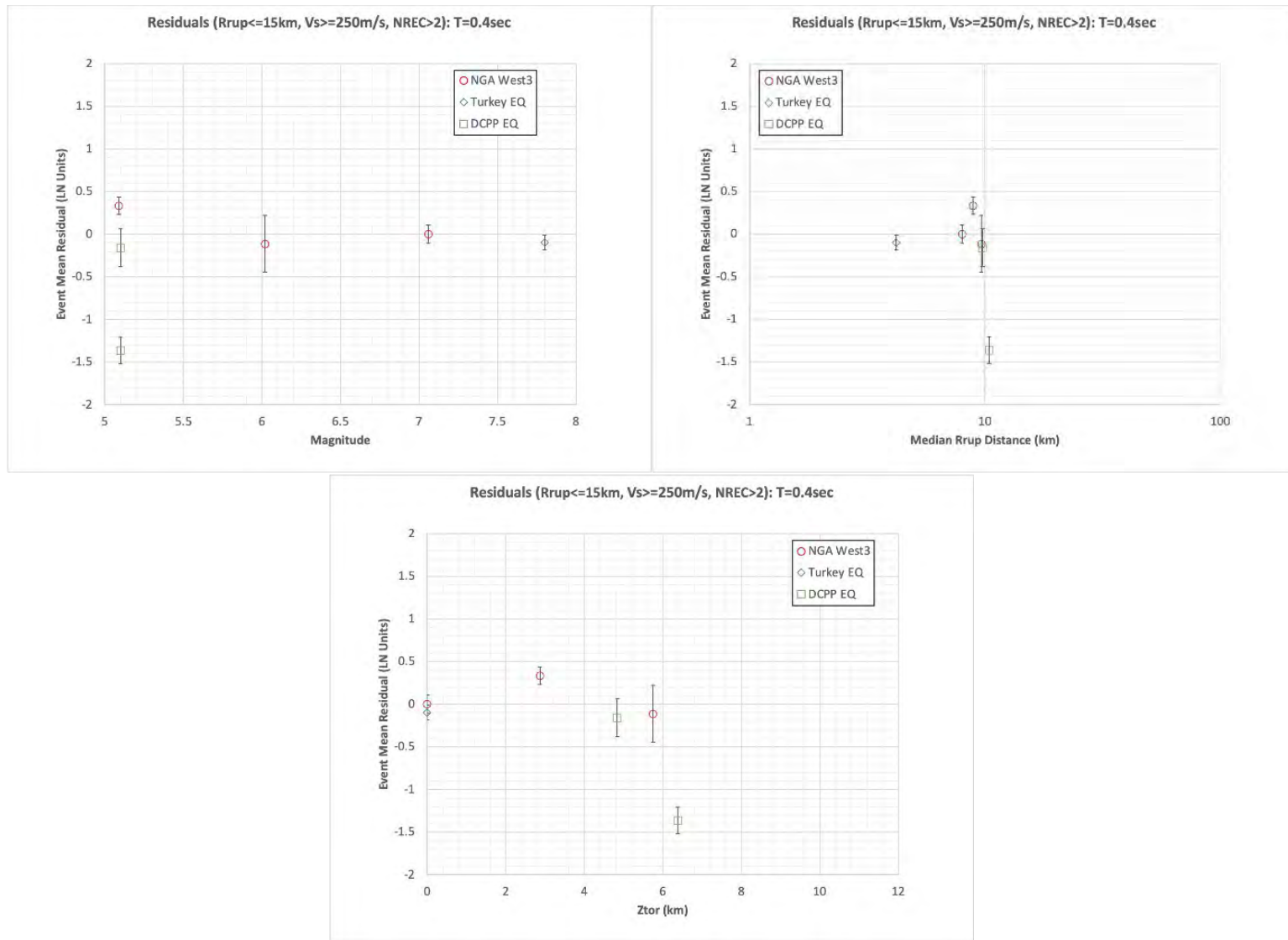


**Figure 7-30. Average and plus- and minus-one standard error residuals for the six earthquakes evaluated from recordings with distances less than 15 km and spectral period of 0.4 sec. Upper left as a function of magnitude, upper right as a function of  $R_{RUP}$  distance, and lower center as a function of  $Z_{TOR}$ .**



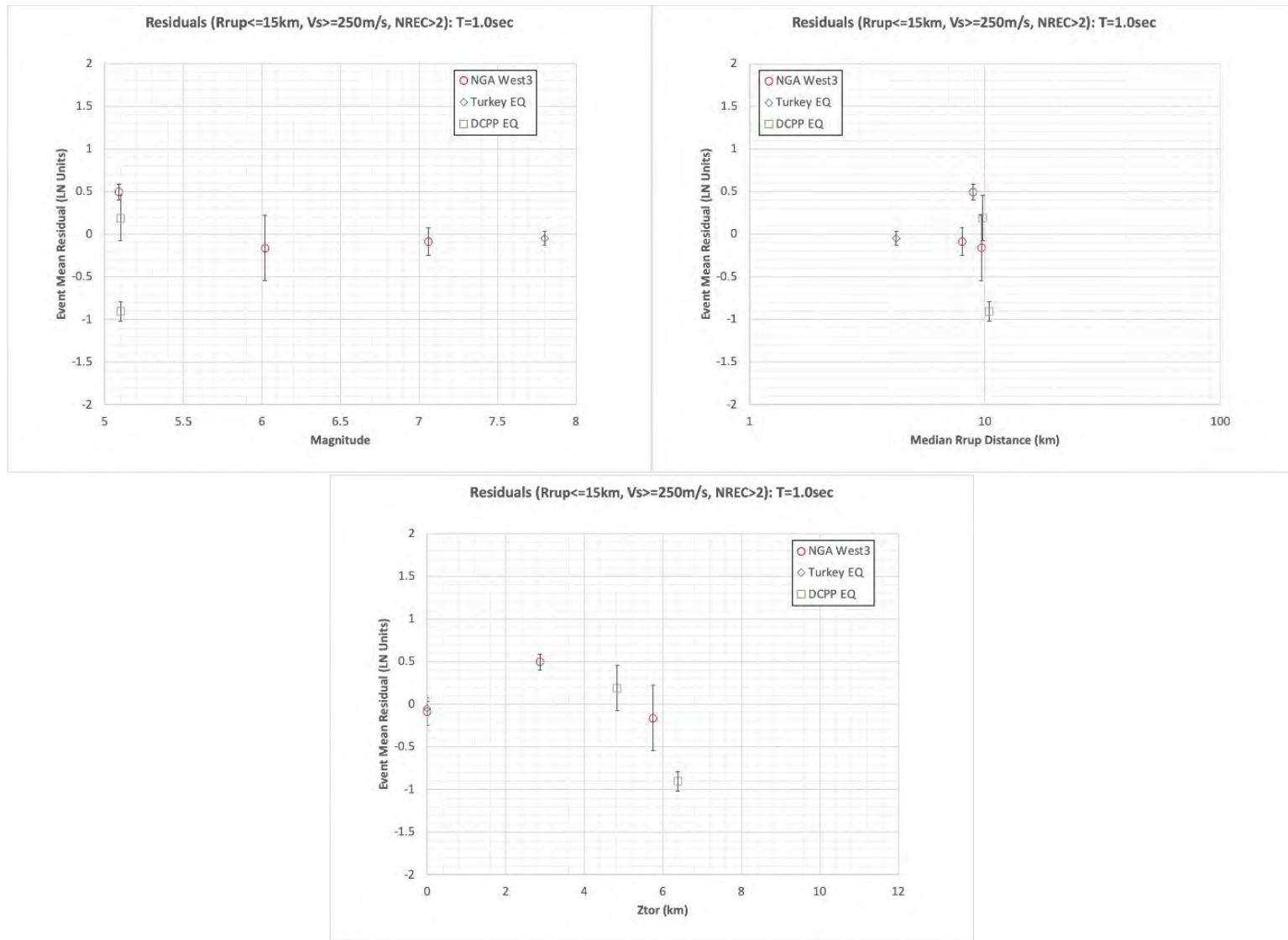


**Figure 7-31. Average and plus- and minus-one standard error residuals for the six earthquakes evaluated from recordings with distances less than 15 km and spectral period of 1.0 sec. Upper left as a function of magnitude, upper right as a function of  $R_{RUP}$  distance, and lower center as a function of  $Z_{TOR}$ .**

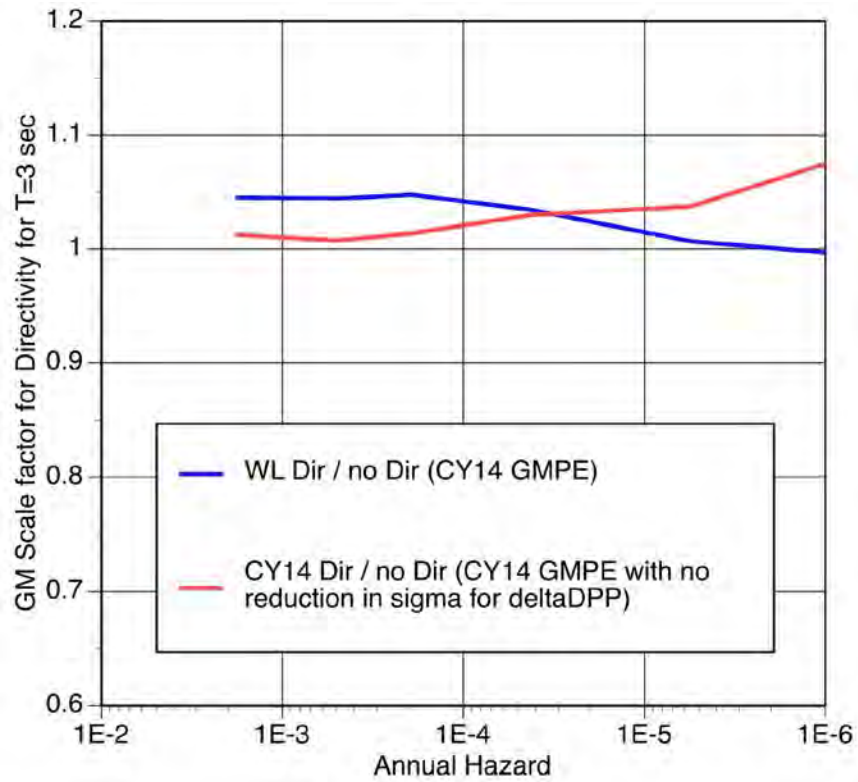


**Figure 7-32. Probabilistic sensitivity analysis of the directivity adjustments to the ground motion at DCP from the Hosgri fault at period of 3 sec. Directivity implementations of Chiou and Youngs (CY14, 2014) and Watson-Lamprey (WL, 2015) are shown (from GeoPentech, 2015, Figure 6.5.2-3).**

### M7, Strike-Slip

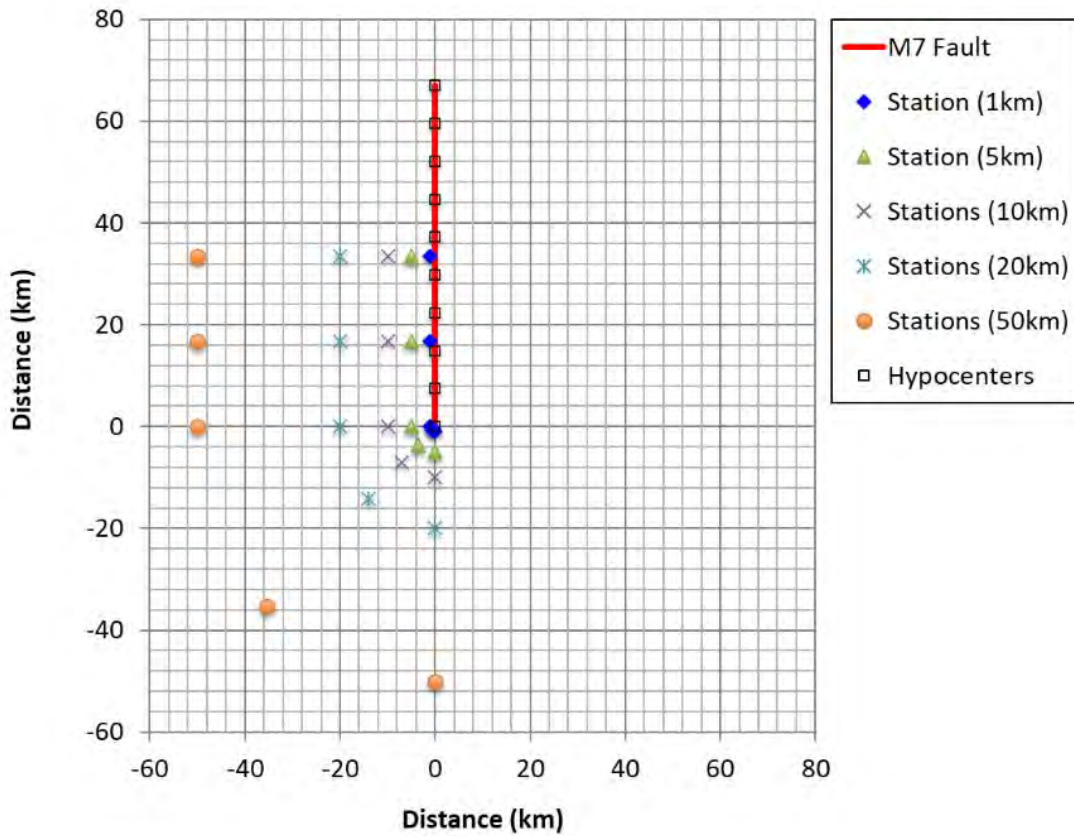


**Figure 7-33. Fault trace (red line), epicentral locations of the hypocenters, and station locations for a simplified strike-slip M 7.0 earthquake rupture. Sites A are located off the end of the fault, Sites B are located at 45° off the end of the fault, Sites C are perpendicular to the end of the fault, Sites D are perpendicular to  $\frac{3}{4}$  of the fault, and Sites E are perpendicular to the middle of the fault (from Al Atik et al., 2023).**

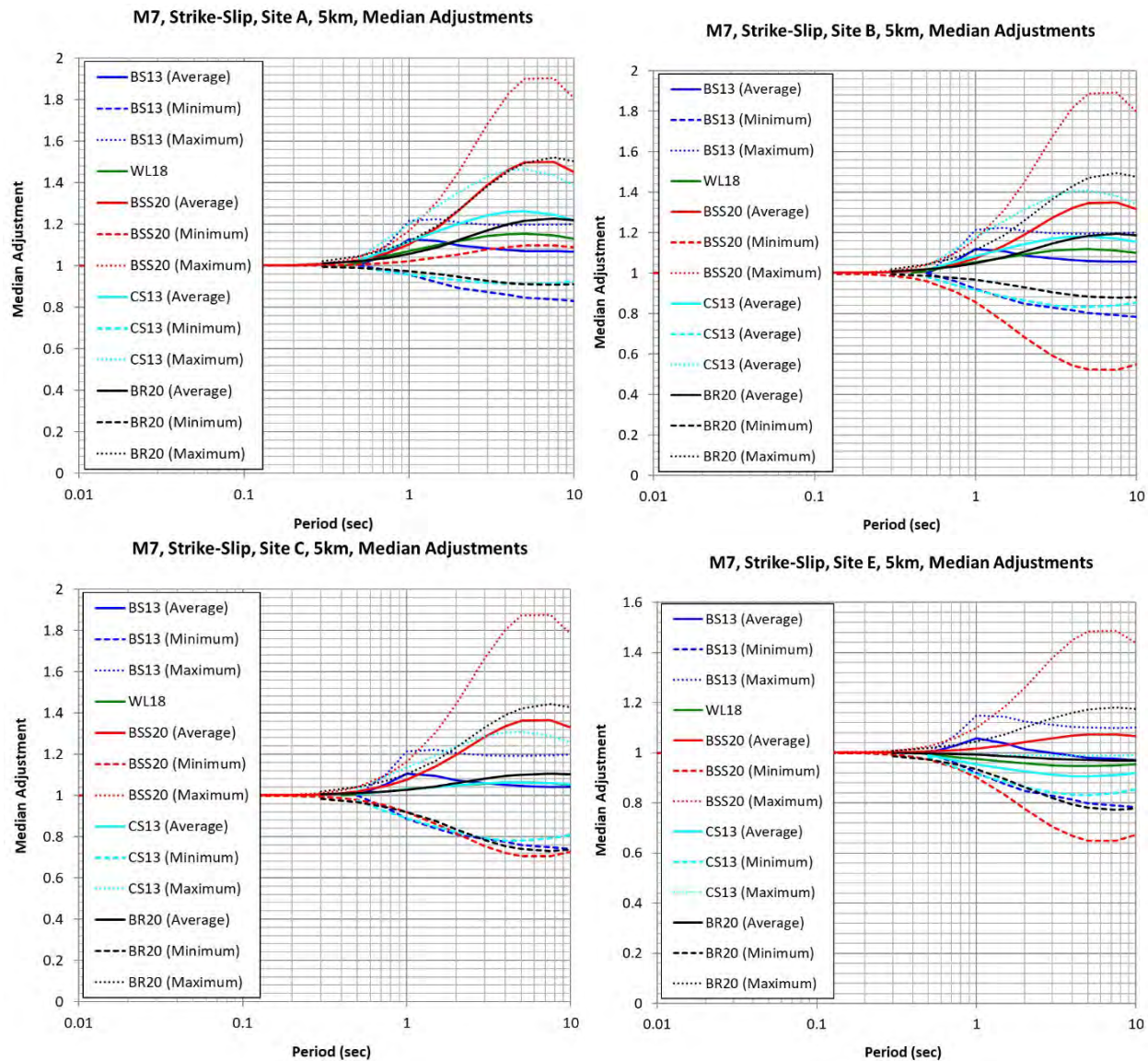
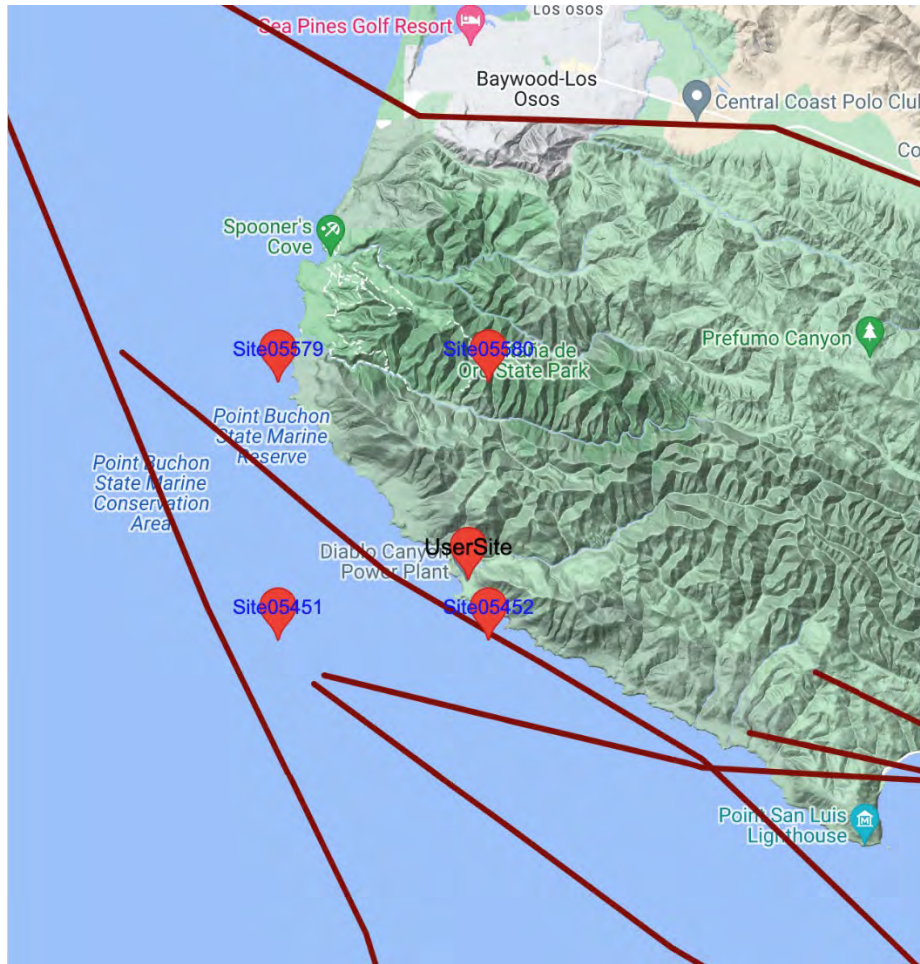
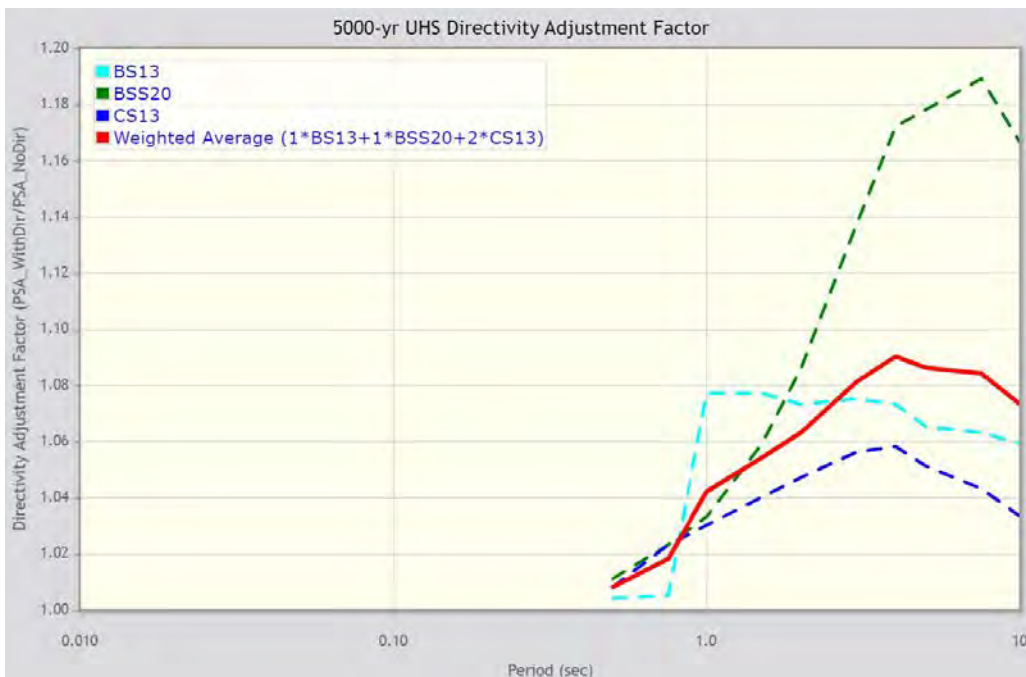
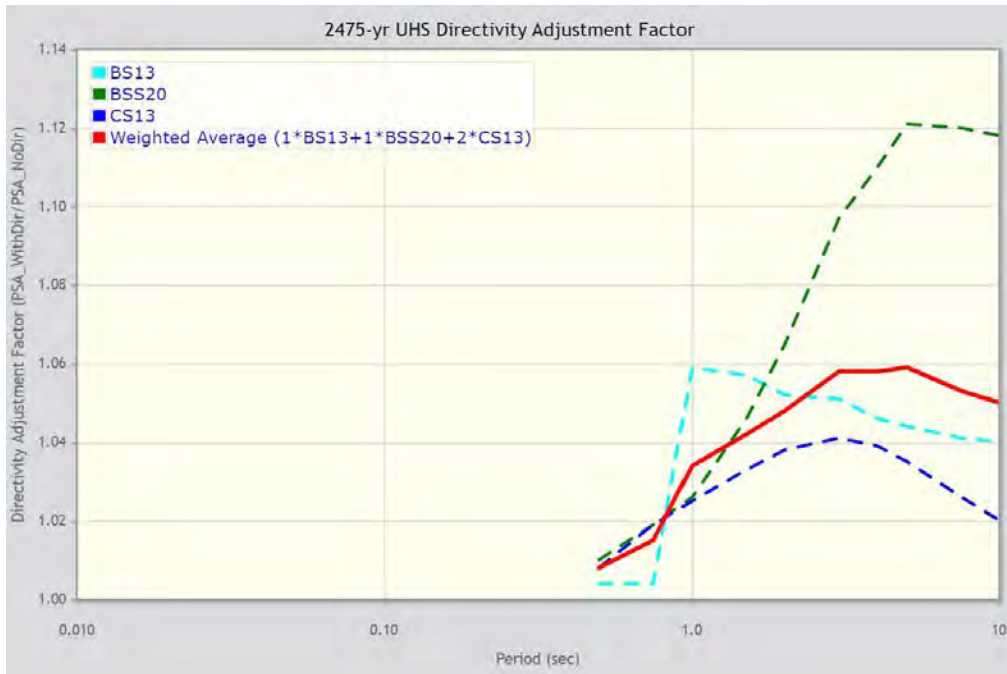


Figure 7-34. Estimated directivity median adjustment factors for a M 7.0 strike-slip case from the BS13, WL18, BSS20, CS13, and BR20 models for Sites A, B, C, and E at a rupture distance of 5 km (from Al Atik et al., 2023).





**Figure 7-35. Location of the DCPP site (labeled “user site”) and the four neighboring sites used to interpolate the probabilistic directivity adjustment factors at DCPP (from Mazzoni et al., 2023). Fault traces are shown in red.**



**Figure 7-36. Probabilistic ground-motion directivity adjustment factors versus spectral periods at the DCPD site for return period of 2,475 yr (top) and 5,000 yr (bottom) (from Mazzoni et al., 2023)**



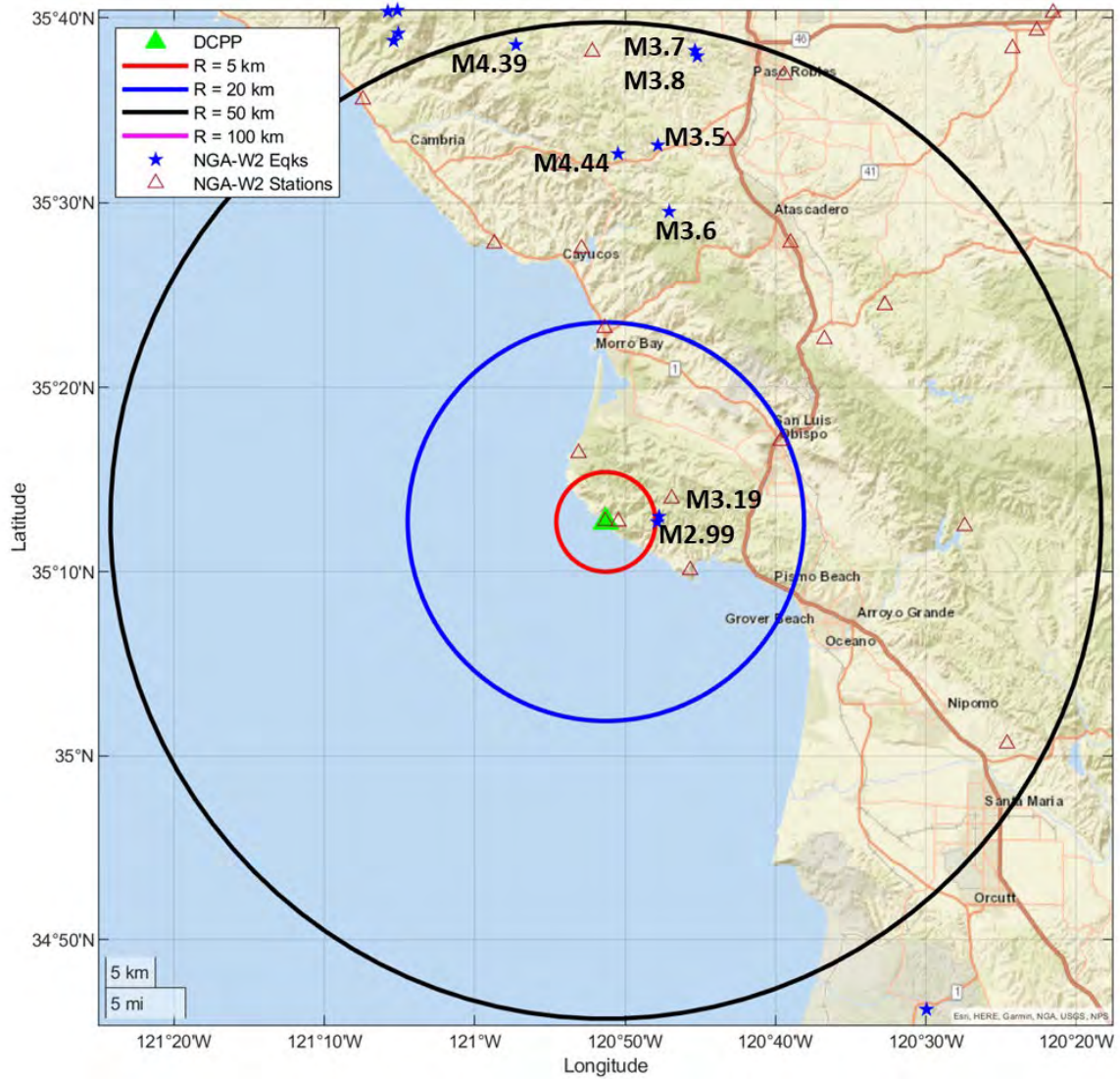


Figure 7-37. Earthquakes and stations in the NGA-West2 database within 50 km of DCP

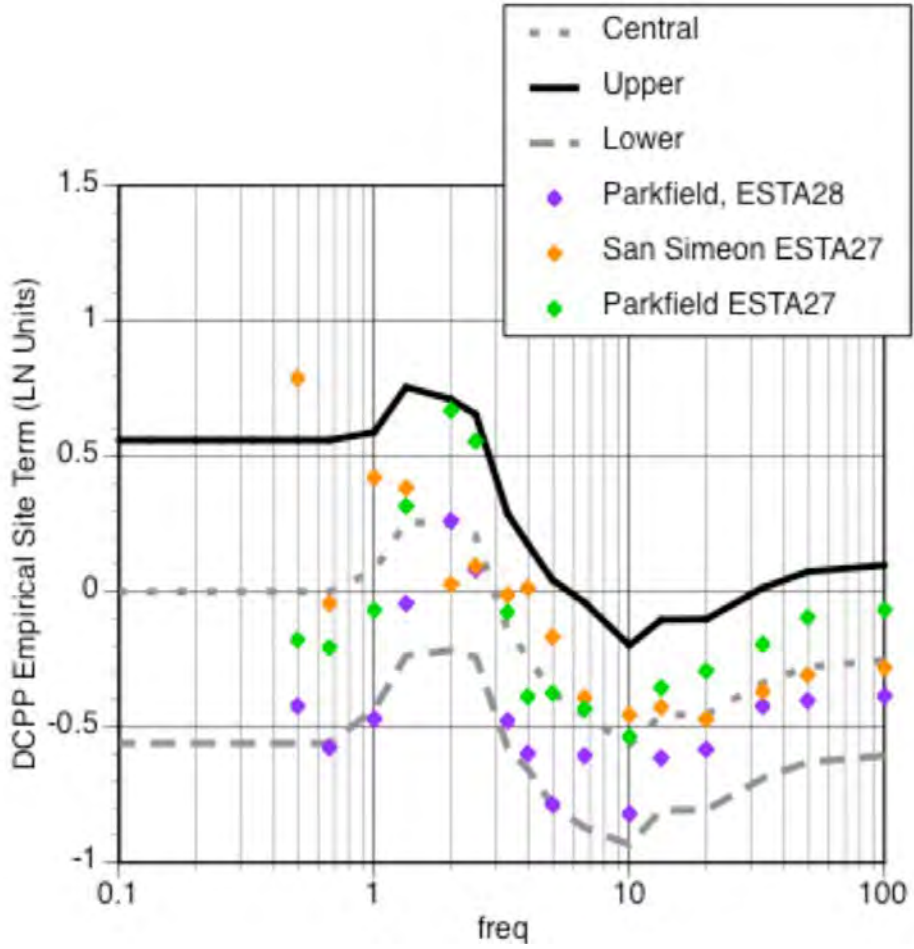
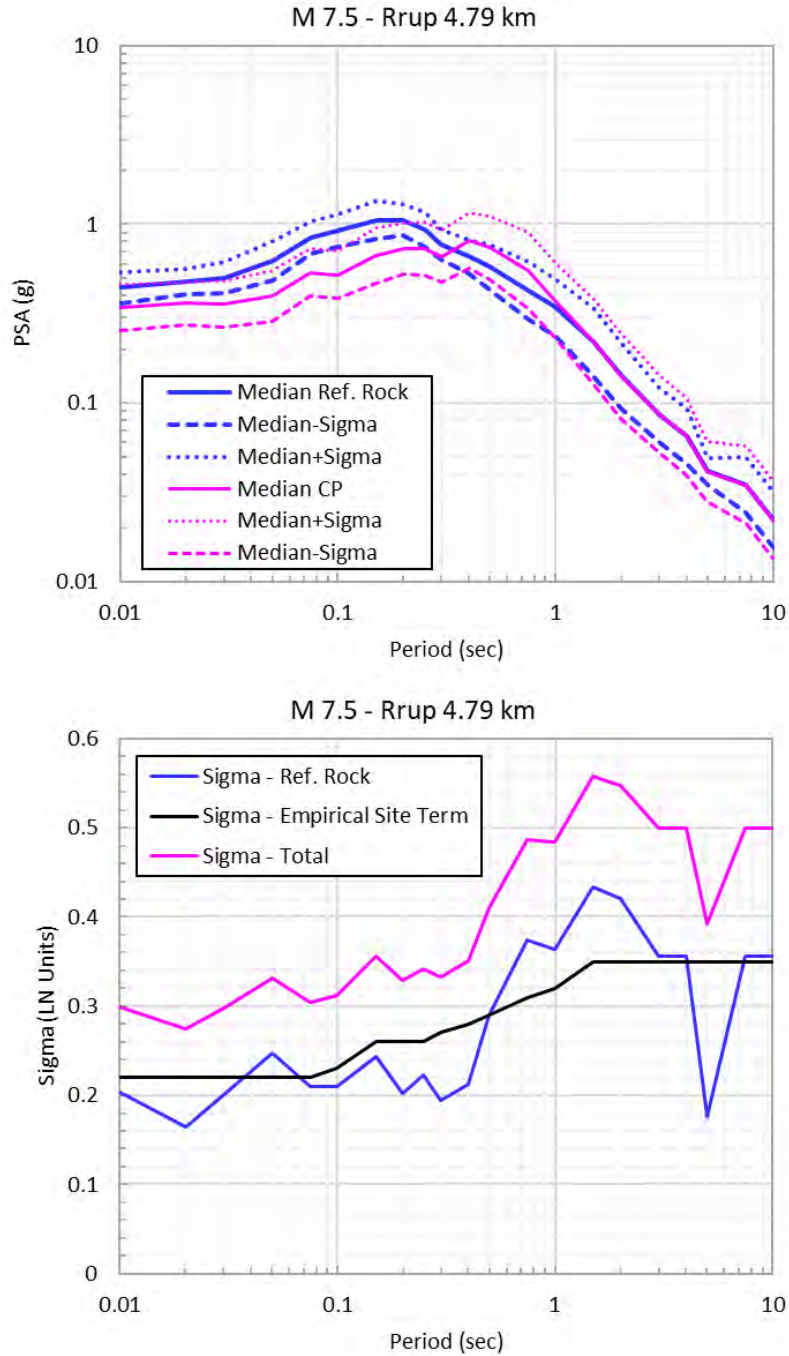
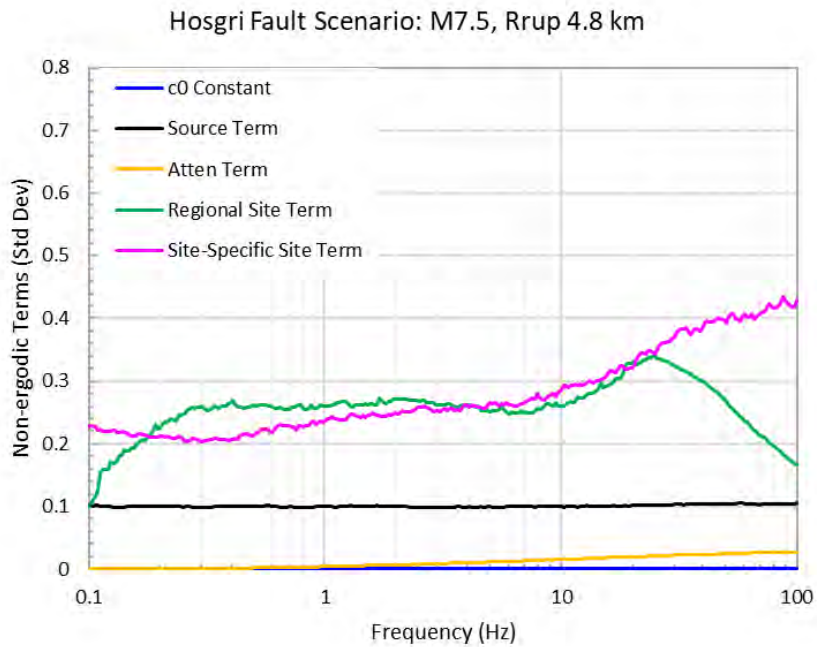
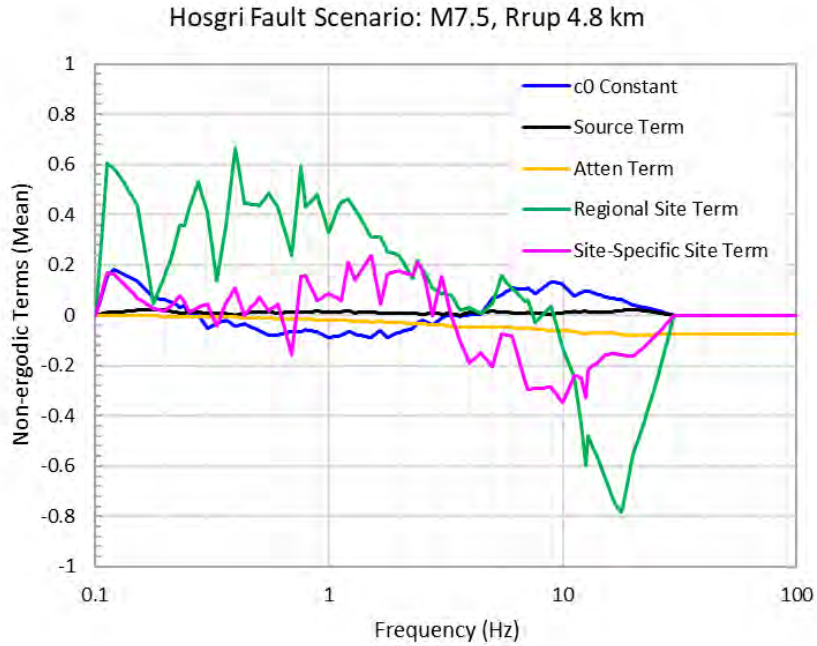


Figure 7-38. DCPD empirical site adjustment factors (from PG&E, 2017b)



**Figure 7-39. Top: Median predicted response spectra for the Hosgri fault scenario for the reference rock model (Ref. Rock) and site-specific conditions at DCPP (CP). Bottom: Epistemic uncertainty standard deviation of the DCPP median ground-motion model.**



**Figure 7-40. Non-ergodic EAS adjustments at DCPD in LN units for the Hosgri fault scenario based on the LAK21 model. The mean (top) and standard deviation (bottom) of the adjustments over 1000 drawn samples are shown.**

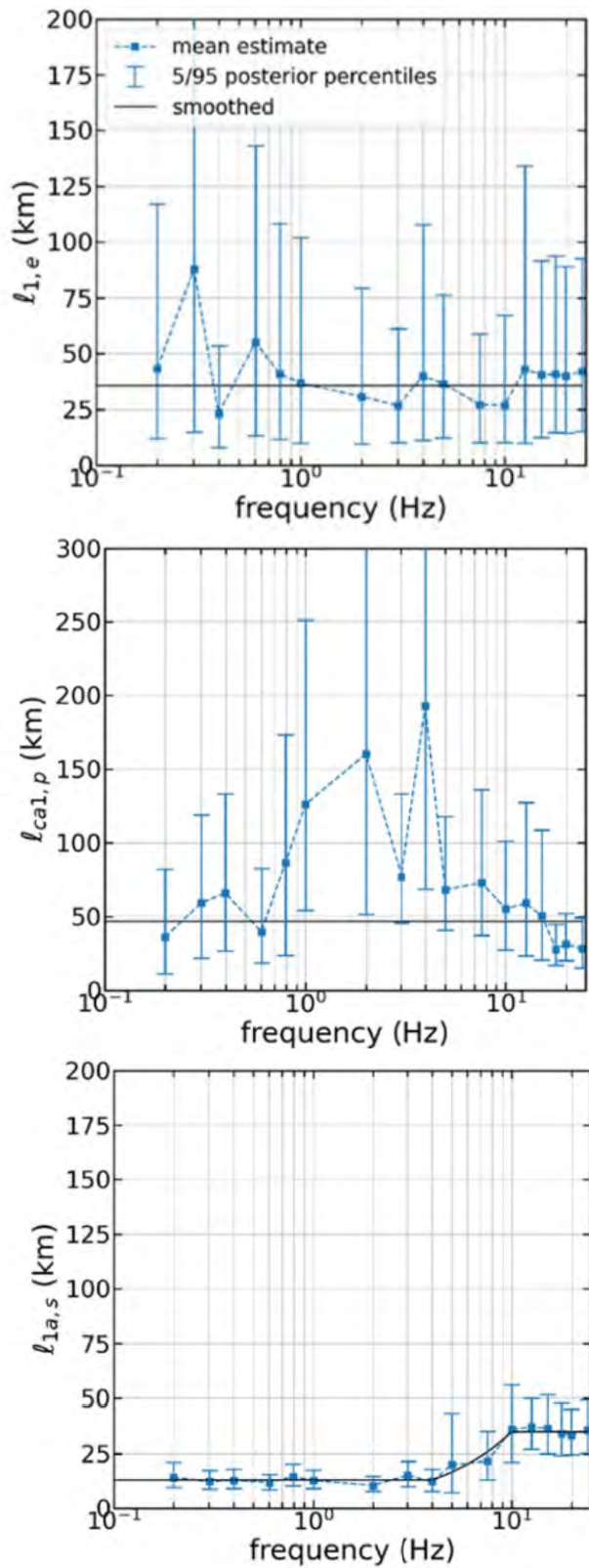
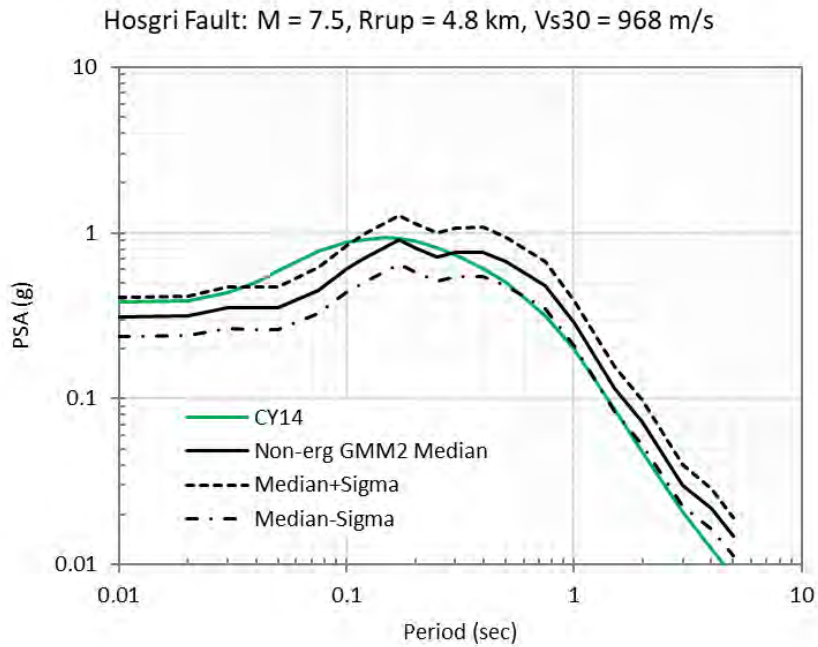
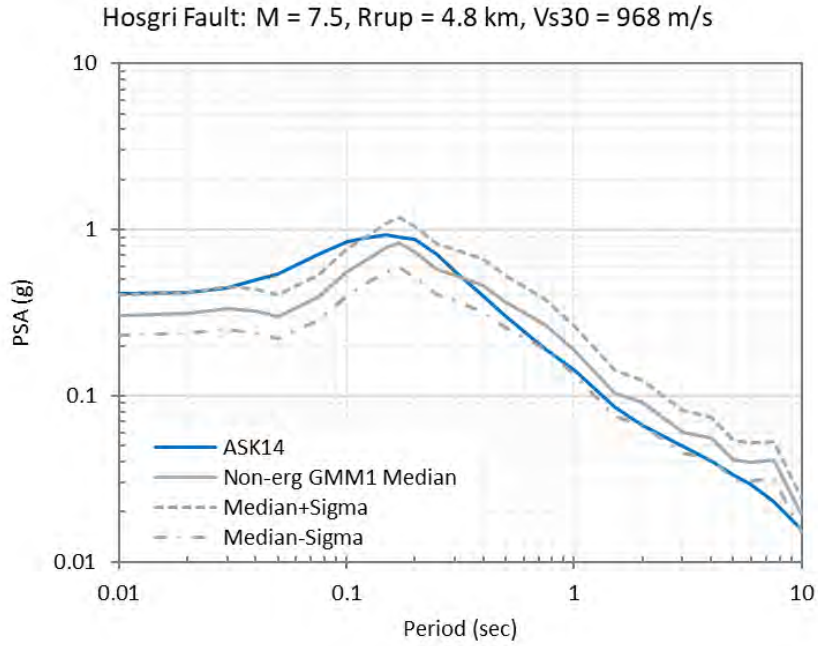


Figure 7-41. Correlation length of the source term ( $\ell_{1,e}$ ), anelastic attenuation term ( $\ell_{ca1,p}$ ), and regional site term ( $\ell_{1a,s}$ ) in the LAK21 model (from Lavrentiadis et al., 2023)





**Figure 7-42. Comparison of predicted median ground motion at DCP for the Hosgri fault scenario for ASK14 and LA23 non-ergodic model 1 (top) and CY14 and LA23 non-ergodic model 2 (bottom)**



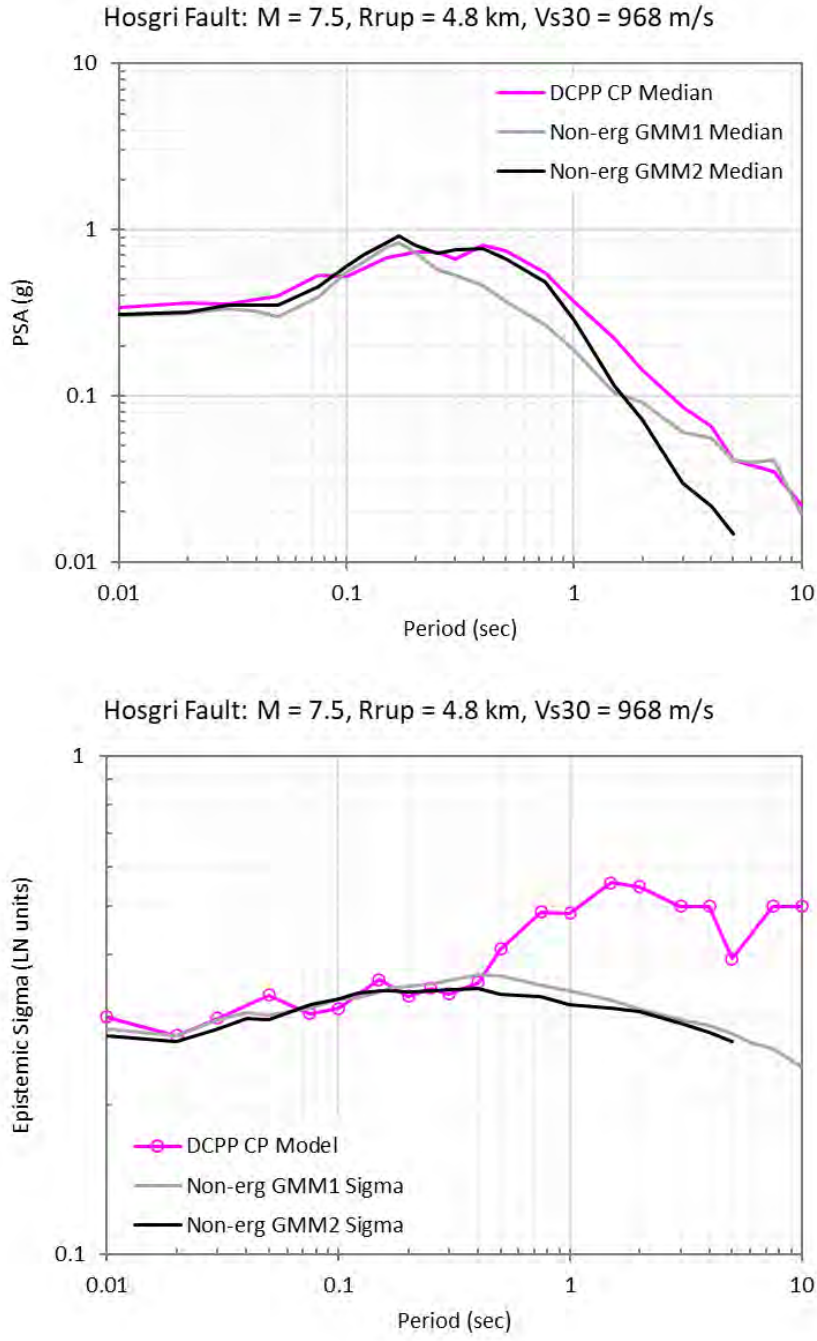


**Figure 7-43. Comparison of predicted median ground motion at the control point at DCP for the Hosgri fault scenario for the DCP model and the LA23 non-ergodic models (top) and of epistemic sigma for the DCP and the LA23 models (bottom)**

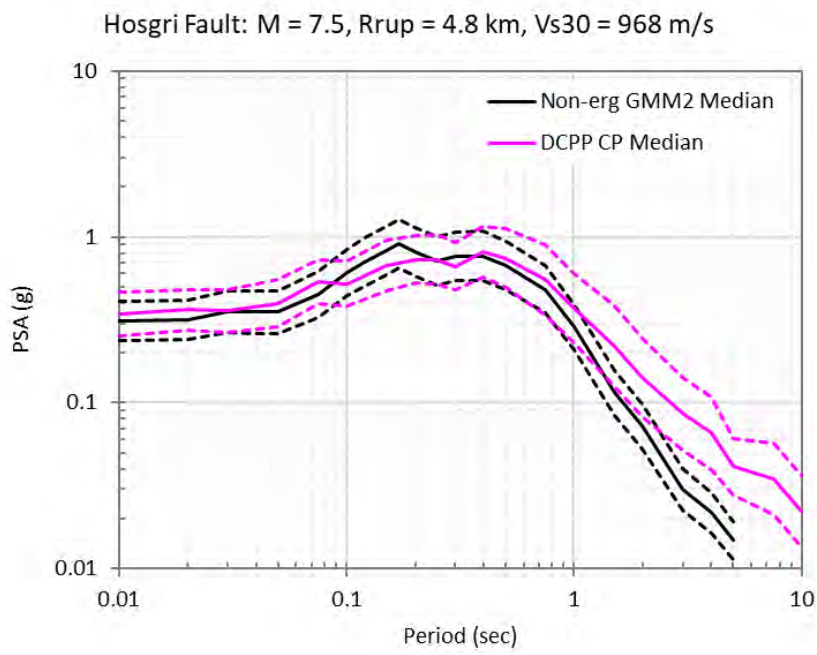
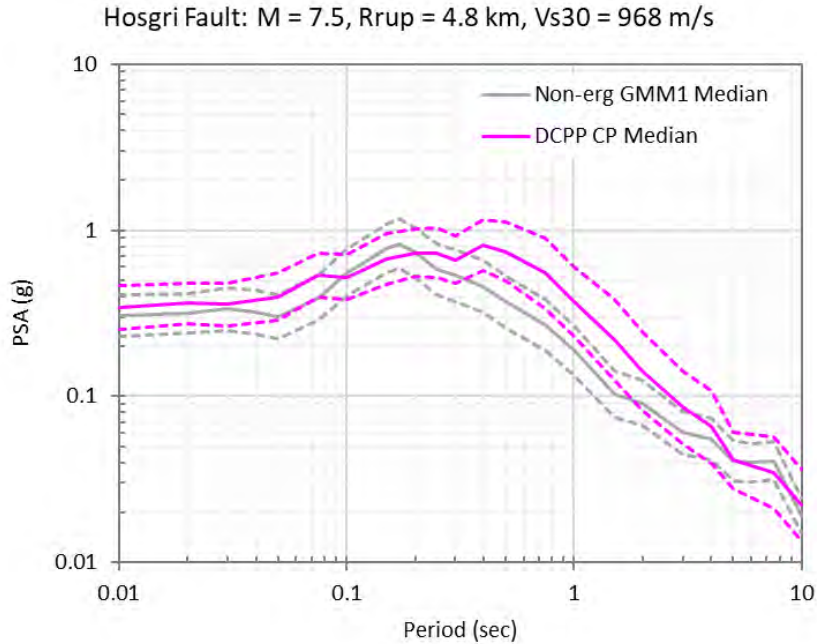


**Figure 7-44. Comparison of the range of predicted median ground motion at the control point at DCPD for the Hosgri fault scenario from the DCPD model and LA23 non-ergodic model 1 (top) and the DCPD model and LA23 non-ergodic model 2 (bottom). Dashed lines show median  $\pm$  sigma.**

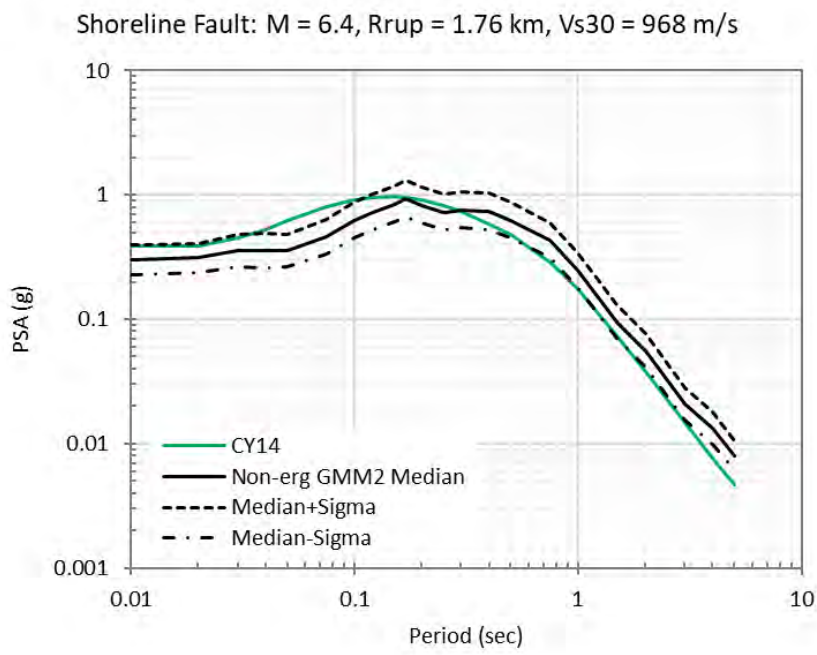
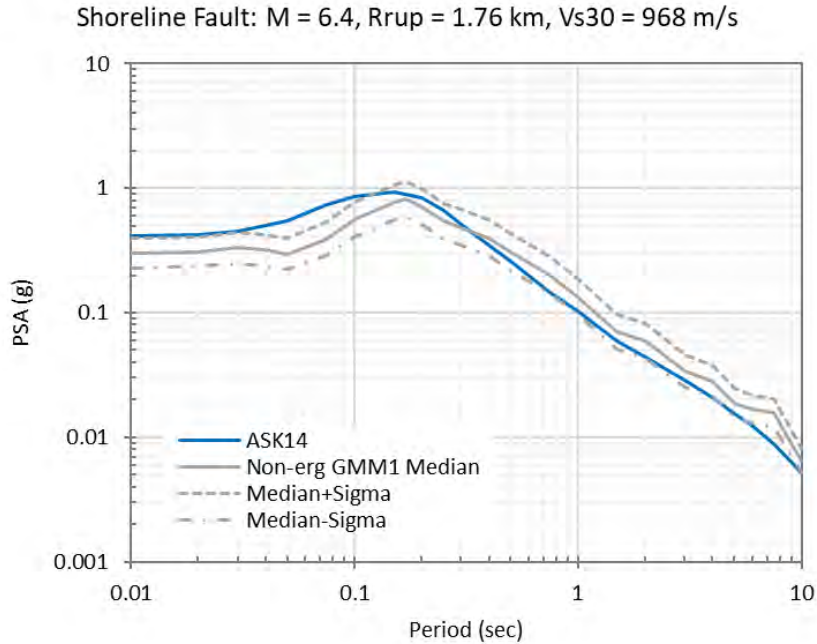


**Figure 7-45. Comparison of predicted median ground motion at DCPD for the Shoreline fault scenario for ASK14 and LA23 non-ergodic model 1 (top) and CY14 and LA23 non-ergodic model 2 (bottom)**

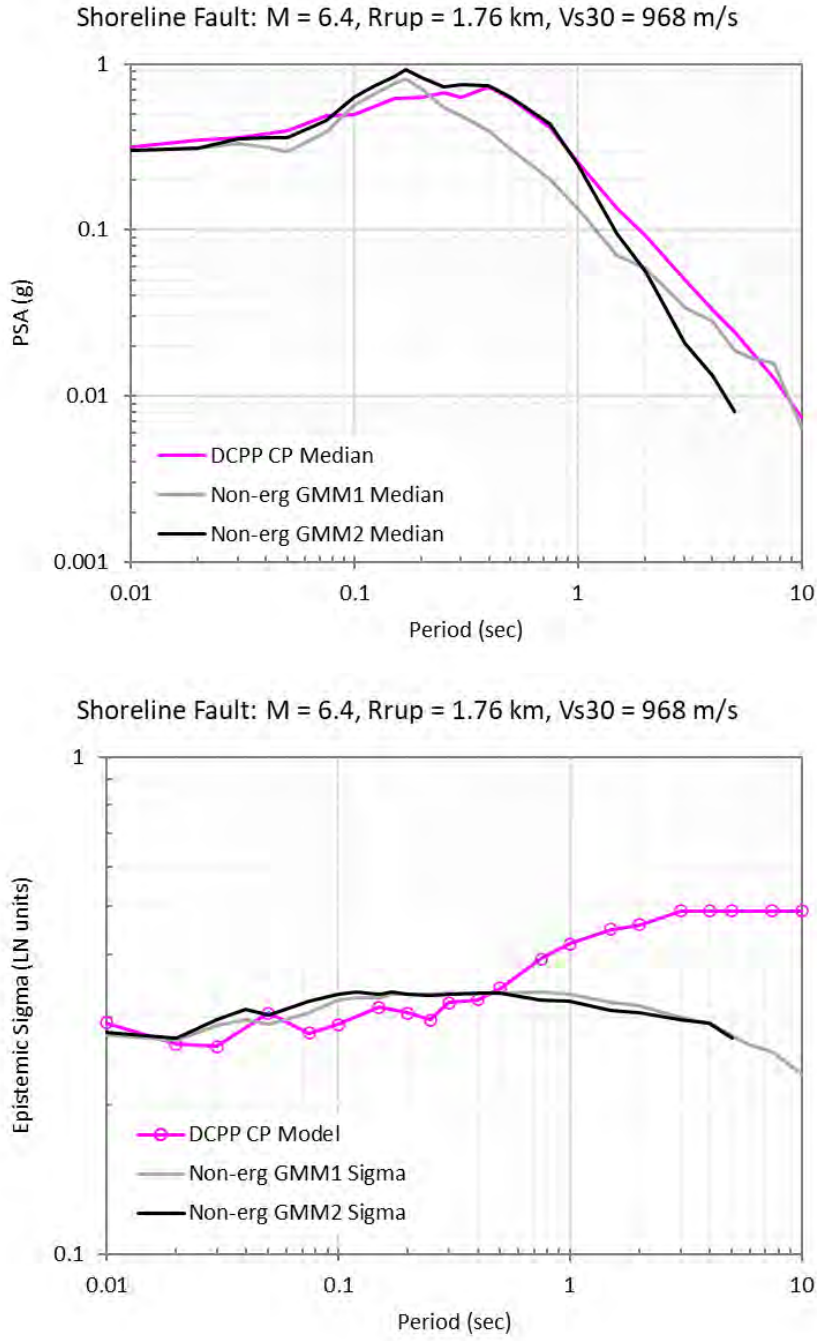


**Figure 7-46. Comparison of predicted median ground motion at the control point at DCPP for the Shoreline fault scenario for the DCPP model and the LA23 non-ergodic models (top) and of epistemic sigma for the DCPP and the LA23 models (bottom)**

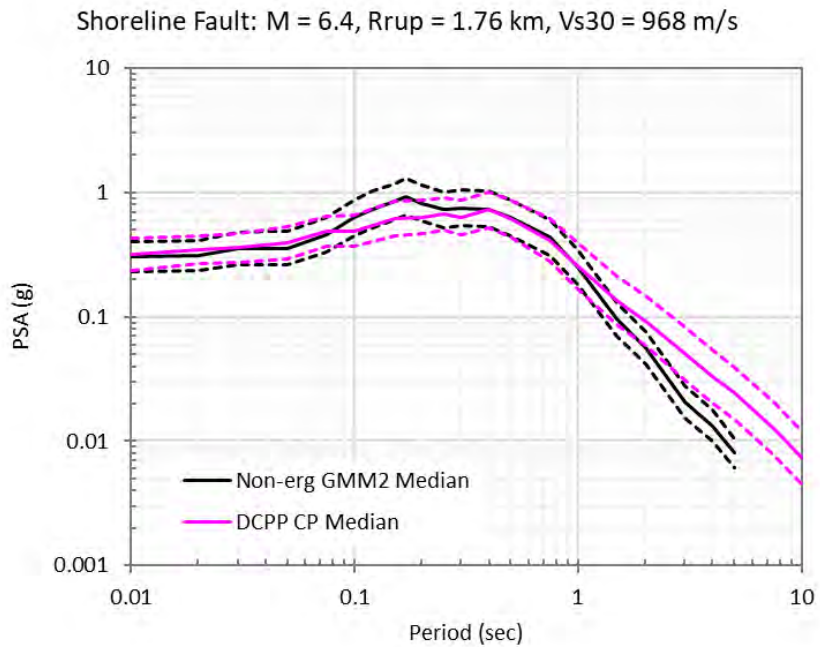
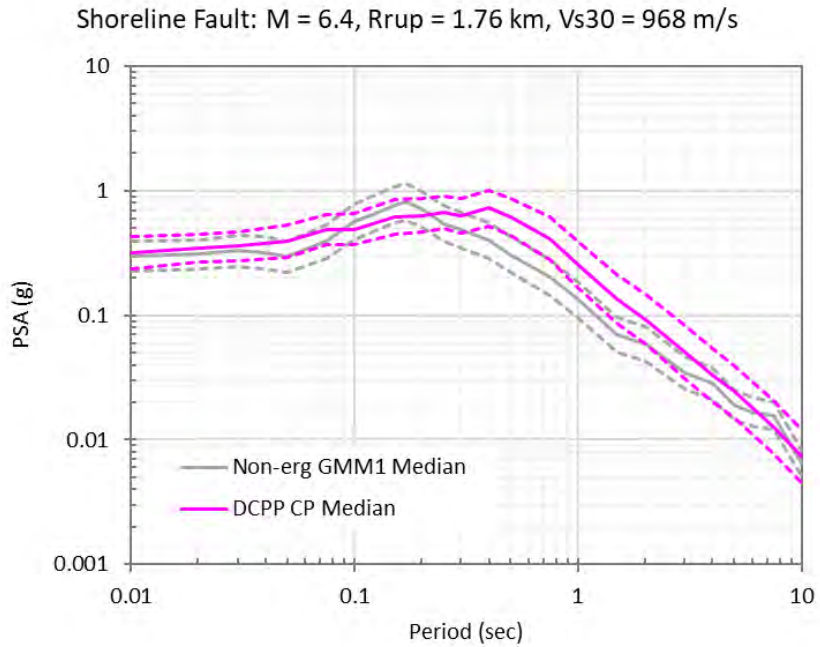


**Figure 7-47. Comparison of the range of predicted median ground motion at the control point at DCPP for the Shoreline fault scenario from the DCPP model and LA23 non-ergodic model 1 (top) and the DCPP model and LA23 non-ergodic model 2 (bottom). Dashed lines show median  $\pm$  sigma.**

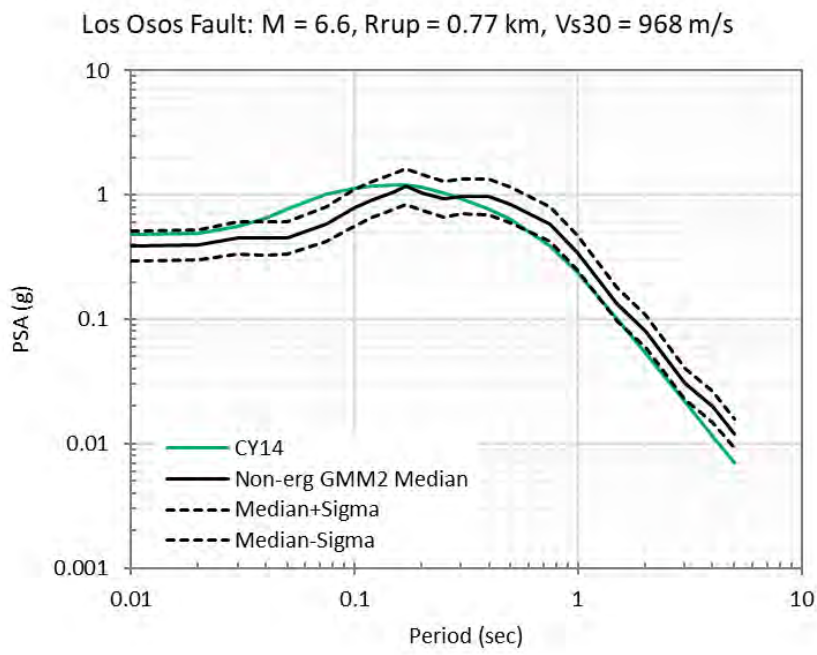
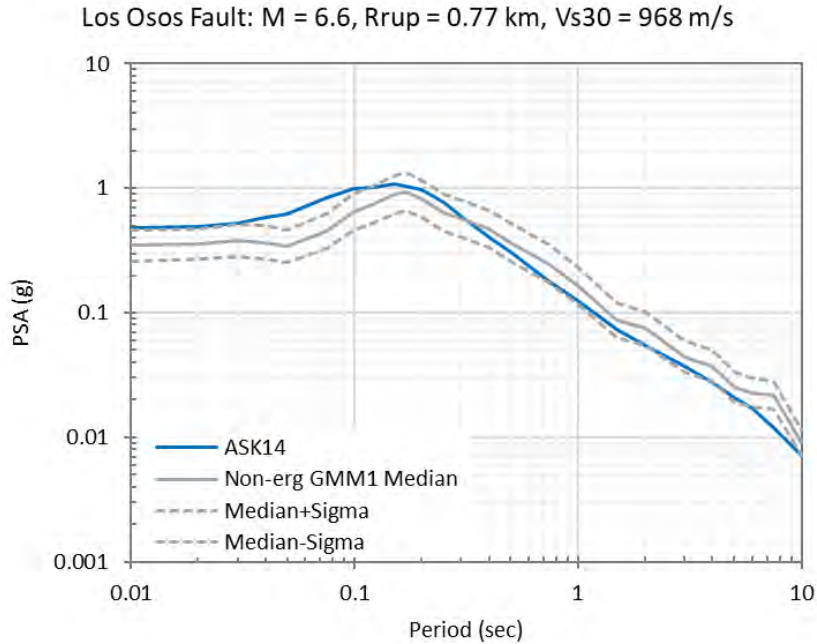


**Figure 7-48. Comparison of predicted median ground motion at DCPD for the Los Osos fault scenario for ASK14 and LA23 non-ergodic model 1 (top) and CY14 and LA23 non-ergodic model 2 (bottom). For the non-ergodic models, the median and median  $\pm$  sigma over 1000 drawn samples are shown.**



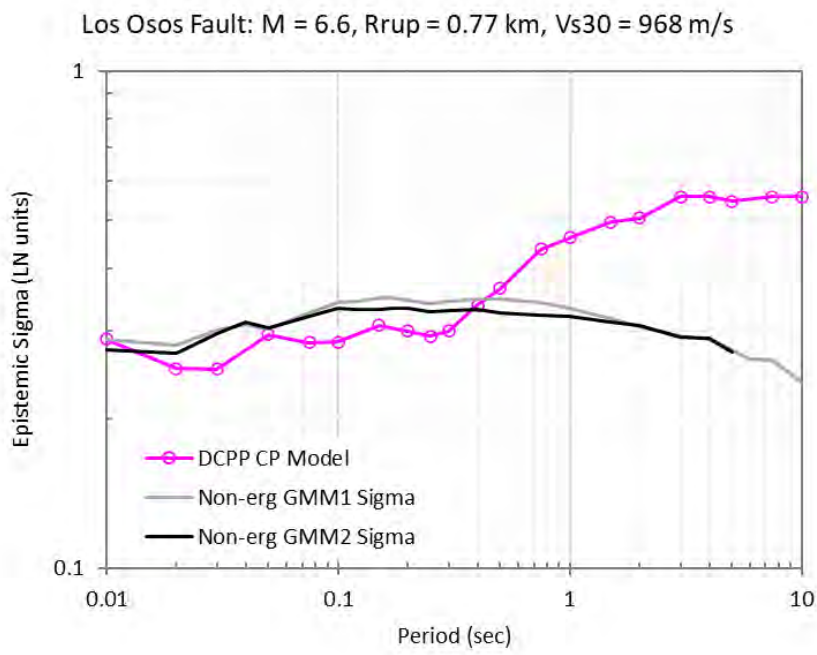
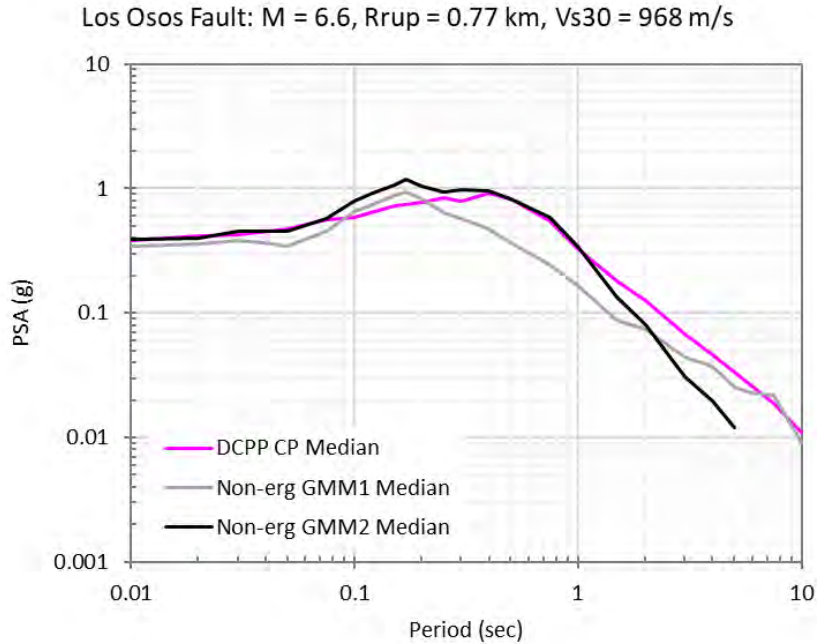


**Figure 7-49. Top: Comparison of predicted median ground motion at the control point at DCPP for the Los Osos fault scenario for the DCPP model and the LA23 non-ergodic models. Bottom: comparison of epistemic sigma for the DCPP and the LA23 models.**

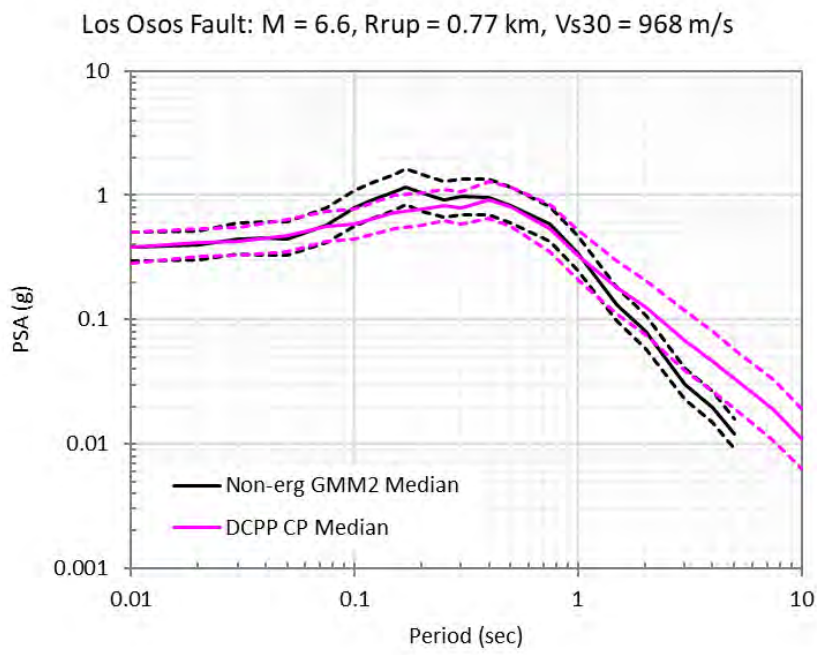
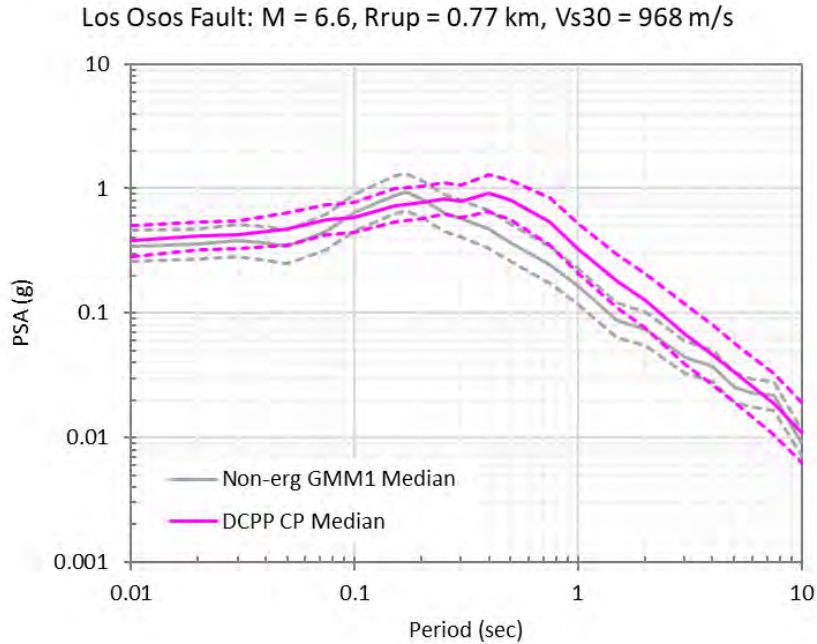


**Figure 7-50. Comparison of the range of predicted median ground motion at the control point at DCPD for the Los Osos fault scenario from the DCPD model and LA23 non-ergodic model 1 (top) and the DCPD model and LA23 non-ergodic model 2 (bottom). Dashed lines show median  $\pm$  sigma.**

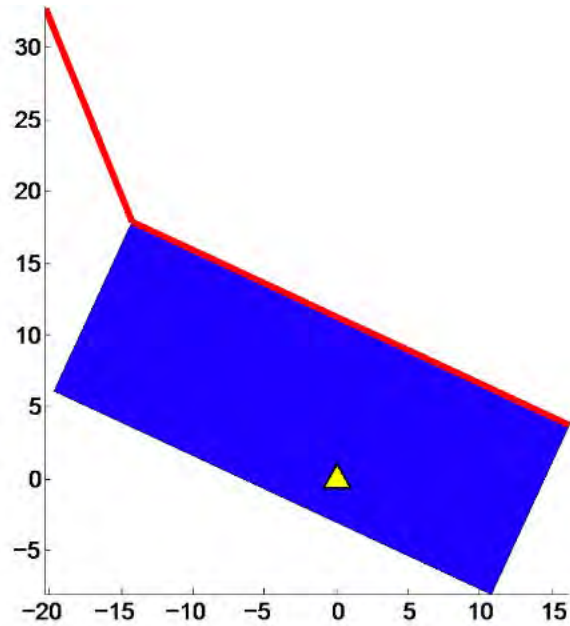


Figure 7-51. Example of a complex rupture with the Hosgri and Los Osos faults (blue area is the surface projection of the Los Osos fault plane). DCP site is indicated with the yellow triangle (from GeoPentech, 2015, Figure 5.2.3-3)

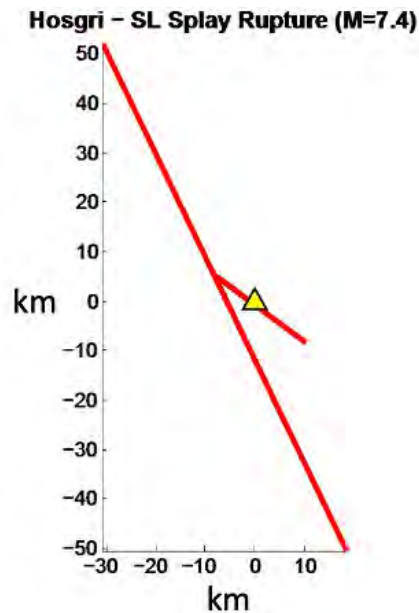
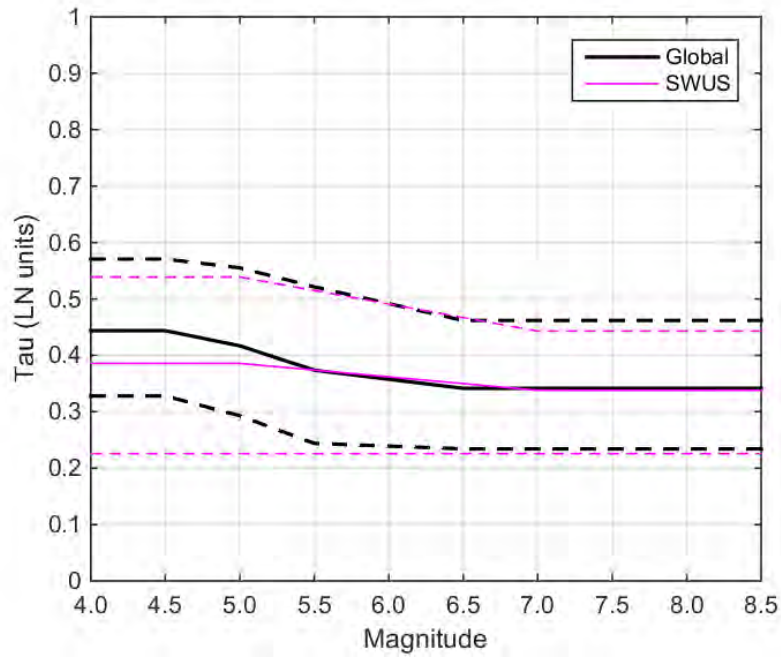


Figure 7-52. Example splay rupture with the Hosgri and Shoreline faults. DCP site is indicated by the yellow triangle (from GeoPentech, 2015, Figure 5.2.3-6)



**Figure 7-53. Comparison of the global  $\tau$  model versus magnitude to the SWUS  $\tau$  model. Both models are period-independent. Solid lines show the median models and dashed lines show the 5<sup>th</sup> and 95<sup>th</sup> percentiles (from INL, 2022)**

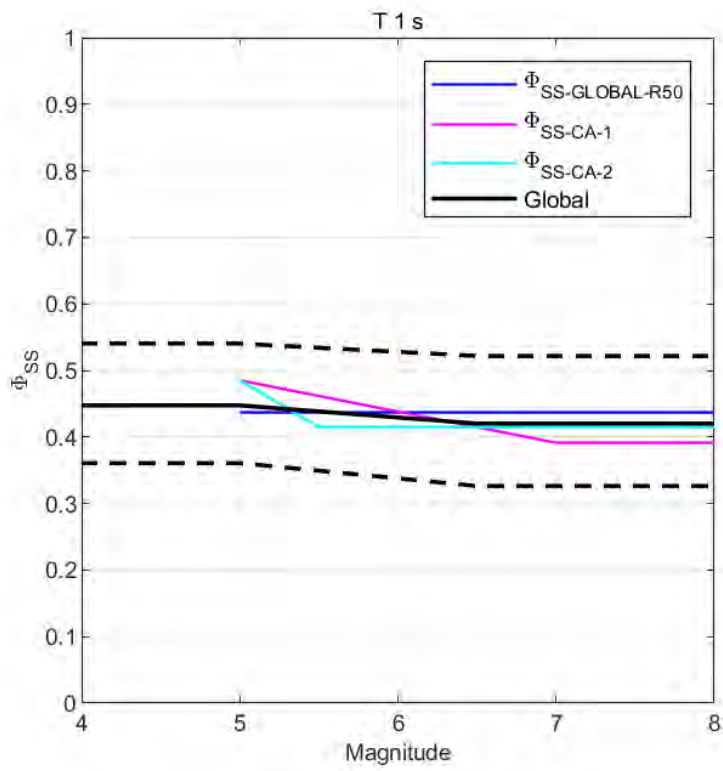
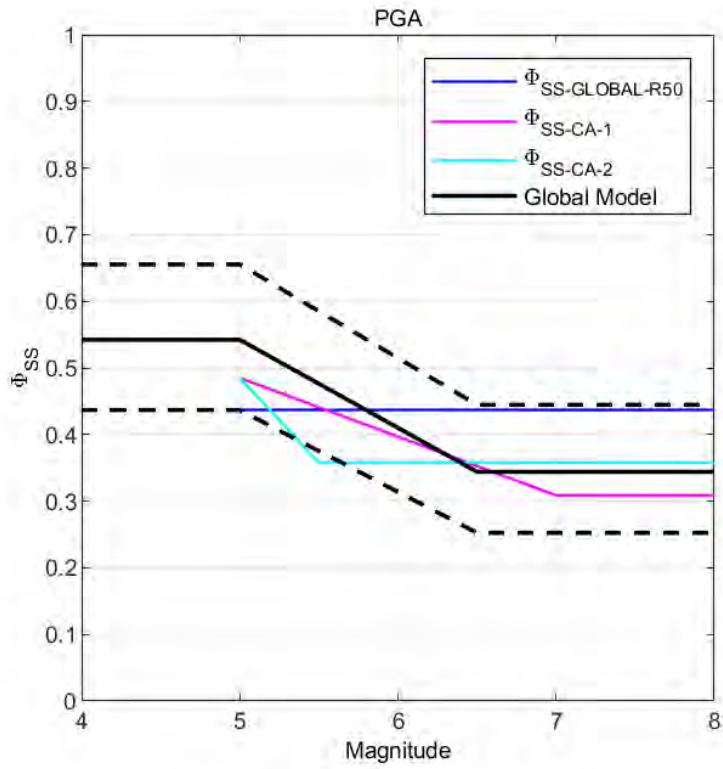


Figure 7-54. Comparison of the global  $\phi_{SS}$  model versus magnitude to the SWUS  $\phi_{SS}$  models for PGA (top) and period of 1 sec (bottom)

## 8. EVALUATION OF VERTICAL GROUND MOTIONS

To assist in the structural analysis of DCP, three-component spectrum-compatible ground-motion time histories were generated based on the horizontal Foundation Input Response Spectra (FIRS) methodology. For the vertical component, the standard state of practice of applying an applicable vertical to horizontal (V/H) spectral ratio to the defined horizontal spectrum was followed (PG&E, 2017a). This methodology for developing the vertical spectrum prevents the potential mismatch of controlling-scenario events one might obtain using a vertical GMM within the PSHA calculation (Gülerce and Abrahamson, 2011).

As part of the vertical FIRS development, the selected scenario event based on the controlling seismic sources from the PSHA study was a magnitude 7 earthquake at a distance of 5 km. In addition, a  $V_{S30}$  value of 969 m/sec for the control point horizon was assigned. Note that as part of the site amplification studies, a  $V_{S30}$  value of 968 m/sec was previously assigned to the DCP site, whereas the PG&E (2017a) calculation used a value of 969 m/sec. This minor difference between the two  $V_{S30}$  values has no significant impact on the calculated results. Given these scenario parameters, the empirically based Gülerce and Abrahamson (2011) V/H model was used to compute the V/H ratio scale factors. This empirically based V/H model was based on the NGA-West1 database for crustal events in active tectonic regions, which was considered applicable for DCP. The V/H value at 1 Hz was applied for frequencies less than 1 Hz. The Gülerce and Abrahamson (2011) V/H ratio model estimates slightly lower V/H values (i.e., down to 0.59) for these lower frequencies (i.e., less than 1 Hz). These V/H ratio values are listed in Table 8-1.

Unlike the development of horizontal GMMs, the development of vertical, and more importantly, V/H spectral ratio models has not followed the same progression; as a result, there are fewer V/H ratio models than horizontal GMMs. Several published models, however, have been developed based on specific datasets, and hence, application regions. For example, Bommer et al. (2011) developed a V/H model for Europe and the Middle East. Chen et al. (2017) developed a model for both onshore and offshore recordings in Japan based on the Kiknet data from Japan. Ramadan et al. (2021) developed a model for Italian events. Phung et al. (2022) developed a V/H ratio model for crustal earthquakes in Taiwan. Pezeshk et al. (2022) developed a V/H ratio model for application to the Central and Eastern United States regions. None of these models would be considered applicable to DCP given its tectonic environment and controlling scenario event.

As part of the NGA-West2 program, Bozorgnia and Campbell (2016 [BC16]) developed a V/H ratio model based on the development of their horizontal GMM (Campbell and Bozorgnia, 2014) and a vertical component model. This model is based on the larger NGA-West2 database compared to the Gülerce and Abrahamson (2011) model and would be considered a potentially applicable V/H model for DCP. One key aspect of this V/H model is its dependency on the horizontal Campbell and Bozorgnia (2014) ground-motion model. For rock site conditions, this horizontal model shows an increase in high frequency ground motions relative to the other NGA-West2 GMMs and the DCP median GMM. Application of the BC16 V/H model with a horizontal ground motion consistent with the Campbell and Bozorgnia (2014) horizontal spectrum will yield vertical motions comparable to the results using the application of the Gülerce and Abrahamson (2011) V/H model with the other NGA-West2 GMMs and DCP median GMM.



Given the scenario event parameters from the PG&E (2017a) calculation, a comparison is presented of the V/H values from the BC16 model. Additional event parameters are required for this model and are assigned as follows:  $Z_{hyp} = 10.4$  km,  $Z_{tor} = 0.13$  km, and  $Z_{2.5} = 0.46$  km. The resulting V/H ratio values for this scenario from the BC16 model are listed in Table and plotted on Figure 8-1, along with the results from the Gülerce and Abrahamson (2011) model reported in PG&E (2017a). The Gülerce and Abrahamson (2011) V/H ratio values envelope the BC16 results across all frequencies; this implies a larger vertical spectrum than one would compute using the BC16 factors alone, or a combination of the two models. The noted observation of a relatively constant V/H model across a broad frequency range from the BC16 model is observed for the DCPD scenario event with a stiff site condition.

**Table 8-1. Vertical to Horizontal (V/H) Spectral Ratio Results for the Scenario Event from the Gülerce and Abrahamson (2011) and Bozorgnia and Campbell (2016) Models**

Gülerce and Abrahamson (2011)		Bozorgnia and Campbell (2016)	
Frequency (Hz)	V/H Spectral Ratios	Frequency (Hz)	V/H Spectral Ratios
100	0.803	100.00	0.603
50	0.803	50.00	0.640
39.84	0.85	33.33	0.653
33.33	0.911	25.00	0.623
25.13	1.002	20.00	0.600
20	1.083	13.33	0.559
16.58	1.09	10.00	0.558
13.33	0.998	6.67	0.504
11.75	0.918	5.00	0.476
10	0.823	4.00	0.463
8.32	0.726	3.33	0.458
6.67	0.651	2.50	0.451
5.89	0.617	2.00	0.451
5	0.58	1.33	0.465
4.47	0.571	1.00	0.475
4	0.563	0.67	0.495
3.71	0.561	0.50	0.518
3.33	0.561	0.33	0.562
2.82	0.563	0.25	0.556
2.5	0.561	0.20	0.583
2.24	0.559	0.13	0.569
2	0.556	0.10	0.486
1.66	0.574		
1.33	0.609		
1.17	0.63		
1	0.63		
0.79	0.63		

<b>Gülerce and Abrahamson (2011)</b>		<b>Bozorgnia and Campbell (2016)</b>	
<b>Frequency (Hz)</b>	<b>V/H Spectral Ratios</b>	<b>Frequency (Hz)</b>	<b>V/H Spectral Ratios</b>
0.67	0.63		
0.58	0.63		
0.5	0.63		
0.4	0.63		
0.33	0.63		

The V/H ratio used in the development of the vertical FIRS is based on a site-specific study. However, there are more general V/H ratios that have been used for ground motion studies for nuclear facilities. Regulatory Guide 1.60 (NRC, 2014) provides a V/H ratio that is equal to 1.0 for frequencies greater than 3.5 Hz, two thirds (0.67) for frequencies less than 0.25 Hz and interpolated for frequencies between 0.25 and 3.5 Hz. NUREG CR-6728 (McGuire et al., 2001) provides V/H ratios for sites located in the Western United States for general rock site conditions. These V/H ratios are defined as a function of the horizontal PGA value with the highest category being for sites with PGAs greater than 0.5 g. The site-specific factors from Gülerce and Abrahamson (2011) are preferred over the generic V/H models as they are based off a dataset more appropriate to the region.

Based on this evaluation of the more recent BC16 V/H model with the understanding of its horizontal counterpart, the Campbell and Bozorgnia (2014) model for high frequency ground motions on rock site conditions, we conclude that the vertical spectrum developed for the FIRS horizon in the PG&E (2017a) calculation is based on the current state of practice. Future evaluations could be conducted with the inclusion of the BC16 V/H model accounting for the differences in the horizontal ground motions based on Campbell and Bozorgnia (2014) GMM and the DCCP median GMM, if the vertical ground motions are identified as being controlling and/or significant for the structural analyses.

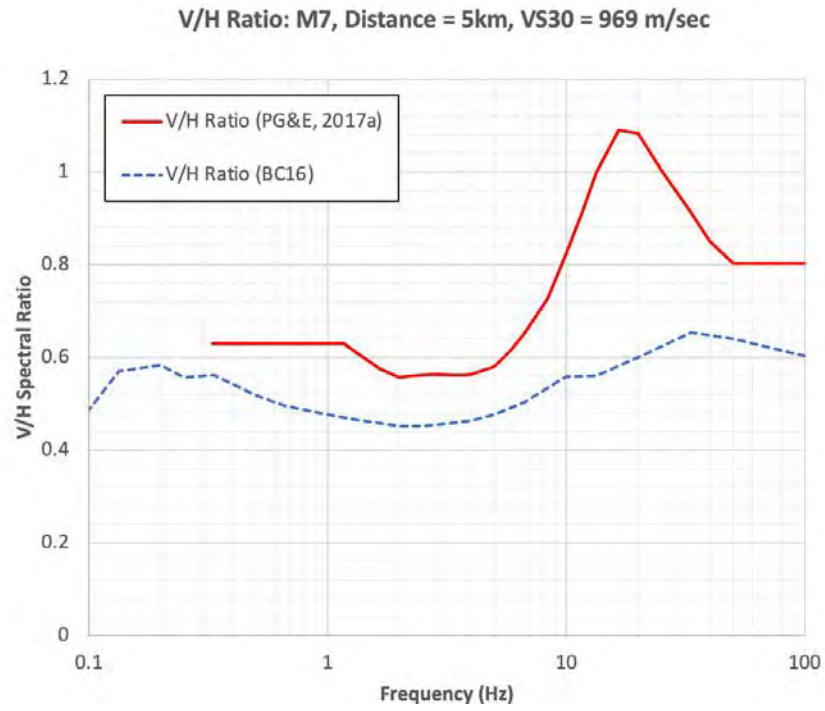


**Figure 8-1. Vertical to Horizontal (V/H) spectral ratio for the controlling scenario event and  $V_{S30}$  of 969 m/sec**

## 9. EVALUATION OF SITE CHARACTERIZATION

Following the conclusions of the SSHAC Level 3 SWUS study (GeoPentech, 2015) and the calculation of reference rock hazard at DCPD (PG&E, 2015c), a site response study was conducted to develop site-specific adjustment factors for DCPD relative to the reference rock site condition with a time-averaged  $V_{S30}$  of 760 m/sec. The reference rock hazard results and the site adjustment factors were used to develop the DCPD site-specific ground-motion response spectrum (GMRS) following approach 3 of NUREG/CR-6728 (McGuire et al., 2001).

In this chapter, we first present an overview of the DCPD site-specific adjustment study. This site response study consists of analytical and empirical approaches and is documented in PG&E (2015c, 2015d, 2017b). Next, the evaluation of the inputs and methods of the site response study in light of new available information since the completion of the DCPD study is presented. The potential impact of these changes on the GMRS is also evaluated.

### 9.1. OVERVIEW OF 2015 MODEL

In the 2015 study, the control point (CP) at DCPD was defined as a hypothetical location with a  $V_S$  profile representative of the range of site conditions over the power block and the turbine building footprint at an elevation of 85 ft (25.9 m). This region is shown on Figure 9-1. The  $V_S$  profile for the control point was defined in the top 125 m based on the 1-D  $V_S$  profiles extracted from the 3-D velocity model of Fugro (2015a) at the grid point locations shown on Figure 9-1. These grid points  $V_S$  profiles are shown on Figure 9-2, along with the central, upper, and lower profiles for the control point. The central profile is based on the geometric mean of the grid points profiles, and the upper and lower profiles correspond to  $\pm 1.6$  standard deviation from the central profile. A minimum range of 10% was applied to the lower and upper profiles. This resulted in a best estimate  $V_{S30}$  of 968 m/sec for the control point.

In the depth range of 125 to 3000 m, the control point  $V_S$  profile was constructed based on the 1-D  $V_P$  profile below the DCPD area (Fugro, 2015b). Below 3000 m, the  $V_S$  profile was extended to a depth of 8 km based on the NGA-West2 reference rock  $V_S$  profile used in Pacific Engineering and Analysis (PE&A, 2015). The resulting central, upper, and lower  $V_S$  profiles for the control point extended to a depth of 8 km are shown on Figure 9-3 compared to the reference  $V_S$  profile used in PE&A (2015).

The development of site adjustment factors for the DCPD control point relative to the reference rock site condition with  $V_{S30} = 760$  m/sec followed an analytical and empirical approach. The analytical approach followed a traditional 1-D site response analysis and is documented in PE&A (2015). The empirical approach relied on the evaluation of three ground-motion recordings recorded in the DCPD region at ESTA27 and ESTA28; these station locations are shown on Figure 9-1. The approach, inputs, and results from the empirical and analytical approach are summarized in the following subsections.

#### 9.1.1. Analytical Approach

A 1-D site response study was conducted by PE&A (2015) to develop site adjustment factors for the control point relative to the reference rock site condition with  $V_{S30} = 760$  m/sec. These site adjustment factors consist of the ratio of surface response spectra for the target control point site condition relative to the surface response spectra for the reference rock site condition. Response

spectra for each of the host and target site conditions were computed using a point-source stochastic model. The input motion consisted of a magnitude 7 earthquake at a depth of 8 km, and a range of point source distances were used to generate a range of input ground-motion levels.

The development of analytical site adjustment factors for DCPD involved the characterization of host and target site conditions in terms of best estimates and epistemic uncertainty in input parameters. For the host site condition, the Kamai et al. (2013) generic reference rock  $V_S$  profile with  $V_{S30}$  of 760 m/sec was used in PE&A (2015) and is shown on Figure 9-3. A kappa estimate of 0.03 sec was used for the host reference rock site condition based on the inversion of the NGA-West2 GMPEs. To accommodate potential nonlinear response in the reference site profile, the Peninsular Range curves (Silva et al., 1996) were used over the top 500 ft (152.4 m), with linear analyses below that depth.

The logic tree for the target site conditions is shown on Figure 9-4. The shallow and deep  $V_S$  profiles discussed above are shown on Figure 9-3. The assigned weights of [0.6], [0.2], and [0.2] on the central, upper and lower profiles, respectively, represent statistical weights on the median, 5<sup>th</sup>, and 95<sup>th</sup> percentiles according to Keefer and Bodily (1983). For each of the three base case profiles, 30 randomized profiles were developed based on the EPRI “Footprint” correlation model (EPRI, 2013). The  $V_S$  values were randomized, whereas the depth to rock was not randomized.

Based on the evaluation of ground-motion recordings at DCPD of the 2003 Deer Canyon earthquake ( $M_L$  3.4), the 2003 San Simeon earthquake ( $M$  6.5), and the 2004 Parkfield earthquake ( $M$  6.0), the kappa value for DCPD was estimated to be in the range of 0.03 to 0.05 sec. Therefore, target kappa values of 0.04, 0.03, and 0.05 sec were used with weights of [0.6], [0.2], and [0.2], respectively.

Three alternative models were used to model nonlinear material properties (damping and modulus reduction curves), as follows: (1) fully linear response (M1), (2) nonlinear EPRI rock model (M2) (EPRI, 1993), and (3) nonlinear Peninsular Range model (M3) (Silva et al., 1996). The modulus reduction and damping curves for the EPRI rock and the Peninsular Range models are shown on Figure 9-5 and Figure 9-6, respectively. The EPRI model consists of five depth ranges between 0 and 500 ft, while the Peninsular Range model has two depth ranges between 0 and 500 ft. Damping was limited to less than 15% and nonlinearity was limited to depths less than 500 ft.

The modulus reduction and damping curves obtained from laboratory testing of the soft-rock material at DCPD conducted by Bechtel (1988) were compared to the alternative linear and nonlinear models used in the analytical site response study. These comparisons are shown on Figure 9-7 and indicate that the range of measured  $G/G_{max}$  for the DCPD soft rock is consistent with the range of the models used, with most of the data showing linear behavior. As a result, the linear and nonlinear models were given equal weights, with the two nonlinear alternatives also given equal weights of [0.25].

Example site adjustment factors resulting from the analytical approach are shown on Figure 9-8 for reference rock peak ground acceleration (PGA) of 0.2, 1.07, and 1.91 g. The reference rock PGA of 0.2 g reflects the linear case, whereas the PGAs of 1.07 and 1.91 g represent the  $10^{-4}$  and  $10^{-5}$  reference rock hazard levels.

### 9.1.2. Empirical Approach

The availability of ground-motion recordings at DCPD allowed for the development of empirical site adjustment factors relative to the reference rock site condition with  $V_{S30} = 760$  m/sec. Ground-motion recordings at DCPD consisted of recordings from the 2003 San Simeon and the 2004 Parkfield earthquakes at station ESTA27 and a recording of the Parkfield earthquake at station ESTA28. The  $V_{S30}$  values at ESTA27 and ESTA28 were estimated as 856 and 777 m/sec, respectively, based on the 3-D velocity model of Fugro (2015a), while  $V_{S30}$  at the control point is 968 m/sec.

The empirical approach consisted of quantifying the average source and path effects and removing them from the ground-motion residuals of the DCPD recordings in order to estimate the remaining average site effects. This approach can be summarized as follows:

- For each of the Parkfield and the San Simeon earthquakes, the average event-specific source and attenuation effects were computed. For the San Simeon earthquake, mean residuals were calculated relative to each of the four NGA-West2 GMPEs (Abrahamson et al., 2014 [ASK14], Boore et al., 2014 [BSSA14], Campbell and Bozorgnia, 2014 [CB14], and Chiou and Youngs, 2014 [CY14]) by averaging the total residuals of recordings with  $R_{RUP}$  of 0 to 100 km. These mean residuals were then averaged over the four NGA-West2 GMPEs to calculate the average source-path term for the San Simeon earthquake at the distance range of interest for DCPD. For the Parkfield earthquake, the average source-path term was calculated similarly using recordings with  $R_{RUP}$  of 50 to 150 km.
- For each of the three recordings at the DCPD stations, the event- and path-corrected residuals were calculated by removing the average source-path term from the total residuals of the ground motion at these stations.
- Given the difference in  $V_{S30}$  between the control point, ESTA27, and ESTA28, the event- and path-corrected residuals of the DCPD recordings were corrected for  $V_{S30}$  scaling differences between the stations and the control point. The  $V_{S30}$  scaling correction was based on the NGA-West2 GMPEs  $V_{S30}$  scaling.
- The empirical site term was estimated based on the weighted average of the event-corrected residuals from the three recordings at DCPD.

Epistemic uncertainty in the empirical site term was quantified to account for the limited number of recordings at DCPD, as well as the uncertainty in other parts of the empirical site term calculation. The components of this epistemic uncertainty are the standard error due to the limited number of observations, the standard error in the estimated average source-path term, and the uncertainty in the  $V_{S30}$  adjustment. Figure 9-9 (top) shows the components of the epistemic uncertainty of the empirical site term and indicates that the standard error due to the limited number of ground-motion recordings at DCPD constitutes the largest component of the total epistemic uncertainty. Figure 9-9 (bottom) shows the smoothed central estimate of the empirical site term for DCPD, as well as the upper and lower estimates that are based on  $\pm 1.6$  times the epistemic standard deviation in natural logarithm units.

### 9.1.3. Implementation and Results

In the evaluation of the empirical and analytical site adjustment factors, the 2015 study assigned weights of [0.33] and [0.67] to the analytical and the empirical approaches, respectively. A



higher weight was assigned to the empirical approach because it reflects actual site-specific effects at DCP. On the other hand, the analytical approach has the advantage of allowing for multiple realizations of earthquake scenarios and of incorporating nonlinear site response. However, it represents a simple 1-D layered model that does not capture lateral heterogeneity that can be captured with the empirical approach. Laboratory testing of DCP soft rock indicated no strong nonlinearity.

The site-specific hazard at DCP—also referred to as “soil hazard”—was computed following approach 3 of NUREG/CR-6728 (McGuire et al., 2001) using the reference rock hazard and the site adjustment factors as inputs. Aleatory variability of the site adjustment factors is included in the single-station sigma model. However, since the NGA-West2 ground motions are mostly in the linear range, additional aleatory variability at high ground-motion levels was added in the soil hazard calculation.

The analytical site adjustment factors were computed relative to the reference rock condition incorporating nonlinearity in the reference rock profile. As a result, the analytical model has different levels of nonlinearity as the ground motion increases above the median level. In contrast, the NGA-West2 GMPEs used in the computation of the reference rock hazard include nonlinearity in the site terms and in the standard deviations but only as a function of the nonlinearity of the median ground-motion level. To address this inconsistency in the treatment of nonlinearity in the analytical site terms and the reference rock GMPEs, an additional set of site factors was applied in the soil hazard calculation to correct the analytical site factors to be relative to linear 760 m/sec. To avoid large nonlinear site effects that may not be reliable, the nonlinear part of the analytical site adjustment factors was limited to be greater than or equal to 0.5 in the soil hazard calculation.

Following the calculation of soil hazard, the GMRS was computed for the DCP control point; the result is shown on Figure 9-10. A sensitivity of the soil hazard to the empirical versus analytical site term approach was conducted. Figure 9-11 shows the  $10^{-4}$  and  $10^{-5}$  UHS curves for the empirical and analytical approaches. This figure indicates that the UHS obtained using the two approaches are generally consistent. Differences can be observed around 10 Hz and 2 Hz.

## **9.2. EVALUATION OF ANALYTICAL SITE FACTORS**

The evaluation of the analytical site factors for DCP involves an assessment of the input parameters used to characterize the host and target site conditions, and the general methodology used in the analytical site response study. The host site condition refers to the average  $V_S$  profile and kappa implicit in the NGA-West2 GMPEs for the reference rock site condition with  $V_{S30} = 760$  m/sec. The target site condition refers to the site-specific conditions for the DCP control point. The evaluation of these aspects of the analytical site factors in light of new available information since the completion of the 2015 DCP study is presented in this section.

### **9.2.1. Approach**

Analytical site factors were developed for DCP using a 1-D site response approach as described in PE&A (2015) and summarized in Section 9.1.1. This approach uses 1-D layered velocity models of the site and relies on broadband point-source stochastic simulations of ground motion for the host and target site conditions. The input motion consisted of a magnitude 7 earthquake at a depth of 8 km and a range of point source distances were used to generate a range of input

ground-motion levels. Unlike the traditional soil-over-rock site response approach that requires the definition of a reference rock at some depth that is treated as the top of an elastic half-space, the DCPD analytical site response approach uses a lateral or one-step site adjustment approach. Under this approach, the ground motion is simulated for the entire profile depth for each of the host and the target  $V_S$  profiles separately. The ratio of the host and target ground motions is used to define the site adjustment factors for different input loading levels.

In recent years, use of the soil-over-rock site response approach has been criticized for being inconsistent with the site response scaling in ground-motion models and potentially leading to unconservative long-period ground motion (Williams and Abrahamson, 2021). Instead, site response correction for the entire  $V_S$  profile, consistent with the PE&A (2015) study approach, has been advocated for and used on several projects. Recent SSHAC Level 3 studies that used the 1-D  $V_S$  profile correction approach are the Idaho National Laboratory study (INL, 2022) and the Natrium study (Natrium, 2024). While the details of these studies differ from the PE&A (2015) study, these studies support the 1-D  $V_S$  profile correction method that was employed for the development of the DCPD analytical site factors. Analytical site response studies used on these large projects and others indicate that the analytical study used for DCPD is still considered the state-of-the practice.

Given the 3-D velocity model for DCPD (Fugro, 2015a), more sophisticated 2-D or 3-D site response studies could be conducted to evaluate the impact of lateral heterogeneities and 3-D effects on the site adjustment factors. Such studies are generally not standard practice in the industry and can be considered as part of the long-term evaluation of site response at DCPD. Moreover, Fugro (2015a) indicated that the lateral variability in the 3-D  $V_S$ -depth model below the DCPD foundation area is relatively modest compared to areas close to the coast. This indicates that 3-D effects below the foundation area may not be pronounced, and that site response might be reasonably approximated with a 1-D model that considers the lateral variability as part of the development of the  $V_S$  profiles, as was done for the 2015 study.

### **9.2.2. Characterization of DCPD Target Site Conditions**

The characterization of target site conditions for the DCPD control point involves target  $V_S$  profile,  $\kappa$ , and nonlinear material properties. Section 9.1.1 discussed the characterization of these target site input parameters in the 2015 study in terms of best estimates and epistemic uncertainty in these estimates or models. The target  $V_S$  profile for the control point was based on the 3-D velocity model of Fugro (2015a) and the 1-D  $V_P$  profile below the DCPD area (Fugro, 2015b), accounting for the uncertainty in the profile and the lateral variability under the power block and the turbine building region. The extensive site data at DCPD provided a well constrained velocity model for depths up to 3 km. As a result, no updates to the target 1-D  $V_S$  profile characterization are deemed necessary.

The characterization at DCPD of the small strain damping parameter  $\kappa$ , which affects the high frequency ground motion, was based on the analysis of ground motion from the Deer Canyon, San Simeon, and Parkfield earthquakes recorded at ESTA27 and ESTA28. Since the completion of the 2015 study, there have been no triggered recordings at these stations. The lack of new ground-motion recordings at DCPD does not trigger a reevaluation of the  $\kappa$  characterization. Recently, the EPRI (2021) study evaluated  $\kappa$  for hard-rock sites in Canada

and in France. Findings from this study for hard-rock site conditions are not applicable to the DCPD soft-rock site.

Modulus reduction and damping curves (MRD) used in nonlinear site response studies are typically based on laboratory testing of material at the target site, which is commonly not available, or curves published in the literature developed based on testing of a large number of soil samples. As a result, the selection of MRD curves typically involves large uncertainty particularly for rock material for which dynamic properties are generally poorly known. Commonly used MRD curves for rock are the EPRI (1993) rock and the Schnabel (1973) curves. The Schnabel (1973) curves are based on Seed and Idriss (1970) and are not directly based on measurements, whereas the EPRI rock curves are based on tests on gravel.

Material nonlinearity at DCPD was characterized using three alternative models: (1) linear behavior with a weight of [0.5], (2) nonlinear EPRI rock model (EPRI, 1993) with a weight of [0.25], and (3) nonlinear Peninsular Range model (Silva et al., 1996) with a weight of [0.25]. The EPRI (1993) curves were used to reflect an upper range on potential nonlinear response and assume that intact rock behaves similar to highly nonlinear gravels (PE&A, 2015). The Peninsular Range curves reflect significantly more linear response than the EPRI rock curves. The use of the linear and two nonlinear models spans a realistic range of dynamic material properties at high-loading levels. Moreover, these curves span the range of behavior based on the testing of soft rock at DCPD (Bechtel, 1988). These curves are, therefore, considered adequate. Future material testing can potentially better constrain the nonlinear behavior at DCPD. Given the weight of [0.33] assigned to the analytical approach, the total weight for the nonlinear modulus reduction and damping models is [0.165]. Given this low weight, changes to the MRD curves are not expected to significantly impact the site terms at DCPD.

### **9.2.3. Characterization of Host Site Conditions**

The PE&A (2015) analytical site response study used the Kamai et al. (2013)  $V_S$  profile and a kappa of 0.03 sec to characterize the host site condition for  $V_{S30}$  of 760 m/sec. The Kamai et al. (2013) profile is a generic profile considered applicable to the WUS region. Generic regional  $V_S$  profiles have been traditionally used to characterize the average  $V_S$  profile implicit in the host region GMPEs. Host kappa is typically estimated based on the spectral shape of GMPEs or model inversions accounting for the tradeoff between the site amplification of the  $V_S$  profile and the kappa scaling at high frequencies.

Recently, Al Atik and Abrahamson (2021) showed that the use of generic host  $V_S$  profiles does not necessarily capture the average site response in the GMPEs. They developed 1-D GMPE-compatible  $V_S$  profiles and kappa values for the NGA-West2 GMPEs for a range of site conditions. These GMPE-compatible  $V_S$  profiles are considered to be a better representation of the average  $V_S$  scaling in the ground-motion models. Figure 9-12 shows a comparison of the GMPE-compatible host  $V_S$  profile for  $V_{S30}$  of 760 m/sec to the reference profile used in the PE&A (2015) analysis. The target control point  $V_S$  profiles are also shown on this figure. Figure 9-13 shows the linear quarter-wavelength site amplifications of the host and target  $V_S$  profiles. These figures indicate differences among the GMPE-compatible profiles and the Kamai et al. (2013) profile at both the shallow and deep layers, leading to differences in the site amplifications at high and low frequencies. Table 9-1 shows a comparison of the host kappa

values for the GMPE-compatible profile method to the host kappa used in the PE&A (2015) analysis. The target DCPD kappa values are also listed in this table.

**Table 9-1. Host Kappa for the NGA-West2 GMPEs for  $V_{S30}$  of 760 m/sec Based on the GMPE-Compatible Method and the PE&A (2015) Analysis**

	Host Kappa (sec)				Target Kappa (sec)
	ASK14	BSSA14	CB14	CY14	
GMPE-Compatible	0.0419	0.0429	0.0315	0.0390	0.04 (0.03 - 0.05)
PE&A (2015)	0.03				

Given the differences in the host  $V_S$  profile and kappa values for the GMPE-compatible  $V_S$  profile method and the PE&A (2015) study, a sensitivity analysis was conducted to evaluate the impact of these differences on the site adjustment factors for DCPD. The inverse random vibration theory (IRVT) approach of Al Atik et al. (2014) was used to convert response spectra from the NGA-West2 GMPEs for a suite of magnitude-distance scenarios for  $V_{S30}$  of 760 m/sec to corresponding Fourier amplitude spectra (FAS). Next, these FAS were adjusted from their host site conditions to the DCPD target site conditions. The host site conditions used the GMPE-compatible  $V_S$  profiles and kappa values for  $V_{S30}$  of 760 m/sec. The target site conditions consisted of the DCPD logic tree shown on Figure 9-4. We note that this sensitivity analysis did not consider nonlinear material behavior. The adjusted FAS were then converted into response spectra using random vibration theory. For each GMPE and each branch of the logic tree, analytical site adjustment factors ( $V_S$ -kappa scaling factors) were computed as the ratio of corrected to initial response spectra.

An example of the obtained  $V_S$ -kappa scaling factors for CY14 is shown on Figure 9-14. These factors were obtained using the GMPE-compatible host  $V_S$  profile and kappa for CY14 and the nine target  $V_S$  profile and kappa branches. The weighted average of the factors over the nine branches is also shown in this figure. A similar approach was used to derive scaling factors for each of the other three NGA-West2 GMPEs. Figure 9-15 shows a comparison of the factors derived for the four GMPEs and their average, giving equal weight to the GMPEs.

Figure 9-16 shows a comparison of the derived  $V_S$ -kappa scaling factors using the GMPE-compatible  $V_S$  profiles and kappa values to the linear average site factors from the PE&A (2015) study. This figure indicates that using the GMPE-compatible profiles and kappa generally leads to comparable site factors to those obtained in PE&A (2015). The biggest observed difference is around the frequency of 6 Hz where the average site factors for the GMPE-compatible host profiles are about 24% larger than those of the PE&A (2015) study. Figure 9-16 indicates that the factors obtained from this sensitivity study are within the range of DCPD empirical site factors. We note that some of the differences between the analytical site factors observed on Figure 9-16 can be attributed to the different methodologies used in the PE&A (2015) analysis and this sensitivity study. Also, given the small weight assigned to the analytical approach—[0.33]—the overall impact of using the GMPE-compatible host  $V_S$  profiles and kappa on the final site factors is expected to be small.

### 9.3. EVALUATION OF EMPIRICAL SITE FACTORS

The evaluation of the empirical site factors developed for DCPD involves an evaluation of empirical ground-motion data available since the completion of the 2015 study and the evaluation of the methodology used to derive the empirical site factors. As discussed in Section 9.1.2, the 2015 empirical site factors were based on three ground-motion recordings at DCPD: recordings of the 2003 San Simeon and the 2004 Parkfield earthquakes at station ESTA27 and a recording of the Parkfield earthquake at station ESTA28. Ground-motion residuals at these stations were corrected for differences in  $V_{S30}$  between ESTA27 (856 m/sec) and ESTA28 (777 m/sec) and the control point (968 m/sec). A larger dataset of recordings from the San Simeon and the Parkfield earthquakes was used to estimate average source-path terms for these earthquakes. The empirical site term was estimated based on the weighted average of the event- and path-corrected residuals from the three recordings at DCPD.

In this section, we present available ground-motion data since the completion of the 2015 study and discuss its use in evaluating the 2015 empirical site factors. Since the completion of the 2015 study, the emergence of non-ergodic ground-motion modeling represents a major development in ground-motion modeling. This approach, however, is still considered preliminary and the dataset compiled for this purpose, as discussed below, is also of preliminary nature. In this section, we evaluate the preliminary application of the non-ergodic ground-motion modeling for the development of empirical site factors for DCPD. The limitations of the approach and dataset used are discussed, as well as preliminary gained insights from this evaluation relative to the empirical site factors from the 2015 study.

#### 9.3.1. *New Information Since 2015*

Available empirical ground-motion data and methods since the completion of the 2015 study were evaluated for a potential update of the empirical site term. Since 2015, additional ground-motion data in the vicinity of DCPD have become available. Preliminary datasets of the post-2015 ground motion were discussed in Section 4.2 (NGA-West3 and DCPD flatfile) and will be further discussed in the next section. Despite the availability of new ground-motion data in the vicinity of DCPD, stations ESTA27 and ESTA28 did not record new ground-motion data since the completion of the 2015 study. Since the empirical site term derived for DCPD relies on site-specific ground-motion recordings at these stations, the 2015 empirical site term is not expected to change given the lack of new recordings at the DCPD stations.

Since the completion of the 2015 study, a major advance in ground-motion modeling involves the development of non-ergodic ground-motion models. These models, discussed in Section 7.2.6, allow for the estimation of repeatable source, path, and site effects and the adjustment of ergodic ground-motion models to become site-, source-, and region-specific. The characterization of these repeatable effects requires the availability of empirical ground-motion data at the site of interest and in the region of interest. The non-ergodic modeling procedure was explored for the evaluation of the empirical site term at DCPD using the three DCPD recordings as well as an updated dataset of ground motion recorded in the vicinity of the site. This represents an independent approach for the evaluation of the empirical site term for DCPD. The dataset, approach, and results obtained from this effort are discussed in the next section.

### 9.3.2. Non-ergodic Modeling

Lavrentiadis et al. (2023) developed a non-ergodic ground-motion model for California for the effective amplitude spectral (EAS) values using the NGA-West2 ground-motion dataset. The Bayless and Abrahamson (2019, [BA18]) EAS ground-motion model was used as the ergodic backbone model to constrain average source, path, and site scaling. EAS represents a smooth rotation-independent Fourier amplitude spectrum of the two horizontal components of an acceleration time history (Goulet, Kottke et al., 2018). The Lavrentiadis et al. (2023) model was developed for EAS instead of the more traditional response spectral accelerations (PSA) because it is easier for the EAS non-ergodic effects estimated from small-magnitude earthquakes to be transferred to large-magnitude earthquakes where data are more limited. Due to the sensitivity of the short-period spectral accelerations to ground motion at frequencies near the peak of the Fourier spectrum, scaling of the short-period spectral acceleration is magnitude-dependent. This magnitude-dependence of PSA scaling and the predominance of small-magnitude earthquakes in the ground-motion database were the driving factors for developing an EAS non-ergodic model that gets converted to PSA using random vibration theory (RVT) (Lavrentiadis and Abrahamson, 2023).

The median non-ergodic ground-motion model of Lavrentiadis et al. (2023) can be written as:

$$f(x, \theta) = (f_{erg}(M, R_{rup}, V_{S30}, \dots) - c_7 R_{rup}) + \delta c_0 + \delta c_{0,e} + \delta c_{1,e} + \delta S2S_{reg} + \delta S2S_{unc} + c_{ca,p} \cdot \Delta R \quad \text{Equation (9.1)}$$

Equation (9.1) shows the non-ergodic median model written as a function of the ergodic backbone model without the anelastic attenuation ( $f_{erg}(M, R_{rup}, V_{S30}, \dots) - c_7 R_{rup}$ ), the non-ergodic terms ( $\delta c_0, \delta c_{0,e}, \delta c_{1,e}, \delta S2S_{reg}, \delta S2S_{unc}$ ), and the cell-specific anelastic attenuation  $c_{ca,p} \cdot \Delta R$ . The model parameters  $\theta$  consist of the non-ergodic terms, the cell-specific coefficients, and aleatory terms and are listed in Table 9-2. The model parameters  $\theta$  follow prior distributions that are defined in terms of hyperparameters  $\theta_{hyp}$  listed in Table 9-2.

The non-ergodic modeling approach of Lavrentiadis et al. (2023) was implemented for this study with the focus on estimating the empirical non-ergodic site term at DCP. The empirical site term,  $\delta S2S$ , can be represented with  $\delta S2S = \delta S2S_{reg} + \delta S2S_{unc}$ , where  $\delta S2S_{reg}$  is a regional site adjustment with a finite correlation length describing the broader adjustments to the backbone model from regional site effects.  $\delta S2S_{unc}$  is a site-specific uncorrelated site adjustment.

In contrast with the non-ergodic approach, the 2015 study followed a partially non-ergodic approach where site-specific effects were characterized. The median site-specific ground-motion model in the 2015 study can be written as follows:

$$f(M, R_{rup}, V_{S30}, \dots) = f_{erg}(M, R_{rup}, V_{S30}, \dots) + \delta S2S \quad \text{Equation (9.2)}$$

where  $f_{erg}(M, R_{rup}, V_{S30}, \dots)$  is the SWUS ergodic median ground-motion model developed for the reference rock condition with  $V_{S30} = 760$  m/sec. Under the empirical approach,  $\delta S2S$  was estimated using the three ground-motion recordings at DCP that allowed for the characterization of the differences in site-specific effects compared to the ergodic model for the reference rock condition. Using the same dataset and ergodic backbone model,  $\delta S2S$  obtained from the non-ergodic modeling approach is not expected to be different from that obtained in the



2015 study. Given the same number of recordings at DCP, the main value of the non-ergodic modeling approach is to derive the two site term components, regional and correlated, and to examine the observed site-specific adjustments at DCP compared to broader regional site effects.

The next subsections describe the preliminary dataset compiled for use in the non-ergodic modeling approach, the performed analysis, and the results and their interpretations. A detailed description of the non-ergodic analysis performed by Dr. Chih-Hsuan “Karen” Sung is provided in Appendix F of this report and summarized herein.

**Table 9-2. Summary of the Lavrentiadis et al. (2023) Model Parameters and Hyperparameters (from Lavrentiadis et al., 2023, Table 2)**

Group Name	Group Notation	Components
Model parameters	$\theta$	$\delta c_0, \delta c_{0,e}, \delta c_{1,e}, \delta c_{1a,s}, \delta c_{1b,s},$ $c_{ca,p}, \delta WS_{e,s}^0, \delta B_e^0$
Model hyperparameters	$\theta_{hyp}$	$\ell_{1,e}, \omega_{1,e}, \ell_{1a,s}, \omega_{1b,s}, \omega_{1b,s},$ $\ell_{ca1,p}, \omega_{ca1,p}, \omega_{ca2,p}, \phi_0, \tau_0$

### 9.3.2.1. Data

A preliminary expanded dataset of Fourier amplitude ground motions was compiled for use in the non-ergodic analysis to estimate updated empirical site terms for DCP. This dataset is compiled as described in Section 4.2.2 (“DCP Data”) but includes ground-motion from earthquakes with  $M \geq 2.5$  that occurred between 1994 and August 2023. A summary of this dataset is described below, followed by a description of the subset of data selected for use in the non-ergodic analysis of Dr. Sung (see Appendix F).

The preliminary “dcp” flatfile was compiled based on a search of ground-motion recordings from earthquakes within 300 km of DCP with  $M \geq 2.5$  that occurred between 1994 and August 2023. This dataset includes overlapping ground-motion recordings with NGA-West2 and more recent post-NGA-West2 recordings. The earthquake epicenters and station locations based on this search criteria are plotted on Figure 9-17. This dataset consists of 20,443 recordings from 844 earthquakes with  $M$  2.5 to 6.7,  $R_{RUP}$  of 3 to 334 km, and  $V_{S30}$  of 133 to 1,464 m/sec. The magnitude-distance distribution of the data is shown on Figure 9-18. Figure 9-19 shows a comparison of the number of earthquakes and stations within 50 km of DCP in the NGA-West2 and the dcp flatfiles. This figure indicates that the NGA-West2 flatfile contained four stations within 20 km of DCP while 17 stations are now available in the dcp flatfile. This increased number of stations within 20 km of DCP will allow for an estimate of the regional correlated site term from the non-ergodic analysis.

Given the preliminary nature of the dcp dataset and short timeframe for compiling it, several key metadata are missing. A total of 609 earthquakes do not have moment magnitude estimates. Moreover, the style-of-faulting and depth-to-top of rupture parameters are missing in this dataset. While most stations do have  $V_{S30}$  estimates, some do not, and most stations do not have basin depth estimates. Also, some stations are sometimes reported to have different  $V_{S30}$  estimates depending on the source of the data. The retrieved ground motions in this dataset were processed

using the automated *GMprocess* script (Hearne et al., 2019). Although this script and its implementation follow a similar standard time history processing methodology as has been used for the NGA projects, differences may be observed in the processed ground motions based on the specifics of the data processing. For recordings that are overlapping between this dataset and the NGA-West2 dataset, no comparisons were performed to evaluate potential differences in the ground-motion processing and data quality. In summary, and based on the limitations discussed here, the preliminary dcpp dataset is only suited for sensitivity analyses. Further reviews, iterations, and checks are needed to improve the quality of this dataset.

For the dcpp dataset, an FAS flatfile was generated with the as-recorded Fourier amplitude spectra calculated as  $\sqrt{0.5 * FAS_{H1}^2 + 0.5 * FAS_{H2}^2}$ , where  $FAS_{H1}$  and  $FAS_{H2}$  are the Fourier spectra of the H1 and H2 components. The usable frequency range was assigned for each recording based on the corner frequencies of the filters applied. Given the usable frequency range of the data, the number of FAS data versus frequency is shown on Figure 9-20. This plot indicates that outside of 0.3 to 11.6 Hz, less than 35% of the data remains due to frequency bandwidth limitations.

Given the dcpp FAS flatfile, Dr. Sung (see Appendix F) selected a subset of data for use in the non-ergodic analysis. This subset consists of earthquakes with a minimum of three recordings, recordings with  $R_{RUP} \leq 100$  km for earthquakes with  $M \leq 6.0$ , and recordings with  $R_{RUP} \leq 200$  km for earthquakes with  $M > 6.0$ . The minimum number of recordings per earthquake is imposed to ensure a reliable estimate of the between-event residuals, while the distance cutoff is applied to avoid potential censoring of the data at large distances. In addition to this subset of data, the three NGA-West2 ground-motion recordings at ESTA27 and ESTA28 from the Parkfield and the San Simeon earthquakes were added, as well as additional NGA-West2 ground-motion recordings from the Parkfield and San Simeon earthquakes with  $R_{RUP}$  range of 50 to 100 km and 0 to 100 km, respectively. These additional NGA-West2 recordings were not available in the preliminary dcpp flatfile. The additional Parkfield and San Simeon recordings were added to calculate an average source term from these earthquakes centered on the distance to DCP, and to remove the average source term from the total residuals, consistent with the 2015 approach.

The final dataset used in the non-ergodic analysis consists of 645 earthquakes and 1,026 stations from the dcpp flatfile (41 stations are within 50 km of DCP), three DCP recordings from the NGA-West2 flatfile, and 16 Parkfield and eight San Simeon recordings from the NGA-West2 flatfile. Total residuals of the FAS ground motion relative to the ergodic BA18 model were calculated. For the dcpp flatfile data, a strike-slip style-of-faulting was assumed in calculating the median ground-motion prediction. The depth-to-top of rupture was estimated using the CY14 relationship with magnitude, and basin depth to  $V_S$  horizon of 1 km/sec (Z1.0) was assumed to be the default value for stations missing Z1.0 estimates. For the DCP recordings,  $V_{S30}$  values of 856 and 777 m/sec were assigned to ESTA27 and ESTA28, respectively, consistent with the 2015 analysis.

### 9.3.2.2. Analysis

Using the subset of FAS residuals relative to the BA18 ergodic model described above, Dr. Sung (see Appendix F) estimated the empirical site term for DCP and its regional and uncorrelated

components using the non-ergodic modeling approach. This analysis, described in detail in Appendix F involves the following steps:

1. Perform a mixed-effects regression analysis to estimate the between-event residuals for the dcpp flatfile data. Figure 9-21 shows the calculated between-event residuals versus magnitude at frequencies of 0.1, 1, 5, 10, 14.7, and 23.3 Hz. An examination of these plots indicates a trend in the between-event residuals as a function of magnitude. This trend could be due to the nonuniform magnitude scale in the dataset and is more pronounced outside of 0.3-11.6 Hz, where the dataset is more limited. A simple linear fit of the between-event residuals versus magnitude was applied as shown on Figure 9-21 (blue lines). These linear fits versus magnitude were then removed from the total residuals to center the magnitude scaling of the non-ergodic model on the data.

For the Parkfield and the San Simeon earthquakes, the between-event residuals were centered on the distance from these earthquakes to DCP. This is done to avoid mapping path effects into the site term given the limited number of recordings at DCP, consistent with the 2015 empirical approach. The DCP recordings were not included in the estimation of these average event-path terms.

2. Perform a mixed-effects regression analysis that removes the trend of the between-event residuals versus magnitude obtained from step 1 and calculate the between-event residuals and the site-to-site ( $\delta S_2 S$ ) residuals (also called between-site residuals). The resulting site-to-site residuals versus  $V_{S30}$  are shown on Figure 9-22 along with the averaged residuals in different  $V_{S30}$  bins at frequencies of 0.1, 1, 5, 10, 14.7, and 23.3 Hz. The average of the binned residuals on Figure 9-22 indicates no significant trends versus  $V_{S30}$ , particularly in the  $V_{S30}$  bins that include a large number of stations.
3. Using the site-to-site ( $\delta S_2 S$ ) residuals calculated above, calculate the regional site term ( $\delta S_2 S_{reg}$ ) in FAS domain using the spatially varying coefficient model (VCM) following the methodology in Lavrentiadis et al. (2023). VCM imposes a spatial correlation on the model coefficients such that they vary continuously from one location to another. The model hyperparameters in this analysis were fixed to those from Lavrentiadis et al. (2023). Next, the uncorrelated site term ( $\delta S_2 S_{unc}$ ) at DCP in FAS domain was estimated as:  $\delta S_2 S_{unc} = \delta S_2 S - \delta S_2 S_{reg}$ .

Figure 9-23 shows the DCP FAS site term ( $\delta S_2 S$ ) and its components ( $\delta S_2 S_{reg}$  and  $\delta S_2 S_{unc}$ ) versus frequency. The regional site term component  $\delta S_2 S_{reg}$  at DCP reflects broader adjustments to the ergodic backbone model due to regional site effects in the vicinity of the site. The left panel of Figure 9-23 indicates that  $\delta S_2 S_{reg}$  is negative at frequencies greater than 1 Hz, indicating that the ground motion in the coastal region surrounding DCP has below-average site effects consistent with the negative observed  $\delta S_2 S$  at DCP at high frequencies.

The epistemic uncertainty in the  $\delta S_2 S_{reg}$  computed from the VCM and in  $\delta S_2 S_{unc}$  computed based on site-to-site variability in the dataset are shown in the bottom panel of Figure 9-23. The epistemic uncertainty for the  $\delta S_2 S_{unc}$  term is larger than that for

$\delta S2S_{reg}$  because there are only three recordings to constrain the site-specific site term at DCPD while the regional site term is constrained by a large dataset at stations in the vicinity.

4. Convert the site term components  $\delta S2S_{reg}$  and  $\delta S2S_{unc}$  from FAS domain to PSA domain using the empirically calibrated random vibration theory (RVT) method by Phung and Abrahamson (2023). For each component of the site term, FAS are computed for the ergodic and the non-ergodic model, including the site term component in question for a scenario earthquake with  $M$  7.5,  $R_{RUP}$  of 4.8 km, and for  $V_{S30} = 760$  m/sec. This earthquake scenario is consistent with a hazard-significant scenario on the Hosgri fault. The ergodic and non-ergodic FAS are converted to PSA and then ratioed to compute the PSA site term components. The total site term  $\delta S2S$  in PSA domain is then calculated by summing the PSA  $\delta S2S_{reg}$  and  $\delta S2S_{unc}$ . Figure 9-24 shows a comparison of the site term and its components in FAS and PSA domains.

Following the analysis described in this section, a sensitivity analysis was performed by Dr. Sung (see Appendix F) to assess the consistency of the site term obtained from the FAS data analysis and converted to the PSA domain, and the site term computed directly in the PSA domain. Given the preliminary nature of the dcpp flatfile, it was not possible to match all the subsets of FAS recordings to corresponding ones in PSA. As a result, a PSA dataset consisting of a subset of the recordings used in the FAS analysis (Data2) and including the three DCPD recordings and the San Simeon and Parkfield recordings was used in the PSA analysis. Figure 9-25 shows the number of recordings versus frequency used in the FAS analysis (Data1) and the sensitivity analysis (Data2).

Given this reduced subset of data (Data2 plus additional DCPD and San Simeon and Parkfield recordings), the FAS analysis described above was repeated to calculate site terms and then convert them to PSA via RVT. The analysis was also repeated using the PSA dataset to compute the site term at DCPD and its components directly in the PSA domain. Figure 9-26 shows a comparison of the PSA site term and its components obtained from the FAS analysis with Data1 and Data2, and directly from the PSA analysis with Data2. Using the same set of data (Data2), Figure 9-26 indicates the PSA site terms obtained from the FAS analysis via RVT versus directly from the PSA analysis are consistent. Therefore, the conversion of the site terms from FAS to PSA domains does not seem to impact the PSA site terms obtained.

A difference, however, can be observed between the PSA site terms (plot g of Figure 9-26) obtained from the different subsets of data used (Data1 and Data2). In principle, the site term at DCPD calculated based on the three available recordings at ESTA27 and ESTA28 should not be dependent on the subset of data used in the analysis. The observed difference in plot g of Figure 9-26 can be attributed to a different overall shift (constant term) in the observed ground-motion data relative to the median non-ergodic ground-motion model for Data1 versus Data2. This sensitivity of the DCPD site term to the dataset used could indicate a lack of robustness of the results obtained.

### 9.3.2.3. Evaluation

The preliminary implementation of the non-ergodic modeling approach (referred to as updated study) for the estimation of the empirical site term for DCPD provides valuable insights into the

regional trend in site effects in the coastal region in the vicinity of DCPD compared to the site term inferred from the available site-specific ground-motion recordings at ESTA27 and ESTA28. Figure 9-27 compares the 2015 empirical site term in LN units to the PSA site term and its components from the non-ergodic analysis. This figure indicates that the total site terms obtained from the 2015 empirical study and from this updated study are comparable, showing a below-average ground motion at DCPD at frequencies greater than 3 Hz due to site effects. The examination of the regional component of the site term on Figure 9-27 also indicates a below-average ground motion in the region due to regional site effects. This regional trend that was estimated through the preliminary non-ergodic modeling analysis provides valuable insights into the cause of the smaller high-frequency ground motions at DCPD. About half of the total ground-motion reduction observed at DCPD is a regional effect, and half of the reduction is a site-specific effect.

Figure 9-28 shows the ratio of the updated empirical site term at DCPD to that obtained from the 2015 study. For frequencies above 0.67 Hz, the ratio is between 0.83 and 1.15 (ratio at 5 Hz). For frequencies below 0.5 Hz, the site terms were not modeled in the 2015 empirical study. Overall, the difference between the 2015 and the updated total site term is not large and can be attributed to the preliminary nature of the dataset used in the non-ergodic modeling approach and potential data quality issues resulting from the automated processing of ground-motion processing. Figure 9-29 provides a comparison of the updated total site term from this preliminary analysis to the site term and its uncertainty from the 2015 study. This figure indicates that differences observed between the 2015 and the updated empirical site terms are small compared to the uncertainty in the empirical site term.

Given the discussion presented in this section, no updates to the 2015 empirical site terms are recommended. Results from the non-ergodic modeling approach and the regional trend in the site term support the use of the 2015 empirical site term. Further refinements of the ground-motion dataset and the implementation of the non-ergodic modeling approach and associated sensitivities are needed before adopting results from this study. Such work can be undertaken as part of a longer-term study.

## 9.4. CONCLUSIONS

In this chapter, we presented an overview of the analytical and empirical site adjustment factors developed in the 2015 study for adjusting the ground motion from the reference rock site condition with  $V_{S30}$  of 760 m/sec to site-specific condition at the control point at DCPD. Results from the 2015 study in terms of site factors and GMRS hazard for the control point were presented.

The 2015 analytical study was evaluated in terms of approach and inputs to the site response analysis. The characterizations of the host and target site conditions were evaluated in light of new available information since the conclusion of the 2015 study. A sensitivity analysis was performed to evaluate the impact of alternative characterization of the host site conditions on the obtained analytical site factors. Overall, this impact on the overall site factors was small, considering the low weight of [0.33] assigned to the analytical approach.

The 2015 empirical site factors were evaluated in terms of available data and methods since the conclusion of the 2015 study and their impact of the site term. The empirical site term is primarily driven by site-specific ground-motion recordings. Since no new ground-motion data

have been recorded at ESTA27 and ESTA28, updates to the empirical site term were not expected to be significant.

Next, the preliminary non-ergodic ground-motion modeling approach was applied to estimate the empirical site term at DCPD and its regional and uncorrelated components. For this purpose, an expanded preliminary dataset was assembled, including recent ground-motion data post NGA-West2, and processed using automated processing tools. Results from the preliminary non-ergodic analysis indicated that the regional site term resulting from broader regional site effects in the vicinity of DCPD shows a below-average trend in ground motion consistent with that observed in the 2015 empirical site term at frequencies greater than 1 Hz. This consistency in the trends between the regional and the site-specific empirical terms provides support and explanation for the 2015 site terms. Overall, the empirical site term obtained from the non-ergodic approach was generally comparable to the 2015 site term. The site term from the non-ergodic analysis was not adopted due to the preliminary nature of the dataset used, as well as the preliminary nature of the analysis performed.



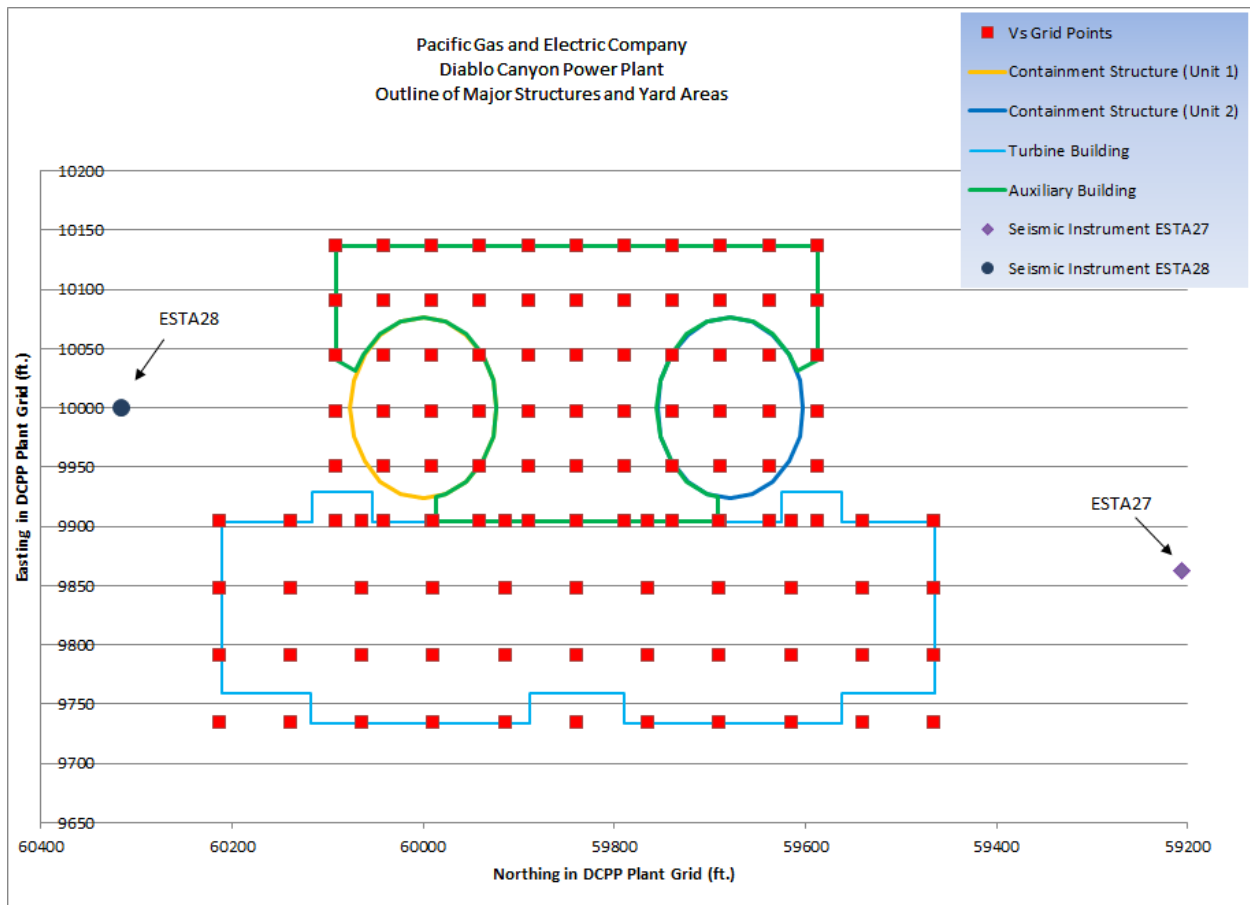


**Figure 9-1. Locations of 1-D profiles in the power block and turbine building region used to define the control point (from PG&E, 2015d)**

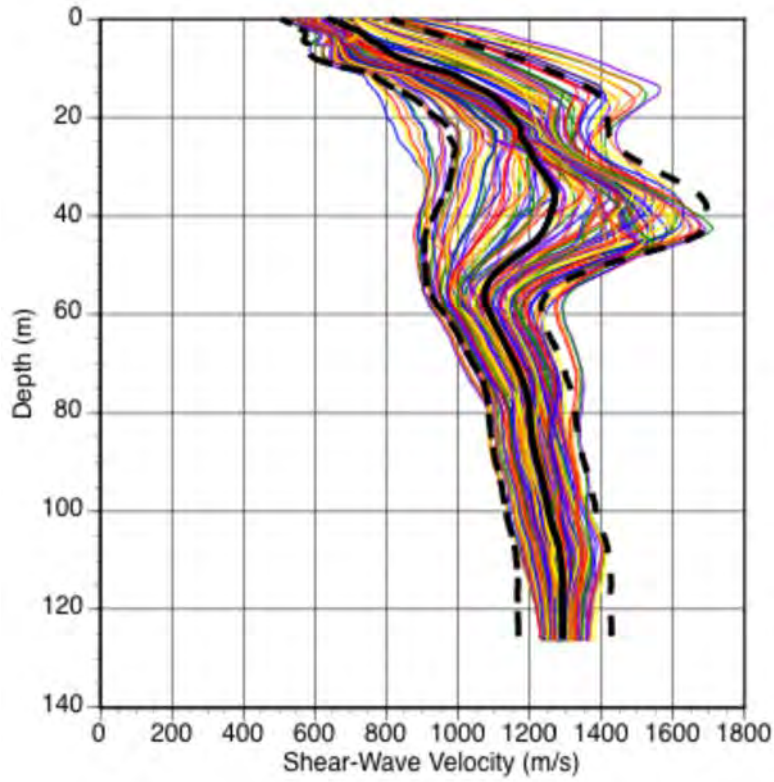


**Figure 9-2. Range of  $V_s$  profiles under the power block and the turbine building regions along with the central, upper, and lower  $V_s$  profiles (shown in black) for the control point (from PG&E, 2015d)**

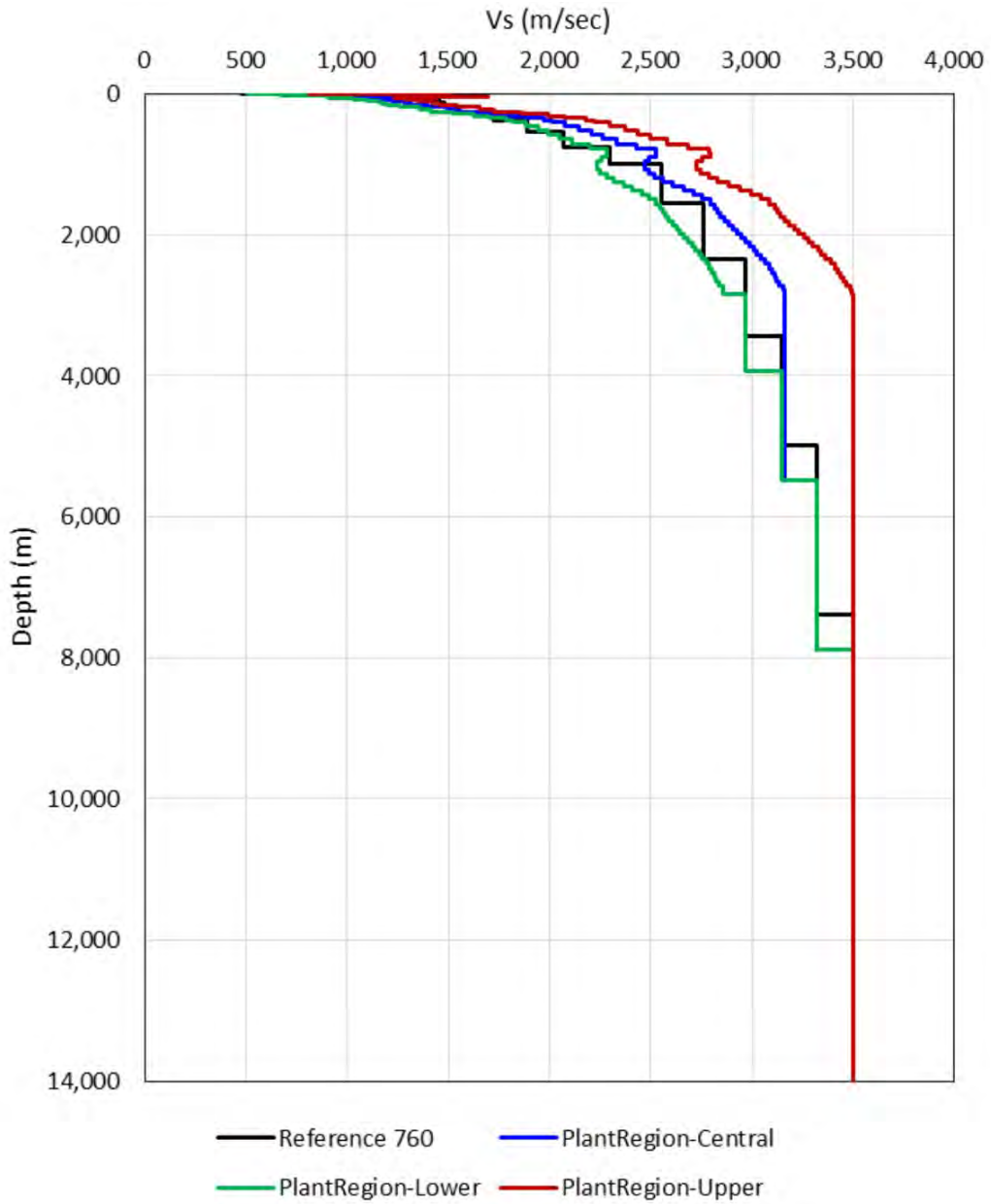


**Figure 9-3. Control point  $V_s$  profiles compared to the WUS host  $V_s$  profile (labeled reference 760) (from PG&E, 2015d)**

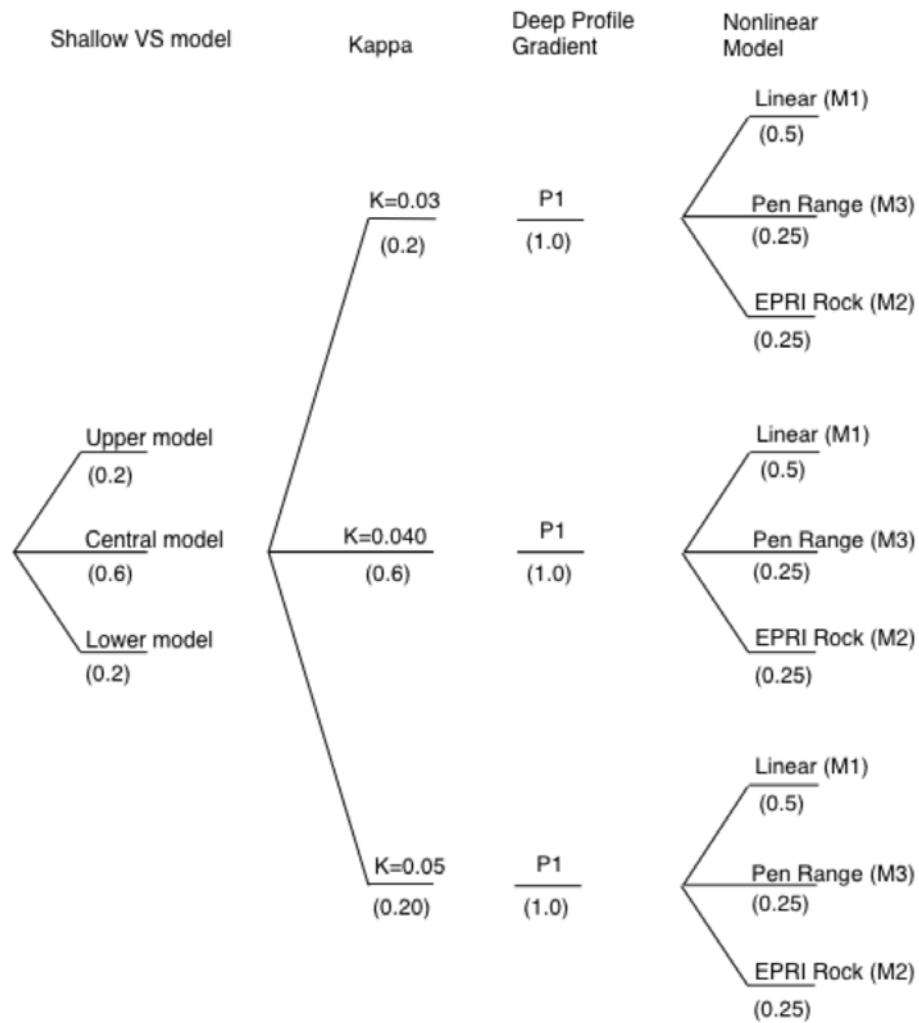
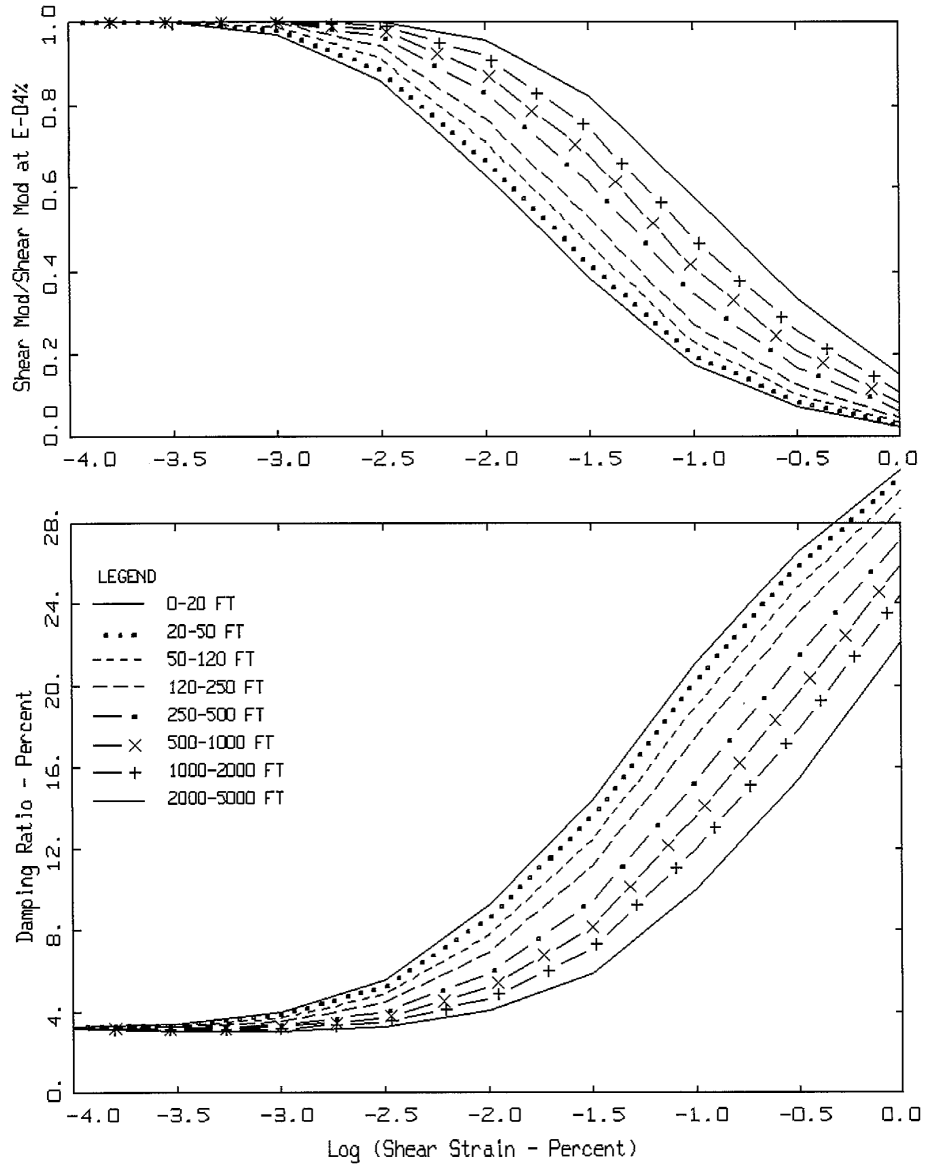
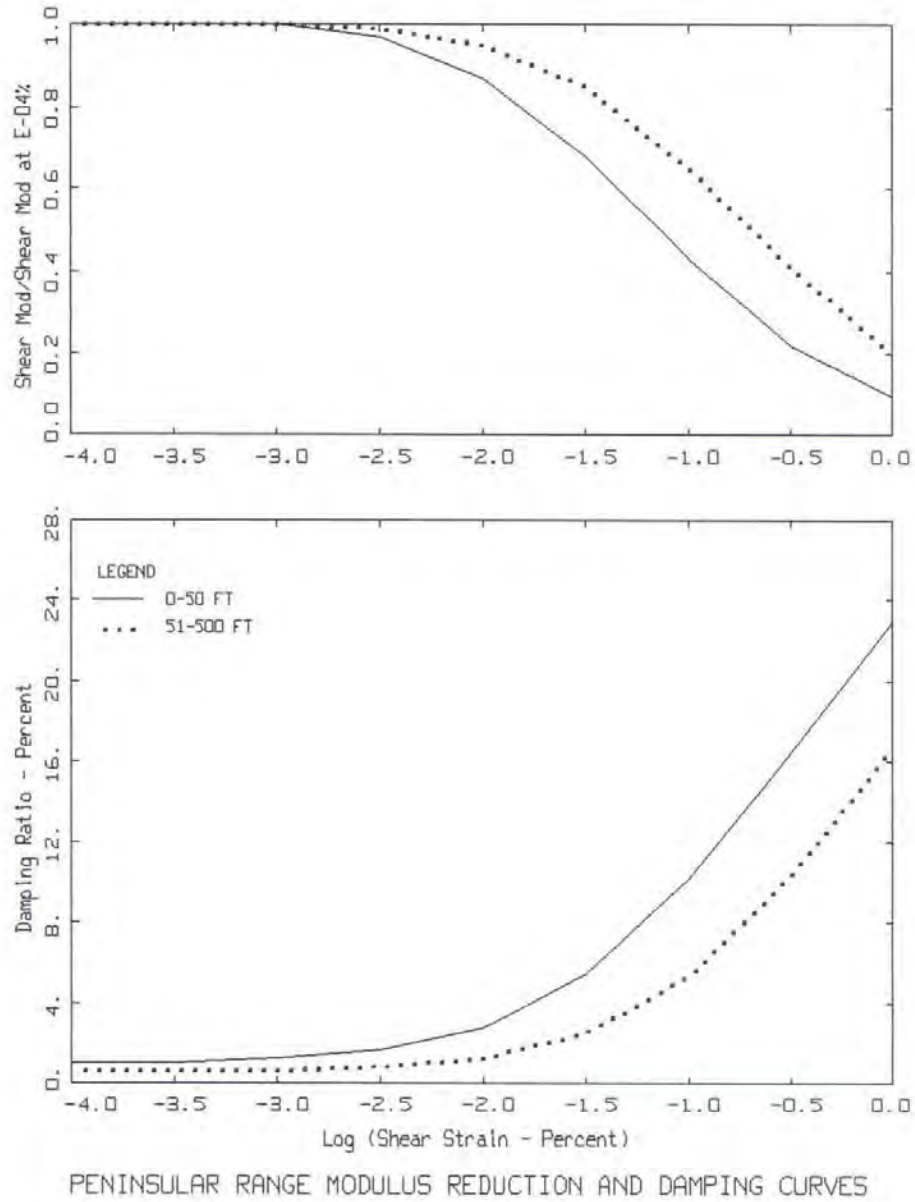


Figure 9-4. Logic tree for the site condition characterization for the DCPD control point used in the PE&A (2015) analytical study (from PG&E, 2015d)



MODULUS REDUCTION AND DAMPING CURVES FOR ROCK (EPRI)

**Figure 9-5. Modulus reduction and damping curves for the EPRI rock model (from PE&A, 2015)**



**Figure 9-6. Modulus reduction and damping curves for the Peninsular Range model (from PE&A, 2015)**



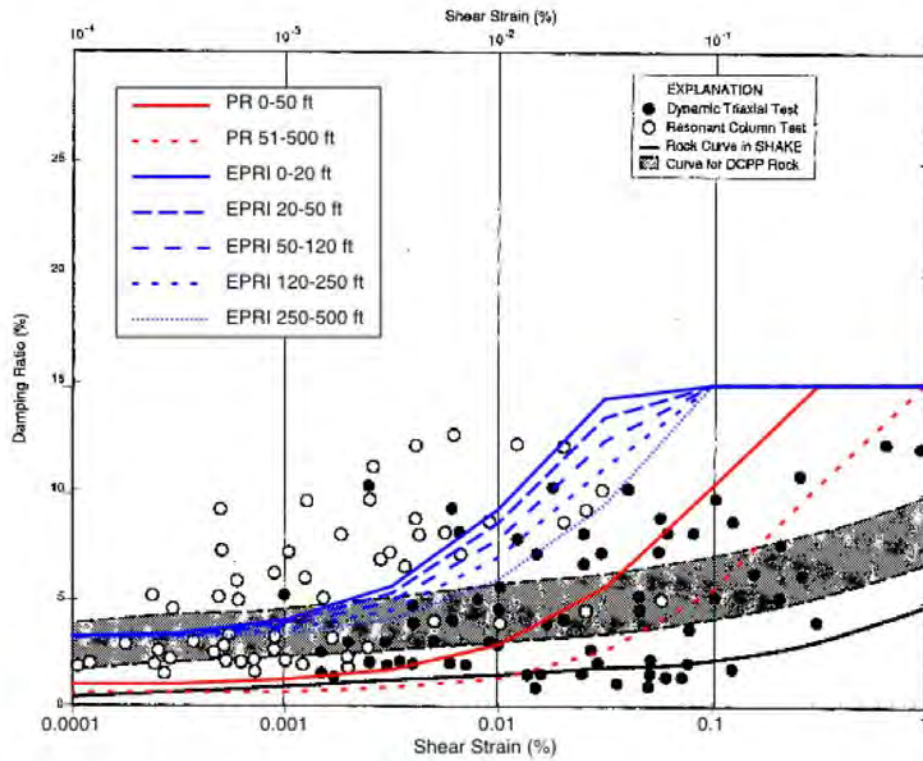
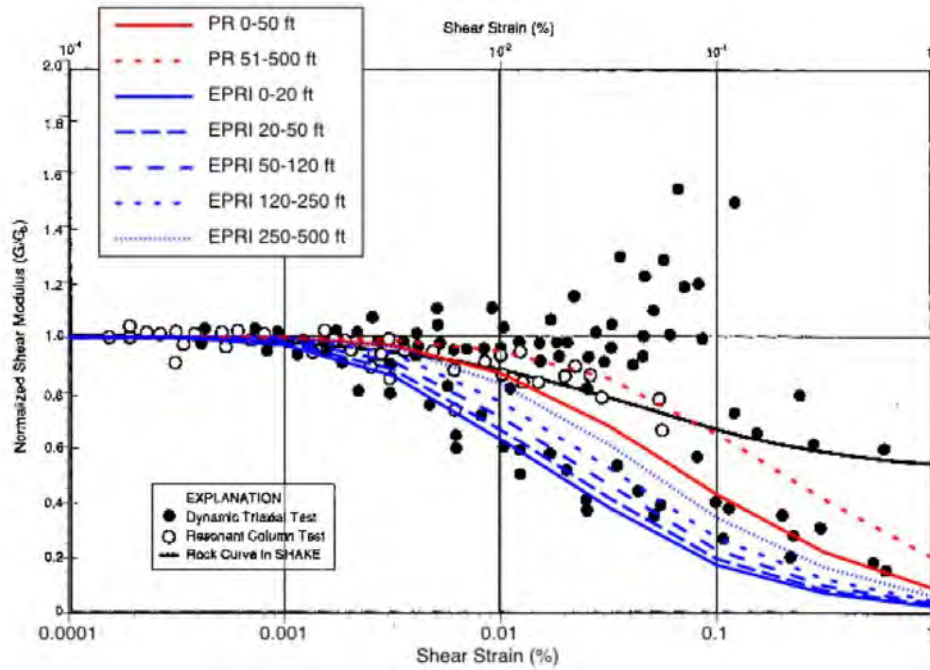
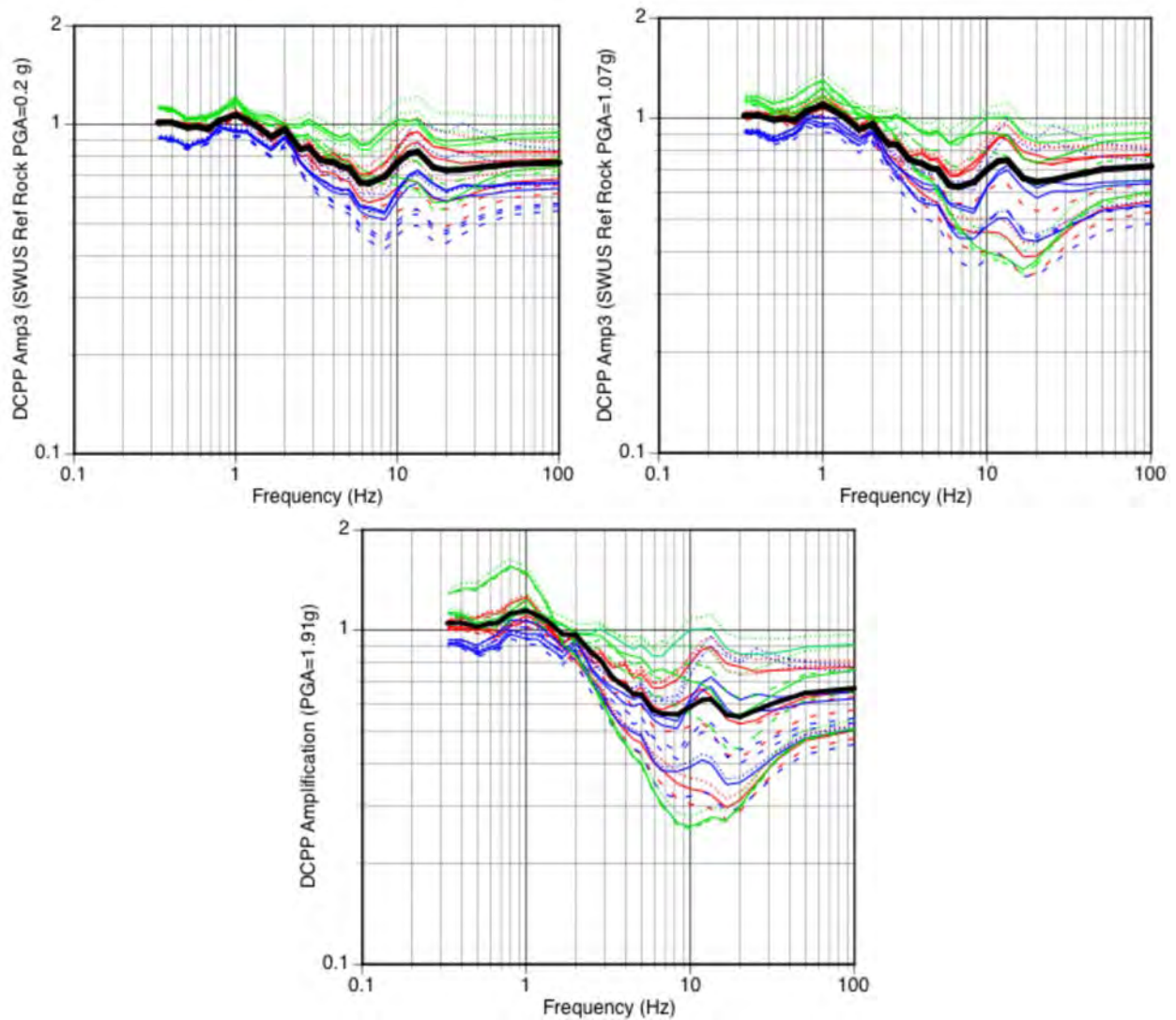
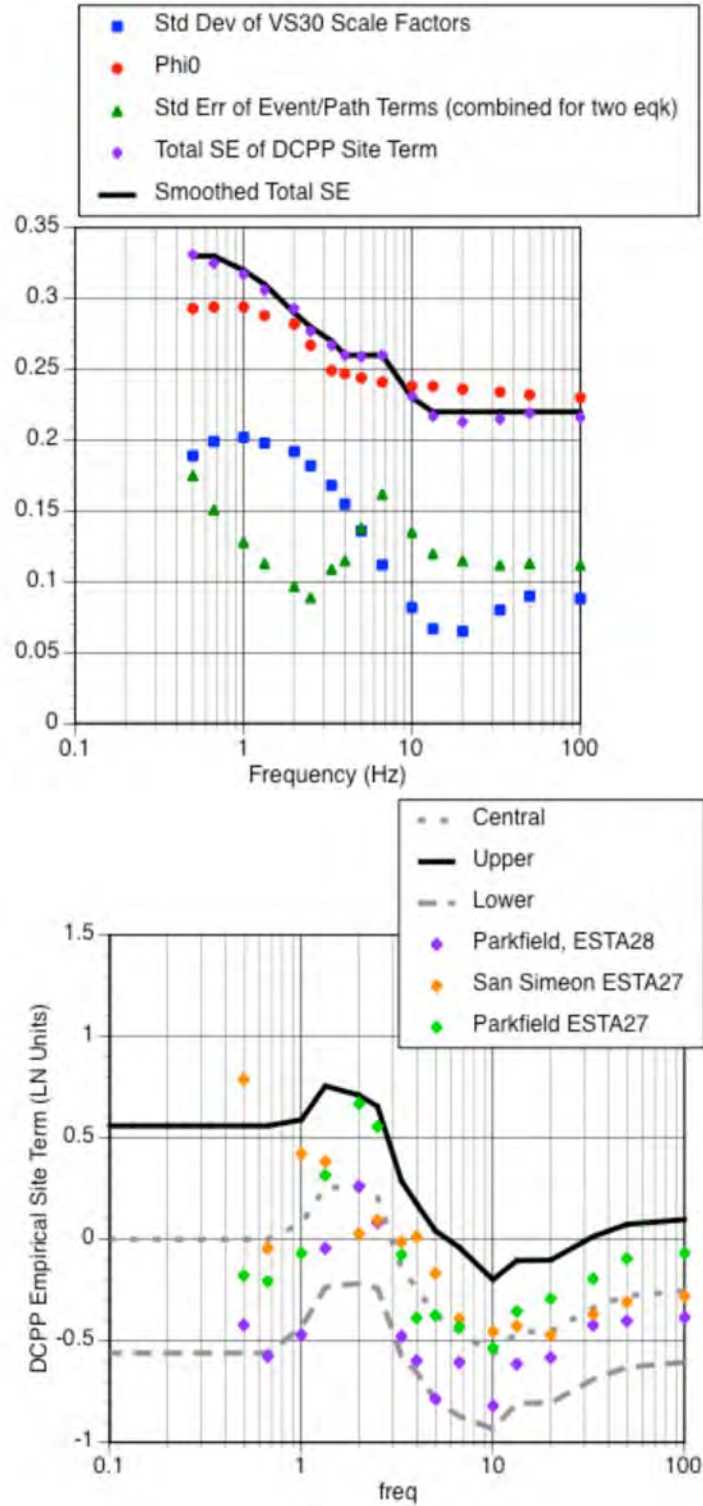


Figure 9-7. Comparison of modulus reduction (top) and damping (bottom) curves from laboratory testing of DCPD soft rock to the EPRI rock and Peninsular Range models (from PG&E, 2015d)



**Figure 9-8. Analytical site adjustment factors for DCP for a reference rock PGA of 0.2 g (top left), 1.07 g (top right), and 1.91 g (bottom). The green, red, and blue curves are for the lower, central, and upper  $V_s$  profiles. The short-dashed lines are for target kappa of 0.03 sec, the long-dashed lines are for target kappa of 0.05 sec, and the solid lines are for target kappa of 0.04 sec. The black line shows the mean factors. (From PG&E, 2015d)**



**Figure 9-9. Top: Components of the epistemic uncertainty of the empirical site term. Bottom: Central, upper, and lower estimates of the empirical site term (from PG&E, 2017b)**

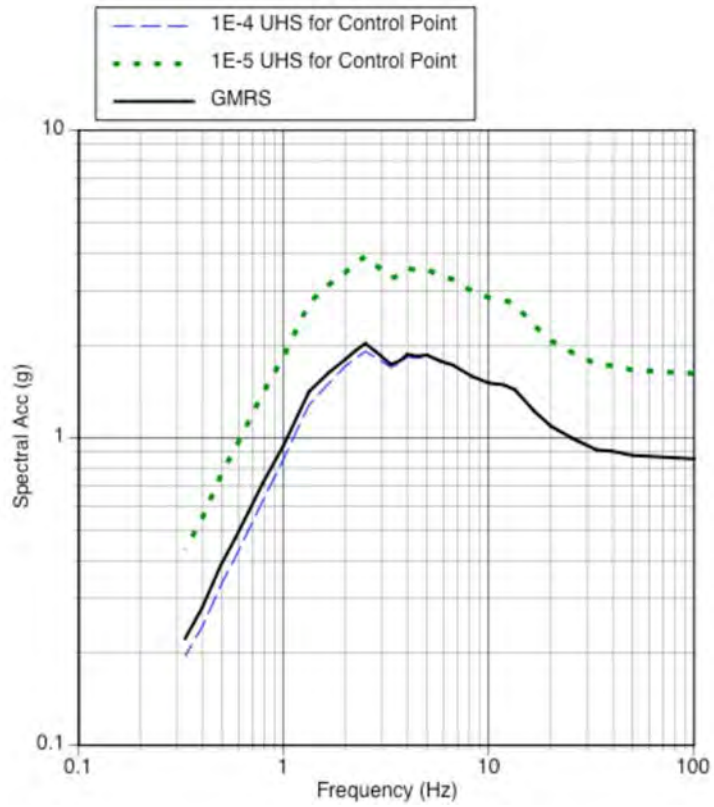


**Figure 9-10. Uniform hazard spectra (UHS) and GMRS for the DCCP control point (from PG&E, 2015d)**

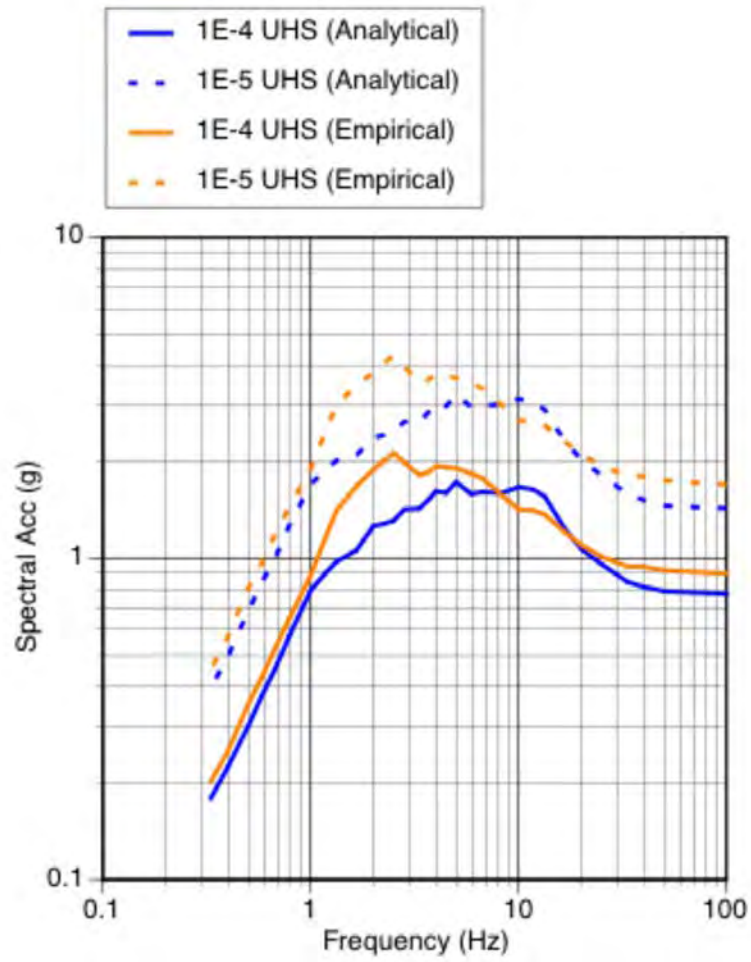
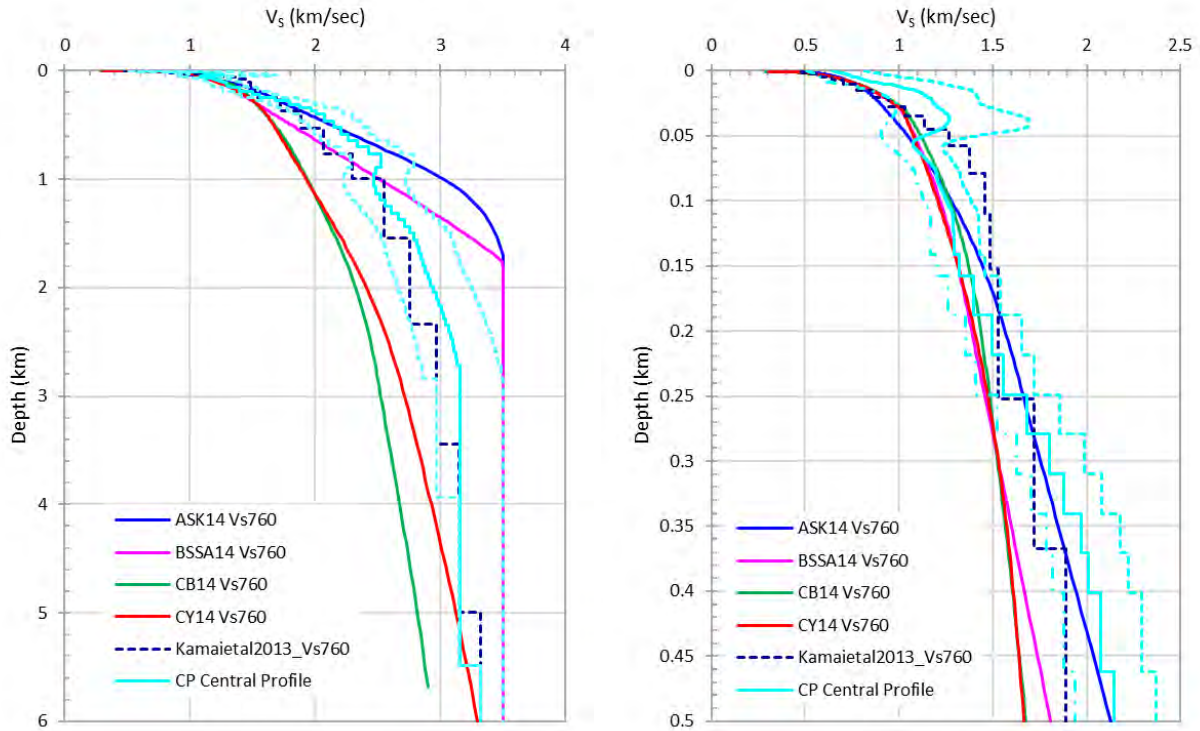
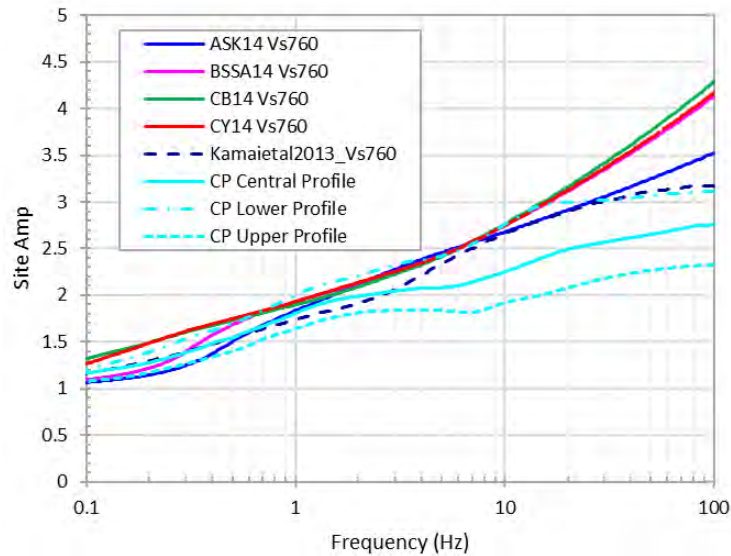


Figure 9-11. Sensitivity of the UHS to the site term approach (from PG&E, 2015d)





**Figure 9-12. Comparison of the GMPE-compatible  $V_s$  profiles for ASK14, BSSA14, CB14, and CY14 to the Kamai et al. (2013) reference  $V_s$  profile for  $V_{s30}$  of 760 m/sec. The control profiles (central, upper, and lower) are shown in cyan. The left panel shows full profile while the right panel shows the profiles in the top 500 m.**



**Figure 9-13. Quarter-wavelength linear site amplifications of the host  $V_s$  profiles and the control point target  $V_s$  profiles**

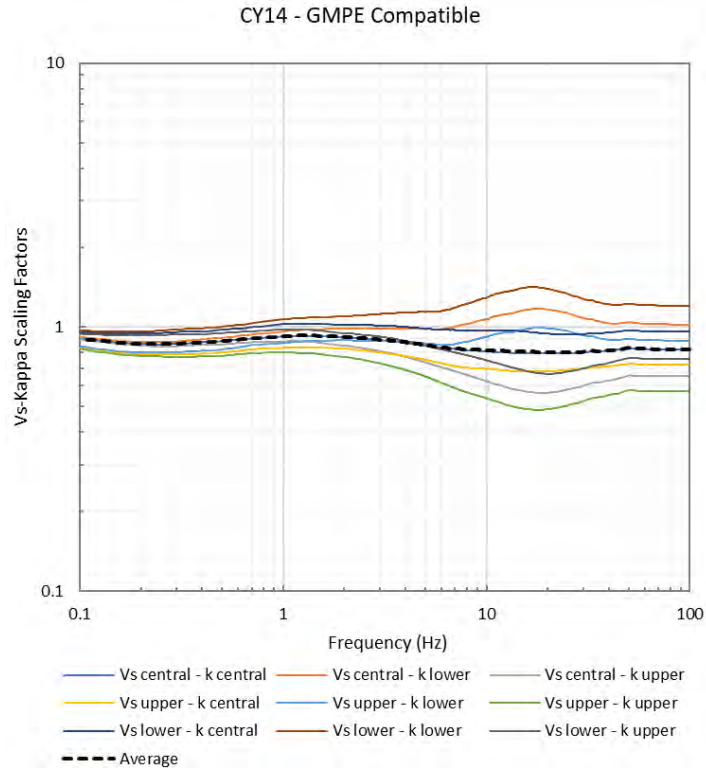


**Figure 9-14.  $V_s$ -kappa scaling factors for CY14 using the GMPE-compatible host  $V_s$  profile and kappa for each of the nine target DCPV  $V_s$  and kappa branches**

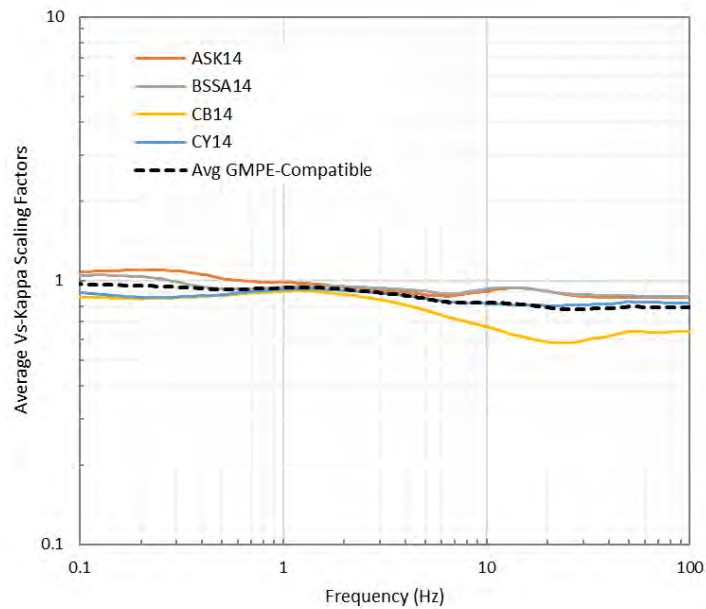


**Figure 9-15. Comparison of the average  $V_s$ -kappa scaling factors for each of the four NGA-West2 GMPEs using the GMPE-compatible host  $V_s$  profiles and kappa. The average of the factors over the four NGA-West2 GMPEs is shown with the black curve.**



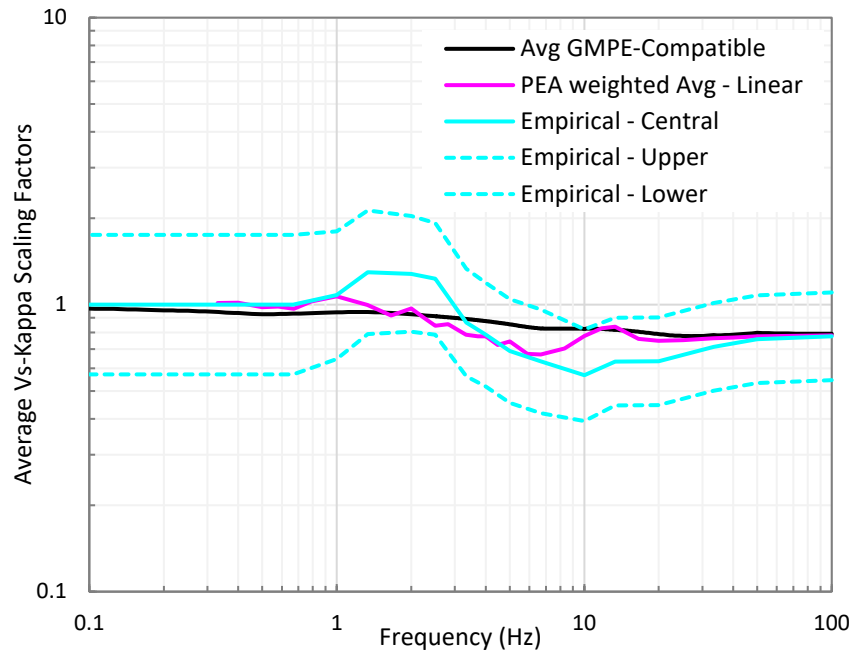


**Figure 9-16. Comparison of the analytical and empirical site factors for DCPD to the analytical factors obtained using the IRVT approach and the GMPE-compatible host  $V_s$  profiles and kappa**

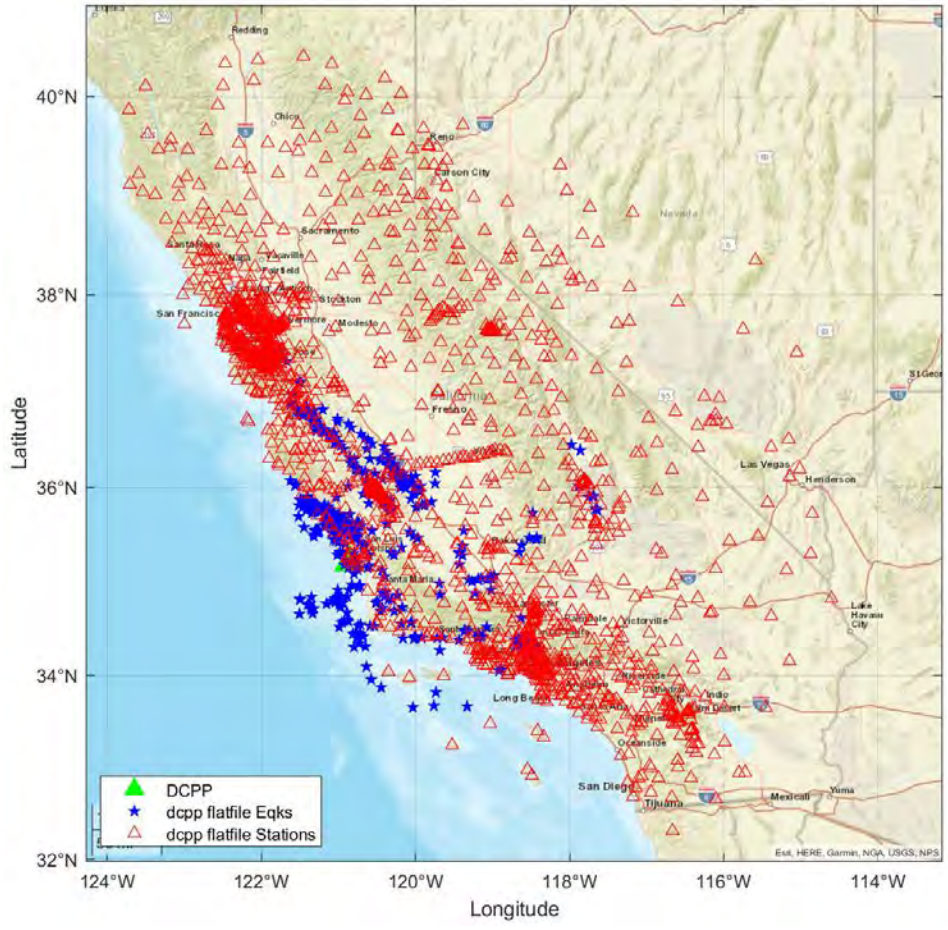


**Figure 9-17. Earthquake epicenters (blue stars) and ground-motion recording station locations (open red triangles) for the DCPP expanded dataset used in the non-ergodic analysis**

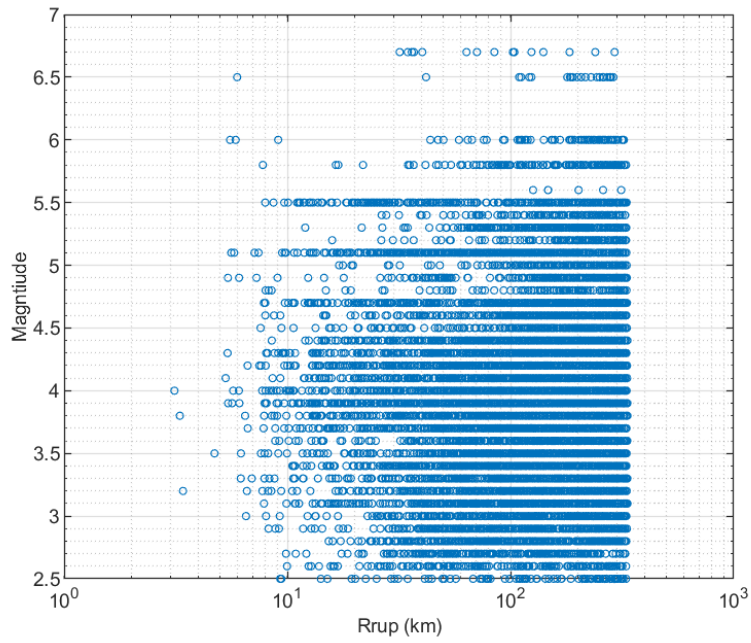


**Figure 9-18. Magnitude-distance distribution of the expanded dcpp flatfile used in the non-ergodic analysis**

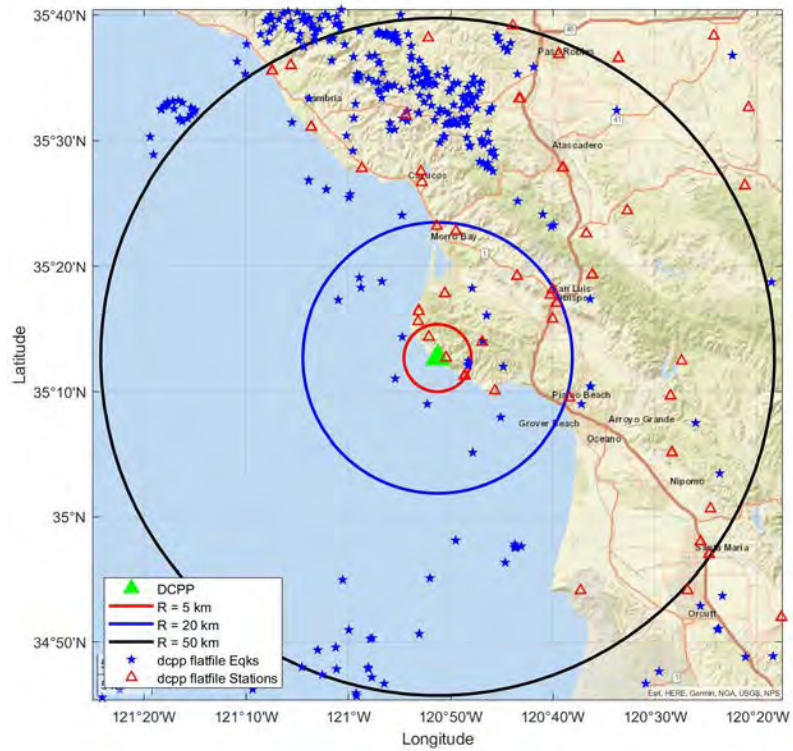
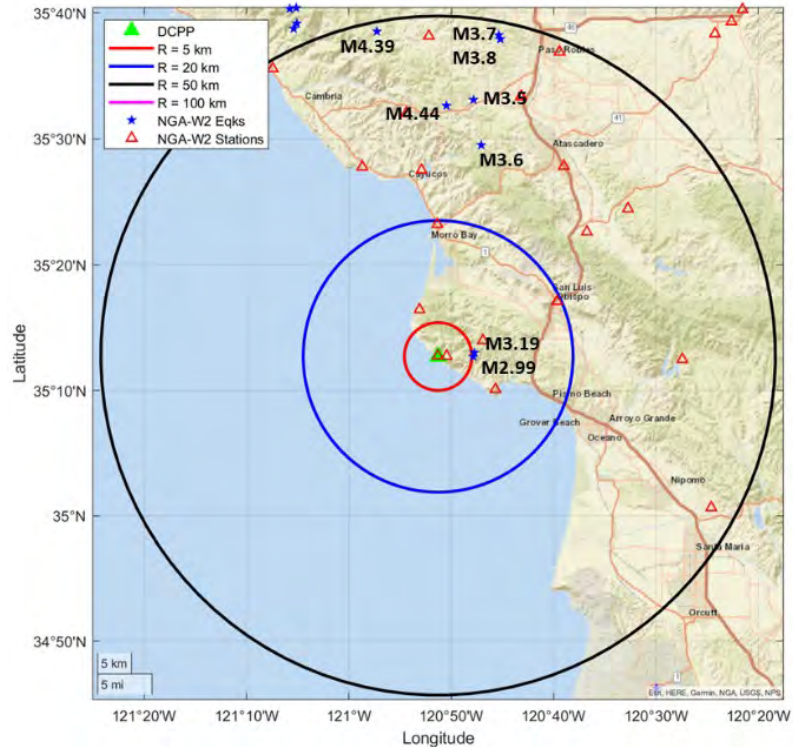


**Figure 9-19. Earthquake epicenters (blue stars) and ground-motion recording station locations (open red triangles) within 50 km of DCP in the NGA-West2 dataset (top) and the expanded preliminary dcpp dataset (bottom)**

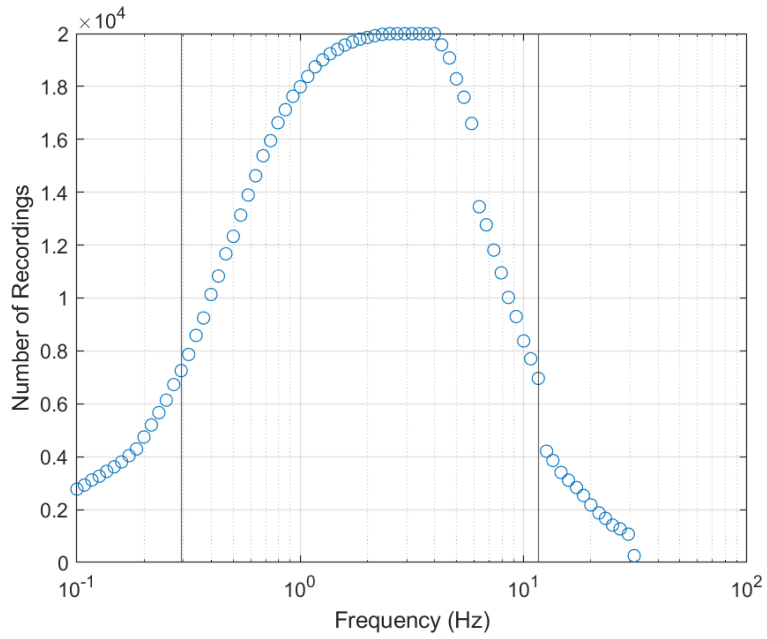


**Figure 9-20. Number of FAS data in the usable frequency range versus frequency in the dcpp flatfile. Vertical lines at 0.3 and 11.6 Hz indicate the range beyond which less than 35% of the data remain.**

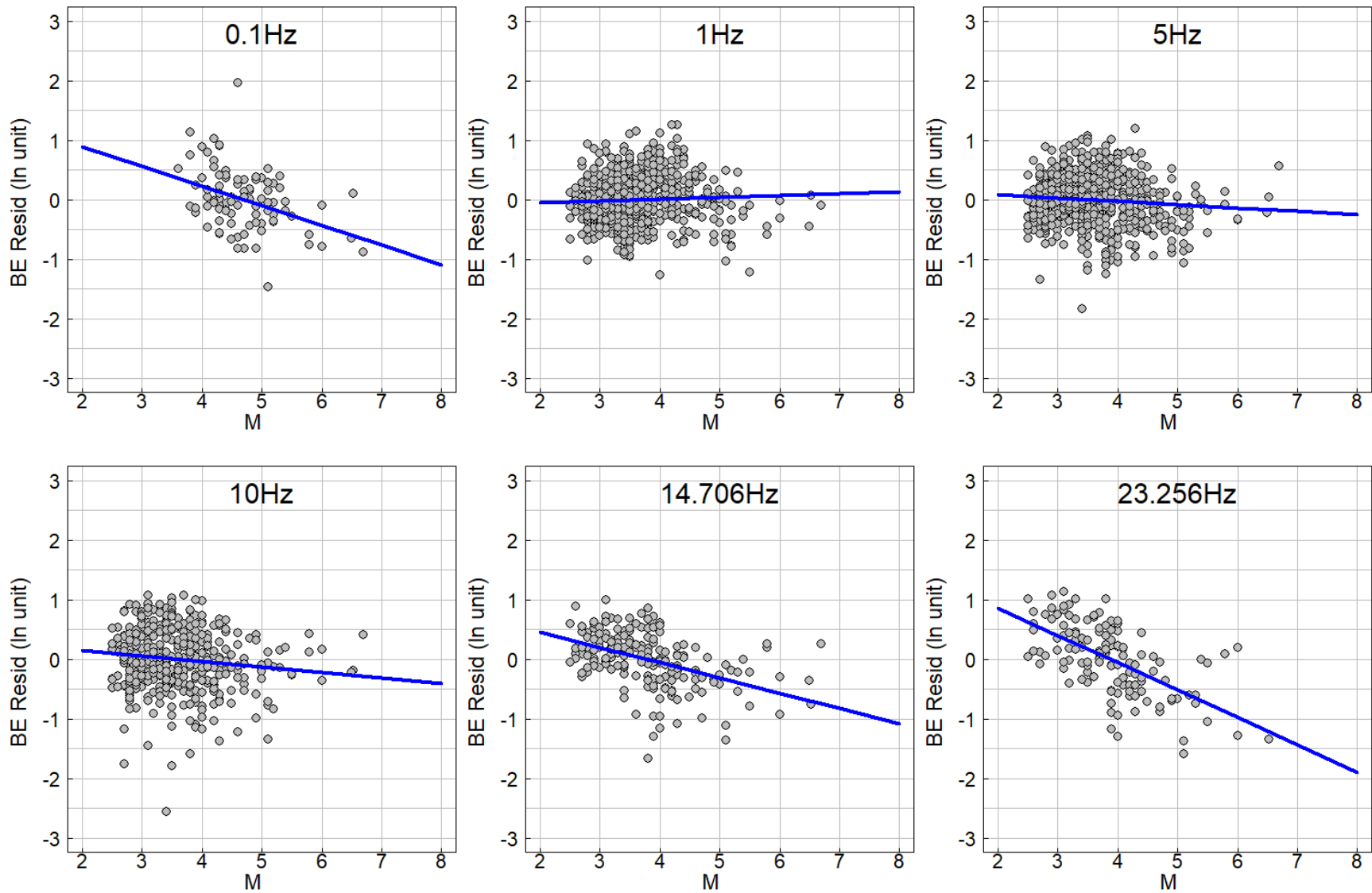


**Figure 9-21. FAS between-event residuals versus magnitude at frequencies of 0.1, 1, 5, 10, 14.7, and 23.3 Hz. The blue lines show the linear fits to the residuals versus magnitude (from Dr. Sung's report in Appendix F)**



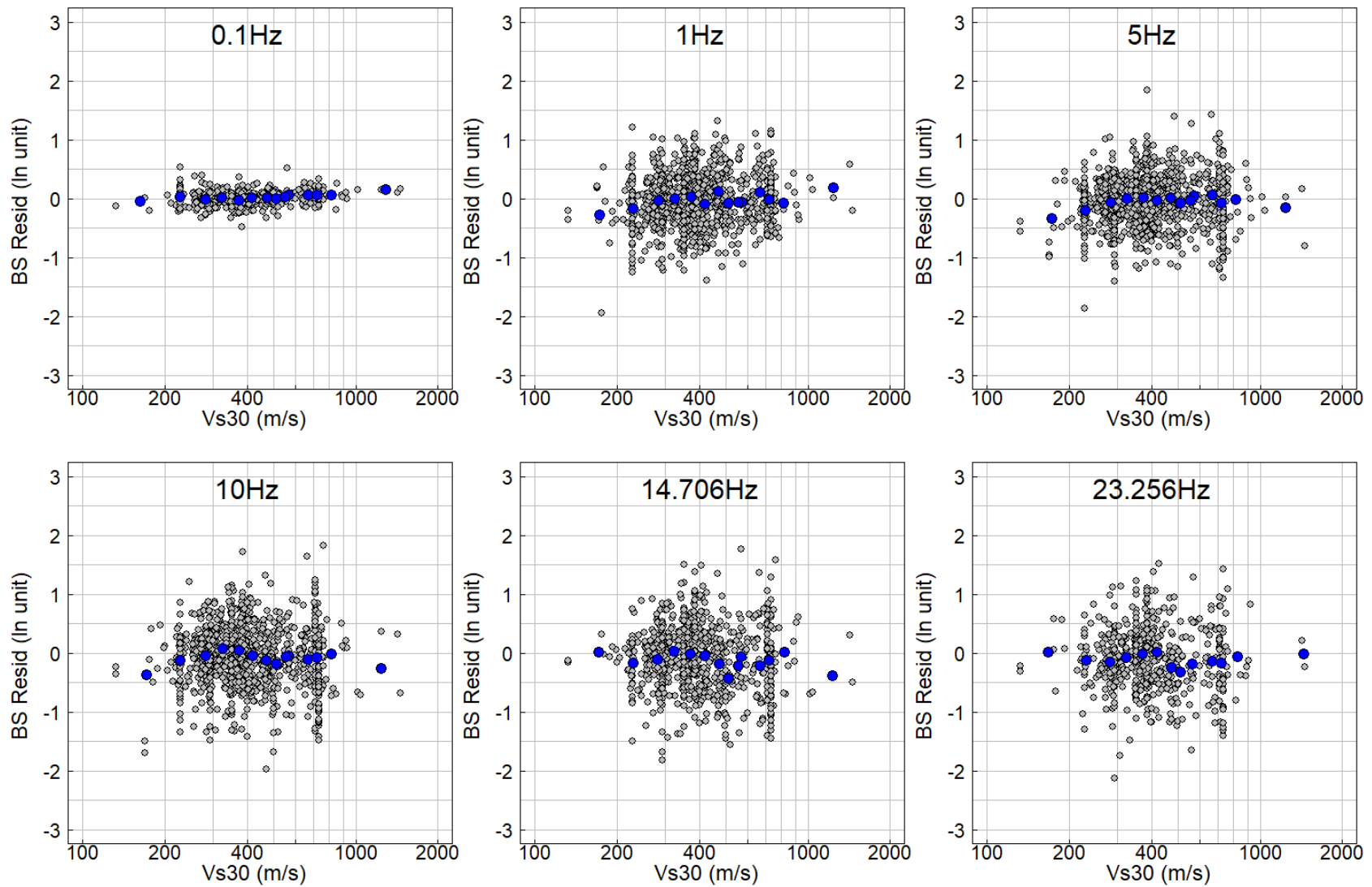


**Figure 9-22. FAS site-to-site terms versus  $V_{s30}$  at frequencies of 0.1, 1, 5, 10, 14.7, and 23.3 Hz. The blue datapoints show bin averages of the site-to-site residuals. (from Dr. Sung's report in Appendix F)**

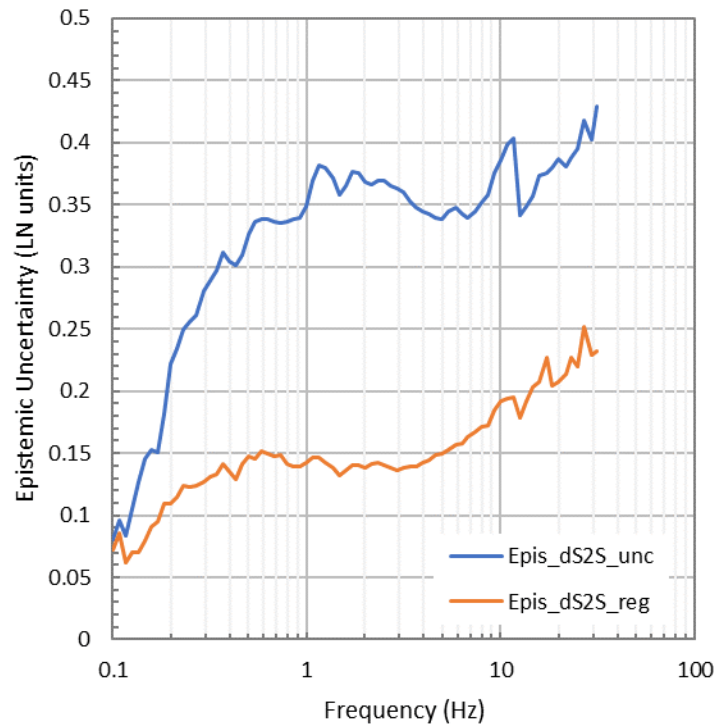
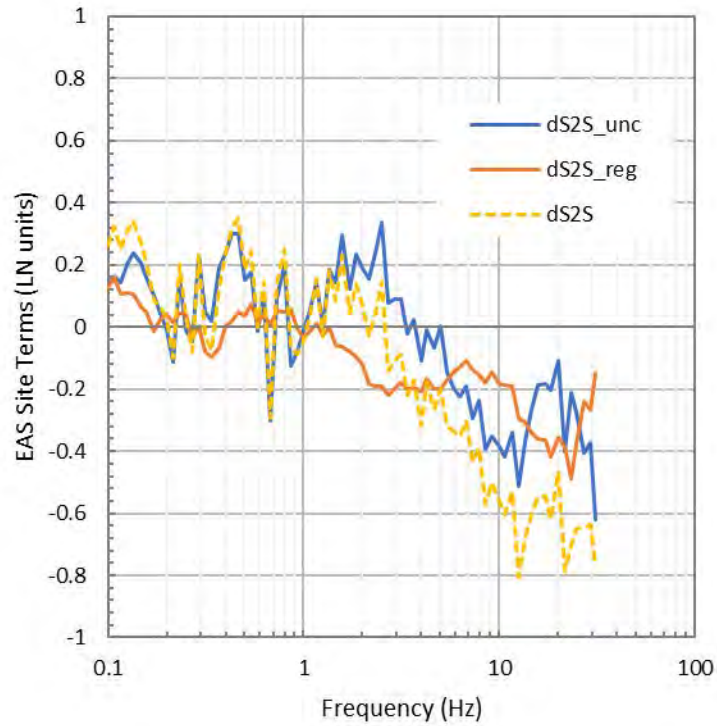


**Figure 9-23. Top: DCP site term ( $\delta S2S$ ) and its regional ( $\delta S2S_{reg}$ ) and uncorrelated ( $\delta S2S_{unc}$ ) components in FAS domain. Bottom: Epistemic uncertainty of the regional and uncorrelated components of the site term.**

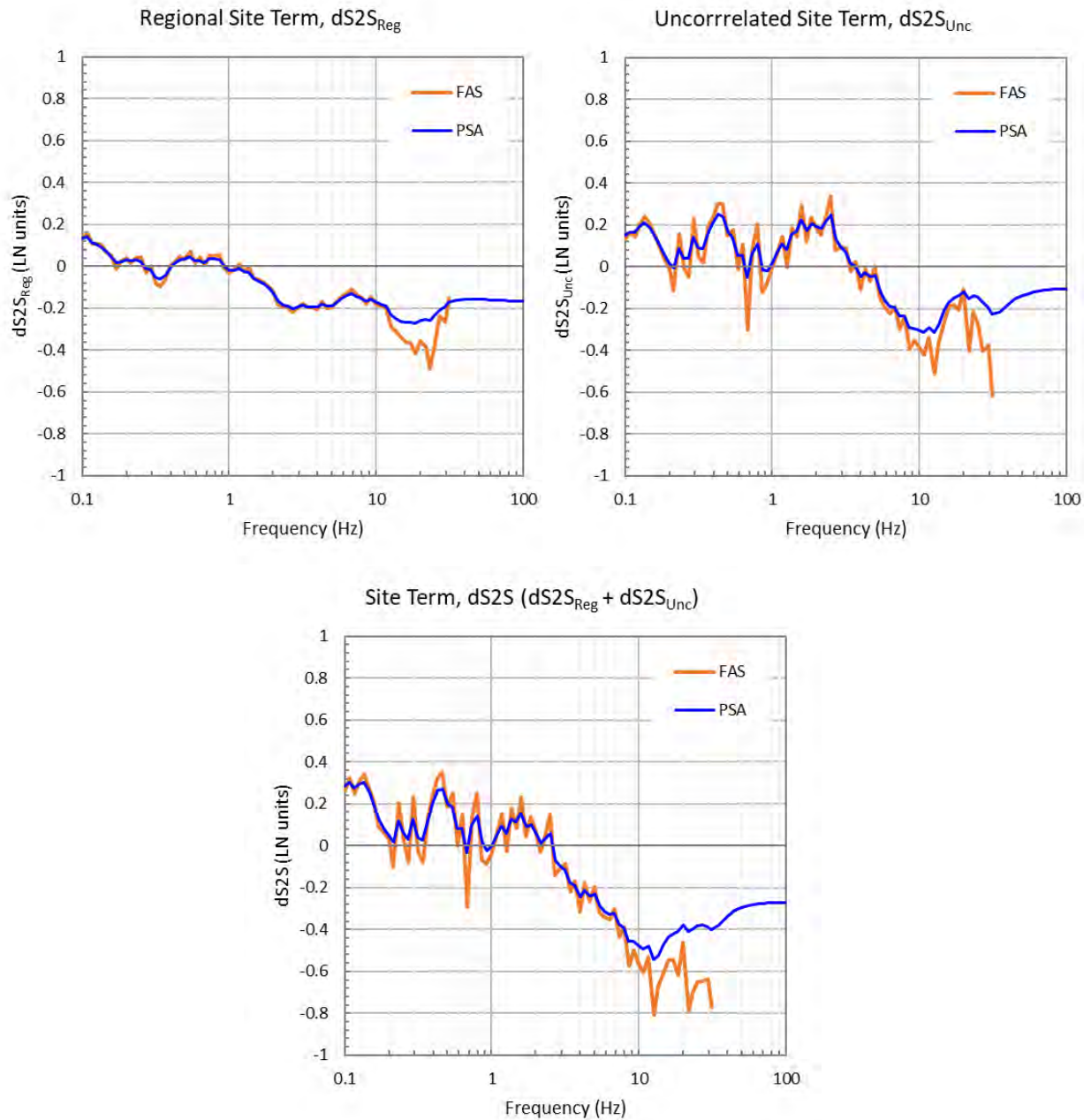


**Figure 9-24. Comparison of site term and its regional and uncorrelated components in the FAS and PSA domains**

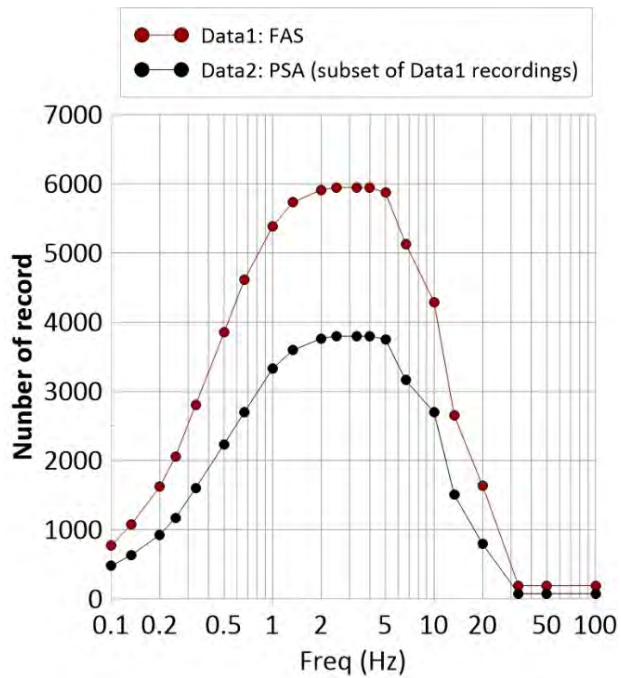


**Figure 9-25. Number of recordings versus frequency for the dataset used in the FAS non-ergodic modeling approach (Data1) and in the PSA sensitivity analysis (Data2) (from Dr. Sung’s report in Appendix F)**

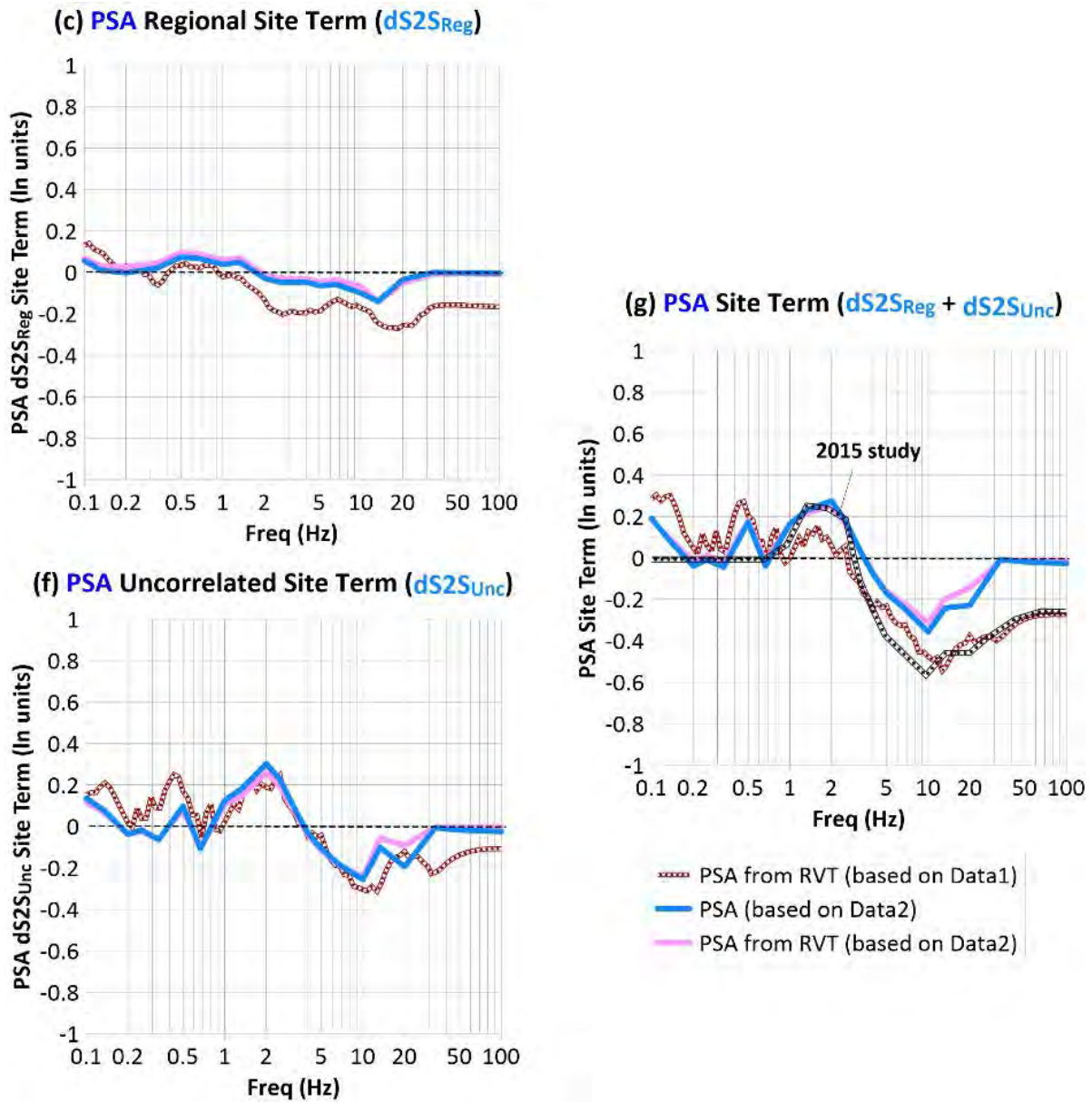
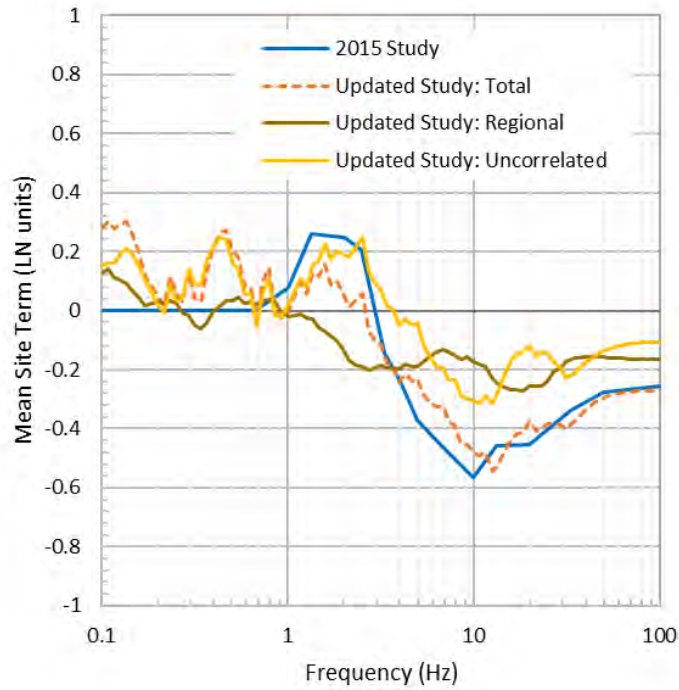
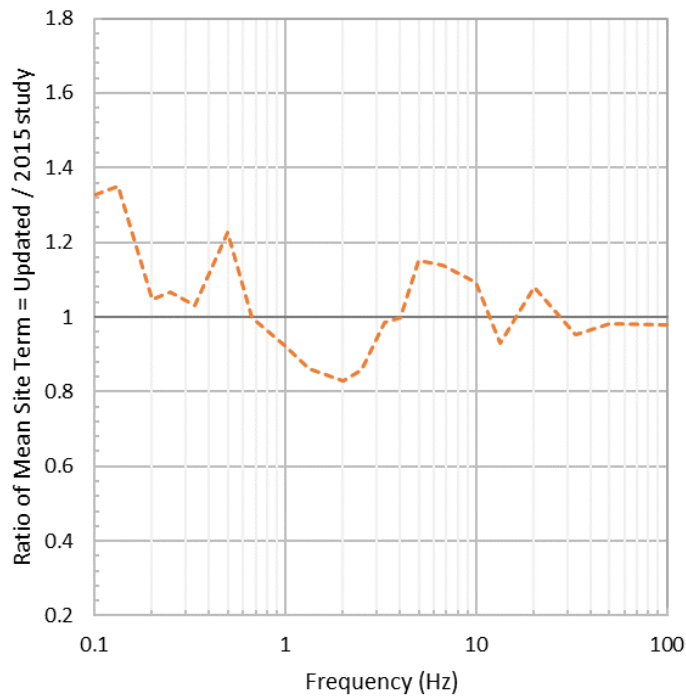


Figure 9-26. Comparison of the PSA regional site term (plot c), uncorrelated site term (plot f), and total site term (plot g) obtained from the FAS analysis via RVT for Data1 and Data2 and directly from the PSA analysis for Data2 (from Dr. Sung's report in Appendix F)



**Figure 9-27. Comparison of the 2015 empirical site term (LN units) for DCPD to the site term and its regional and uncorrelated components obtained from the non-ergodic approach (updated study) with the preliminary expanded ground-motion dataset**



**Figure 9-28. Ratio of the empirical site term for DCPD obtained from the non-ergodic modeling approach (updated) to the 2015 site term**



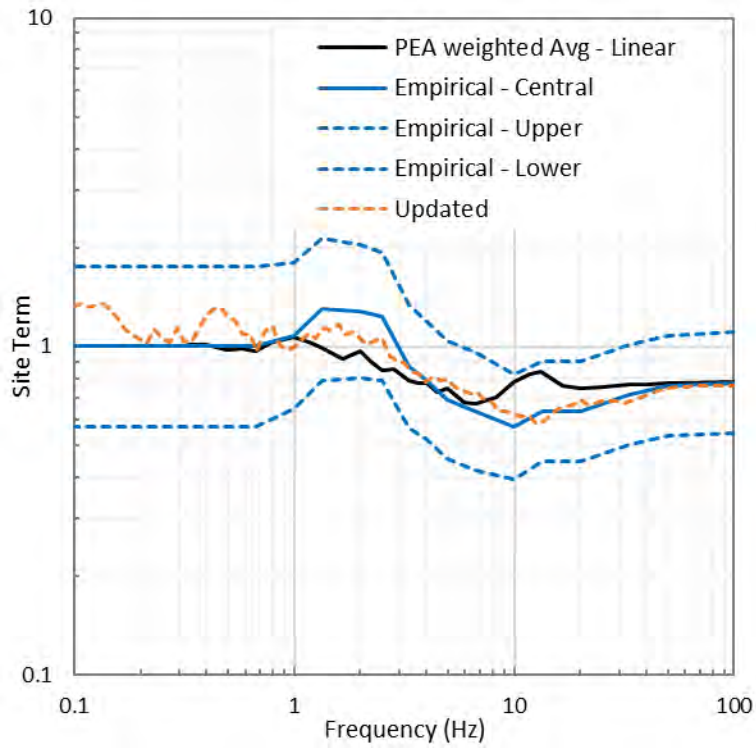


**Figure 9-29. Comparison of the 2015 site term and its epistemic uncertainty (5<sup>th</sup> and 95<sup>th</sup> percentile labeled as lower and upper, respectively) and the updated empirical site term obtained from the non-ergodic modeling approach. The average analytical linear site term is shown in black.**

## 10. HAZARD CALCULATIONS AND RESULTS

For the evaluation of the hazard results, the previous conclusions from the evaluation of the SSC and GMC models are incorporated. As noted earlier in this report, the SSC model evaluation results in an adjustment for the mean slip rates associated with the Hosgri and Los Osos faults. There is also a recommended adjustment for the EPHR for the Hosgri fault. Adjustments for the other seismic sources (PG&E, 2015a) are not considered. From the GMC model evaluation, the recommended conclusion is that the median SWUS ground-motion model and aleatory model used in the 2015 study (GeoPentech, 2015) are still acceptable, given the evaluation of the more recent empirical data and models. Based on these recommendations for the SSC and GMC models, a simplified scaling approach is performed to evaluate the potential impact on the resulting hazard curves and ground motions given these adjustments.

### 10.1. CALCULATION PROCESS

Probabilistic seismic hazard analysis calculations are based on the integration of the hazard integral over all seismic sources. For a given seismic source, the integration is performed over the probability density function for magnitude, the probability density function for distance given the source and site location, and the conditional probability of exceedance at the given ground motions dependent on the median and aleatory ground-motion models. In addition to these components of the hazard integral, the frequency of occurrence from a given seismic source is linearly scaled by the frequency of occurrence of each event (i.e., magnitude and location) in the integration procedure. For seismic fault sources in which the frequency of occurrence is defined based on a slip rate, the scaling of the slip rate directly results in a scaling of the hazard curve results keeping all of the aspects of the hazard integration the same. This scaling is performed on the hazard values (i.e., y-axis values) as there is no change in the shape of the hazard curve. For this reason, the adjustments recommended earlier to account for the change in the slip rates for the Hosgri and Los Osos faults can be directly implemented with a change in the hazard curves from these two sources. For the recommended change in the EPHR for the Hosgri fault, the same scaling approach is adopted, as the implementation of the EPHR is also a direct linear scale factor on the hazard results.

For the evaluation of the impact of the recommended changes to the mean slip rate for the Hosgri and Los Osos faults and for the recommended change to the Hosgri fault EPHR, the following approach is implemented. These steps are presented for the reference rock horizon calculations.

- Extract the hazard curves from the Hosgri and Los Osos fault sources from the 2015 results.
- Scale the Hosgri fault hazard curve based on the adjustment for the mean slip rate.
- Scale the Hosgri fault hazard curve based on the adjustment for the EPHR.
- Scale the Los Osos fault hazard curve based on the adjustment for the mean slip rate.
- Combine the scaled Hosgri and Los Osos fault hazard curves with the original hazard curves (PG&E, 2015a) from the other seismic sources to compute the scaled total hazard curve.

This process is performed for each of the 17 spectral frequencies from 100 Hz (PGA) to 0.333 Hz. Following this process, scaled updated mean hazard curves for each spectral frequency for the reference rock horizon are computed and the resulting uniform hazard spectra and GMRS are

estimated. Comparisons will be presented for these resulting ground motions with the original results from the 2015 study.

## **10.2. REFERENCE ROCK HAZARD AND GROUND MOTION COMPARISONS**

As presented earlier in this report, two sets of scaling factors are recommended for the Hosgri fault source. The first is related to the adjustment of the mean slip rate of the Hosgri fault. The second factor is based on the adjustment of the EPHR for the Hosgri fault. Given that these two scaling factors are both applied as a linear scaling factor to the hazard curves, they can be combined (i.e., multiplicative) as a single scaling factor. The summary of the individual factors and the resulting combined scaling factor of 1.30 are listed in Table 10-1. For each spectral frequency, the Hosgri fault hazard curve is scaled by this 1.30 factor for the update analysis.

For the Los Osos fault, individual scaling factors are developed for the OV, SW, and NE seismic source models. These factors are listed in Table 10-2. Following the procedure outlined above, these factors are first applied to the individual Los Osos fault hazard curves from each of the three seismic source models, and then recombined to compute the updated Los Osos fault hazard curve.

**Table 10-1. Scaling Factors for the Adjustment to the Mean Slip Rate, EPHR, and Combined Factor for the Hosgri Fault Source**

<b>Hosgri Fault Source</b>	<b>Value</b>	<b>Scale Factor</b>
Mean Slip Rate (2015 Study)	1.7	
Mean Slip Rate (Update Study)	2.14	
Slip Rate Scale Factor (Update/2015)		1.26
EPHR (2015 Study)	1.2	
EPHR (Update Study)	1.24	
EPHR Scale Factor (Update/2015)		1.03
Combined Scale Factor		1.30

**Table 10-2. Scaling Factors for the Adjustment to the Mean Slip Rate for the Los Osos Fault Source**

<b>Los Osos Fault Source</b>	<b>Scale Factor</b>
OV Fault Model	0.85
SW Fault Model	0.89
NE Fault Model	0.93

### **10.2.1. Reference Rock Hazard Curves Comparisons**

The scaling factors are applied to the Hosgri and Los Osos fault hazard curves for each spectral frequency. For each of the 17 spectral frequencies, the original 2015 total mean hazard curve,

scaled updated total mean hazard curve, and the hazard curve ratio (i.e., updated hazard curve divided by the 2015 hazard curve) are listed in Table 10-3 through Table 10-19. Based on these results, the comparison of the mean hazard curves for each of the 17 spectral frequencies is plotted on Figure 10-1 through Figure 10-17. Note that the other individual hazard curves from the other seismic sources are not plotted in these figures since they are not changed between the 2015 study and this calculation. Based on the relative contribution from the Hosgri and the Los Osos faults, respectively, the change in the total hazard curve varies as a function of ground motion and spectral frequency. For the lower spectral frequencies, the relative contribution from the Hosgri fault to the total hazard increases, leading to a larger increase in the updated hazard curves when compared to the intermediate and higher spectral frequencies where the relative contribution from just the Hosgri fault is smaller. For the 5 Hz case, it is observed that the ratio in hazard curves is approximately constant for hazard levels of about  $10^{-4}$  and lower.

**Table 10-3. Mean Total Hazard Curve from the 2015 Study, Updated Mean Total Hazard Curve, and Hazard Curve Ratio for the 100 Hz (PGA) Spectral Frequency**

PSA (g)	Total Mean Hazard Curve (2015)	Total Mean Hazard Curve (Updated)	Hazard Curve Ratio (Updated/2015)
0.0100	2.21E-01	2.486E-01	1.124
0.0500	3.31E-02	3.482E-02	1.053
0.1000	1.28E-02	1.377E-02	1.073
0.2000	4.50E-03	4.957E-03	1.103
0.4000	1.42E-03	1.590E-03	1.119
0.8000	2.72E-04	3.044E-04	1.120
1.5000	3.21E-05	3.579E-05	1.113
2.0000	1.04E-05	1.151E-05	1.110
3.0000	1.84E-06	2.034E-06	1.103
5.0000	1.68E-07	1.840E-07	1.094
10.0000	4.30E-09	4.639E-09	1.078
20.0000	6.01E-11	6.359E-11	1.059

**Table 10-4. Mean Total Hazard Curve from the 2015 Study, Updated Mean Total Hazard Curve, and Hazard Curve Ratio for the 50 Hz Spectral Frequency**

<b>PSA (g)</b>	<b>Total Mean Hazard Curve (2015)</b>	<b>Total Mean Hazard Curve (Updated)</b>	<b>Hazard Curve Ratio (Updated/2015)</b>
0.0100	2.24E-01	2.522E-01	1.126
0.0500	3.38E-02	3.559E-02	1.053
0.1000	1.32E-02	1.417E-02	1.073
0.2000	4.70E-03	5.179E-03	1.103
0.4000	1.53E-03	1.705E-03	1.118
0.8000	3.06E-04	3.424E-04	1.117
1.5000	3.79E-05	4.212E-05	1.110
2.0000	1.25E-05	1.379E-05	1.107
3.0000	2.27E-06	2.496E-06	1.100
5.0000	2.13E-07	2.328E-07	1.091
10.0000	5.72E-09	6.153E-09	1.076
20.0000	8.53E-11	9.023E-11	1.058

**Table 10-5. Mean Total Hazard Curve from the 2015 Study, Updated Mean Total Hazard Curve, and Hazard Curve Ratio for the 33.333 Hz Spectral Frequency**

<b>PSA (g)</b>	<b>Total Mean Hazard Curve (2015)</b>	<b>Total Mean Hazard Curve (Updated)</b>	<b>Hazard Curve Ratio (Updated/2015)</b>
0.0100	2.37E-01	2.693E-01	1.136
0.0500	3.76E-02	3.966E-02	1.054
0.1000	1.51E-02	1.615E-02	1.071
0.2000	5.48E-03	6.031E-03	1.100
0.4000	1.82E-03	2.031E-03	1.116
0.8000	3.98E-04	4.432E-04	1.114
1.5000	5.45E-05	6.039E-05	1.107
2.0000	1.86E-05	2.056E-05	1.104
3.0000	3.57E-06	3.921E-06	1.099
5.0000	3.59E-07	3.912E-07	1.091
10.0000	1.06E-08	1.147E-08	1.078
20.0000	1.82E-10	1.938E-10	1.065

**Table 10-6. Mean Total Hazard Curve from the 2015 Study, Updated Mean Total Hazard Curve, and Hazard Curve Ratio for the 20 Hz Spectral Frequency**

<b>PSA (g)</b>	<b>Total Mean Hazard Curve (2015)</b>	<b>Total Mean Hazard Curve (Updated)</b>	<b>Hazard Curve Ratio (Updated/2015)</b>
0.0100	2.64E-01	3.051E-01	1.155
0.0500	4.82E-02	5.076E-02	1.053
0.1000	2.01E-02	2.138E-02	1.065
0.2000	7.57E-03	8.269E-03	1.092
0.4000	2.64E-03	2.938E-03	1.112
0.8000	7.17E-04	7.992E-04	1.114
1.5000	1.29E-04	1.431E-04	1.109
2.0000	4.89E-05	5.401E-05	1.104
3.0000	1.06E-05	1.166E-05	1.099
5.0000	1.24E-06	1.349E-06	1.090
10.0000	4.56E-08	4.912E-08	1.077
20.0000	1.03E-09	1.097E-09	1.061

**Table 10-7. Mean Total Hazard Curve from the 2015 Study, Updated Mean Total Hazard Curve, and Hazard Curve Ratio for the 13.333 Hz Spectral Frequency**

<b>PSA (g)</b>	<b>Total Mean Hazard Curve (2015)</b>	<b>Total Mean Hazard Curve (Updated)</b>	<b>Hazard Curve Ratio (Updated/2015)</b>
0.0100	3.01E-01	3.555E-01	1.183
0.0500	6.28E-02	6.619E-02	1.054
0.1000	2.68E-02	2.847E-02	1.061
0.2000	1.07E-02	1.156E-02	1.086
0.4000	3.86E-03	4.286E-03	1.111
0.8000	1.18E-03	1.328E-03	1.121
1.5000	2.58E-04	2.899E-04	1.124
2.0000	1.06E-04	1.186E-04	1.122
3.0000	2.51E-05	2.808E-05	1.118
5.0000	3.23E-06	3.588E-06	1.112
10.0000	1.35E-07	1.483E-07	1.100
20.0000	3.52E-09	3.818E-09	1.085



**Table 10-8. Mean Total Hazard Curve from the 2015 Study, Updated Mean Total Hazard Curve, and Hazard Curve Ratio for the 10 Hz Spectral Frequency**

<b>PSA (g)</b>	<b>Total Mean Hazard Curve (2015)</b>	<b>Total Mean Hazard Curve (Updated)</b>	<b>Hazard Curve Ratio (Updated/2015)</b>
0.0100	3.27E-01	3.946E-01	1.205
0.0500	7.36E-02	7.768E-02	1.055
0.1000	3.13E-02	3.317E-02	1.059
0.2000	1.25E-02	1.356E-02	1.081
0.4000	4.62E-03	5.112E-03	1.106
0.8000	1.51E-03	1.685E-03	1.116
1.5000	3.70E-04	4.128E-04	1.115
2.0000	1.61E-04	1.788E-04	1.112
3.0000	4.11E-05	4.548E-05	1.106
5.0000	5.72E-06	6.288E-06	1.099
10.0000	2.67E-07	2.901E-07	1.087
20.0000	7.91E-09	8.482E-09	1.072

**Table 10-9. Mean Total Hazard Curve from the 2015 Study, Updated Mean Total Hazard Curve, and Hazard Curve Ratio for the 6.667 Hz Spectral Frequency**

<b>PSA (g)</b>	<b>Total Mean Hazard Curve (2015)</b>	<b>Total Mean Hazard Curve (Updated)</b>	<b>Hazard Curve Ratio (Updated/2015)</b>
0.0100	3.50E-01	4.262E-01	1.217
0.0500	8.38E-02	8.815E-02	1.051
0.1000	3.53E-02	3.720E-02	1.053
0.2000	1.41E-02	1.520E-02	1.077
0.4000	5.25E-03	5.793E-03	1.105
0.8000	1.79E-03	2.007E-03	1.119
1.5000	4.91E-04	5.524E-04	1.126
2.0000	2.26E-04	2.544E-04	1.127
3.0000	6.18E-05	6.957E-05	1.126
5.0000	9.17E-06	1.030E-05	1.124
10.0000	4.60E-07	5.135E-07	1.117
20.0000	1.45E-08	1.608E-08	1.108

**Table 10-10. Mean Total Hazard Curve from the 2015 Study, Updated Mean Total Hazard Curve, and Hazard Curve Ratio for the 5 Hz Spectral Frequency**

<b>PSA (g)</b>	<b>Total Mean Hazard Curve (2015)</b>	<b>Total Mean Hazard Curve (Updated)</b>	<b>Hazard Curve Ratio (Updated/2015)</b>
0.0100	3.62E-01	4.443E-01	1.228
0.0500	8.43E-02	8.856E-02	1.050
0.1000	3.46E-02	3.632E-02	1.051
0.2000	1.34E-02	1.435E-02	1.074
0.4000	4.83E-03	5.314E-03	1.101
0.8000	1.63E-03	1.819E-03	1.120
1.5000	4.38E-04	4.951E-04	1.129
2.0000	2.00E-04	2.261E-04	1.132
3.0000	5.41E-05	6.131E-05	1.134
5.0000	8.00E-06	9.077E-06	1.135
10.0000	4.01E-07	4.552E-07	1.135
20.0000	1.26E-08	1.426E-08	1.133

**Table 10-11. Mean Total Hazard Curve from the 2015 Study, Updated Mean Total Hazard Curve, and Hazard Curve Ratio for the 4 Hz Spectral Frequency**

<b>PSA (g)</b>	<b>Total Mean Hazard Curve (2015)</b>	<b>Total Mean Hazard Curve (Updated)</b>	<b>Hazard Curve Ratio (Updated/2015)</b>
0.0100	3.62E-01	4.444E-01	1.228
0.0500	7.94E-02	8.320E-02	1.048
0.1000	3.15E-02	3.306E-02	1.049
0.2000	1.17E-02	1.258E-02	1.072
0.4000	4.09E-03	4.504E-03	1.100
0.8000	1.32E-03	1.471E-03	1.119
1.5000	3.25E-04	3.659E-04	1.127
2.0000	1.42E-04	1.597E-04	1.128
3.0000	3.63E-05	4.095E-05	1.129
5.0000	5.06E-06	5.702E-06	1.127
10.0000	2.34E-07	2.628E-07	1.122
20.0000	6.77E-09	7.536E-09	1.113

**Table 10-12. Mean Total Hazard Curve from the 2015 Study, Updated Mean Total Hazard Curve, and Hazard Curve Ratio for the 3.333 Hz Spectral Frequency**

<b>PSA (g)</b>	<b>Total Mean Hazard Curve (2015)</b>	<b>Total Mean Hazard Curve (Updated)</b>	<b>Hazard Curve Ratio (Updated/2015)</b>
0.0100	3.57E-01	4.371E-01	1.224
0.0500	7.27E-02	7.588E-02	1.045
0.1000	2.78E-02	2.913E-02	1.047
0.2000	9.91E-03	1.061E-02	1.070
0.4000	3.32E-03	3.645E-03	1.099
0.8000	9.87E-04	1.101E-03	1.115
1.5000	2.11E-04	2.357E-04	1.118
2.0000	8.63E-05	9.642E-05	1.118
3.0000	2.07E-05	2.310E-05	1.117
5.0000	2.71E-06	3.027E-06	1.116
10.0000	1.17E-07	1.296E-07	1.111
20.0000	3.11E-09	3.443E-09	1.106

**Table 10-13. Mean Total Hazard Curve from the 2015 Study, Updated Mean Total Hazard Curve, and Hazard Curve Ratio for the 2.5 Hz Spectral Frequency**

<b>PSA (g)</b>	<b>Total Mean Hazard Curve (2015)</b>	<b>Total Mean Hazard Curve (Updated)</b>	<b>Hazard Curve Ratio (Updated/2015)</b>
0.0100	3.36E-01	4.051E-01	1.205
0.0500	5.87E-02	6.106E-02	1.040
0.1000	2.15E-02	2.253E-02	1.047
0.2000	7.26E-03	7.777E-03	1.072
0.4000	2.32E-03	2.557E-03	1.104
0.8000	6.21E-04	6.995E-04	1.127
1.5000	1.19E-04	1.356E-04	1.140
2.0000	4.75E-05	5.450E-05	1.146
3.0000	1.13E-05	1.307E-05	1.155
5.0000	1.50E-06	1.744E-06	1.164
10.0000	6.70E-08	7.889E-08	1.178
20.0000	1.96E-09	2.348E-09	1.195

**Table 10-14. Mean Total Hazard Curve from the 2015 Study, Updated Mean Total Hazard Curve, and Hazard Curve Ratio for the 2 Hz Spectral Frequency**

<b>PSA (g)</b>	<b>Total Mean Hazard Curve (2015)</b>	<b>Total Mean Hazard Curve (Updated)</b>	<b>Hazard Curve Ratio (Updated/2015)</b>
0.0010	7.86E-01	1.535E+00	1.953
0.0100	3.10E-01	3.660E-01	1.182
0.0500	4.70E-02	4.871E-02	1.036
0.1000	1.66E-02	1.734E-02	1.045
0.2000	5.38E-03	5.766E-03	1.073
0.4000	1.70E-03	1.885E-03	1.110
0.8000	4.16E-04	4.711E-04	1.133
1.5000	6.89E-05	7.880E-05	1.144
2.0000	2.57E-05	2.949E-05	1.147
3.0000	5.54E-06	6.373E-06	1.150
5.0000	6.43E-07	7.399E-07	1.151
10.0000	2.33E-08	2.688E-08	1.152

**Table 10-15. Mean Total Hazard Curve from the 2015 Study, Updated Mean Total Hazard Curve, and Hazard Curve Ratio for the 1.333 Hz Spectral Frequency**

<b>PSA (g)</b>	<b>Total Mean Hazard Curve (2015)</b>	<b>Total Mean Hazard Curve (Updated)</b>	<b>Hazard Curve Ratio (Updated/2015)</b>
0.0100	2.33E-01	2.624E-01	1.125
0.0500	2.70E-02	2.787E-02	1.031
0.1000	8.85E-03	9.261E-03	1.047
0.2000	2.75E-03	2.989E-03	1.086
0.4000	8.23E-04	9.299E-04	1.130
0.8000	1.75E-04	2.030E-04	1.163
1.5000	2.67E-05	3.152E-05	1.182
2.0000	9.72E-06	1.155E-05	1.188
3.0000	2.04E-06	2.436E-06	1.194
5.0000	2.30E-07	2.759E-07	1.200
10.0000	8.08E-09	9.745E-09	1.206
20.0000	1.75E-10	2.120E-10	1.213

**Table 10-16. Mean Total Hazard Curve from the 2015 Study, Updated Mean Total Hazard Curve, and Hazard Curve Ratio for the 1 Hz Spectral Frequency**

<b>PSA (g)</b>	<b>Total Mean Hazard Curve (2015)</b>	<b>Total Mean Hazard Curve (Updated)</b>	<b>Hazard Curve Ratio (Updated/2015)</b>
0.0010	6.83E-01	1.141E+00	1.671
0.0100	1.66E-01	1.791E-01	1.081
0.0500	1.59E-02	1.640E-02	1.029
0.1000	5.04E-03	5.333E-03	1.057
0.2000	1.60E-03	1.776E-03	1.112
0.4000	4.48E-04	5.214E-04	1.163
0.8000	8.00E-05	9.564E-05	1.196
1.5000	1.04E-05	1.261E-05	1.211
2.0000	3.57E-06	4.343E-06	1.215
3.0000	6.95E-07	8.478E-07	1.220
5.0000	7.16E-08	8.773E-08	1.225
10.0000	2.24E-09	2.760E-09	1.230

**Table 10-17. Mean Total Hazard Curve from the 2015 Study, Updated Mean Total Hazard Curve, and Hazard Curve Ratio for the 0.667 Hz Spectral Frequency**

<b>PSA (g)</b>	<b>Total Mean Hazard Curve (2015)</b>	<b>Total Mean Hazard Curve (Updated)</b>	<b>Hazard Curve Ratio (Updated/2015)</b>
0.0010	5.76E-01	8.509E-01	1.478
0.0100	9.18E-02	9.565E-02	1.042
0.0500	7.51E-03	7.755E-03	1.032
0.1000	2.26E-03	2.446E-03	1.085
0.2000	6.63E-04	7.652E-04	1.154
0.4000	1.50E-04	1.810E-04	1.204
0.8000	2.08E-05	2.556E-05	1.231
1.5000	2.20E-06	2.729E-06	1.241
2.0000	6.93E-07	8.622E-07	1.245
3.0000	1.20E-07	1.496E-07	1.249
5.0000	1.06E-08	1.330E-08	1.253
10.0000	2.66E-10	3.336E-10	1.255

**Table 10-18. Mean Total Hazard Curve from the 2015 Study, Updated Mean Total Hazard Curve, and Hazard Curve Ratio for the 0.5 Hz Spectral Frequency**

PSA (g)	Total Mean Hazard Curve (2015)	Total Mean Hazard Curve (Updated)	Hazard Curve Ratio (Updated/2015)
0.0010	4.82E-01	6.513E-01	1.351
0.0100	5.56E-02	5.699E-02	1.025
0.0500	4.24E-03	4.425E-03	1.043
0.1000	1.19E-03	1.325E-03	1.111
0.2000	2.90E-04	3.411E-04	1.175
0.4000	5.11E-05	6.207E-05	1.215
0.8000	5.95E-06	7.353E-06	1.237
1.5000	5.83E-07	7.273E-07	1.248
2.0000	1.80E-07	2.251E-07	1.252
3.0000	3.05E-08	3.833E-08	1.256
5.0000	2.68E-09	3.382E-09	1.261
10.0000	6.79E-11	8.589E-11	1.266

**Table 10-19. Mean Total Hazard Curve from the 2015 Study, Updated Mean Total Hazard Curve, and Hazard Curve Ratio for the 0.333 Hz Spectral Frequency**

PSA (g)	Total Mean Hazard Curve (2015)	Total Mean Hazard Curve (Updated)	Hazard Curve Ratio (Updated/2015)
0.0010	3.50E-01	4.251E-01	1.214
0.0100	2.74E-02	2.761E-02	1.007
0.0500	1.75E-03	1.882E-03	1.074
0.1000	4.05E-04	4.690E-04	1.160
0.2000	7.22E-05	8.717E-05	1.207
0.4000	8.66E-06	1.060E-05	1.224
0.8000	6.72E-07	8.263E-07	1.229
1.5000	4.65E-08	5.713E-08	1.230
2.0000	1.22E-08	1.504E-08	1.230
3.0000	1.65E-09	2.026E-09	1.228
5.0000	1.06E-10	1.300E-10	1.226
10.0000	1.62E-12	1.976E-12	1.221

**10.2.2. Reference Rock Horizon Uniform-Response Spectra Comparisons**

Given the suite of updated mean total hazard curves, the UHS are computed for the three hazard levels of  $10^{-4}$ ,  $10^{-5}$ , and  $10^{-6}$ . These results, along with the original 2015 UHS for the same three

hazard levels, are listed in Table 10-20 and plotted on Figure 10-18. Given that the Hosgri fault source contributes more than the Los Osos fault source to the total hazard, the overall result in the UHS is an increase in the ground motions. The ratios of the UHS for the three hazard levels are listed in Table 10-21 and plotted on Figure 10-19. These ratio values are a function of hazard level and spectral frequency, with larger resultant values for the lower frequencies (i.e., up to about 5–7% increase at the lowest frequency of 0.333 Hz), as is expected given the relative increase in the contribution from the Hosgri fault to the total hazard. For the intermediate and higher frequencies, the increase is on the order of about 4% or less.

**Table 10-20. Original 2015 UHS and Updated UHS for the Three Hazard Levels of  $10^{-4}$ ,  $10^{-5}$ , and  $10^{-6}$**

Frequency (Hz)	UHS 2015 ( $10^{-4}$ ) (g)	UHS 2015 ( $10^{-5}$ ) (g)	UHS 2015 ( $10^{-6}$ ) (g)	UHS Updated ( $10^{-4}$ ) (g)	UHS Updated ( $10^{-5}$ ) (g)	UHS Updated ( $10^{-6}$ ) (g)
100.000	1.0739	2.0171	3.4183	1.1093	2.0669	3.4889
50.000	1.1205	2.1075	3.5811	1.1573	2.1584	3.6531
33.333	1.2383	2.3299	3.9807	1.2794	2.3858	4.0610
20.000	1.6180	3.0425	5.2284	1.6674	3.1109	5.3230
13.333	2.0315	3.7728	6.4567	2.0983	3.8767	6.6022
10.000	2.3033	4.3268	7.4182	2.3755	4.4356	7.5666
6.667	2.5803	4.8849	8.3524	2.6782	5.0344	8.5723
5.000	2.4789	4.7097	8.0925	2.5769	4.8722	8.3338
4.000	2.2179	4.1901	7.2080	2.2993	4.3226	7.4005
3.333	1.9070	3.6015	6.2293	1.9767	3.7027	6.3793
2.500	1.5837	3.0954	5.4716	1.6513	3.2107	5.6629
2.000	1.3167	2.5670	4.5027	1.3795	2.6628	4.6551
1.333	0.9638	1.9840	3.5446	1.0160	2.0766	3.6968
1.000	0.7313	1.5163	2.7413	0.7856	1.5968	2.8796
0.667	0.4614	0.9816	1.8252	0.4935	1.0414	1.9273
0.500	0.3060	0.6766	1.2960	0.3295	0.7239	1.3757
0.333	0.1755	0.3816	0.7183	0.1890	0.4064	0.7596



**Table 10-21. UHS Ground Motion Ratios (Updated/2015) for the Three Hazard Levels of  $10^{-4}$ ,  $10^{-5}$ , and  $10^{-6}$**

Frequency (Hz)	Ratio (Updated/2015) ( $10^{-4}$ )	Ratio (Updated/2015) ( $10^{-5}$ )	Ratio (Updated/2015) ( $10^{-6}$ )
100.000	1.033	1.025	1.021
50.000	1.033	1.024	1.020
33.333	1.033	1.024	1.020
20.000	1.031	1.022	1.018
13.333	1.033	1.028	1.023
10.000	1.031	1.025	1.020
6.667	1.038	1.031	1.026
5.000	1.040	1.034	1.030
4.000	1.037	1.032	1.027
3.333	1.037	1.028	1.024
2.500	1.043	1.037	1.035
2.000	1.048	1.037	1.034
1.333	1.054	1.047	1.043
1.000	1.074	1.053	1.050
0.667	1.070	1.061	1.056
0.500	1.077	1.070	1.061
0.333	1.077	1.065	1.057

### **10.2.3. Reference Rock Horizon GMRS Comparisons**

The GMRS is defined based on the UHS results for the  $10^{-4}$  and  $10^{-5}$  hazard levels. The mathematical function form for the GMRS is defined as:

$$\text{GMRS}(f) = \text{UHS}_{10^{-4}}(f) * \text{DF} \quad \text{Equation (10-1)}$$

where

$$\text{DF}(f) = \text{MAX}[0.6 * \text{AR}^{0.8}, 1] \quad \text{Equation (10-2)}$$

and

$$\text{AR} = \text{UHS}_{10^{-5}}(f) / \text{UHS}_{10^{-4}}(f) \quad \text{Equation (10-3)}$$

Original 2015 and updated GMRS for the reference rock horizon based on the hazard curve and UHS results are listed in Table 10-22 and Table 10-23, respectively. These two GMRS are plotted on Figure 10-20. In addition, the ratios of the GMRS ground-motion values are listed in Table 10-24 and plotted on Figure 10-21. The ratio results for the GMRS are similar to the UHS

ratio results. For lower frequencies, the increase is on the order of about 7% or less, and for the intermediate to high frequency ranges the increase is approximately 3%.

**Table 10-22. Original 2015 GMRS for the Reference Rock Horizon**

Frequency (Hz)	UHS 2015 (10 <sup>-4</sup> ) (g)	AR	DF	GMRS 2015 (g)
100.000	1.0739	1.878	1.000	1.0739
50.000	1.1205	1.881	1.000	1.1205
33.333	1.2383	1.882	1.000	1.2383
20.000	1.6180	1.880	1.000	1.6180
13.333	2.0315	1.857	1.000	2.0315
10.000	2.3033	1.878	1.000	2.3033
6.667	2.5803	1.893	1.000	2.5803
5.000	2.4789	1.900	1.003	2.4854
4.000	2.2179	1.889	1.000	2.2179
3.333	1.9070	1.889	1.000	1.9070
2.500	1.5837	1.955	1.026	1.6243
2.000	1.3167	1.950	1.024	1.3477
1.333	0.9638	2.058	1.069	1.0303
1.000	0.7313	2.073	1.075	0.7863
0.667	0.4614	2.128	1.098	0.5064
0.500	0.3060	2.211	1.132	0.3464
0.333	0.1755	2.175	1.117	0.1960

**Table 10-23. Updated GMRS for the Reference Rock Horizon**

Frequency (Hz)	UHS Updated (10 <sup>-4</sup> ) (g)	AR	DF	GMRS Updated (g)
100.000	1.109	1.863	1.000	1.1093
50.000	1.157	1.865	1.000	1.1573
33.333	1.279	1.865	1.000	1.2794
20.000	1.667	1.866	1.000	1.6674
13.333	2.098	1.848	1.000	2.0983
10.000	2.375	1.867	1.000	2.3755
6.667	2.678	1.880	1.000	2.6782
5.000	2.577	1.891	1.000	2.5769
4.000	2.299	1.880	1.000	2.2993
3.333	1.977	1.873	1.000	1.9767
2.500	1.651	1.944	1.021	1.6865
2.000	1.379	1.930	1.015	1.4008
1.333	1.016	2.044	1.063	1.0800

Frequency (Hz)	UHS Updated ( $10^{-4}$ ) (g)	AR	DF	GMRS Updated (g)
1.000	0.786	2.033	1.058	0.8314
0.667	0.494	2.110	1.090	0.5382
0.500	0.329	2.197	1.126	0.3711
0.333	0.189	2.150	1.107	0.2092

**Table 10-24. GMRS Ratios for the 2015 Study Results and the Updated Results for the Reference Rock Horizon**

Frequency (Hz)	GMRS 2015 (g)	GMRS Updated (g)	GMRS Ratio (Updated/2015)
100.000	1.0739	1.1093	1.0330
50.000	1.1205	1.1573	1.0328
33.333	1.2383	1.2794	1.0332
20.000	1.6180	1.6674	1.0306
13.333	2.0315	2.0983	1.0329
10.000	2.3033	2.3755	1.0313
6.667	2.5803	2.6782	1.0379
5.000	2.4854	2.5769	1.0368
4.000	2.2179	2.2993	1.0367
3.333	1.9070	1.9767	1.0365
2.500	1.6243	1.6865	1.0383
2.000	1.3477	1.4008	1.0394
1.333	1.0303	1.0800	1.0482
1.000	0.7863	0.8314	1.0573
0.667	0.5064	0.5382	1.0626
0.500	0.3464	0.3711	1.0713
0.333	0.1960	0.2092	1.0673

### 10.3. CONCLUSIONS

Updated hazard curves and UHS for the reference rock horizon are computed based on the recommended adjustments for the Hosgri and Los Osos mean slip rates and the Hosgri EPHR. The 2015 ground-motion model was used in this analysis as recommended in Chapter 7. These source parameter adjustments are implemented as linear scaling factors to the original 2015 hazard curves from the Hosgri and Los Osos seismic sources. The updated total hazard is computed based on these updated scaled hazard curves from these two seismic sources along with the original hazard curves from the other seismic sources. In comparison with the original 2015 results, the increase in the hazard curves is a function of spectral frequency and hazard level. For the 5 Hz spectral frequency, the hazard curve ratio is approximately constant for hazard levels of about  $10^{-4}$  and lower. UHS ground-motion results are computed from these

updated seismic hazard curves for the three hazard levels of  $10^{-4}$ ,  $10^{-5}$ , and  $10^{-6}$ . These results in comparison with the previous 2015 UHS results show an increase in ground motions in a range of 5–7% in the lowest frequencies range, decreasing to about 3–4% in the intermediate to high frequency ranges. This observed increase in the scaled ground-motion values is well within the epistemic uncertainty from the 2015 study. For example, the ratio of 95<sup>th</sup> percentile ground motions divided by the 5<sup>th</sup> percentile ground motions for the UHS for the hazard levels between  $10^{-4}$  to  $10^{-6}$  is in the range of ground motion ratios of 3 – 5 (i.e., scaling factors of 300 – 500%) across the range of spectral frequencies.

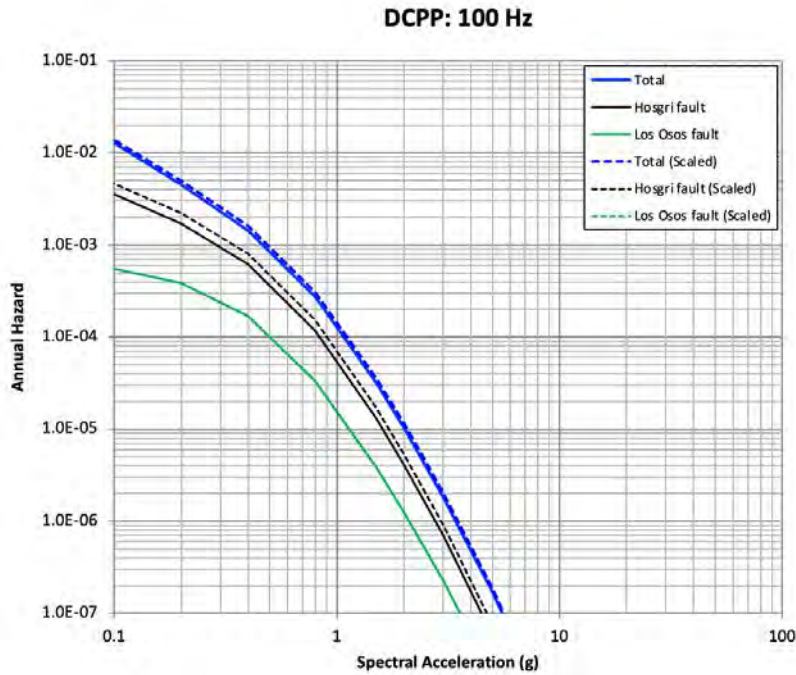


**Figure 10-1. Mean hazard curves from the 2015 study (solid lines) and updated scaled results (dashed lines) for the Los Osos fault source (green lines), Hogгри fault source (black lines) and total hazard curves (blue lines) for 100 Hz (PGA)**

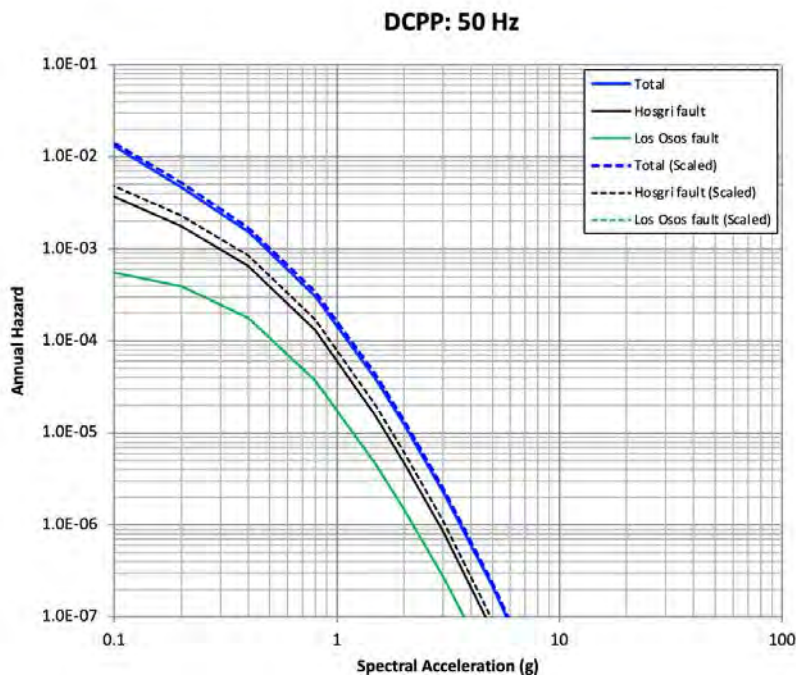


**Figure 10-2. Mean hazard curves from the 2015 study (solid lines) and updated scaled results (dashed lines) for the Los Osos fault source (green lines), Hogгри fault source (black lines) and total hazard curves (blue lines) for 50 Hz**

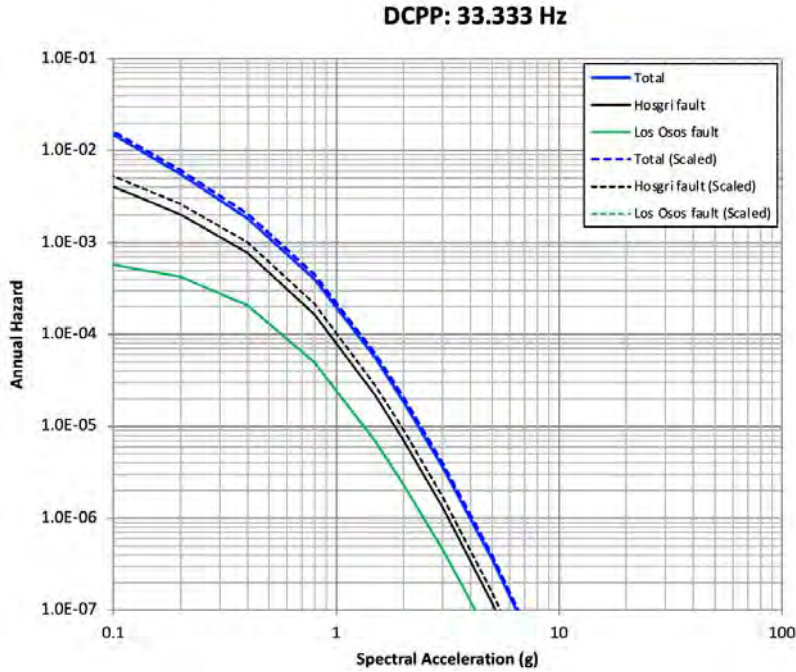


**Figure 10-3. Mean hazard curves from the 2015 study (solid lines) and updated scaled results (dashed lines) for the Los Osos fault source (green lines), Hosgri fault source (black lines) and total hazard curves (blue lines) for 33.333 Hz**

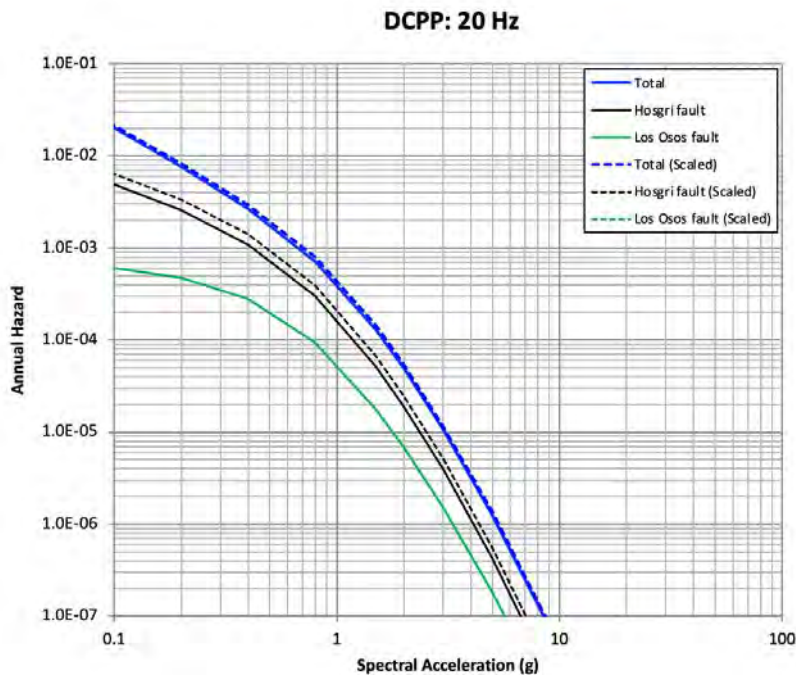


**Figure 10-4. Mean hazard curves from the 2015 study (solid lines) and updated scaled results (dashed lines) for the Los Osos fault source (green lines), Hosgri fault source (black lines) and total hazard curves (blue lines) for 20 Hz**

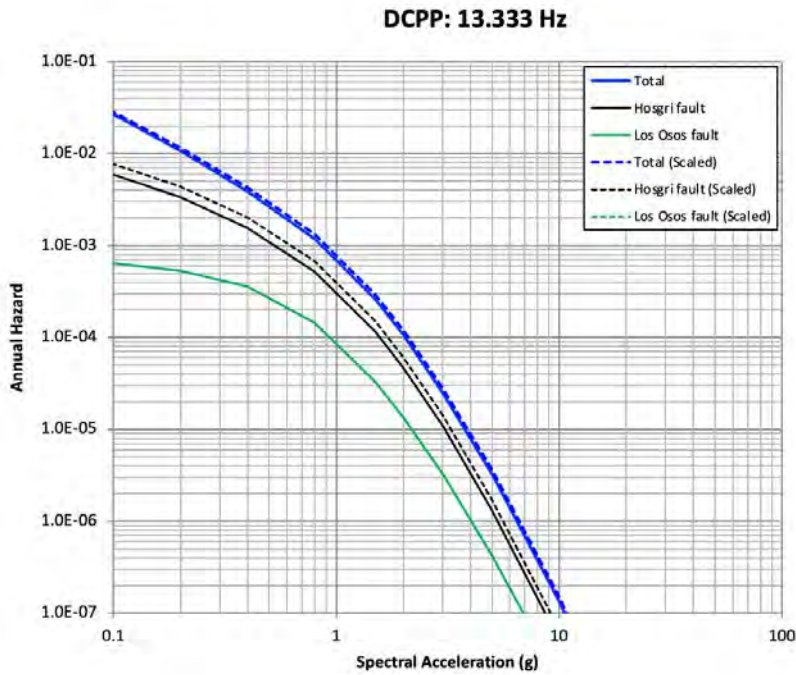


**Figure 10-5. Mean hazard curves from the 2015 study (solid lines) and updated scaled results (dashed lines) for the Los Osos fault source (green lines), Hosgri fault source (black lines) and total hazard curves (blue lines) for 13.333 Hz**

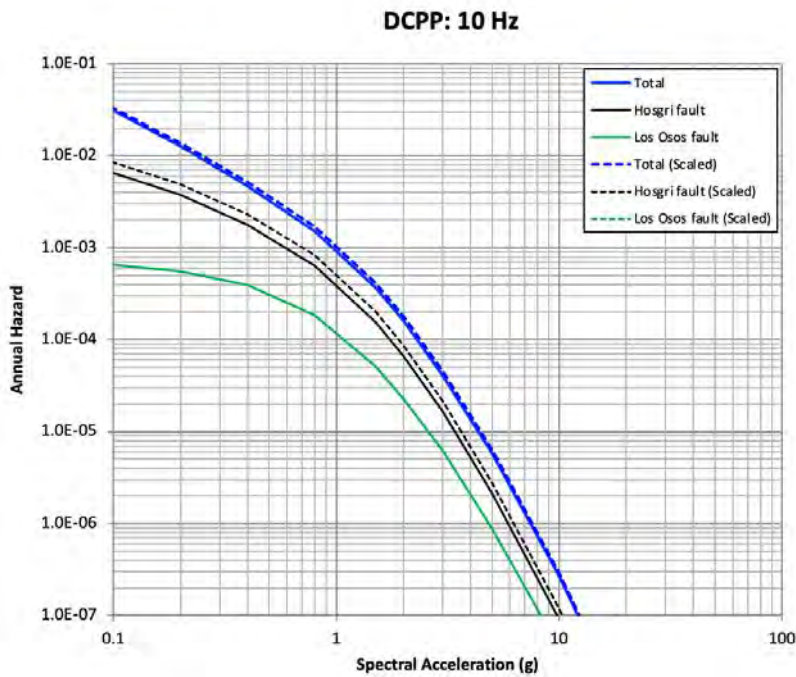


**Figure 10-6. Mean hazard curves from the 2015 study (solid lines) and updated scaled results (dashed lines) for the Los Osos fault source (green lines), Hosgri fault source (black lines) and total hazard curves (blue lines) for 10 Hz**



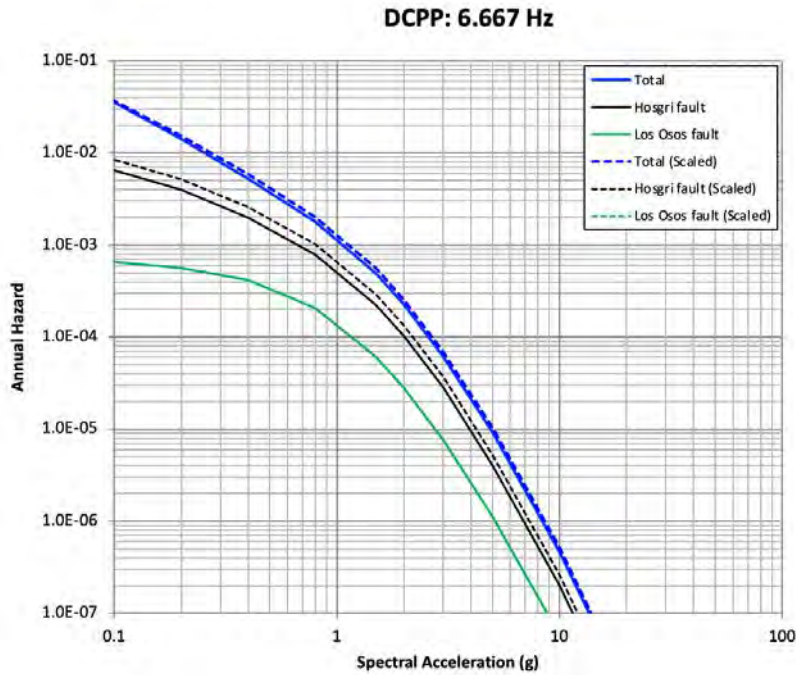


**Figure 10-7. Mean hazard curves from the 2015 study (solid lines) and updated scaled results (dashed lines) for the Los Osos fault source (green lines), Hoggri fault source (black lines) and total hazard curves (blue lines) for 6.667 Hz**

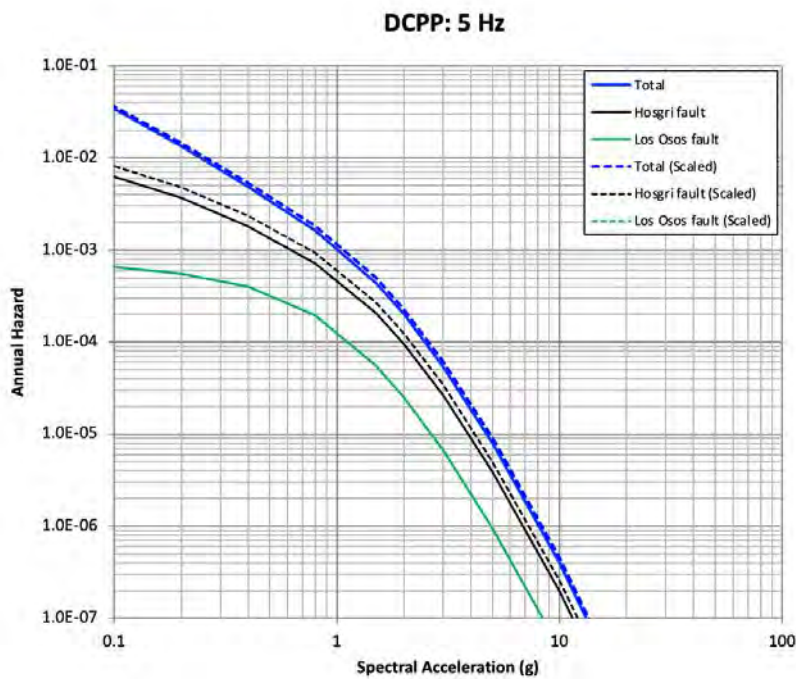


**Figure 10-8. Mean hazard curves from the 2015 study (solid lines) and updated scaled results (dashed lines) for the Los Osos fault source (green lines), Hoggri fault source (black lines) and total hazard curves (blue lines) for 5 Hz**

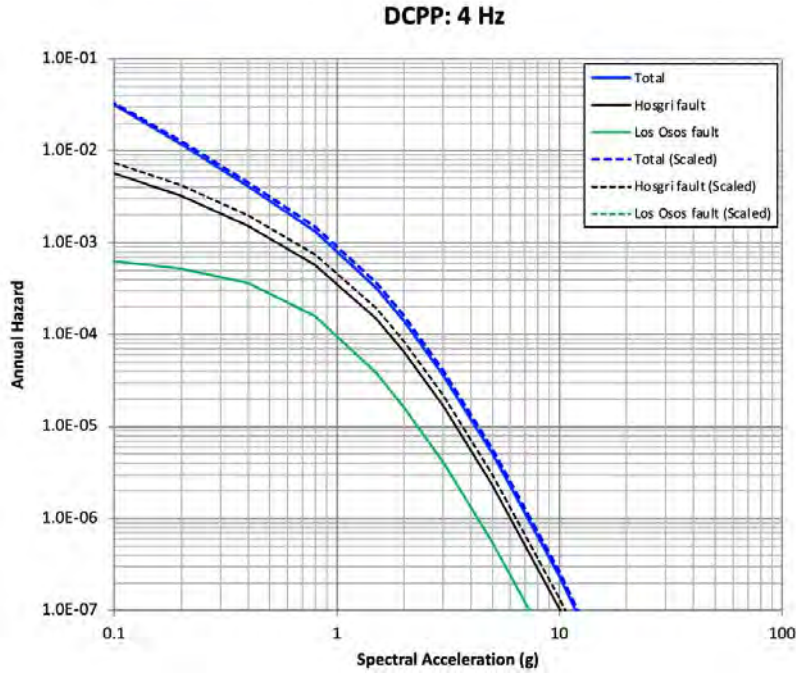


**Figure 10-9. Mean hazard curves from the 2015 study (solid lines) and updated scaled results (dashed lines) for the Los Osos fault source (green lines), Hogгри fault source (black lines) and total hazard curves (blue lines) for 4 Hz**

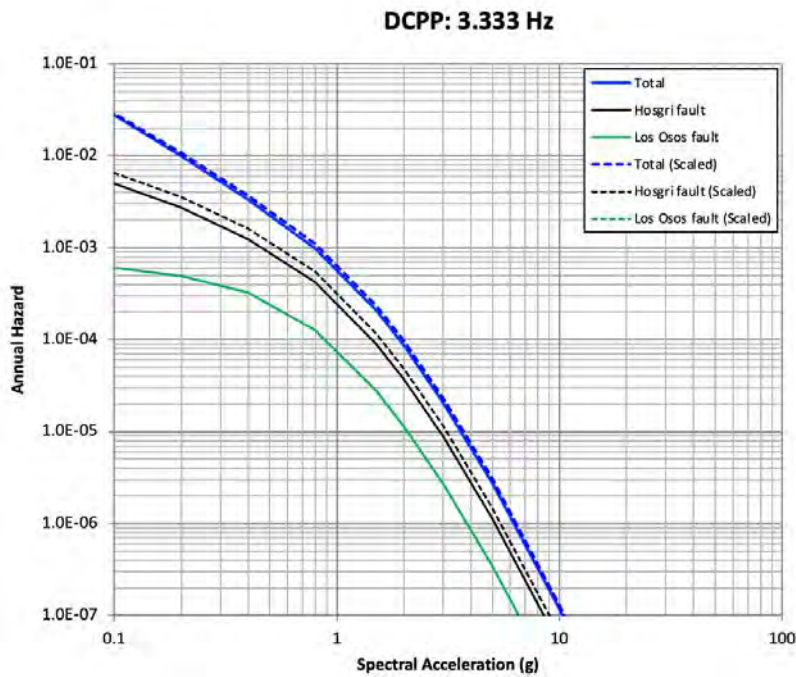


**Figure 10-10. Mean hazard curves from the 2015 study (solid lines) and updated scaled results (dashed lines) for the Los Osos fault source (green lines), Hogгри fault source (black lines) and total hazard curves (blue lines) for 3.333 Hz**

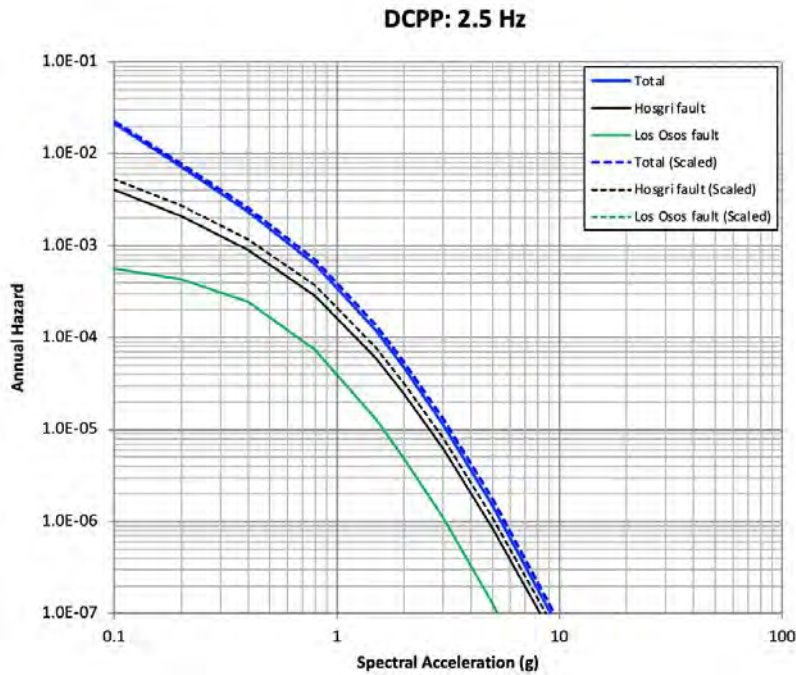


Figure 10-11. Mean hazard curves from the 2015 study (solid lines) and updated scaled results (dashed lines) for the Los Osos fault source (green lines), Hogгри fault source (black lines) and total hazard curves (blue lines) for 2.5 Hz

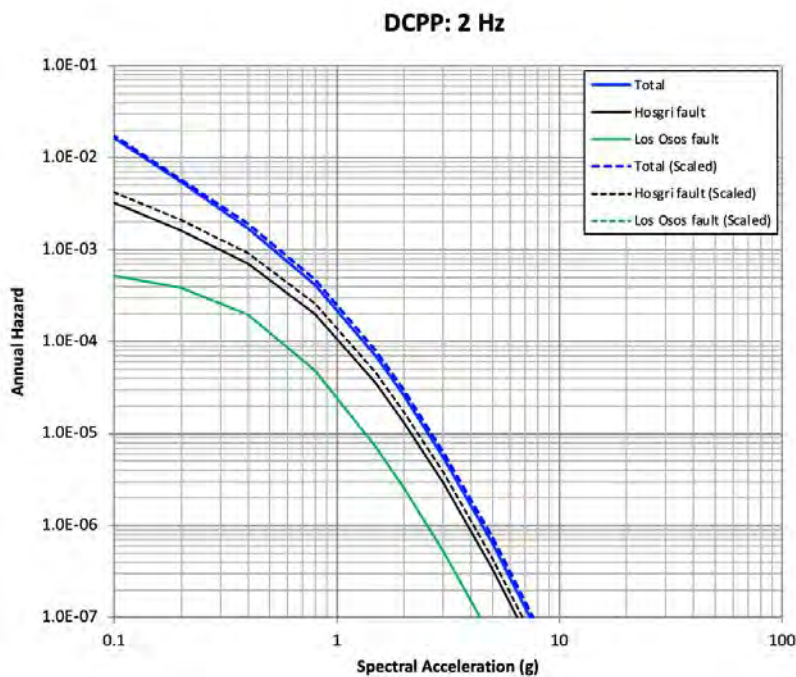


Figure 10-12. Mean hazard curves from the 2015 study (solid lines) and updated scaled results (dashed lines) for the Los Osos fault source (green lines), Hogгри fault source (black lines) and total hazard curves (blue lines) for 2 Hz



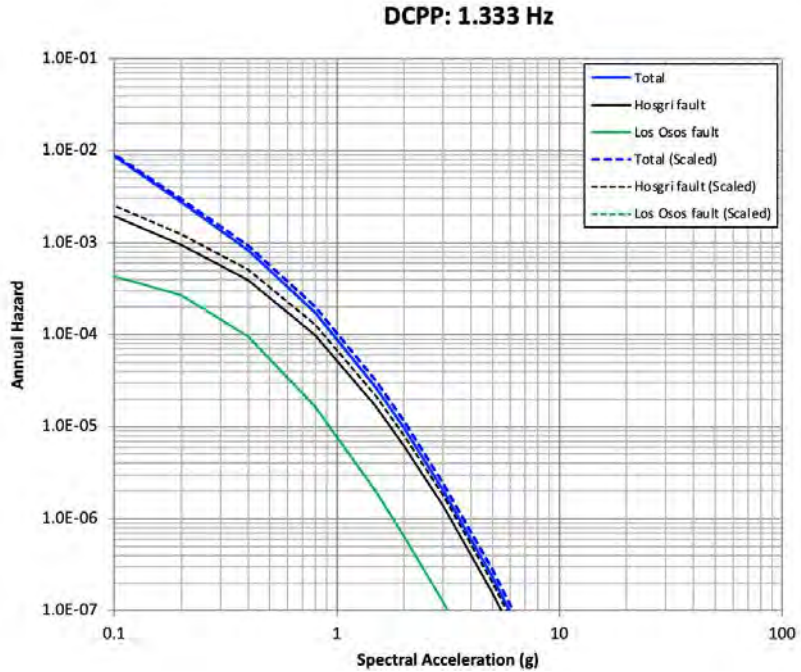


Figure 10-13. Mean hazard curves from the 2015 study (solid lines) and updated scaled results (dashed lines) for the Los Osos fault source (green lines), Hosgri fault source (black lines) and total hazard curves (blue lines) for 1.333 Hz

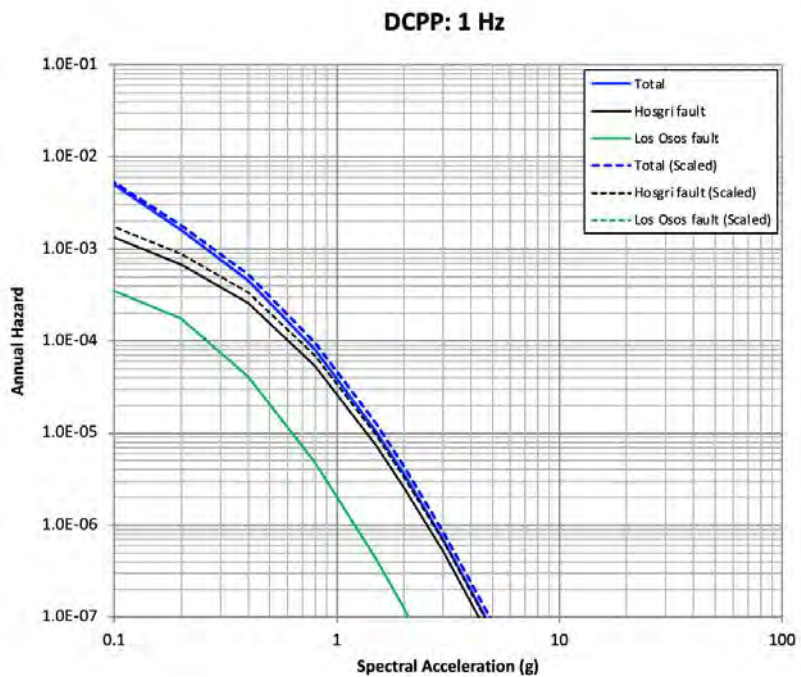


Figure 10-14. Mean hazard curves from the 2015 study (solid lines) and updated scaled results (dashed lines) for the Los Osos fault source (green lines), Hosgri fault source (black lines) and total hazard curves (blue lines) for 1 Hz

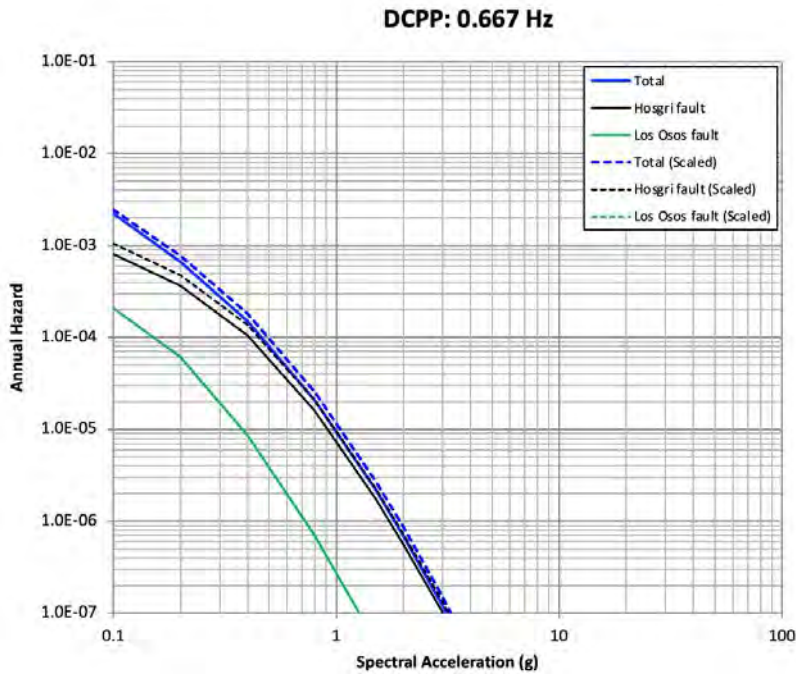


Figure 10-15. Mean hazard curves from the 2015 study (solid lines) and updated scaled results (dashed lines) for the Los Osos fault source (green lines), Hogгри fault source (black lines) and total hazard curves (blue lines) for 0.667 Hz

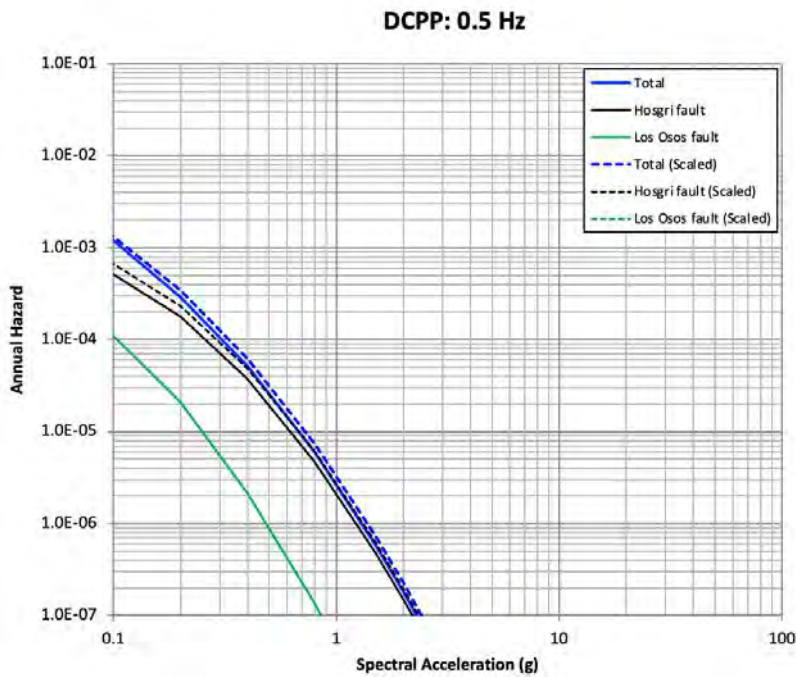
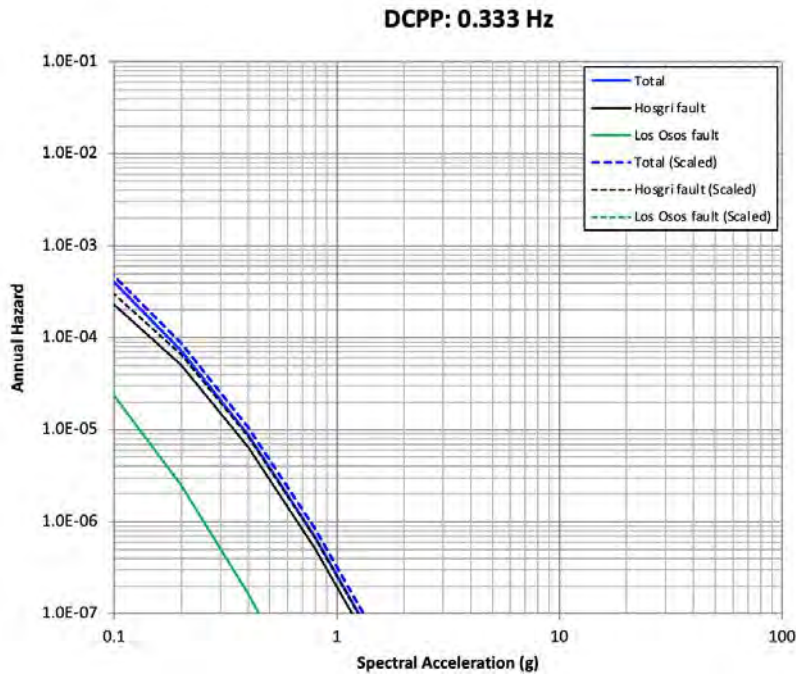
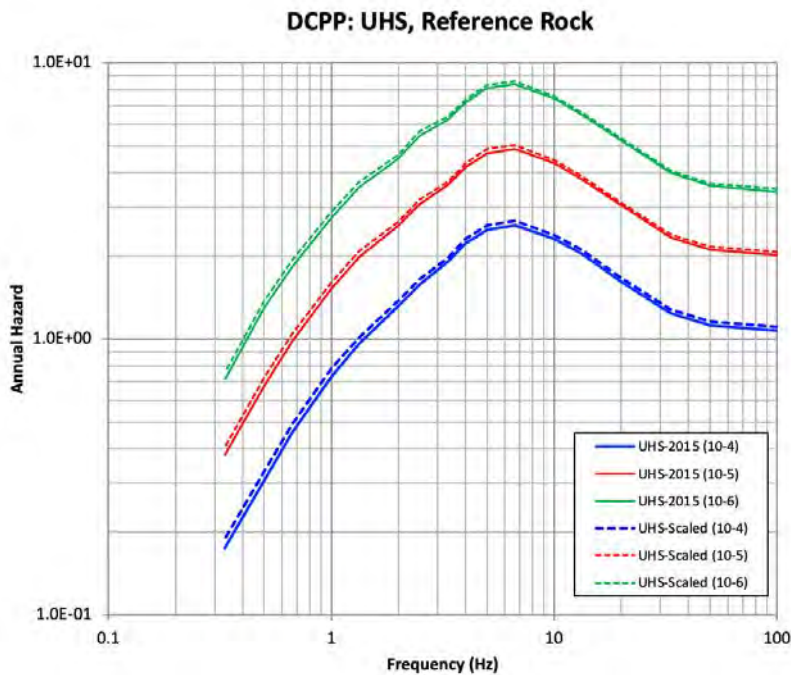


Figure 10-16. Mean hazard curves from the 2015 study (solid lines) and updated scaled results (dashed lines) for the Los Osos fault source (green lines), Hogгри fault source (black lines) and total hazard curves (blue lines) for 0.5 Hz



**Figure 10-17. Mean hazard curves from the 2015 study (solid lines) and updated scaled results (dashed lines) for the Los Osos fault source (green lines), Hosgri fault source (black lines) and total hazard curves (blue lines) for 0.333 Hz**



**Figure 10-18. UHS from the 2015 study (solid lines) and the updated results (dashed lines) for hazard levels of  $10^{-4}$  (blue lines),  $10^{-5}$  (red lines), and  $10^{-6}$  (green lines)**

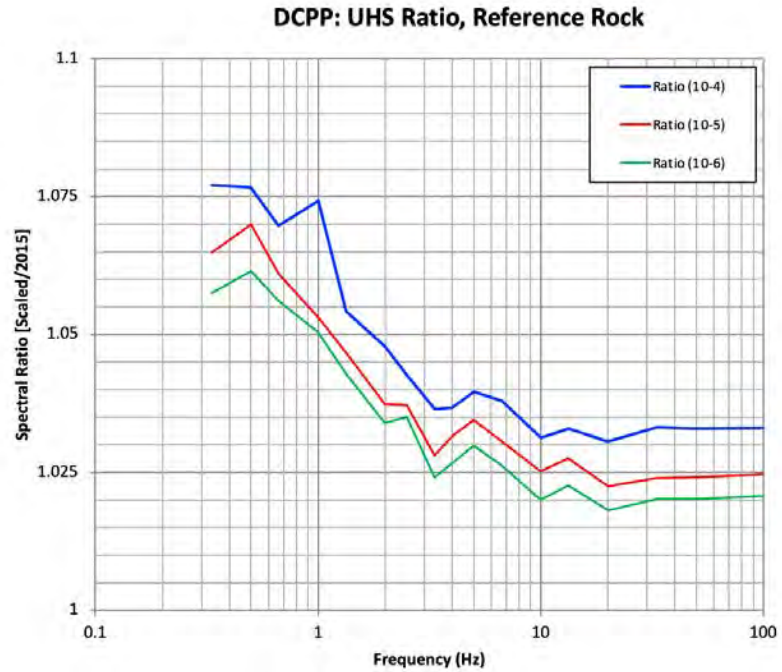


Figure 10-19. Ratio of UHS from the 2015 study and the updated results for hazard levels of 10<sup>-4</sup> (blue line), 10<sup>-5</sup> (red line), and 10<sup>-6</sup> (green line)

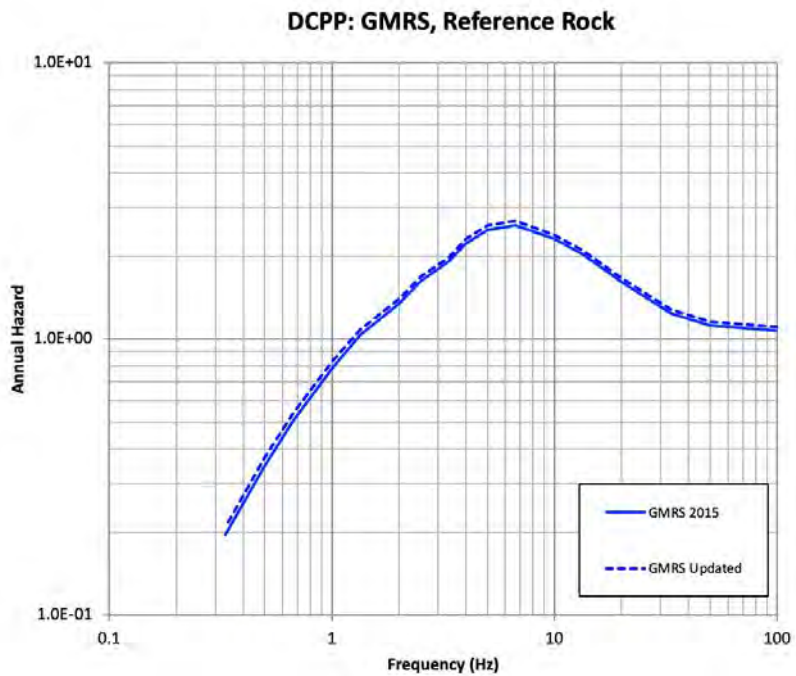
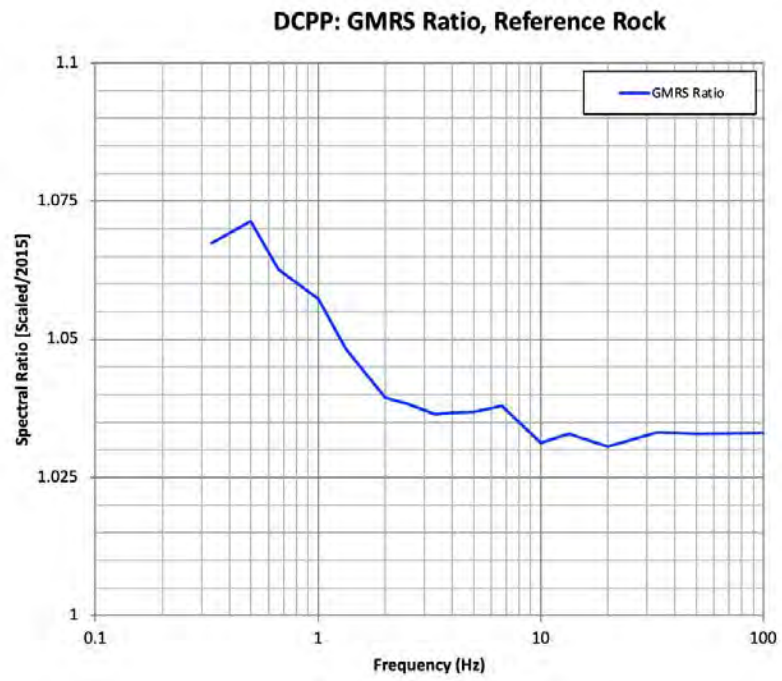


Figure 10-20. GMRS for the reference rock horizon from the 2015 study (solid line) and updated results (dashed line)





**Figure 10-21. GMRS spectral ratio (Updated/2015) for the reference rock**

## 11. CONTROL-POINT HAZARD FOR RISK ASSESSMENT

The probabilistic risk analysis (PRA) is based on the hazard curves and ground motions for the control point horizon. Specifically, the hazard curve for the 5 Hz spectral frequency is used as input into the PRA. Given the sensitivity from the recommended adjustments of the Hosgri and Los Osos faults mean slip rates and the adjustment of the EPHR for the Hosgri source, an evaluation of the adjustment to the hazard curves for the control point horizon is presented. The impact of these adjustments on the reference rock horizon has been previously presented.

### 11.1. DEVELOPMENT OF SITE ADJUSTMENT FACTORS

Site adjustment factors were previously developed based on the empirical ground-motion recordings from two instruments at DCPD and analytical studies (PG&E, 2015b). As noted, these site adjustment factors were applied to the hazard results for the reference rock horizon to estimate the hazard curves and ground motions for the control-point horizon. As part of this study and documented earlier in this report, the evaluation of the site adjustment factors based on new, more recent data, models, and methodologies led to the conclusion that the site adjustment factors used in the 2015 study are still acceptable. This is the same conclusion reached for the 2015 GMC model (GeoPentech, 2015). Based on these evaluations and the conclusions, the scale factors developed for the reference rock horizon are assumed to be applicable to the control-point horizon results. This assumption is based on the observation of the site adjustments having a linear scaling behavior rather than a strong nonlinear scaling behavior.

### 11.2. CONTROL-POINT HAZARD CURVES

Hazard curves for the control-point horizon are estimated based on the hazard curve ratio factors developed from the reference rock horizon scaling results with the assumption that the original site adjustment factors are applicable for this evaluation. Given this assumption, which is supported by the evaluation of the site adjustment factors, the hazard curve ratio factors (i.e., ratio of the scaled hazard values divided by the original hazard values) based on the reference rock horizon hazard curves can be directly applied to the control-point hazard curves (i.e., hazard values not ground-motion values) from the 2015 study. As described earlier, this scaling is based on the evaluation and adjustment of the mean slip rate and EPHR rate for the Hosgri fault and the mean slip rate for the Los Osos fault.

The hazard ratio values (i.e., scaled hazard value divided by 2015 hazard value) for 100 Hz (PGA) are plotted on Figure 11-1 as a function of the original total hazard (solid blue line) or the scaled total hazard (dashed green line). Similar results are observed for these two cases. For both results, the annual hazard ratio varies between values of about 1.05 and 1.12. As an approximation, a single scale factor is selected based on the results for the  $10^{-5}$  hazard level. This scale factor of 1.11 is plotted on Figure 11-1 with the dashed red line. The selection of the scaling factor at the  $10^{-5}$  hazard level is based on the overall shape of the scaling factors and the PRA results that show that the hazard level of importance is in the  $10^{-4}$  to  $10^{-5}$  range. Figure 11-1 shows that the selected scale factor overestimates the hazard for hazard levels greater than about  $8 \times 10^{-2}$  and lower than  $10^{-5}$ , but slightly underestimates the hazard in the range of  $10^{-3}$  to  $10^{-4}$ .

Similar results are presented on Figure 11-2 through Figure 11-7 for spectral frequencies of 20, 10, 5, 2.5, 1 and 0.5 Hz. Given the importance of the 5 Hz results for the PRA (see Figure 11-4), it should be stated that the scale factor is approximately constant for hazard levels less than about

10<sup>-4</sup> and thus selecting the scale factor at the 10<sup>-5</sup> hazard level is consistent with the 10<sup>-4</sup> value. The other spectral frequencies show a larger variation in the scale factors than the 5 Hz case. The resulting scale factors are listed in Table 11-1 for these seven spectral frequencies, and plotted on Figure 11-8 as a function of spectral frequencies. It is observed that for frequencies greater than 5 Hz, the selected 10<sup>-5</sup> hazard value scale factor is less than the 5 Hz value of 1.135. For lower spectral frequencies, however, the opposite is observed with larger scale factors for the selected 10<sup>-5</sup> hazard level. Given this larger value of 1.233 for the 0.5 Hz spectral frequency, it can be used as a potential bounding study value in place of the 1.135 value associated with the 5 Hz spectral frequency in a PRA sensitivity study.

**Table 11-1. Selected Scale Factors for the Control Point Hazard Curves Based on the Scaling Adjustments**

Frequency (Hz)	Scale Factor
100.0000	1.110
20.0000	1.100
10.0000	1.100
<b>5.0000</b>	<b>1.135</b>
2.5000	1.155
1.0000	1.212
0.5000	1.233

### 11.3. CONCLUSIONS

Given the results from the reference rock horizon hazard curve scaling based on the recommended adjustments to the Hosgri and Los Osos fault characterizations with the assumption that the site adjustment factors from the previous 2015 study are still applicable, selected scaling factors are recommended for the control-point horizon hazard curves. These scaling factors, which can be applied to the total control-point hazard from the 2015 study, are based on the computed factors for the 10<sup>-5</sup> hazard level, which is the approximate range of importance for the PRA study. Given that the PRA study is based on the 5 Hz hazard curves, the recommended scaling factor is 1.135. For a bounding sensitivity study, a slightly higher scaling factor of 1.233 that is based on the 0.5 Hz results can be used. For the other spectral frequencies considered, the scaling factors are less than the 1.233 value.

### DCPP: 100 Hz

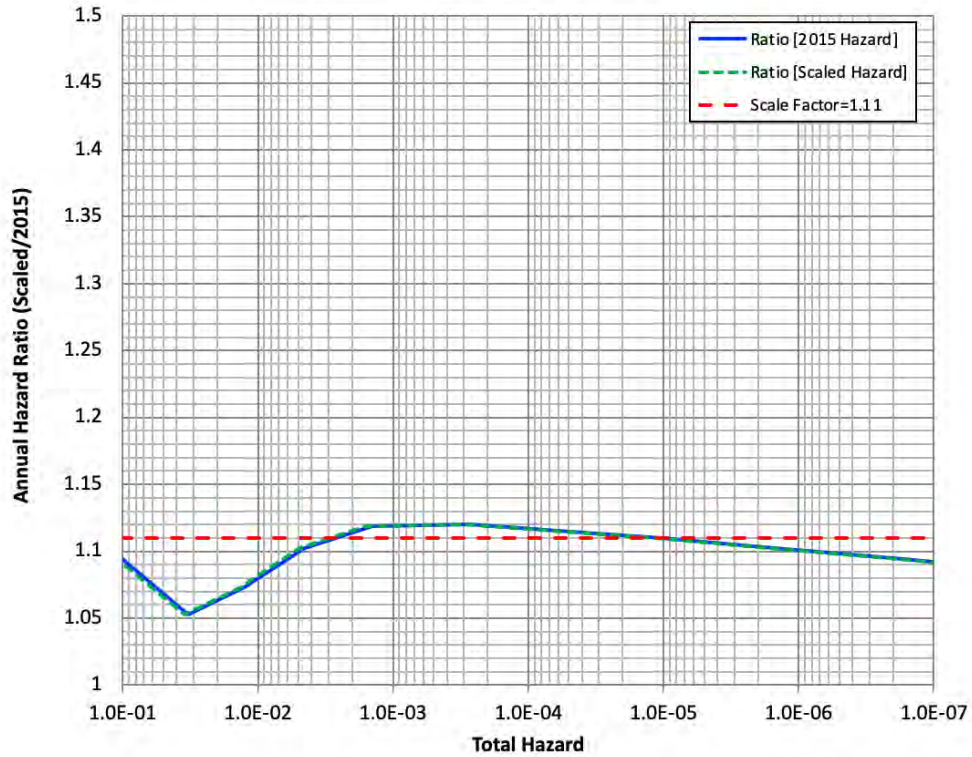


Figure 11-1. Hazard curve ratio (i.e., scaled hazard divided by 2015 hazard) plotted as a function of 2015 total hazard (solid blue line), scaled total hazard (dashed green line), and selected scale factor (dashed red line) for 100 Hz (PGA)

### DCPP: 20 Hz

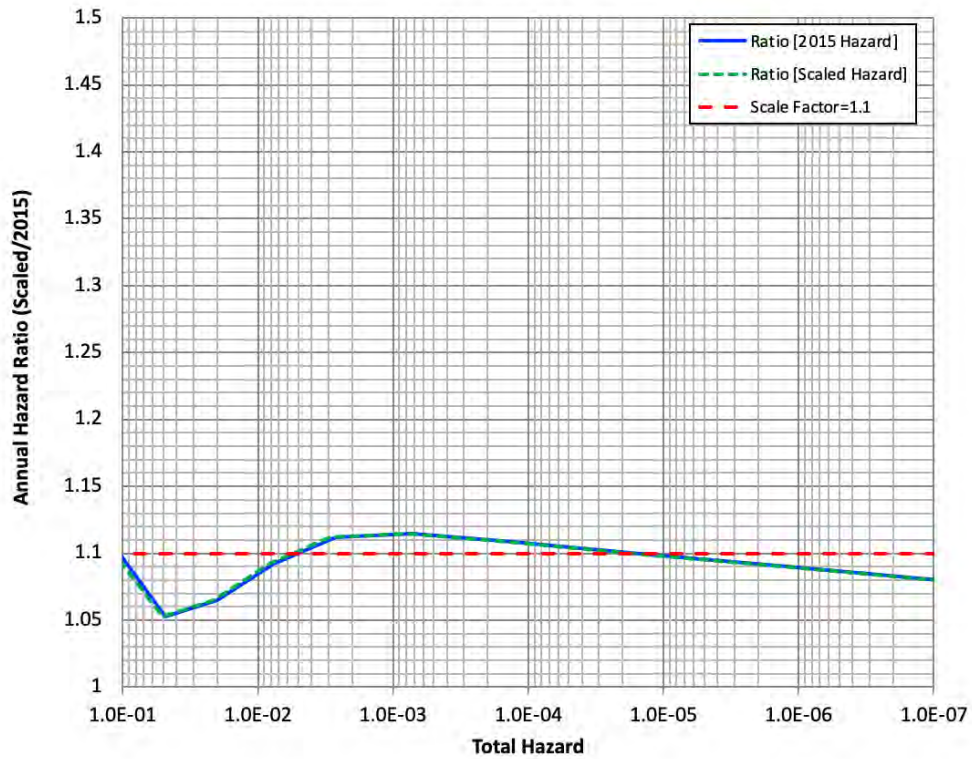


Figure 11-2. Hazard curve ratio (i.e., scaled hazard divided by 2015 hazard) plotted as a function of 2015 total hazard (solid blue line), scaled total hazard (dashed green line), and selected scale factor (dashed red line) for 20 Hz

### DCPP: 10 Hz

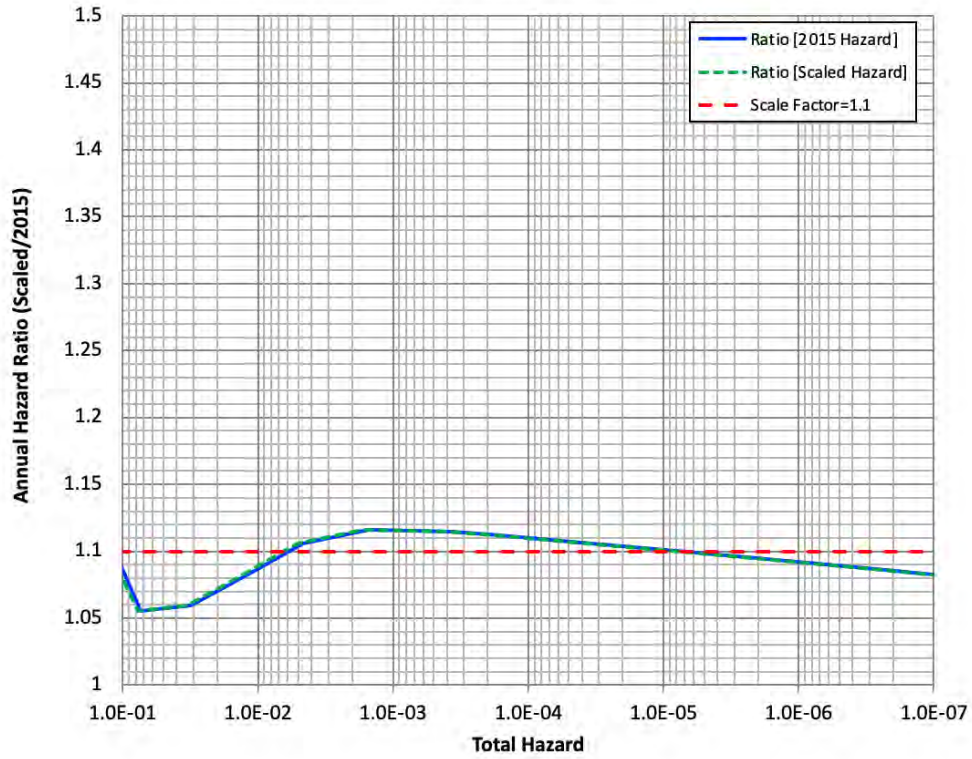


Figure 11-3. Hazard curve ratio (i.e., scaled hazard divided by 2015 hazard) plotted as a function of 2015 total hazard (solid blue line), scaled total hazard (dashed green line), and selected scale factor (dashed red line) for 10 Hz

### DCPP: 5 Hz

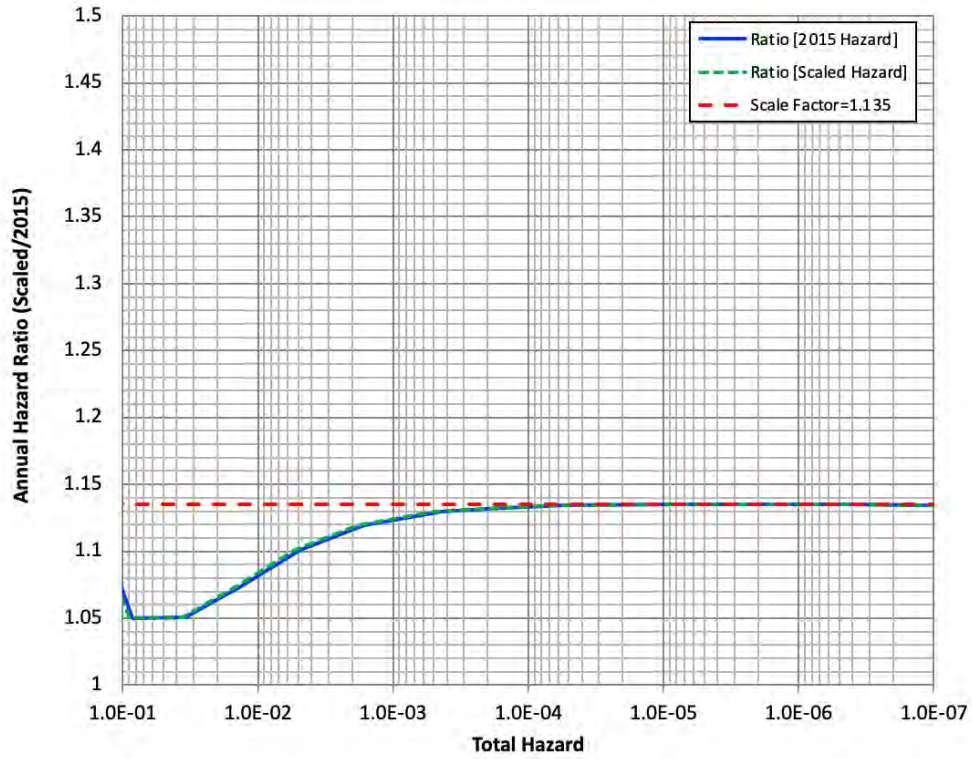


Figure 11-4. Hazard curve ratio (i.e., scaled hazard divided by 2015 hazard) plotted as a function of 2015 total hazard (solid blue line), scaled total hazard (dashed green line), and selected scale factor (dashed red line) for 5 Hz



DCPP: 2.5 Hz

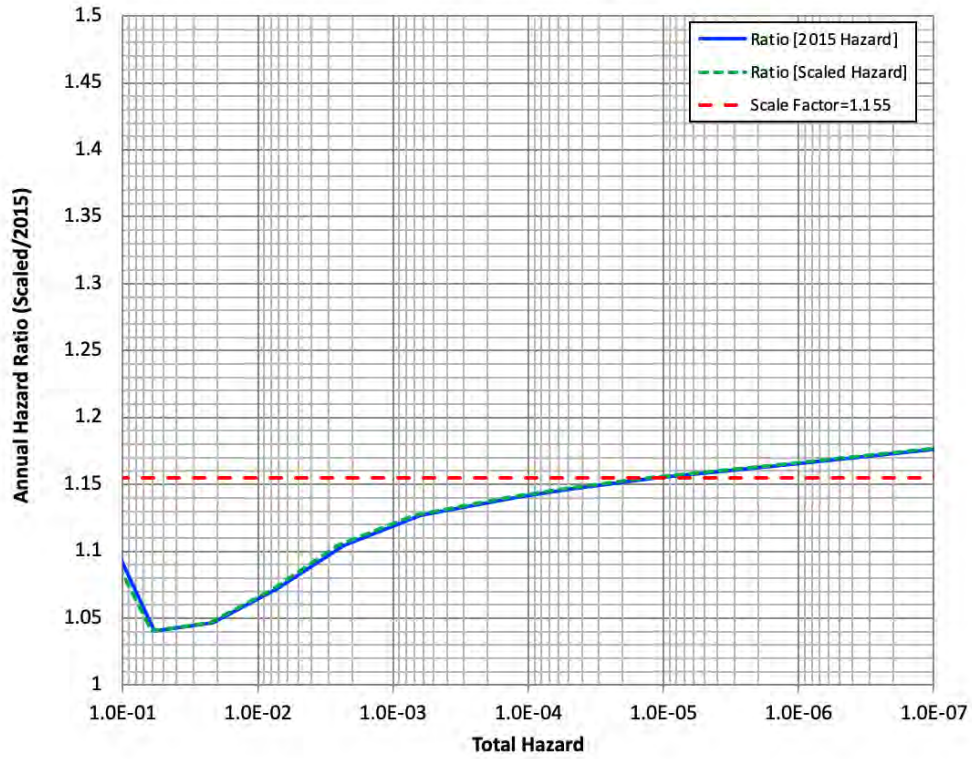
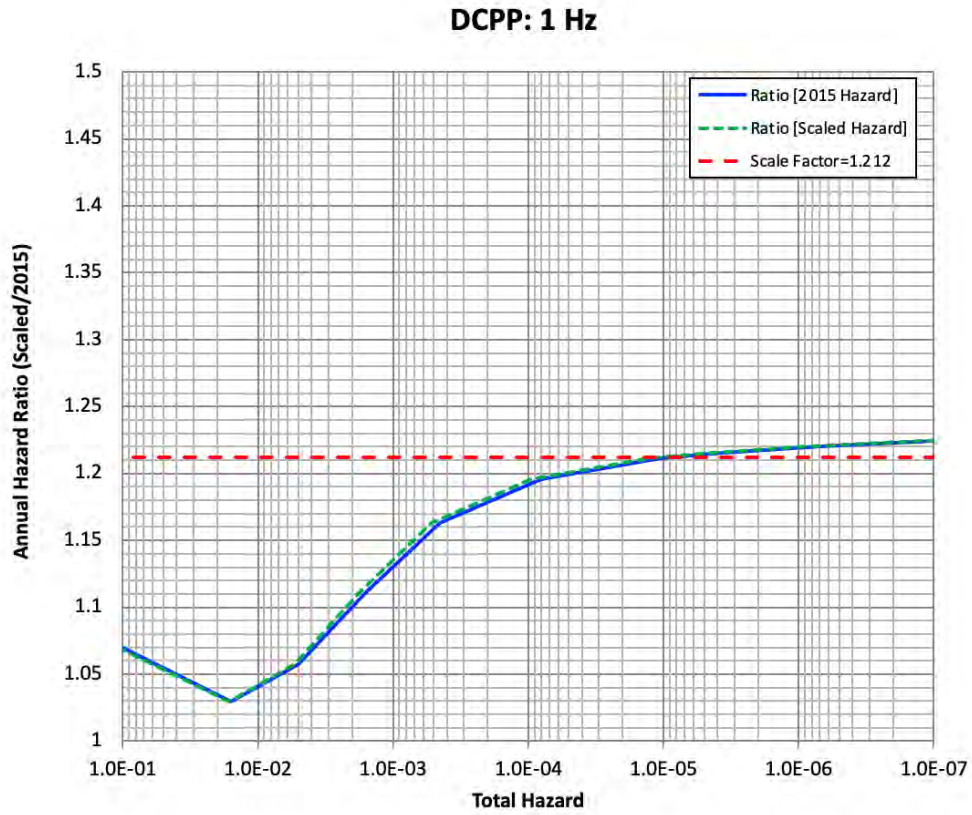


Figure 11-5. Hazard curve ratio (i.e., scaled hazard divided by 2015 hazard) plotted as a function of 2015 total hazard (solid blue line), scaled total hazard (dashed green line), and selected scale factor (dashed red line) for 2.5 Hz



**Figure 11-6. Hazard curve ratio (i.e., scaled hazard divided by 2015 hazard) plotted as a function of 2015 total hazard (solid blue line), scaled total hazard (dashed green line), and selected scale factor (dashed red line) for 1 Hz**

DCPP: 0.5 Hz

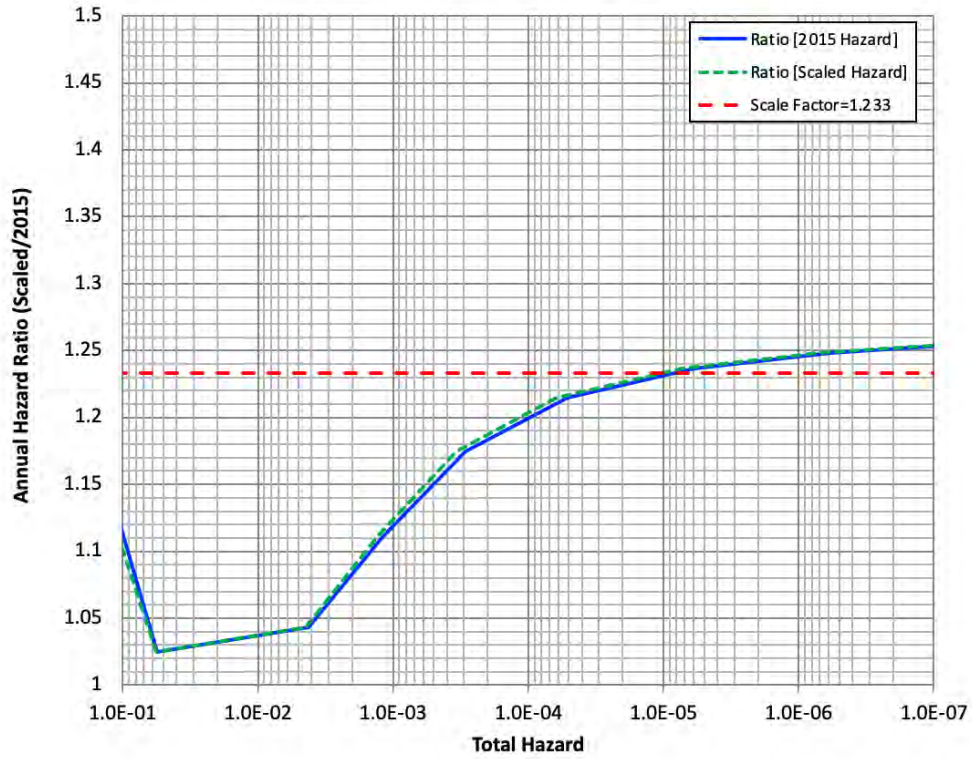


Figure 11-7. Hazard curve ratio (i.e., scaled hazard divided by 2015 hazard) plotted as a function of 2015 total hazard (solid blue line), scaled total hazard (dashed green line), and selected scale factor (dashed red line) for 0.5 Hz

### DCPP: Hazard Scale Factors

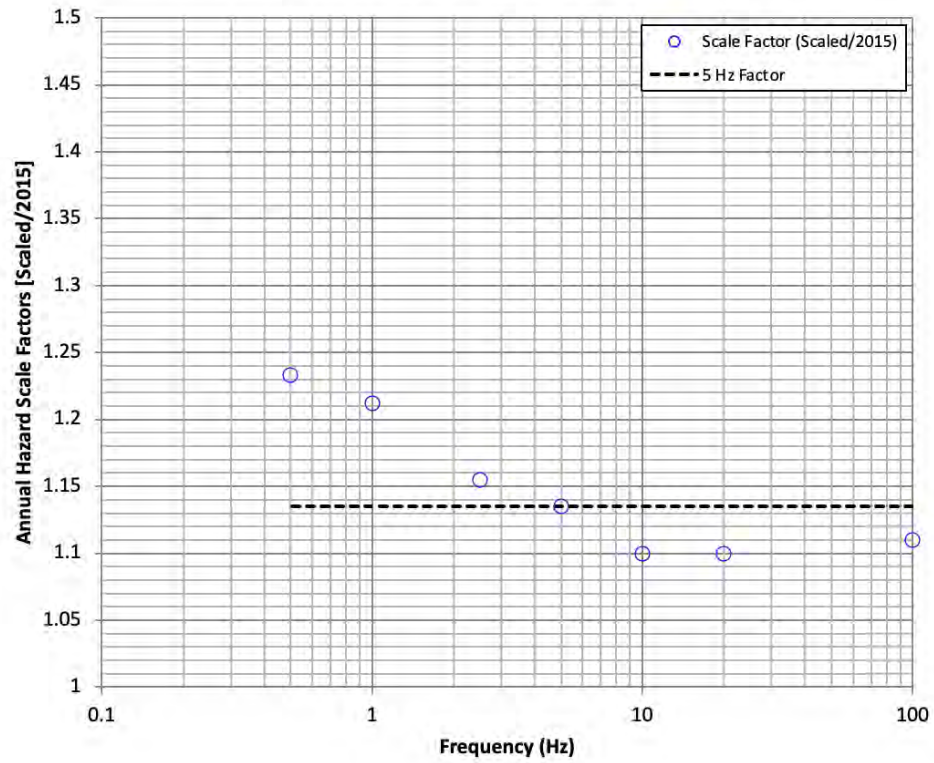


Figure 11-8. Selected scale factors (open blue circles) for the seven spectral frequencies and 5 Hz value (dashed black line)

## 12. RISK ASSESSMENT

SB-846 requires that PG&E conduct an “updated seismic assessment.” There are a number of different approaches with varying degrees of detail that could be used to conduct an updated seismic assessment. These approaches could range from assessing the change in the seismic hazard itself (source characterization, ground-motion modeling updates, etc.) to a more complete assessment of the risk impact starting with the change in seismic hazard and then assessing the change in risk to operation of the plant itself, which would be expressed in terms of core damage frequency and large early release frequency. The latter approach was chosen by PG&E to perform the SB-846 seismic risk assessment.

As part of PG&E’s LTSP, the state of knowledge of earthquake sources and hazards are monitored. Formal updates to the SPRA are made once the understanding of the new information is mature and the magnitude of the impact on the plant risk is significant enough to require an update. One method used to identify the need for further risk analysis is from the NRC’s Process of Assessment of Natural Hazard Impacts (POANHI) (NRC, 2023) screening process.

This assessment provides a conservative approximation of the change in plant risk. A detailed assessment that reduces conservatism would involve additional assessments including:

- The impact of a change in the hazard spectral shape on the fragility assessments that are used in the Diablo Canyon Probabilistic Risk Assessment (PRA) model,
- Full development of a new hazard (the current approach only approximates the impact based on scaling factors), and a
- Full update of the SPRA model that incorporates fragility adjustments and updated hazard.

### 12.1. CALCULATION PROCESS

The plant risk assessment sensitivity study utilizes the current Diablo Canyon PRA model of record, which is a full scope model including internal events, internal flooding, internal fire, and seismic hazards. This model was recently updated in August of 2023 (PG&E, 2023) and includes updates to equipment reliability data as well as resolutions to industry peer-review comments.

The plant risk assessment sensitivity study, PRA 23-05 (PG&E, 2024), involved the following steps:

1. Identify a scaling factor for the seismic hazard information previously used in the DCP 50.54(f) NTTF recommendation 2.1 response. This involved updated source characterization and ground-motion assessments and is discussed earlier in this report.
2. Perform a series of sensitivity assessments using the Diablo Canyon seismic PRA model. The first sensitivity used a 5-Hz hazard scaling factor of 1.05. This was performed prior to completion of the final hazard scaling factors to confirm the impact of a scaling factor on plant risk. The next step was to directly use the new hazard information to provide sensitivity assessments for plant risk. These sensitivity studies utilized scaling factors of 1.135 and 1.233 for the 5 Hz and 0.5 Hz hazards, respectively. These scaling factors effectively increase the hazard frequency across the full range of accelerations by 13.5% to 23.3%. Use of the bounding 0.5 Hz scaling factor provides additional assurance that the risk model is conservatively assessing the change in hazard. The results of the PRA

model sensitivity analysis were compared against the change in core damage frequency ( $\Delta$ CDF) and change in the Large Early Release Frequency  $\Delta$ LERF criteria commonly used in the nuclear industry (Regulatory Guide 1.174 criteria).

3. To confirm that the relative importance of systems, structures and components (SSCs) does not change, SSC fragility Fussell-Vesely and Risk Achievement Worth (RAW) importance were reviewed. No changes to SSC importance were identified. This was expected because the sensitivity analysis involved a linear increase in hazard frequency for all return periods.

## **12.2. DISCUSSION AND CONCLUSIONS**

The results of this assessment indicate that the total CDF and LERF for DCPP remain below region II risk criteria from Regulatory Guide 1.174 Revision 3: Total CDF and LERF are less than  $10^{-4} \text{ yr}^{-1}$  and  $10^{-5} \text{ yr}^{-1}$  (1E-04/yr and 1E-05/yr), respectively for all of the hazard scaling factors used in this assessment. The region II risk acceptance guidelines are used to identify the region of risk for which small risk changes are allowed and is the region that virtually all U.S. nuclear facilities fall into.

## 13. SUMMARY AND CONCLUSIONS

A site-specific seismic hazard assessment for DCPD was performed to satisfy the covenant for the performance of a seismic update associated with the State of California Senate Bill (SB) 846 plant license extension. Site-specific probabilistic seismic hazard analysis (PSHA) is calculated from three model elements: (1) a seismic source characterization (SSC) that models the locations, magnitudes, and rates of earthquakes; (2) a ground-motion characterization (GMC) that models vibratory ground motions at the site from the earthquakes for a reference site condition; and (3) a site characterization that models how to adjust the vibratory ground motions to account for the specific physical properties underlying the site.

The SB-846 seismic hazard assessment consisted of a focused review and evaluation of new data, models, and methods that have become available since the latest comprehensive seismic hazard studies for DCPD were completed in 2015. These hazard studies included a site-specific SSC model developed under a Senior Seismic Hazard Analysis Committee (SSHAC) Level 3 process (PG&E, 2015b), a GMC model for the southwestern United States (SWUS, including DCPD) developed under a SSHAC level 3 process (GeoPentech, 2015), and a site characterization study performed for DCPD that utilized 3-D seismic velocity data (Fugro, 2015a).

The outcome of the evaluation is a targeted update to the seismic hazard at DCPD, which is captured through a sensitivity analysis. The review of new information (Section 13.1) shows that no changes are warranted to the GMC and site characterization models and most aspects of the SSC model. The SSC evaluation concludes that updates to the Hosgri and Los Osos fault slip rates are warranted based on recently published data and models. Changes to the fault slip rates impact the calculated rate of earthquakes from these fault sources, and in turn the rate of ground-motion exceedance (hazard curves). The seismic hazard sensitivity analysis (Section 13.2) consists of hazard curve scaling for a suite of spectral frequencies based on the recommended changes to the mean fault slip rates.

The resulting scaling of the 5-Hz hazard curve for the control-point horizon was further used in a sensitivity analysis for the probabilistic risk assessment (PRA) of DCPD.

### 13.1. MODEL EVALUATIONS

The evaluations of new information for the SSC, GMC, and site condition models are provided in the subsections that follow.

#### 13.1.1. *Source Characterization*

Chapter 5 of this report presents an evaluation of the site-specific SSC model for the DCPD. The chapter starts with an overview of the 2015 SSC model (PG&E, 2015b) and documentation that the seismic sources contributing most to the hazard include the Hosgri, Los Osos, Shoreline, and San Luis Bay faults, as well as the Local seismic source zone. Hazard sensitivities document that fault slip rates are the SSC model parameters that contribute most to hazard uncertainty.

The review of new data, models, and methods that may impact the 2015 SSC model focused on information from the published literature, technical reports, and publicly released datasets. The review focused on those seismic sources and source parameters that contributed most to hazard and hazard uncertainty. The review in Chapter 5 does not address proponent models offered



through testimony, such as the recent testimony statements by Dr. Peter Bird. Such proponent models are discussed in Chapter 6 of this report and do not impact the 2023 hazard update because they are either not suitable or mature enough for a site-specific hazard evaluation or are not technically defensible.

For most aspects of the 2015 SSC model, recently published data, models, and methods are consistent with information available to the 2015 SSC SSHAC TI team, and no new information warrants changes to the model. The exception to this general finding is several publications containing new information relevant to the calculation of the Hosgri and Los Osos fault slip rates. New research on the stratigraphy and age of a sea-floor feature near Point Estero called the cross-Hosgri slope (CHS) is presented in Kluesner et al. (2023) and Medri et al. (2023). These new data and analyses have substantiated and broadened the earlier understanding of the origin of the CHS and its use for calculating the slip rate of the Hosgri fault (Johnson et al., 2014). Based on this new information, the geologic slip rate of the Hosgri fault at the CHS is revised, and the weighting of the Point Estero (CHS) slip rate site is increased relative to the three other Hosgri fault slip rate sites used in the 2015 SSC model to calculate the Hosgri fault slip rate near DCP. The result of the updated calculations is a 26% increase in the weighted mean Hosgri fault source slip rate from 1.70 mm/yr in the 2015 SSC model to 2.14 mm/yr. This increase in mean slip rate also results in a change in the SSC model element (the equivalent Poisson hazard ratio, or EPHR) used to capture uncertainty related to time-dependent earthquake recurrence behavior of the Hosgri fault source. The change in mean EPHR related to the increase in mean slip rate is an increase of approximately 3%, from an EPHR of 1.20 in the 2015 SSC model to 1.24.

The Los Osos fault slip rate is also revised due to a new model of tectonic uplift rate as recorded by marine terraces along the central California coast published by Simms et al. (2016). This model utilizes the same marine terrace stratigraphic and elevation information from earlier models (e.g., Hanson et al., 1994), but estimates paleosea levels based on the incorporation of local glacio-isostatic adjustment (GIA) effects rather than global average conditions. The new Simms et al. (2016) model results in an approximately 30% decrease in the calculated uplift rate of the hanging wall of the Los Osos fault. The update to the 2015 SSC model consisted of weighting the Simms et al. (2016) model along with two alternative models for hanging wall uplift rate and recalculating the Los Osos fault slip rates for three alternative fault geometry models. Revised weighted mean slip rates are 0.22, 0.17, and 0.39 mm/yr for the OV, SW, and NE models, respectively, which represent a decrease in mean slip rate compared to the 2015 SSC model on the order of 9% to 15%. The magnitudes of the changes in mean slip rate are on the order of 0.02 to 0.04 mm/yr, which are an order of magnitude less than the 0.44 mm/yr change in mean slip rate for the Hosgri fault source. No changes to the mean EPHR for the Los Osos slip rate were made.

### **13.1.2. Ground Motion Characterization**

The evaluation of the 2015 GMC model is presented in detail in Chapter 7 of this report. The 2015 GMC model (GeoPentech, 2015) consists of a median ground-motion model and an aleatory uncertainty model. Each of these components was reviewed and evaluated given the compilation of more recently recorded earthquake ground motions in the area around DCP. In addition, a literature review was performed to evaluate the potential of any new ground-motion models (GMMs) that may be applicable for DCP.

The 2015 study followed a Sammon (1969) mapping process using candidate GMMs to fully sample the distribution space for the median model. The 2015 study was the first full implementation of the Sammon's mapping process for a SSHAC Level 3 study and subsequent SSHAC Level 3 studies have implemented this methodology. This process has become the standard state of practice for these types of high-level studies and no adjustment is required for the 2015 methodology. It is also concluded that there are no new available GMMs that would be considered as candidate models for the Sammon's mapping process.

Recently recorded empirical data as part of the NGA-West3 project, the recent large crustal earthquakes in Türkiye, and other recently compiled ground motions from events located around the DCPD site were evaluated. Using this preliminary dataset, a residual analysis was conducted to compare the median GMM from the SWUS study for DCPD with the new empirical data. Overall, the results of this residual study led to the conclusion that the SWUS median GMM for DCPD is consistent with this new empirical data and that no adjustment to the median GMM model was deemed necessary for the hazard sensitivity analyses.

A review of the implemented hanging wall model in the 2015 study was performed by reviewing other hanging wall models. The model implemented in the 2015 study was guided by numerical simulations, and since that study, no additional simulations have been completed that would apply to the fault geometry for DCPD. In addition, there have been no new processed data for earthquakes and strong ground-motion recordings from dipping reverse fault events that would help evaluate the robustness of the 2015 hanging wall model. Based on these factors, the hanging wall model used in the 2015 model is still acceptable.

For the 2015 study, the effects of rupture directivity were not included but were noted in the documentation. In their final letter, the PPRP noted limitations of the directivity evaluation and integration in the SWUS study. Since the 2015 study, several newer directivity models have been developed and have been published in the literature. All of these models provide median ground-motion adjustments for longer spectral period (i.e., greater than about 1 sec). Deterministic comparisons of these new models and other existing models were presented for a representative Hosgri fault scenario event. These models were evaluated and show a wide range in median adjustment; there are technical considerations regarding the centering of some of these models and their treatment of aleatory variability. For these reasons, combined with the expected small impact of potential directivity adjustments on the DCPD hazard and the longer spectral period range of these adjustments, it was concluded that the effects of directivity do not need to be considered for this sensitivity study. This is the same conclusion reached for the original 2015 study.

Since the conclusion of the 2015 study, fully non-ergodic ground-motion models have become available for ground-motion data-rich locations such as California. These models allow for the characterization of non-ergodic source, path, and site effects based on recorded ground-motion data at and around a site of interest. The non-ergodic model of Lavrentiadis and Abrahamson (2023) was evaluated and compared to the partially non-ergodic site-specific median ground-motion predictions from the 2015 study for DCPD. Deterministic median ground-motion predictions for hazard-significant scenarios indicated consistent results between the 2015 study and the non-ergodic model of Lavrentiadis and Abrahamson (2023). This consistency is the result of limitations in the available ground-motion data in the DCPD region, and the fact that non-ergodic adjustments, which are primarily driven by site-specific effects, were also

incorporated in the 2015 study. As a result, it was concluded that no adjustments to the 2015 GMC median model were necessary.

Given the complexity of the SSC model with both splay and complex ruptures, the 2015 GMC model provided a methodology for estimating the median ground motions from these types of earthquakes. In reviewing the approach and the simulations developed for the 2015 study, combined with the lack of any new simulations, the conclusion was reached that the original methodology of taking the square root of the sum of the squares for either splay or complex ruptures is acceptable.

The aleatory variability model developed as part of the 2015 study was evaluated in terms of new data and models. It was concluded that the available preliminary ground-motion datasets do not currently allow for an update to the calculation of components of aleatory variability for the large magnitude and short distance range of interest for DCP (e.g.,  $M > 5$  and  $R_{RUP} < 50$  km). Existing models for the components of aleatory variability were also evaluated and compared to 2015 models. These comparisons indicated consistency in the approach, the elements of the logic tree, and the results in the magnitude and distance range of interest for DCP. As a result, the SWUS aleatory variability model developed for DCP is still considered acceptable.

### **13.1.3. Site Characterization**

The evaluation of the 2015 study for the development of site-adjustment factors is presented in detail in Chapter 9 of this report. These adjustment factors were developed based on analytical and empirical methodologies and applied to correct the reference rock hazard for DCP to the site-specific conditions at the control point. The inputs, methodologies, and results were evaluated for each of the analytical and the empirical approaches.

For the analytical approach, a review of the methodology and input parameters in terms of host and target site characterizations was performed. This evaluation indicated that the methodology used for the analytical study as well as the characterization of target site conditions are acceptable. A sensitivity analysis was performed to evaluate the impact of alternative characterization of the host site conditions on the obtained analytical site factors. Overall, this impact on the overall site factors was observed to be small, considering the low weight of [0.33] assigned to the analytical approach. As a result, no updates to the analytical site study were recommended.

The 2015 empirical site factors were evaluated considering data and methods that have become available since the conclusion of the 2015 study and their impact of the site term. Since the 2015 study, there have been no new empirical ground-motion recordings at ESTA27 and ESTA28 that would cause a reevaluation of the empirical site term at DCP.

The novel non-ergodic ground-motion modeling approach was applied to estimate the empirical site term at DCP and its regional and uncorrelated components using a preliminary expanded ground-motion dataset in the region surrounding DCP. This analysis provided insights into the cause of the smaller high-frequency ground motions at DCP: about half of the reduction is a regional effect and half of the reduction is a site-specific effect.

This consistency in the trends between the regional and the site-specific empirical terms provided support for the 2015 site terms. As a result of this consistency, and given the

preliminary nature of the expanded dataset and the non-ergodic analysis performed, no updates to the empirical site term were recommended.

## **13.2. HAZARD ANALYSIS**

The hazard analysis sensitivities based on the recommended adjustments from the SSC model are presented in full detail in Chapter 11 and Chapter 12 of this report.

### **13.2.1. Hazard Curve Scaling**

Given the recommended adjustments to the Hosgri and Los Osos mean slip rates and the recommended adjustment to the Hosgri EPHR rate, the reference rock hazard curves were scaled based on the multiplicative ratio factor of the change in the rates (i.e., slip rate and EPHR rate). For the Hosgri fault source, this led to a scaling factor increase of 1.30. For the Los Osos fault source, the scaling factor led to a reduction on the order of 0.85 to 0.93 depending on the tectonic model (i.e., OV, NE, or SW). Applying these scale factors and keeping the contribution from the other seismic sources the same, the resulting change in the ground motions from the scaled hazard is approximately a 5–7% increase in the low frequency range (i.e., frequencies less than about 2.5 Hz), and smaller increases of about 4% in the higher frequency range from the reference rock horizon. These results are over the hazard levels of  $10^{-4}$  to  $10^{-6}$  and also include the reference rock horizon GMRS. Larger ratios (i.e., of about 10–20%) of the total reference rock hazard as opposed to the ratio of the ground motions are observed from the scaling results. These results are dependent on the relative contribution of the Hosgri fault source to the total hazard with the lower frequencies having a larger contribution from the Hosgri fault source than the higher frequencies.

Based on the evaluation of new data and methodologies and the resulting conclusion that the site adjustments used in the 2015 study (PG&E, 2015b) are applicable, the scaling factors developed for the reference rock horizon were applied to hazard curves for the control-point horizon. Specifically, based on the PRA for DCPH being based on the 5-Hz control-point hazard curves, a scaling factor of 1.135 is recommended. This scaling factor is approximately equal to the ratio of the scaled hazard curve to the 2015 hazard curve over the hazard levels of  $10^{-4}$  to  $10^{-7}$ . Based on the PRA calculations, the hazard level of interest is approximately in the  $10^{-4}$  to  $10^{-5}$  range. Scale factors for six other spectral frequencies (100, 20, 10, 2.5, 1, and 0.5 Hz) were also selected based on the ratio at the  $10^{-5}$  hazard level. For frequencies less than 5 Hz, these selected scaling factors are slightly larger, with the largest value of 1.233 for 0.5 Hz. For frequencies higher than 5 Hz, the scale factors are less than the 5-Hz value of 1.135. As part of the PRA sensitivity analysis, the largest value of 1.233 associated with the 0.5-Hz results can be used as a bounding value to be applied to the 5-Hz PRA analysis.

### **13.2.2. Summary of Comparisons**

Based on the review and evaluation of the SSC and GMC (GeoPentech, 2015) models and the site adjustment factors, a scaling of the hazard curves was implemented to assist in the sensitivity evaluation of the seismic hazard at DCPH based on new information. Scaling factors for the Hosgri and Los Osos fault sources were developed and implemented with this scaling exercise. Based on the evaluation of the GMC, the previous 2015 model is still acceptable, and no adjustments are needed for these sensitivity analyses. Ratio values between the scaled hazard

curves and previous 2015 hazard curves were estimated along with the ground-motion ratio values. This ratio is also applicable to the control-point hazard given the conclusion that the 2015 site adjustment factors are acceptable. Finally, it is recommended that the selected hazard value scale factor of 1.135 for the 5-Hz hazard curve be applied for the PRA sensitivity analysis, as discussed in Chapter 12.

## 14. REFERENCES

- Abrahamson, N.A., Silva, W.J., and Kamai, R., 2014. Summary of the ASK14 ground motion relation for active crustal regions: *Earthquake Spectra* **30** (3): 1025–1055.
- Aki, K., 1965. Maximum likelihood estimate of  $b$  in the formula  $\log N = a - bM$  and its confidence limits: *Bulletin of the Earthquake Research Institute* [University of Tokyo] **43**: 237–239.
- Akkar, S., Sandikkaya, M.A., and Bommer, J.J., 2014a. Empirical ground-motion models for point- and extended-source crustal earthquake scenarios in Europe and the Middle East: *Bulletin of Earthquake Engineering* **12** (1): 359–387, doi:10.1007/s10518-013-9461-4.
- Akkar, S., Sandikkaya, M.A., and Bommer, J.J., 2014b. Erratum to: Empirical ground-motion models for point- and extended-source crustal earthquake scenarios in Europe and the Middle East: *Bulletin of Earthquake Engineering* **12** (1), 389–390, doi:10.1007/s10518-013-9508-6.
- Akkar, S., Sandikkaya, M.A., Senyurt, M., Azari Sisi, A., Ay., B.Ö., Traversa, P., Douglas, J., Cotton, F., Luzi, L., Hernandez, B., and Godey, S., 2014c. Reference database for seismic ground-motion in Europe (RESORCE): *Bulletin of Earthquake Engineering* **12** (1): 311–339, doi:10.1007/s10518-013-9506-8.
- Al Atik, L., 2015. NGA-East: *Ground-motion Standard Deviation Models for Central and Eastern North America*, Report PEER 2015–07, Pacific Earthquake Engineering Research Center, University of California, Berkeley.
- Al Atik, L., and Abrahamson, N., 2021. A methodology for the development of 1D reference  $V_s$  profiles compatible with ground-motion prediction equations: Application to NGA-West2 GMPEs: *Bulletin of the Seismological Society of America* **111** (4): 1765–1783.
- Al Atik, L., Abrahamson, N., Bommer, J.J., Scherbaum, F., Cotton, F., and Kuehn, N., 2010. The variability of ground-motion prediction models and its components: *Seismological Research Letters* **81** (5): 794–801.
- Al Atik, L., Gregor, N., Mazzoni, S., and Bozorgnia, Y., 2023. *Directivity-Based Probabilistic Seismic Hazard Analysis for the State of California: Report 2, Directivity Implementation*, Report GIRS 2023–05 prepared for the Department of Civil and Environmental Engineering, University of California, Los Angeles.
- Al Atik, L., Kottke, A., Abrahamson, N., and Hollenback, J., 2014. Kappa ( $\kappa$ ) scaling of ground-motion prediction equations using an inverse random vibration theory approach: *Bulletin of the Seismological Society of America* **104** (1): 336–346, doi:[10.1785/0120120200](https://doi.org/10.1785/0120120200).
- Al Atik, L. and Youngs, R.R., 2014. Epistemic uncertainty for NGA-West2 models: *Earthquake Spectra* **30** (3): 1301–1318, doi:10.1193/062813EQS173M.

Ancheta, T.D., Darragh, R.B., Stewart, J.P., Seyhan, E., Silva, W.J., Chiou, B.S.-J., Wooddell, K.E., Graves, R.W., Kottke, A.R., Boore, D.M., Kishida, T., and Donahue, J.L., 2014. NGA-West2 Database: *Earthquake Spectra* **30** (3): 989–1005, doi:10.1193/070913EQS197M.

Anderson, J.G., and Brune, J.N., 1999. Probabilistic seismic hazard analysis without the ergodic assumption: *Seismological Research Letters* **70** (1): 19–28.

Bayless, J., and Abrahamson, N.A., 2019. Summary of the BA18 ground-motion model for Fourier amplitude spectra for crustal earthquakes in California: *Bulletin of the Seismological Society of America* **109** (5): 2088–2105, doi:10.1785/0120190077.

Bayless J., and Somerville, P.G., 2013. Chapter 2: Bayless and Somerville model: in Spudich, P. (editor), Bayless, J., Baker, J.W., Chiou, B.S.-J., Rowshandel, B., Shahi, S.K., and Somerville, P.G., *Final Report of the NGA-West2 Directivity Working Group*, Report PEER 2013-09, Pacific Earthquake Engineering Research, University of California, Berkeley: 29–46.

Bayless, J., Somerville, P.G., and Skarlatoudis, A., 2020. *A Rupture Directivity Adjustment Model Applicable to the NGA-West2 Ground Motion Models and Complex Fault Geometries*, Final Technical Report, U.S. Geological Survey Award No. G18AP00092.

Bechtel Power Corporation (Bechtel), 1988. *Final Report on the Diablo Canyon Long Term Seismic Program Soil Structure Interaction Analysis*, final report prepared for Pacific Gas & Electric, July 1988.

Biasi, G.P., Parsons, T., Weldon, R.J., II, and Dawson, T.E., 2013. Appendix J—Fault-to-Fault Rupture Probabilities: in Field, E.H., Biasi, G.P., Bird, P., Dawson, T.E., Felzer, K.R., Jackson, D.D., Johnson, K.M., and 11 others [Working Group on California Earthquake Probabilities], *Uniform California Earthquake Rupture Forecast, Version 3 (UCERF3)—The Time-Independent Model*, U.S. Geological Survey Open-File Report 2013–1165/ California Geological Survey Special Report 228/ and Southern California Earthquake Center Publication 1792, 20 pp.

Biasi, G.P., Weldon, R.J., II, Fumal, T.E., and Seitz, G.G., 2002. Paleoseismic event dating and the conditional probability of large earthquakes on the southern San Andreas fault, California: *Bulletin of the Seismological Society of America* **92** (7): 2761–2781.

Biasi, G.P., and Thompson, S.C., 2018. Estimating time-dependent seismic hazard of faults in the absence of an earthquake recurrence record: *Bulletin of the Seismological Society of America* **108** (1): 39–50.

Biasi, G.P., and Wesnousky, S.G., 2016. Steps and gaps in ground ruptures: empirical bounds on rupture propagation: *Bulletin of the Seismological Society of America* **106** (3): 1110–1124.

Biasi, G.P., and Wesnousky, S.G., 2017. Bends and ends of surface ruptures: *Bulletin of the Seismological Society of America* **107** (6): 2543–2560.



- Bird, P., 2012. *NeoKinema Fault-Based Deformation Model of the California Region for UCERF3, with Focus on the DCPD Region*, presentation at DCPD SSHAC Workshop 2, November 7.
- Bird, P., 2023a. *Declaration of Dr. Peter Bird in the Matter of Proposed Rule: Renewing Nuclear Power Plant Operating Licenses - Environmental Review*, Docket No. 2018-0296, dated 2 May 2023.
- Bird, P., 2023b. *Opening Testimony of Dr. Peter Bird on Behalf of San Luis Obispo Mothers for Peace on Phase 1 Track 2 Issues*: Testimony before the Public Utilities Commission of the State of California regarding Implementing Senate Bill 846 Concerning Potential Expansion of Diablo Canyon Power Plant Operations, Docket No. R.23-01-007, dated 30 June 2023.
- Bird, P., and Liu, Z., 2007. Seismic hazard inferred from tectonics: California: *Seismological Research Letters* **78** (1): 37–48, doi:10.1785/gssrl.78.1.37.
- Bird, P., and Kagan, Y.Y., 2004. Plate-tectonic analysis of shallow seismicity: Apparent boundary width, beta, corner magnitude, coupled lithosphere thickness, and coupling in seven tectonic settings: *Bulletin of the Seismological Society of America* **94** (6): 2380–2399.
- Bird, P., and Kreemer, C., 2015. Revised tectonic forecast of global shallow seismicity based on version 2.1 of the Global Strain Rate Map: *Bulletin of the Seismological Society of America* **105** (1): 152–166, doi:10.1785/0120140129.
- Bird, P., Kreemer, C., and Holt, W.E., 2010. A long-term forecast of shallow seismicity based on the Global Strain Rate Map: *Seismological Research Letters* **81** (2): 184–194, plus electronic appendices.
- Bommer, J.J., Akkar, S., and Kale, O., 2011. A model for vertical-to-horizontal response spectral ratios for Europe and the Middle East: *Bulletin of the Seismological Society of America* **101** (4): 1783–1806.
- Bommer, J.J., Coppersmith, K.J., Coppersmith, R.T., Hanson, K.T., Mangongolo, A., Neveling, J., Rathje, E.M., Rodriguez-Marek, A., Scherbaum, F., Shelembe, R., Stafford, P.J., and Strasser, F.O., 2015. A SSHAC Level 3 probabilistic seismic hazard analysis for a new-build nuclear site in South Africa: *Earthquake Spectra* **31** (2): 661–698.
- Boore, D.M., Stewart, J.P., Seyhan, E., and Atkinson, G.M., 2014. NGA-West2 equations for predicting PGA, PGV, and 5% damped PSA for shallow crustal earthquakes: *Earthquake Spectra* **30** (3): 1057–1085.
- Bozorgnia, Y., and Campbell, K.W., 2016. Ground motion model for the Vertical-to-Horizontal (V/H) ratios of PGA, PGV, and response spectra: *Earthquake Spectra*, **32** (2): 951–978.
- Bozorgnia, Y., Abrahamson, N.A., Al Atik, L., Ancheta, T.D., Atkinson, G.M., Baker, J.W., Baltay, A., Boore, D.M., Campbell, K.W., Chiou, B.S.-J., Darragh, R., Day, S., Donahue, J., Graves, R.W., Gregor, N., Hanks, T., Idriss, I.M., Kamai, R., Kishida, T., Kottke, A., Mahin,

- S.A., Rezaeian, S., Rowshandel, B., Seyhan, E., Shahi, S., Shantz, T., Silva, W., Spudich, P., Stewart, J.P., Watson-Lamprey, J., Wooddell, K., and Youngs, R., 2014. NGA-West2 Research Project: *Earthquake Spectra* **30** (3): 973–987.
- Bradley, B.A., Razafindrakoto, H.N.T., and Polak, V., 2017. Ground-motion observations from the 14 November 2016 Mw 7.8 Kaikoura, New Zealand, earthquake and insights from broadband simulations: *Seismological Research Letters* **88** (3): 1–17, [doi:10.1785/0220160225](https://doi.org/10.1785/0220160225).
- Budnitz, R.J., Apostolakis, G., Boore, D.M., Cluff, L.S., Coppersmith, K.J., Cornell, C.A., and Morris, P.A., 1997. *Recommendations for Probabilistic Seismic Hazard Analysis: Guidance on Uncertainty and Use of Experts*, report prepared by the Senior Seismic Hazard Analysis Committee, Lawrence Livermore National Laboratory, Volume 1, Main Report, NUREG/CR-6372, UCRL-ID-122160, 280 pp.
- Campbell, K.W., and Bozorgnia, Y., 2014. NGA-West2 ground motion model for the average horizontal components of PGA, PGV, and 5% damped linear acceleration response spectra: *Earthquake Spectra* **30** (3): 1087–1115.
- Chen, B.K., Wang, D.S., Li, H.N., Sun, Z.G., and Li, C., 2017. Vertical-to-horizontal response spectral ratio for offshore ground motions: Analysis and simplified design equation: *Journal Central South University* **24**: 203–216, [doi:10.1007/s11771-017-3421-0](https://doi.org/10.1007/s11771-017-3421-0).
- Chiou, B.S.J., and Spudich, P., 2013. Chapter 6: The Chiou and Spudich NGA-West2 directivity predictor DPP: in Spudich, P. (editor), Bayless, J., Baker, J.W., Chiou, B.S.J., Rowshandel, B., Shahi, S.K., and Somerville, P.G., *Final report of the NGA-West2 Directivity Working Group*, Report PEER 2013-09, Pacific Earthquake Engineering Research: 85–94.
- Chiou, B.S.J., and Youngs, R.R., 2014. Update of the Chiou and Youngs NGA model for the average horizontal component of peak ground motion and response spectra: *Earthquake Spectra* **30** (3): 1117–1153.
- Cornell, C.A., and Vanmarcke, E.H., 1969. The major influences on seismic risk, *Proceedings of the Fourth World Conference on Earthquake Engineering, Santiago, Chile, Paper No. A-1*: 69–93.
- CyberShake, 2017. CyberShake Study 17.3, [https://strike.scec.org/scecpedia/CyberShake\\_Study\\_17.3](https://strike.scec.org/scecpedia/CyberShake_Study_17.3)
- Dawood, H.M., Rodriguez-Marek, A., Bayless, J., Goulet, C. and Thompson, E., 2015. A flatfile for the Kik-net database processed using an automated protocol: *Earthquake Spectra* **32** (2), [doi:10.1193/071214EQS106](https://doi.org/10.1193/071214EQS106).
- DeMets, C., Márquez-Azúa, B., Cabral-Cano, E., 2014. A new GPS velocity field for the Pacific Plate – Part 2: implications for fault slip rates in western California: *Geophysical Journal International* **199** (3): 1900–1909, [doi:10.1093/gji/ggu347](https://doi.org/10.1093/gji/ggu347).

Donahue, J., and Abrahamson, N.A., 2014. Simulation-based hanging-wall effects: *Earthquake Spectra* **30** (3): 1269–1284, doi:10.1193/071113EQS200M.

Donahue, J., Stewart, J.P., Gregor, N., and Bozorgnia, Y., 2019. *Ground-motion Directivity Modeling for Seismic Hazard Applications*, Report PEER 2019-3, Pacific Earthquake Engineering Research Center, University of California, Berkeley.

Electric Power Research Institute (EPRI), 1993. Guidelines for Determining Design Basis Ground Motions, Technical Report No. TR–102293, 1 December 1993.

Electric Power Research Institute (EPRI), 2013. *Seismic Evaluation Guidance: Screening, Prioritization and Implementation Details (SPID) for the Resolution of Fukushima Near-Term Task Force Recommendation 2.1: Seismic*, Technical Report No. TR–102587, 28 February 2013, 220 pp.

Electric Power Research Institute (EPRI), 2021. *Seismic Hazard Research: Kappa and High-Frequency Ground Motion Effects at Hard-Rock Sites*, Report No. 3002020750, 8 November 2021, Palo Alto, California.

EPRI/DOE/NRC (Electric Power Research Institute [EPRI], U.S. Department of Energy [DOE], and U.S. Nuclear Regulatory Commission [NRC]), 2012. *Central and Eastern United States Seismic Source Characterization for Nuclear Facilities*, Technical Report, Palo Alto, California, available at <http://www.ceus-ssc.com/index.htm>.

Evans, E.L., 2022. A dense block model representing Western Continental United States deformation for the 2023 update to the National Seismic Hazard Model: *Seismological Research Letters* **93** (6): 3024–3036.

Felzer, K.R., 2013. Appendix K—The UCERF3 earthquake catalog: in Field, E.H., Biasi, G.P., Bird, P., Dawson, T.E., Felzer, K.R., Jackson, D.D., Johnson, K.M., and 11 others [Working Group on California Earthquake Probabilities], 2013. *Uniform California Earthquake Rupture Forecast, Version 3 (UCERF3)—The Time-Independent Model*, U.S. Geological Survey Open-File Report 2013-1165.

Field, E.H., Arrowsmith, R.J., Biasi, G.P., Bird, P., Dawson, T.E., Felzer, K.R., Jackson, D.D., Johnson, K.M., Jordan, T.H., Madden, C. and Michael, A.J., 2014. Uniform California earthquake rupture forecast, version 3 (UCERF3)—The time-independent model: *Bulletin of the Seismological Society of America* **104** (3): 1122–1180.

Field, E.H., Biasi, G.P., Bird, P., Dawson, T.E., Felzer, K.R., Jackson, D.D., Johnson, K.M., Jordan, T.H., Madden, C., Michael, A.J., Milner, K.R., Page, M.T., Parsons, T., Powers, P.M., Shaw, B.E., Thatcher, W.R., Weldon, R.J., II, and Zeng, Y. [Working Group on California Earthquake Probabilities], 2013. *Uniform California Earthquake Rupture Forecast, Version 3 (UCERF3)—The Time-Independent Model*, U.S. Geological Survey Open-File Report 2013–1165/ California Geological Survey Special Report 228/ and Southern California Earthquake Center Publication 1792, 115 pp., available at <http://pubs.usgs.gov/of/2013/1165/>.

Field, E.H., Dawson, T.E., Felzer, K.R., Frankel, A.D., Gupta, V., Jordan, T.H., Parsons, T., Petersen, M.D., Stein, R.S., Weldon II, R.J., and Wills, C.J., 2008. *The Uniform California Earthquake Rupture Forecast, Version 2 (UCERF2)*, U.S. Geological Survey Open File Report, 2007-1437.

Field, E.H., Jordan, T.H., Page, M.T., Miller, K.R., Shaw, B.E., Dawson, T.E., Biasi, G.P., Parsons, T., Hardebeck, J.L., Michael, A.J., and 10 others, 2017. A synoptic view of the Third Uniform California Earthquake Rupture Forecast (UCERF3): *Seismological Research Letters* **88** (5): 1259–1267.

Field, E.H., Milner, K.R., Hatem, A.E., Powers, P.M., Pollitz, F.F., Llenos, A.L., Zeng, Y., and 17 others, 2023. The USGS 2023 Conterminous U.S. Time-Independent Earthquake Rupture Forecast: *Bulletin of the Seismological Society of America*, doi:10.1785/0120230120.

Fitzenz, D.D., Ferry, M.A., and Jalobeanu, A., 2010. Long-term slip history discriminates among occurrence models for seismic hazard assessment: *Geophysical Research Letters* **37** (2): L20307, doi:10.1029/2010GL044071.

Fugro, 2015a. *Update of the Three-dimensional Velocity Model for the Diablo Canyon Power Plant (DCPP) Foundation Area*, Final Report prepared for PG&E, dated May 2015.

Fugro, 2015b. *1-D  $V_p$  Profile Below the DCPP Area*, memorandum from D. O’Connell, A. Fernandez, and T. Travararou (Fugro) to N. Abrahamson (PG&E), dated 14 December 2015.

Gauchery, T., Campiani, E., Rovere, M., Pellegrini, C., Cattaneo, A., and Trincardi, F., 2021. Factors controlling margin instability during the Plio-Quaternary in the Gela Basin (Strait of Sicily, Mediterranean Sea): *Marine and Petroleum Geology* **123**, 104767, 21 pp., doi:10.1016/j.marpetgeo.2020.104767.

GEER Association, 2023. *February 6, 2023 Turkiye Earthquakes: Report on Geoscience and Engineering Impacts*: GEER Association Report 082, 6 May 2023.

GeoPentech, 2015. *Southwestern United States Ground Motion Characterization SSHAC Level 3: Technical Report, Rev. 2*, Report prepared for Arizona Public Service Company and Pacific Gas and Electric Company, 10 March 2015.

Gerstenberger, M.C., Van Dissen, R.J., Rollins, C., DiCaprio, C., Thingbaijam, K.K.S., Bora, S., Chamberlain, C., Christophersen, A., Coffey, G.L., Ellis, S.M., Iturrieta, P., Johnson, K.M., and 30 others, 2024. The seismicity rate model for the 2022 Aotearoa New Zealand National Seismic Hazard Model: *Bulletin of the Seismological Society of America*, doi:10.1785/0120230165.

Goulet, C., Bozorgnia, Y., Abrahamson, N., Kuehn, N., Al Atik, L., Youngs, R., and Graves, R., 2018. *Central and Eastern North America Ground-Motion Characterization - NGA-East Final Report*, Report PEER 2018/08, Pacific Earthquake Engineering Research Center, University of California, Berkeley.

Goulet, C., Kottke, A., Boore, D., Bozorgnia, Y., Hollenback, J., Kishida, T., Der Kiureghian, A., Ktenidou, O., Kuehn, N., Rathje, E., and Thompson, E., 2018. Effective amplitude spectrum (EAS) as a metric for ground motion modeling using Fourier amplitudes, *Proceedings of the 2018 Seismology of the Americas Meeting, Miami, Florida, USA*, 14-17 May, 2018; abstract published in *Seismological Research Letters* **89** (2B): 844.

Graymer, R.W., 2012. *Irish Hills Geologic Cross Section*, presentation at DCPD SSHAC Workshop 2, 7 November 2012.

Gülerce, Z., and Abrahamson, N.A., 2011. Site-specific design spectra for vertical ground motion: *Earthquake Spectra* **27** (4): 1023-1047.

Gutenberg, B., and Richter, C.F., 1944. Frequency of earthquakes in California: *Bulletin of the Seismological Society of America* **34**: 185–188.

Hall, T., Hunt, T.D., and Vaughan, P.R., 1994. Holocene behavior of the San Simeon fault zone, south-central coastal California: in Alterman, I.B., McMullen, R.B., Cluff, L.S., and Slemmons, D.B. (editors), *Seismotectonics of the Central California Coast Ranges*: Geological Society of America Special Paper **292**: 167–189.

Hamilton, D.B., 2012a. *Direct testimony of Douglas Hamilton before the Public Utilities Commission of the State of California*, Application of Pacific Gas and Electric Company for approval of ratepayer funding to perform additional seismic studies recommended by the California Energy Commission (U 39), Application No. 10-01-014, 10 February 2012.

Hamilton, D.B., 2012b. *Irish Hills and San Luis Range Fault Model*, presentation at DCPD SSHAC Workshop 2, 6 November 2012; available at <http://www.pge.com/mybusiness/edusafety/systemworks/dcpp/SSHAC/workshops/index.shtml>.

Hanks, T.C., 1979. The 1927 Lompoc, California, earthquake (November 4, 1927;  $M = 7.3$ ) and its aftershocks: *Bulletin of the Seismological Society of America* **69** (2): 451–462.

Hanks, T.C., and Bakun, W.H., 2014.  $M$ -log $A$  models and other curiosities: *Bulletin of the Seismological Society of America* **104** (5): 2604–2610.

Hanson, K.L., and Lettis, W.R., 1994. Estimated Pleistocene slip rate for the San Simeon fault zone, south-central coastal California: in Alterman, I.B., McMullen, R.B., Cluff, L.S., and Slemmons, D.B. (editors), *Seismotectonics of the Central California Coast Range*: Geological Society of America Special Paper **292**: 133–150.

Hanson, K.L., Wesling, J.R., Lettis, W.R., Kelson, K.I., and Mezger, L., 1994. Correlation, ages, and uplift rates of Quaternary marine terraces, south-central California: in Alterman, I.B., McMullen, R.B., Cluff, L.S., and Slemmons, D.B. (editors), *Seismotectonics of the Central California Coast Ranges*: Geological Society of America Special Paper **292**: 45–72 + 2 plates.

Hanson, K.L., Lettis, W.R., McLaren, M.K., Savage, W.U., and Hall, N.T., 2004. Style and rate of Quaternary deformation of the Hosgri fault zone, offshore south-central California: in Keller,

- M.A. (editor), *Evolution of Sedimentary Basins/Onshore Oil and Gas Investigations—Santa Maria Province*: U.S. Geological Survey Bulletin **1995-BB**, 33 pp.
- Hardebeck, J.L., 2010. Seismotectonics and fault structure of the California central coast: *Bulletin of the Seismological Society of America* **100** (3): 1031–1050.
- Hardebeck, J.L., 2013. Geometry and earthquake potential of the Shoreline fault, Central California: *Bulletin of the Seismological Society of America* **103** (1): 447–462.
- Hardebeck, J.L., 2014a. *Earthquake Epicenter Locations in Updated Seismicity Relocation Catalog for the California Central Coast*, unpublished data file provided to PG&E, dated 19 February 2014.
- Hardebeck, J.L., 2014b. *Seismicity and Fault Structure of Estero Bay and the Irish Hills*, presentation at DCPD SSHAC Workshop 3, 26 March 2014.
- Harris, R.A., and Day, S.M., 1999. Dynamic 3D simulations of earthquakes on en echelon faults: *Geophysical Research Letters* **26**: 2089–2092, doi:10.1029/1999GL900377.
- Hatem, A.E., Collett, C.M., Briggs, R.W., Gold, R.D., Angster, S.J., Powers, P.M., Field, E.H., and 21 others, 2022. *Earthquake Geology Inputs for the U.S. National Seismic Hazard Model (NSHM) 2023 (Western US)*, version 2.0, February 2022: U.S. Geological Survey data release, doi:10.5066/P9AU713N.
- Hatem, A.E., Reitman, N.G., Briggs, R.W., Gold, R.D., Thompson Jobe, J.A., and Burgette, R.J., 2022a. Western U.S. geologic deformation model for use in the U.S. National Seismic Hazard Model 2023: *Seismological Research Letters* **93** (6), 3068–3086, doi:10.1785/0220220154.
- Hatem, A.E., Reitman, N.G., Briggs, R.W., Gold, R.D., Thompson Jobe, J.A., and Burgette, R.J., 2022b. *Western U.S. geologic deformation model for use in the U.S. National Seismic Hazard Model 2023*, version 1.0: U.S. Geological Survey Data Release, doi: 10.5066/P9W63WOZ.
- Hearne, M., Thompson, E.M., Schovanec, H., Rekoske, J., Aagaard, B.T., and Worden, C.B., 2019. *USGS Automated Ground Motion Processing Software*: U.S. Geological Survey Software Release, doi:10.5066/P9ANQXN3.
- Hecker, S., Abrahamson, N.A., and Wooddell, K.E., 2013. Variability of displacement at a point: Implications for earthquake-size distribution and rupture hazard on faults: *Bulletin of the Seismological Society of America* **103**: 651–674.
- Helmberger, D.V., Somerville, P.G., and Garnero, E., 1992. The location and source parameters of the Lompoc, California, earthquake of 4 November 1927: *Bulletin of the Seismological Society of America* **82**: 1678–1709.
- Hirakawa, E., Parker, G.A., Baltay, A. and Hanks, T., 2023. Rupture directivity of the 25 October 2022 Mw 5.1 Alum Rock earthquake: *The Seismic Record* **3** (2): 144–155, doi:10.1785/0320230013.

Idaho National Laboratory (INL), 2022. *Idaho National Laboratory Sitewide SSHAC Level 3 Probabilistic Seismic Hazard Analysis*, Technical Report INL/RPT-22-70233, dated November 2022, 2487 pp.

Idriss, I.M., 2014. An NGA-West2 empirical model for estimating the horizontal spectral values generated by shallow crustal earthquakes: *Earthquake Spectra* **30** (3): 1155-1177, doi:10.1193/070613EQS195M.

Ishibe, T., and Shimazaki, K., 2012. Characteristic earthquake model and seismicity around late Quaternary active faults in Japan: *Bulletin of the Seismological Society of America* **102** (3): 1041–1058.

Johnson, K.M., Hammond, W.C., and Weldon, R.J., II, 2024. Review of geodetic and geologic deformation models for 2023 US National Seismic Hazard Model: *Bulletin of the Seismological Society of America*, doi:10.1785/0120230137.

Johnson, S.Y., Hartwell, S.R., and Dartnell, P., 2014. Offset of latest Pleistocene shoreface reveal slip rate on the Hosgri strike-slip fault, offshore central California: *Bulletin of the Seismological Society of America* **104** (4): 1650–1662.

Johnson, S.Y., and Watt, J.T., 2012. Influence of fault trend, bends, and convergence on shallow structure and geomorphology of the Hosgri strike-slip fault, offshore central California: *Geosphere* **8** (6): 1632–1656.

Johnson, S.Y., Watt, J.T., Hartwell, S.R., and Kluesner, J.W., 2018. Neotectonics of the Big Sur Bend, San Gregorio-Hosgri fault system, central California: *Tectonics* **37**: 1930–1954. doi:10.1029/2017TC004724.

Jordan, T.H., Abrahamson, N., Anderson, J.G., Biasi, G., Campbell, K., Dawson, T., DeShon, H., and 12 others, 2023. Panel review of the USGS 2023 Conterminous U.S. Time-Independent Earthquake Rupture Forecast: *Bulletin of the Seismological Society of America*, doi:10.1785/0120230140.

Kagan, Y.Y., 1993. Statistics of characteristic earthquakes: *Bulletin of the Seismological Society of America* **83** (1): 7–24.

Kagan, Y.Y., Jackson, D.D., and Geller, R.J., 2012. Characteristic earthquake model, 1884–2011, R.I.P: *Seismological Research Letters* **83** (6): 951–953, doi:10.1785/0220120107

Kamai, R., Abrahamson, N., and Silva, W., 2013. *Nonlinear Horizontal Site Response for the NGA-West2 Project*, Report PEER 2013-12, Pacific Earthquake Engineering Research Center, University of California, Berkeley.

Keefer, D.L. and Bodily, S.E., 1983. Three-point approximations for continuous random variables: *Management Science* **29** (5): 595–609.



Kishida, T., Kayen, R.E., Ktenidou, O.-J., Silva, W., Darragh, R., and Watson-Lamprey, J., 2014. *Arizona Strong Motion Database and GMPEs Evaluation*, Report PEER 2014-09, Pacific Earthquake Engineering Research Center, University of California, Berkeley, 135 pp.

Kluesner, J.W., Johnson, S.Y., Nishenko, S.P., Medri, E., Simms, A.R., Greene, H.G., Gray, H.J., and 5 others, 2023. High-resolution geophysical and geochronological analysis of a relict shoreface deposit offshore central California: Implications for slip rate along the Hosgri fault: *Geosphere* **19** (6): 1788–1811, doi:10.1130/GES02657.1

Kreemer, C., and Young, Z.M., 2022. Crustal strain rates in the Western United States and their relationship with earthquake rates: *Seismological Research Letters* **93**: 2990–3008, doi:10.1785/0220220153

Kucks, Robert P., 1999. *Bouguer gravity anomaly data grid for the conterminous US*: U.S. Geological Survey Digital Data Series DDS-9, <https://mrdata.usgs.gov/metadata/usgravboug.html>.

Lambeck, K., Purcell, A., and Dutton, A., 2012. The anatomy of interglacial sea levels: the relationship between sea levels and ice volumes during the Last Interglacial: *Earth and Planetary Science Letters* **315-316**: 4–11.

Langenheim, V.E., Jachens, R.C., Graymer, R.W. and Wentworth, C.M., 2008, Implications for fault and basin geometry in the central California Coast Ranges from preliminary gravity and magnetic data: *Proceedings of the American Geophysical Fall Meeting, San Francisco, California, USA*, 15-19 December 2008; *Supplement, Eos, Transactions, American Geophysical Union* **89** (53), Abstract #GP43B-0811.

Langenheim, V.E., Watt, J.T., and Denton, K.M., 2012. Magnetic map of the Irish Hills and surrounding areas, San Luis Obispo County, central California: Open-File Report 2012-1080, scale 1:24,000, U.S. Geological Survey.

Lavrentiadis, G. and Abrahamson, N.A., 2023. A non-ergodic spectral acceleration ground motion model for California developed with random vibration theory: *Bulletin of Earthquake Engineering* **21** (11): 5265-5291, doi:10.1007/s10518-023-01689-9.

Lavrentiadis, G., Abrahamson, N.A. and Kuehn, N.M., 2023. A non-ergodic effective amplitude ground-motion model for California: *Bulletin of Earthquake Engineering* **21** (1): 5233-5264, doi:10.1007/s10618-021-02106-w.

Lawrence, M., McCann, M., Ostenaar, D., Wong, I., Unruh, J., Hanson, K., Olig, S., Clague, J., LaForge, R., Lettis, W., Swan, B., Zachariasen, J., Youngs, R., and Addo, K., 2014. The BC Hydro SSHAC Level 3 Seismic Source Model, *Proceedings of the 10th National Conference on Earthquake Engineering, Anchorage, Alaska*, 21-25 July 2014.

Lettis, W.R., and Hall, N.T., 1994. Los Osos fault zone, San Luis Obispo County, California: in Alterman, I.B., McMullen, R.B., Cluff, L.S., and Slemmons, D.B. (editors), *Seismotectonics of the Central California Coast Ranges*: Geological Society of America Special Paper **292**: 73–102.

Lettis, W.R., Kelson, K.I., Wesling, J.R., Angell, M., Hanson, K.L., and Hall, N.T., 1994. Quaternary deformation of the San Luis Range, San Luis Obispo County, California: in Alterman, I.B., McMullen, R.B., Cluff, L.S., and Slemmons, D.B. (editors), *Seismotectonics of the Central California Coast Ranges*: Geological Society of America Special Paper **292**: 111–132.

Lewandowski, N., 2014. *Analysis of Stress and Strain in the Central Coast, California*, presentation at DCPD SSHAC Workshop 3, 25 March 2014.

Llenos, A.L., and Michael, A.J., 2020. Regionally optimized background earthquake rates from ETAS (ROBERE) for probabilistic seismic hazard assessment: *Bulletin of the Seismological Society of America* **110**: 1172–1190, doi:10.1785/0120190279.

Lin, P.S., Chiou, B., Abrahamson, N., Walling, M., Lee, C.T. and Cheng, C.T., 2011. Repeatable source, site, and path effects on the standard deviation for empirical ground-motion prediction models: *Bulletin of the Seismological Society of America* **101** (5): 2281–2295.

Liu, H., Jiang, J., Lin, C., Zhang, Z., Zhang, B., Tian, H., and Zhang, M., 2022. Shelf-margin architecture and deposition variability across the mid-Pleistocene climate transition, northeastern South China Sea: *Marine Geology* **443**, 106690, 17 pp., doi:10.1016/j.margeo.2021.106690

Lowry, A., and Pérez-Gussinyé, M., 2011. The role of crustal quartz in controlling Cordilleran deformation: *Nature* **471**: 353–357, doi:10.1038/nature09912.

Lozos, J., Oglesby, D., Duan, B., and Wesnousky, S., 2011. The effects of double fault bends on rupture propagation: a geometrical parameter study: *Bulletin of the Seismological Society of America* **101**: 385–398.

Lozos, J.C., Oglesby, D.D., Brune, J.N., and Olsen, K.B., 2015. Rupture propagation and ground motion of strike-slip stepovers with intermediate fault segments: *Bulletin of the Seismological Society of America* **105** (1): 387–399, doi:10.1785/0120140114.

Lozos, J.C., 2021. The effect of along-strike variation in dip on rupture propagation on strike-slip faults: *Geosphere* **17** (6): 1616–1630, doi:10.1130/GES02391.1

Maechling, P.J., Silva, F., Callaghan, S. and Jordan, T.H., 2015. SCEC broadband platform: System architecture and software implementation: *Seismological Research Letters* **86** (1): 27–38, doi:10.1785/0220140125.

Marzocchi, W., and Taroni, M., 2014. Some thoughts on declustering in probabilistic seismic-hazard analysis: *Bulletin of Seismological Society of America* **104**: 1838–1845, doi:10.1785/0120130300.

- Matthews, M.V., Ellsworth, W.L. and Reasenber, P.A., 2002. A Brownian model for recurrent earthquakes: *Bulletin of the Seismological Society of America* **92** (6): 2233–2250.
- Mazzoni, S., Al Atik, L., Gregor, N., and Bozorgnia, Y., 2023. *Directivity-Based Probabilistic Seismic Hazard Analysis for the State of California: Report 3, Datasets & Tools*, Report GIRS 2023-06 prepared for the Department of Civil and Environmental Engineering, University of California, Los Angeles.
- McGuire, R.K., Silva, W.J., and Costantino, C.J., 2001. *Technical Basis for Revision of Regulatory Guidance on Design Ground Motions: Hazard- and Risk-Consistent Ground Motions Spectra Guidelines*, Report NUREG/CR-6728 prepared for the Division of Engineering Technology, U.S. Nuclear Regulatory Commission, Washington D.C.
- McLaren, M.K., and Savage, W.U., 2001. Seismicity of south-central coastal California: October 1987 through January 1997: *Bulletin of the Seismological Society of America* **91** (6): 1629–1658.
- McLaren, M.K., Hardebeck, J.L., van der Elst, N., Unruh, J.R., Bawden, G.W., and Blair, J.L., 2008. Complex faulting associated with the 22 December 2003  $M_w$  6.5 San Simeon, California earthquake, aftershocks and postseismic surface deformation: *Bulletin of the Seismological Society of America* **98** (4): 1659–1680.
- Medri, E., Nishenko, S.P., Simms, A.R., Kluesner, J., Johnson, S.Y., Greene, H.G., and Conrad, J. E., 2023. Subaqueous clinoforms created by sandy wave-supported gravity flows: Lessons from the central California shelf: *Marine Geology* **456**: 106977, 13 pp., doi:10.1016/j.margeo.2022.106977.
- Mestdagh, T., Lobo, F.J., Llave, E., Hernandez-Molina, F.J., and Van Rooij, D., 2019. Review of the late Quaternary stratigraphy of the northern Gulf of Cadiz continental margin: New insights into controlling factors and global implications: *Earth-Science Reviews* **198**: 102944, 29 pp., doi:10.1016/j.earscirev.2019.102944.
- Muhs, D.R., Simmons, K.R., Schumann, R.R., Groves, L.T., Laurel, D., and Mitrovica, J.X., 2012. Sea-level history during the Last Interglacial complex on San Nicolas Island, California: Implications for glacial isostatic adjustment processes, paleozoogeography and tectonics: *Quaternary Science Reviews* **37**: 1–25.
- Nakada, M., and Lambeck, K., 1987. Glacial rebound and relative sea-level variations: a new appraisal: *Geophysical Journal of the Royal Astronomical Society* **90**: 171–224.
- Natrium Demonstration Project (Natrium), 2024. *Natrium SSHAC Level 3 Probabilistic Seismic Hazard Analysis*, Report under review.
- Neely, J.S., Salditch, L., Spencer, B.D., and Stein, S., 2022. A more realistic earthquake probability model using long-term fault memory: *Bulletin of the Seismological Society of America* **113** (2): 843–855, doi:10.1785/0120220083.

Nishenko, S., Greene, H.G., Hogan, P., and Bergkamp, B., 2018. Geometry and late Pleistocene displacement of the Shoreline and Oceano fault zones, San Luis Obispo Bay, California: *Bulletin of the Seismological Society of America* **108** (6): 3225–3247, doi:10.1785/0120160177.

Nitchman, S.P., 1988. “Tectonic geomorphology and neotectonics of the San Luis Range, San Luis Obispo County, California,” M.S. thesis, University of Nevada, Reno, 120 pp.

Nuclear Regulatory Commission (NRC), 1991. *Diablo Canyon SSER 34* (Safety Evaluation Report Related to the Operation of Diablo Canyon Nuclear Power Plant, Units 1 and 2, Docket Nos. 50-275 and 50-323, NUREG-0675, Supplement No. 34), USNRC NULL (NULL), 353 pp.

Nuclear Regulatory Commission (NRC), 2012a, *Practical Implementation Guidelines for SSHAC Level 3 and 4 Hazard Studies*, Technical Report NUREG-2117, dated February 2012 .

Nuclear Regulatory Commission (NRC), 2012b. Letter from E.J. Leeds and M.R. Johnson (NRC) to All Power Reactor Licensees and Holders of Construction Permits in Active or Deferred Status “Request for Information Pursuant to Title 10 of the Code of Federal Regulations 50.54(f) Regarding Recommendations 2.1, 2.3, and 9.3 of the Near-Term Task Force Review of Insights from the Fukushima Dai-Ichi Accident,” NRC Accession No. ML12053A340, dated 12 March 2012.

Nuclear Regulatory Commission (NRC), 2014. *Regulatory Guide 1.60 Design Response Spectra for Seismic Design of Nuclear Power Plants*, USNRC Report, Revision 2.

Nuclear Regulatory Commission (NRC), 2016. Letter from F. Vega to E.D. Halpin (PG&E), “Diablo Canyon Power Plant, Unit Nos. 1 and 2 – Staff Assessment of Information Provided Under Title 10 of the Code of Federal Regulations Part 50, Section 50.54(f), Seismic Hazard Reevaluation for Recommendation 2.1 of the Near-Term Task Force Review of Insights from the Fukushima Dai-Ichi Accident,” NRC Accession No. ML16341C057, 21 December.

Nuclear Regulatory Commission (NRC), 2018. *An Approach for Using Probabilistic Risk Assessment in Risk-Informed Decisions on Plant-Specific Changes to the Licensing Basis*, Regulatory Guide 1.174 Revision 3, NRC Accession No. ML17317A256, January.

Nuclear Regulatory Commission (NRC), 2019. Letter from L. Lund to J. Welsch (PG&E), “Diablo Canyon Power Plant, Unit Nos. 1 and 2 – Staff Review of Seismic Probabilistic Risk Assessment Associated with the Reevaluated Seismic Hazard Implementation of the Near-Term Task Force Recommendation 2.1: Seismic,” NRC Accession No. ML18254A040, 22 January.

Nuclear Regulatory Commission (NRC), 2023. *NRC Process for the Ongoing Assessment of Natural Hazard Information (POANHI)*, <https://www.nrc.gov/reactors/operating/ops-experience/poanhi/seismic-activities.html>

O’Connell, D.R.H. and Turner, J., 2023. Hosgri fault transpressional slip rates reproduce observed central California Coast uplift rates: *The Seismic Record* **3** (3): 182–193, doi:10.1785/0320220047.

Oglesby, D.D., 2020. What can surface-slip distributions tell us about fault connectivity at depth?: *Bulletin of the Seismological Society of America* **110** (3): 1025–1036, doi:10.1785/0120190245

Oppenheimer, D.H., Bakun, W.H., and Lindh, A.G., 1990. Slip partitioning of the Calaveras fault, California, and prospects for future earthquakes: *Journal of Geophysical Research*, **95**: 8483-8498.

Pacific Engineering and Analysis (PE&A), 2015. *Development of amplification factors for the Diablo Canyon Nuclear Power Plant: Site-wide profiles*, Report to PG&E, 24 November.

Pacific Gas and Electric Company (PG&E), 1991. Letter from J.D. Shiffer to United States Nuclear Regulatory Commission “Benefits and Insights of the Long-Term Seismic Program,” Letter No. DCL-91-091, NRC Accession No. ML16342B761, 17 April.

Pacific Gas and Electric Company (PG&E), 2011. *Report on the Analysis of the Shoreline Fault Zone, Central Coastal California*, report to the U.S. Nuclear Regulatory Commission, January; available at [www.pge.com/myhome/edusafety/systemworks/dcpp/shorelinereport/](http://www.pge.com/myhome/edusafety/systemworks/dcpp/shorelinereport/).

Pacific Gas and Electric Company (PG&E), 2014a. *Central Coastal California Seismic Imaging Project (CCCSIP)*, report to the California Public Utilities Commission; available at <http://www.pge.com/en/safety/systemworks/dcpp/seismicsafety/report.page>.

Pacific Gas and Electric Company (PG&E), 2014b. Letter from E.D. Halpin to United States Nuclear Regulatory Commission, “Central Coastal California Seismic Imaging Project, Shoreline Fault Commitment,” Letter No. DCL-14-081, NRC Accession No. ML14253A490, dated 10 September.

Pacific Gas and Electric Company (PG&E), 2015a. *Seismic Source Characterization for the Diablo Canyon Power Plant, San Luis Obispo County, California*; report on the results of SSHAC level 3 study, Rev. A, March; available at <http://www.pge.com/depp-ltsp>.

Pacific Gas and Electric Company (PG&E), 2015b. *Seismic Hazard Screening Report, Diablo Canyon Power Plant, Units 1 and 2*, PG&E Letter DCL-15-035 to U.S. Nuclear Regulatory Commission, 11 March.

Pacific Gas and Electric Company (PG&E), 2015c. Response to NRC request for information pursuant to 10 CFR 50.54(f) regarding the seismic aspects of recommendation 2.1 of the near-term task force review of insights from the Fukushima Dai-ichi accident: in *Seismic Hazard and Screening Report, Diablo Canyon Power Plant, Units 1 and 2*, PG&E Letter DCL-15-035 to U.S. Nuclear Regulatory Commission, 11 March.

Pacific Gas and Electric Company (PG&E), 2015d. *Response to NRC request for additional information dated October 1, 2015, and November 13, 2015, regarding recommendation 2.1 of the near-term task force seismic hazard and screening report*, PG&E Letter DCL-15-154 to U.S. Nuclear Regulatory Commission, 21 December.

Pacific Gas and Electric Company (PG&E), 2017a. *Development of FIRS for Unit 1 and Unit 2 Containment Turbine Building, and AUX Building*, PG&E Geosciences Calculation No. GEO.DCPP.CAL.16.01, 14 April.

Pacific Gas and Electric Company (PG&E), 2017b. *Updated DCPG GMRS Using the Analytical and Empirical Site Term Approaches*, PG&E Geosciences Calculation No. GEO.DCPP.15.02, Revision 3, 9 October.

Pacific Gas and Electric Company (PG&E), 2018. Letter from J.M. Welsch to the United States Nuclear Regulatory Commission “Seismic Probabilistic Risk Assessment for the Diablo Canyon Power Plant, Units 1 and 2 – Response to NRC Request for Information Pursuant to 10 CFR 50.54(f) Regarding Recommendations 2.1, 2.3, and 9.3 of the Near-Term Task Force Review of Insights from the Fukushima Dai-Ichi Accident,” Letter No. DCL-18-027, NRC Accession No. ML18120A201, 24 April.

Pacific Gas and Electric Company (PG&E), 2023. Assessment Associated with the Reevaluated Seismic Hazard Implementation of the Near-Term Task Force Recommendation 2.1: Seismic,” NRC Accession No. ML18254A040, 22 January.

Pacific Gas and Electric Company (PG&E), 2024. *PRA Calculation File 23-05, Revision 0*, “SB 846 Risk Assessment,” January.

Pacific Northwest National Laboratory (PNNL), 2014. *Hanford Sitewide Probabilistic Seismic Hazard Analysis*, Report prepared for the U.S. Department of Energy, November.

Page, M.T., Alderson, D., and Doyle, J., 2011. The magnitude distribution of earthquakes near Southern California faults: *Journal of Geophysical Research: Solid Earth* **116** (B12), doi:10.1029/2010JB007933.

Page, M.T., Field, E.H., Milner, K.R., and Powers, P.M., 2013. Grand inversion implementation and testing: in Field, E.H., Biasi, G.P., Bird, P., Dawson, T.E., Felzer, K.R., Jackson, D.D., Johnson, K.M., and 11 others, *Uniform California Earthquake Rupture Forecast, Version 3 (UCERF3)—The Time-Independent Model*: U.S. Geological Survey Open-File Report 2013-1165, Appendix N, 38 pp., California Geological Survey Special Report 228, and Southern California Earthquake Center Publication 1792; available at [pubs.usgs.gov/of/2013/1165/pdf/ofr2013-1165\\_appendixN.pdf](https://pubs.usgs.gov/of/2013/1165/pdf/ofr2013-1165_appendixN.pdf).

Parsons, T., and Geist, E.L., 2009. Is there basis for preferring characteristic earthquakes over Gutenberg-Richter distributions on individual faults in probabilistic earthquake forecasting?: *Bulletin of the Seismological Society of America* **99** (3): 2012–2019.

Parsons, T., Geist, E.L., Console, R., and Carluccio, R., 2018. Characteristic earthquake magnitude frequency distributions on faults calculated from consensus data in California: *Journal of Geophysical Research: Solid Earth* **123** (12): 10,761–10,784, doi:10.1029/2018JB016539.

Petersen, M.D., Powers, P.M., Shumway, A.M., Field, E.H., Moschetti, M.P., Jaiswal, K.S., Milner, K., and 14 others, 2023. 2023 U.S. 50-State National Seismic Hazard Model: Overview and implications: *Earthquake Spectra*, doi:1177/87552930231215428.

Pezeshk, S., Farhadi, A., and Haji-Soltani, A., 2022. A new model for vertical-to-horizontal response spectral ratios for Central and Eastern North America: *Bulletin of the Seismological Society of America*, **112** (4): 2018-2030.

Phung, V-B. and Abrahamson, N.A., 2023. Conditional ground-motion model based on RVT spectral moments for converting Fourier amplitude spectra to response spectra: *Bulletin of Earthquake Engineering*, **21** (11): 5175-5207, doi:10.1007/s10518-022-01559-w.

Phung, V.B., Abrahamson, N.A., Haung, B.S., and Loh, C.H., 2022. Vertical ground-motion prediction equation and the vertical-to-horizontal spectral ratio for crustal earthquakes in Taiwan: *Earthquake Spectra* **38** (2): 1189-1222.

Pollitz, F.F., 2022. Viscoelastic fault-based model of crustal deformation for the 2023 update to the U.S. National Seismic Hazard Model: *Seismological Research Letters* **93** (6): 3087–3099, doi:10.1785/0220220137.

Pollitz, F.F., Evans, E.L., Field, E.H., Hatem, A.E., Hearn, E.H., Johnson, K., Murray, J.R., and 4 others, 2022. Western U.S. deformation models for the 2023 update to the U.S. National Seismic Hazard Model: *Seismological Research Letters* **93** (6): 3068–3086, doi:10.1785/0220220143.

Ramadan, F., Smerzini, C., Lanzano, G., and Pacor F., 2021. An empirical model for the vertical-to-horizontal spectral ratios for Italy: *Earthquake Engineering and Structural Dynamics* **50**: 4121–4141.

Ridente, D., 2016. Releasing the sequence stratigraphy paradigm: Overview and perspectives: *Journal of the Geological Society* **173**: 845–853, doi:10.1144/jgs2015-140.

Rockwell, T.K., Dawson, T.E., Young-Ben Horton, J., and Seitz, G., 2015. A 21 event, 4,000-year history of surface ruptures in the Anza seismic gap, San Jacinto fault and implications for long-term earthquake production on a major plate boundary fault: *Pure and Applied Geophysics* **172** (5): 1143–1165, doi:10.1007/s00024014-0955-z.

Rowshandel, B., 2013. Chapter 3: Rowshandel's NGA-West2 directivity model: in Spudich, P. (editor), Bayless, J., Baker, J.W., Chiou, B.S.J., Rowshandel, B., Shahi, S.K., and Somerville, P.G., *Final Report of the NGA-West2 Directivity Working Group*, Report PEER 2013-09, Pacific Earthquake Engineering Research, University of California, Berkeley, 47–69.

Rowshandel, B., 2018. Directivity centering of GMPEs and of directivity models: *Eleventh U.S. National Conference on Earthquake Engineering IINCEE*, 25-29 June 2018, Los Angeles, California.

Rowshandel, B., 2020. Personal Correspondence.



Salditch, L., Stein, S., Neely, J.S., Spencer, B.D., Brooks, E., Agnon, M.A., and Liu, M., 2020. Earthquake supercycles and long-term fault memory: *Tectonophysics* **774**, Article 228289, doi:10.1016/j.tecto.2019.228289.

Salisbury, J.B., Rockwell, T.K., Middleton, T.J., and Hudnut, K.W., 2012. LiDAR and field observations of slip distribution for the most recent surface ruptures along the central San Jacinto fault: *Bulletin of the Seismological Society of America* **102** (2): 598–619.

Sammon, J.W., 1969. A nonlinear mapping for data structure analysis: *IEEE Transactions on Computers* **C-18**: 401–409.

Satake, K., and Somerville, P., 1992. Location and size of the 1927 Lompoc, California earthquake from tsunami data: *Bulletin of the Seismological Society of America* **82**: 1710–1725.

Schnabel, P.B., 1973. “Effects of Local Geology and Distance from Source on Earthquake Ground Motions,” Ph.D. Thesis, University of California, Berkeley, 140 pp.

Scharer, K.M., Biasi, G.P., Weldon, R.J., and Fumal, T.E., 2010. Quasi-periodic recurrence of large earthquakes on the southern San Andreas fault: *Geology* **38**: 555–558, doi:10.1130/G30746.1.

Scherbaum, F., Kuehn, N.M., Ohrnberger, M., and Koehler, A., 2010. Exploring the proximity of ground-motion models using high-dimensional visualization techniques: *Earthquake Spectra* **26** (4): 1117–1138, doi:10.1193/1.3478697.

Schwartz, D.P., and Coppersmith, K.J., 1984. Fault behavior and characteristic earthquakes: Examples from the Wasatch and San Andreas fault zones: *Journal of Geophysical Research* **89** (B7): 5681–5698.

Seed, H.B., and Idriss, I.M., 1970. *Soil Modulus and Damping Factors for Dynamic Response Analysis*, Report No. EERC-70/10, Earthquake Engineering Research Center, University of California, Berkeley.

Shen, Z.-K., and Bird, P., 2022. NeoKinema deformation model for the 2023 update to the US National Seismic Hazard Model: *Seismological Research Letters* **93** (6): 3037–3052, doi:10.1785/0220220179.

Silva, W.J., Abrahamson, N., Toro, G. and Costantino, C., 1996. *Description and validation of the stochastic ground motion model*, Report prepared by Pacific Engineering and Analysis (PE&A) for the Department of Nuclear Energy, Brookhaven National Laboratory, Associated Universities, Inc., Upton, New York, Contract No. 770573, 15 November.

Simms, A.R., Rouby, H., and Lambeck, K., 2016. Marine terraces and rates of vertical tectonic motion: The importance of glacio-isostatic adjustment along the Pacific coast of central North America: *Geological Society of America Bulletin* **128** (1-2): 81–93, doi:10.1130/B31299.1.

Simms, A.R., Rood, D.H., and Rockwell, T.K., 2020. Correcting MIS5e and 5a sea-level estimates for tectonic uplift, an example from southern California: *Quaternary Science Reviews* **248**: 106571, doi:10.1016/j.quascirev.2020.106571.

Simpson, R.W., Jachens, R.C., Blakely, R.J., and Saltus, R.W., 1986. A new isostatic residual gravity map of the conterminous United States with a discussion of the significance of isostatic residual anomalies: *Journal of Geophysical Research* **91** (B5): 8348–8372.

Spudich, P., Bayless, J.R., Baker, J.W., Chiou, B.S., Rowshandel, B., Shahi, S.K. and Somerville, P., 2013. *Final Report of the NGA-West2 Directivity Working Group*, Report PEER 2013-09, Pacific Earthquake Engineering Research Center, University of California, Berkeley.

Stirling, M.W., Wesnousky, S.G., and Shimizaki, K., 1996. Fault trace complexity, cumulative slip, and the shape of the magnitude-frequency distribution for strike-slip faults: A global survey: *Geophysical Journal International* **124** (3): 833–868.

State of California, 2022, Senate Bill No. 846, Chapter 239, “SB 846, Dodd. Diablo Canyon powerplant: extension of operations,” available at [https://leginfo.ca.gov/faces/billNavClient.xhtml?bill\\_id=202120220SB846](https://leginfo.ca.gov/faces/billNavClient.xhtml?bill_id=202120220SB846).

State of California, 2006, Assembly Bill No. 1632, Chapter 722, “AB 1632, Blakeslee. Energy: Planning and forecasting.”

Styron, R., 2019. The impact of earthquake cycle variability on neotectonic and paleoseismic slip rate estimates: *European Geosciences Union, Solid Earth* **10** (1): 15–25, doi:10.5194/se-10-15-2019.

Sung, C-H., Abrahamson, N., and Lacour, M. 2023. Methodology for including path effects due to 3D velocity structure in nonergodic ground-motion models: *Bulletin of the Seismological Society of America* **113** (5): 2144–2163.

U.S. Geological Survey (USGS), 2017. *Advanced National Seismic System (ANSS) Comprehensive Catalog of Earthquake Events and Products*, product of the U.S. Geological Survey Earthquake Hazards Program, doi:10.5066/F7MS3QZH.

van der Elst, N.J., 2021. B-Positive: A robust estimator of aftershock magnitude distribution in transiently incomplete catalogs: *Journal of Geophysical Research: Solid Earth* **126**: e2020JB021027, doi:10.1029/2020JB021027.

Villasenor, T., Jaeger, J.M., Marsaglia, K.M., and Browne, G.H., 2015. Evaluation of the relative roles of global versus local sedimentary controls on Middle to Late Pleistocene formation of continental margin strata, Canterbury Basin, New Zealand: *Sedimentology* **62**: 1118–1148, doi:10.1111/sed.12181.

Watson-Lamprey, J.A., 2015. *Capturing Directivity Effects in the Mean and Aleatory Variability of the NGA-West 2 Ground Motion Prediction Equations*, Pacific Earthquake Engineering Research Center PEER Report (in preparation).

- Watson-Lamprey, J.A., 2018. *Capturing Directivity Effects in the Mean and Aleatory Variability of the NGA-West2 Ground-Motion Prediction Equations*, Report PEER 2018-04, Pacific Earthquake Engineering Research Center, University of California, Berkeley, doi:10.55461/USOP6050.
- Wesnousky, S.G., 2006. Predicting the endpoints of earthquake ruptures: *Nature* **444**: 358–360.
- Wesnousky, S.G., 2008. Displacement and geometrical characteristics of earthquake surface ruptures: Issues and implications for seismic-hazard analysis and the process of earthquake rupture: *Bulletin of the Seismological Society of America* **98**: 1609–1632.
- Wesnousky, S.G., Scholz, C.H., Shimazaki, K., and Matsuda, T., 1983. Earthquake frequency distribution and the mechanics of faulting: *Journal of Geophysical Research* **88**: 9331–9340.
- Williams T., Abrahamson N., 2021. Site-response analysis using the shear-wave velocity profile correction approach: *Bulletin of the Seismological Society of America* **111** (4): 1989–2004.
- Xu, W., Feng, G., Meng, L., Zhang, A., Ampuero, J.P., Burgmann, R. and Fang, L., 2018. Transpressional rupture cascade of the 2016 M<sub>w</sub> 7.8 Kaikoura Earthquake, New Zealand: *Journal of Geophysical Research: Solid Earth* **123**: 2396–2409.
- Youngs, R.R., and Coppersmith, K.J., 1985. Implications of fault slip rates and earthquake recurrence models to probabilistic hazard estimates: *Bulletin of the Seismological Society of America* **75**: 939–964.
- Zaliapin, I., and Ben-Zion, Y., 2020. Earthquake declustering using the nearest-neighbor approach in space-time-magnitude domain: *Journal of Geophysical Research* **125** (4), e2018JB017120, doi:10.1029/2018JB017120.
- Zeng, Y., 2022a. GPS velocity field of the western United States for the 2023 National Seismic Hazard Map Update: *Seismological Research Letters* **93** (6): 3121–3134, doi:10.1785/0220220180.
- Zeng, Y., 2022b. A fault-based crustal deformation model with deep driven dislocation sources for the 2023 Update to the U.S. National Seismic Hazard Model: *Seismological Research Letters* **93** (6): 3170–3185, doi:10.1785/0220220209.
- Zhao, J.X., Zhang, J., Asano, A., Ohno, Y., Oouchi, T., Takahashi, T., Ogawa, H., Irikura, K., Thio, H.K., Somerville, P.G., Fukushima, Y. and Fukushima, Y., 2006. Attenuation relations of strong ground motion in Japan using site classification based on predominant period: *Bulletin of the Seismological Society of America* **96** (3): 898–913, doi:10.1785/0120050122.
- Zhao, J.X., and Lu, M., 2011. Magnitude-scaling rate in ground motion prediction equations for response spectra from large, shallow crustal earthquakes: *Bulletin of the Seismological Society of America* **101** (6): 2643–2661, doi:10.1785/0120100350.

Zhao, J.X., Zhou, S., Zhou, J., Zhao, C., Zhang, H., Zhang, Y., Gao, P., Lan, X., Rhoades, D., Fukushima, Y., Somerville, P.G., and Irikura, K., 2016. Ground-motion prediction equations for shallow crustal and upper-mantle earthquakes in Japan using site class and simple geometric attenuation functions: *Bulletin of the Seismological Society of America* **106** (4): 1552-1569.

Zhuo, H., Nie, X., Su, M., Zhou, W., Lei, Y., Wang, Y., Peng, X., Qiu, Y., Yan, W, and Lin, L., 2023. Quaternary stratigraphic architecture of the Pearl River Mouth continental shelf, northern South China Sea: Unraveling stratigraphic imprints of tectonism, paleoceanography, and climate change: *Sedimentary Geology* **459**, 106548, doi:10.1016/j.sedgeo.2023.106548.

## **Appendix A**

# **Project Plan for 2023 DCPP Updated Seismic Assessment**



Title: Project Plan for 2023 DCPD Updated Seismic Assessment

Project Name: 2023 DCPD Updated Seismic Assessment

Total No. of Pages 12

Prepared by: E-SIGNED by William Horstman  
on 2023-11-16 01:27:01 GMT Date: 11/15/2023  
(Name/Signature)

Reviewed by: E-SIGNED by albert kottke  
on 2023-11-22 18:47:20 GMT Date: 11/16/2023  
(Name/Signature)

Approved by: E-SIGNED by Jeffery Bachhuber  
on 2023-11-23 00:40:49 GMT Date: 11/16/2023  
(Name/Signature)

**Record of Revisions**

Rev. No.	Reasons for Revision	Revision Date
0	Initial Release	11/16/2023



**Table of Contents**

List of Figures	3
1. PROJECT SCOPE	4
1.1 Background	4
1.2 Project Objective	5
1.3 Summary of Scope	7
1.3.1 Topics for the Technical Integration Teams	8
2. PROJECT ORGANIZATION	8
3. DELIVERABLES	10
4. SCHEDULE	10
5. QUALITY REQUIREMENTS	10
5.1 Project Documents	10
5.2 Vendors/Consultants	11
5.3 Application of the SSHAC Process	11
6. REFERENCES	11

**List of Figures**

FIGURE 1: FLOWCHART FOR A SSHAC LEVEL 1 PSHA STUDY, INDICATING THE REVIEW CRITERIA AND POTENTIAL QUESTIONS AT EACH POINT OF ENGAGEMENT BY THE PPRP .....	6
FIGURE 2: DECISION AND EVALUATION PROCESSES USED IN THE SEISMIC HAZARD PERIODIC REEVALUATION METHODOLOGY FOR EXISTING NUCLEAR FACILITIES THAT ARE CLASSIFIED AS SEISMIC DESIGN CATEGORY 3.....	7
FIGURE 3: ORGANIZATIONAL STRUCTURE FOR THIS PROJECT.....	9

## 1. PROJECT SCOPE

This document presents a project plan for a seismic hazard assessment update for the Pacific Gas & Electric Company's (PG&E) Diablo Canyon Power Plant (DCPP) to satisfy the covenant for the performance of a seismic update associated with the State of California Senate Bill (SB) 846<sup>(Reference [1])</sup> plant license extension. SB 846 states that the loan agreement with the California Department of Water Resources (DWR) must include:

*A covenant that the operator shall conduct an updated seismic assessment.*

The purpose of the work addressed in this updated seismic assessment project plan is to address this covenant by no later than the end of August 2024, which is prior to the expiration of the current operating licenses for DCPP. The Diablo Canyon Independent Safety Committee (DCISC), and DWR are invited to be observers during the performance of this assessment and are herein referred to as the stakeholders.

The project plan was developed by the PG&E Geosciences Department, which will manage the work, at the request of the DCPP License Renewal Project (Notification No. 51199572<sup>[2]</sup>).

### 1.1 Background

Since initial start of operation of the plant (1984 and 1985 for Units 1 and 2, respectively), numerous studies and updates of the seismic hazard and seismic risk have been performed. In addition, PG&E has maintained a Geosciences Department and the Long-Term Seismic Program (LTSP) focused on monitoring earthquakes, keeping track of scientific studies and state of knowledge on earthquake sources and hazards applicable to the site, and directing and funding new research through collaboration with the U.S. Geological Survey and various academic institutions. To sustain this work, PG&E and the U.S. Nuclear Regulatory Commission (NRC) agreed to an operating license commitment to continue the Geosciences Department and LTSP for the duration of the plant's operating licenses<sup>[3]</sup>.

In addition to the studies performed by PG&E under the LTSP, additional studies related to the seismic hazards applicable to the DCPP were performed by PG&E following the recommendations of the California Energy Commission (CEC) in response to State of California Assembly Bill 1632<sup>[4]</sup> were performed between 2006 and 2014<sup>[5]</sup>. These included new information characterizing seismic sources, velocity structure, and reliability of the plant. Also, in responding to the NRC's Request for Information related to Recommendation 2.1 (Seismic) of the Near Term Task Force (NTTF) Review of Insights from the Fukushima Dai-Ichi Accident<sup>[6]</sup> PG&E updated seismic hazard and seismic probabilistic risk assessments for DCPP<sup>[7]</sup>. This work included a Probabilistic Seismic Hazard Analysis (PSHA) which was completed in 2015. The PSHA followed the NRC guidelines for a Senior Seismic Hazard Analysis Committee (SSHAC) Level 3 hazard study described in NUREG-2117<sup>[8]</sup> and included a Participatory Peer Review Panel (PPRP) to provide the confident technical basis and mean-centered estimates of the ground motions. This multi-year study addressed all aspects of the seismic hazard

at the DCPP. In December 2016, the NRC stated that the reevaluated seismic hazard for DCPP (i.e., the results of the PSHA) is suitable for use in the other seismic assessments associated with the 50.54(f) letter<sup>[9]</sup>. The seismic hazards developed through the PSHA served as input to the updated DCPP seismic probabilistic risk assessment (SPRA). In January of 2019, the NRC stated that the updated SPRA met the requirements specified in the 10 CFR 50.54(f) letter and that no further response or regulatory actions are required<sup>[10]</sup>.

Since the completion of the AB 1632 and NTTF Recommendation 2.1 studies, monitoring of earthquakes and targeted research under the ongoing LTSP have continued, with updates provided to the California Public Utilities Commission (CPUC) Independent Peer Review Panel (IPRP) and the Diablo Canyon Independent Safety Committee (DCISC). These continuing studies and reviews have served to keep DCPP current on seismic activity around the plant and new sources, ground motion and hazard data or methods that could potentially impact hazard or risk at the plant. This information provides a basis for the proposed SB 846 seismic update addressed in this workplan.

## **1.2 Project Objective**

To develop the scope for the SB 846 seismic update several aspects were considered: the previous PSHA was recently completed, PG&E has continued monitoring and research/data collection under the LTSP, there is limited time for new information or new methodologies to be developed during this project, and the importance of seismic safety to both PG&E and the public. With these considerations, PG&E will follow an incremental hazard assessment process that first evaluates new information and models (i.e., comparison of hazard inputs) in a qualitative approach. If no significant changes in models or inputs are identified, the assessment will be complete with no further assessment required. If sufficient differences are found with inputs used in the 2015 assessment, then the study is extended to include quantitative analyses with integration and recalculation of hazard.

Nuclear Regulatory Commission (NRC) NUREG-2213<sup>[11]</sup>, provides updated guidelines on implementing SSHAC studies including a flow chart for the SSHAC Level 1 process (Figure 1, and the interaction with the PPRP. The initial scope of this project is the “Evaluation” portion in the Figure 1 flowchart, where the 2015 model is evaluated against potential new information to decide if the Integration step is warranted.

In this process, interaction with stakeholders will take place during the development of the study plan, summary of the evaluation, and if necessary once hazard calculations are completed. Stakeholders will have the opportunity to observe and provide written feedback.

There are three means to extend the study to the Integration phase where hazard is calculated. First, during the evaluation phase, the project team will use the guidance in Figure 2, (Payne et. al.<sup>[12]</sup>) to determine whether changes in data, models and methods warrant an escalation.

Second, additional considerations by the project team will include: if any hazard significant discrepancies are found with the previous study; if updated inputs are outside of the center, body, and range of the previous study; and if evaluators do not have confidence in their assessment.

Finally, the results of the findings will be presented to the stakeholders, and upon review may recommend that an elevated quantitative study be initiated.

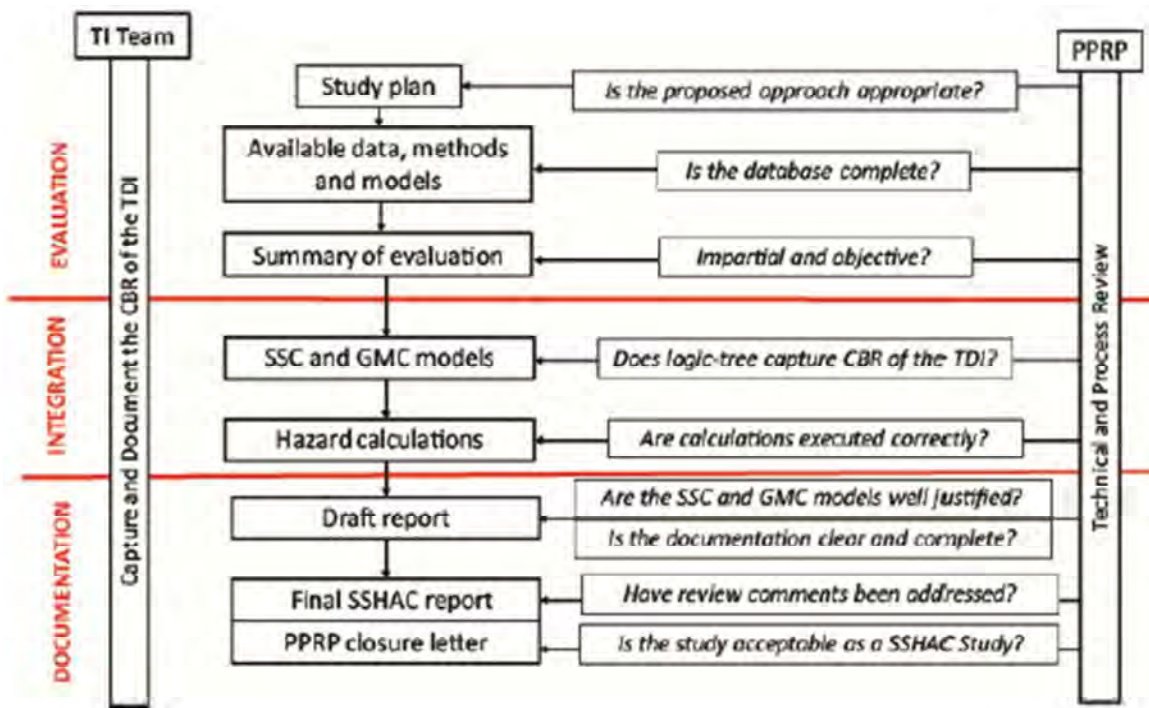


**Figure 1: Flowchart for a SSHAC Level 1 PSHA study, indicating the review criteria and potential questions at each point of engagement by the PPRP (Figure 3-2 of NRC NUREG-2213<sup>[11]</sup>).**

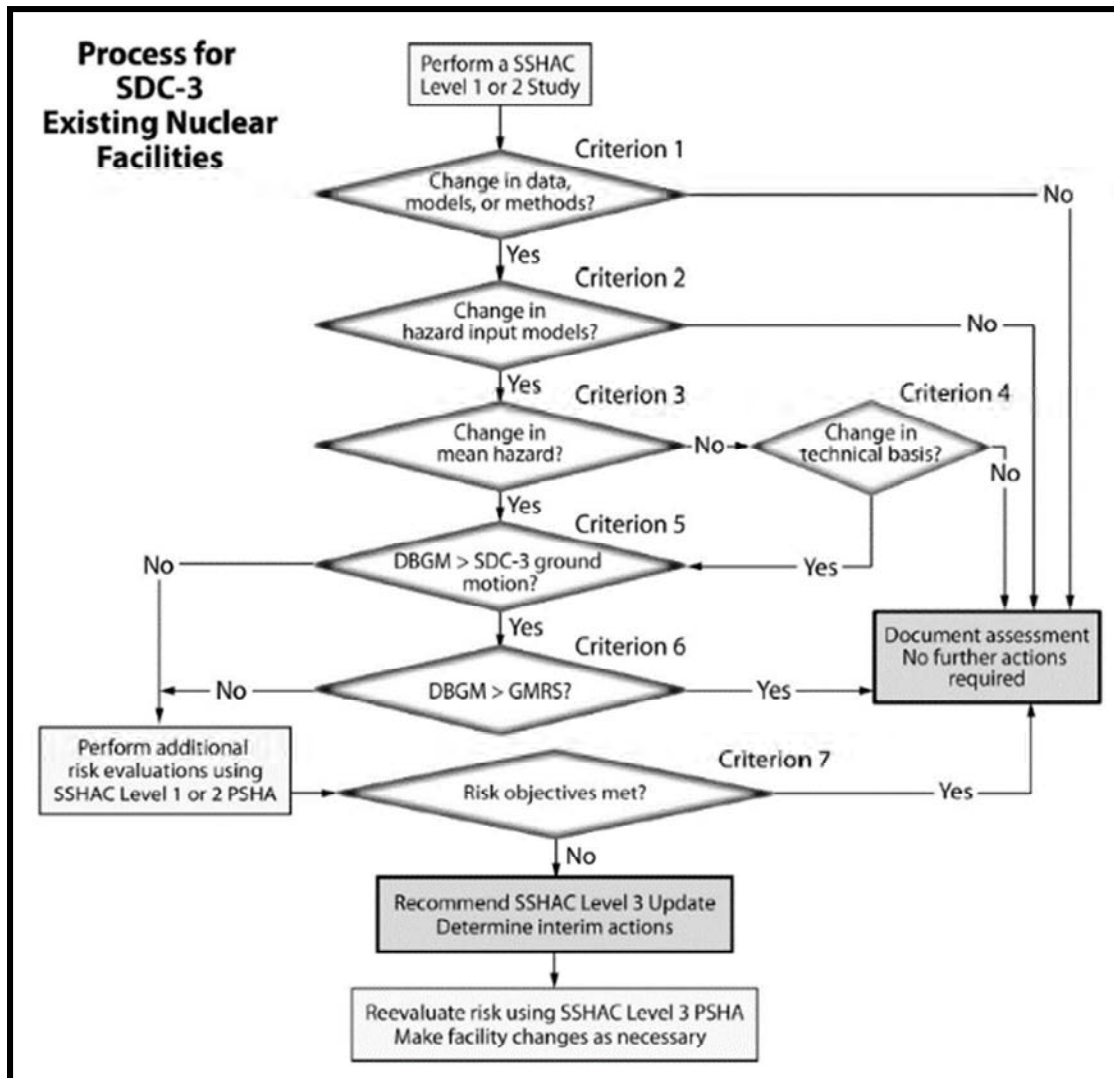


**Figure 2: Decision and evaluation processes used in the Seismic Hazard Periodic Reevaluation Methodology for existing nuclear facilities that are classified as Seismic Design Category 3 (Figure 1 of Payne, et. al. (2017)<sup>[12]</sup>).**

### 1.3 Summary of Scope

This SB 846 updated seismic assessment will be conducted using working meetings, workshops, and other technical activities. The final scope of model components considered will be developed by the project team including reviewers. The following areas have been identified as initial potential topics for consideration by the Technical Integration Team.

### **1.3.1 Topics for the Technical Integration Teams**

#### **1.3.1.1 Refinement of Inputs for the Seismic Source Characterization (SSC)**

- 1) New data, models, or methods with the potential to change hazard - significant seismic source parameters, especially for seismic sources closest to the plant, including the Hosgri, Los Osos, San Luis Bay and Shoreline faults and the Background source. Tornado plots from the 2015 study can be used to identify hazard-significant source parameters and help understand the impact of parameter changes.
- 2) Updated earthquake catalog – over 6000 earthquake events have been recorded by the PG&E Central Coast Seismic Network (CCSN) since 2015 and may inform fault geometry and rates of aerial source zones
- 3) Background model – accounts for earthquakes that occur off recognized fault sources or secondary low slip rate sources

#### **1.3.1.2 Refinement of Parameters for the Ground Motion Characterization (GMC)**

- 1) Review of Ground Motion Models (GMM) to include: Median; Variability; and Uncertainty – there have been no new models since the Southwestern United States (SWUS) project (one of the elements of the PSHA described in Reference [7]). However, it is relevant to review the logic trees and implementation of the models.
- 2) Directivity models
- 3) Updates to the local earthquake catalog; in particular, the four events within 100 km with a magnitude greater than M4.
- 4) Non-ergodic models and their potential application – these models are still being developed, but many advancements have been made.

#### **1.3.1.3 Additional Topics**

- 1) Potential updates to empirical site amplification models - There are two instruments near the project site; one is on the site property and records triggered events, the other is off-site and provides a continuous record.
- 2) Recent modifications to the software HAZ used to compute the PSHA - Review modifications made to the code HAZ and impact of those changes. The end goal of this task is to run old hazard inputs on a new executable.

## **2. PROJECT ORGANIZATION**

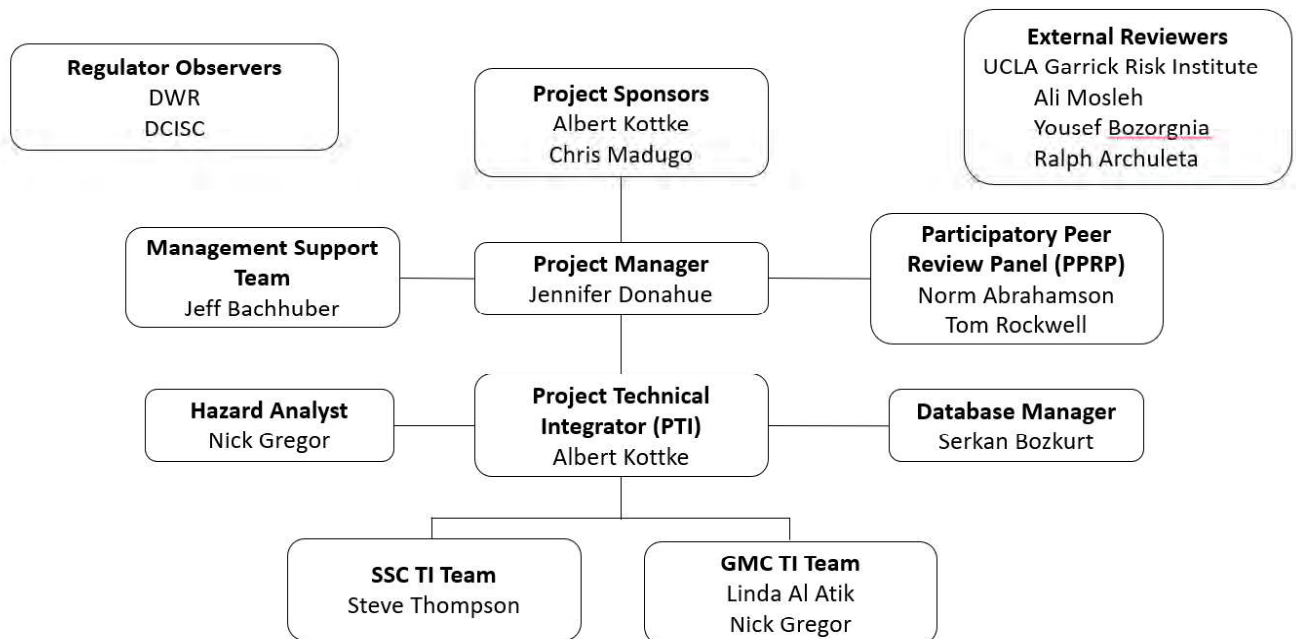
The project organization is composed of the following members (see organization chart in Figure 3):

- Two PG&E Project Sponsors - The Project Sponsors provide financial support and “own” the results of the study in the sense of property ownership. The



Project Sponsors will attend project meetings, review project documents, and facilitate data gathering.

- One Project Manager (PM) - The PM is responsible for managing the schedule, and budget and coordinates the execution of the project. In addition, the PM interacts with the Project Sponsors to keep them informed on the progress.
- Three Technical Integration (TI) Team members - The TI Team is a team of Evaluator Experts with PSHA experience that are responsible for conducting the evaluation and integration process. Two members of the TI Team will review the GMC and one member, along with staff, will review the SSC. These team members were involved in the previous and were selected based on their experience with the previous efforts and expertise in the field.
- Two Participatory Peer Review Panel (PPRP) members – The PPRP is a panel of experts with SSHAC methodology and PSHA experience capable of evaluating the technical judgments of the TI Team.
- Three External Reviewers – The external reviewers are also experts with SSHAC methodology and PSHA experience. They will provide external review of the process, methodology and documentation of the project. They will ensure that it is consistent with the intent of the covenant.
- One Technical Writer – The technical writer will be editing report content and working closely with the various members of the organizational team.



Note: Specialty Contractors, Resource Experts, and Proponent Experts are not included on this project

**Figure 3: Organizational structure for this project**



---

### 3. DELIVERABLES

The results of the evaluation will first be presented to the PPRP and External reviewers during workshops. The TI Teams will prepare a report that presents what new information was considered and an evaluation of the potential impact.

The PPRP will review the documentation and provide comments back to the TI Team. The TI Team will then review and incorporate comments, as necessary, then present the final results to the PPRP and the External Reviewers. This presentation will be followed by the Final Report and submitted to the PPRP. The PPRP will provide a closure letter, if appropriate, and will send all documentation to the External Reviewers for review before review and acceptance by the Diablo Canyon Power Plant team.

### 4. SCHEDULE

A detailed schedule will be developed to meet the project requirements and ensure the ability to track progress.

### 5. QUALITY REQUIREMENTS

The DCPP work request for this project<sup>[2]</sup> indicates that the classification of the work is “Graded Quality.” Therefore, the work is not classified as “Safety Related” and the DCPP Quality Assurance Program does not apply. In accordance with DCPP Procedure No. AD9.ID2<sup>[15]</sup>, the DCPP Quality Verification group developed the Quality Verification Plan (QVP) for this project, as documented in DCPP Notification No. 51200395<sup>[14]</sup>, to define the quality requirements applicable to the various aspects of the project.

#### 5.1 Project Documents

Documentation developed in support of this project shall be subject to the following general requirements:

- Geosciences Department-generated input reviewed by another competent PG&E personnel to assure that the results are reasonable, including inputs and assumptions.
- Vendor-generated input and results reviewed and accepted by PG&E personnel to assure that the results are reasonable, including inputs and assumptions.

The vendor-generated results shall be processed in accordance with one of the following DCPP procedures, as applicable to the document type:

- Procedure No. CF7.ID4, “Processing of Documents Received from Suppliers”
- Procedure No. CF3.ID17, “Design and Analysis Documents Prepared by External Contractors”

---

## 5.2 Vendors/Consultants

The project team is comprised of a combination of PG&E personnel and consultants (see Project Organization Chart in Figure 3). Consultants shall be classified as “Task Specialists” in accordance with DCPP Procedure No. TQ2.ID4 (Training Program Implementation<sup>[16]</sup>) and their qualifications documented in accordance with this procedure.

## 5.3 Application of the SSHAC Process

As indicated in Section 1.2, this project will be performed in a similar manner to the Level 1 SSHAC process (NUREG-2213<sup>[11]</sup>), which includes explicit internal reviews. In accordance with the SSHAC process, the analyses performed by the TI Team will be scrutinized by the PPRP. Additionally, this project includes the use of an External Review Team who will examine the methods, process and documentation.

This methodology will provide added assurance of the validity of the updated seismic assessment.

## 6. REFERENCES

1. State of California, Senate Bill No. 846, “SB 846, Dodd. Diablo Canyon power plant: extension of operations,” ([https://leginfo.legislature.ca.gov/faces/billNavClient.xhtml?bill\\_id=202120220SB846](https://leginfo.legislature.ca.gov/faces/billNavClient.xhtml?bill_id=202120220SB846)), 2022
2. PG&E DCPP “Geosc. Work Request – SB-846,” Notification No. 51199572, dated August 9, 2023
3. PG&E Letter from J.D. Shiffer to United States Nuclear Regulatory Commission, “Benefits and Insights of the Long-Term Seismic Program” Letter No. DCL-91-091, dated April 17, 1991, NRC Accession No. ML16342B761
4. State of California, Assembly Bill No. 1632, “AB 1632, Blakeslee. Energy: Planning and forecasting,” Chapter 722, Statutes of 2006
5. PG&E Letter from E.D. Halpin to United States Nuclear Regulatory Commission, “Central Coastal California Seismic Imaging Project, Shoreline Fault Commitment,” Letter No. DCL-14-081, dated September 10, 2014, NRC Accession No. ML14253A490
6. NRC Letter from E.J. Leeds and M.R. Johnson (NRC) to All Power Reactor Licensees and Holders of Construction Permits in Active or Deferred Status “Request for Information Pursuant to Title 10 of the Code of Federal Regulations 50.54(f) Regarding Recommendations 2.1, 2.3, and 9.3 of the Near-Term Task Force Review of Insights from the Fukushima Dai-Ichi Accident,” dated March 12, 2012, NRC Accession No. ML12053A340

7. PG&E Letter from J.M. Welsch to the United States Nuclear Regulatory Commission, "Seismic Probabilistic Risk Assessment for the Diablo Canyon Power Plant, Units 1 and 2 – Response to NRC Request for Information Pursuant to 10 CFR 50.54(f) Regarding Recommendations 2.1, 2.3, and 9.3 of the Near-Term Task Force Review of Insights from the Fukushima Dai-Ichi Accident," Letter No. DCL-18-027, dated April 24, 2018, NRC Accession No. ML18120A201
8. NRC, "Practical Implementation Guidelines for SSHAC Level 3 and 4 Hazard Studies," NUREG-2117, dated February 2012
9. NRC Letter from F. Vega to E.D. Halpin (PG&E), "Diablo Canyon Power Plant, Unit Nos. 1 and 2 – Staff Assessment of Information Provided Under Title 10 of the Code of Federal Regulations Part 50, Section 50.54(f), Seismic Hazard Reevaluation for Recommendation 2.1 of the Near-Term Task Force Review of Insights from the Fukushima Dai-Ichi Accident," dated December 21, 2016, NRC Accession No. ML16341C057
10. NRC Letter from L. Lund to J. Welsch (PG&E), "Diablo Canyon Power Plant, Unit Nos. 1 and 2 – Staff Review of Seismic Probabilistic Risk Assessment Associated with the Reevaluated Seismic Hazard Implementation of the Near-Term Task Force Recommendation 2.1: Seismic," dated January 22, 2019, NRC Accession No. ML18254A040
11. NRC, "Updated Implementation Guidelines for SSHAC Hazard Studies," NUREG-2213, dated October 2018 (<https://www.nrc.gov/reading-rm/doc-collections/nuregs/staff/sr2213/index.html>)
12. Payne, S., Coppersmith, K., Coppersmith, R., Montaldo-Falero, V., Youngs, R., Rodriguez-Marek, A., and Silva, W. "Assessing the Need for an Update of a Probabilistic Seismic Hazard Analysis using a SSHAC Level 1 Study and the Seismic Hazard Periodic Reevaluation Methodology," Nuclear Engineering and Design, v. 323, p. 103-119. 2017
13. PG&E DCP Notification "Geosc. Work Request – SB-846," Notification No. 51199572, dated August 9, 2023
14. PG&E DCP Notification "QVP: 2023 Seismic Hazard Assessment," Notification No. 51200395, dated August 16, 2023
15. PG&E DCP Procedure "Procurement of Services," Procedure No. AD9.ID2, Rev. 20
16. PG&E DCP Procedure "Training Program Implementation," Procedure No. TQ2.ID4, Rev. 56

## **Appendix B**

### **Minutes from the Working Meeting #1 Held on 21 July 2023**

## 2023 DCPD Updated Seismic Assessment

---

### Working Meeting

#### Introduction

On July 21, 2023, the first Working meeting took place at Pacific Gas and Electric Company's (PG&E) Oakland Office at 300 Lakeside Drive, Oakland, California. The meeting was attended by the following personnel:

- Mr. Jeffery Bachhuber, PG&E Director of Geosciences
- Dr. Albert Kottke, PG&E, Project Sponsor
- Dr. Chris Madugo, PG&E, Project Sponsor
- Dr. Mahdi Bahrapouri, PG&E, Project Sponsor
- Dr. Jennifer Donahue, JL Donahue Engineering, Project Manager
- Dr. Norman Abrahamson, UC Berkeley, PPRP
- Dr. Tom Rockwell, San Diego State University, PPRP
- Dr. Yousef Bozorgnia, UCLA, Regulatory Observer
- Dr. Ali Mosleh, UCLA, Regulatory Observer
- Dr. Linda Al Atik, Linda Al Atik Consulting, Ground Motion Technical Integration Team Member
- Dr. Nick Gregor, Nicholas Gregor Consulting, Ground Motion Technical Integration Team Member
- Dr. Steve Thompson, LCI, Source Characterization Technical Integration Team Member
- Dr. Ralph Archuleta, UC Santa Barbara, Regulatory Observer (*by phone*)
- Ms. Nora Lewandowski, LCI, Source Characterization Technical Integration Team Member (*by phone*)
- Mr. Ferman Wardell, DCISC, Observer (*by phone*)

#### Meeting Content and Action Items

##### Introduction – Dr. Kottke

The meeting began with an introduction by Dr. Kottke. He provided an introduction to the project, details on the qualitative approach for the seismic hazard review, expectations of the technical integration teams, roles of personnel on the project, and the timeline of major deliverables.

Dr. Abrahamson had questions regarding whether hazard curves would be recalculated. He mentioned that it would be difficult to assess the change in the hazard without the full calculations. Mr. Bachhuber recommended that some calculations should be done. It was agreed that the simplified 4-source fault model with local zones would be an easy means to implement, if needed. Relative changes could then be compared to the final results of the 2015 SSHAC Level 3 study.

## Ground Motion Review and Topics – Dr. Gregor

Dr. Gregor provided an overview of the Ground Motion Characterization (GMC). In the 2015 SSHAC Level 3 study, hazard was dominated by events less than 15 km away, which included both fault sources and a local background zone. Other important topics for the GMC included hanging wall terms, complex ruptures, splay ruptures, and directivity.

Dr. Gregor commented that the optimization models are robust for close in events. No directivity models were included in the 2015 study.

### Action Items for GMC:

- Develop a comprehensive list of ground motion topics that have been advanced in the last 8 years.
- Compare non-ergodic models from Abrahamson and Lavrentiadis Varying Coefficient Model (VCM). What are the changes in median and distribution? Is the spatial source different and should it be used?
- Compare common form median ground motion models to updated ground motion database empirical recordings from NGA-West3 through residual analyses.
- Compile and evaluate any empirical recordings in the Central Coast region of California from more recent earthquakes since the completion of the SWUS study.
- Although directivity is a long-period issue, a UCLA study has shown some further increase beyond the 2015 study (~10% vs 5%). However, the NRC has not been concerned with directivity because it is a long-period issue and DCPD is sensitive to short-period ground motions.
- Should multi-segment ruptures be included in the earthquake ground motion models.
- Review the approach used for the estimation of vertical ground motions.
- Review the recently completed INL SSHAC Level 3 Study for sigma (median ground motion model would not be applicable for DCPD).
- Review of Sammon's maps. Because this was the first time they were used, it may be prudent to review if they were incorporated and run correctly.

## Site Amplification Review and Topics – Dr. Al Atik

Dr. Al Atik provided an overview of the site amplification factors and methodology used for DCPD. She reviewed both the analytical and empirical methodologies that were used.

Key highlights include that Dr. Al Atik commented that there is no new data for the two stations ESTA27 and ESTA28. There are also different nonlinearity models from UT Austin, to include Dardanelli, that could be reviewed, however nonlinearity isn't significant at the DCPD site.

### Action Items for Site Amplification:

- Develop a comprehensive list of site amplification topics that have been advanced in the last 8 years.
- Analytical
  - Review changes in host-profiles and kappa.
  - Review if new analysis of the 3D velocity structure should be performed. This may be a long-term item for consideration in the Long-Term Seismic Program (LTSP).
  - Review of EPRI report on Kappa.
- Empirical

- Compile and evaluate any empirical recordings in the vicinity of DCPD for applicability to the estimation of empirical site adjustment factors.
- Review correlation length from non-ergodic models to see the correction for  $V_{s30}$  and application of other stations.

### Seismic Source Review and Topics – Dr. Thompson

Dr. Thompson provided an overview of the seismic source characterization (SSC) for DCPD from the 2015 SSC SSHAC study. He identified the four SSC parameters that contributed most to hazard uncertainty as the following: the Hosgri slip rate, the Hosgri EPR (time dependency uncertainty) model, the San Luis-Pismo Block (SLPB) EPR model and the SLPB geometry model. Dr. Thompson also described how the SSC addressed multi-fault or multi-segment, linked ruptures and described the source characterization for “complex” and “splay” ruptures that allowed ruptures to change style of faulting (rake) along strike and allowed simultaneous rupture on two faults. Dr. Thompson also noted the importance of floating ruptures over the longest rupture topologies, and that this differed from some traditional fault source approaches where the total length of the source is used to define the expected characteristic earthquake magnitude.

On the topic of the time-dependent uncertainty model, Dr. Thompson described the EPR as a ratio or scale factor that is applied to the mean earthquake rate for each source. The EPR model used in the 2015 SSC SSHAC and hazard model uses information on earthquake recurrence coefficient of variation (CV) from empirical data collected on other faults with better paleoseismic information, and it considers a variety of recurrence distribution forms, including lognormal, Brownian-passage time, and Weibull. An important aspect of the model is the requirement that it quantify the uncertainty in time dependent behavior in the absence of any fault-specific paleoseismic constraints. For the faults closest to DCPD, none have high quality, detailed paleoseismic data about the timing or size of the most recent large earthquake closest to the plant.

Dr. Thompson also reviewed the background, or areal source zones, used for the DCPD study. There are three zones (Local, Vicinity, and Regional), for which the Local Source Zone is similar in contribution to the San Luis Bay or Los Osos faults. The Local source zone includes the volume of crust beneath DCPD, the Irish Hills, and Estero Bay. Ruptures within the Local source zone are modeled using alternative, parallel fault traces with a range in dip and dip directions and alternative strike-slip and reverse styles of faulting. The rate of earthquakes is based on the relocated seismicity catalog. Dr. Thompson noted that double counting of the earthquake rate of  $M$  5.0 to ~6.5 is present in the model, as the rate of these events is not adjusted to account for the rate of smaller events modeled to occur on the Los Osos, San Luis Bay, and Shoreline fault sources, which occupy the same volume of crust. The impact of double counting has not been evaluated.

#### Action Items for SSC:

- Develop a comprehensive list of topics that have been advanced in the last 8 years.
- Source Characterization (Faults):
  - Time dependency model
    - Has subsequent hazard modeling changed this distribution?
    - Examine assumptions made in the 2015 study.
  - Review Hosgri slip rate information, including new publications.



- Review the new models of paleosea level and the impact on estimating the uplift rates and ages of marine terraces.
  - Review the new information on the cross-Hosgri slope slip rate site off Point Estero (USGS effort).
  - Review the models and assumptions for all Hosgri fault slip rate sites from the onshore San Simeon site to the offshore sites analyzed as part of the AB1632 seismic studies.
- Geometry models – no new site-specific publications but should review the most recent USGS catalog data. Further reanalysis of alternative geometry models may be a future LTSP task.
- Review literature of earthquake rupture linkages and complexities that are challenges to rupture propagation. Review any new “rules” that may be considered for defining characteristic earthquake magnitudes or other rupture topologies.
- Source Characterization (Source zones):
  - Review potential impact of double-counting from Local fault zone.
  - Review recent catalog data and if the rate has changed in the background.
  - Review whether the point-source approximation used for the Vicinity and Regional source zones is adequate.

### Proponent Positions – Dr. Madugo

Dr. Madugo reviewed the current positions of Interveners and Proponents on seismic source characterization, including recent declarations and testimony to the NRC and CPUC by Dr. Peter Bird on behalf of the San Luis Obispo Mothers for Peace. Documentation will be provided to the SSC TI Team and PPRP by PG&E. Significant topics included how published geodetic and kinematic finite element models, off-fault deformation and seismicity and alternative models for characterizing seismicity rates are considered in the SSC model. The Inferred Coastline Thrust (ICT) is a proponent model for faulting beneath the Irish Hills that is similar to Inferred Offshore fault and San Luis Range thrust model considered in the 2015 Seismic Source Characterization.

#### Action Items for SSC:

- Review Neokinema kinematic finite element model
  - Consider a simplistic approach to run and assess Neokinema, including applicability to site-specific seismic hazard.
  - Review USGS reviewer comments that declined the integration of the off-fault deformation portion of the model into the 2023 update to the National Seismic Hazard Map
- Review Seismic Hazard Inferred From Tectonics (SHIFT) method to develop magnitude frequency distribution (MFD) encoded in the program Long\_Term\_Seismicity\_v12.
- Review basis for ICT model.

## **Appendix C**

### **Minutes from the Preliminary Results Meeting #1 Held on 19 September 2023**

## 2023 DCPD Updated Seismic Assessment

---

### Workshop #1

#### Introduction

On September 19, 2023 the first Workshop took place at Pacific Gas and Electric Company's (PG&E) Oakland Office at 300 Lakeside Drive, Oakland, California. The following personnel attended the meeting:

- Mr. Jeffery Bachhuber, PG&E Director of Geosciences
- Mr. Jearl Strickland, PG&E Management Support Team
- Ms. Maureen Zawalick, PG&E Diablo Canyon
- Mr. Tom Jones, PG&E Diablo Canyon
- Dr. Albert Kottke, PG&E, Project Sponsor
- Dr. Chris Madugo, PG&E, Project Sponsor
- Mr. Bill Horstman, PG&E
- Dr. Mahdi Bahrapouri, PG&E
- Dr. Norman Abrahamson, UC Berkeley, PPRP
- Dr. Yousef Bozorgnia, UCLA, Regulatory Observer
- Dr. Ali Mosleh, UCLA, Regulatory Observer
- Dr. Ralph Archuleta, UC Santa Barbara, Regulatory Observer
- Dr. Linda Al Atik, Linda Al Atik Consulting, Ground Motion Technical Integration Team Member
- Dr. Nick Gregor, Nicholas Gregor Consulting, Ground Motion Technical Integration Team Member
- Dr. Steve Thompson, LCI, Source Characterization Technical Integration Team Member
- Mr. Eric Wulff, DWR, Observer
- Mr. Christian Arechavaleta, DWR, Observer
- Mr. Mark Krausse, PG&E (*by phone*)
- Mr. Thomas Vargas, PG&E (*by phone*)
- Dr. Jennifer Donahue, JL Donahue Engineering, Project Manager (*by phone*)
- Dr. Tom Rockwell, San Diego State University, PPRP (*by phone*)
- Ms. Delphine Hou, DWR, Observer (*by phone*)
- Ms. Deb Luchsinger, DWR, Observer (*by phone*)
- Dr. Robert Budnitz, DCISC, Observer (*by phone*)
- Mr. Ferman Wardell, DCISC, Observer (*by phone*)
- Mr. Rick McWhorter, DCISC, Observer (*by phone*)

## Meeting Content and Action Items

### Introduction – Dr. Kottke

The meeting began with an introduction by Dr. Kottke. He provided a safety and security orientation, re-introduction to the project, and the timeline of major deliverables.

### Ground Motion Review and Topics – Dr. Gregor

Dr. Gregor began with a review of the PG&E 2015 PSHA Study and the results in the form of hazard curves and disaggregation plots to show which sources had the greatest contribution to hazard.

He then reviewed the empirical and simulation databases with events post-2015. With a wealth of new data from various sources, there is a general zero bias for the mean residuals for four out of the five events.

Hanging wall models were also reviewed, but since 2015, there has been no new empirical or simulation data.

For Directivity, the PRRP letter from the 2015 SWUS study noted a limitation because directivity models were not applied. Since 2015, there have been new publications for the Watson-Lamprey, Chiou and Spudich, Rowshandel, and Bayless and Somerville models. There was also a statewide PSHA study performed with UCERF3 and directivity models in 2023. Directivity studies are still ongoing and there may be an impact for long periods.

Next, non-ergodic model updates were provided. The median and epistemic uncertainty of ground motion predictions at DCP agree well with the non-ergodic models at frequencies greater than 1 Hz. At long periods the median predictions and epistemic uncertainty are larger than those of the non-ergodic model.

Splay and Complex Ruptures were then discussed. These types of ruptures have low rates of occurrence and a minimal contribution to the total hazard. Since 2015, there has been no substantial empirical data or new or additional simulation results.

Finally, the SWUS Sigma model was discussed. The models for Tau and Phi-SS models were consistent with state of the practice and may be updated following the NGA-W3 study. Dr. Abrahamson recommended that the Phi-SS from Dr. Lavrentiadis's non-ergodic model be compared with the Phi-SS from the SWUS model.

### Site Amplification Review and Topics – Dr. Al Atik

Dr. Al Atik provided the preliminary results for the site amplification review. She discussed the development of the site factors used to compute soil hazard and the GMRS at the control point, as well as analytical site factors and empirical factors.

First, she provided background for control point and how the velocity profile was developed. She then described the analytical site factors that were computed by PE&A in 2015 relative to the SWUS reference rock condition.

The empirical site factors were developed based on events recorded at DCP. During the evaluation for this project, PG&E provided information to develop the “DCP flat file.” This flat file is composed of a total of 7,116 recordings from 2014 to the present and was used to enhance the development of the empirical site factors.

In summary, there are some potential updates for the site characterization and the MRD curves for the analytical site factors. This might have a small overall impact. For the empirical site factors there is no additional data at the two stations at DCP that could re-evaluate the site-specific site adjustments. However, there is a possibility to make use of trends in the vicinity. Dr. Abrahamson recommended that current work by Dr. Sung be used to look at non-ergodic site factors.

### Seismic Source Review and Topics – Dr. Thompson

Dr. Thompson presented the DCP Seismic Source Characterization Review and started with a description of which sources, either faults or source zones, were the greatest contribution to hazard during the 2015 study. He then provided details on what the latest information is available for each of the sources.

The Hosgri fault slip rate had the highest contribution to hazard and was discussed first. Since 2015, there has been considerable geologic and geophysical work done by multiple entities. There is now increased confidence in the understanding of the Hosgri fault and slip rate, meaning that there could be a change to the weighting of the slip rate interpretation from the 2015 study.

Next, the Los Osos slip rate was discussed. Again, there has been considerable geologic and geophysical research done on this feature. Based on the research, the uplift rate may decrease with a net slip rate also decreasing.

The San Luis Bay model was discussed next. In 2023 there was a paper published by O’Connell and Turner regarding the uplift rates in the region and the uplift rate boundary could be explained by the Hosgri fault. And it was found that Dr. Bird’s proponent model of thrusting was inconsistent with the observed uplift for this feature. It could be concluded that the San Luis Bay faults source is not required and again that the Los Altos fault slip rate may be lower.

For the Shoreline fault, new geologic information was reviewed and is consistent with previous studies.

Dr. Thompson provided a great deal of discussion on the Western US Deformation models for the 2023 National Seismic Hazard Model Project (NSHMP). He discussed the five models that were proposed, which includes the Neokinema model, and each uses a distinct set of approaches and assumptions. During the 2015 DCP study, a prior generation of geodesy-based models were considered but were not used directly in the fault slip rate model. Dr. Thompson provided a deformation model comparison for each of the considered faults that comparing the 2015 SSHAC model, 2013 UCERF3 model, and the 2023 NSHMP model.

The background model, or seismic source zones, were then discussed. He provided background on the sub-parallel virtual fault model used for the Local Source zone and the Gutenberg-Richter a-, b-value calculations. Since 2023, there has been no change in the local seismicity rates and the a-, b-value pairs are still consistent with the prior study. For the Magnitude-Frequency Distributions (MFD) of the local

source zones there was suggestion by Dr. Bird to consider geodetic model-based off-fault deformations. These were not modeled as part of the 2013 UCERF3 project and will not be implemented in the 2023 NSHMP. There are multiple concerns about the off-fault deformation. It was recommended to Dr. Thompson that more information and documentation should be requested from the USGS as to why they did not use Dr. Bird's model.

Dr. Thompson stated that the USGS process for capturing background seismicity based on an earthquake catalog is consistent with PG&E current process and the process followed by other nuclear projects. Geodetic based moments rates are only used on projects without local information. This subject could be explored for consistency as part of LTSP longer research efforts.

In conclusion, Dr. Thompson stated there is no new information with major consequences for the SSC model. Since the slip rates are the most important, the Hosgri slip rate has new geologic data that may require new weighting. This may increase the mean hazard rate. For the Los Osos, San Luis Bay, and Shoreline fault sources, the geologic data is generally consistent with the previous study. If the Los Osos fault slip rate were revised, it would likely result in a decrease in the mean hazard. The local source zone is consistent with the previous study based on the updated seismicity catalog which was updated with the events from the past 10 years. For the 2023 NSHMP data, there are updated geologic models, but the data is considered unreliable for direct input for DCPD for multiple reasons.

Regarding the Dr. Bird testimonies, several inconsistencies were found with site-specific data including the current tectonic regime, that his testimony statements and proponent model are inconsistent with published Neokinema results, and his SHIFT methodology and regional geodetic based on-fault and off-fault deformation models are not appropriate for a site-specific SHA with relatively well-mapped faults.

The PPRP asked if the rates that the current model has accommodate the new geodetic information. Dr. Thompson responded that yes, they do fit and include both the faults and the background sources.

The PPRP asked whether the SHIFT model would decrease the hazard versus the Neokinema model. This concept would need more consideration and could be included in a future model. Jearl Strickland mention that this may be a part of the Long-Term Seismic Program (LTSP).

There was general discussion regarding running sensitivities with reweighting schemes, new moment rates, increasing the  $M_{\max}$  to 8 and rebalancing, and creating a new simplified source model would be possible. Dr. Thomspson responded that they may not have time to do this work prior to the report and this may be a candidate for the Long-Term Seismic Program. There was agreement that these concepts would be best served in the LTSP.

## **Appendix D**

### **Minutes from the Workshop #2 Held on 7 November 2023**



## 2023 DCPD Updated Seismic Assessment

---

### Workshop #2

#### Introduction

On November 7, 2023 the second Workshop took place at Pacific Gas and Electric Company's (PG&E) Oakland Office at 300 Lakeside Drive, Oakland, California. The following personnel attended the meeting:

#### Attendees:

- Mr. Jeffery Bachhuber, PG&E Director of Geosciences
- Mr. Jearl Strickland, PG&E Management Support Team
- Dr. Albert Kottke, PG&E, Project Sponsor
- Dr. Chris Madugo, PG&E, Project Sponsor
- Mr. Bill Horstman, PG&E
- Dr. Jennifer Donahue, JL Donahue Engineering, Project Manager
- Dr. Norman Abrahamson, UC Berkeley, PPRP
- Dr. Tom Rockwell, San Diego State University, PPRP
- Dr. Nick Gregor, Nicholas Gregor Consulting, Ground Motion Technical Integration Team Member
- Dr. Linda Al Atik, Linda Al Atik Consulting, Ground Motion Technical Integration Team Member
- Dr. Steve Thompson, LCI, Source Characterization Technical Integration Team Member
- Dr. Robert Budnitz, DCISC, Observer
- Ms. Deb Luchsinger, DWR, Observer
- Ms. Delphine Hou, DWR, Observer
- Mr. Eric Wulff, DWR, Observer
- Mr. Christian Arechavaleta, DWR, Observer
- Mr. Thomas Vargas, PG&E (*by phone*)
- Mr. Mark Krause, PG&E (*by phone*)
- Mr. Nathan Barber, PG&E (*by phone*)
- Dr. Yousef Bozorgnia, UCLA, Regulatory Observer (*by phone*)
- Dr. Ali Mosleh, UCLA, Regulatory Observer (*by phone*)
- Dr. Ralph Archuleta, UC Santa Barbara, Regulatory Observer (*by phone*)
- Mr. Rick McWhorter, DCISC, Observer (*by phone*)

#### Meeting Content and Action Items

##### Introduction – Dr. Kottke

The meeting began with an introduction by Dr. Kottke. He provided a safety and security orientation, and short re-introduction to the project.

Mr. Strickland confirmed that a preliminary version of the report could be delivered to DCISC prior to its public release. This was strongly supported by DWR.

### Seismic Source Review and Topics – Dr. Thompson

Dr. Thompson provided an update on the changes to the fault source slip rates for hazard sensitivity to include the new slip rate characterization for the cross Hosgri slope (CHS) site, new weighting for the four Hosgri slip rate sites, and new preferred estimate for the EPHR to account for uncertainty and time dependency.

For the CHS, Dr. Thompson provided a discussion on the uncertainties in the shoreface offset which were broadened. He also discussed the offset feature age, which included additional information published in 2023 and required that the probability density function also be broadened to account for uncertainty. For the CHS, the mean slip rate decreased from 2.6 to 2.5 m/ky.

For the 2015 SSHAC study, the weights for the Hosgri slip rate sites were originally more distributed. There is now a higher confidence in the CHS compared to other sites, meaning that the weighting for all sites is more skewed towards the CHS. At the CHS, the weighting increases from 0.2 to 0.5. At Estero Bay site (closest to the site) the weighting decreased from 0.3 to 0.2. Dr. Abrahamson suggested that weighting is subjective and that it should be documented, making sure that there is a basis for how the weights were evaluated, essentially if put it into three bins: preferred, alternatives, questionable, and to have justification for the difference between Estero Bay and San Simeon Terrace.

For the Hosgri slip rate, the mean slip rate increases from 1.7 to 2.14 mm/yr, which is a 26% increase.

Regarding the deformation models, the UCERF3 and ERF-2023 models were compared. The preferred values are generally sampled across the distribution but within model uncertainties and offshore faults are poorly understood, mainly because there is only a 242-year record for this site. Re-interpreting the mean EPHR for the upgraded Hosgri slip rate results in a mean EPHR of 1.24 given the 2.14 mm/year slip rate.

The Irish Hills slip rates were also reviewed with a new model of paleo sea level and updated uplift rate uncertainties for the Los Osos slip rate. The weights across the three different models resulted in a decrease from 0.27 to 0.23, a 13% decrease.

No changes are proposed for the Shoreline or San Luis Bay slip rates. Further, there are no changes proposed to the local area source zones and virtual faults. The level of conservatism will be documented in the report.

During the discussions after Dr. Thompson's presentation, it was noted that the slip rate uncertainty compares well with geodetic models. Also, it was recommended that it might be valuable to research the Oceanic fault to understand the motion at Pacific Plate margin. There was also a question regarding the basis for equally weighing Simms and Hanson, which will be addressed in the report.

### Ground Motion Review and Topics – Dr. Gregor

Dr. Gregor presented the scaling methodology based on the SSC model adjustments. He began with the results and significant seismic sources of the PSHA from the 2015 SSHAC study. He then explained the

scaling methodology, which is consistent with the 2015 SWUS model. Hazard curves are linearly scalable as a function of the slip rate. For this process, the Hosgri and Los Osos faults will be separated from the larger SSC model, scaled, and recombined for each source and the total hazard. All other sources will remain the same. He then showed what the rupture groups will look like.

The scaling will still occur at the reference rock horizon,  $V_{s30} = 760$  m/s, and will include an evaluation of hazard curves, and the UHS at three different hazard levels.

Dr. Abrahamson questioned how much of the hazard is coming from nearby faults. It may be necessary to disaggregate the results to look at relative contribution of nearby Hosgri sources relative to more distant Hosgri sources. This information might be helpful for selecting the weights on the slip rate sites. Mr. Horstman requested the GMRS in addition to the UHS.

In general, all members in attendance and on the phone seem to support this scaling approach. Dr. Abrahamson and Dr. Bozorgnia specifically support it.

### Site Amplification Review and Topics – Dr. Al Atik

Dr. Al Atik provided updates to the site terms. She began with discussion of the DCPD flat file. This flat file has a total of over 20,000 recordings between 1994 and August of 2023, yet there are issues of the data quality, such as magnitudes other than moment magnitude ( $M_w$ ), missing parameters, and the reliability of very low or very high frequencies.

Next, updates to the non-ergodic site term were then discussed and preliminary results from Dr. Sung were presented. Dr. Abrahamson noted that one of the graphs did not look correct and Dr. Al Atik said that she would continue working with Dr. Sung.

During the discussion period it was noted that this part of the coast of California has lower than average spectral values, because this part of the coast has less high-frequency energy. This was seen earlier and doubted by NRC, but then confirmed by their own independent data.

It was also asked if Dr. Al Atik would be running new ground motions, to which the answer was no, not as part of this project.

It was particularly noted that there is a significant difference in the results between 2 Hz and 10 Hz. Mr. Horstman noted that 5 Hz is the most important frequency for the PRA, but that 2.5 Hz is used for the containment buildings. According to the current results, there is a factor of 1.2 increase in site amplification at 5 Hz. There was a great deal of discussion and suggestions on how to deal with this. Mr. Barber suggested running the analyses for both 5 Hz and 10 Hz, but needed to investigate the situation more thoroughly and would make a recommendation on how to move forward within a week. Dr. Budnitz then recommended making an approximation that seems reasonable but making sure to document.

## Probabilistic Risk Assessment Topics – Mr. Barber

Mr. Barber gave an initial report on his planned activities. He stated that this will be an update to the 2017 PRA and hazard fractiles ranging from 0.5 g to 10 g.

Because there is a plan to scale the hazard, all 100 of the fractiles will also scale. Mr. Barber said that he will provide a brief report on the results to include changes to the risk of components and structures of DCP. Not knowing how the results will turn out, Mr. Strickland and Mr. Horstman recommended to perform a parametric study. There was also a question by Dr. Abrahamson who wondered if the spectral shape would change based on the results.

The methodology and results of Mr. Barber's study will be presented at the next meeting.

## **Appendix E**

### **Minutes from the Final Results Meeting Held on 7 December 2023**

## 2023 DCPD Updated Seismic Assessment

---

### Final Results

#### Introduction

On December 7, 2023, the Final Results meeting took place via MS Teams. The following personnel virtually attended the meeting:

#### Attendees:

- Mr. Jeffery Bachhuber, PG&E Director of Geosciences
- Mr. Jearl Strickland, PG&E Management Support Team
- Dr. Albert Kottke, PG&E, Project Sponsor
- Dr. Chris Madugo, PG&E, Project Sponsor
- Ms. Angie Gibson, PG&E
- Mr. Nathan Barber, PG&E
- Dr. Jennifer Donahue, JL Donahue Engineering, Project Manager
- Dr. Norman Abrahamson, UC Berkeley, PPRP
- Dr. Tom Rockwell, San Diego State University, PPRP
- Dr. Yousef Bozorgnia, UCLA, Regulatory Observer
- Dr. Ali Mosleh, UCLA, Regulatory Observer
- Dr. Ralph Archuleta, UC Santa Barbara, Regulatory Observer
- Dr. Nick Gregor, Nicholas Gregor Consulting, Ground Motion Technical Integration Team Member
- Dr. Linda Al Atik, Linda Al Atik Consulting, Ground Motion Technical Integration Team Member
- Dr. Steve Thompson, LCI, Source Characterization Technical Integration Team Member
- Dr. Robert Budnitz, DCISC, Observer
- Mr. Rick McWhorter, DCISC, Observer
- Ms. Deb Luchsinger, DWR, Observer
- Ms. Delphine Hou, DWR, Observer
- Mr. Eric Wulff, DWR, Observer
- Mr. Ferman Wardell, DCISC, Observer
- Ms. Tania Gonzalez, Earth Consultants International, Technical Editor

#### Meeting Content and Action Items

##### Introduction – Dr. Kottke

The meeting began with an introduction by Dr. Kottke. He provided a safety and security orientation, and short re-introduction to the project.

### Seismic Source Review and Topics – Dr. Thompson

Dr. Thompson provided a concise overview of the 2023 SSC Model. He found that the previous 2015 SSC model used for the SSHAC study was reliable for the 2023 SB-846 seismic hazard assessment with the following updates, the Hosgri fault source mean slip rate, the Hosgri fault source mean EPHR, and the Los Osos fault source slip rate. These updates can be achieved by scaling the appropriate pieces of the 2015 SSC model.

He then provided a summary of the changes that were recommended. The Hosgri slip rate scale factor would be 1.259. The scale factor for the mean EPHR Hosgri slip rate would be 1.033. The scale factors for the Irish Hills slip rate would be OV=0.846, SW=0.895, and NE=0.929.

There were no questions for Dr. Thompson.

### Ground Motion Review and Topics – Dr. Gregor

Dr. Gregor presented the results of the hazardous scaling based on the SSC model adjustments. The methodology he used linearly scales the hazard curves as a function of the slip rate and EPHR. The Hosgri and Lo Osos faults, part of the larger SSC model, were separated into their contributing hazard curves. These curves were then scaled based on the mean slip rate and EPHR changes. They were then recombined for each source and the total hazard. Twenty (20) spectral periods ranging from 0.01 to 3 seconds were calculated.

Dr. Gregor then presented the hazard scaling results, in the form of hazard curves and spectral ratios. He also provided the Uniform Hazard Spectra (UHS) and the UHS Ratio for the reference rock condition ( $V_{s30} = 760$  m/s) at the various annual frequencies.

In conclusion, for the reference rock hazard curves and the UHS, at low frequencies, the ground motions increased up to approximately 7.5%. At intermediate to high frequencies, the ground motions increased approximately 4% or less. At the control point, assuming there is no change in site amplification factors, and the scale factor at the  $10^{-5}$  hazard level, the scale factor at 5 Hz is equal to 1.135. There are smaller factors for higher frequencies and larger factors, up to 1.233, for lower frequencies.

There were no additional questions for Dr. Gregor.

### Site Amplification Review and Topics – Dr. Al Atik

Dr. Al Atik provided the results for the site adjustment factors evaluation. She began with an overview of the methodology and resulting site factors developed for the 2015 study, which included both analytical and empirical approaches.

For the analytical approach, she found that the methodology used in 2015 is still considered state-of-the-practice and valid. Regarding target site conditions, she found that there was no new data for either the  $V_s$  profile characterization or Kappa based on the analyses of recordings from stations near DCP. The Modulus-Reduction and Damping (MRD) curves used in 2015 are commonly used and still valid. For the host site conditions, she concluded that there are no updates required to the analytical site factors.



For the empirical site factors, there is new ground motion data in the vicinity of DCPD that can be used, but no new data recorded at DCPD. For a non-ergodic GMM approach, she worked with Dr. Sung, providing a step-by-step methodology to update the non-ergodic site terms. She found that the total residuals were similar to those from the GMM model by Chiou and Youngs 2014. Additionally, she found that there were consistent results obtained when using the same data set for both an FAS and PSA analysis.

In conclusion, the results obtained from the independent analyses of the empirical site terms are generally consistent with the 2015 study. Differences with the 2015 study could be due to the preliminary nature of the data set and differences in methodology. She also concluded that there are no updates to the 2015 empirical site terms recommended at this time, because there have been no new recordings at DCPD. There is an overall consistency with the 2015 results.

The use of non-ergodic site terms is a new and upcoming topic. It was agreed that this topic should be carried into the LTSP.

### Probabilistic Risk Assessment Topics – Mr. Barber

Mr. Barber provided the background and methodology for the SB-846 seismic risk assessment. The model used in this assessment was completed in August of 2023 and included updated plant specific reliability data and addressed peer review findings from the internal events peer review. No seismic model parameters have changed since the 2017 seismic model update.

The methodology used the scale factors for the annual hazard to scale the hazard fractals used in DCPD PRA model. The use of the uniform scaling factor for the seismic hazard for all return periods results in a linear impact on CDF and LERF. The PRA model was quantified using the scale factor for 5 Hz to confirm the model response and the 0.5 Hz scaling factor was applied to bound the risk assessment results. The component and structure risk importances were reviewed to identify significant changes.

As a result, using the 5 Hz scaling factor increased the seismic CDF to approximately  $4 \times 10^{-6}$  /year. The results for using the conservative 0.5 Hz scaling factor allowed DCPD to remain in Region II, meaning that changes in the risk of less than  $1 \times 10^{-5}$  /year are allowed in this region. As a result, no significant change in importance was identified.

## **Appendix F**

# **Evaluation of Site Terms at DCPD using Updated Methods and Data**

Evaluation of Site Terms at DCPD using Updated Methods and Data

Prepared by: Chih-Hsuan Sung

Reviewed by: Norman Abrahamson

December 12, 2023

## Introduction

The 2015 models for site effects at DCPD used a partially non-ergodic approach (single-station sigma). In this approach, the site-specific site term was estimated using both an empirical approach based on the recorded ground-motion data at DCPD and an analytical approach using 1-D site response calculations. Since 2015, there have been advances in the development of non-ergodic ground-motion models and additional ground-motion data collected in the region.

The main changes to the methodology are to (1) use Fourier amplitude spectra (FAS) rather than response spectra (SA) for developing the non-ergodic terms and then convert these FAS to SA using random vibration theory (RVT), and (2) separate the non-ergodic site term into a spatially correlated regional term and a spatially uncorrelated site-specific term.

In this report, we apply the new methodology with the expanded data sets to estimate the site terms for DCPD relative to the ergodic ground-motion model (GMM) for a reference VS30 of 760 m/s used in the hazard calculation.

## Data Sets

There is no new ground-motion data at the DCPD site, but there is additional ground-motion data from the region.

### Ground-Motion Data at DCPD

The ground motion data at DCPD consists of three recordings from the 2004 Parkfield and 2003 San Simeon earthquakes. The meta data for these three recordings are listed in Table 1.

Table 1. Ground-motion data at DCPD

rsn	eqid	M	R <sub>RUP</sub>	Z <sub>TOR</sub>	SOF	VS30
8167	177	6.52	37.97	2	1	856
8168	179	6	78.32	2.5	0	777
21540	179	6	78.32	2.5	0	856

### Regional Ground-Motion Data

The expanded data set for the region was provided by Al-Atik. This data set includes earthquakes between Jan 1994 and Aug 2023 with magnitudes greater than and equal to 2.5.

There are missing meta data for this data set including the style-of-faulting class and the depth to the top of rupture (Z<sub>TOR</sub>). The basin depth (Z<sub>1.0</sub>) is also not available for all sites. The magnitudes include a range of magnitude types (i.e., they are not all moment magnitude).

For this initial evaluation, the following values were used for computing the residuals relative to a GMM. (1) the style of faulting is strike slip for all events; (2) the Z<sub>TOR</sub> is set using the default values for the magnitude; the missing Z<sub>1.0</sub> values are set using the default relation between Z<sub>1.0</sub> and VS30; and the magnitudes are assumed to be moment magnitudes.

This preliminary data set did not include all of the ground-motion data for the 2003 San Simeon and 2004 Parkfield earthquakes that were available in the NGA-W2 data base. As these data are key to estimating the site terms at DCPP, these additional recordings were added to the ground-motion data set.

Data Set used in Evaluation

The following selection criteria were applied to the regional data set:

- (1) A minimum of 3 recordings per earthquake
- (2) A maximum distance of 100 km for  $M \leq 6$
- (3) A maximum distance of 200 km for  $M > 6$

For isolating the DCPP site terms from regional path effects, it is important to have the event terms centered on the distance to DCPP, but with enough recordings to reliably estimate the event term. For the 2004 Parkfield earthquake, (distance to DCPP of 85 km), the data were restricted to 50-150 km, and for the 2003 San Simeon earthquake (distance to DCPP of 35 km), the data were restricted to 0-100 km. Over these ranges, there is not a strong trend of the residuals with distance, indicating that the events terms are not biased by the path terms.

The locations of stations and earthquakes in the final data is shown on Figure 1, and a summary of the data set sampling is given in Table 2.

Table 2. Final Data set

Subset	Number of earthquakes	Number of recordings	Number of stations within 50 km of DCPP
Regional data set	645	1026	41
Recordings at DCPP	2	3	
2004 Parkfield data set	1	16	
2003 San Simeon data set	1	8	

The total residuals from this data set were provided by Al-Atik. They were computed relative to the Bayless and Abrahamson (2019) ergodic model for effective amplitude spectral (EAS) and was used as the reference model by Lavrentiadis *et al.* (2023a).

**Residuals**

The total residuals from the ergodic GMM were separated into between-event residual,  $\delta B$ , is and within-event residuals,  $\delta W$ :

$$\delta = \delta B + \delta W$$

The between-event residuals,  $\delta B$ , are shown as a function of magnitude on Figure 2 for a representative set of frequencies. At some frequencies, there is a trend in the residuals. This trend was removed by fitting a simple linear model for the adjustment to the magnitude scaling:

$$\Delta GMM(M) = c_1 + c_2 M$$

With this adjustment to center the magnitude scaling, the total (uncorrelated) non-ergodic site terms were included in the model:

$$\delta = \Delta GMM(M) + \delta S2S + \delta B + \delta WS$$

in which  $\delta S2S$  is the total non-ergodic site term, and  $\delta WS$  is the within-site residual. The  $\delta S2S$  were estimated using random effects and are plotted as a function of VS30 on Figure 3. There are no clear trends with VS30 indicating that the VS30 scaling in the ergodic GMM is consistent with the data set.

For estimating site terms, it is important to avoid mapping path terms into the site term. Following the approach used in the 2015 study, the within-event residuals for the DCPD site were computed relative to the reference GMM with the between-event residual computed from a limited range of distances for the San Simon earthquake (0-100 km) and for the Parkfield earthquake (50-150 km). The within-event residuals are shown on Figure 4. The residuals are centered for the distances to DCPD for these two events.

### New Methodology for Site Terms

The current methodology for non-ergodic site terms (Lavrentiadis *et al.*, 2023a, 2023b) includes both a regional site term that is spatially correlated,  $\delta S2S_{reg}$ , and a site-specific site term that is uncorrected spatially,  $\delta S2S_{unc}$ . The statistical model for the residual is given by:

$$\delta - \Delta GMM(M) = \delta S2S_{reg} + \delta S2S_{unc} + \delta B + \delta WS$$

The median regional site terms,  $\delta S2S_{reg}$ , and the epistemic uncertainty of the regional site terms are estimated using the varying coefficient model (VCM) approach with the hyperparameters fixed at the values from Lavrentiadis *et al.* (2023a).

The EAS site terms are converted to response spectral values (PSA) using the empirically calibrated RVT method by Phung and Abrahamson (2023). This median EAS is computed for a representative scenario, and the non-ergodic site term is added to the median. The RVT method is then used to convert both the ergodic median EAS and the non-ergodic median EAS. The ratio of the PSA values is computed and gives the non-ergodic site term in PSA. The reason for taking the ratio is that any bias in the RVT method would be in both the numerator and the denominator and tend to cancel out.

$$\delta S2S_{PSA-reg} = \ln \left( \frac{f_{RVT}(EAS_{med}(M, R) \exp(S2S_{reg}))}{f_{RVT}(EAS_{med}(M, R))} \right)$$

$$\delta S2S_{PSA-unc} = \ln \left( \frac{f_{RVT}(EAS_{med}(M, R) \exp(S2S_{unc}))}{f_{RVT}(EAS_{med}(M, R))} \right)$$

in which  $f_{RVT}$  is the RVT model used to convert EAS to PSA.

## Results

Maps of the median and epistemic uncertainty of the regional site terms ( $\delta S2S_{reg}$ ) for 0.1 Hz, 1 Hz, and 10 Hz are shown on Figure 5.

The median and epistemic uncertainty of the  $\delta S2S_{reg}$  and  $\delta S2S_{unc}$  at the DCPD site location are plotted as a function of frequency on Figure 6. The epistemic uncertainty is larger for the  $\delta S2S_{unc}$  term because there are only three recordings to constrain this term.

The non-ergodic site terms converted to SA using the RVT method are shown on Figures 6c and 6f. The  $\delta S2S_{reg}$  for SA (Figure 6c) is near zero for low frequencies (0.2 - 1Hz) and near -0.2 for high frequencies (> 2 Hz). This indicates that this region of coastal California has lower high-frequency ground motions than average sites in California. The  $\delta S2S_{unc}$  for PSA (Figure 6f) is more variable due to only three recordings. At low frequencies, the average  $\delta S2S_{unc}$  is about 0.1. At high frequencies (> 5 Hz), the average  $\delta S2S_{unc}$  is about -0.2.

At high frequencies, the contributions of the regional site term and the site-specific site term to the total non-ergodic site term at DCPD are about equal (both near -0.2). At low frequencies, the contribution to the total site-specific term is from the site-specific term,  $\delta S2S_{unc}$ .

The total median non-ergodic site terms from the 2015 study are compared to the results from this evaluation on Figure 7. The two results are similar for frequencies above 0.5 Hz. For the 2015 study, the site terms for frequencies less than 0.5 Hz were not modeled.

### Comparison of methods: EAS with RVT compared to direct use of SA

As a check of the approach that converts the EAS non-ergodic terms to PSA non-ergodic terms, the analysis described above was repeated using PSA data; however, the PSA values were not available for the full EAS data set. The number of recordings with EAS data and with PSA data are compared on Figure 8. There is a large reduction in the number of SA values as compared to the number of PSA values.

To check the RVT method, we used the smaller data set with SA values to repeat the analysis for both EAS with RVT and for the PSA directly. The resulting non-ergodic site terms are compared on Figure 9. The two methods lead to similar non-ergodic site terms, indicating that the EAS with RVT method is working well.



## Limitations

The data sets used in this analysis are preliminary and need further checks to improve the metadata (M, SOF,  $Z_{TOR}$ ,  $Z_{1.0}$ ), and to have the PSA values for the full data set. Automated data processing also should be checked.

The ergodic EAS GMM used for computing the residuals was adjusted for the magnitude scaling to be centered on the selected data set, but this is not a full update of the EAS GMM to be consistent with the expanded data set. A set of updated EAS GMMs are currently being developed as part of the NGA-W3 project. Once completed, this suite of GMMs will provide a more stable evaluation of the site terms for DCPD.

## Conclusions

This study applies the advances in modeling non-ergodic ground motions that have been developed after the completion of the 2015 study. These advanced non-ergodic GMMs are new, and this study is one of the first applications. These results should be considered as preliminary, but they provide valuable insights into the cause of the smaller high-frequency ground motions at DCPD: about half of the reduction is a regional effect and half of the reduction is a site-specific effect.

## References

- Bayless, J. and N. Abrahamson (2019). "Summary of the BA18 Ground-Motion Model for Fourier Amplitude Spectra for Crustal Earthquakes in California", *Bulletin of the Seismological Society of America*, October 2019, Volume. 109, pp. 2088–2105, doi: 10.1785/0120190077.
- Lavrentiadis, G., N. Abrahamson, and N. Kuehn (2023a). "A non-ergodic effective amplitude ground-motion model for California", *Bull Earthquake Eng*, Volume. 21, pp. 5233–5264.
- Lavrentiadis, G., N. Abrahamson, N. Kuehn, Y. Bozorgnia, C. Goulet, A. Babic, J. Macedo, M. Dolsek, N. Gregor, A. Kottke, M. Lacour, C. Liu, Z. Meng, V-B Phung, C-H Sung, and M. Walling (2023b). "Overview and introduction to development of non-ergodic earthquake ground-motion models", *Bull Earthquake Eng*, Volume. 21, pp. 5121–5150.
- Phung, V-B. and N. Abrahamson (2023). "Conditional Ground-Motion Model Based on RVT Spectral Moments for Converting Fourier Amplitude Spectra to Response Spectra", *Bull Earthquake Eng*, Volume. 21, pp. 5175–5207.

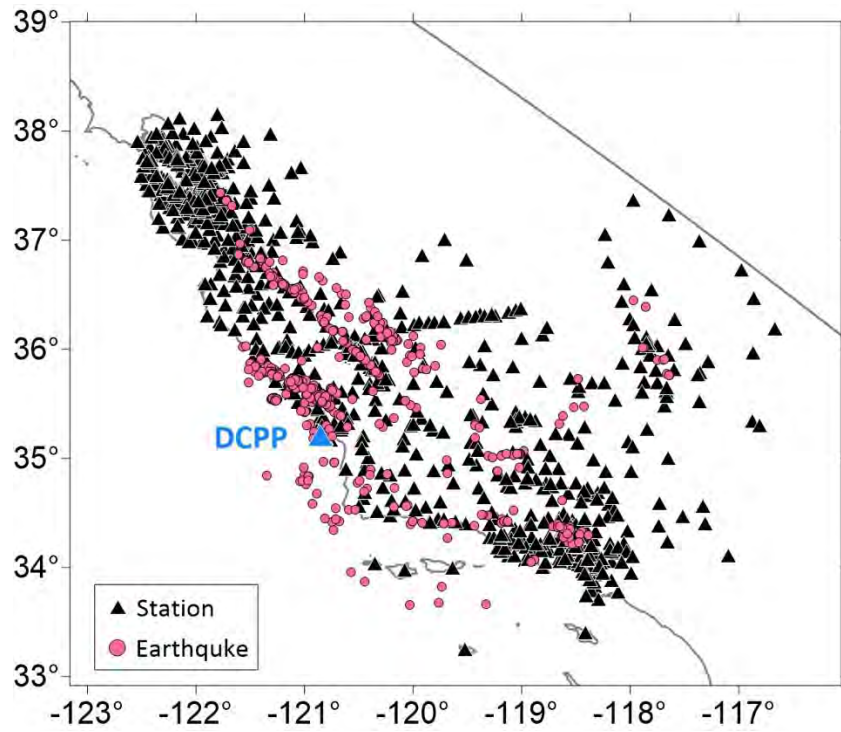


Figure 1. The distribution of the stations and earthquakes from the final dataset which was used in this study. There are 41 stations around the DCPP within 50 km.

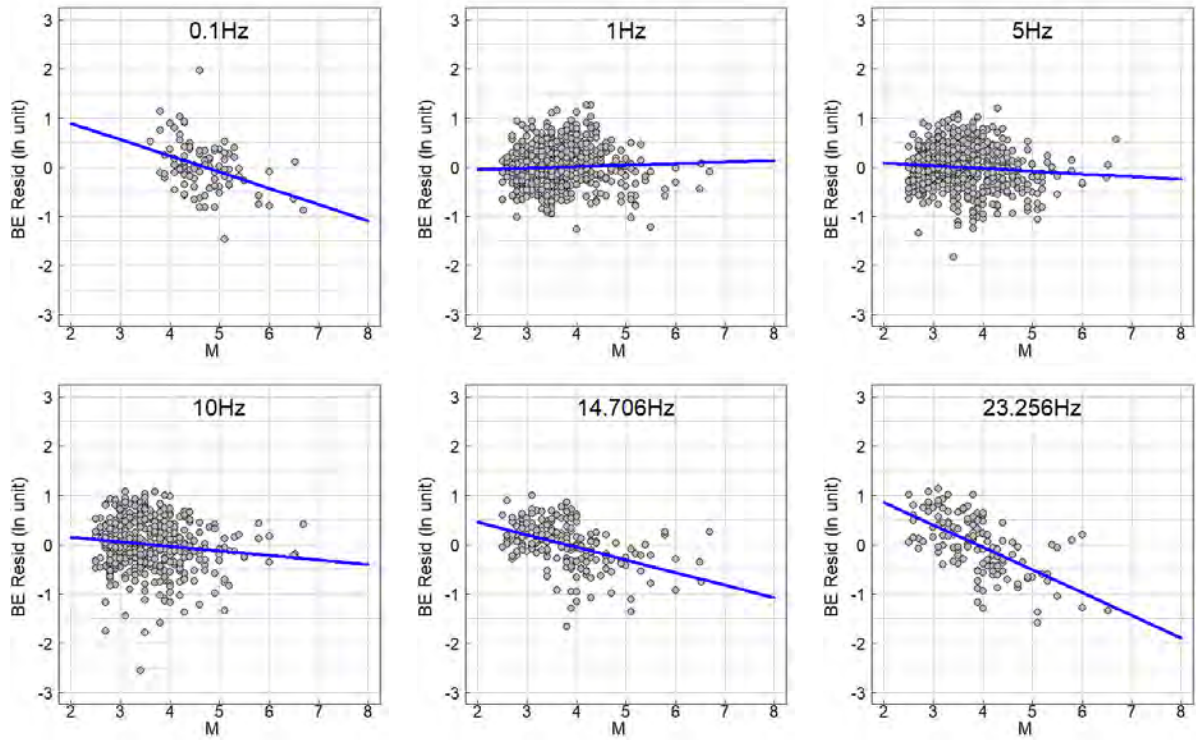


Figure 2. Between-event residuals versus Magnitude ( $M_L$  or  $M_w$ ). The  $\Delta GMM(M)$  fit is shown in by the blue lines. The between-event residuals are estimated from a data set without the recordings at DCP.

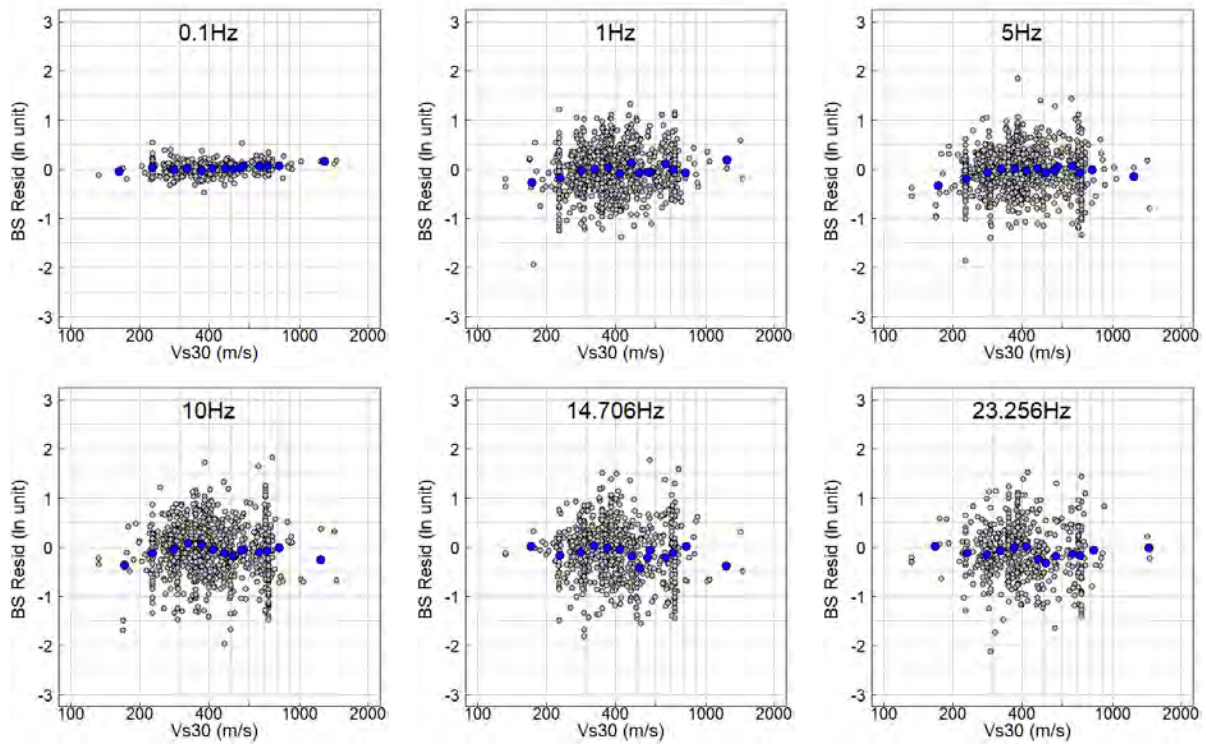


Figure 3. Between-site residuals versus Vs30. Blue points are the mean residual for each Vs30 bin.

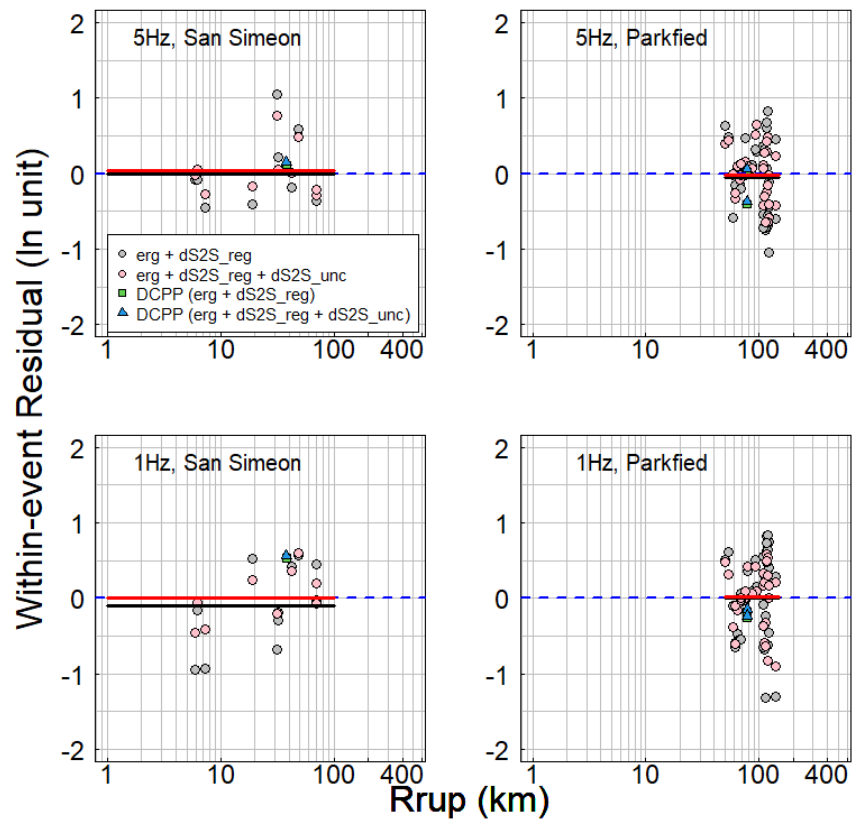


Figure 4. Residuals from the 2003 San Simeon and 2004 Parkfield earthquakes for 5 Hz and 1 Hz.

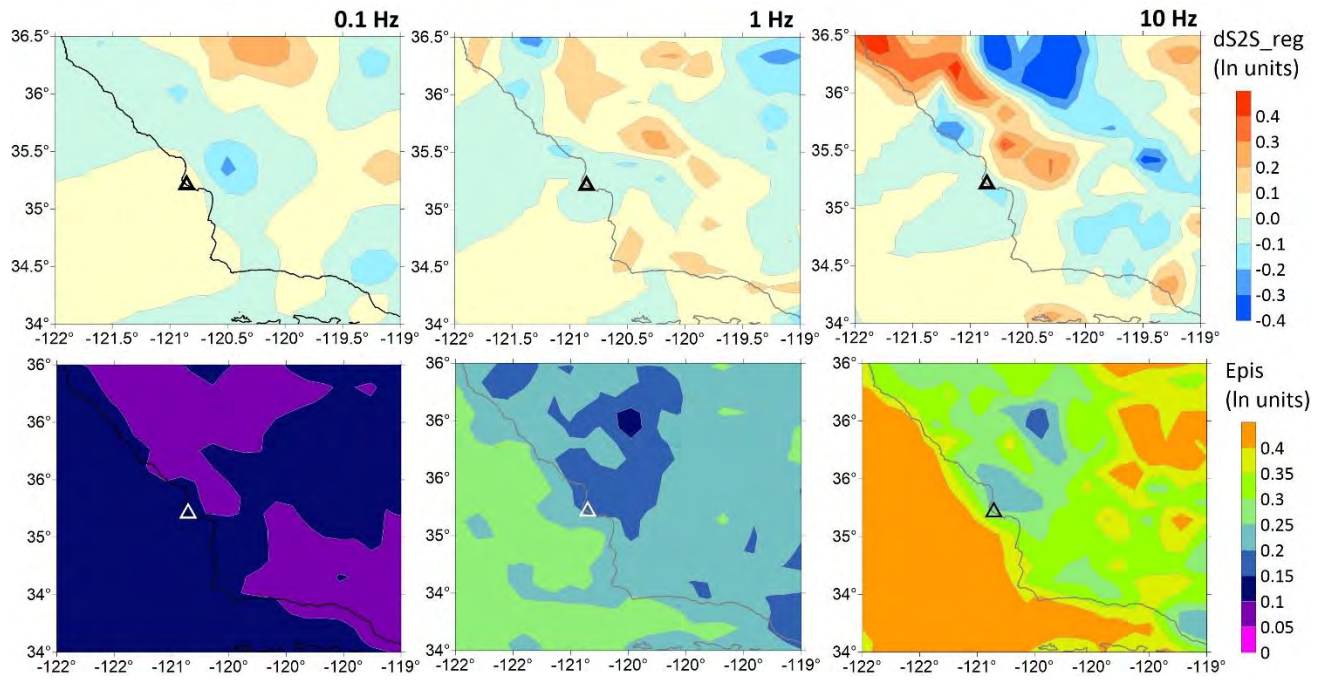


Figure 5. The upper frames show the regional site terms,  $\delta S2S_{reg}$ , for the EAS at 0.1 Hz, 1 Hz, and 10 Hz. The bottom frames show the epistemic uncertainty of  $\delta S2S_{reg}$  for 0.1 Hz, 1Hz, 10Hz.



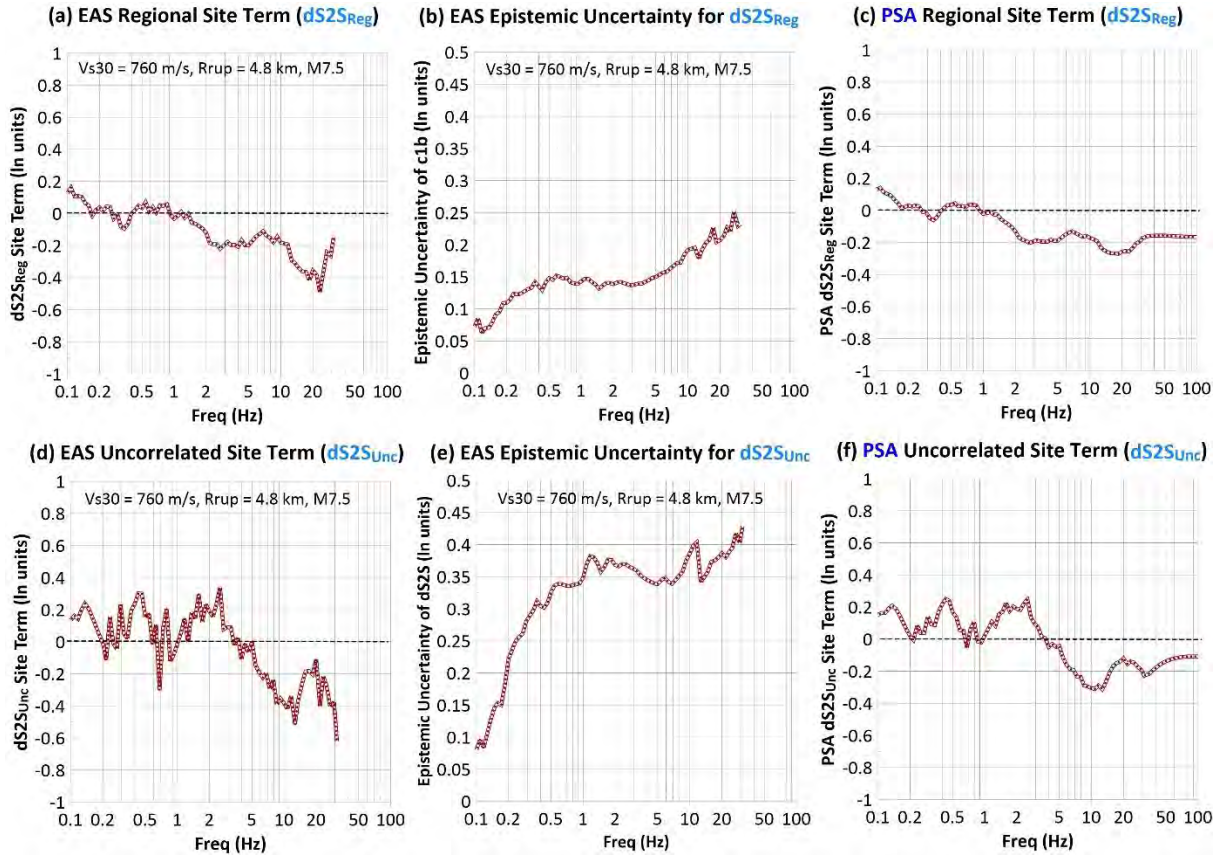


Figure 6. (a) Median  $\delta S2S_{reg}$  for EAS. (b) Epistemic uncertainty of  $\delta S2S_{reg}$  for EAS. (c) Median  $\delta S2S_{reg}$  for response spectra values using RVT. (d) Median  $\delta S2S_{unc}$  for EAS. (e) Epistemic uncertainty of  $\delta S2S_{unc}$  for EAS. (f) Median  $\delta S2S_{unc}$  for response spectra values using RVT.



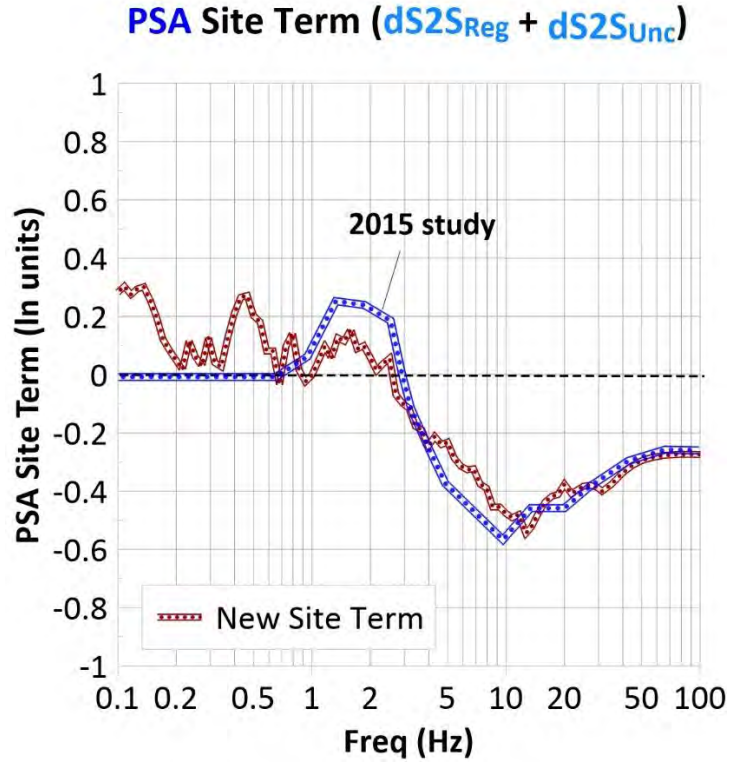


Figure 7. Comparison of the total non-ergodic site term for SA ( $\delta S2S_{reg} + \delta S2S_{unc}$ ) from the current evaluation with the results from the 2015 study.

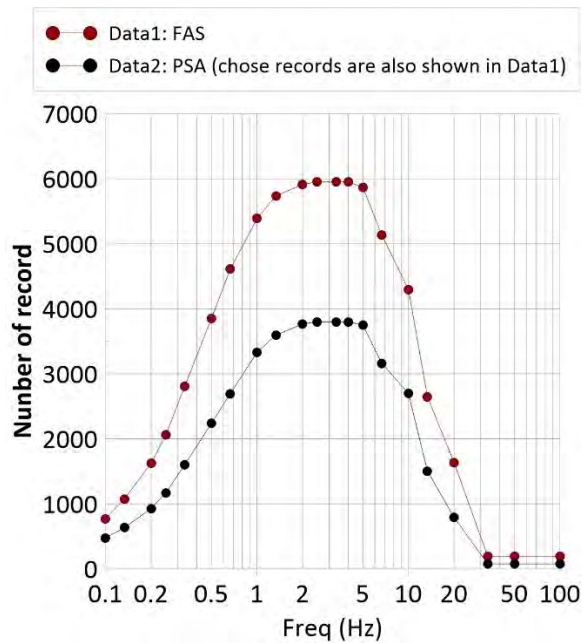


Figure 8. Comparison of the size of the data set with EAS data and with PSA data.

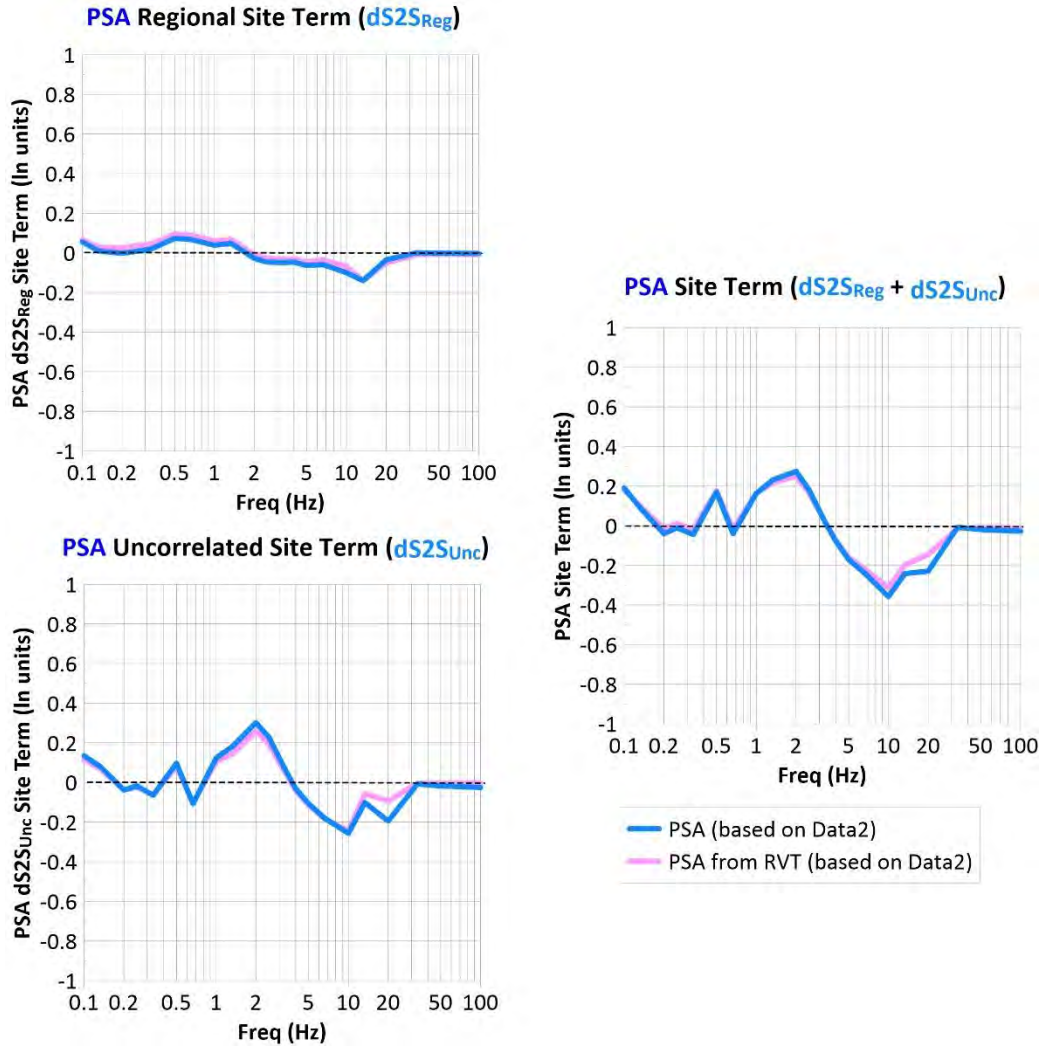


Figure 9. Comparison of site terms using the EAS with RVT approach with the direct PSA approach. This analysis uses the smaller data set with SA values for both the EAS and the PSA approaches.

# **Appendix G**

## **Closure Letters**

January 26, 2024

Drs. Albert Kottke and Chris Madugo  
Pacific Gas & Electric Company  
300 Lakeside Dr #130  
Oakland, CA 94612

**Subject: Diablo Canyon Nuclear Power Plant Seismic Hazard Re-Evaluation Project**

Dear Drs. Kottke and Madugo

In response to Senate Bill 846, an update of the 2015 PSHAs (DCPP SSC SSHAC 3 and SWUS SSHAC 3) was conducted for the Diablo Canyon Power Plant (DCPP). The Participatory Peer Review Panel (“PPRP”) is pleased to issue this PPRP Closure Letter containing our findings with respect to the Diablo Canyon Seismic Assessment Update. The PPRP was actively engaged in all phases and activities of the Projects implementation, including final development of the Project Plan and planning and execution of the evaluation and integration activities, which are at the core of the participatory assessment process.

Our role as the PPRP was to conduct a review of both the *process* followed and the *technical assessments* made by the Technical Integration (TI) Team. This letter documents the activities that the PPRP has carried out in its review of the process followed, and its findings regarding the technical adequacy of the PSHA update of the 2015 SSHAC Level 3 PSHA. Although this update is not formally a SSHAC study, main principles of a SSHAC level 1 process were followed. The project included bi-weekly on-line TI Team meetings, in person working meetings that included the sponsor, TI Teams, the PPRP and outside reviewers, an on-line final review of results, and a final report summarizing the updates to the 2015 SSHAC 3 PSHA.

**PPRP Activities for the DCPP PSHA Update Peer Review**

The purpose of a participatory peer review process, which is the continual review of a project from its start to finish, is to assure that both the process and technical assessments are conducted in such a fashion as to assure that the final product meets the highest standards and captures the center, body and range (CBR) of technically defensible interpretations (TDI). This requires adequate opportunities during the project duration for the PPRP to absorb the data used for the assessment, understand the analyses performed, and evaluate the TI Team’s assessment and integration of the data into the final model. The activities of the PPRP for the DCPP PSHA Update are summarized in the table below, which includes oral and written reviews and comments during various stages of the project.

During the *Evaluation* phase of the DCPP PSHA Update, the TI Team considered new data, models, and methods that have become available in the technical community since the previous DCPP PSHA projects (DCPP SSC SSHAC Level 3, PG&E 2015; SWUS GMC SSHAC Level 3, LCI, 2015) were completed in 2015. In particular, the TI Team incorporated new information on slip rate for the Hosgri and Los Osos faults, which resulted in an increase in hazard at DCPP. On the GMC side, the TI Team concluded that GMMs used in the 2015 study are consistent with new data, models, and

methods for ground motion developed after the 2015 study, so the 2015 GMMs remain applicable to DCP. The PPRP concludes that the TI Team’s evaluation process and documentation in the PSHA Update report are sufficient.

As the PPRP, we provided feedback to the TI teams during the various meetings. This included review of the TI Team’s analyses and evaluations of data, models, and methods at multiple times during the project, as summarized in the table below. The PPRP comments on the approaches used for the evaluation of the new information and the method used to adjust the 2015 seismic hazard results to reflect the new information were addressed in the final PSHA update report. The PPRP concludes that the technical aspects of the project have been adequately addressed.

Date	PPRP Activity
June 26, 2023	Workshop No. 0: On-line Kickoff Meeting; PPRP members attended on-line as observers
July 10, 2023	First of many bi-weekly on-line meetings. PPRP members attended as observers.
July 21, 2023	Working Meeting No. 1 in Oakland: Significant Issues and Data Needs; PPRP members attended in person as observers
September 19, 2023	Working Meeting No. 2 in Oakland: Alternative Interpretations; PPRP members attended in person or online as observers
November 7, 2023	Working Meeting No. 3 in Oakland: Update on Findings and Hazard Feedback
December 7, 2023	Online Working Meeting: Final Review of Results
January 10, 2024	Submittal of Written Comments on the Draft PSHA Update Report
January 26, 2024	Submittal of DCP PSHA Update PPRP Closure Letter

## Conclusions

The PPRP agrees with the conclusion that the new information for the SSC and GMC that has been developed since the 2015 seismic hazard study does not significantly change the estimate of the seismic risk for DCP.

Some of the new data and methods are not advanced enough to be applied at this time. As these data and methods become more mature, their potential impact on the seismic risk estimates at DCP should be evaluated as part of PG&E's Long-Term Seismic Program.

Based on its review of the DCPD PSHA Update, the PPRP concludes that the process and technical aspects of the assessment adequately address Senate Bill 846.

We appreciate the opportunity to provide our review of the project.

Sincerely,

DCPD PSHA Update PPRP Members

Dr. Norman Abrahamson



Dr. Thomas Rockwell



January 27, 2024

Dr. Albert Kottke and Dr. Chris Madugo, PG&E Project Sponsors  
Dr. Jennifer Donahue, Project Manager  
Diablo Canyon Updated Seismic Assessment

**SUBJECT: DCPD SSHAC Level 1 External Peer Review Panel (EPRP) Final Closure Letter**

Dear Dr. Kottke, Dr. Madugo and Dr. Donahue:

In 2022 the State of California passed a Senate Bill, SB-846, to extend operation of the Pacific Gas & Electric Company (PG&E) Diablo Canyon power plant (DCPP). In response to SB-846, PG&E carried out a study, “*Diablo Canyon Updated Seismic Assessment*” (DCUSA). The goal of the DCUSA study was to review and evaluate new seismic hazard methods, data and models that have been developed since 2015 and assess their impacts on the seismic hazard of the DCPP. The last extensive Probabilistic Seismic Hazard Analysis (PSHA) for the DCPP was completed in 2015 under the Senior Seismic Hazard Analysis Committee (SSHAC) Level 3 process. The DCUSA study was organized following a SSHAC Level 1 study (NUREG-2213), which included a Technical Integration (TI) team and a Participatory Peer Review Panel (PPRP).

For the DCUSA study, an external peer review panel (EPRP) was also formed to provide an external review that focused on the evaluation and procedural processes of the study. The EPRP consisted of three members, the undersigned, from the University of California (UC) Los Angeles Garrick Risk Institute and UC Santa Barbara.

The EPRP members reviewed the DCUSA workplan and participated in multiple conference calls and in-person meetings covering different technical aspects of the PSHA including seismic source characterization (SSC) and ground motion characterization (GMC). The EPRP has also reviewed the draft final report issued on December 18, 2023, and its revised version dated January 23, 2024. The DCUSA study, as documented in its final report, showed minor changes in SSC and no changes warranted for the median and aleatory variability models of GMC. The EPRP provided multiple comments on the evaluation process and technical issues covered in the DCUSA draft report. These comments have all been considered by the TI team of the DCUSA and the report has been updated accordingly. The EPRP agrees with the findings of the study as documented in the final report.

Based on the review of the process conducted in the DCUSA study, and documented in its final report, the EPRP concludes that the process and technical aspects of the DCUSA study meet the guidance and current expectations for a SSHAC Level 1 study.

Sincerely,



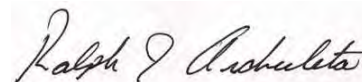
**Ali Mosleh, PhD, NAE**  
Distinguished Professor of  
Engineering, and Director of  
Garrick Institute for Risk  
Sciences

University of California,  
Los Angeles



**Yousef Bozorgnia, PhD, PE**  
Professor of Civil and  
Environmental Engineering, and  
Director of Natural Hazards Risk  
and Resiliency Research Center

University of California,  
Los Angeles



**Ralph Archuleta, PhD**  
Distinguished Professor Emeritus,  
Department of Earth Science  
University of California,  
Santa Barbara